

Carbon Materials: Chemistry and Physics 8  
Series Editors: Franco Cataldo · Paolo Milani

Mihai V. Putz  
Ottorino Ori *Editors*

# Exotic Properties of Carbon Nanomatter

Advances in Physics and Chemistry

 Springer

# **Carbon Materials: Chemistry and Physics**

Volume 8

## **Series Editors**

Franco Cataldo

Soc. Lupi Chemical Research Institute Dipto. Ricerca e Sviluppo

Roma

Italy

Paolo Milani

Università Milano-Bicocca Dipto. Fisica

Milano

Italy

*Carbon Materials: Chemistry and Physics* aims to be a comprehensive book series with complete coverage of carbon materials and carbon-rich molecules. From elemental carbon dust in the interstellar medium, to the most specialized industrial applications of the elemental carbon and derivatives. With great emphasis on the most advanced and promising applications ranging from electronics to medicinal chemistry.

The aim is to offer the reader a book series which not only should be made of self-sufficient reference works, but should stimulate further research and enthusiasm.

More information about this series at <http://www.springer.com/series/7825>

Mihai V. Putz • Ottorino Ori  
Editors

# Exotic Properties of Carbon Nanomatter

Advances in Physics and Chemistry

 Springer



*Editors*

Mihai V. Putz  
West University of Timișoara  
Timișoara  
Romania

Ottorino Ori  
Actinium Chemical Research  
Rome  
Italy

ISSN 1875-0745

ISSN 1875-0737 (electronic)

ISBN 978-94-017-9566-1

ISBN 978-94-017-9567-8 (eBook)

DOI 10.1007/978-94-017-9567-8

Springer Dordrecht Heidelberg New York London

Library of Congress Control Number: 2014953928

© Springer Science+Business Media Dordrecht 2015

This work is subject to copyright. All rights are reserved by the Publisher, whether the whole or part of the material is concerned, specifically the rights of translation, reprinting, reuse of illustrations, recitation, broadcasting, reproduction on microfilms or in any other physical way, and transmission or information storage and retrieval, electronic adaptation, computer software, or by similar or dissimilar methodology now known or hereafter developed. Exempted from this legal reservation are brief excerpts in connection with reviews or scholarly analysis or material supplied specifically for the purpose of being entered and executed on a computer system, for exclusive use by the purchaser of the work. Duplication of this publication or parts thereof is permitted only under the provisions of the Copyright Law of the Publisher's location, in its current version, and permission for use must always be obtained from Springer. Permissions for use may be obtained through RightsLink at the Copyright Clearance Center. Violations are liable to prosecution under the respective Copyright Law.

The use of general descriptive names, registered names, trademarks, service marks, etc. in this publication does not imply, even in the absence of a specific statement, that such names are exempt from the relevant protective laws and regulations and therefore free for general use.

While the advice and information in this book are believed to be true and accurate at the date of publication, neither the authors nor the editors nor the publisher can accept any legal responsibility for any errors or omissions that may be made. The publisher makes no warranty, express or implied, with respect to the material contained herein.

Printed on acid-free paper

Springer is part of Springer Science+Business Media ([www.springer.com](http://www.springer.com))

# Preface

Forefront advancements in modeling and characterization of fundamental and newly designed Carbon based nanocomposites (graphenes, fullerenes, polymers, crystals and allotropic forms, aromatic systems, carbohydrates, PAHs, etc.) are nowadays envisaged in various research fields targeting the nano-formation, quantification, indexing and interpretation of physical and chemical exotic properties related with space-time structure-evolution, phase transitions, chemical reactivity, topology, structure-property relationships etc., and related structural and optical/spectroscopic features and interactions.

These challenges are addressed by the present edited book in an integrated manner, approaching Carbon nanomatter and its exotic features along three main directions:

- Carbon elemental forms, from simple compounds to fullerenes, graphenes and nanotubes
- Topological, geometrical and molecular analysis of Carbon nanomatter
- Bondonic chemistry

The first direction unfolds the so called generalist approach to Carbon extended structures: it offers the introduction to Carbon allotropes (diamond, graphite, fullerene, and hydrocarbon fragments as diamondoids and benzenoids) in Chap. 1; the graphenic patterning for  $C_n$  fullerenes generation from  $n = 60$  to  $n = 100$  in Chap. 2; the physical characterization of graphenes by interpreting the spectra associated to collective excitations, phonons and plasmons, in Chap. 3; detailed investigations on exohedral reactivity of endohedral metallofullerenes with the aid of Diels-Alder reactivity in Chap. 4; the epitaxial growth of silicon carbide nanowires (SiC-NWs) with related phenomenology and experimental fingerprints (X-ray photoelectron spectroscopy, electronic microscopy) in Chap. 5; the ending section of the volume, Chap. 14, about van der Waals interactions in layered 2D structures of graphene (vs. those made of  $MoS_2$ ) which are modifiable and tunable by external electric fields, completes this book by an outstanding communication on both theoretical and experimental perspectives of Carbon nanosystems.

The second direction focuses on the mathematical and computational characteristics of various Carbon nano-structures: reviewing the topological and group properties of Carbon armchair/zig-zag polyhex towards combined  $C_4C_8$  nanotubes

and nanotori, in Chap. 6; the bridge graphs modeled by Zagreb indices accounting for chemical bonding in comb nanolattices, polymers, nanostars and dendrimers, spirochains and caterpillar trees or cycles are mathematically exposed (for future QSAR applications) in Chap. 7; recently invented  $D_5$  allotropic diamantine structures are analyzed by topological and energetical advanced methods predicting exotic possible intermediates in the synthesis of some hyper-graphenes, in Chap. 8; protein-protein/ligand interaction is modeled by surface pocket analysis driven by fractal dimension while computations exploit all available data bases to unveil chemical key properties of protein surfaces towards biological functionalization and activity; all these topics are discussed in Chap. 9, closing this second direction centered on the conceptual-computational aspects of *micro-to-macro* Carbon structures;

The third direction of the book, intended as a “small treatise of chemical bonding by bondons”, goes through the advanced bosonic-bondons picture, being the bondon the new quantum quasi-particles associated to the chemical bonding field, by various approaches and prospects: Chap. 10 introduces the bondon within the quantum relativistic Dirac framework that, combined to the sub-quantum Bohmian treatment of the quantum potential, predicts the bondonic mass, reformulating the bonding-antibonding chemical space of bonding as *the bondon-antibondon universe*, with deeper insights in entangled chemistry, and bondonic identification by teleportation of the chemical bonding on the graphenic lattices; Chap. 11 reloads the bondonic mass prediction within quantum non-relativistic Schrödinger “classical” approach, deriving further extensions and space-time-gravity bosonic-fermionic information to characterize the chemical bond as *the bosonization of the condensation of pairing fermions*, paralleling the structure-reactivity analysis of benchmarking Carbon systems to confirm the validity of the bondonic paradigm in chemical bonding. Chap. 12 complements previous chapter information – bondonic velocity, charge, life-time and bondonic mass general behaviors compared with electron characteristics – and introduces the specific chemical bonding with illustrative applications to a series of silanes for which chemical metallic behavior is prognosticated, confirming the “unit cell” approach for complex silicene simulation; on the way of discovering the *bondonic existence*, Chap. 14 deals with Raman-IR spectroscopic methodology applied on a relevant series of ionic liquids (IL), with inherent dipole moment and fluctuating anionic-cationic polarization affecting ground and excited IL states, showing intimate correlations between the chemical bonding by bondons and the recorded biological activity, posing new exiting issues for studies in the near future.

Edited volumes are somehow more demanding than authorship monographs. This because editors face several possible directions of the book which evolve as the single contributions come, prompting editors to rearrange the frame of the book in order to preserve volume uniform flow and identity. If we succeed in completing the present venture is just because we benefited by exquisite contributions of eminent Scientists from Europe, America, and Asia that gave their best to help the understanding of the Carbon phenomenology and Carbon nanomatter either existing or designed. We do thank them all for the consistent support they encompassed in contributing first-class scientific chapters providing the audience with broad perspectives on chemical exotic structures and frontier modeling in general and of those involving Carbon in particular!

Special thanks are due to Professor Dr. Franco Cataldo, the main coordinator of the Springer Carbon Materials Series, for enthusiastically supporting the present editorial project, as well to the Springer Chemistry Team, chiefly to its Senior Editor for Chemistry Books Dr. Sonia Ojo and the Springer Production Editor for Books Karin de Bie for their patience and constructive assistance in all stages towards the publication of the present . . . exotic yet highly vanguardist volume!

Mihai V. Putz  
Ottorino Ori

# Contents

<b>1</b>	<b>Ode to the Chemical Element Carbon</b> .....	<b>1</b>
	Alexandru T. Balaban	
<b>2</b>	<b>Origami: Self Organizing Polyhexagonal Carbon Structures for Formation of Fullerenes, Nanotubes and Other Carbon Structures</b> .....	<b>19</b>
	István László and Ibolya Zsoldos	
<b>3</b>	<b>Collective Excitations in Monolayer Graphene on Metals: Phonons and Plasmons</b> .....	<b>33</b>
	Antonio Politano and Gennaro Chiarello	
<b>4</b>	<b>Understanding the Exohedral Functionalization of Endohedral Metallofullerenes</b> .....	<b>67</b>
	Marc Garcia-Borràs, Sílvia Osuna, Josep M. Luis, Marcel Swart and Miquel Solà	
<b>5</b>	<b>Cubic Silicon Carbide Nanowires</b> .....	<b>101</b>
	Marco Negri, Francesca Rossi, Giovanni Attolini, Filippo Fabbri, Sathish Chander Dhanabalan, Francesco Boschi, Matteo Bosi, Marco Vittorio Nardi and Giancarlo Salviati	
<b>6</b>	<b>Geometry and Topology of Nanotubes and Nanotori</b> .....	<b>131</b>
	Fatemeh Koorepazan-Moftakhar, Ali Reza Ashrafi, Ottorino Ori and Mihai V. Putz	
<b>7</b>	<b>The First and Second Zagreb Indices of Several Interesting Classes of Chemical Graphs and Nanostructures</b> .....	<b>153</b>
	Ali Iranmanesh and Mahdieh Azari	
<b>8</b>	<b>Exotic Allotropes of Carbon</b> .....	<b>185</b>
	Mircea V. Diudea, Beata Szeffler, Csaba L. Nagy and Attila Bende	

<b>9</b>	<b>Web-based Computational Tools Used in Protein Surface Analysis and Characterization. Applications for Protein–Protein and Protein–Ligand Interactions</b> . . . . .	203
	Adriana Isvoran	
<b>10</b>	<b>Bondonic Chemistry: Physical Origins and Entanglement Prospects</b> . . . . .	229
	Mihai V. Putz and Ottorino Ori	
<b>11</b>	<b>Bondonic Chemistry: Non-classical Implications on Classical Carbon Systems</b> . . . . .	261
	Mihai V. Putz, Laura Pitulice, Daniela Dascălu and Delia Isac	
<b>12</b>	<b>Bondonic Chemistry: Consecrating Silanes as Metallic Precursors for Silicenes Materials</b> . . . . .	323
	Mihai V. Putz, Corina Duda-Seiman, Daniel M. Duda-Seiman and Constantin Bolcu	
<b>13</b>	<b>Bondonic Chemistry: Predicting Ionic Liquids’ (IL) Bondons by Raman-IR Spectra</b> . . . . .	347
	Mihai V. Putz, Nicoleta A. Dudaş and Ana-Maria Putz	
<b>14</b>	<b>Electric Field Effects on Graphene Materials</b> . . . . .	383
	Elton J. G. Santos	
	<b>Index</b> . . . . .	393

# Contributors

**Ali Reza Ashrafi** Department of Nanocomputing, Institute of Nanoscience and Nanotechnology, University of Kashan, Kashan, I. R. Iran

**Giovanni Attolini** Istituto dei Materiali per l'Elettronica ed il Magnetismo, Consiglio Nazionale delle Ricerche, Parma, Italy

**Mahdieh Azari** Department of Mathematics, Kazerun Branch, Islamic Azad University, Kazerun, Iran

**Alexandru T. Balaban** Texas A&M University at Galveston, TX, USA

**Attila Bende** Molecular and Biomolecular Physics Department, National Institute for R&D of Isotopic and Molecular Technologies, Cluj-Napoca, Romania

**Constantin Bolcu** Laboratory of Organic Chemistry, Department of Biology-Chemistry, Faculty of Chemistry, Biology, Geography, West University of Timișoara, Timișoara, Romania

**Francesco Boschi** Istituto dei Materiali per l'Elettronica ed il Magnetismo, Consiglio Nazionale delle Ricerche, Parma, Italy

Facoltà di fisica, Università degli studi di Parma, Parma, Italy

**Matteo Bosi** Istituto dei Materiali per l'Elettronica ed il Magnetismo, Consiglio Nazionale delle Ricerche, Parma, Italy

**Gennaro Chiarello** Dipartimento di Fisica, Università degli Studi della Calabria, Rende (Cs), Italy

**Daniela Dascălu** Department of Biology-Chemistry, Faculty of Chemistry, Biology, Geography, West University of Timișoara, Timișoara, Romania

**Sathish Chander Dhanabalan** Istituto dei Materiali per l'Elettronica ed il Magnetismo, Consiglio Nazionale delle Ricerche, Parma, Italy

Facoltà di fisica, Università degli studi di Parma, Parma, Italy

**Mircea V. Diudea** Faculty of Chemistry and Chemical Engineering, Babes-Bolyai University, Cluj-Napoca, Romania

**Corina Duda-Seiman** Laboratory of Computational and Structural Physical-Chemistry for Nanosciences and QSAR, Department of Biology-Chemistry, Faculty of Chemistry, Biology, Geography, West University of Timișoara, Timișoara, Romania

Laboratory of Organic Chemistry, Department of Biology-Chemistry, Faculty of Chemistry, Biology, Geography, West University of Timișoara, Timișoara, Romania

**Daniel M. Duda-Seiman** Department of Medical Ambulatory, Medical Emergencies, University of Medicine and Pharmacy “Victor Babes”, Timișoara, Timișoara, Romania

**Nicoleta A. Dudaș** Laboratory of Computational and Structural Physical-Chemistry for Nanosciences and QSAR, Department of Biology-Chemistry, Faculty of Chemistry, Biology, Geography, West University of Timișoara, Timișoara, Romania

**Filippo Fabbri** Istituto dei Materiali per l’Elettronica ed il Magnetismo, Consiglio Nazionale delle Ricerche, Parma, Italy

**Marc Garcia-Borràs** Institut de Química Computacional i Catàlisi (IQCC) and Departament de Química, Universitat de Girona, Campus de Montilivi, Girona, Catalonia, Spain

**Ali Iranmanesh** Department of Mathematics, Tarbiat Modares University, Tehran, Iran

**Delia Isac** Department of Biology-Chemistry, Faculty of Chemistry, Biology, Geography, West University of Timișoara, Timișoara, Romania

**Adriana Isvoran** Department of Biology-Chemistry, West University of Timișoara, Timișoara, Romania

**Fatemeh Koorepazan-Moftakhar** Department of Nanocomputing, Institute of Nanoscience and Nanotechnology, University of Kashan, Kashan, I. R. Iran

**István László** Department of Theoretical Physics, Institute of Physics, Budapest University of Technology and Economics, Budapest, Hungary

**Josep M. Luis** Institut de Química Computacional i Catàlisi (IQCC) and Departament de Química, Universitat de Girona, Campus de Montilivi, Girona, Catalonia, Spain

**Csaba L. Nagy** Faculty of Chemistry and Chemical Engineering, Babes-Bolyai University, Cluj-Napoca, Romania

**Marco Vittorio Nardi** Institut für Physik, Humboldt-Universität zu Berlin, Berlin, Germany



**Marco Negri** Istituto dei Materiali per l'Elettronica ed il Magnetismo, Consiglio Nazionale delle Ricerche, Parma, Italy

Facoltà di fisica, Università degli studi di Parma, Parma, Italy

**Sílvia Osuna** Institut de Química Computacional i Catàlisi (IQCC) and Departament de Química, Universitat de Girona, Campus de Montilivi, Girona, Catalonia, Spain

**Ottorino Ori** Actinium Chemical Research, Rome, Italy

Laboratory of Computational and Structural Physical-Chemistry for Nanosciences and QSAR, Department of Biology-Chemistry, Faculty of Chemistry, Biology, Geography, West University of Timișoara, Timișoara, Romania

**Laura Pitulice** Department of Biology-Chemistry, Faculty of Chemistry, Biology, Geography, West University of Timișoara, Timișoara, Romania

**Antonio Politano** Dipartimento di Fisica, Università degli Studi della Calabria, Rende (Cs), Italy

**Mihai V. Putz** Laboratory of Computational and Structural Physical-Chemistry for Nanosciences and QSAR, Department of Biology-Chemistry, Faculty of Chemistry, Biology, Geography, West University of Timișoara, Timișoara, Romania

**Ana-Maria Putz** Laboratory of Computational and Structural Physical-Chemistry for Nanosciences and QSAR, Department of Biology-Chemistry, Faculty of Chemistry, Biology, Geography, West University of Timișoara, Timișoara, Romania

Institute of Chemistry Timișoara of the Romanian Academy, Timișoara, Romania

**Francesca Rossi** Istituto dei Materiali per l'Elettronica ed il Magnetismo, Consiglio Nazionale delle Ricerche, Parma, Italy

**Giancarlo Salviati** Istituto dei Materiali per l'Elettronica ed il Magnetismo, Consiglio Nazionale delle Ricerche, Parma, Italy

**Elton J. G. Santos** School of Engineering and Applied Sciences, Harvard University, Cambridge, USA

Department of Chemical Engineering, Stanford University, Stanford, USA

**Miquel Solà** Institut de Química Computacional i Catàlisi (IQCC) and Departament de Química, Universitat de Girona, Campus de Montilivi, Girona, Catalonia, Spain

**Marcel Swart** Institut de Química Computacional i Catàlisi (IQCC) and Departament de Química, Universitat de Girona, Campus de Montilivi, Girona, Catalonia, Spain

Institució Catalana de Recerca I Estudis Avançats (ICREA), Barcelona, Catalonia, Spain

**Beata Szefer** Department of Physical Chemistry, Collegium Medicum, Nicolaus Copernicus University, Bydgoszcz, Poland

**Ibolya Zsoldos** Faculty of Technology Sciences, Széchenyi István University  
Egyetem tér 1, Győr, Hungary

# Chapter 1

## Ode to the Chemical Element Carbon

Alexandru T. Balaban

**Abstract** If an element deserves praise, then this element is carbon. Its nucleus, along with N and O, catalyzes the fusion of H into He in the sun and sun-like stars. Its minor stable isotope allows chemical structure to be elucidated by  $^{13}\text{C}$ -NMR, along with  $^1\text{H}$ -NMR. Its long-lived radioisotope  $^{14}\text{C}$  allows radiocarbon dating, and reaction mechanisms or bioactivities of medicines to be understood by isotopic labeling. Its short-lived radioisotope  $^{11}\text{C}$  is used for PET scans. The 16th part of its atomic weight serves as *unified atomic mass unit*, also called “dalton”. Its allotropes (diamond, graphite, fullerenes) have extremely useful properties. And this above all: it is the element that life is based upon, the central element of organic chemistry, and the element that is present in most of the  $7 \times 10^7$  substances registered till now. Due to this fact and to the multiple uses of carbon compounds, although it is now known that they do not differ from inorganic compounds, Organic Chemistry is still a distinct part of chemistry. Because carbon atoms form molecules with covalent bonds that can be represented by hydrogen-depleted molecular graphs, this makes molecular structure search the best scientific documentation among all sciences. Substantial consideration is dedicated to carbon allotropes and to derived hydrocarbon fragments such as diamondoids and benzenoids, emphasizing the author’s theoretical contributions to these research fields.

### 1.1 Isotopic Carbon Nuclei

Six protons need six or seven neutrons in order for the nuclear strong force to hold together all these nucleons for a longer time than about  $10^{15}$  years (resulting in what are called ‘stable nuclides’). “Stable” is a relative notion, connected with our ability of detecting radioactive decays; probably in the future when this ability will increase, deuterium and other nuclides may be found to be very weakly radioactive, having very long half-lives, longer than those of the naturally-occurring primordial nuclides  $^{232}\text{Th}$ ,  $^{233}\text{U}$ ,  $^{235}\text{U}$ ,  $^{238}\text{U}$ . With only five neutrons, the  $^{11}\text{C}$  nucleus is a positron-emitter with a half-life of 20.4 min; with eight neutrons, the  $^{14}\text{C}$  nucleus is an

---

A. T. Balaban (✉)

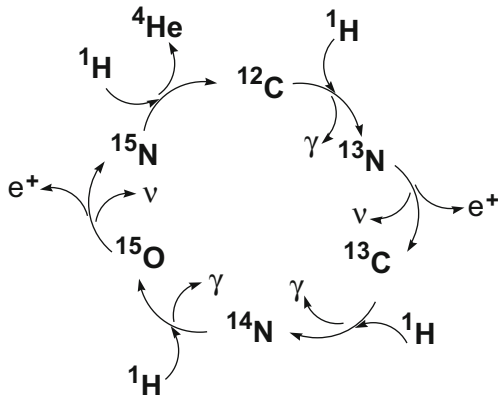
Texas A&M University at Galveston, 200 Seawolf Parkway, 77553 Galveston, TX, USA  
e-mail: balabana@tamug.edu

© Springer Science+Business Media Dordrecht 2015

M. V. Putz, O. Ori (eds.), *Exotic Properties of Carbon Nanomatter*,

Carbon Materials: Chemistry and Physics, DOI 10.1007/978-94-017-9567-8\_1

**Fig. 1.1** The fusion of four protons ( $^1\text{H}$ ) affording a  $^4\text{He}$  nucleus ( $\alpha$ -particle)



electron-emitter with a half-life of 5730 years. We will examine briefly each of these four carbon nuclides.

First, starting with the stable  $^{12}\text{C}$ , which accounts for 89.9% of all carbon atoms, it is formed in the interior of stars by the triple-alpha process. It is no longer a mystery how three  $\alpha$ -particles interact in the nucleus despite the electrostatic repulsion (two  $\alpha$ -particles cannot form a stable  $^8\text{Be}$  nuclide): it was recently calculated that in the ground state of the  $^{12}\text{C}$  nucleus, three  $\alpha$ -particles form a triangle cluster, whereas with low-energy excitation they form a kinked obtuse-angle cluster (so-called Hoyle state) shaped like a bent arm (Epelbaum et al. 2011; Lee et al. 2012). Pairing of nuclear spins for protons and neutrons in even-even nuclei such as  $^2\text{He}$ ,  $^{12}\text{C}$ ,  $^{16}\text{O}$  results in such nuclei to be devoid of magnetic moments.

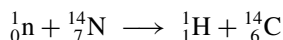
In the sun and other sun-like stars, fusion of hydrogen nuclei to helium involves a process discovered by Hans Bethe, who was honored for it in 1967 with the Nobel Prize for Physics. A catalytic cycle involving  $^{12}\text{C}$ ,  $^{13}\text{C}$ ,  $^{13}\text{N}$ ,  $^{14}\text{N}$ ,  $^{15}\text{N}$ , and  $^{15}\text{O}$  nuclei allows this fundamental process to occur; 2 positrons, 2 neutrinos, and 3 gamma photons carrying away the fusion energy are also released (Fig. 1.1). In the Bethe cycle there are four stable nuclides ( $^{12}\text{C}$ ,  $^{13}\text{C}$ ,  $^{14}\text{N}$ ,  $^{15}\text{N}$ ) and two positron + neutrino-emitters:  $^{13}\text{N}$  ( $T_{1/2} = 10$  min) and  $^{15}\text{O}$  ( $T_{1/2} = 2$  min). Positrons undergo rapid annihilation on encountering electrons, further increasing the emitted fusion energy during the life-time of the star.

An important characteristic of the  $^{12}\text{C}$  and  $^{13}\text{C}$  nuclei is their small cross-section for neutron capture. Thus, despite their higher mass than that of deuterons or protons, which could thermalize better the fast neutrons released during the fission of  $^{235}\text{U}$ , the first nuclear reactor was built by E. Fermi and coworkers in Chicago by using pure graphite as moderator. This use of graphite has several drawbacks: (i) small amounts of impurities reduce substantially its efficiency, and this is why Hitler's Germany opted for using heavy water as moderator in the 1940s; (ii) nuclear radiations cause lattice defects ("E. P. Wigner defects") which may release large amounts of energy, as it happened in 1957 in the Windscale reactor fire in UK; (iii) at higher temperature

it can burn, as it happened in the Chernobyl disaster, Ukrainian Soviet Republic in 1986.

*Second*, the  $^{13}\text{C}$  nucleus accompanying  $^{12}\text{C}$  as a minor constituent (about 1 % of all carbon atoms) has a magnetic moment, and as such allows nuclear magnetic resonance of carbon atoms in organic compounds.

*Third*, for archaeology the existence of the long-lived beta-emitter  $^{14}\text{C}$  has been a blessing, allowing radiocarbon dating of any old organic finds between a few 100 years and about 60,000 years. Willard Libby was awarded the 1960 Nobel Prize in chemistry for this work. All living organisms assimilate during their lifetime a small amount of radiocarbon because high-energy neutrons from cosmic rays convert continuously a small amount of  $^{14}\text{N}$  nuclei into  $^{14}\text{C}$  nuclei via the following nuclear reaction, in which a proton is released:



The resulting carbon atoms are immediately oxidized to  $\text{CO}_2$  that mixes in the earth's atmosphere; then photo-assimilation and metabolic reactions cause an equilibrium concentration of radiocarbon in all organic constituents. As long as the plants or animals are alive, the amount of radiocarbon remains constant, but after their death the radioactivity decays exponentially according to the well-known first-order kinetics. Tree rings allow the calibration of radioactive dating, and one can see the spike due to atmospheric nuclear bomb tests in the 1960s. Libby demonstrated the accuracy of radiocarbon dating by estimating the age of wood for which the age was known, including an ancient Egyptian barge of 1850 before the Christian era.

*Fourth*, compounds labeled with positron-emitting nuclei such as  $^{11}\text{C}$ ,  $^{13}\text{N}$ ,  $^{15}\text{O}$  and  $^{18}\text{F}$  are used for positron emission tomography; [ $^{11}\text{C}$ ]glucose or [ $^{18}\text{F}$ ]fluorodeoxyglucose can detect metastasis spreading of cancer cells; other  $^{11}\text{C}$ -labeled compounds may be used to diagnose Alzheimer disease or leukemia. The short half-life ensures the rapid disappearance of radioactivity but requires a facility for producing the radionuclide and incorporating the label in the proximity of the medical facility. Positrons are immediately converted into easily-detected gamma-rays by annihilation with electrons.

## 1.2 Carbon Atoms

Mendeleev's crucial discovery of the Periodic System was based on atomic weights of the elements known at that time, and on his intuition that a deeper principle must govern this *system* (this is why he used this word, instead of today's term "periodic table"). He dared to "stick out his neck" by inverting the order between I and Te (and later between Ar and K) and also by predicting properties of three new elements, Sc, Ga, Ge. Mendeleev was fortunate to see them discovered during his lifetime. Despite many nominations, the Nobel Foundation never honored him.

The first atomic mass unit (*amu*) was taken by J. Dalton to be the mass of a hydrogen atom (1803). Binary hydrides are, however, less common than binary

oxides, so that oxygen was more convenient and the *amu* was defined as the 16<sup>th</sup> part of the atomic mass of oxygen. Refined methods were used for exact measurements of atomic weights, correcting some erroneous data that had been confusing in Mendeleev's time. T. W. Richards was awarded the 1914 Chemistry Nobel Prize (distributed in 1915) for his work on atomic mass determinations. However, after 1912 when the newly invented mass spectrometer revealed the existence of <sup>17</sup>O and <sup>18</sup>O stable isotopes along with the predominating <sup>16</sup>O (99.66%), physicists based their determinations on the atomic weight of <sup>16</sup>O, whereas chemists continued to use the old definition of *amu*, involving the weighted average of all three stable oxygen isotopes; thus chemists had a unit which was more massive by 1.00028 than the physicists' unit. It was only in 1961 that IUPAC, IUPAP, and IUB agreed on redefining the "unified atomic mass unit" as the 12<sup>th</sup> part of the mass of a <sup>12</sup>C atom. After the SI unit "kg" was redefined in 2012, the present-day definition of atomic weights remains based on carbon atoms and Avogadro's number ( $N_A$ ) as 1 dalton (Da) =  $0.001/N_A$  (in kg) (Holden 2004). However, there is an ongoing discussion on the compatibility between the three related SI units (mole, kilogram, and dalton) after fixing the Planck constant and Avogadro's constant (Leonard 2012).

After discussing the role of carbon in the thermonuclear cosmic formation of helium from hydrogen, it is not surprising that carbon is the *4th most abundant element in the universe by mass*, after <sup>1</sup>H, <sup>2</sup>He, and <sup>8</sup>O. One should not forget that 2 and 8 are magic numbers of nucleons (protons and neutrons), so that <sup>4</sup>He, <sup>16</sup>O are double-magic nuclei.

Carbon is the *15th most abundant element in the Earth's crust*, and it is the *2nd most abundant element by mass in the human body* (18.5%) after oxygen (65%); it is followed by hydrogen (10%) and nitrogen (3%).

The most important chemical reaction occurring naturally on this planet is the photo-assimilation of carbon dioxide. In this reaction (catalyzed by chlorophyll in plants and algae, or by phycocyanin in cyanobacteria) the energy of sun's photons is driving the conversion of carbon dioxide and water vapor into glucose and oxygen.



All the oxygen in our atmosphere originates in this reaction, and the energy released in the reverse reaction allows animals feeding on plants to proceed with their metabolism. Glucose and other simple raw materials such as phosphate, ammonia, and mineral salts are processed by living cells into all constituents of living cells: other carbohydrates, lipids, proteins, and polynucleotides.

Carbon dioxide from the atmosphere is replenished by the well-known *carbon cycle* with the participation of carbon sources from the geosphere, hydrosphere, biosphere, and pedosphere. The amount of carbon (in Tt, teratonnes,  $10^{15}$  kg) in the major reservoirs is 0.7 for the atmosphere, 40 for the hydrosphere, and 75,000 for the geosphere (60,000 for the sedimentary carbonates and 15,000 for kerogens). Even carbon from the calcium/magnesium carbonate rocks is recycled via volcanic emissions triggered by plate tectonics. Throughout most of our planet's history, volcanoes provided the highest turnout of CO<sub>2</sub>, but after the industrial revolution,

human contribution by the increasing burning of non-renewable fossil fuels (all based on carbon, namely coal, natural gas, and petroleum) has outpaced volcanic emissions hundredfold. The estimated amount of carbon in accessible fossil fuels is about 5 Tt.

### 1.3 Carbon Chemical Bonding

Atomic orbitals 2s and 2p host the four valence electrons of carbon in the ground state configuration  $1s^2 2s^2 2p^2$ , but the covalent bonds have different energies and geometries (length and bond angle) according to the hybridization. Having an electronegativity situated midway between the extremes (fluorine and cesium), similarly to hydrogen, carbon is able to form stable long chains or rings with itself. Divalent sulfur also has this property, but this leads only to sulfur element allotropes. Alternating SiO bonds can also lead to long chains, and the resulting mineral silicates form a large part of the Earth's crust. However, only carbon's bonds were selected by the evolution of life on our planet. The huge diversity of carbon compounds makes this unique element the central constituent of the  $7 \times 10^7$  substances indexed till now in the *Chemical Abstracts Registry* database, and this fact justifies the study of Organic Chemistry in a distinct class of chemical compounds. Indeed, more than 95 % of the 70 million substances are organic. Unlike the combinatorial large but finite number of inorganic substances (excluding silicates), the number of possible hydrocarbons is infinite. Along with carbon and hydrogen, most of the known organic substances contain only a small number of other elements: O, S, N, P, F, Cl, Br, I. The element carbon appears as a tetravalent anion only in few methides ( $Al_4C_3$  and  $Be_2C$ ) that produce methane with water or acids; other carbides contain  $C_2^{2-}$  or  $C_3^{4-}$  and afford acetylene or allene/propyne, respectively (Cotton et al. 1999). Silicon and boron form with carbon hard covalent tridimensional lattices. Although stable carbocations, free radicals, or carbenes exist when electronic delocalization is present, the overwhelming majority of carbon compounds form molecular covalent bonds.

Although it is impossible to enumerate all the uses and applications of organic compounds, one should mention that the marked increase of life expectancy during the last centuries is mainly due to the progress of medicinal chemistry and detergents; local and general anesthetics allow surgeons to perform operations and organ replacements that were unimaginable a century ago; nowadays plastics tend to become the preferred materials; dyestuffs and synthetic textiles surround us; Alfred Nobel's fortune was due to the invention of dynamite, an organic explosive; pesticides and herbicides contribute to increasing productivity of agriculture; organic compounds contribute to the electronic industry, liquid crystals for color screens, heat transfer agents for air conditioners and refrigerators, etc.

Living cells produce powerful catalysts, enzymes, which are proteins. In many cases biosynthetic reactions proceed on the basis of effects caused by carbonyl groups. The chemical reactions allowing chemists to synthesize new organic compounds involve, however, bonds with other types of atoms. As an illustration, the following paragraph contains a list of such atoms (in brackets) associated with the

name of a chemist awarded Chemistry Nobel Prizes for the discovery of efficient synthetic procedures. The list is far from being exhaustive.

V. Grignard 1912 (Mg); K. Ziegler and G. Natta 1963 (Ti, Al); E. O. Fischer, G. Wilkinson 1973 (Fe, Cr); H. C. Brown 1979 (B, H); G. Wittig 1979 (P); R. F. Heck, A. Suzuki 2010 (Pd); E. Negishi 2010 (Zn, Pd); R. H. Grubbs, R. R. Schrock 2005 (Ru, Rh). A few other names follow that have not been honored by the Nobel Foundation, yet they have discovered important organic reactions involving various other heteroatoms: E. Frankland (Zn); H. Gilman (Cu); J. K. Stille (Sn).

## 1.4 Chemical Abstracts Service: Documentation in Chemistry versus Other Sciences

On the occasion of its centennial anniversary in 2007, Chemical Abstracts Service (CAS) issued a Special Issue of *Chemical & Engineering News* in which the CEO of CAS, Robert J. Massie, gave details of what CAS is and what it does (Massie 2007). CAS qualifies as a “national treasure”. Moreover, by adopting a graph-theoretical approach to chemical structures represented as hydrogen-depleted molecular graphs that can be traced on a computer screen and then linked to the CAS database, it is possible to learn in a matter seconds if any covalent structure has ever been described in a publication or a patent. Thus chemistry, considered to be the Central Science (Brown et al. 2011; Balaban and Klein 2006) because it bridges the hard sciences such as mathematics, physics, or astronomy with the soft sciences such as biomedical, economic and social sciences, is nowadays also the best-documented science. One can never be certain if a mathematical theorem or a physical property has been described earlier, because these are expressed in words, and the association between words and the corresponding theorems, properties, or ideas is not unique. Of course, this limitation applies also to chemistry when it uses words and not structural formulas.

Before the “computer age”, the IUPAC Nomenclature Committee had devised elaborate rules for naming chemical substances: the “Red Book” for inorganic substances, and the thicker “Blue Book” for organic substances. Yet despite spending hours or days in the library for looking into the Collective Molecular Formula Indices of *Chemisches Zentralblatt* (till 1945) or *Chemical Abstracts* (1907–1986), one could never be quite sure that one could access all documentation for a given substance because of the intricacy of chemical isomerism and nomenclature. All this uncertainly is now a problem of the past, as long as one can draw a constitutional formula as a hydrogen-depleted molecular graph, provided that one has access to SciFinder. An agreement between CAS and FIZ Karlsruhe gave rise to STN International, which is an online database service that provides global access to published research, journal literature, patents, structures, sequences, properties, and other data.



**Table 1.1** Comparison between diamond and graphite

Property	Diamond	Graphite
Aspect	Transparent, highly refractive	Opaque, black
Crystalline system	Cubic	Hexagonal
Density ( $\text{g} \times \text{cm}^{-3}$ )	3.514	2.266
Hardness (Mohs scale)	10	Between 1 and 2
Electrical conductivity	Low	High
Thermal conductivity	High	Low

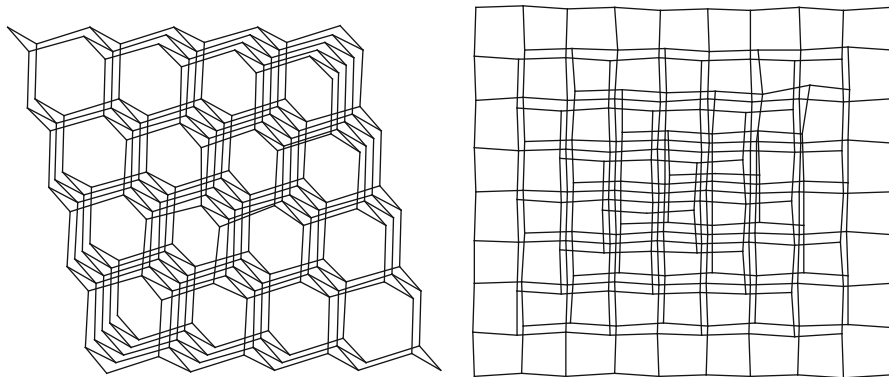
## 1.5 The Hard and Dense Carbon Allotrope, Diamond, and Its Diamondoid Hydrocarbon Relatives

We will discuss *infinite nets* whose peripheral bonds (usually connected to heteroatoms such as H or O) can be neglected, as well as *molecules*, all of whose atoms have to be taken into account. In the present survey the molecules to be discussed will be hydrocarbons, considered to be smaller fragments of the nets with hydrogen atoms connected to the peripheral dangling bonds. Whenever trillions of billions of molecules are identical we call them “substances”, otherwise we have mixtures. With two exceptions, natural or synthetic macromolecular polymers are mixtures with various degrees of dispersion. The narrower the dispersion, the closer is the polymer to a pure substance. The two exceptions (macromolecular compounds that are at the same time pure substances) are the natural polymers proteins and polynucleotides.

The hardest material on the Mohs scale is a carbon allotrope, diamond, formed in the earth’s interior at high temperatures and high pressures (HTHP), and brought to the surface by forces derived from tectonic plate movements. In 1946, P. W. Bridgman was awarded the Nobel Prize for Physics for his research on high-pressure devices. “Bridgman’s opposed anvils” were essential in General Electric’s HTHP method that used graphite and nickel at pressures of 5.4 GPa (54 kbar) and temperatures around 1720 K. At normal temperatures and pressures, graphite is thermodynamically more stable than diamond by about 0.2 kcal/mol, but the interconversion kinetics has a huge activation barrier so that “diamonds are forever”. Table 1.1 illustrates a comparison between the two common carbon allotropes.

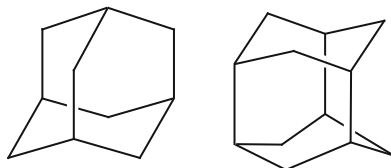
In diamond (Fig. 1.2) all carbon atoms have  $sp^3$  hybridization, all CC bonds have bond distances of 1.54 Å and bond angles of 109.5°. The conformation of CC bonds is staggered, minimizing the electrostatic repulsions, so that one can distinguish adamantane cells in the cubic lattice, which is identical to the zinc sulfide sphalerite lattice.

A different carbon allotropic hexagonal lattice is present in lonsdaleite, which contains iceane units having eclipsed CC bonds with Pitzer strain and a hexagonal (wurtzite) lattice. Figure 1.3 presents hydrogen-depleted formulas of adamantane ( $\text{C}_{10}\text{H}_{16}$ ) and iceane ( $\text{C}_{12}\text{H}_{18}$ ).



**Fig. 1.2** A portion of the diamond lattice seen sideways (*left*) and up-front (*right*)

**Fig. 1.3** Hydrogen-depleted formulas of adamantane (on the *left*) and icane (on the *right*)



Recently, two exoplanets supposed to have huge amounts of diamond layers have been discovered when astronomers observed them transiting across their host star. The first one gravitates around a millisecond pulsar at a distance of 4,000 light years from us, and has a radius about ten times larger than that of earth, whereas the second one is at a distance of only 40 light years, has a radius twice larger than that of earth, and circles around 55 Cancri. Mass and radius estimates of this “55 Cancri e” planet suggested that it has a molten iron core surrounded by successive layers of silicon carbide, silicates, graphite and diamond (Madhusudhan et al. 2012).

The diamond lattice may be expanded theoretically by replacing each C–C bond by the sequence C–C≡C–C, affording thereby “polyyne-diamond” (Melnichenko 1982; Kijima 2005); this replacement may be carried out in one, two, or three dimensions, and combines  $sp^3$  with  $sp$  hybridization. It was emphasized by Kroto that a one-dimensional carbon allotrope with  $sp$  hybridization (carbyne) has no chance of existence as a stable substance (Kroto 2010).

Other theoretical possibilities of carbon nets, combining this time  $sp^3$  and  $sp^2$  hybridizations, were calculated more than 40 years ago (Balaban et al. 1968) and continued in later years; the topic has been reviewed by the present author in book chapters (Balaban 1989, 1998, 2013a). He collaborated with Roald Hoffmann and K. M. Merz in order to predict the stability of infinite nets having ordered arrangements of  $sp^3$  and  $sp^2$  hybridized carbon atoms (Merz et al. 1987). Interconversions between diamond and graphite must start with local hybridization changes, which were investigated theoretically (Balaban and Klein 1997). The near coincidence between certain interatomic distances in the diamond and graphite nets allowed some calculations of diamond-graphite hybrids (Balaban et al. 1994).

In books edited by Diudea (Diudea 2005; Diudea and Nagy 2013) one may read about some other possible types of diamond nets. It is stimulating to look at an ornamental diamond jewel with dimensions  $d$  measured in millimeters, and to think that one can look at this single *macromolecule* in which the carbon atoms constitute most of the atoms (their number is proportional to  $d^3$ ), whereas any peripheral atoms such as H are much less numerous (their number is proportional to  $d^2$ ).

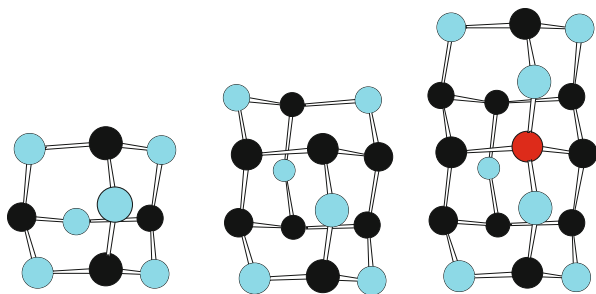
The history of diamond hydrocarbons (or diamondoids for short) starts in 1933 with Landa's discovery of adamantane in petroleum (Landa and Mahacek 1933), confirmed a few years later by its elaborate synthesis (Prelog and Seiwert 1941). The story might have ended there but for two fortuitous events. The first was Schleyer's serendipitous finding that  $\text{AlCl}_3$  catalyzes the isomerization of the hydrogenated cyclopentadiene dimer into adamantane (Schleyer 1957, 1990). This discovery was made possible by adamantane's incredible volatility, paradoxically associated with a high melting point (actually adamantane sublimates around  $270^\circ$  without melting) (Mansoori et al. 2012). Soon afterwards Schleyer and his coworkers succeeded in synthesizing diamantane and triamantane using similar isomerizations (Cupas et al. 1965; Williams et al. 1966; Fort and Schleyer 1964; Fort 1976). The driving force in these reactions is increased thermodynamic stability: diamondoids are the perfect hydrocarbons for  $\text{sp}^3$  hybridization. Unfortunately, the labyrinth of 1, 2-rearrangements becomes too complicated and only one tetramantane isomer could be obtained synthetically (Burns et al. 1976; McKerver 1980).

The IUPAC name of diamondoid hydrocarbons ( $[n]$ polymantanes) based on von Baeyer's conventions for polycyclic hydrocarbons becomes extremely awkward as the number  $n$  of adamantane units increases, as will be seen in the next paragraph. One must also take into account that starting with  $n = 4$  more than one isomer is possible, so that one needs a shorter and simpler name, as well as a coding system and an understanding on how the carbon atoms are partitioned among quaternary, tertiary, and secondary groups. This was achieved by means of dualists (inner dual graphs) whose vertices are the centers of adamantane units and whose edges connect adjacent vertices corresponding to adamantane units sharing a cyclohexane ring. The code is simply a sequence of digits 1, 2, 3, or 4 representing the four tetrahedral directions around a carbon atom according to simple conventions of minimizing the number in that sequence (Balaban and Schleyer 1978). Dualists are a special kind of graphs, in which the angles between edges do matter. For specifying substituent positions, however, IUPAC names have to be used; a general procedure to find IUPAC names exists for zigzag catamantanes (Balaban and Rucker 2013).

Adamantane is tricyclo[3.3.1.1<sup>3,7</sup>]decane; it has molecular formula  $\text{C}_{10}\text{H}_{16}$  and partitioned formula  $(\text{CH})_4(\text{CH}_2)_6$ . Diamantane is pentacyclo[7.3.1.1<sup>4,12</sup>.0<sup>2,7</sup>.0<sup>6,11</sup>]tetradecane and has code [1]; it has molecular formula  $\text{C}_{14}\text{H}_{22}$  and partitioned formula  $(\text{CH})_6(\text{CH}_2)_8$ . Triamantane is heptacyclo[7.7.1.1<sup>3,15</sup>.0<sup>1,12</sup>.0<sup>2,7</sup>.0<sup>4,13</sup>.0<sup>5,11</sup>]octadecane and has code [12]; it has molecular formula  $\text{C}_{18}\text{H}_{26}$  and partitioned formula  $\text{C}(\text{CH})_8(\text{CH}_2)_9$ . These diamondoids are unique isomers (Fig. 1.4), but starting with  $n = 4$ , more than one isomeric  $[n]$ polymantane are possible.

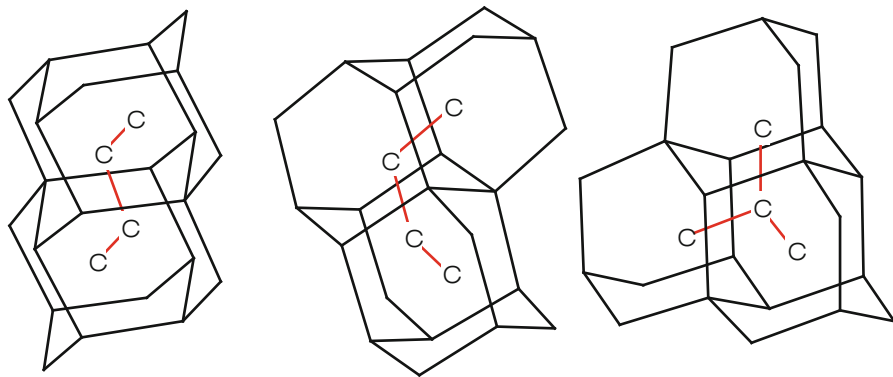
By means of dualists it was possible to classify polymantanes into *catamantanes* when their dualists are acyclic, *perimantanes* when they have dualists containing

**Fig. 1.4** Adamantane, diamantane, and triamantane; *red, black, and blue* denote *quaternary, tertiary, and secondary* carbon atoms



6-membered rings, and coronamantanes when they have dualists with larger rings that are not peripheries of condensed 6-membered rings. The dualist of a catamantane mimics the carbon skeleton of a staggered alkane. In turn,  $[n]$ catamantanes can be regular when their molecular formula is  $C_{4n+6}H_{4n+12}$ , or irregular when they have lower numbers of C and H atoms for a given  $n$  value. Codes of irregular catamantanes have one or more repeated digits  $a$  in a code sequence  $\dots abca \dots$ . So far, all possible  $[n]$ polymantanes with  $n < 8$  have been theoretically discussed. Some of them, like [123]tetramantane, are chiral, and exist as two distinct stable stereoisomers (Fig. 1.5).

The second fortuitous event was the discovery of large amounts of diamondoids in petroleum condensates that were blocking pipelines for natural gas from Chevron's offshore platforms in the Gulf of Mexico. Again, the explanation for this phenomenon involves volatility, paradoxically associated with high melting point and low solubility. Dahl, Carlson and their associates succeeded in perfecting the technology for isolating and purifying diamondoids taking advantage of their higher thermal stability and resistance to oxidation in comparison with other petroleum hydrocarbons (Dahl et al. 2003). Reactions of diamondoids were studied by Schreiner and coworkers



**Fig. 1.5** Isomeric tetramantanes: [121]tetramantane, [123]tetramantane (one of the two enantiomers), and [1(2)1]tetramantane with branched dualist. Dualists are represented by *red* edges connecting the centers of adamantane units indicated by letters C

**Table 1.2** Regular catamantanes with  $n = 4, 5, 6,$  and  $7$  adamantane units. Upper row: *quaternary-tertiary-secondary* carbon atoms; lower row (red color): degrees of dualist (1, 2, 3, and 4)

$n$	C	Formula	Zero branches	One branch	Two branches	Three branches
3	18	$C_{18}H_{24}$	1-10-7 2, 1, 0, 0			
4	22	$C_{22}H_{28}$	2-12-8 2, 2, 0, 0	3-10-9 3, 0, 1, 0		
5	26	$C_{26}H_{32}$	3-14-9 2, 3, 0, 0	4-12-10 3, 1, 1, 0		6-8-12 4, 0, 0, 1
6	30	$C_{30}H_{36}$	4-16-10 2, 4, 0, 0	5-14-11 3, 2, 1, 0	6-12-12 4, 0, 2, 0	7-10-13 4, 1, 0, 1
7	34	$C_{34}H_{40}$	5-18-11 2, 5, 0, 0	6-16-12 3, 3, 1, 0	7-14-13 4, 1, 2, 0	8-12-14 4, 2, 0, 1 9-10-15 5, 0, 1, 1

in collaboration with Carlson, Dahl, and their coworkers from Chevron. They studied how to obtain regioselective functionalization by substituting hydrogens from tertiary or secondary positions (Schwertfeger et al. 2008).

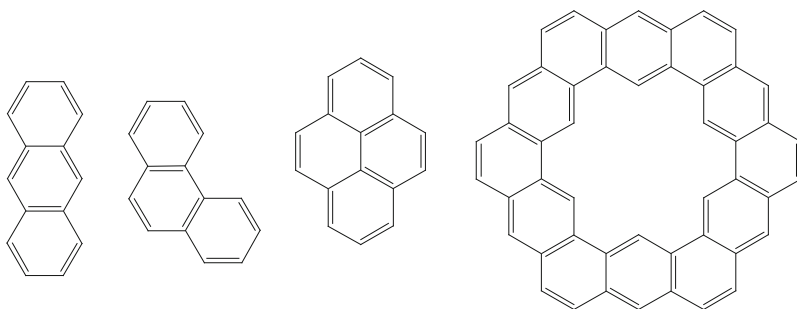
A highly symmetric *formula periodic table* of regular catamantanes results (Table 1.2).when considering all isomers in terms of the number  $n$  of adamantane units and the number  $b$  of branches in the dualist (Balaban 2013b). Diamondoids have partitioned formulas  $C_Q(CH)_T(CH_2)_S$ . Regular catamantanes have the following partitioned formula:  $C_{n+b-2}(CH)_{2n-2b+4}(CH_2)_{n+b+4}$ . The numbers of quaternary and secondary carbon atoms increase according to the number  $n$  of units and number  $b$  of branches, whereas the number of tertiary CH groups increases twice as fast. The three components of the triplet  $Q$ - $T$ - $S$  indicating the numbers of C, CH, and  $CH_2$  groups, respectively, are:

$$Q = n + b - 2 = S - 6 \quad (1.1)$$

$$T = 2(n - b + 2) \quad (1.2)$$

$$S = n + b + 4 \quad (1.3)$$

Till now all possible  $[n]$ diamondoids with  $n < 8$  have been enumerated theoretically (Balaban and Schleyer 1978), and their partitions have been discussed (Balaban 2012, 2013b). Computer programs for enumerating higher polymantanes are urgently needed. The present author collaborated with Klein, Dahl and Carlson in finding molecular descriptors for QSPR correlations with diamondoid chromatographic data (Balaban et al. 2007).



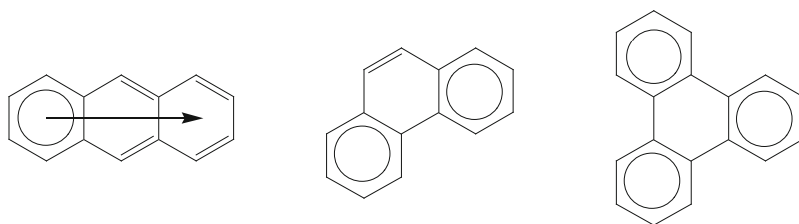
**Fig. 1.6** Hydrogen-depleted structures of two catafusenes (isomeric anthracene and phenanthrene  $C_{14}H_{10}$ ), one perifusene (pyrene,  $C_{16}H_{10}$ ), and one coronafusene (kekulene,  $C_{48}H_{24}$ ).

## 1.6 A Soft Carbon Allotrope, Graphite; Graphene; and Benzenoid Hydrocarbon Relatives

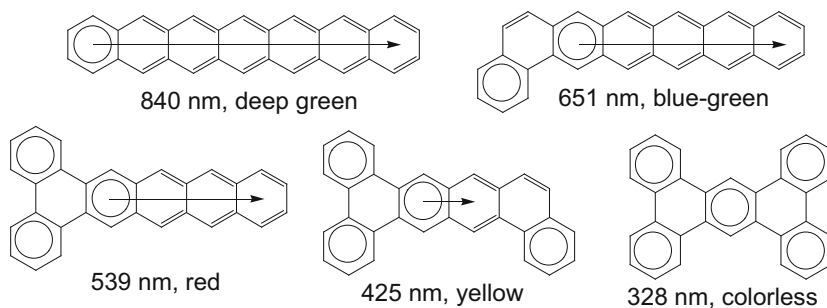
Naturally-occurring graphite is a soft, black carbon allotrope in which carbon atoms have  $sp^2$  hybridization with interatomic distances of 1.41 Å, and form huge planar sheets stacked upon one another with inter-sheet distances of 3.35 Å, which are rigid in two directions but may glide in the third spatial direction, explaining thereby the low hardness (see Table 1.1). Geim's and Novoselov's discovery that one can isolate such one-atom thick sheets was honored with the 2010 Nobel Prize in Physics. Again, now for the different  $sp^2$  hybridization, the graphene sheet is the perfect lattice, both as far as bond angles are concerned, and taking aromaticity into account. Graphene properties, especially the electrical conductivity, are astounding (Geim 2009).

Aromaticity started with August Kekulé, and was subsequently developed by well-known chemists, too many to mention (Balaban 1980; Randić 2003; Balaban et al. 2005). There are two ways of defining benzenoid hydrocarbons (or benzenoids, for short): (i) a restrictive definition, as planar fragments of the graphene lattice, and (ii) a more relaxed definition, which includes non-planar helicenes, and considers just the presence of benzenoid rings sharing CC bonds. The traditional classification into cata-condensed and peri-condensed benzenoids (or for short catafusenes and perifusenes, respectively) was based on the absence or presence of internal carbon atoms, respectively. A simpler and more comprehensive classification was advanced (Balaban and Harary 1968; Balaban 1969) on the basis of dualists (centers of hexagons, connected by an edge for adjacent hexagons sharing a CC bond): catafusenes, perifusenes, and coronafusenes have dualists that are acyclic, contain triangles, or larger rings that are not perimeters of triangle aggregates, respectively. The examples for all these types of benzenoids presented in Fig. 1.6 are all crystalline colorless compounds.

According to Erich Hückel, on the basis of quantum-chemical arguments, whenever the perimeter of a monocyclic or polycyclic benzenoid catafusene has an odd number of double bonds (i. e.  $4n + 2\pi$ -electrons with  $n = 0, 1, 2$ , etc.), enhanced



**Fig. 1.7** Clar structures of anthracene, phenanthrene, and triphenylene



**Fig. 1.8** Heptacatafusene isomers  $C_{30}H_{18}$  with increasing numbers of Clar sextets from 1 to 5: longest absorption wavelength (in *nanometers*), and corresponding color

stability and many other characters associated with aromaticity are present. *Hückel's*  $4n + 2\pi$ -*electron rule* as a necessary and sufficient condition for planar aromatic systems applies also to ionic and to heterocyclic structures. For the simplest benzenoid, benzene, which has a  $\pi$ -electron sextet and is the prototype of perfect aromaticity, one can write two Kekulé valence structures. For  $[k]$ acenes with  $k$  linearly condensed benzenoid rings one can write  $n + 1$  Kekulé structures, but for kinked benzenoids such as phenanthrene or branched ones such as triphenylene, the number of Kekulé structures is higher.

Sir Robert Robinson invented formulas with a circle symbolizing a  $\pi$ -electron sextet. Eric Clar observed that electronic absorption spectra of benzenoids, which account for the colors of these hydrocarbons, are correlated with formulas (nowadays called Clar structures) using the sextet circle under the assumption that in polycyclic benzenoids there is a tug-of-war between rings trying to own  $\pi$ -electron sextets (Clar 1972). In acenes, the unique Clar sextet can move along and this is symbolized by arrows, as seen in Fig. 1.7. Clar formulas must have the maximum possible number of sextet rings; a ring can either have a sextet, or one or two double bonds; no sextets can be written in adjacent rings.

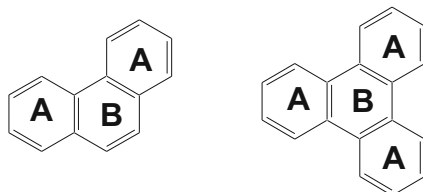
In Fig. 1.8 one can see Clar structures of five isomeric heptacatafusenes, starting with heptacene which absorbs red photons (and is therefore colored deep green, having  $k = 7$  and 1 Clar sextet), and ending with tetrabenzanthracene which has 5 Clar sextets and absorbs only in the ultraviolet region and is therefore colorless.

**Table 1.3** Various kinds of partitions of  $\pi$ -electrons in two benzenoids

Hydrocarbon	Phenan threne		Triphe nylene	
Partition	A-ring	B-ring	A-ring	B-ring
Equipartition	5.00	4.00	5.00	3.00
$\pi$ -Electron partition	5.20	3.60	5.33	2.00
Clar partition	6.00	2.00	6.00	0.00

Not only color, but also several other properties of polycyclic benzenoids can be correlated with two simple parameters: the number of benzenoid rings and the number of linearly-condensed rings: kinetics of cycloaddition with maleic anhydride (Balaban et al. 1985), redox potentials (Balaban et al. 2011; Singh et al. 2006), etc. (Balaban and Pompe 2007).

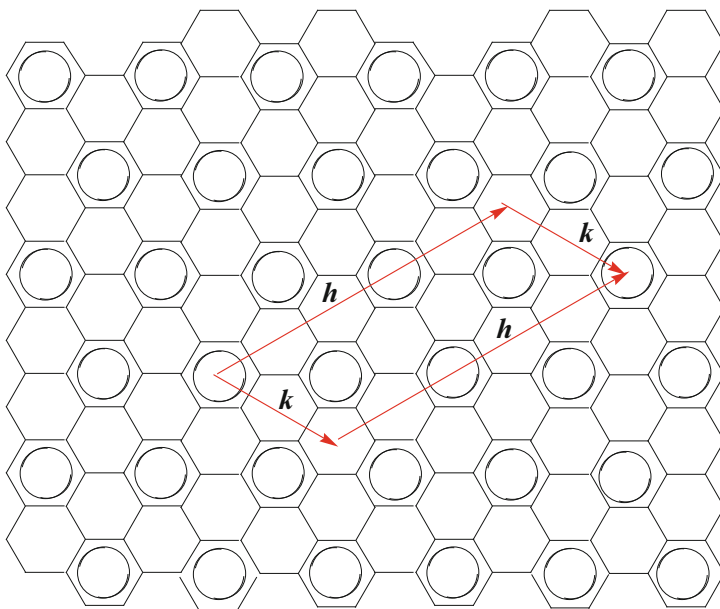
If one considers that each  $sp^2$ -hybridized carbon atom is associated with one  $\pi$ -electron, then equipartition would assign one  $\pi$ -electron to carbon atoms that are not shared to adjacent rings and 0.5  $\pi$ -electrons when a carbon atom is shared with another ring. A more reasonable partition of  $\pi$ -electrons, reviewed in a book chapter (Balaban and Randić 2011), considers the average of all Kekulé valence structures weighted equally. Finally, Clar structures yield partitions according to the principle “winner takes all” (Balaban 2011). The 14  $\pi$ -electrons of phenanthrene and the 18  $\pi$ -electrons of triphenylene can be distributed according to the above types of partitions as shown in Table 1.3. By the same arguments, equipartition would assign two  $\pi$ -electrons to each carbon atoms in graphene because the sharing is between three rings.



## 1.7 The Newer Allotropes of Carbon: Fullerenes, Nanotubes, Nanocones, Nanotori

After the discovery of fullerenes by Smalley, Curl and Kroto (1996 Nobel Prize for Chemistry) by mass spectrometry (Kroto et al. 1985), it was possible to find experimental conditions for producing larger amounts of  $C_{60}$  and  $C_{70}$ , and for purifying them, arriving for the first time at *molecular carbon allotropes*, i. e. at *pure substances* containing exclusively carbon atoms (Krätschmer 1990). Buckminsterfullerene  $C_{60}$  is an assembly of carbon atoms arranged as a truncated icosahedron one,





**Fig. 1.9** Part of a graphene sheet with  $h = 5$  and  $k = 2$  vectors between two “sextet” hexagons

of the 13 Archimedean semiregular polyhedra. Higher fullerenes can be multiple-walled (“onion fullerenes”), or ellipsoidal double-capped nanotubes. Long nanotubes (Ijima 1991) have more complicated geometries (zigzag, armchair, chiral) and so far have been obtained only as mixtures. The same is true of nanocones (Balaban 2005; Klein and Balaban 2006) and nanotori (Klein and Balaban 2006). An interesting aspect of nanotubes is that their electrical conductance depends on the orientation of benzenoid rings with respect to the nanotube axis. It was shown that a simple rationalization of these experimental and theoretical data could be obtained by applying Clar’s ideas to the folding of graphene sheets in forming single-wall nanotubes (SWNTs). Virtual Clar sextets in graphene must have conjugation along a poly-*para*-phenylenic direction, as seen in Fig. 1.9.

The folding obeys the vector rules  $(h, k)$  as indicated in Fig. 1.9 and Eq. (1.4). When  $k = 0$ , the folding occurs along an acenic portion leading to an achiral SWNT with a zigzag edge. In this case a congruent folding of Clar sextet rings occurs only if  $h$  is a multiple of 3. When  $h = k$ , the folding occurs along a poly-*para*-phenylenic direction affording also an achiral SWNT but now with an armchair edge. In this case a congruent folding occurs if  $h - k$  is a multiple of 3. Otherwise (when  $h \neq k \neq 0$ ) chiral SWNTs result, and congruent folding occurs only whenever Eq. 1.4 is fulfilled, which covers also the previous situations with achiral SWNTs.

$$h - k \equiv 0 \pmod{3} \quad (1.4)$$

The resulting bandgap is zero (when curvature variations of the Hückel parameters are neglected) so that the nanotube will have a metallic conductivity, and otherwise it will behave as a semiconductor. As a result, all armchair SWNTs and one-third of zigzag and chiral SWNTs are metallic, whereas two-thirds are semiconducting (Klein and Balaban 2011).

## 1.8 Concluding Remarks

Having had for many years an interest in carbon nets, the present author witnessed many astonishing developments connected to the chemical element carbon. The aromaticity associated with  $sp^2$ -hybridized carbon atoms in certain cyclic structures is responsible for the amazing formation of fullerenes and nanotubes, as well as for the isolation of sturdy one-atom thick graphene sheets. The minimized electronic repulsion associated with staggered conformation of  $sp^3$ -hybridized C–C bonds is responsible for diamond being one of the hardest materials, for the presence of diamondoid hydrocarbons (diamondoids) in petroleum, and for the promising semiconductors obtained by epitaxial deposition yielding diamond-like films. The discovery of methods to isolate and purify naturally occurring diamondoids opened new perspectives for using such hydrocarbons in various applications after functionalization.

However, most praise should be addressed not to the element carbon, but to its compounds. Already from the infinity of chemical compounds, more than  $7 \times 10^7$  organic substances have been characterized and registered, and they are by far more numerous than compounds of all other elements heavier than hydrogen. It is not due to chance that life is based on carbon compounds. What is amazing is that the element carbon with an abundance of only 0.08 % in the accessible earth's crust, oceans, and atmosphere (14th place among all elements) in its most oxidized form of carbon dioxide can be converted (at all latitudes on land or in oceans by bacteria, algae, and plants using water vapor and sun's energy) into carbohydrates and oxygen, thanks to the elaborate machinery of photo-assimilation. In the not too distant future, when mankind will have exhausted all fossil fuels (oil, coal, and natural gas) returning the element carbon to the climate-foe  $CO_2$  due to greenhouse-effects, much more energy will be needed to make foods, plastics, and textiles by gaining access to carbon from calcium carbonate rocks. Will we be ready?

## References

- Balaban AT (1969) *Tetrahedron* 25:2949–2956
- Balaban AT (1980) *Pure Appl Chem* 52:1409–1429
- Balaban AT (1989) *Computers Math Applic* 17:397–416 (Reprinted In: Hargittai I (ed) *Symmetry II*, Pergamon Press, Oxford, pp. 397–416)
- Balaban AT (1998) In: Parkanyi C (ed) *Theoretical organic chemistry*. Elsevier, Amsterdam, pp. 381–404

- Balaban AT (2005) In: Diudea MV (ed) Nanostructures novel architecture. Nova Publishers, New York, pp. 113–142
- Balaban AT (2011) *Phys Chem Chem Phys* 13:20649–20658
- Balaban AT (2012) *J Chem Inf Model* 52:2856–2869
- Balaban AT (2013a) In: Diudea MV, Nagy CL (eds) Diamond and related nanostructures. Springer, Berlin
- Balaban AT (2013b) *J Math Chem* 51:1045–1055
- Balaban AT, Aziz S, Manikpuri AD, Khadikar PV (2011) *J Indian Chem Soc* 88:87–97
- Balaban AT, Biermann D, Schmidt W (1985) *Nouv J Chim* 9:443–449
- Balaban AT, Harary F (1968) *Tetrahedron* 24:2505–2516
- Balaban AT, Klein DJ (1997) *Carbon* 35:247–251
- Balaban AT, Klein DJ (2006) *Scientometrics* 69:615–637
- Balaban AT, Klein DJ (2009) *J Phys Chem C* 113:19123–19133
- Balaban AT, Klein DJ, Dahl JE, Carlson RMK (2007) *Open Org Chem J* 1:13–31
- Balaban AT, Klein DJ, Folden CA (1994) *Chem Phys Lett* 217:266–270
- Balaban AT, Pompe M (2007) *J Phys Chem A* 111:2448–2454
- Balaban AT, Randić M (2011) In: Putz MV (ed) Carbon bonding and structures: advances in physics and chemistry. Carbon materials: chemistry and physics 5. Springer Science + Business Media, London pp. 159–204
- Balaban AT, Rentia CC, Ciupitu E (1968) *Rev Roum Chim* 13:231–247
- Balaban AT, Rucker C (2013) *Central Eur J* 11:1423–1430
- Balaban AT, Schleyer PvR (1978) *Tetrahedron* 34:3599–3609
- Balaban AT, Schleyer PvR, Rzepa HS (2005) *Chem Rev* 105:3436–3447
- Brown TE, LeMay EH, Bursten BE, Murphy C, Woodward P (2011) *Chemistry: the central science*, 12th ed. Prentice Hall, New Jersey
- Burns W, Mitchell TRB, McKervey MA, Rooney JJ, Ferguson G, Roberts P (1976) *Chem Commun* 893–895
- Clar E (1972) *The Aromatic sextet*. Wiley, London
- Cotton FA, Wilkinson G, Murillo CA, Bochmann M (1999) *Advanced inorganic chemistry*. Wiley, New York, pp. 208–257
- Cupas CA, Schleyer PvR, Trecker DJ (1965) *J Am Chem Soc* 87:917–918
- Dahl JE, Liu SG, Carlson RMK (2003) *Science* 299:96–99
- Diudea MV (ed) (2005) Nanostructures. Novel architecture. Nova Publishers, New York
- Diudea MV, Nagy CL (eds) (2013) Diamond and related nanostructures. Springer, Berlin
- Epelbaum E, Krebs H, Lee D, Meissner U-G (2011) *Phys Rev Lett* 106:192501
- Fort Jr RC (1976) Adamantane. The chemistry of diamond molecules. Marcel Dekker, New York
- Fort Jr RC, Schleyer PvR (1964) *Chem Rev* 64:277–300
- Geim A (2009) *Science* 324:1530–1534
- Holden NE (2004) *Chem Internat* 26:4–7
- Ijima S (1991) *Nature* 354:56–58
- Kijima M (2005) In: Polyynes. Synthesis, properties, and applications (Cataldo F ed), CRC Press, Boca Raton pp. 197–218
- Klein DJ, Balaban AT (2006) *J Chem Inf Model* 46:307–320
- Klein DJ, Balaban, AT (2011) *Open Org Chem J* 5(Suppl. 1-M1):27–61
- Krätschmer W, Lamb LD, Fostiropoulos K, Huffman DR (1990) *Nature* 347:354–358
- Kroto HW (2010) *RSC Chemistry world*. November issue
- Kroto HW, Heath JR, O'Brien SC, Curl RF, Smalley RE (1985) *Nature* 318:162–163
- Landa S, Mahacek V (1933) *Coll Czech Chem Commun* 5:1–5
- Lee D, Epelbaum E, Krebs H, Lähde TA, Meissner U-G (2012) *Phys Rev Lett* 109:252501
- Leonard, BP (2012) *Metrologia* 49:487–491
- Madhusudhan N, Lee KKM, Mousis O (2012) *Astrophys J Lett*
- Mansoori GA, de Araujo PLB, de Araujo ES (2012) Diamondoid molecules with applications in biomedicine, materials science, nanotechnology and petroleum science. Wiley, New York

- Massie RJ (2007) *Chem Eng News* 85(24):56–57
- McKervey MA (1980) *Tetrahedron* 36:971–992
- Melnichenko VM, Nikulin YI, Sladkov AM (1982) *Dokl Akad Nauk SSSR* 267:1150–1154
- Merz Jr KM, Hoffmann R, Balaban AT (1987) *J Am Chem Soc* 109:6742–6751
- Prelog V, Seiwerth B (1941) *Ber dtsch chem Ges* 74:1644–1648, 1679–1772
- Randić M (2003) *Chem Rev* 103:3449–3606
- Schleyer, PvR (1957) *J Am Chem Soc* 79:3292
- Schleyer PvR (1990) *Cage Hydrocarbons* (Olah GA ed). Wiley, New York, pp. 1–38
- Schwertfeger H, Fokin AA, Schreiner PT (2008) *Angew Chem Int Ed* 47:1022–1036
- Singh J, Singh S, Meer S, Agrawal VK, Khadikar PV, Balaban AT (2006) *Arkivoc* (xv):104–109
- Williams Jr VZ, Schleyer PvR, Gleicher GJ, Rodewald LB (1966) *J Am Chem Soc* 88:3862–3863

# Chapter 2

## Origami: Self Organizing Polyhexagonal Carbon Structures for Formation of Fullerenes, Nanotubes and Other Carbon Structures

István László and Ibolya Zsoldos

**Abstract** The selective production of fullerenes and nanotubes is a challenging problem. Molecular dynamics calculations can reveal the physical and chemical properties of various carbon nanostructures and can help to devise the possible formation pathways. In our previous publications we have presented various graphene patterns which could transform in a self organising way into the desired structure. The processes were realized in molecular dynamics simulations. In the present publication we review the molecular dynamics method used in our previous calculations and give further graphene patterns for  $C_n$  fullerenes from  $C_{60}$  to  $C_{100}$ . Also the possibility of experimental realizations will be discussed.

### 2.1 Introduction

The idea of graphene origami emerged already nearly a decade before the famous graphene paper was published in 2004 (Novoselov et al. 2004). In 1995 Ebbesen and Hiura published namely an article with the title: “Graphene in 3-Dimension: toward graphite origami” (Ebbesen and Hiura 1995). These authors suggested that graphene could be folded up to a variety of shapes and cutting well-defined patterns can allow to design nanotubes with given diameters. Even earlier Kroto et al. wrote in their “ $C_{60}$ :Buckminsterfullerene” paper (Kroto et al. 1985): “Our rationalization of these results is that in the laser vaporization, fragments are torn from the surface as pieces of the planar graphite fused six-membered ring structure. We believe that the distribution is fairly representative of the nascent distribution of larger ring fragments. When these hot ring clusters are left in contact with high-density helium, the clusters

---

I. László (✉)

Department of Theoretical Physics, Institute of Physics,  
Budapest University of Technology and Economics, 1521 Budapest, Hungary  
e-mail: laszlo@eik.bme.hu

I. Zsoldos

Faculty of Technology Sciences, Széchenyi István University,  
Egyetem tér 1, 9036 Győr, Hungary  
e-mail: zsoldos@sze.hu

equilibrate by two- and three-body collisions towards the most stable species, which appears to be unique cluster containing 60 atoms.”

These early suggestions, however, were based on larger graphene sheets in the case of nanotubes or they supposed degradation or fusion of various ring fragments. In our recent molecular dynamics simulations we have shown the existence of various patterns cut out from the graphene which transformed to  $C_{60}$  and  $C_{70}$  fullerenes or nanotubes depending on the initial pattern structures (László and Zsoldos 2012a, b, 2014). The greater application of fullerenes and nanotubes faces the lack of selective growth and assembly processes. Our results can initiate new experimental researches for improving the existing carbon nanostructure productions and to develop a new, structure selective nanolithography of fullerenes, nanotubes and other carbon structures. We are aware of the fact that nowadays patterning of graphene is not yet at atomic precision, but there are promising experimental achievements (Avouris et al. 2007; Chen et al. 2007; Tapasztó et al. 2008; Feng et al. 2012).

First we review the molecular dynamics method which was used in our previous calculations (László and Zsoldos 2012a, b, 2014), after the methods of experimental patterning will be shown. Then we present various geometrical patterning of graphene which are not applicable for self organizing production of fullerenes. Than we present the method of coding the final structure in the initial one. As new results we suggest new patterns for formation of  $C_n$  fullerenes with ( $72 \leq n \leq 100$ ). In the conclusion we analyse our results and regarding new experimental results we extend the meaning of patterning to hydrocarbon patterns as well.

## 2.2 Tight Binding Molecular Dynamics Calculation

Although our system contained only about 100 carbon atoms we were using a tight binding method in our molecular dynamics simulations as we had to make a great number of runs. The inter atomic forces were calculated with the help of a density functional tight binding (DFTB) model (Porezag et al. 1995). In such a model the total energy is written in the form of

$$E = \sum_{k=1}^N \frac{P_k^2}{2M_k} + E_{\text{bond}} + E_{\text{rep}} \quad (2.1)$$

where

$$E_{\text{bond}} = \sum_i n_i \varepsilon_i \quad (2.2)$$

is the tight binding electronic energy where the summation goes over all of the eigenstates of the tight binding Hamiltonian matrix  $H$ . The value  $n_i$  of the occupation number is 2, 1 or 0 depending of the occupation of the eigenfunctions

$$\psi_i(\mathbf{r}) = \sum_v^m C_{vi} \phi_v(\mathbf{r} - \mathbf{R}_v) \quad (2.3)$$

Here the atom-centred basis function  $\phi_\nu((\mathbf{r}-\mathbf{R}_\nu))$  is centred around the atom with the position vector  $\mathbf{R}_\nu$  and  $m$  equals to the number of basis functions centred on the atoms in the positions  $\mathbf{R}_k$  with  $1 \leq k \leq N$  where  $N$  is the number of atoms and  $\mathbf{R}_\nu$  equals to one of the vectors  $\mathbf{R}_k$ .  $\mathbf{P}_k$  is the momentum of the atom  $k$  with the mass  $M_k$ . The eigenvalues and the eigenvectors are determined by the equations

$$\sum_{\nu=1}^m C_{\nu i} (H_{\mu\nu} - \varepsilon_i S_{\mu\nu}) = 0 \quad (2.4)$$

For each  $\mu$  and  $i$ , where

$$H_{\mu\nu} = \langle \phi_\mu | H | \phi_\nu \rangle \quad (2.5)$$

and

$$S_{\mu\nu} = \langle \phi_\mu | \phi_\nu \rangle \quad (2.6)$$

is the overlap integral. The  $H_{\mu\nu}$  and  $S_{\mu\nu}$  off diagonal matrix elements are given with the help of the function  $H_{\text{sp}\sigma}(R)$ ,  $H_{\text{pp}\sigma}(R)$ ,  $H_{\text{ss}\sigma}(R)$ ,  $H_{\text{pp}\pi}(R)$ ,  $S_{\text{sp}\sigma}(R)$ ,  $S_{\text{pp}\sigma}(R)$ ,  $S_{\text{ss}\sigma}(R)$ ,  $S_{\text{pp}\pi}(R)$ . Namely we were using only carbon atoms and each of them was supplied by one s orbital and three p orbital. That is  $\phi$  was s,  $p_x$ ,  $p_y$  or  $p_z$  orbital. The corresponding functions are given in ref. (Porezag et al. 1995) with the help of Chebyshev polynomials. The matrix element were given with the help of the Slater-Koster relations (Slater and Koster 1954).

$$H_{\text{ss}}(\mathbf{R}_j - \mathbf{R}_i) = H_{\text{ss}\sigma}(\mathbf{R}_{ij}) \quad (2.7)$$

$$H_{\text{sx}}(\mathbf{R}_j - \mathbf{R}_i) = \cos(\alpha_x) H_{\text{sp}\sigma}(\mathbf{R}_{ij}) \quad (2.8)$$

$$H_{\text{xx}}(\mathbf{R}_j - \mathbf{R}_i) = \cos^2(\alpha_x) H_{\text{pp}\sigma}(\mathbf{R}_{ij}) + (1 - \cos^2(\alpha_x)) H_{\text{pp}\pi}(\mathbf{R}_{ij}) \quad (2.9)$$

$$H_{\text{xy}}(\mathbf{R}_j - \mathbf{R}_i) = \cos(\alpha_x) \cos(\alpha_y) H_{\text{pp}\sigma}(\mathbf{R}_{ij}) - \cos(\alpha_x) \cos(\alpha_y) H_{\text{pp}\pi}(\mathbf{R}_{ij}) \quad (2.10)$$

$$H_{\text{xz}}(\mathbf{R}_j - \mathbf{R}_i) = \cos(\alpha_x) \cos(\alpha_z) H_{\text{pp}\sigma}(\mathbf{R}_{ij}) - \cos(\alpha_x) \cos(\alpha_z) H_{\text{pp}\pi}(\mathbf{R}_{ij}) \quad (2.11)$$

Here we have supposed that the atomic orbital  $\phi_\mu$  was centred at  $\mathbf{R}_i$  and the atomic orbital  $\phi_\nu$  was centered on the atom at  $\mathbf{R}_j$ . The direction cosines of the vector  $\mathbf{R}_j - \mathbf{R}_i \neq 0$  are  $\cos(\alpha_x)$ ,  $\cos(\alpha_y)$  and  $\cos(\alpha_z)$ .  $\mathbf{R}_{ij}$  is the distance between the two atoms. If the atomic orbitals  $\phi_\mu$  and  $\phi_\nu$  are centred on the same atom,  $H_{\text{ss}} = -13.573eV$  and  $H_{\text{xx}} = H_{\text{yy}} = H_{\text{zz}} = -5.3715eV$  for  $\mu = \nu$  and  $H_{\mu\nu} = 0$  for  $\mu \neq \nu$ . The other matrix elements can be generated with the help of symmetry.

Similar relations are valid for the  $S_{\mu\nu}$  overlap matrix elements as well. That is,

$$S_{\text{ss}}(\mathbf{R}_j - \mathbf{R}_i) = S_{\text{ss}\sigma}(\mathbf{R}_{ij}) \quad (2.12)$$

$$S_{\text{sx}}(\mathbf{R}_j - \mathbf{R}_i) = \cos(\alpha_x) S_{\text{sp}\sigma}(\mathbf{R}_{ij}) \quad (2.13)$$

$$S_{\text{xx}}(\mathbf{R}_j - \mathbf{R}_i) = \cos^2(\alpha_x) S_{\text{pp}\sigma}(\mathbf{R}_{ij}) + (1 - \cos^2(\alpha_x)) S_{\text{pp}\pi}(\mathbf{R}_{ij}) \quad (2.14)$$

$$S_{xy}(\mathbf{R}_j - \mathbf{R}_i) = \cos(\alpha_x) \cos(\alpha_y) S_{pp\sigma}(\mathbf{R}_{ij}) - \cos(\alpha_x) \cos(\alpha_y) S_{pp\pi}(\mathbf{R}_{ij}) \quad (2.15)$$

$$S_{xz}(\mathbf{R}_j - \mathbf{R}_i) = \cos(\alpha_x) \cos(\alpha_z) S_{pp\sigma}(\mathbf{R}_{ij}) - \cos(\alpha_x) \cos(\alpha_z) S_{pp\pi}(\mathbf{R}_{ij}) \quad (2.16)$$

for basis functions centred on different atoms and if the two basis functions are centred on the same atom,  $S_{ss} = S_{xx} = S_{yy} = S_{zz} = 1$  if  $\mu = \nu$  and  $S_{\mu\nu} = 0$  for  $\mu \neq \nu$ .

The  $E_{\text{rep}}$  repulsive par potential is also given in ref. (Porezag et al. 1995) with the help of Chebyshev polynomials.

The atomic force

$$\mathbf{F}_k = - \sum_i \sum_{\mu,\nu}^m n_i \left( C_{i\mu} C_{i\nu} \left[ \frac{\partial H_{\mu\nu}}{\partial \mathbf{R}_k} - \varepsilon_i \frac{\partial S_{\mu\nu}}{\partial \mathbf{R}_k} \right] \right) - \frac{\partial E_{\text{rep}}}{\partial \mathbf{R}_k} \quad (2.17)$$

is calculated from the Hellmann-Feynman theorem.

In the canonical ensemble molecular dynamics calculations the constant environmental temperature was controlled with the help of Nosé-Hoover thermostat (Nosé 1984; Hoover 1985; Allen and Tildesley 1996; Frenkel and Smit 1996). In this thermostat the environmental temperature is  $T_{\text{env}}$ , and the force acting on the atom in the position  $\mathbf{R}_k$  is determined as

$$\mathbf{F}_k^{\text{NH}} = - \sum_i \sum_{\mu,\nu}^m n_i \left( C_{i\mu} C_{i\nu} \left[ \frac{\partial H_{\mu\nu}}{\partial \mathbf{R}_k} - \varepsilon_i \frac{\partial S_{\mu\nu}}{\partial \mathbf{R}_k} \right] \right) - \frac{\partial E_{\text{rep}}}{\partial \mathbf{R}_k} - \xi \mathbf{P}_k \quad (2.18)$$

The friction coefficient  $\xi$  is given by the first-order differential equation

$$\dot{\xi} = \frac{f}{Q} k_B (T - T_{\text{env}}) \quad (2.19)$$

where  $k_B$  is the Boltzmann constant,  $Q$  is a thermal inertial parameter,  $f = 3N$  is the number of degrees of freedom and the kinetic temperature is

$$T = \frac{1}{3Nk_B} \sum_{k=1}^N \frac{\mathbf{P}_k^2}{2M_k} \quad (2.20)$$

The thermal inertial parameter determines the time scale of the kinetic temperature oscillation and strength of interaction with the environment. The detailed nature of the dynamics depends on the value of  $Q$  chosen but the average properties are less sensitive to its value, thus it can be arbitrary.

The equation of motion was solved with the help of the Verlet algorithm (Verlet 1967)

$$\mathbf{V}_k(t) = \frac{\mathbf{R}_k(t + \Delta t) - \mathbf{R}_k(t - \Delta t)}{2\Delta t} \quad (2.21)$$

$$\mathbf{P}_k(t) = M_k \mathbf{V}_k(t) \quad (2.22)$$



$$R_k(t + \Delta t) = 2R_k(t) - R_k(t - \Delta t) + \frac{F_k^{NH}(t)}{M_k} \Delta t^2 \quad (2.23)$$

where  $\Delta t$  is the time step. The Euler algorithm

$$\xi(t) = \xi(t - \Delta t) + \frac{f}{Q} k_B (T(t) - T_{env}) \Delta t \quad (2.24)$$

gives the solution of the friction coefficient  $\xi$ .

## 2.3 Patterning of Graphene

### 2.3.1 *Experimental Patterning*

Patterning of graphene comes from the need of constructing graphene based electronic devices. Although the flat and wide graphene is semimetal, the band gap of nanoribbons scales inversely with their widths (Feng et al. 2012). The graphene patterning methods are the electron and/or ion beam irradiation (Chen et al. 2007; Fischbein and Drndić 2008; Meyer et al. 2008; Huang et al. 2009; Girit et al. 2009; Lemme et al. 2009; Bell et al. 2009; Huang et al. 2010; Shi et al. 2011; Song et al. 2011) the scanning tunnelling lithography (McCarley et al. 1992, Hiura 2004, Tapasztó et al. 2008) and various etching techniques (Zhang et al. 2011; Han et al. 2007; Bai et al. 2009, 2010; Kim et al. 2012; Sinitskii and Tour 2010; Li 2008; Datta et al. 2008; Ci et al. 2008; Dimiev et al. 2011; Kosynkin 2009; Jiao et al. 2009, 2010). In electron beam lithography nanoribbons with a width of 10–15 nm were fabricated (Chen et al. 2007; Han et al. 2007). Scanning tunnelling microscope lithography reached the nanoribbon width of 2.5 nm (Tapasztó et al. 2008).

With redesigned zinc patterns single atomic layer resolution lithography was found on graphene (Björk et al. 2011).

### 2.3.2 *Geometrical Patterning Including Multiples of Some Atoms*

Many authors working on carbon nanostructures start their talks with a picture presenting a graphene sheet containing various cut out patterns which are turning into fullerenes and nanotubes (Geim and Novoselov 2007). These processes follow the text book geometric construction of fullerenes and nanotubes and explain the fact that the graphene is “Mother of all graphitic forms” (Geim and Novoselov 2007). Following the mathematical construction these initial patterns contain usually more carbon atoms than needed in the final structure. Several of these atoms are identified during the geometric constructions. Beaton for example presented patterns which could be transformed into fullerenes by further cutting along given lines and

cut out of hexagons. The fullerenes were obtained by overlapping and gluing given hexagons (Beaton 1995). In the projection method the pentagons of the fullerenes are constructed from the honeycomb lattice by removing a triangular region (Dresselhaus et al. 1996). The nanotubes can be imagined as rolled up parallelograms or nanoribbons (Dresselhaus et al. 1996). In all of the previous graphene patterns the initial structures have more carbon atoms than the final fullerene or nanotube. Thus they can not be used as self organizing patterns.

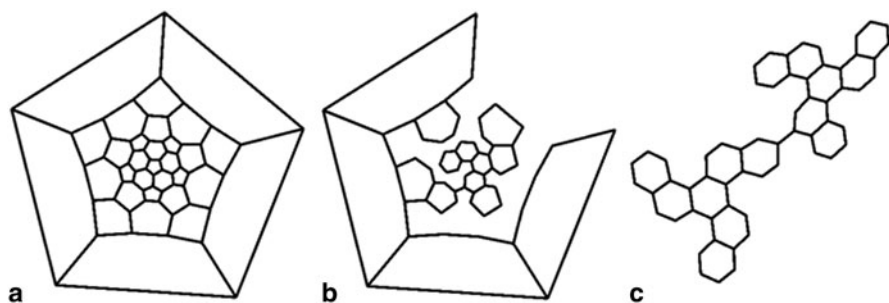
### 2.3.3 Geometrical Patterning for Self Organizing Processes

We are looking for patterns which have the same number of carbon atoms as the final structure and they can be transformed into the desired arrangement in a self organizing way.

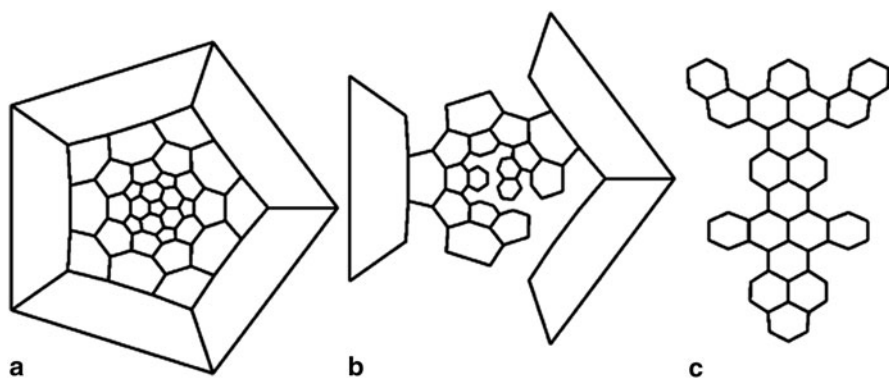
In biology the information is encoded in the amino acid sequence. This sequence determines the structure and properties of the protein. In our previous publications (László and Zsoldos 2012a, b, 2014) the final structure of the fullerenes and nanotubes was coded in the geometrical structure of the graphene patterns. The conditions of the coding were the followings: (1) A pattern contains only hexagons. (2) There are some fourth neighbouring atoms on the perimeter which can approach each other during their heat motion by constructing new pentagonal or hexagonal faces. (3) After the formation of new faces other carbon atoms will be in appropriate positions to produce new bonds. Repeating steps (2) and (3) we obtain the final structure selected by the initial pattern.

In Figs. 2.1–2.17 we present 17 examples of isolated pentagon  $C_n$  fullerenes for each possible even values of  $n$  in the ranges ( $n = 60$ ) and ( $70 \leq n \leq 100$ ). These patterns fulfil the above mentioned conditions. Applying the isolated-pentagon rule (IPR) there is only one isomer for  $C_{60}$ ,  $C_{70}$ ,  $C_{72}$  and  $C_{74}$ . For ( $62 \leq n \leq 68$ ) there is not any fullerene having the IPR. As  $n$  increases, the number of isomers increases significantly. For ( $n = 76$ ) the number of isomers is two only, but for ( $n = 100$ ) it reaches the value of 450 (Fowler and Manolopoulos 1995). In Figs. 2.1–2.17 also the Schlegel diagrams of the corresponding fullerenes are presented with the cut out pattern in the Schlegel diagram and the same cut out pattern in the graphene sheet. For the notation of the fullerenes and the spiral codes we used the definitions given in reference (Fowler and Manolopoulos 1995).

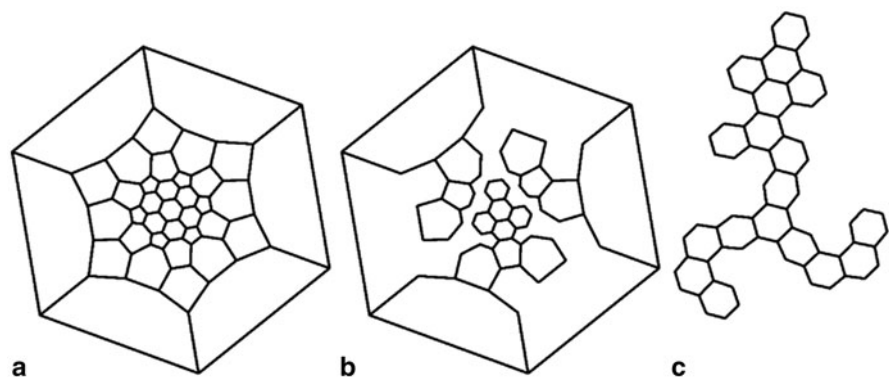
In tight binding molecular dynamics simulations the patterns of Figs. 2.1 and 2.2 developed into the desired  $C_{60}$  and  $C_{70}$  fullerenes (László and Zsoldos 2012a, b, 2014). In these publications the possibility of transforming into the desired structures was presented several fullerene and nanotube patterns. These processes were controlled by applying appropriate environmental temperature conditions in the frame work of the Nosé-Hoover thermostat.



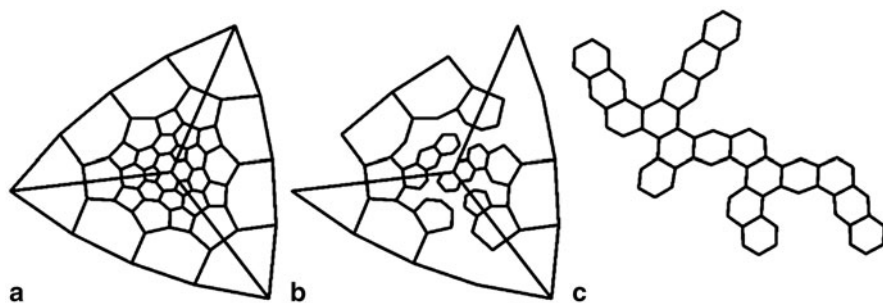
**Fig. 2.1** The  $C_{60-1}$  fullerene of symmetry  $I_h$  and ring spiral (1,7, 9,11, 13,15, 18,20, 22,24, 26,32). The Schlegel diagram (a), the pattern in the Schlegel diagram (b), the pattern in the graphene lattice



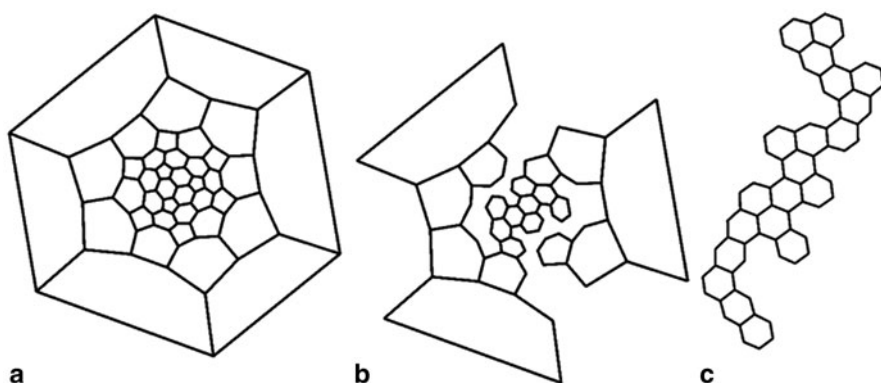
**Fig. 2.2** The  $C_{70-1}$  fullerene of symmetry  $D_{5h}$  and ring spiral (1,7, 9,11, 13,15, 27,29, 31,33, 35,37). The Schlegel diagram (a), the pattern in the Schlegel diagram (b), the pattern in the graphene lattice



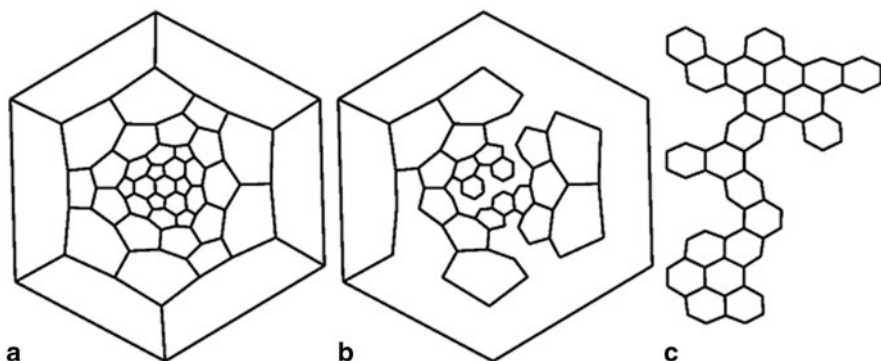
**Fig. 2.3** The  $C_{72-1}$  fullerene of symmetry  $D_{6d}$  and ring spiral (1,7, 9,11, 13,18, 22,24, 27,34, 36,38). The Schlegel diagram (a), the pattern in the Schlegel diagram (b), the pattern in the graphene lattice



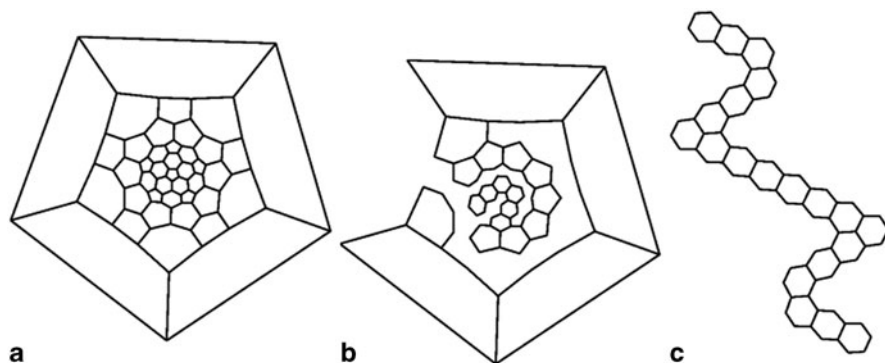
**Fig. 2.4** The  $C_{74-1}$  fullerene of symmetry  $D_{3h}$  and ring spiral (1,7, 9,11, 14,23, 26,28, 30,32, 35,38). The Schlegel diagram (a), the pattern in the Schlegel diagram (b), the pattern in the graphene lattice



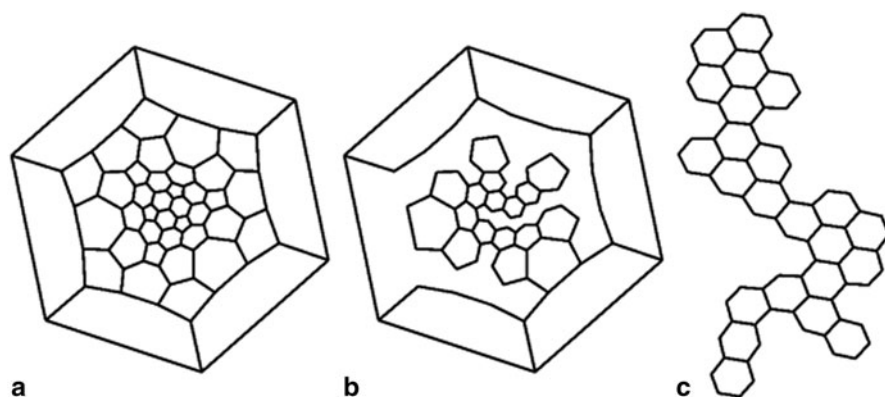
**Fig. 2.5** The  $C_{76-2}$  fullerene of symmetry  $T_d$  and ring spiral (1,7, 9,12, 14,21, 26,28, 30,33, 35,38). The Schlegel diagram (a), the pattern in the Schlegel diagram (b), the pattern in the graphene lattice



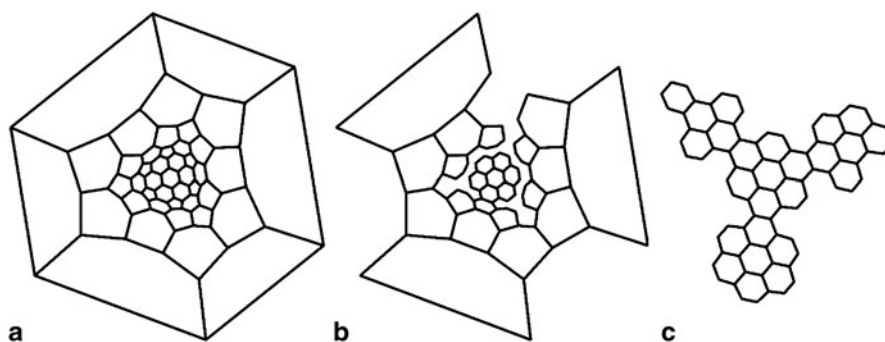
**Fig. 2.6** The  $C_{78-4}$  fullerene of symmetry  $D_{3h}$  and ring spiral (1,7, 9,11, 15,18, 22,25, 33,37, 39,41). The Schlegel diagram (a), the pattern in the Schlegel diagram (b), the pattern in the graphene lattice



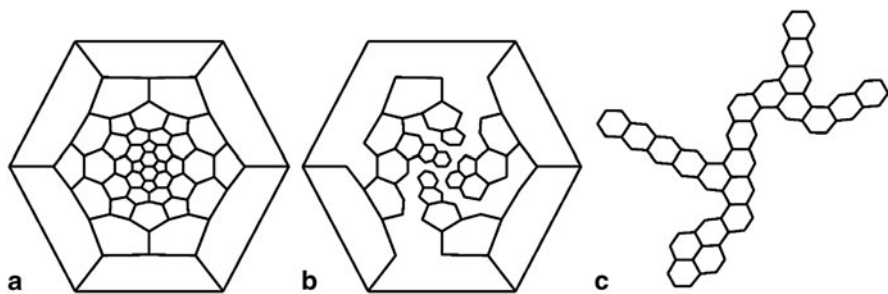
**Fig. 2.7** The  $C_{80,6}$  fullerene of symmetry  $D_{5h}$  and ring spiral (1,7, 10,12, 14,19, 26,28, 32, 34, 39,42). The Schlegel diagram (a), the pattern in the Schlegel diagram (b), the pattern in the graphene lattice



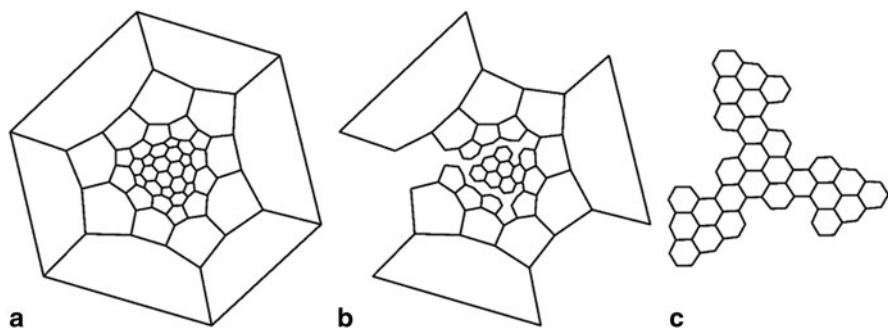
**Fig. 2.8** The  $C_{82,7}$  fullerene of symmetry  $C_{3v}$  and ring spiral (1,7, 9,12, 14,20, 27,32, 34,36, 38,40). The Schlegel diagram (a), the pattern in the Schlegel diagram (b), the pattern in the graphene lattice



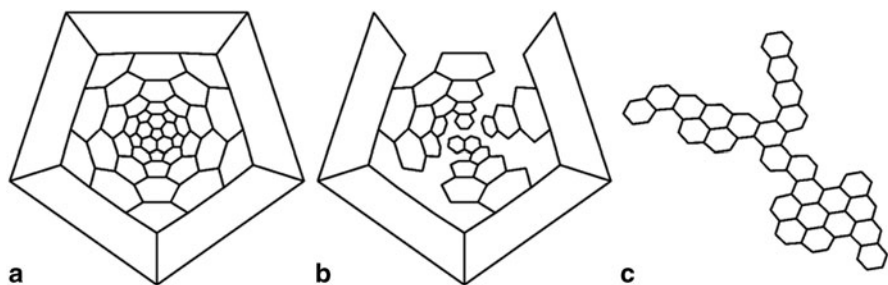
**Fig. 2.9** The  $C_{84,20}$  fullerene of symmetry  $T_d$  and ring spiral (1,7, 9,13, 20,23, 25,28, 33,37, 39,41). The Schlegel diagram (a), the pattern in the Schlegel diagram (b), the pattern in the graphene lattice



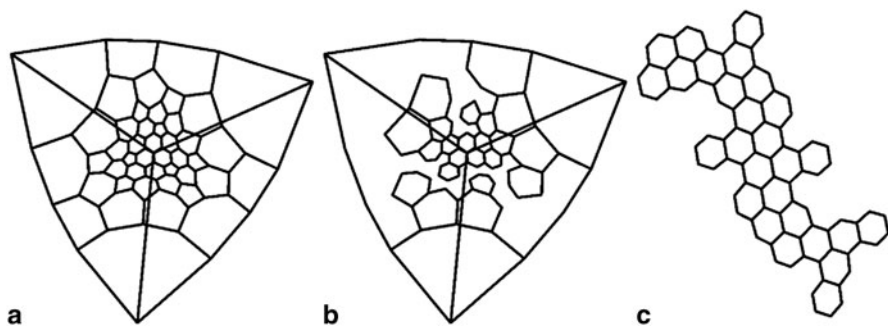
**Fig. 2.10** The  $C_{86_9}$  fullerene of symmetry  $C_{2v}$  and ring spiral (1,7, 9,11, 23,25, 27,29, 33,41, 43,45). The Schlegel diagram (a), the pattern in the Schlegel diagram (b), the pattern in the graphene lattice



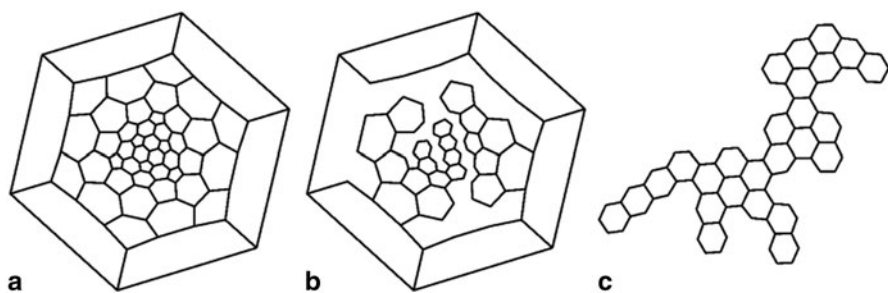
**Fig. 2.11** The  $C_{88_{34}}$  fullerene of symmetry  $T$  and ring spiral (1,7, 9,12, 24,27, 31,33, 35,38, 40,42). The Schlegel diagram (a), the pattern in the Schlegel diagram (b), the pattern in the graphene lattice



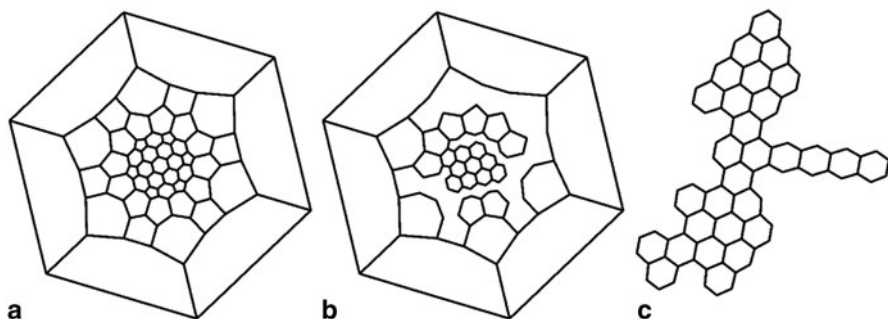
**Fig. 2.12** The  $C_{90_1}$  fullerene of symmetry  $D_{5h}$  and ring spiral (1,7, 9,11, 13,15, 37,39, 41, 43, 45,47). The Schlegel diagram (a), the pattern in the Schlegel diagram (b), the pattern in the graphene lattice



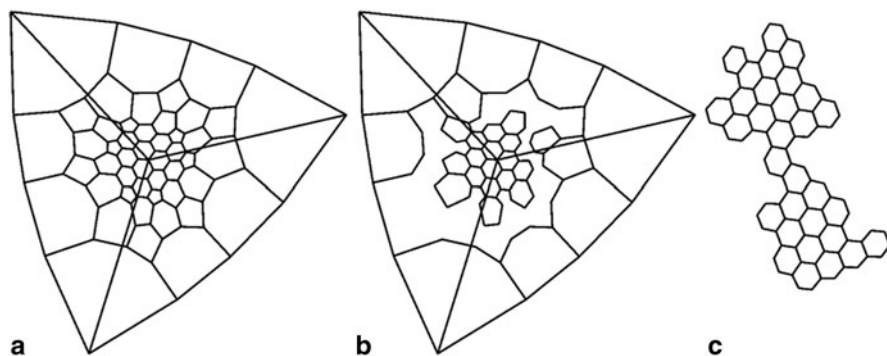
**Fig. 2.13** The  $C_{92,28}$  fullerene of symmetry  $D_3$  and ring spiral (1,7,9,11,24,26,30,32,34,37,39,48). The Schlegel diagram (a), the pattern in the Schlegel diagram (b), the pattern in the graphene lattice.



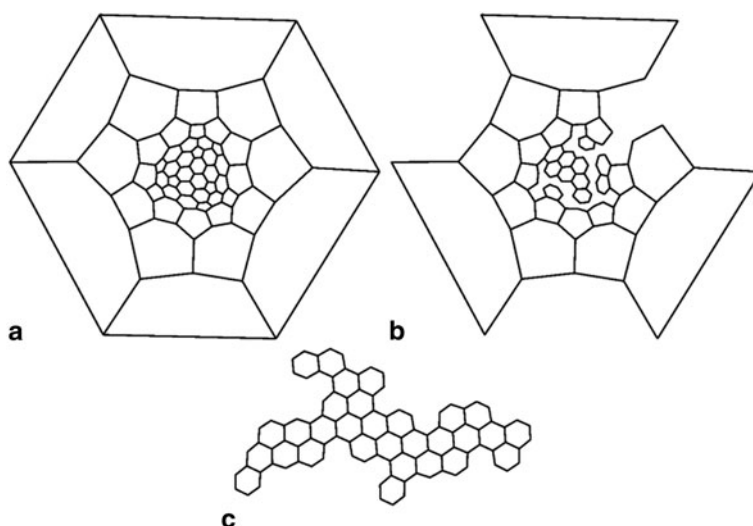
**Fig. 2.14** The  $C_{94,134}$  fullerene of symmetry  $C_{3v}$  and ring spiral (1,7,10,13,25,28,30,32,34,36,39,49). The Schlegel diagram (a), the pattern in the Schlegel diagram (b), the pattern in the graphene lattice



**Fig. 2.15** The  $C_{96,184}$  fullerene of symmetry  $D_{6h}$  and ring spiral (1,7,10,14,19,27,33,35,37,43,48,50). The Schlegel diagram (a), the pattern in the Schlegel diagram (b), the pattern in the graphene lattice



**Fig. 2.16** The  $C_{98_{66}}$  fullerene of symmetry  $D_{6h}$  and ring spiral (1,7, 9,11, 23,29, 34,36, 40, 42, 47,49). The Schlegel diagram (a), the pattern in the Schlegel diagram (b), the pattern in the graphene lattice



**Fig. 2.17** The  $C_{100_{321}}$  fullerene of symmetry  $T$  and ring spiral (1,7, 9,22, 24,27, 31,33, 36, 39, 41,51). The Schlegel diagram (a), the pattern in the Schlegel diagram (b), the pattern in the graphene lattice

## 2.4 Conclusions

We have shown that there are special graphene cut out patterns which can transform into predetermined structures in molecular dynamics simulations. The driving force of these transformations comes from the formation of new bonds during accidentally heat motion of the atoms. Such kind of formation process was observed in transmission electron microscopy experiment (Chuvilin et al. 2010).



Revising the recent experimental techniques it can be seen that they are not yet at the technical level to produce patterns with atomic precisions. In the laser-induced conversion of polycyclic aromatic hydrocarbon, however, the initial structure  $C_{60}H_{30}$  is very similar to our pattern of Fig. 2.1. In realistic experimental situations this initial structure turned into fullerene after removal of hydrogens by laser irradiation (Boorum et al. 2001; Scott et al. 2002). Thus if we include hydrocarbon patterns as well into the set of initial patterns their experimental production is much more possible than that of graphene cut out patterns. The graphene cut out patterns can give ideas for such possible hydrocarbon structures which can transform into the desired structures after removing the hydrogens by laser irradiation.

**Acknowledgements** The authors thank for the support of grant TAMOP-4.2.2.A-11/1/ KONV-2012-0029.

## References

- Allen MP, Tildesley DJ (1996) Computer simulation of liquids. Clarendon Press, Oxford
- Avouris P, Chen Z, Perebeinos V (2007) *Nat Nanotechnol* 2:605
- Bai JW, Duan XF, Huang Y (2009) *Nano Lett* 9:2083–2087
- Bai JW, Zhong X, Jiang S, Huang Y, Duan XF (2010) *Nat Nanotechnol* 5:190–194
- Beaton JM (1995) *J Chem Educ* 72:863
- Bell DC, Lemme MC, Stern LA, Rwilliams J, Marcus CM (2009) *Nanotechnology* 20:455301
- Björk J, Stafström S, Hanke F (2011) *J Am Chem Soc* 133:14884
- Boorum MM, Vasil'ev YV, Drewello T, Scott LT (2001) *Science* 294:828
- Chen Z, Lin Y, Rooks MJ, Avouris P (2007) *Physica E* 40:228–232
- Chuvilin A, Kaiser U, Bichoutsskaia E, Besley NA, Khlobystov AN (2010) *Nat Chem* 2:450
- Ci L, Xu ZP, Wang LL, Gau W, Ding F, Kelly KF, Yakobson BI, Ajayan PM (2008) *Nano Res* 1:116–122
- Datta SS, Strachan DR, Khamis SM, Johnson ATC (2008) *Nano Lett* 8:1912–1915
- Dimiev A, Kosynkin DV, Sinitskii A, Slesarev A, Sun Z, Tour JM (2011) *Science* 331:1168
- Dresselhaus MS, Dresselhaus G, Eklund PC (1996) *Science of fullerenes and carbon nanotubes*. Academic Press, New York
- Ebbesen TW, Hiura H (1995) *Adv Mater* 7:582–586
- Feng J, Li W, Qian X, Qi J, Qi L, Li J (2012) *Nanoscale* 4:4883–4899
- Fischbein MD, Drndić M (2008) *Appl Phys Lett* 93:3
- Fowler PW, Manolopoulos DE (1995) *San atlas of fullerenes*. Clarendon Press, Oxford
- Frenkel D, Smit B (1996) *Understanding molecular simulation*. Academic Press, San Diego
- Geim AK, Novoselov KS (2007) *Nat Mater* 6:183–191
- Girit CO, Meyer JC, Erni R, Rossell MD, Kisielowski C, Yang L, Park C-H, Crommie MF, Cohen ML, Louie SG, Zettl A (2009) Graphene at the edge: stability and dynamics. *Science* 323:1705–1708
- Han MY, Ozyilmaz B, Zhang YB, Kim P (2007) *Phys Rev Lett* 98:206805
- Hiura HF (2004) *Appl Surf Sci* 222:374–381
- Hoover WG (1985) *Phys Rev A* 31:1695–1697
- Huang JY, Ding F, Yakobson BI, Lu P, Qi L, Li J (2009) *Proc Natl Acad Sci U S A* 106:10103–10108
- Huang JY, Qi L, Li J (2010) *Nano Res* 3:43–50
- Jiao LY, Zhang L, Wang X, Diankov G, Dai H (2009) *Nature* 458:877–880
- Jiao LY, Wang XR, Diankov G, Wang HL, Dai HJ (2010) *Nat Nanotechnol* 5:321–325

- Kim T, Kirn H, Kwon SW, Kim Y, Park WK, Yoon DH, Jang AR, Shin HS, Suh KS Yang WS (2012) *Nano Lett* 12:743–748
- Kosynkin DV, Higginbotham, Sinitiskii A, Lomeda JR, Dimiev, Price BK, Tour JM (2009) *Nature* 458: 872–876
- Kroto HW, Heath JR, O'Brien SC, Curl RF, Smalley RE (1985) *Nature* 318:162–163
- László I, Zsoldos I (2012a) *Europhys Lett* 99:63001
- László I, Zsoldos I (2012b) *Phys Status Solidi* 249:2616–2619
- László I, Zsoldos I (2014) *Physica E* 56:422–426
- Lemme MC, Bell DC, Williams JR, Stern LA, Baughter BWH, Jarillo-Herrero P, Marcus CM (2009) *ACS Nano* 3:2674–2676
- Li X, Wang X, Zhang L, Lee S, Dai H (2008) *Science* 319:1229–1232
- McCarley RL, Hendricks SA, Bard AJ (1992) *J Phys Chem* 96:10089–10092
- Meyer JC, Girit CO Crommie MF, Zettl A (2008) *Appl Phys Lett* 92:123110
- Nosé S (1984) *Mol Phys* 52:255–268
- Novoselov KS, Geim AK, Morozov SV, Jiang D, Zhang Y, Dubonos SV, Grigorieva IV, Firsov AA (2004) *Science* 306:666–669
- Porezag D, Frauenheim T, Köhler T, Seifert G, Kaschner R (1995) *Phys Rev B* 51:12947–12957
- Scott LT, Boorum MM, McMahon BJ, Hagen S, Mack J, Blank J, Wegner H, de Meijere A (2002) *Science* 295:1500
- Shi ZW, Yang R, Zhang LC, Wang Y, Liu DH, Shi DX, Wang EG, Zhang GY (2011) *Adv Mater* 23:3061
- Sinitiskii A, Tour JM (2010) *J Am Chem Soc* 132:14730–14732
- Slater JC, Koster GF (1954) *Phys Rev* 94:1498–1524
- Song B, Schneider GF, Xu Q, Pandraud G, Dekker C, Zandbergen H (2011) *Nano Lett* 11:2247–2250
- Tapasztó L, Dobrik G, Lambin P, Bíró LP (2008) *Nat Nanotechnol* 3:397
- Verlet L (1967) *Phys Rev* 159:98–103
- Zhang LM, Diao SO, Nie YF, Yan K, Liu N, Dai BY, Xie Q, Reina A, Kong J, Liu ZF (2011) *J Am Chem Soc* 133:2006–2713

# Chapter 3

## Collective Excitations in Monolayer Graphene on Metals: Phonons and Plasmons

Antonio Politano and Gennaro Chiarello

**Abstract** In this chapter, we report on experiments on collective excitations in graphene/metal interfaces by means of electron energy loss spectroscopy. Many of the peculiar graphene's properties are related to its electronic collective excitations, even if their understanding is still missing. We have found a linear dispersion of the sheet plasmon in metals and such behaviour is attributed to the nonlocal screening of the plasmon mode of graphene caused by the underlying metal substrate. Due to its low energy and its linear dispersion, the sheet plasmon is expected to play an important role in graphene dynamics. This could be especially relevant for future graphene-based nano-optical devices, since the rippled, nanostructured surface of graphene on metal substrates provides an interesting scenario to couple acoustic surface plasmons and light. Measurements on plasmon modes also indicate that  $\pi$  electrons in graphene/metal interfaces behave as an interacting electron gas. We also report on collective modes due to the lattice dynamics of the graphene sheet. From experimental phonon dispersions, therefore it is possible to draw conclusions about the interaction strength in graphene/metal interfaces. Such investigation is of fundamental importance for graphene-based devices as both electronic and optical excitations can be scattered by phonon states or decay into vibrational excitations.

### Abbreviations

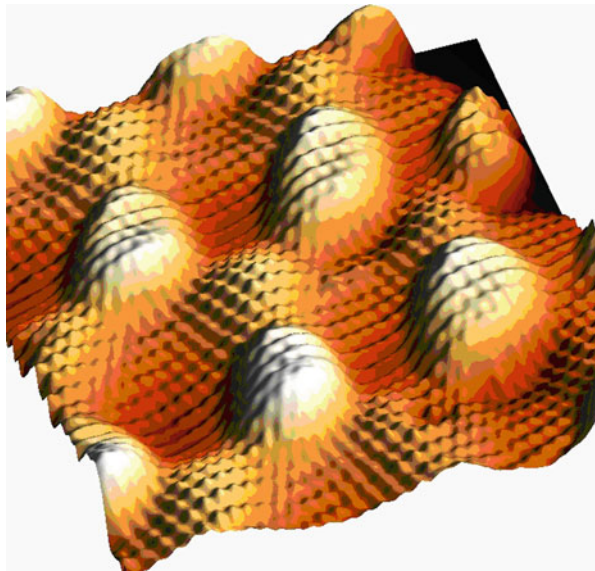
2DEG	(Two-dimensional electron gas)
AES	(Auger electron spectroscopy)
ARPES	(Angle-resolved photoemission spectroscopy)
ASP	(Acoustic surface plasmon)
CVD	(Chemical vapour deposition)
FWHM	(Full-width at half maximum)
HOPG	(highly oriented pyrolytic graphite)
HREELS	(High-resolution electron energy loss spectroscopy)
KA	(Kohn anomalies)

---

A. Politano (✉) · G. Chiarello  
Dipartimento di Fisica, Università degli Studi della Calabria, 87036 Rende (Cs), Italy  
e-mail: antonio.politano@imdea.org

© Springer Science+Business Media Dordrecht 2015  
M. V. Putz, O. Ori (eds.), *Exotic Properties of Carbon Nanomatter*,  
Carbon Materials: Chemistry and Physics, DOI 10.1007/978-94-017-9567-8\_3

**Fig. 3.1** Periodically rippled graphene



LEED	(Low-energy electron diffraction)
MLG	(Monolayer graphene)
SPE	(Single-particle excitation)
UHV	(Ultra-high vacuum)
VA-SWCNT	(Vertically-aligned single-walled carbon nanotubes)

### 3.1 Preface

Graphene, a single atom-thick sheet of graphite (Novoselov et al. 2006), is an allotropic form of carbon that allows a low energy manifestation of Quantum Electrodynamics at surfaces (Novoselov et al. 2005). Graphene is an extraordinary material that presents fascinating new properties due to the linear energy dispersion of the conduction and valence bands near the Fermi level, giving rise to massless charge carriers that behave as Dirac fermions with a group velocity  $\approx 1/300$  of the speed of light (Novoselov et al. 2005), exhibit chiral behavior, display ballistic transport of charge (room temperature mobilities of up to  $1.5 \times 10^4 \text{cm}^2/\text{V}\hat{\text{A}}\cdot\text{s}$ ) and spin (spin relaxation length up to microns) and an anomalous, half-integer Quantum Hall Effect at 300 K (Giesbers et al. 2009). (Fig. 3.1)

Graphene is lightweight, inexpensive, robust, chemically stable. Moreover, the use of graphene for transparent conducting electrodes (Nair et al. 2010), to realize photosensitive transistors (Cao et al. 2009), ultracapacitors (Wang et al. 2009), or novel chemical sensors (Yang et al. 2010) is envisioned.

Graphene was realized experimentally in 2004 (Novoselov et al. 2004). Since then, there has been intense interest in this material, stemming both from graphene's unusual physical properties and from the possible applications of graphene in high-speed analogical or digital electronics, electro-mechanical systems, sensors, energy storage, etc (Lee et al. 2010). In particular, the high mobility of electrons in graphene and the strong electric field effect encourage work to realize graphene-based electronics (Wu et al. 2008).

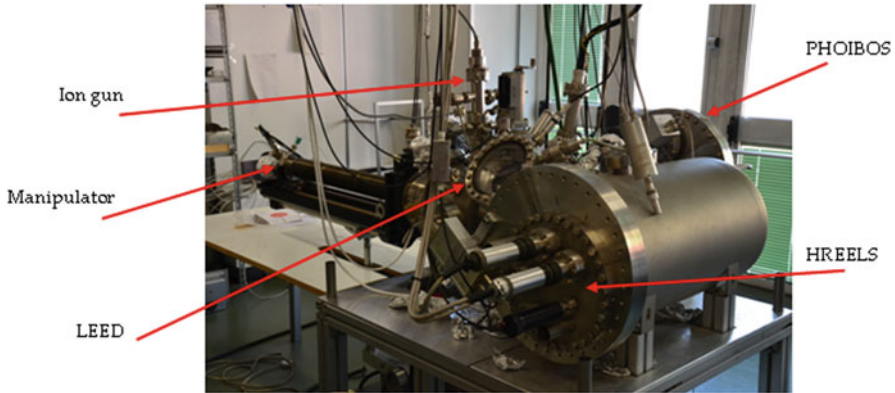
Graphene is manufactured mainly in three ways: by exfoliation from HOPG (Hale et al. 2011), by the epitaxial growth in silicon carbide (Wu et al. 2009) and by the epitaxial growth on metals (Politano et al. 2011a, b; Borca et al. 2010; Martoccia et al. 2010). The initial methods of preparation of graphene by peeling graphite or vaporizing SiC suffered from an inherent lack of control and were not scalable and they have been replaced almost universally by methods to grow controlled epitaxial graphene on different substrates.

Graphene layers were grown on the surfaces of many transition metals upon annealing in a hydrocarbon atmosphere. What is nowadays a technique, was an unwanted side effect in catalytic processes, as it lead to the passivation of catalysts, known as poisoning. The chemical deposition of carbon on metal substrates has been extensively studied from the 1970s to 1990s (Shikin et al. 1998, 1999). A major motivation for studying these graphite films was the passivation of catalysts by carbon films known as poisoning, but the properties of graphene were not investigated in detail.

The epitaxial growth of large, highly perfect graphene monolayers is indeed a prerequisite for most practical applications of this “wonder” material. Most of these epitaxial graphene layers are spontaneously nanostructured in a periodic array of ripples by the Moiré patterns caused by the difference in lattice parameter with the different substrates such as Ru(0001) (Borca et al. 2010), Ir(111) (Müller et al. 2011) or Pt(111) (Politano 2011c, d; 2012a, b, c). The careful characterization of these superlattices is important because nanostructuring graphene (in superlattices, stripes or dots), in turn, may reveal new physical phenomena and fascinating applications. In addition, it is crucial to understand the interaction of graphene with the surfaces of substrates of different nature (oxides, semiconductors or metals), as well as with adsorbed molecules, in view of the relevance of metallic contacts, and the sensitivity of the conduction properties of graphene to gating materials and doping by adsorbed molecules (Politano 2011a, c).

All these topics can be characterized in detail in what has become one of the benchmarks for epitaxial graphene: a self-organized, millimeter large, periodically “rippled” epitaxial monolayer of graphene grown by soft CVD under UHV conditions on single crystal metal substrates with hexagonal symmetry. The superb control that allows the UHV environment facilitates the characterization of the system down to the atomic scale.

In this chapter we report on HREELS investigations on both the vibrational and electronic properties of graphene grown on Pt(111).



**Fig. 3.2** UHV chamber

In Sect. 3.2, we introduce our measurement techniques, in Sects. 3.3. and 3.4 LEED and HREEL spectroscopy has been used for studying MLG epitaxially grown on Pt(111) surface.

Our studies have clarified that acoustic-like plasmons exist in epitaxial graphene. We have also found that graphene/Pt(111) is characterized by phonon modes which are very similar to that ones of graphite. In particular, KAs are found in this system, in contrast with results for graphene/Ni(111). This finding is ascribed to the quasi-freestanding nature of the graphene sheet on Pt(111).

## 3.2 Experimental Methods

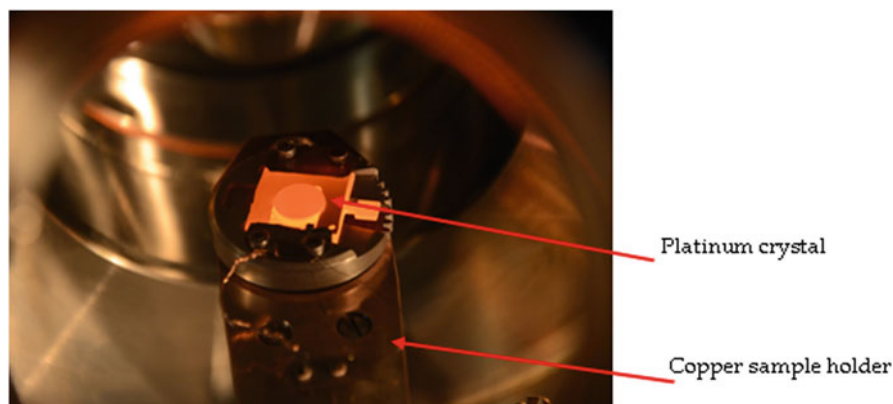
### 3.2.1 UHV Chamber

In Fig. 3.2 is shown the UHV chamber (with a base pressure of  $5\hat{A}\cdot 10^{-9}\text{Pa}$ ) used for our experiments.

Our system is a stainless steel vacuum chamber with a variety of pumps attached, which allows us to obtain UHV. The pumps used on our system include a scroll pump, two turbo pumps, a titanium sublimation pump and an ion pump. It is equipped with an electron analyser (Phoibos 100, Specs), a high-resolution electron energy loss spectrometer (Delta 0.5, Specs, Figs. 3.8, 3.9), an apparatus for low-energy electron diffraction, a quadrupole spectrometer, and an ion gun for sputtering. Leak valves are used for controlled gas inlet in the UHV chamber.

AES and LEED were used as control techniques for checking the cleanliness of the order of the surface.

The sample was a single crystal of Pt(111), delivered from MaTecK GmbH (Germany). The substrate was cleaned by repeated cycles of ion sputtering and annealing at 1300 K. (Fig. 3.3)



**Fig. 3.3** Sample holder

### 3.2.2 The EELS Technique

EELS is an experimental technique that permit the study of materials through the analysis of their electronic and vibrational excitations. In contrast to infrared spectroscopy, EELS is not limited by strict dipole selection rules, which often hinder observation of important modes and adsorbates. In EELS both long-range *dipole* and short-range *impact* scattering mechanisms are operable and they may be effectively studied as a function of scattering angle and impact energy. Information obtained from EELS ideally complements data obtained with other surface spectroscopies, and offers ease of interpretation for the experimentalist.

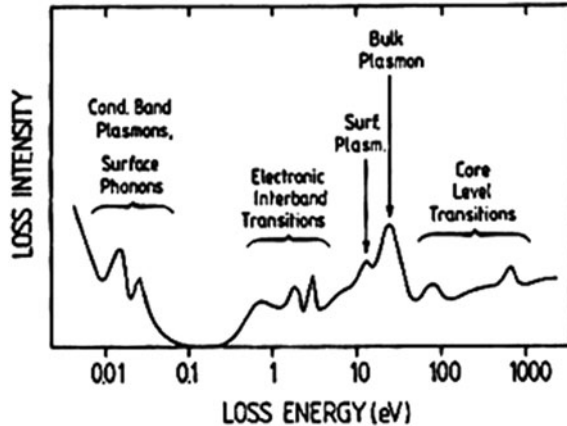
In this spectroscopy, a monochromatic electron beam is sent to the surface of a solid material, these primary electrons are partially inelastically scattered and their kinetic energy distribution is analyzed using an electron energy analyzer (Ibach and Mills 1982), the energy losses are due to the excitation of electronic and vibrational transition of the investigated materials and so provide a tool for analysing them. The EELS technique can be used in various configurations by changing the geometrical and physical parameters. For example different spectra and information can be obtained by changing the electronic energy or the incidence angle of the impinging primary beam, or the angle of analysis of diffused electrons (Ibach and Mills 1982).

The various excitations in a EEL spectrum cover a wide energy range which extends from some meV, as for phonons and vibrations of atoms or molecules adsorbed onto the surface, some eV, as for interband transitions and plasmonic excitations, up to hundreds of eV, as for the excitations of core electrons (Lüth 1995) (Fig. 3.4).

Energy losses are due mainly to three processes:

1. excitations of network vibrations of atoms on the clean surface (optical phonons surface, acoustic phonons surface) and/ or vibrations of atomic and molecular species adsorbed on the surface;

**Fig. 3.4** Regions of characteristic losses



2. excitations of valence band transitions that can be divided into single particles electronic excitations (inter-band and intra-band excitations) and collective excitations (surface, volume and interface plasmons);
3. excitations of core levels electrons to conduction band levels.

The mentioned excitations hold a very large energy range, which extends from around tens meV (for phonons) up to a few thousands eV needed to excite core electrons to states above the Fermi level.

Thus, EELS plays an important role in the investigation of surface chemical reactions (Politano et al. 2008) and dynamic screening properties (Politano 2011d) of metal systems.

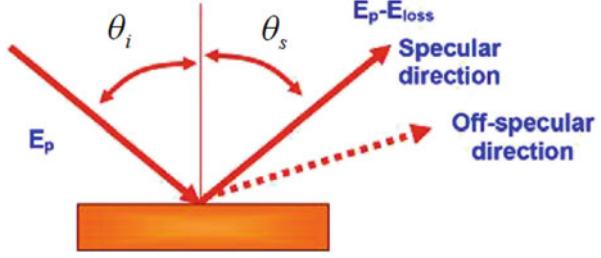
The great diffusion of this technique in the last two decades is mainly due to the development of a new generation of high-resolution EEL spectrometers by prof. Harald Ibach (Ibach 1993; Ibach et al. 1996), whose resolution ranges from 0.5 to 5 meV. This allows HREELS to have an energy resolution similar to inelastic helium atom scattering (Benedek et al. 2001) and optical techniques as infrared absorption spectroscopy (Hoffmann and Weisel 1992) or second-harmonic generation (Balzer and Rubahn 2000). The recent development of novel spectrometers for spin-polarized EELS (Ibach et al. 2006) is expected to further contribute to the diffusion of this spectroscopy.

The analysis of kinetic energy of electrons inelastically back-scattered provides information about excited modes at the surface. Electrons scattered from the sample are analyzed as a function of  $E_{loss} = \Delta E = E_p - E_s$ , where  $E_{loss}$  is the energy lost by electrons,  $E_p$  is the primary electron beam energy, and  $E_s$  is the energy of scattered electrons. If the electron excites a surface mode  $\hbar\omega_0$ , after the interaction with the sample its energy will be  $E_s = E_p - \hbar\omega_0$ . Hence, if electrons lost  $E^*$  they will give rise to loss peaks at energy  $E_p - E^*$ .

In inelastic processes the energy change should equal the quantum energy of an electronic or vibrational surface mode, by respecting conservation laws of energy



**Fig. 3.5** Scattering geometry in HREELS experiments



and wave-vector parallel to the surface.

$$\begin{cases} E_{loss} = E_p - E_s \\ \hbar \vec{q}_{||} = \hbar(\vec{k}_i \sin \theta_i - \vec{k}_s \sin \theta_s) \end{cases} \quad (3.1)$$

Where  $q_{||}$  is the parallel momentum transfer,  $\vec{k}_i$  is the wave-vector of incident electrons,  $\vec{k}_s$  is the wave-vector of scattered electrons,  $\theta_i$  and  $\theta_s$  are the angles formed with the normal to the surface by incident and scattered electrons, respectively (Fig. 3.5).

Thus an expression linking  $q_{||}$  with  $E_p$ ,  $E_{loss}$ , and  $\theta_i$ ,  $\theta_s$  could be obtained:

$$q_{||} = \frac{\sqrt{2mE_p}}{\hbar} \left( \sin \theta_i - \sqrt{1 - \frac{E_{loss}}{E_p}} \sin \theta_s \right) \quad (3.2)$$

Likewise, it is possible to obtain the indeterminacy on  $q_{||}$ , that is the window in the reciprocal space which also depends on the angular acceptance of the apparatus  $\alpha$  (Rocca 1995), usually ranging between 0.5 and 1.0 degrees:

$$\Delta q_{||} = \frac{\sqrt{2mE_p}}{\hbar} \left( \cos \theta_i - \sqrt{1 - \frac{E_{loss}}{E_p}} \cos \theta_s \right) \cdot \alpha \quad (3.3)$$

Thus  $\Delta q_{||}$  is minimized for low impinging energies and for grazing scattering conditions.

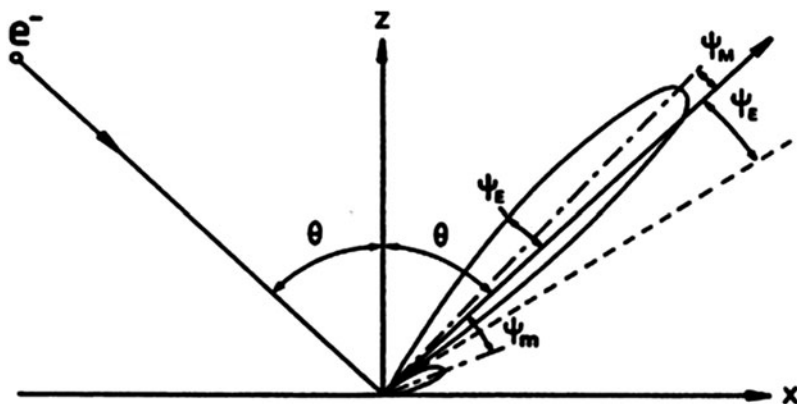
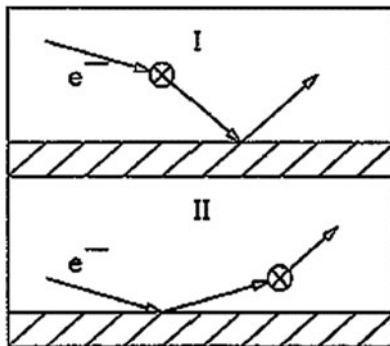
Three scattering mechanisms for impinging electrons are possible: *dipole*, *impact* and *resonant scattering* (Ibach and Mills 1982). The last mechanism is prevalent for molecules in gaseous phase (see Ref. (Ibach and Mills 1982) for more details) and thus it is not important for plasmonic excitations.

Concerning *dipole scattering*, it is worth remembering that the Coulombian field produced by incoming electrons interacts at long range (about 100 Å) with the surface. Loss events may occur both before and after diffusion from the surface (Rocca 1995), as shown in Fig. 3.6.

According to Mills (Mills 1975), the differential cross section  $d^2S/d\omega d\Omega$ , is given by:

$$\frac{d^2S}{d\omega d\Omega} = \frac{(mev_{\perp})^2}{2\pi^2\hbar^5 \cos \theta_i} \frac{k_s}{k_i} \frac{P(q_{||}, \omega)}{q_{||}^2} \frac{|v_{\perp} q_{||} (R_s + R_i) + i(R_s - R_i)(\omega - v_{||} q_{||})|^2}{[(v_{\perp} q_{||})^2 + (\omega - v_{||} q_{||})^2]^2} \quad (3.4)$$

**Fig. 3.6** Loss events before (I) and after (II) diffusion from the surface



**Fig. 3.7** Angular dependence of dipole scattering and its concentrations in a lobe with semi-amplitude  $\Psi_E$  along specular directions

where  $v_{\parallel}$  are  $v_{\perp}$  the parallel and perpendicular components of the velocity of impinging electrons with respect to the surface, respectively, and  $P(q_{\parallel}, \omega)$  is the surface loss function.  $R_i$  and  $R_s$  are the amplitude of complex reflectivity for initial and final energies. The maximum inelastic scattering occurs for  $\omega = v_{\parallel}q_{\parallel}$ , in correspondence of a minimum in the denominator of (3.4). Such condition corresponds to the interaction of electrons with partial waves with phase velocity  $\omega/q_{\parallel} = v_{\parallel}$ . By defining  $\theta$  as the deviation from trajectory of electrons inelastically scattered from specular direction, thus for  $\hbar\omega \ll E_p$  and  $\theta \ll 1$ , the denominator of (3.4) may be written as:

$$(v_{\perp}q_{\parallel})^2 + (\omega - v_{\parallel}q_{\parallel})^2 = 4E_i^2 (\theta^2 + \Psi_E^2) \cos^2\theta; \tag{3.5}$$

where  $\Psi_E = \hbar\omega/2E_p$ . The Eq. (2.6) determines the angular dependence of dipole scattering and its concentrations in a lobe with semi-amplitude  $\Psi_E$  along specular directions. Dipole scattering dominates for small transfer momenta.

As shown in Fig. 3.7, a principal maximum exists (which corresponds to the condition  $\omega = v_{\parallel}q_{\parallel}$ ), even if a secondary maximum also exists.

For short-range interactions *impact scattering* occurs. Within this scattering mechanism, electrons are diffused in every possible solid angle, even beyond the incidence plane. Both perpendicular and parallel component of the wave-vector (with respect to the sample normal) are not conserved. As a consequence of such complexity, theory which describes such interactions is not deeply developed. The cross section is defined as (Ibach and Mills 1982):

$$\frac{d\sigma}{d\Omega} = \frac{mE_p \cos^2 \theta_s}{2\pi^2 \hbar^2 \cos \theta_i} |M|^2 \quad (3.6)$$

where  $M$  is the matrix element for the transition and  $m$  is the mass of electrons. The cross section presents only minimal changes with scattering angle.

### 3.2.3 HREEL Spectrometer

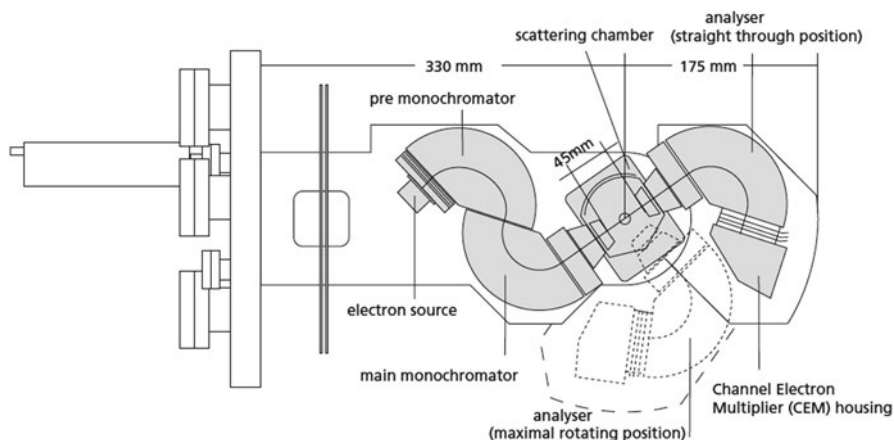
We used an instrument manufactured by SPECS GmbH under licence of Forschungszentrum Jülich, Germany, distributed worldwide under the name DELTA 0.4. This spectrometer, designed by prof. Harald Ibach and shown in Figs. 3.8–3.9, is constituted by a two-step monochromator and by a rotating analyser which the peculiarity of having 151 ° cylindrical deflectors. This results in an ultimate resolution of 0.5 meV and a significant increase of intensity in the high resolution range.

The basic concept of the DELTA 0.5 spectrometer is a fixed double stage monochromator and a rotatable single stage analyser. In order to allow the probing of the largest possible fraction of the surface BZ the maximum rotation angle of the DELTA 0.5 analyzer stage was increased to > 90 °. The impact energy is variable from 0 to 250 eV.

## 3.3 Phonon Modes of Epitaxial Graphene

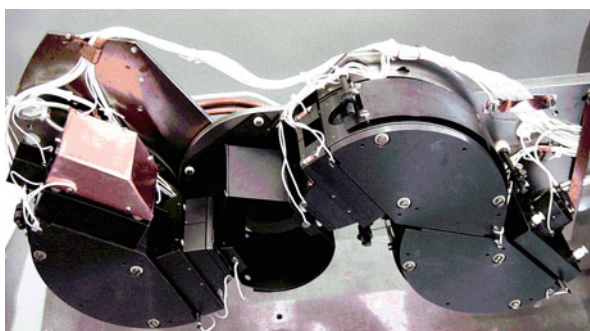
### 3.3.1 Structure of Graphene on Pt(111)

The graphene-metal interface is a model system where the interaction between the graphene  $\pi$ -bands and the metal bands can be investigated. This has relevance to contacting of graphene with metal electrodes. The carbon hybridization and also the epitaxial relationship with the metal substrate were proposed to influence the contact transmittance (Nemec et al. 2006) and cause local doping of graphene (Giovannetti et al. 2008). A variety of situations regarding the interplay of graphene and its metal support is realized depending on the support material. One type with strong bonding between metal graphene and a typical metal-graphene distance smaller than a metal-metal bond (around 1.4–2.2 Å) and one with weak bonds and a typical metal-graphene distance which is much larger than the bonds between the substrate atoms (around 3.2–3.7 Å).



**Fig. 3.8** Schematics of the DELTA0.5 HREELS spectrometer, designed by Prof. Harald Ibach and commercialized by SPECS

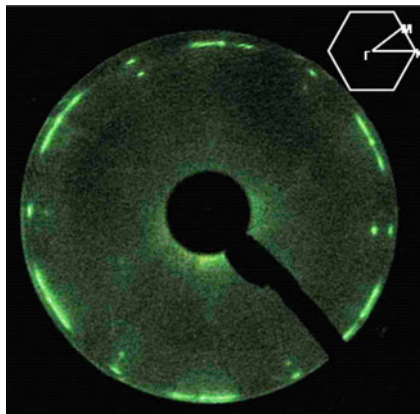
**Fig. 3.9** DELTA0.5 HREELS spectrometer, designed by Prof. Harald Ibach and commercialized by SPECS



The difference in bonding also reflects in the phonon modes of graphene. A softening of the phonon modes indicating weakened C-C bonds is observed in the case of strong binding, whereas in the case of weak binding the phonon frequencies stay close to the bulk values known from HOPG (Benedek and Onida 1993). The electronic structure ranges from almost no interaction in the case of Pt(111) (Politano 2011c) to deep a modification in the case of a graphene monolayer on Ni(111) (Wang et al. 2011) or Ru(0001) (Borca et al. 2009, 2010).

For platinum the lattice constant is  $a = 3.92 \text{ \AA}$  and the nearest neighbour distance between atoms is  $d = 2.77 \text{ \AA}$ . For graphene the lattice constant is  $a = 2.46 \text{ \AA}$  and the nearest neighbour is  $d = 1.42 \text{ \AA}$ . As can be seen from a comparison of the close-packed layer of atoms of the Pt(111) surface and the honeycomb structure of graphene, they both have hexagonal symmetry. This similarity should make Pt(111) a natural fit for growing well-ordered graphene on the surface. However, the presence of a difference in lengths of the lattice constants, results in a mismatch of approximately 11 %.

**Fig. 3.10** LEED pattern of graphene on Pt(111), recorded at  $E_p = 74.7$  eV and for a sample temperature of 100 K



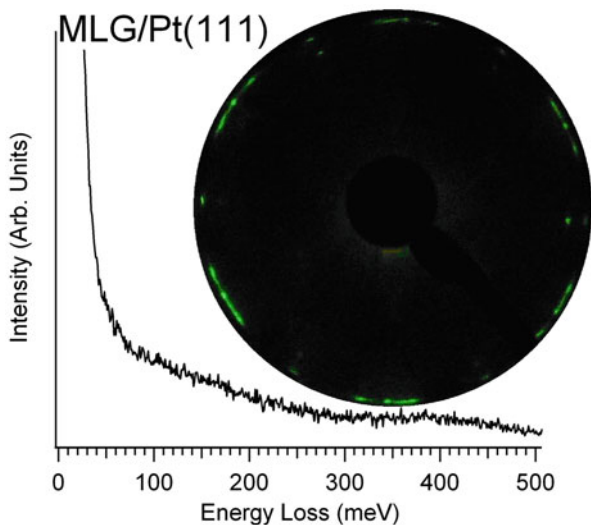
Such system is ideal for a study of phonon modes and elastic properties due to the absence of corrugation of the graphene overlayer found on other substrates (Borca et al. 2009, 2010) which has been demonstrated to be caused by the hybridization with the substrate. The growing strength of hybridization is accompanied by a gradual change in graphene morphology from nearly flat for MLG/Pt(111) to strongly corrugated in MLG on other substrates (Preobrajenski et al. 2008). Thus, MLG on Pt(111) behaves as nearly-flat free-standing graphene, as also confirmed by angle-resolved photoemission spectroscopy experiments (Sutter et al. 2009).

Graphene was obtained by dosing ethylene onto the clean Pt(111) substrate held at 1150 K. At a certain temperature, the hydrocarbon is catalytically dissociated and hydrogen desorbs, remaining carbon adsorbed species can then form graphene. Moreover, the high temperature of the sample during depositions favours the increase of the size of MLG islands (Zhang et al. 2009) and allows maintaining the substrate clean so as to avoid any contaminant-induced effect on graphene growth. The completion of the first layer was reached upon an exposure of  $3 \hat{\text{A}} \cdot 10^{-8}$  mbar for ten minutes ( $24 \text{ L}, 1 \text{ L} = 1.33 \hat{\text{A}} \cdot 10^{-6}$  mbar $\hat{\text{A}} \cdot \text{s}$ ). After removing the  $\text{C}_2\text{H}_4$  gas from the chamber the temperature was held at 1150 K for further 60 s.

The attained LEED pattern (shown in Figs. 3.10, 3.11) is essentially similar to that one reported in Ref. (Gao et al. 2011). The ring pattern indicates the existence of different domains. Nonetheless, preferred orientations aligned with the substrate ( $R_0$ ) are clearly distinguished. The presence of well-resolved spots in the LEED pattern is a clear fingerprint of the order of the MLG over-structure, also evidenced by the high electron reflectivity of the obtained surface (even higher with respect to the bare Pt substrate). (Fig. 3.11)

Despite the presence of other domains, the predominance of  $R_0$  in the whole sample has been clearly inferred by the analysis of phonon dispersion measurements performed along the  $\bar{\Gamma} - \bar{K}$  and the  $\bar{\Gamma} - \bar{M}$  directions (inset of Fig. 3.10).

**Fig. 3.11** HREEL spectrum of MLG/Pt(111), recorded with an impinging energy of 4 eV and in specular scattering conditions. In the inset the LEED pattern recorded with  $E_p = 74.7$  eV is reported



### 3.3.2 Phonon Dispersion

The dynamics of atoms at surfaces plays an important role in many chemical and physical processes. In particular, lattice vibrations can afford essential information on many physical properties, such as thermal expansion, heat capacity, sound velocity, magnetic forces, and thermal conductivity (Chis and Benedek 2011). Recently, phonon modes of graphene sheets are attracting much attention (Allard and Wirtz 2010) as they influence many of the novel and unusual properties of graphene (Efetov and Kim 2010).

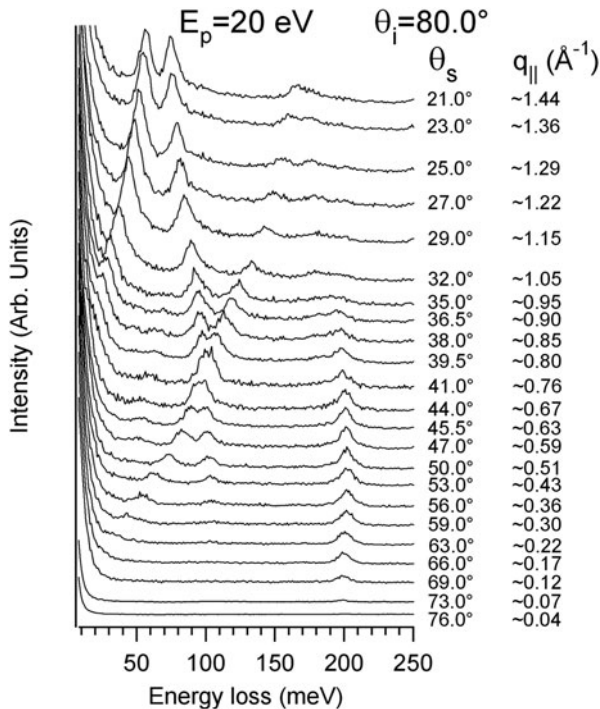
Due to the high energy of phonon modes in graphitic materials, several techniques as inelastic helium atom scattering can not be used. Infrared or Raman spectroscopy can not probe the whole Brillouin zone, while neutron or inelastic ion scattering are not always applicable. Among various detection methods for phonon dispersion, HREELS is a powerful tool to gain knowledge on phonons in graphene.

Present HREELS measurements show the dispersion relation of phonon modes in MLG/Pt(111). Results have been compared with recent calculations in Ref. (Karssemeijer and Fasolino 2011).

The energy resolution of the spectrometer was degraded to 4 meV so as to increase the signal-to-noise ratio of loss peaks. Dispersion of the loss peaks, i.e.,  $E_{\text{loss}}(q_{\parallel})$ , was measured by moving the analyzer while keeping the sample and the monochromator in a fixed position (See Chap. 2). To measure the dispersion relation, values for the parameters  $E_p$ , impinging energy and  $\theta_i$ , the incident angle, were chosen so as to obtain the highest signal-to-noise ratio. The primary beam energy used for the dispersion,  $E_p = 20$  eV, provided, in fact, the best compromise among surface sensitivity, the highest cross-section for mode excitation and  $q_{\parallel}$  resolution.

All measurements were made at room temperature.

**Fig. 3.12** HREEL spectra for MLG/Pt(111) in the  $\bar{\Gamma} - \bar{k}$  direction as a function of the scattering angle. The incidence angle is  $80.0^\circ$  and the impinging energy is 20 eV



The phonon dispersion was measured along the  $[\bar{2}11]$  direction of the Pt substrate which corresponds to the  $\bar{\Gamma} - \bar{K}$  direction of the MLG.

Loss measurements of MLG/Pt(111) recorded at  $E_p = 20$  eV as a function of the scattering angle  $\theta_s$  are reported in Fig. 3.12, while the dispersion relation  $E_{\text{loss}}(q_{\parallel})$  is shown in Fig. 3.13.

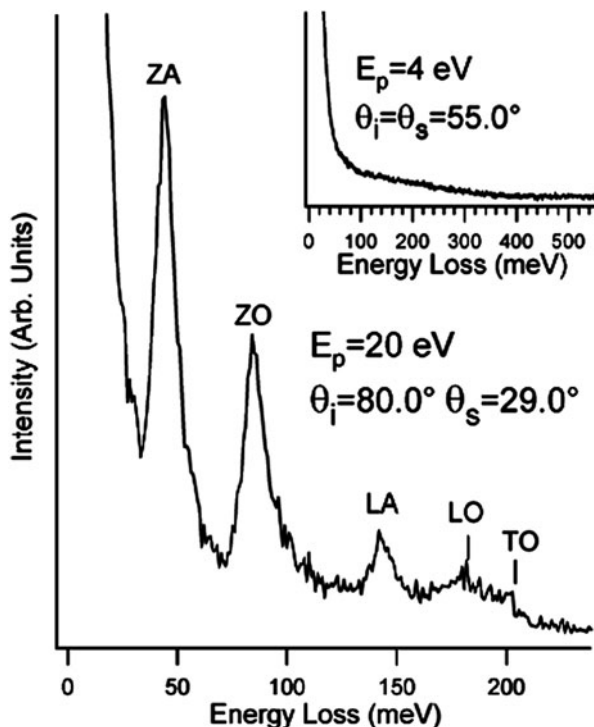
Measurements were repeated for several preparations of the MLG over-structure also by using different impinging energies and incident angles. All these experiments provided the same phonon dispersion. Such reproducibility further support the occurrence of a predominant graphene domain.

HREEL spectra show several dispersing features as a function of the scattering angle, all assigned to phonon excitations (Fig. 3.12). The energy and the dispersion of phonon modes indicate a negligible interaction between MLG and the underlying Pt substrate, in agreement with previous works. Accordingly, MLG may be considered as a quasi-freestanding sheet physisorbed on the underlying Pt substrate.

As for graphite (Wirtz and Rubio 2004), vibrations of the graphene lattice are characterized by two types of phonons: those ones vibrating in the plane of the sheet with transverse and longitudinal acoustic (TA and LA) and optical (TO and LO) branches, and those ones with vibrations out of the plane of the layer—the so-called flexural phonons (ZA and ZO). Modes classified with “T” are shear in-plane phonon excitations; “L” modes are longitudinal in-plane vibrations; while “Z” indicates out-of-plane polarization. In general, the ZO mode is significantly softened with respect



**Fig. 3.13** Phonon modes of graphene



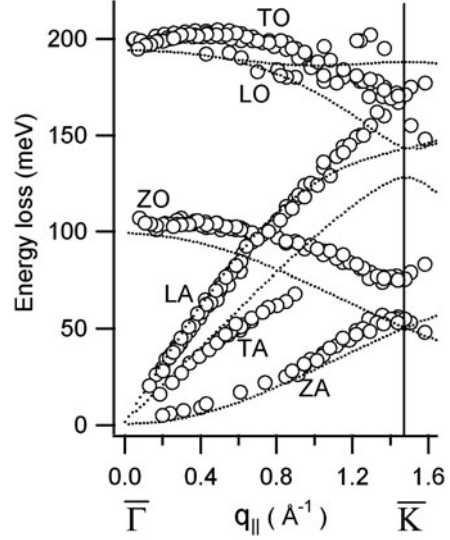
to the other two optical modes, i.e. TO and LO. This is due to the higher freedom for atom motion perpendicularly to the plane with respect to the in-plane motion. All observed phonons are similar to those ones of bulk graphite.

This is quite expected for modes associated with vibrations of carbon atoms in the direction of the  $\sigma$  bonds, i.e. the LA and LO phonons (except a stiffening of the LO mode at  $\bar{\Gamma}$  by 5 meV). In particular, a careful comparative analysis with respect to graphite showed a softening of the TA mode (with a maximum difference of 18 meV). On the other hand, by comparing the phonon dispersion relation of MLG/Pt(111) with that one recorded for MLG/Ni(111) (Shikin et al. 1999; Farías et al. 2000), we notice a significant energy shift by 10–15 meV at the  $\bar{\Gamma}$  point for the ZA and ZO modes, which are connected to perpendicular vibrations of carbon atoms with respect to the surface. In particular, in MLG/Ni(111) the ZA phonon is stiffened while the ZO mode is softened with respect to MLG/Pt(111). This is caused by of the orbital mixing of the  $\pi$ -states of the MLG with Ni d-bands (Mittendorfer et al. 2011).

A particular attention should be devoted to the ZA phonon, as it was recently found that the ZA modes in suspended graphene carry most of the heat (Seol et al. 2010). It is a bending mode in which the two atoms in the unit cell are involved in an in-phase motion in the out-of-plane direction. At long wavelengths it bends the MLG sheet so as to induce rippling in graphene. While the TA and the LA phonons are



**Fig. 3.14** Dispersion relation for phonon modes in MLG/Pt(111) in the  $\bar{\Gamma} - \bar{k}$  direction (empty circles). The dotted line represents the calculated phonon dispersion



characterized by a linear dispersion, the ZA mode has a quadratic dispersion near the  $\bar{\Gamma}$  point (Fig. 3.14), as also in layered crystals (Hartmut 2001). Its dispersion depends on the bending rigidity  $\tau$ , which is an important parameter for mechanical properties of membranes:

$$\omega_{ZA}(q_{||}) = \sqrt{\frac{\tau}{\rho_{2D}}} |\vec{q}_{||}|^2$$

where  $\rho_{2D} = 4m_C/(3\sqrt{3}a^2)$  is the two-dimensional mass density ( $m_C$  is the atomic mass of carbon atoms;  $a$  is the in-plane lattice parameter). We found that the bending rigidity  $\tau$  could be estimated to be about 2 eV, in agreement with results in Ref. (Perebeinos and Tersoff 2009).

The dispersion relation of phonons in MLG/Pt(111) have been compared with recent calculations for free-standing graphene derived from Long-range Carbon Bond Order Potential (Karssemeijer and Fasolino 2011) (dotted line in Fig. 3.14). In particular, we note an excellent agreement with calculations for the LA mode. The recorded dispersion for the flexural phonon ZA apparently does not match the behavior predicted by theory. However, it is worth remembering that the bending rigidity strongly depends on temperature and an increase by about 40 % was found in the range 0–300 K (Fasolino et al. 2007). The temperature dependence of the bending rigidity implies that also the ZA mode should depend on temperature. Hence, comparison of the calculated dispersion of ZA phonons at 0 K with experiments at 300 K is not straightforward.

Interestingly, the ZA/ZO degeneracy at  $\bar{k}$ , predicted by theoretical calculations for free-standing graphene (Karssemeijer and Fasolino 2011) and bulk graphite (Maultzsch et al. 2004), is lifted and a “gap” of 20 meV in MLG/Pt(111) appears.

Allard and Wirtz demonstrated in Ref. (Allard and Wirtz 2010) that this is a direct consequence of symmetry reduction in supported graphene systems. In fact, for free-standing graphene all carbon atoms of the graphene unit cell are equivalent, while for adsorbed graphene both atop and three-fold adsorption sites exist. Thus, some atoms are directly connected to the substrate while other ones are unconnected. In the ZA mode, the unconnected atoms are performing a perpendicular motion while the bonded atoms are at rest. For the ZO branch, the opposite occurs. This implies a higher energy for the ZA phonon. Thus, the ZA/ZO gap can be taken as a fingerprint for graphene adsorption on solid substrates, in fact, it occurs also for MLG/Ni(111) (Shikin et al. 2009; Aizawa et al. 1990). By decoupling the MLG from the substrate through Ag intercalation, the gap can be removed (Farfás et al. 1999, 2000).

By contrast, the degeneracy of LA and LO phonons at  $\bar{K}$  was observed, even if the energy of such degenerate mode at  $\bar{K}$  is blue-shifted by 25 meV with respect to the calculated value in Refs. (Viola et al. 2009) and (Karssemeijer and Fasolino 2011).

### 3.3.3 KAs

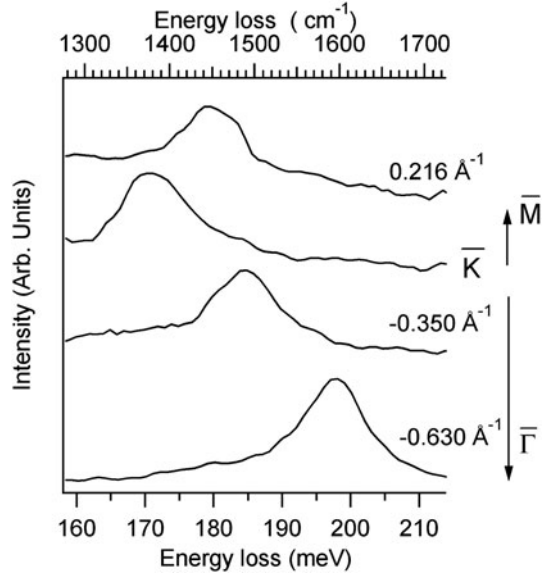
Atomic vibrations could be screened by electrons and, moreover, screening can change rapidly for vibrations associated with high-symmetry points of the Brillouin zone. This phenomenon leads to an anomalous behaviour of the phonon dispersion around such points, which is called KA (Kohn 1959). Their occurrence is completely determined by the shape of the Fermi surface.

Inelastic x-ray scattering experiments (Piscanec et al. 2004) that graphite exhibits two KAs for the  $\bar{\Gamma} - E_{2g}$  and  $\bar{K} - A'_1$  modes. In details, only the highest optical branches (HOB) show KAs, which are evidenced in the phonon dispersion curve by two sharp kinks. Their existence is intimately related to the dispersion of the  $\pi$  bands around the high-symmetry point  $\bar{K}$ .

With regard to graphene, several theoretical studies predicted the existence of KAs (Lazzeri and Mauri 2006). However, recently it has been demonstrated (Allard and Wirtz 2010) that the electron-phonon coupling in epitaxial graphene systems can be strongly modified by the interaction with the underlying metal substrate. Allard and Wirtz (Allard and Wirtz 2010), analyzing previous phonon measurements (Shikin et al. 1999) performed on MLG grown on a Ni(111) surface suggested a complete suppression of KAs for such system. Therein it was suggested that the absence of KAs in MLG/Ni(111) is caused by the hybridization of the graphene  $\pi$ -bands with the Ni d bands which lifts the linear crossing of the  $\pi$  bands at  $\bar{K}$ .

Experiments on phonon dispersion showed that, in contrast with the case of MLG/Ni(111), KAs could be detected in MLG/Pt(111). We ascribe this finding to the nearly quasi-freestanding behaviour of  $\pi$  bands in this system. Such results could be important to evaluate the interaction strength between the graphene layer and the underlying metallic substrate.

**Fig. 3.15** HREEL spectra for MLG/Pt(111) as a function of the scattering angle around the high-symmetry point  $\bar{K}$ . The incident angle is fixed to  $86.0^\circ$  with respect to the sample normal



MLG/Pt(111) loss spectra around the high-symmetry point  $\bar{K}$  show (Fig. 3.15) a softening by about 30 meV of the TO mode (characterized by  $A'_1$  symmetry), which reaches a minimal loss energy at  $\bar{K}$  (172 meV).

The impinging energy is 20 eV. All measurements have been carried out at room temperature.

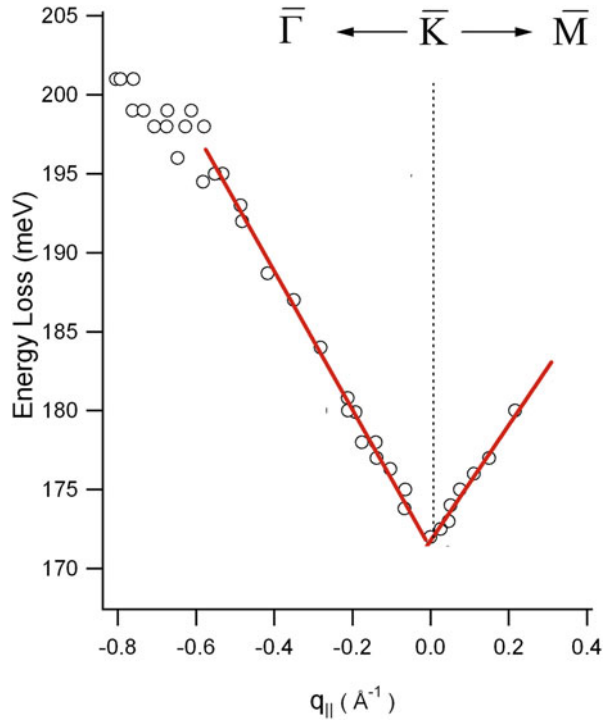
Figures 3.16 and 3.17 report the dispersion relation of the HOB as a function of  $q_{||}$  around the  $\bar{K}$  and  $\bar{\Gamma}$  symmetry points, respectively. The most striking feature of these dispersions is the discontinuity in the derivative of the HOB ( $A'_1$  and  $E_{2g}$ , respectively) at  $\bar{K}$  and  $\bar{\Gamma}$ , which is a direct evidence of the existence of KAs. This should be put in relationship with the abrupt change in the screening of lattice vibrations by conduction electrons. On the other hand, for MLG/Ni(111), the dispersion of the HOB is almost flat at both  $\bar{K}$  and  $\bar{\Gamma}$  symmetry points. This means that the interaction with the substrate leads to a complete suppression of KAs, as a consequence of the strong hybridization of the graphene  $\pi$ -bands with Ni d-bands (Giovannetti et al. 2008). In fact, the hybridization induces around  $\bar{K}$  the appearance of a “gap” of almost 4 eV between unoccupied and occupied  $\pi$ -bands.

## 3.4 Electronic Collective Excitations in Epitaxial Graphene

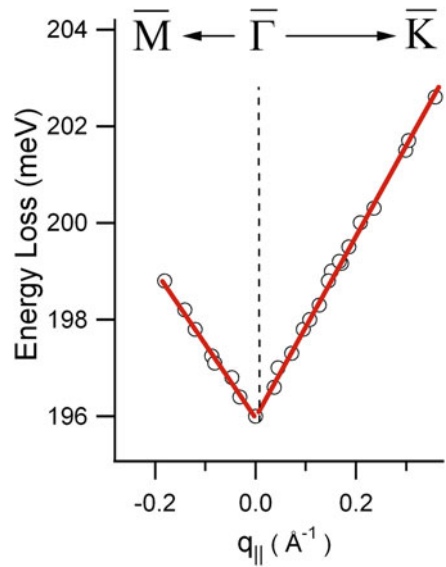
### 3.4.1 General Consideration on Plasmons in Graphene

Low-energy collective excitations in graphene are attracting much interest in recent years (Apalkov et al. 2007) as they influence many of the peculiar properties of graphene samples. In particular, the dispersion and damping of plasmons in epitaxial

**Fig. 3.16** Graphene HOB in the nearness of the  $\bar{K}$  of the Brillouin zone.



**Fig. 3.17** Graphene HOB in the nearness of the  $\bar{\Gamma}$  of the Brillouin zone.



graphene have recently been studied for the case of graphene deposited on SiC(0001) (Langer et al. 2010; Tegenkamp et al. 2011) and Ir(111) (Langer et al. 2011). The understanding of plasmonic excitations of graphene plays a key role in tailoring the properties of novel graphene-based devices (Bostwick et al. 2010).

Indeed, many of the peculiar graphene's properties are related to its electronic collective excitations (Yuan et al. 2011; Yan et al. 2011), even if their understanding is still missing. In particular, it is essential to shed the light on plasmon modes in graphene/metal interfaces to understand dynamical processes and screening in such systems.

The electronic structure of MLG on Pt(111) resembles that of isolated graphene (Sutter et al. 2009). In particular, the linear dispersion of  $\pi$  bands in the so-called Dirac cones, which gives rise to many manifestations of massless Dirac fermions, is preserved. ARPES experiments do not show any remarkable hybridization of graphene  $\pi$  states with metal  $d$  states. They just represent a superposition of graphene and metal-derived states, with minimal interaction between them. The MLG on Pt(111) is hole doped by charge transfer to the Pt substrate (Gao et al. 2010). The Fermi energy  $E_F$  of the graphene layer shifts  $0.30 \pm 0.15$  eV below the Dirac-energy crossing point of the bands, with the Fermi wave vector  $k_F = 0.09 \text{ \AA}^{-1}$ . Epitaxial graphene on Pt(111) thus behaves as an ideal 2D system, sustaining a purely 2DEG system whose collective excitations (plasmon modes) are able to propagate along the sheet. The dielectric response of the 2DEG system is determined by plasmon dispersion, which could be measured by high-resolution electron energy loss spectroscopy.

The 2D plasmon, characterized by its square-root-like dispersion, has been predicted (Stern 1967) and observed in metal layers on semiconductors (Nagao et al. 2001a, b). On the other hand, the ASP with a linear dispersion was demonstrated to exist on semiconductor quantum wells with two interacting quantum well minibands (Chen et al. 1989). Successively, ASP has been experimentally revealed on Be(0001) (Diaconescu et al. 2007) and on noble-metal surfaces (Park and Palmer 2010; Pohl et al. 2010). The acoustic-like dispersion is a consequence of the combination of the nonlocality of the 3D response and the spill-out of the 3D electron density into the vacuum, both providing incomplete screening of the 2D electron-density oscillations.

Previous measurements on MLG/SiC(0001) showed a nonlinear dispersion for the sheet plasmon in MLG. Such behaviour could be described by the Stern's model (Stern 1967). It is interesting to study the behaviour of collective excitations of MLG grown on a metal substrate in order to shed light on the screening mechanisms of the sheet plasmon in the presence of an underlying metal substrate. Present measurements by HREELS show a linear dispersion for the sheet plasmon in MLG/Pt(111). Our results indicate that the sheet Plasmon of MLG survives up to a high energy, i.e., 3 eV. This is a consequence of the fact that intraband excitations have negligible influence on the propagation of the plasmon mode. On the other hand, the dispersion curve of the sheet Plasmon overlaps with the continuum of interband transitions above the Fermi wave vector. This broadens the plasmon peak but does not cause its disappearance, in contrast with the behaviour found for ordinary sheet plasmons in 2DEG and ASP.

### 3.4.2 Evidence for Acoustic-Like Plasmons

To measure plasmon dispersion (see Sect. 3.2), values for the parameters  $Ep$ , impinging energy, and  $\theta_i$ , the incident angle, were chosen so as to obtain the highest signal-to-noise ratio. The primary beam energy used for the dispersion,  $Ep = 7\text{--}12$  eV, provided, in fact, the best compromise among surface sensitivity, the highest cross section for mode excitation and momentum resolution.

To obtain the energies of loss peaks, a polynomial background was subtracted from each spectrum. The resulting spectra were fitted by a Gaussian line shape (not shown herein). All measurements were made at room temperature.

Measurements were performed for both symmetry directions ( $\Gamma\text{--}K$  and  $\Gamma\text{--}M$ ), but no remarkable differences were recorded as a consequence of the existence of differently oriented domains on the sample, as observed in previous low-energy electron microscopy experiments (Sutter et al. 2009). Loss measurements of MLG/Pt(111) recorded as a function of the scattering angle  $\theta_s$  are reported in Fig. 3.18. HREEL spectra show a low-energy feature which develops and disperses up to 3 eV as a function of the scattering angle. This resonance exhibits a clear linear dispersion and its frequency approaches zero in the long-wavelength limit. We assign it to the sheet plasmon of MLG, in agreement with theoretical (Hill et al. 2009; Horing 2010a; Hwang and Das Sarma 2007, 2009; Hwang et al. 2010) and experimental (Langer et al. 2010, 2011; Tegenkamp 2011; Liu and Willis 2010; Lu et al. 2009) results.

The dispersion of the sheet plasmon for MLG on SiC(0001) well agrees with Stern's (Stern 1967) prediction ( $\omega \propto \sqrt{q_{\parallel}}$ ). However, the plasmon dispersion recorded in our experiments (Fig. 3.19) is well described by a linear relationship, as in the case of ASP on bare metal surfaces (Diaconescu et al. 2007; Park and Palmer 2010; Pohl et al. 2010):

$$\hbar\omega_{2D} = Aq_{\parallel}$$

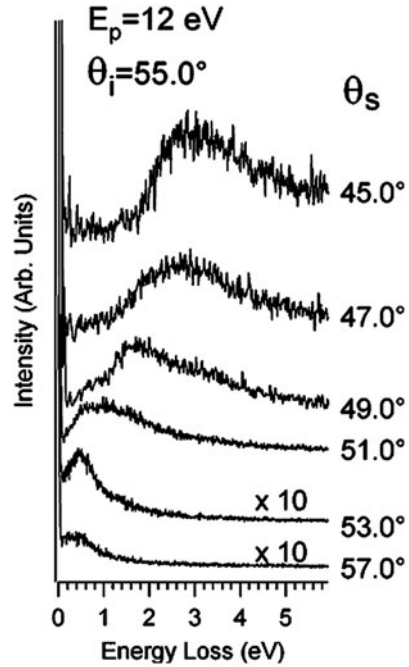
where  $A = 7.4 \pm 0.1$  eV Å.

The sheet plasmon with a linear dispersion owes its existence to the interplay of the underlying metal substrate with the  $\pi$ -charge density in the MLG in the same region of space. It resembles the ASP in metal surfaces that support a partially occupied surface state band within a wide bulk energy gap (Silkin et al. 2004, 2005).

The nonlocal character of the dielectric function (Horing 2010b) and the screening processes in graphene (Yan et al. 2011; Schilfgaarde and Katsnelson 2011) prevent the sheet plasmon from being screened out by the 3D bulk states of Pt(111).

Recently, Horing (Horing 2010a) predicted that the linear plasmon in graphene systems may arise from the Coulombian interaction between the native sheet plasmon ( $\omega \propto \sqrt{q_{\parallel}}$ ) in MLG and the surface plasmon of a nearby thick substrate hosting a semi-infinite plasma. Calculations taking into account the electronic response of the Pt substrate could in principle put this effect in evidence, but this is not trivial due to the existence of a Moiré reconstruction in the MLG lattice on top of the Pt(111) substrate. The slope of the dispersion relation of the sheet plasmon in MLG/Pt(111)

**Fig. 3.18** HREEL spectra of MLG/Pt(111) acquired as a function of the scattering angle. The incident angle is  $54.0^\circ$ . The impinging energy  $E_p$  is 12 eV



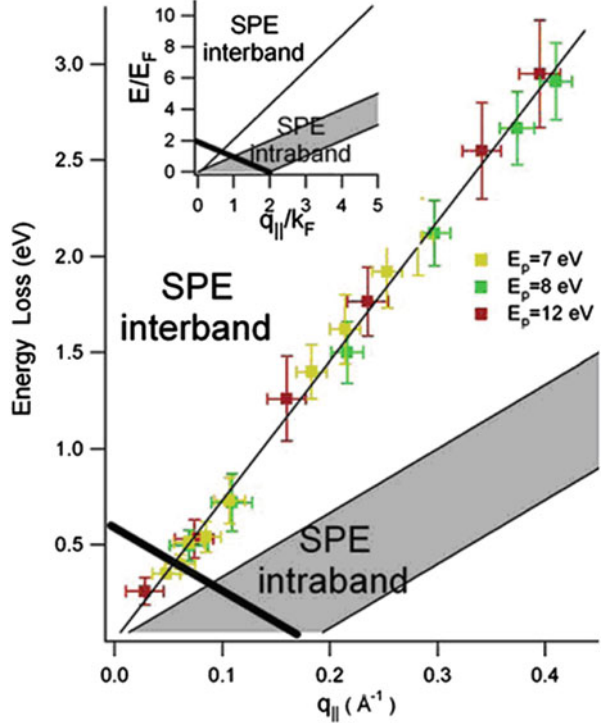
and the ones of acoustic-like excitations provide information about group velocities of the plasmon mode. We found that the group velocity of the sheet plasmon in MLG/Pt(111) ( $1.1 \pm 0.2 \times 10^6 \text{ m/s}$ ) is similar to the ones calculated for ASP (Silkin et al. 2005). The group velocity of the sheet plasmon in MLG/Pt(111) is about 2 orders of magnitude lower than the speed of light, thus its direct excitation by light is not possible. However, nanometer-size objects at surfaces, such as atomic steps or molecular structures, can allow coupling between sheet plasmon and light.

The linear behaviour of its dispersion implies that both phase and group velocities of the collective excitation are the same, so signals can be transmitted undistorted along the surface. Hence, this finding could be of significant importance in future graphene-based nano-optical devices, especially if we have in mind that the Moiré pattern of MLG on metal substrates offers a naturally nanostructured system (Borca et al. 2010).

In Fig. 3.19, we also show the electron-hole continuum or SPE region, which determines the absorption (Landau damping) of the external field at given frequency.

It was calculated on the basis of results in Refs. (Hwang and Das Sarma 2007; Hwang et al. 2010; Polini et al. 2008) by substituting the values of  $E_F$  and  $k_F$  for MLG/Pt(111) obtained by ARPES (Sutter et al. 2009). For a normal 2D system, only indirect transition is possible within the band. However, for graphene, both intraband and interband transitions are possible, and the boundaries are given in Fig. 3.19. Due to the phase-space restriction, the interband SPE continuum has a gap at small momenta.

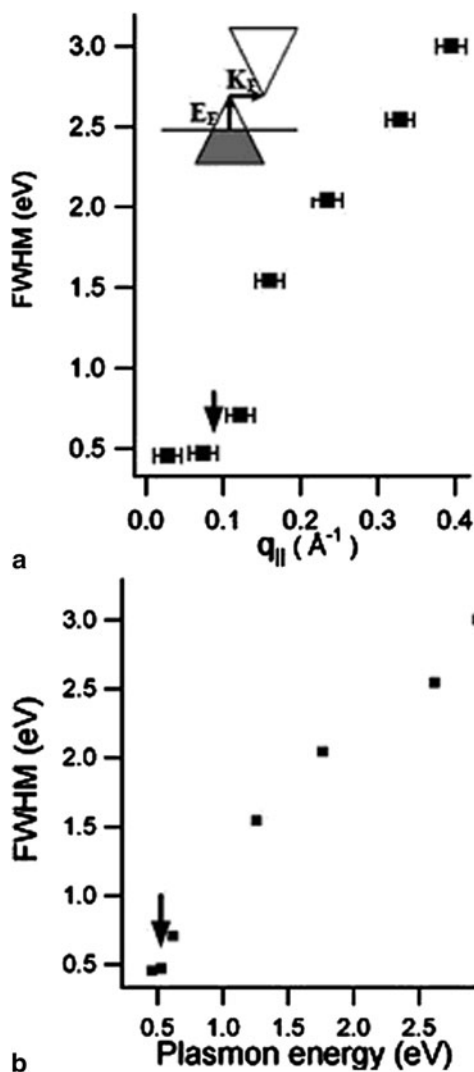
**Fig. 3.19** Plasmon dispersion in MLG/Pt(111). Data have been acquired for three different impinging energies. The thin solid line represents the best fit for experimental points. The dashed area indicates the continuum of intraband SPEs. The thick solid line represents the boundary for the continuum of interband SPEs. The plasmon mode enters the Landau damping regime by interband electron-hole excitations when its dispersion relation intercepts the boundary for the continuum of interband SPEs. In the inset, the curves are reported with respect to the dimensionless units  $E/E_F$  and  $q_{||}/k_F$



For  $q_{||} = 0$ , the transition is not allowed at  $0 < E < 2E_F$ . If the collective mode enters the SPE continuum, the plasmon mode can be damped. The plasmon lies inside the interband SPE continuum, thus decaying into electron-hole pairs, above the Fermi wave vector. Plasmon can propagate without damping only in the region (see Fig. 3.19) not included in the continuum of SPE (interband and intraband). Such considerations are fully confirmed by the analysis of the FWHM of the plasmon peak as a function of both  $q_{||}$  [Fig. 3.20] and the plasmon energy [Fig. 3.20]. Landau damping for the MLG sheet plasmon occurs for momenta above the Fermi wave vector (about  $0.09 \text{ \AA}^{-1}$ ) and for energies above 0.5 eV, as revealed by the sudden increase of the FWHM. Interestingly, the sheet plasmon does not enter into the intraband SPE continuum and it exists for all wave vectors. By contrast, for ASP, Landau damping occurs via intraband transitions and the plasmon mode exists only up to a few hundreds meV (Diaconescu et al. 2007; Park and Palmer 2010; Pohl et al. 2010). On the other hand, for MLG on SiC(0001), the FWHM continuously increases with the momentum (Langer et al. 2010; Liu et al. 2008). For such system, it has been shown (Langer et al. 2010) that the existence of steps or grain boundaries is a source of strong damping, while the dispersion is rather insensitive to defects.



**Fig. 3.20** FWHM of the plasmon peak as a function of **a** the parallel momentum transfer  $q_{\parallel}$  and of **b** the plasmon energy. The inset in the top panel shows the origin of interband SPEs from  $\pi$  to  $\pi^*$  bands. The Fermi wave vector represents the onset where plasmon enters the damping region



### 3.4.3 Dispersion and Damping Processes of $\pi$ Plasmon

The electronic response of graphene systems is related to the collective excitations of the electrons which combine in-plane and inter-plane interactions. Herein we want to investigate the nature and the dispersion of  $\pi$  plasmon in MLG grown on a metal substrate. The  $\pi$  plasmon is a sensitive probe of the graphene band structure near the Fermi level (Sun et al. 2010). Its physical origin is the electric dipole transition between the  $\pi$  energy bands ( $\pi \rightarrow \pi^*$ ) mainly in the region of the M

point of the Brillouin zone of graphitic systems. Recently, it has been demonstrated (Yan et al. 2011) that in the presence of a free-electron substrate the plasmonic excitation of the graphene sheet are nearly completely quenched, as a consequence of the dynamical Coulomb interaction between induced charges in the substrate and graphene. However, in the case of graphene on Ni(111), the  $\pi$  plasmon was found to exist (Generalov and Dedkov 2012). It is thus interesting to characterize the  $\pi$  plasmon mode also in the case of a graphene sheet weakly bonded to the metal substrate, as occurs for MLG/Pt(111).

HREELS measurements show a quadratic dispersion for the  $\pi$  plasmon in MLG/Pt(111), in contrast with results obtained for MLG/6H-SiC(0001) (Lu et al. 2009) and in agreement with very recent findings for MLG/Ni(111) (Generalov and Dedkov 2012). However, the quadratic coefficient of the dispersion relation of  $\pi$  plasmon in MLG/Pt(111) is higher by a factor  $\sim 8$  with respect to the case of MLG/Ni(111) while it is similar to the value reported for graphite.

Moreover, we found that the plasmon peak is blue-shifted by about 1.5 eV with respect to free-standing graphene and MLG/6H-SiC(0001). The presence of the metal substrate also decreases the lifetime of the plasmonic excitation, as evidenced by a careful analysis of its damping processes.

To measure the dispersion relation, primary beam energies,  $E_p = 30\text{--}70$  eV, were used. Spectra recorded for MLG on Pt(111) with the substrate oriented in the  $\bar{\Gamma} - M$  direction are reported in Fig. 3.21a (for a primary energy  $E_p$  of 70 eV) and 3.21b (for  $E_p = 30$  eV).

It is worth mentioning that, due to the very weak intensity of loss peaks ( $\approx 10^{-4}$  with respect to the intensity of the elastic peak), an acquisition time of several hours has been required for each spectrum to reach a sufficient signal-to-noise ratio. All measurements were made at room temperature.

A peak showing clear dispersion from 6.2 to 8.2 eV has been recorded as a function of the parallel momentum transfer  $q_{\parallel}$ . It has been assigned to  $\pi$  plasmon of graphene, in agreement with previous (Lu et al. 2009; Generalov and Dedkov 2012; Kramerberger et al. 2008; Rosei et al. 1984) works.

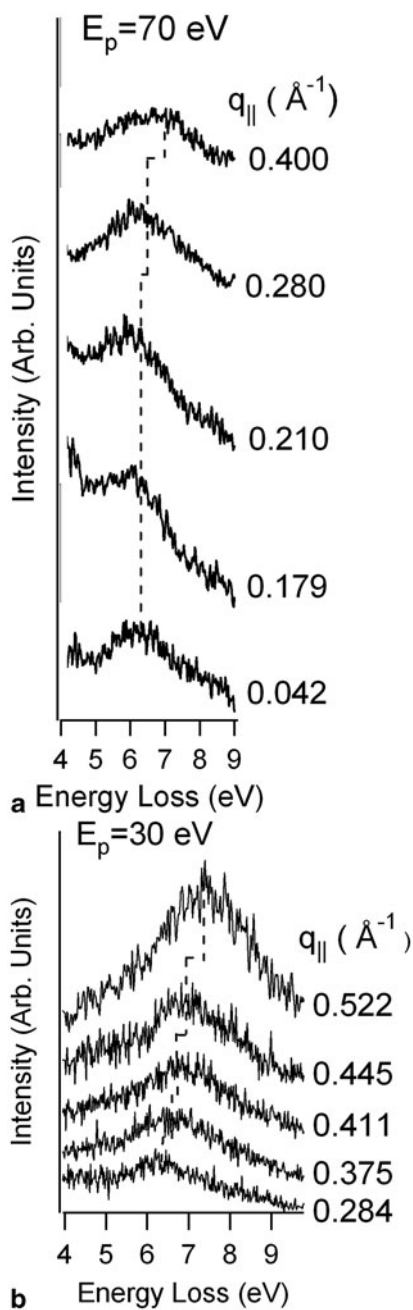
The intensity of the backscattering yield around the  $\pi$  plasmon energy versus the off-specular angle clearly demonstrates that the plasmon mode has a dipolar nature because it is nearly peaked in the specular direction (Rocca 1995; Politano et al. 2009).

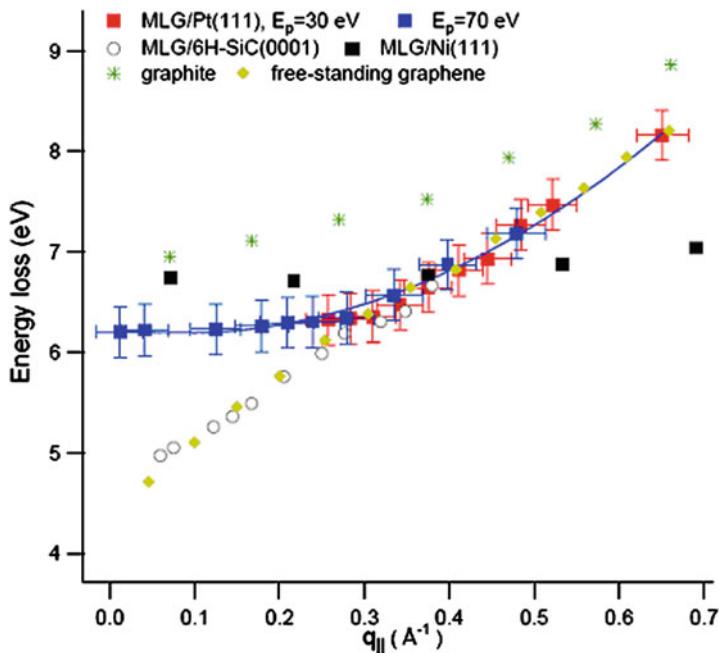
The measured dispersion curve  $E_{loss}(q_{\parallel})$  in Fig. 3.22 was fitted by a second-order polynomial given by:

$$E_{loss}(q_{\parallel}) = E_{loss}(0) + Aq_{\parallel}^2 = E_{loss}(0) + \alpha \frac{\hbar^2}{m} q_{\parallel}^2$$

Where  $E_{loss}(0) = (6.2 \pm 0.1) \text{ eV}$ ,  $A = (4.1 \pm 0.2) \text{ eV} \cdot \text{\AA}^2$ ,  $\alpha = 0.53$ .

**Fig. 3.21** HREEL spectra for MLG/Pt(111) as a function of the parallel momentum transfer  $q_{\parallel}$ . **a** Loss spectra acquired by using an impinging energy of 70 eV and an incidence angle of  $65^\circ$ . **b** Spectra acquired with an impinging energy of 30 eV and an incidence angle of  $55^\circ$ .





**Fig. 3.22** Dispersion relation of the  $\pi$  plasmon for MLG/Pt(111) (our data, acquired for two different scattering geometries), MLG/Ni(111), MLG/6H-SiC(0001), graphite and calculations for free-standing graphene

The same measurements were repeated for the  $\bar{\Gamma} - \bar{K}$  direction, giving a similar dispersion. This is a consequence of the existence on the sample of differently oriented domains with a preferential orientation aligned with respect to the substrate (Sect. 3.3 (Gao et al. 2011)). These findings agree with the conclusions of previous low-energy electron microscopy experiments (Sutter et al. 2009).

Important information on graphene systems is provided by the analysis of the frequency of the  $\pi$  plasmon in the long-wavelength limit ( $q_{||} \approx 0$ ), reported in Table 3.1 for various carbon-based systems. It can be noticed that it ranges between 4.7 eV (free-standing graphene) [2010] and 6.5–7.0 eV (graphite).

As regards graphite, it is important to notice that  $\pi$  plasmon energy in the long-wavelength limit (small momenta) strongly depends on the modality of the EELS experiment. In fact, EELS measurements in the reflection mode provide an energy of 6.5 eV (Diebold et al. 1988; Papageorgiou et al. 2000), while transmission measurements yield approximately 7 eV (Büchner 1977; Zeppenfeld 1969).

Intermediate values have been recorded for VA-SWCNT (Kramberger et al. 2008) and MLG on 6H-SiC(0001) (Lu et al. 2009) (about 5 eV) and magnetically aligned bundles of SWCNT (Liu et al. 2001) (about 6 eV).

**Table 3.1** Energy and line-width of the  $\pi$  plasmon in the long wavelength limit (small momenta) for different systems

	$E_{\text{loss}}(q_{\parallel} = 0)$ in eV	FHWM ( $q_{\parallel} = 0$ ) in eV
Free-standing graphene	4.7 (Kramberger et al. 2008; Liu et al. 2001) $\sim$ 6 (Yuan et al. 2011)	0.45
MLG/6H-SiC(0001), data taken from Ref. (Lu et al. 2009)	4.9	0.95
VA-SWCNT, data taken from Ref. (Kramberger et al. 2008)	3.1	1.00
Bilayer graphene on SiC(0001), data taken from Ref. (Lu et al. 2009)	3.3	1.10
Magnetically-aligned bundled SWCNT, data taken from Ref. (Liu et al. 2001)	6.0	1.25
MLG/Pt(111) (our data)	6.2	1.40
3–4 layers graphene on SiC(0001), data taken from Ref. (Lu et al. 2009)	6.3	1.70
Graphite, data taken from Ref. (Diebold et al. 1988)	6.5 (Diebold et al. 1988; Papageorgiou et al. 2000) $\sim$ 7 (Büchner 1977; Zeppenfeld 1969)	2.90
MLG/Ni(111), data taken from Refs. (Generalov and Dedkov 2012; Rosei et al. 1984)	6.7 (Generalov and Dedkov 2012) 7.5 (Rosei et al. 1984)	$\sim$ 3

A HREELS investigation on graphene grown on 6H-SiC(0001) showed the existence of a blue-shift of the  $\pi$  plasmon energy (Lu et al. 2009) as a function of the number of graphene layers. In fact, it shifted from 4.9 (MLG) to 4.3 eV for bilayer graphene and to 6.2 eV for 3–4 layers of graphene.

The red-shift of the plasmon energy (at small momenta) when going from bulk graphite to quasi-two-dimensional graphene is caused by a decrease of the screening and of the interlayer coupling. This also influences the dispersion relation of the plasmon frequency. A linear dispersion was found for both VA-SWCNT (Kramberger et al. 2008) and MLG on 6H-SiC(0001) (Lu et al. 2009). On the other hand, a quadratic dispersion has been recorded for bulk graphite (Papageorgiou et al. 2000), stage-1 ferric-chloride-intercalated graphite (Ritsko and Rice 1979) and multilayer graphene on 6H-SiC(0001) (Lu et al. 2009). For the latter case, it is clear that the realistic band structure of the system changes the dispersion of the  $\pi$  plasmon from linear to quadratic as a function of the number of graphene layers.

The dispersion relations that we obtained for MLG on Pt(111) (Fig. 3.22) indicate a quadratic dispersion for the  $\pi$  plasmon. Even if a negligible hybridization between Pt and graphene states has been observed by angle-resolved photoemission spectroscopy measurements (Sutter et al. 2009), the dispersion relation of the  $\pi$  plasmon

is quadratic already for the MLG, as a consequence of the screening of the collective mode by the metal substrate. The screening in MLG on metal substrates is clearly more effective with respect to the case of graphene layers grown on the semiconductor silicon carbide substrate. This should explain the quadratic dispersion recorded in MLG/Ni(111) (Ref. Generalov and Dedkov 2012) and MLG/Pt(111) (our data), in spite of the very different band structure of such two graphene/metal interfaces. We also remind that the plasmon dispersion in the long-wavelength limit is predicted to be quadratic with respect to momentum for the interacting electron gas (Pines 1964).

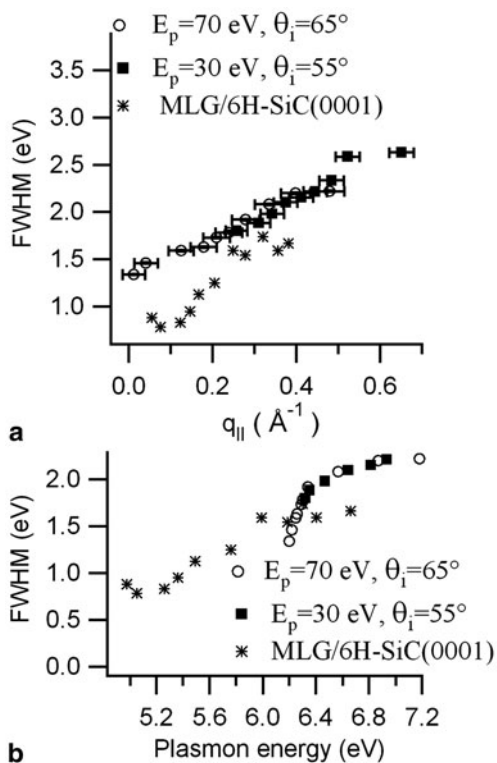
Another issue to be considered is the interlayer coupling. Concerning supported graphene, the interlayer interaction varies as a function of the electron density in the layers. At higher electron density the overlap between orbitals of adjacent layers increases, thus increasing the interlayer coupling (López-Sancho et al. 2007). Hence, in principle the fact that MLG is hole-doped by charge transfer from the Pt substrate (Fermi level below Dirac point) (Gao et al. 2010) could influence the electronic response of the interface. As regards graphite, it is worth mentioning that its interlayer coupling is still under debate. Band structure calculations predicted an interlayer coupling much larger than the values deduced by c-axis conductivity measurements (Dion et al. 2004; Nilsson et al. 2006).

A key factor in the propagation of the plasmonic excitation is its lifetime, which is limited by the decay into electron-hole pairs (Landau damping) (Yuan and Gao 2008). The damping of the plasmon peak is clearly revealed by the trend of the FWHM versus  $q_{\parallel}$ , reported in Fig. 3.23. The width of the plasmon rapidly increases with  $q_{\parallel}$  due to the occurrence of Landau damping. It is worth remembering that, in contrast with the low-energy sheet plasmon (Politano et al. 2011d; Langer et al. 2010), the  $\pi$ -plasmon is a mode which lies inside the continuum of particle-hole excitations and therefore it will be damped even at  $q_{\parallel} \rightarrow 0$  (Yuan et al. 2011).

On the other hand, the width of the  $\pi$  plasmon in MLG/6H-SiC(0001) initially decreased up to  $0.1 \text{ \AA}^{-1}$ , followed by a steep increase as a function of  $q_{\parallel}$ . A similar behaviour has been recorded on graphite (Papageorgiou et al. 2000), where the turning point has been found at  $0.3\text{--}0.4 \text{ \AA}^{-1}$ . The absence of a turning point in MLG/Pt(111) could be related to the nearly-linear dispersion of  $\pi$  bands in the Dirac cones (Sutter et al. 2009). Instead, substrate interactions in graphene on silicon carbide are known to distort the linear dispersion near the Dirac point in the first graphene layer (Zhou et al. 2007). They cause the appearance of a 260 meV energy gap and enhanced electron-phonon coupling (Zhou et al. 2007). This gap decreases as the sample thickness increases and eventually approaches zero for multilayer graphene. The behavior of the FWHM as a function of the plasmon energy (Fig. 3.23b) showed that for MLG/Pt(111) there is an enhanced broadening of the plasmon peak around 6.3 eV. These findings indicate that the Landau damping processes of the  $\pi$  plasmon in MLG/Pt(111) are mainly due to  $\pi$ - $\pi^*$  interband transitions centered around 6.3 eV.

By comparing the FWHM in the long wave-length limit for various graphene systems (Table 3.1), it is quite evident that the presence of out-of-plane decay channels reflects into a wider line-width of the plasmon peak, i.e. a shorter lifetime of the plasmon mode. As demonstrated for graphite (Marinopoulos et al. 2004), they cause additional damping of plasmons, which result in a more diffuse shape for the loss

**Fig. 3.23** Behaviour of the FWHM of the  $\pi$  plasmon of MLG/Pt(111) acquired for two different scattering conditions as a function of **a** the parallel momentum transfer and **b** the plasmon energy. Data for MLG/6H-SiC(0001) are shown for a comparison



spectrum. As a matter of fact, the FWHM increases by a factor 6 from free-standing graphene to graphite.

Results for graphene on 6H-SiC(0001) showed that the  $\pi$  plasmon peak becomes broader and blue-shifted as the thickness of the epitaxial graphene increases. In fact, the  $\pi$  plasmon of 3–4 layer epitaxial graphene includes spectral contribution from both the out-of-plane and in-plane excitations of graphitic origin. This may be due to the three-dimensional band structure of graphite which allows interlayer coupling and out-of-plane excitation.

Moreover, it is worth noticing that the  $\pi$  plasmon in MLG/Pt(111) (our data) and MLG/Ni(111) (Generalov and Dedkov 2012) has a shorter life-time (higher FWHM) than in MLG/6H-SiC(0001) and free-standing graphene as a consequence of enhanced screening by the metal substrate. This implies a broadening of the plasmon peak due to Landau damping via the creation of electron-hole pairs.

## References

- Aizawa T, Souda R, Ishizawa Y, Hirano H, Yamada T, Tanaka K-I, Oshima C (1990) Phonon dispersion in monolayer graphite formed on Ni(111) and Ni(001). *Surf Sci* 237(1–3):194–202
- Allard A, Wirtz L (2010) Graphene on metallic substrates: suppression of the Kohn anomalies in the phonon dispersion. *Nano Lett* 10(11):4335–4340
- Apalkov V, Wang XF, Chakraborty T (2007) Collective excitations of Dirac electrons in graphene. *Int J Mod Phys B* 21(8–9):1165–1179
- Balzer F, Rubahn HG (2000) Interference effects in the optical second harmonic generation from ultrathin alkali films. *Opt Commun* 185(4–6):493–499
- Benedek G, Onida G (1993) Bulk and surface dynamics of graphite with the bond charge model. *Phys Rev B* 47(24):16471–16476
- Benedek G, Brusdeylins G, Senz V, Skofronick JG, Toennies JP, Traeger F, Vollmer R (2001) Helium atom scattering study of the surface structure and dynamics of in situ cleaved MgO(001) single crystals. *Phys Rev B* 64(12):125421
- Borca B, Calleja F, Hinarejos JJ, Vázquez de Parga AL, Miranda R (2009) Reactivity of periodically rippled graphene grown on Ru(0001). *J Phys-Condens Mat* 21(13):134002
- Borca B, Barja S, Garnica M, Minniti M, Politano A, Rodriguez-García JM, Hinarejos JJ, Farías D, Vázquez de Parga AL, Miranda R (2010) Electronic and geometric corrugation of periodically rippled, self-nanostructured graphene epitaxially grown on Ru(0001). *New J Phys* 12(9):093018
- Bostwick A, Speck F, Seyller T, Horn K, Polini M, Asgari R, MacDonald AH, Rotenberg E (2010) Observation of plasmarons in quasi-freestanding doped graphene. *Science* 328(5981):999–1002
- Büchner U (1977) Wave-vector dependence of the electron energy losses of boron nitride and graphite. *Phys Status Solidi B* 81(1):227–234
- Cao Y, Liu S, Shen Q, Yan K, Li P, Xu J, Yu D, Steigerwald ML, Nuckolls C, Liu Z, Guo X (2009) High-performance photoresponsive organic nanotransistors with single-layer graphenes as two-dimensional electrodes. *Adv Funct Mater* 19(17):2743–2748
- Chen Y, Hermanson JC, Lapeyre GJ (1989) Coupled plasmon and phonon in the accumulation layer of InAs(110) cleaved surfaces. *Phys Rev B* 39(17):12682
- Chis V, Benedek G (2011) Phonon-induced surface charge density oscillations in quantum wells: a first-principles study of the  $(2 \times 2)$ -K overlayer on Be(0001). *J Phys Chem A* 115(25):7242–7248
- Diaconescu B, Pohl K, Vattuone L, Savio L, Hofmann P, Silkin VM, Pitarke JM, Chulkov EV, Echenique PM, Farías D, Rocca M (2007) Low-energy acoustic plasmons at metal surfaces. *Nature* 448:57–59
- Diebold U, Preisinger A, Schattschneider P, Varga P (1988) Angle resolved electron energy loss spectroscopy on graphite. *Surf Sci* 197(3):430–443
- Dion M, Rydberg H, Schröder E, Langreth DC, Lundqvist BI (2004) Van der Waals density functional for general geometries. *Phys Rev Lett* 92(24):246401
- Efetov DK, Kim P (2010) Controlling electron-phonon interactions in graphene at ultrahigh carrier densities. *Phys Rev Lett* 105(25):256805
- Farías D, Shikin AM, Rieder KH, Dedkov YS (1999) Synthesis of a weakly bonded graphite monolayer on Ni(111) by intercalation of silver. *J Phys-Condens Mat* 11(43):8453–8458
- Farías D, Rieder KH, Shikin AM, Adamchuk VK, Tanaka T, Oshima C (2000) Modification of the surface phonon dispersion of a graphite monolayer adsorbed on Ni(111) caused by intercalation of Yb, Cu and Ag. *Surf Sci* 454(1–2):437–441
- Fasolino A, Los JH, Katsnelson MI (2007) Intrinsic ripples in graphene. *Nat Mater* 6(11):858–861
- Gao M, Pan Y, Zhang C, Hu H, Yang R, Lu H, Cai J, Du S, Liu F, Gao HJ (2010) Tunable interfacial properties of epitaxial graphene on metal substrates. *Appl Phys Lett* 96(5):053109
- Gao M, Pan Y, Huang L, Hu H, Zhang LZ, Guo HM, Du SX, Gao HJ (2011) Epitaxial growth and structural property of graphene on Pt(111). *Appl Phys Lett* 98(3):033101
- Generalov AV, Dedkov YS (2012) EELS study of the epitaxial graphene/Ni(111) and graphene/Au/Ni(111) systems. *Carbon* 50(1):183–191



- Giesbers AJM, Zeitler U, Ponomarenko LA, Yang R, Novoselov KS, Geim AK, Maan JC (2009) Scaling of the quantum Hall plateau-plateau transition in graphene. *Phys Rev B* 80(24):241411
- Giovannetti G, Khomyakov PA, Brocks G, Karpan VM, van den Brink J, Kelly PJ (2008) Doping graphenewith metal contacts. *Phys Rev Lett* 101(2):026803
- Hale PJ, Hornett SM, Moger J, Horsell DW, Hendry E (2011) Hot phonon decay in supported and suspended exfoliated graphene. *Phys Rev B* 83(12):121404
- Hartmut Z (2001) Phonons in layered compounds. *J Phys Condens Matter* 13(34):7679
- Hill A, Mikhailov SA, Ziegler K (2009) Dielectric function and plasmons in graphene. *Europhys Lett* 87(2):27005
- Hoffmann FM, Weisel MD (1992) Characterization of potassium promoter states under CO hydrogenation conditions on Ru(001): an in situ study with FT-IRAS. *Surf Sci* 269–270(C):495–499
- Horing NJM (2010a) Linear grapheneplasmons. *IEEE Trans Nanotechnol* 9(6):679–681
- Horing NJM (2010b) Aspects of the theory of graphene. *Philos Trans A Math Phys Eng Sci* 368(1932):5525–5556
- Hwang EH, Das Sarma S (2007) Dielectric function, screening, and plasmons in two-dimensional graphene. *Phys Rev B* 75(20):205418
- Hwang EH, Das Sarma S (2009) Plasmon modes of spatially separated double-layer graphene. *Phys Rev B* 80(20):205405
- Hwang EH, Sensarma R, Das Sarma S (2010) Plasmon-phonon coupling in graphene. *Phys Rev B* 82(19):195406
- Ibach H (1993) Electron energy loss spectroscopy with resolution below 1 meV. *J Electron Spectrosc Relat Phenom* 64–65:819–823
- Ibach H, Mills DL (1982) *Electron energy loss spectroscopy and surface vibrations*. Academic, San Francisco
- Ibach H, Balden M, Lehwald S (1996) Recent advances in electron energy loss spectroscopy of surface vibrations. *J Chem Soc Faraday Transac* 92(23):4771–4774
- Ibach H, Etzkorn M, Kirschner J (2006) Electron spectrometers for inelastic scattering from magnetic surface excitations. *Surf Interface Anal* 38(12–13):1615–1617
- Karssemeijer LJ, Fasolino A (2011) Phonons of graphene and graphitic materials derived from the empirical potential LCBOP. *Surf Sci* 605(17–18):1611–1615
- Kohn W (1959) Image of the Fermi surface in the vibration spectrum of a metal. *Phys Rev Lett* 2(9):393–394
- Kramberger C, Hambach R, Giorgetti C, Rümmeli MH, Knupfer M, Fink J, Büchner B, Reining L, Einarsson E, Maruyama S, Sottile F, Hannewald K, Olevano V, Marinopoulos AG, Pichler T (2008) Linear plasmon dispersion in single-wall carbon nanotubes and the collective excitation spectrum of graphene. *Phys Rev Lett* 100(19):196803
- Langer T, Baringhaus J, Pfnür H, Schumacher HW, Tegenkamp C (2010) Plasmon damping below the Landau regime: the role of defects in epitaxial graphene. *New J Phys* 12(3):033017
- Langer T, Förster DF, Busse C, Michely T, Pfnür H, Tegenkamp C (2011) Sheet plasmons in modulated graphene on Ir(111). *New J Phys* 13(5):053006
- Lazzeri M, Mauri F (2006) Nonadiabatic Kohn anomaly in a doped graphenemonolayer. *Phys Rev Lett* 97(26):266407
- Lee H, Ihm J, Cohen ML, Louie SG (2010) Calcium-decorated graphene-based nanostructures for hydrogen storage. *Nano Lett* 10(3):793–798
- Liu Y, Willis RF (2010) Plasmon-phonon strongly coupled mode in epitaxial graphene. *Phys Rev B* 81(8):081406
- Liu Y, Willis RF, Emtsev KV, Seyller T (2008) Plasmon dispersion and damping in electrically isolated two-dimensional charge sheets. *Phys Rev B* 78(20):201403
- Liu X, Pichler T, Knupfer M, Golden MS, Fink J, Walters DA, Casavant MJ, Schmidt J, Smalley RE (2001) An electron energy-loss study of the structural and electronic properties of magnetically aligned single wall carbon nanotubes. *Synth Met* 121(1–3):1183–1186
- López-Sancho MP, Vozmediano MAH, Guinea F (2007) Transverse transport in graphite. *Eur Phys J-Spec Top* 148(1):73–81

- Lu J, Loh KP, Huang H, Chen W, Wee ATS (2009) Plasmon dispersion on epitaxial graphene studied using high-resolution electron energy-loss spectroscopy. *Phys Rev B* 80(11):113410
- Lüth H (1995) *Surfaces and interfaces of solid materials*. Springer, Berlin
- Marinopoulos AG, Reining L, Rubio A, Olevano V (2004) Ab initio study of the optical absorption and wave-vector-dependent dielectric response of graphite. *Phys Rev B* 69(24):245419
- Martocchia D, Björck M, Schlepütz CM, Brugger T, Pauli SA, Patterson BD, Greber T, Willmott PR (2010) Grapheneon Ru(0001): a corrugated and chiral structure. *New J Phys* 12(4):043028
- Maultzsch J, Reich S, Thomsen C, Requardt H, Ordejón P (2004) Phonon dispersion in graphite. *Phys Rev Lett* 92(7):075501
- Mills DL (1975) The scattering of low energy electrons by electric field fluctuations near crystal surfaces. *Surf Sci* 48(1):59–79
- Mittendorfer F, Garhofer A, Redinger J, Klimeš J, Harl J, Kresse G (2011) Graphene on Ni(111): Strong interaction and weak adsorption. *Phys Rev B* 84(20):201401
- Müller F, Grandthyll S, Zeitz C, Jacobs K, Hüfner S, Gsell S, Schreck M (2011) Epitaxial growth of graphene on Ir(111) by liquid precursor deposition. *Phys Rev B* 84(7):075472
- Nagao T, Hildebrandt T, Henzler M, Hasegawa S (2001a) Two-dimensional plasmon in a surface-state band. *Surf Sci* 493(1–3):680–686
- Nagao T, Hildebrandt T, Henzler M, Hasegawa S (2001b) Dispersion and damping of a two-dimensional plasmon in a metallic surface-state band. *Phys Rev Lett* 86(25):5747–5750
- Nair RR, Blake P, Blake JR, Zan R, Anissimova S, Bangert U, Golovanov AP, Morozov SV, Geim AK, Novoselov KS, Latychevskaia T (2010) Graphene as a transparent conductive support for studying biological molecules by transmission electron microscopy. *Appl Phys Lett* 97(15):153102
- Nemec N, Tománek D, Cuniberti G (2006) Contact dependence of carrier injection in carbon nanotubes: an ab initio study. *Phys Rev Lett* 96(7):076802
- Nilsson J, Castro Neto AH, Peres NMR, Guinea F (2006) Electron-electron interactions and the phase diagram of a graphene bilayer. *Phys Rev B* 73(21):214418
- Novoselov KS, Geim AK, Morozov SV, Jiang D, Zhang Y, Dubonos SV, Grigorieva IV, Firsov AA (2004) Electric field effect in atomically thin carbon films. *Science* 306(5696):666–669
- Novoselov KS, Geim AK, Morozov SV, Jiang D, Katsnelson MI, Grigorieva IV, Dubonos SV, Firsov AA (2005) Two-dimensional gas of massless Dirac fermions in graphene. *Nature* 438(7065):197–200
- Novoselov KS, McCann E, Morozov SV, Fal'ko VI, Katsnelson MI, Zeitler U, Jiang D, Schedin F, Geim AK (2006) Unconventional quantum Hall effect and Berry's phase of  $2\pi$  in bilayer graphene. *Nat Phys* 2(3):177–180
- Papageorgiou N, Portail M, Layet JM (2000) Dispersion of the interband  $\pi$  electronic excitation of highly oriented pyrolytic graphite measured by high resolution electron energy loss spectroscopy. *Surf Sci* 454–456(1–2):462–466
- Park SJ, Palmer RE (2010) Acoustic plasmon on the Au(111) surface. *Phys Rev Lett* 105(1):016801
- Perebeinos V, Tersoff J (2009) Valence force model for phonons in graphene and carbon nanotubes. *Phys Rev B* 79(24):241409
- Pines D (1964) *Elementary excitations in solids*. Benjamin, New York
- Piscanec S, Lazzeri M, Mauri F, Ferrari AC, Robertson J (2004) Kohn anomalies and electron-phonon interactions in graphite. *Phys Rev Lett* 93(18):185503
- Pohl K, Diaconescu B, Vercelli G, Vattuone L, Silkin VM, Chulkov EV, Echenique PM, Rocca M (2010) Acoustic surface plasmon on Cu(111). *EPL (Europhys Lett)* 90(5):57006
- Polini M, Asgari R, Borghi G, Barlas Y, Pereg-Barnea T, MacDonald AH (2008) Plasmons and the spectral function of graphene. *Phys Rev B* 77(8):081411
- Politano A, Formoso V, Chiarello G (2008) Alkali-promoted CO dissociation on Cu(111) and Ni(111) at room temperature. *J Chem Phys* 129(16):164703
- Politano A, Agostino RG, Colavita E, Formoso V, Chiarello G (2009) Collective excitations in nanoscale thin alkali films: Na/Cu(111). *J Nanosci Nanotechnol* 9(6):3932–3937

- Politano A, Marino AR, Formoso V, Chiarello G (2011a) Hydrogen bonding at the water/quasi-freestanding graphene interface. *Carbon* 49(15):5180–5184
- Politano A, Borca B, Minniti M, Hinarejos JJ, Vázquez de Parga AL, Farías D, Miranda R (2011b) Helium reflectivity and Debye temperature of graphene grown epitaxially on Ru(0001). *Phys Rev B* 84(3):035450
- Politano A, Marino AR, Formoso V, Chiarello G (2011c) Water adsorption on graphene/Pt(111) at room temperature: a vibrational investigation. *AIP Adv* 1(4):042130
- Politano A, Marino AR, Formoso V, Farías D, Miranda R, Chiarello G (2011d) Evidence for acoustic-like plasmons on epitaxial graphene on Pt(111). *Phys Rev B* 84(3):033401
- Politano A, Marino AR, Chiarello G (2012a) Phonon dispersion of quasi-freestanding graphene on Pt(111). *J Phys Condens Matter* 24(10):104025
- Politano A, Marino AR, Formoso V, Chiarello G (2012b) Evidence of Kohn anomalies in quasi-freestanding graphene on Pt(111). *Carbon* 50(2):734–736
- Politano A, Marino AR, Formoso V, Farías D, Miranda R, Chiarello G (2012c) Quadratic dispersion and damping processes of  $\pi$  plasmon in monolayer graphene on Pt(111). *Plasmonics* 7(2):369–376
- Preobrajenski AB, Ng ML, Vinogradov AS, Mårtensson N (2008) Controlling graphene corrugation on lattice-mismatched substrates. *Phys Rev B* 78(7):073401
- Ritsko JJ, Rice MJ (1979) Plasmon spectra of ferric-chloride-intercalated graphite. *Phys Rev Lett* 42(10):666–669
- Rocca M (1995) Low-energy EELS investigation of surface electronic excitations on metals. *Surf Sci Rep* 22(1–2):1–71
- Rosei R, Modesti S, Sette F, Quaresima C, Savoia A, Perfetti P (1984) Electronic structure of carbidic and graphitic carbon on Ni(111). *Phys Rev B* 29(6):3416–3422
- van Schilfgaarde M, Katsnelson MI (2011) First-principles theory of nonlocal screening in graphene. *Phys Rev B* 83:081409
- Seol JH, Jo I, Moore AL, Lindsay L, Aitken ZH, Pettes MT, Li X, Yao Z, Huang R, Broido D, Mingo N, Ruoff RS, Shi L (2010) Two-dimensional phonon transport in supported graphene. *Science* 328(5975):213–216
- Shikin AM, Farías D, Rieder KH (1998) Phonon stiffening induced by copper intercalation in monolayer graphite on Ni(111). *Europhys Lett* 44(1):44–49
- Shikin AM, Farías D, Adamchuk VK, Rieder KH (1999) Surface phonon dispersion of a graphite monolayer adsorbed on Ni(111) and its modification caused by intercalation of Yb, La and Cu layers. *Surf Sci* 424(1):155–167
- Shikin AM, Adamchuk VK, Rieder KH (2009) Formation of quasi-free graphene on the Ni(111) surface with intercalated Cu, Ag, and Au layers. *Phys Solid State* 51:2390–2400
- Silkin VM, Garcia-Lekue A, Pitarke JM, Chulkov EV, Zaremba E, Echenique PM (2004) Novel low-energy collective excitation at metal surfaces. *Europhys Lett* 66(2):260–264
- Silkin VM, Pitarke JM, Chulkov EV, Echenique PM (2005) Acoustic surface plasmons in the noble metals Cu, Ag, and Au. *Phys Rev B* 72(11):115435
- Stern F (1967) Polarizability of a two-dimensional electron gas. *Phys Rev Lett* 18(14):546–548
- Sun J, Hannon JB, Tromp RM, Johari P, Bol AA, Shenoy VB, Pohl K (2010) Spatially-resolved structure and electronic properties of graphene on polycrystalline Ni. *ACS Nano* 4(12):7073–7077
- Sutter P, Sadowski JT, Sutter E (2009) Graphene on Pt(111): growth and substrate interaction. *Phys Rev B* 80(24):245411
- Tegenkamp C, Pfnür H, Langer T, Baringhaus J, Schumacher HW (2011) Plasmon electron–hole resonance in epitaxial graphene. *J Phys Condens Matter* 23(1):012001
- Viola Kusminskiy S, Campbell DK, Castro Neto AH (2009) Lenosky’s energy and the phonon dispersion of graphene. *Phys Rev B* 80(3):035401
- Wang Y, Shi Z, Huang Y, Ma Y, Wang C, Chen M, Chen Y (2009) Supercapacitor devices based on graphenematerials. *J Phys Chem C* 113(30):13103–13107

- Wang Y, Page AJ, Nishimoto Y, Qian H-J, Morokuma K, Irlé S (2011) Template effect in the competition between haeckelite and graphenegrowth on Ni(111): quantum chemical molecular dynamics simulations. *J Am Chem Soc* 133(46):18837–18842
- Wirtz L, Rubio A (2004) The phonon dispersion of graphite revisited. *Solid State Commun* 131(3–4):141–152
- Wu X, Sprinkle M, Li X, Ming F, Berger C, de Heer WA (2008) Epitaxial-graphene/graphene-oxide junction: an essential step towards epitaxial graphene electronics. *Phys Rev Lett* 101(2):026801
- Wu X, Hu Y, Ruan M, Madiomanana NK, Hankinson J, Sprinkle M, Berger C, De Heer WA (2009) Half integer quantum Hall effect in high mobility single layer epitaxial graphene. *Appl Phys Lett* 95(22):223108
- Yan J, Thygesen KS, Jacobsen KW (2011) Nonlocal screening of plasmons in graphene by semi-conducting and metallic substrates: first-principles calculations. *Phys Rev Lett* 106(14):146803
- Yang WR, Ratinac KR, Ringer SP, Thordarson P, Gooding JJ, Braet F (2010) Carbon nanomaterials in biosensors: should you use nanotubes or graphene? *Angew Chem Int Edit* 49(12):2114–2138
- Yuan Z, Gao S (2008) Landau damping and lifetime oscillation of surface plasmons in metallic thin films studied in a jellium slab model. *Surf Sci* 602(2):460–464
- Yuan S, Roldán R, Katsnelson MI (2011) Excitation spectrum and high-energy plasmons in single-layer and multilayer graphene. *Phys Rev B* 84(3):035439
- Zeppenfeld K (1969) Wavelength dependence and spatial dispersion of the dielectric constant in graphite by electron spectroscopy. *Opt Commun* 1(3):119–122
- Zhang H, Fu Q, Cui Y, Tan D, Bao X (2009) Growth mechanism of graphene on Ru (0001) and O<sub>2</sub> adsorption on the graphene/Ru (0001) surface. *J Phys Chem C* 113(19):8296–8301
- Zhou SY, Gweon GH, Fedorov AV, First PN, de Heer WA, Lee DH, Guinea F, Castro Neto AH, Lanzara A (2007) Substrate-induced bandgap opening in epitaxial graphene. *Nat Mater* 6(10):770–775

# Chapter 4

## Understanding the Exohedral Functionalization of Endohedral Metallofullerenes

Marc Garcia-Borràs, Sílvia Osuna, Josep M. Luis, Marcel Swart and Miquel Solà

**Abstract** The endohedral metallofullerenes (EMFs) and their exohedral functionalized derivatives present an increasing attention due to their potential applications in materials science and medicine. However, the current understanding of the reactivity of endohedral metallofullerenes is still very incomplete. In this chapter, we present a thorough study of the Diels-Alder (DA) reactivity of  $D_{3h}$ - $C_{78}$ ,  $Sc_3N@D_{3h}$ - $C_{78}$ ,  $Y_3N@D_{3h}$ - $C_{78}$ ,  $Ti_2C_2@D_{3h}$ - $C_{78}$ ,  $Sc_3N@D_{5h}$ - $C_{80}$ ,  $Lu_3N@D_{5h}$ - $C_{80}$ ,  $Gd_3N@D_{5h}$ - $C_{80}$ ,  $Sc_3N@I_h$ - $C_{80}$ ,  $Lu_3N@I_h$ - $C_{80}$ - $C_{80}$ ,  $Gd_3N@I_h$ - $C_{80}$ ,  $Y_3N@I_h$ - $C_{80}$ ,  $La_2@I_h$ - $C_{80}$ ,  $Y_3@I_h$ - $C_{80}$ ,  $Sc_3C_2@I_h$ - $C_{80}$ ,  $Sc_4C_2@I_h$ - $C_{80}$ ,  $Sc_3CH@I_h$ - $C_{80}$ ,  $Sc_3NC@I_h$ - $C_{80}$ ,  $Sc_4O_2@I_h$ - $C_{80}$ ,  $Sc_4O_3@I_h$ - $C_{80}$ , and  $La@C_{2v}$ - $C_{82}$ . We have studied both the thermodynamic and the kinetic regioselectivity, taking into account when it was required the free rotation of the metallic cluster inside the fullerene. This systematic investigation was possible only because we use the Frozen Cage Model, which is a low-cost approach to determine the EMF exohedral regioselectivity. Our study has allowed the correction of two wrong experimental assignments of DA adducts, highlighting the key role of computational studies to achieve a deep understanding of exohedral reactivity of the EMFs. The incarceration of the metallic cluster reduces the reactivity of the EMFs respect to the hollow fullerenes. Our results also show that bond distances, pyramidalization angles, LUMOs shape, charge transfer, and cluster volume are the key factors that determine the DA regioselectivity of the fullerenes and EMFs. However, none of them can be used alone to predict which bond will

---

M. Garcia-Borràs (✉) · S. Osuna · J. M. Luis · M. Swart · M. Solà  
Institut de Química Computacional i Catàlisi (IQCC) and Departament de Química,  
Universitat de Girona, Campus de Montilivi, 17071 Girona, Catalonia, Spain  
e-mail: marc.garcia@udg.edu

M. Swart  
Institució Catalana de Recerca i Estudis Avançats (ICREA), Pg. Lluís Companys 23, 08010  
Barcelona, Catalonia, Spain  
e-mail: marcel.swart@udg.edu

S. Osuna  
e-mail: silvia.osuna@udg.edu

J. M. Luis  
e-mail: josepm.luis@udg.edu

M. Solà  
e-mail: miquel.sola@udg.edu

be attacked. Finally, we focus our attention on the essential role of the dispersion interactions to reproduce the experimental results of the exohedral cycloaddition on EMFs.

## 4.1 Introduction

### 4.1.1 Endohedral Metallofullerenes

The encapsulation of metals and small molecules inside a fullerene cavity, i.e. the formation of endohedral fullerenes, was considered right after the  $C_{60}$  discovery (Heath et al. 1985; Kroto et al. 1985). Endohedral metallofullerenes (EMFs) have attracted increasing attention in the last few years for several reasons: (i) the production yield of EMFs is generally higher than for other endohedral fullerenes, (ii) the potential application of these molecules in medicine and materials science, (iii) the metal cluster strongly interacts with the fullerene cavity leading to quite unique materials (Akasaka and Nagase 2002; Chaur et al. 2009; Lu et al. 2012; Osuna et al. 2011a; Rodríguez-Forteza et al. 2011; Yang et al. 2011).

The first example of stable endohedral metallofullerene,  $La@C_{82}$ , was reported in (Chai et al. 1991) In 1999, the synthesis, isolation, and characterization of the first member of the metallic tri-nitride template (TNT) family, i.e.  $Sc_3N@C_{80}$  was reported. (Stevenson et al. 1999) In fact,  $Sc_3N@C_{80}$  is the third most abundant fullerene only after  $C_{60}$  and  $C_{70}$ . Since then, many other EMFs have been synthesized that range from single metal atoms to metallic carbides, nitrides, oxides, and sulfides. (Chaur et al. 2009) A variety of EMFs with fullerene carbon cages that range from  $C_{68}$  to  $C_{104}$  and metal atoms that are generally from Group 3 or lanthanides have been reported (Chaur et al. 2009; Yang et al. 2011).

Nowadays it is well-known that fullerenes can encapsulate atoms, ions, metallic clusters, and small molecules such as  $H_2$ ,  $CO$ ,  $H_2O$ ,  $NH_3$  or  $CH_4$  (for reviews see (Liu and Sun 2000; Guha and Nakamoto 2005; Murata et al. 2008; Yamada et al. 2010; Rodríguez-Forteza et al. 2011; Lu et al. 2011; Chaur et al. 2009). These endohedral fullerenes (EFs) can be classified in different classes: (Chaur et al. 2009) (i) Classical EFs of the type  $X@C_{2n}$ ,  $X_2@C_{2n}$ , and  $X_3@C_{2n}$ , with  $X$  = metal, noble gas, small molecule and  $60 \leq 2n \leq 88$ ); (ii) metallic nitride EMFs such as  $M_3N@C_{2n}$ , with  $M$  = metal and  $68 \leq 2n \leq 96$ ; (iii) metallic carbide EMFs like  $M_2C_2@C_{2n}$ ,  $M_3C_2@C_{2n}$ ,  $M_4C_2@C_{2n}$ , hydrogenated metallic carbide  $M_3CH@C_{2n}$ , and metallic nitrogen carbide  $M_3CN@C_{2n}$  with  $68 \leq 2n \leq 92$ ; (iv) metallic oxide EMFs of the type  $M_4O_2@C_{2n}$  and  $M_4O_3@C_{2n}$ ; and v) metallic sulfide  $M_2S@C_{2n}$ .

The isolated-pentagon rule (IPR) formulated by Kroto (1987) states that all pentagons must be surrounded by hexagons to alleviate the strain produced by two fused pentagons (a pentalene unit). While the isolated pentagon rule (IPR) is strictly obeyed by all pure-carbon fullerenes isolated to the date, (Lu et al. 2008) an increasing number of EMFs have been synthesized that present non-IPR cages. Therefore, the IPR rule appears to be more a suggestion than a rule for these species (Kobayashi

et al. 1997) and in general for any charged fullerene. (Aihara 2001) Very recently, we have shown in a systematic study that the selection of the most suitable cage for the formation of all of the most common  $C_{2n}$  ( $2n = 66-104$ ) EMFs reported to date is governed by the maximum aromaticity criterion (MARC), which determines that the most aromatic negatively charged fullerene cage is the most stable one (Garcia-Borràs et al. 2013b). This rule is based on one of the unique features of these EMFs species, which is the formal electronic transfer that occurs from the metal cluster to the fullerene cage. It has been shown that this negatively charge transferred to the carbon structure is mainly located on five membered rings (5-MRs), (Rodríguez-Forteza et al. 2010) which makes them more aromatic (Garcia-Borràs et al. 2013b). As a whole, there are two main factors that determine the stability of the fullerenes: strain energy and aromaticity. The aromaticity of the hollow neutral fullerenes is very low, and then reducing strain energy is the main factor that governs their stability. That is why all empty fullerenes follow the IPR rule. On the contrary, in highly charged fullerenes or EMFs, the aromaticity plays a major role. Thus, maximizing the total aromaticity is the main stabilizing factor, which could lead to both an IPR or non-IPR isomer as the most stable fullerene cage.

The structure, stability, and reactivity of the fullerene cage among other factors depend on: (i) the size of the metal cluster encapsulated inside, and (ii) the formal electronic transfer from the metal cluster to the fullerene cage. For those species involving small rare-earth atoms, i.e. Sc, Y, and lanthanides from Gd to Lu, the  $I_h-C_{80}$  cage is usually the most abundant (Chaur et al. 2007; Stevenson et al. 2004). The  $I_h-C_{80}$  fullerene is also considered to be the best cage for trapping TNT or  $M_2$  clusters, although is the most unstable among the seven IPR structures of  $C_{80}$  fullerene (Stevenson et al. 1999; Lu et al. 2012). Similar situations are found for other fullerene cages such as the  $D_{3h}-C_{78}$ ,  $C_{2v}-C_{78}$ , and  $C_{2v}-C_{82}$ . The preference for the  $I_h-C_{80}$  cage among all possible  $C_{80}$  IPR and non-IPR isomers is mainly attributed to the higher aromaticity of the negatively charged  $I_h-C_{80}$  cage in the EMFs (Garcia-Borràs et al. 2013b). In addition to that, the inner cavity of  $I_h-C_{80}$  is relatively large; the shape of the cage maximizes the separation between the negatively charged 12 pentagons (the so-called maximum pentagon separation rule); (Rodríguez-Forteza et al. 2010) and  $I_h-C_{80}$  presents a large LUMO+3-LUMO+4 gap (Campanera et al. 2005; Rodríguez-Forteza et al. 2010; Valencia et al. 2007). Apart from the highly stable TNT EMF,  $Sc_3N@I_h-C_{80}$ , and the related  $X_3N@I_h-C_{80}$  ( $X = Sc, Y, Gd, Tb, Dy, Ho, Er, Tm, Lu$ ) and mixed metal nitride clusterfullerenes  $M_xSc_{3-x}N@I_h-C_{80}$ , ( $X = Gd, Dy, Lu, Y, Ce, Nd, Tb, Er, Lu, Ti$ ) and  $M_xL_{3-x}N@I_h-C_{80}$  ( $Lu_xY_{3-x}, CeLu_2, Y_2Ti$ ), many other  $I_h-C_{80}$  cluster-based EMFs have been reported (Yang et al. 2011; Lu et al. 2012). For instance, the metal clusters  $La_2$ ,  $Ce_2$ , and  $Y_3$ , (Guldi et al. 2010; Popov et al. 2010; Akasaka et al. 1997; Suzuki et al. 1995) the metal carbides  $Sc_3C_2$  and  $Sc_4C_2$ , (Tan and Lu 2006; Tan et al. 2006) the metal hydrocarbides  $Sc_3CH$ , (Krause et al. 2007) metal carbonitride  $Sc_3CN$ , (Wang et al. 2010b) and metal oxides  $Sc_4O_2$  and  $Sc_4O_3$  have been encapsulated inside the  $I_h-C_{80}$  cage. (Stevenson et al. 2008; Mercado et al. 2010) Interestingly, all these  $X@I_h-C_{80}$  species have a formal charge transfer from the metal cluster to the cage of six electrons, i.e.  $X^{6+}@I_h-C_{80}^{6-}$ .

The experimental isolation of some of these EMFs species led to the wrong assignment of the fullerene cage and cluster encapsulated inside due to experimental difficulties in the characterization of these EMFs. It should be emphasized that EMFs are obtained generally in low yield and are often difficult to isolate. For instance, the first example of a carbide cluster EMF, the  $\text{Sc}_2\text{C}_2@D_{2d}(23)\text{-C}_{84}$  was initially assumed to be  $\text{Sc}_2@\text{C}_{86}$  (Wang et al. 1999, 2001). Similarly, a theoretical study on the smallest metal carbide EMFs synthesized up to date  $\text{Sc}_2\text{C}_2@C_{2v}(7854)\text{-C}_{68}$ , argued that the synthesized EMF corresponds to  $\text{Sc}_2@C_{2v}(7854)\text{-C}_{70}$  (Shi et al. 2006; Zheng et al. 2012). On the other hand, neither  $\text{Y}_2\text{C}_{82}$  nor  $\text{Y}_3\text{C}_{80}$  were found to be metal carbide EMFs and they were assigned to be  $\text{Y}_2@\text{C}_{82}$  and  $\text{Y}_3@\text{C}_{80}$  classical EFs (Nishibori et al. 2006; Popov et al. 2010). Interestingly, the initially assigned  $\text{Ti}_2@\text{C}_{80}$  later was found to be  $\text{Ti}_2\text{C}_2@D_{3h}(78:5)\text{-C}_{78}$  by  $^{13}\text{C}$  NMR and density functional theory (DFT) calculations (Cao et al. 2001; Jaffiol et al. 2003; Iwasaki et al. 2004; Tan and Lu 2005; Yumura et al. 2005). The  $D_{3h}(78:5)\text{-C}_{78}$  cage in  $\text{Ti}_2\text{C}_2@D_{3h}(78:5)\text{-C}_{78}$  represents the smallest fullerene cage obeying the isolated pentagon rule (IPR) that has a metal carbide encapsulated. For non-IPR cages, the smallest metal carbide disclosed so far is  $\text{Sc}_2\text{C}_2@\text{C}_{68}$  (Shi et al. 2006). From an electronic point of view, metal carbides can formally transfer four electrons to the fullerene cage as in  $(\text{Sc}_2\text{C}_2)^{4+}@\text{(C}_{82})^{4-}$  or six electrons like in  $(\text{Ti}_2\text{C}_2)^{6+}@\text{(C}_{78})^{6-}$  or  $(\text{Sc}_3\text{C}_2)^{6+}@\text{(C}_{80})^{6-}$  (Valencia et al. 2008). These observations demonstrate the paramount importance of both experiment and theory to correctly characterize these fascinating compounds.

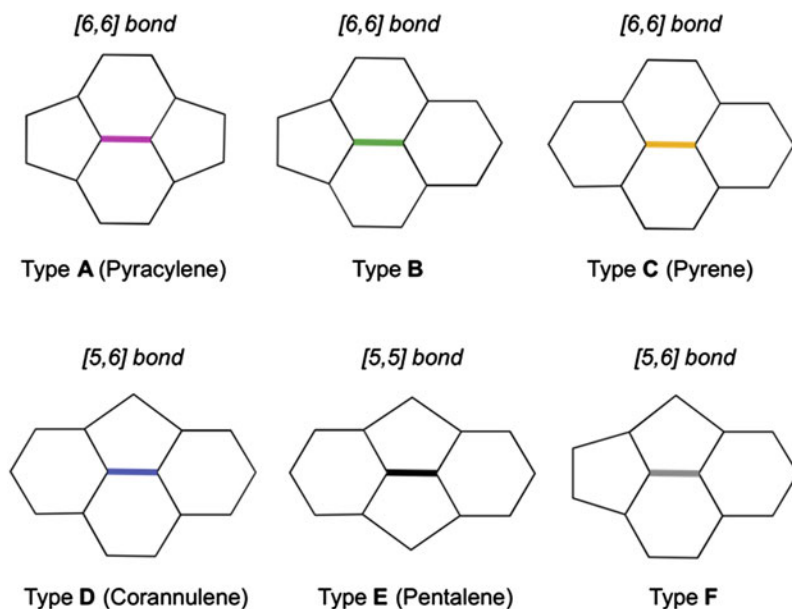
The above-mentioned electron-transfer confers EMFs a different reactivity than the hollow counterparts. The exohedral functionalization of EMFs is essential for the final goal of obtaining new materials of interest for future applications in the fields of biomedicine and materials science. These species have interesting physicochemical properties with many potential interesting applications in the fields of magnetism, superconductivity, nonlinear optical (NLO) properties, radioimmunotherapy, and magnetic resonance imaging (MRI) contrast agents, among others. The most remarkable example is the gadolinium based EMFs  $\text{Gd}_3\text{N}@I_h\text{-C}_{80}$ . This fullerene can be effectively used in MRI as contrast agent (Fatouros et al. 2006).

### 4.1.2 Exohedral Functionalization of Endohedral Metallofullerenes

In fullerene structures at least six possible different C–C bonds might be present: types A to F (represented in Fig. 4.1). Adjacent pentagon pairs (APPs) are present in non-IPR carbon cages where types E and F can be found.

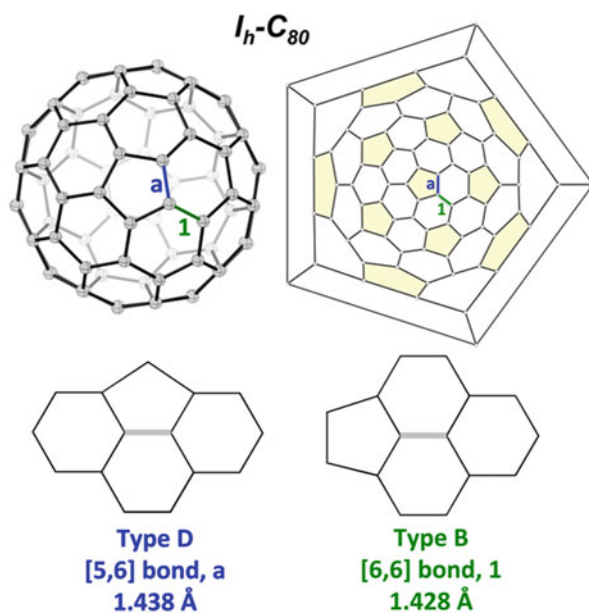
Because  $\text{X}@I_h\text{-C}_{80}$  EMFs are those most abundant, their exohedral functionalization have been intensively explored in the quest for new materials of interest for future applications in biomedicine and materials science (Rivera-Nazario et al. 2013). The first exohedral functionalization of an EMF was a Diels-Alder (DA) cycloaddition of 6,7-methoxyisochrom-3-one on  $\text{Sc}_3\text{N}@I_h\text{-C}_{80}$  (Iezzi et al. 2002). The icosahedral  $I_h\text{-C}_{80}$  cage is highly symmetric (see Fig. 4.2), and taking into account





**Fig. 4.1** Representation of the different [6, 6], [5, 6] and [5, 5] bond types that are more commonly found in fullerene structures

the free rotation of the metallic cluster only two different regioisomers are possible after functionalization: the adduct on a corannulenic [5, 6] bond type (type D, Figs. 4.1 and 4.2) or the adduct on the type B [6, 6] bond (see Figs. 4.1 and 4.2). DFT calculations at BP86/TZP level showed that addition at the corannulene [5, 6] bond (type D) is at least 11 kcal mol<sup>-1</sup> more stable than the adduct on the [6, 6] bond. (Campanera et al. 2006; Osuna et al. 2011b) Moreover, the Prato reaction on M<sub>3</sub>N@I<sub>h</sub>-C<sub>80</sub> was also achieved. The *N*-ethylazomethine ylide addition on Sc<sub>3</sub>N@I<sub>h</sub>-C<sub>80</sub> takes place regioselectively at the corannulene [5, 6] bond, but the [5, 6] and [6, 6] regioisomers are obtained for Y<sub>3</sub>N@I<sub>h</sub>-C<sub>80</sub> (Cardona et al. 2006). The two adducts are also observed in the synthesis of *N*-tritylpyrrolidino derivative of Sc<sub>3</sub>N@I<sub>h</sub>-C<sub>80</sub> (Cai et al. 2006a). Rodríguez-Forteza and coworkers reported that the [6, 6] and [5, 6] pyrrolidino adducts are almost degenerate in the case of Y<sub>3</sub>N@I<sub>h</sub>-C<sub>80</sub>. (Rodríguez-Forteza et al. 2006) They suggested a pirouette-type mechanism for the observed [6, 6]-to-[5, 6] isomerization under thermal conditions instead of via retrocycloaddition (Rodríguez-Forteza et al. 2006). On the other hand, the Bingel-Hirsch cyclopropanation on M<sub>3</sub>N@I<sub>h</sub>-C<sub>80</sub> takes place regioselectively on the [6, 6] bond for M = Sc, Lu, Y, and Er. However, a higher reactivity for yttrium and erbium-based EMFs were observed (Lukoyanova et al. 2007). Finally, Sc<sub>3</sub>N@I<sub>h</sub>-C<sub>80</sub> were found to react photochemically with disilirane to afford the corresponding adduct (Iiduka et al. 2005a).



**Fig. 4.2** Different [5, 6] (*a*, in blue) and [6, 6] (*1*, in green) nonequivalent bonds present in the  $I_h-C_{80}$  cage. The Schlegel diagram, which converts the 3D fullerene into a 2D representation, is also shown. (Reprinted with permission from (Garcia-Borràs et al. 2013c). Copyright 2013 Wiley)

Other non-TNT EMFs based on the  $I_h-C_{80}$  cage have also been exohedrally functionalized. The 1,3-dipolar cycloaddition was successfully produced on  $La_2@I_h-C_{80}$  and  $Ce_2@I_h-C_{80}$  (Yamada et al. 2006; Yamada et al. 2009). Two different regioisomers were obtained corresponding to the addition to [5, 6] and [6, 6] bonds. Interestingly, the two metal atoms were fixed at the slantwise positions on the mirror plane in the [6, 6]-adducts, whereas they were collinear with the pyrrolidino ring in the [5, 6]-pyrrolidinodimetallofullerenes (Yamada et al. 2009). The Prato cycloaddition between  $La_2@I_h-C_{80}$  and 3-triphenylmethyl-5-oxazolidinone has been achieved to give the  $La_2@I_h-C_{80}(CH_2)_2NTrt$  (Trt = triphenylmethyl) adduct (Yamada et al. 2006). The products obtained experimentally correspond to the attack over both [5, 6] and [6, 6] bonds. Very recently, another Prato reaction between 11,11,12,12-tetracyano-9,10-anthra-*p*-quinodimethane and  $La_2@I_h-C_{80}$  was produced affording [5, 6]-metallofulleropyrrolidines (Takano et al. 2012). On the other hand, the carbene addition on  $La_2@I_h-C_{80}$  and  $Ce_2@I_h-C_{80}$  was found to occur at the [6, 6] position leading to an open adduct. Interestingly, both La and Ce atoms were positioned collinearly with spiro carbons of the [6, 6]-open adduct (Ishitsuka et al. 2011; Yamada et al. 2008). Similarly, the chemical functionalization of the  $Sc_3C_2@C_{80}$  molecule by adamantylidene carbene (Ad) was carried out to obtain the [6, 6]-cycloadduct,  $Sc_3C_2@C_{80}(Ad)$ , (Iiduka et al. 2005b) whereas the Prato reaction (Wang et al. 2010a) to  $Sc_3C_2@I_h-C_{80}$  occurred at the [5, 6] ring junction. Finally, the cycloaddition of

tetrazine (Kurihara et al. 2012) to  $\text{Sc}_3\text{C}_2@I_h\text{-C}_{80}$  took place at a 1,4 position of a six-membered ring.

From the experimental examples seen above, it becomes apparent that endohedral clusters play a major role in directing the addition sites of the exohedral reactivity of the fullerene cage. This fact has been computationally reinforced by a series of thermodynamic and kinetic studies performed by some of us and reported in this chapter on the DA reaction between *s-cis*-1,3-butadiene and several EMFs:  $\text{Sc}_3\text{N}@D_{3h}\text{-C}_{78}$ , (Osuna et al. 2008)  $\text{Y}_3\text{N}@D_{3h}\text{-C}_{78}$ , (Osuna et al. 2009a)  $\text{Y}_3\text{N}@C_{2v}\text{-C}_{78}$ , (Osuna et al. 2009a)  $\text{Ti}_2\text{C}_2@D_{3h}\text{-C}_{78}$ , (Garcia-Borràs et al. 2012a)  $\text{X}@I_h\text{-C}_{80}$  ( $\text{X} = \emptyset, \text{Sc}_3\text{N}, \text{Lu}_3\text{N}, \text{Y}_3\text{N}, \text{La}_2, \text{Y}_3, \text{Sc}_3\text{C}_2, \text{Sc}_4\text{C}_2, \text{Sc}_3\text{CH}, \text{Sc}_4\text{O}_2, \text{and Sc}_4\text{O}_3$ ) (Garcia-Borràs et al. 2013c) and  $\text{X}_3\text{N}@D_{5h}\text{-C}_{80}$  ( $\text{X} = \text{Sc}, \text{Lu}, \text{Gd}$ ) (Osuna et al. 2012b).

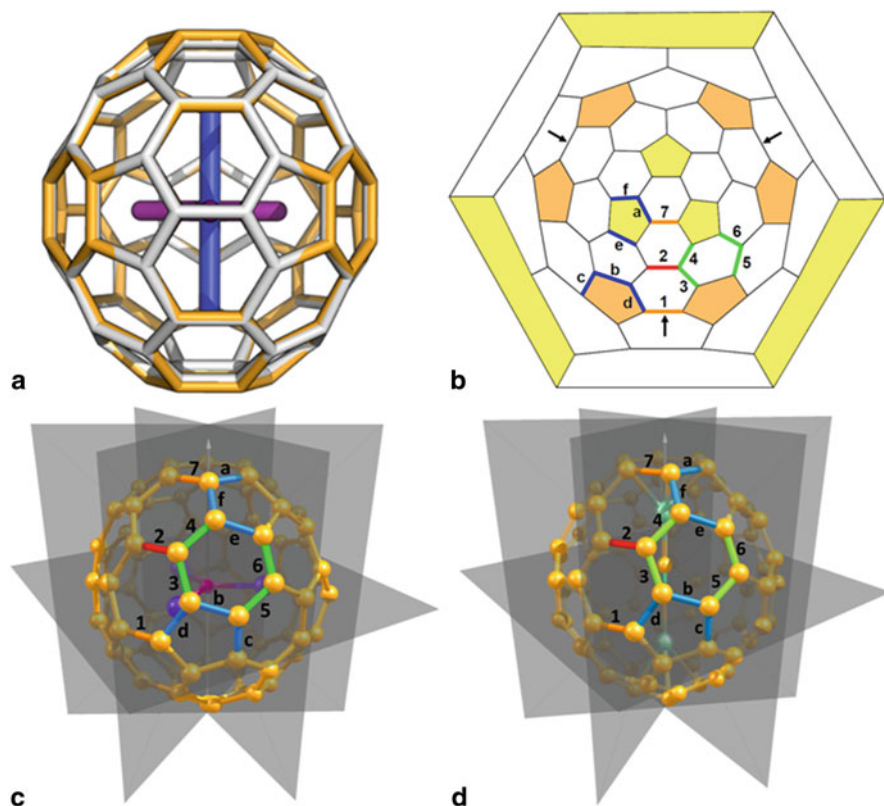
In the next sections, we summarize the results obtained in all these previous studies. First, in order to analyze the changes on the regiochemistry due to: (i) the size and orientation of the metallic clusters; (ii) the deformation and strain induced on the carbon structure by the encapsulated moiety; and (iii) the different amounts of charge transferred from the metallic cluster to the fullerene cage, we studied the DA cycloaddition involving  $\text{X}@D_{3h}\text{-C}_{78}$  ( $\text{M} = \emptyset, \text{Sc}_3\text{N}, \text{Y}_3\text{N}$  and  $\text{Ti}_2\text{C}_2$ ) species. (Osuna et al. 2008, 2009a; Garcia-Borràs et al. 2012a) The different nature, size and shape of  $\text{Sc}_3\text{N}, \text{Y}_3\text{N}$  and  $\text{Ti}_2\text{C}_2$  metallic clusters, which remain immobile inside the  $D_{3h}\text{-C}_{78}$  cage, make them as perfect candidates to achieve our goals. Then, we compared the TNT based EMFs reactivity between  $I_h\text{-C}_{80}$  and  $D_{5h}\text{-C}_{80}$  hosting cages (Osuna et al. 2012b). The  $I_h\text{-C}_{80}$  cage encapsulating different metal clusters is one of the EMF cages for which more experimental work has been reported. For this reason, in a subsequent study we selected a number of  $I_h\text{-C}_{80}$ -based EMFs to perform an exhaustive analysis of the influence of the metal cluster in their chemical reactivity using our recently proposed FCM approach for exploring all the possible cluster orientations inside the  $I_h\text{-C}_{80}$  cage (Garcia-Borràs et al. 2012b, 2013c).

Next, we discussed the importance of including van der Waals dispersion corrections in DFT calculations involving fullerenes in order to obtain reaction barriers and energies much closer to the experimental ones (Osuna et al. 2011b). Finally, we show that different experimentally observed product stabilities for  $\text{La}@C_{2v}\text{-C}_{82}\text{Cp}$  ( $\text{Cp} = \text{cyclopentadiene}$ ) and  $\text{La}@C_{2v}\text{-C}_{82}\text{Cp}^*$  ( $\text{Cp}^* = 1,2,3,4,5\text{-pentamethylcyclopentadiene}$ ) adducts can only be explained when the dispersion interaction energies are considered (Garcia-Borràs et al. 2013a).

## 4.2 Metal Effects on Diels-Alder Cycloaddition Regioselectivity

### 4.2.1 The Diels-Alder Reaction on $D_{3h}\text{-C}_{78}$ and $\text{Sc}_3\text{N}, \text{Y}_3\text{N}, \text{Ti}_2\text{C}_2$ Related EMFs: The Role of Fullerene Strain Energy

In some experimental studies, it was observed that exohedral reactivity of EMFs is highly affected by the nature of the encapsulated cluster (Cardona et al. 2005a). In order to evaluate the effect of the metal cluster on the exohedral reactivity of the



**Fig. 4.3** **a** Representation of superimposed  $\text{Ti}_2\text{C}_2@D_{3h}\text{-C}_{78}$  (yellow cage and blue cluster) and  $\text{Sc}_3\text{N}@D_{3h}\text{-C}_{78}$  (light gray cage and lila cluster). **b** Schlegel diagram (2D representation) of  $D_{3h}\text{-C}_{78}$  fullerene where all non-equivalent bonds are highlighted and different bond types are marked: Type A in orange; Type B in green; Type C in red; Type D in blue. Black arrows indicate the position of Sc atoms facing the different bonds. **c** Representation of the  $\text{Sc}_3\text{N}@D_{3h}\text{-C}_{78}$  structure. **d** Representation of the  $\text{Ti}_2\text{C}_2@D_{3h}\text{-C}_{78}$  structure. (Adapted with permission from (Garcia-Borràs et al. 2012a). Copyright 2012 Wiley)

fullerene cages, we decided to study the DA reaction on the empty  $D_{3h}\text{-C}_{78}$  fullerene and its related  $\text{Sc}_3\text{N}$ ,  $\text{Y}_3\text{N}$  and  $\text{Ti}_2\text{C}_2$  EMFs. In contrast to what happens in larger cages such as  $I_h\text{-C}_{80}$ , the metal cluster is not able to rotate inside the  $D_{3h}\text{-C}_{78}$  cavity. Because of the different position that TNT clusters and titanium carbide adopt inside the  $D_{3h}\text{-C}_{78}$  cage (see Fig. 4.3a), and the different nature of the metal clusters, we expected to find significant differences in their reactivity towards DA reaction.

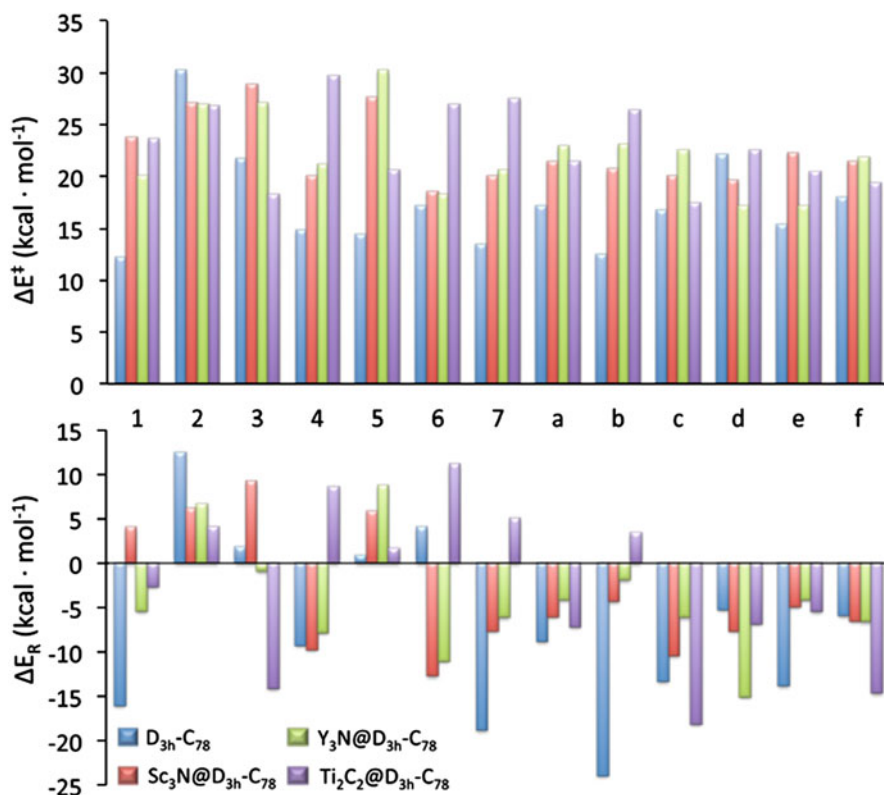
In general, for fullerenes and EMFs it is considered that the more pyramidalized the C–C bond being attacked, the closer to the  $\text{sp}^3$  bonding situation of the final adduct, and the lower the deformation energy is needed for the Diels-Alder adducts formation. Thus, when the strain of the C–C bond due to the presence of large inner

metal cluster increases (a more pyramidalized bond), the more reactive the considered bond should be. Moreover, in EMFs, the electronic transfer from the metal clusters to the carbon cage implies a reduction of the reactivity of the fullerene because of the destabilization of the EMF LUMOs disfavoring their interaction with the HOMO of the diene (in Diels-Alder reaction fullerene compounds act as a dienophile). It is usually found in fullerenes and EMFs that cycloadditions occur preferentially on short C–C bonds with lobes of opposite sign on each C atom in some of the accessible LUMOs of the fullerene cage. The double bond character and appropriate shape of the LUMO of these C–C bonds facilitate the interaction with the HOMO of the diene. Thus, bonds with high pyramidalized angles, short C–C distances and correct LUMO shape should be those more reactive in cycloaddition reactions involving EMFs.

Based on these observations, we present here a study on the Diels-Alder [4 + 2] reaction at the BP86/TZP//BP86/DZP level of theory over the 13 non-equivalent bonds of the  $D_{3h}$ - $C_{78}$  pristine cage, and its  $Sc_3N$ ,  $Y_3N$ , and  $Ti_2C_2$  EMFs. In  $D_{3h}$ - $C_{78}$  related EMFs, as opposite to the  $C_{80}$  systems described in previous sections where the metal clusters can freely rotate, the rotation of TNTs and carbide unit encapsulated is highly impeded. Thus, we can directly investigate the changes in the reactivity of the different non-equivalent bonds (13 in total, see Fig. 4.3) due to the presence of the different metal clusters: different orientation, shape, and strain on the fullerene cage (see Fig. 4.3). The fullerene deformation energies found at BP86/TZP//BP86/DZP level are 32.2, 67.5, and 39.9 kcal mol<sup>-1</sup> for  $Sc_3N$ ,  $Y_3N$ , and  $Ti_2C_2$ , respectively, indicating that the  $Y_3N$  cluster (the largest one) induces the larger strain on  $D_{3h}$ - $C_{78}$  cage, followed by  $Ti_2C_2$  and  $Sc_3N$  in this order.

In Fig. 4.4 we report the activation barriers and reaction energies for each addition site for  $D_{3h}$ - $C_{78}$ ,  $Sc_3N@D_{3h}$ - $C_{78}$ ,  $Y_3N@D_{3h}$ - $C_{78}$ , and  $Ti_2C_2@D_{3h}$ - $C_{78}$ .  $D_{3h}$ - $C_{78}$ ,  $Sc_3N@D_{3h}$ - $C_{78}$  and  $Ti_2C_2@D_{3h}$ - $C_{78}$  have 7 different [6, 6] type bonds: (i) Type A (pyracenylic) bonds 1 and 7; (ii) Type B bonds 2, 4, 5, and 6; and (iii) Type C (pyrenic) bond 2. Furthermore, there are 6 [5, 6] type bonds, all of them corresponding to the Type D (corannulene), bonds a-f (see Figs. 4.1 and 4.3 for bond types and nomenclature used here). The large yttrium based TNT cluster occupies the same position as the  $Sc_3N$  one, but it is forced to adopt a pyramidal configuration inside the  $D_{3h}$ - $C_{78}$  cage. Therefore, two clearly differentiated areas are present: the so-called *up* region, which is more influenced by the nitrogen atom, and the *down* region which has the yttrium atoms in close contact. In each area, the 13 non-equivalent bonds might be considered to take into account all the different addition sites.

Our results indicate that, as a general trend, reaction energies became less exothermic (less favorable) and reaction barrier heights increase when a metallic cluster is encapsulated (see Fig. 4.4). For the three EMFs, the formal charge transferred from the metal cluster to the fullerene cage is six electrons, inducing a reduction of the electron affinity of the carbon cage. Moreover, it is worth to mention here that there exists a good correspondence between the products obtained under thermodynamic conditions (those more stable) and those that exhibit lower reaction activation barriers, i.e., the kinetic control products (Garcia-Borràs et al. 2012b). But the most important observation is the largely different regioselectivities found for all four systems.



**Fig. 4.4** Comparison of the reaction energy barriers and reaction energies (in kcal mol<sup>-1</sup>) for the DA reaction over all non-equivalent bonds of X@D<sub>3h</sub>-C<sub>78</sub> (X = ∅, Sc<sub>3</sub>N, Y<sub>3</sub>N, and Ti<sub>2</sub>C<sub>2</sub>) EMFs. For Y<sub>3</sub>N@D<sub>3h</sub>-C<sub>78</sub> only energies for the down region are reported here (see ref. (Osuna et al. 2009a)). (Reprinted with permission from (Garcia-Borràs et al. 2012a). Copyright 2012 Wiley)

The most reactive bonds for the D<sub>3h</sub>-C<sub>78</sub> pristine cage are the pyracylene (type A) [6, 6] bonds **1** and **7** and the corannulene (type D) [5, 6] bond **b** (for bond **1**:  $\Delta E_R = -16.0$  kcal mol<sup>-1</sup>,  $\Delta E^\ddagger = 12.2$  kcal mol<sup>-1</sup>; for bond **7**:  $\Delta E_R = -18.8$  kcal mol<sup>-1</sup>,  $\Delta E^\ddagger = 13.5$  kcal mol<sup>-1</sup>; and for bond **b**:  $\Delta E_R = -23.9$  kcal mol<sup>-1</sup>,  $\Delta E^\ddagger = 12.5$  kcal mol<sup>-1</sup>). It is important to remark here that pyracylene bonds are also the most favorable addition sites for C<sub>60</sub>.

When the scandium based metal cluster is encapsulated, the regioselectivity changes towards the additions over type B [6, 6] bonds **6** and **4**, and the type D [5, 6] bond **c** (for bond **6**:  $\Delta E_R = -12.7$  kcal mol<sup>-1</sup>,  $\Delta E^\ddagger = 18.5$  kcal mol<sup>-1</sup>; for bond **4**:  $\Delta E_R = -9.7$  kcal mol<sup>-1</sup>,  $\Delta E^\ddagger = 20.0$  kcal mol<sup>-1</sup>; and for bond **c**:  $\Delta E_R = -10.4$  kcal mol<sup>-1</sup>,  $\Delta E^\ddagger = 20.1$  kcal mol<sup>-1</sup>). And when the yttrium TNT EMF is considered (Y<sub>3</sub>N@D<sub>3h</sub>-C<sub>78</sub>, the largest cluster studied), the most favorable additions are those corresponding to the attack over type D [5, 6] bond **d** ( $\Delta E_R = -15.0$

kcal mol<sup>-1</sup>,  $\Delta E^\ddagger = 17.1$  kcal mol<sup>-1</sup>), type B [6, 6] bond **6** ( $\Delta E_R = -11.0$  kcal mol<sup>-1</sup>,  $\Delta E^\ddagger = 18.3$  kcal mol<sup>-1</sup>), and type D [5, 6] bond **e** ( $\Delta E_R = -4.1$  kcal mol<sup>-1</sup>,  $\Delta E^\ddagger = 17.2$  kcal mol<sup>-1</sup>), situated all of them in the down region. Finally, the titanium carbide  $D_{3h}\text{-C}_{78}$  based EMF ( $\text{Ti}_2\text{C}_2@D_{3h}\text{-C}_{78}$ ) most favored additions correspond to the cycloaddition over type D [5, 6] **c** bond ( $\Delta E_R = -18.1$  kcal mol<sup>-1</sup>,  $\Delta E^\ddagger = 17.4$  kcal mol<sup>-1</sup>), type B [6, 6] **3** bond ( $\Delta E_R = -14.1$  kcal mol<sup>-1</sup>,  $\Delta E^\ddagger = 18.2$  kcal mol<sup>-1</sup>) and type D [5, 6] **f** bond ( $\Delta E_R = -14.6$  kcal mol<sup>-1</sup>,  $\Delta E^\ddagger = 19.3$  kcal mol<sup>-1</sup>). In Fig. 4.4 the different reactivity for all nonequivalent bonds is compared.

In Table 4.1 we report the C–C bond distances and pyramidalization angles for each studied system. As can be seen there, for the empty fullerene and  $\text{Sc}_3\text{N}@D_{3h}\text{-C}_{78}$  EMF (the least strained cage as discussed before), the most favorable addition sites present the shortest C–C bond distances (**1**, **7**, and **b** for  $D_{3h}\text{-C}_{78}$ , and **4**, **6** and **c** for  $\text{Sc}_3\text{N}@D_{3h}\text{-C}_{78}$ ). But there are some bonds that although they present similar bond distances, their reaction energies are clearly different (for instance, bonds **6** and **7** in  $\text{Sc}_3\text{N}@D_{3h}\text{-C}_{78}$ ). As it happens with bond distances, the prediction of the fullerene reactivity analyzing the pyramidalization angles is not clear. These observations indicate that in the case of endohedral compounds, there is not an overall correlation between C–C bond distances, pyramidalization angles and reaction energies.

It is usually said that in DA reactions it is very important to have good overlaps between the HOMO orbital of the diene and the LUMO orbital of the dienophile. In the present case, *s-cis*-1,3-butadiene acts as the diene while fullerenes and EMF compounds act as the dienophiles. In Fig. 4.5 we report the 3 lowest-energy unoccupied molecular orbitals (LUMOs) of  $D_{3h}\text{-C}_{78}$  and the related  $\text{Ti}_2\text{C}_2@D_{3h}\text{-C}_{78}$  EMF. As can be seen there, because of the largely delocalized molecular orbitals, there are many bonds that present the correct shape to interact with the HOMO of the diene. For example, for the titanium EMF the bonds that present similar suitable antibonding character to interact correctly with the diene are: **a**, **c**, **f**, **1**, **2**, **3**, **4**, **5**, and **7**. However, three of these bonds (**4**, **5**, and **7**) present endothermic reaction energies. Hence, predictions of the fullerene and EMF reactivities based on the LUMO orbitals analysis are also too imprecise, as one finds too many bonds suitable to interact, although some of them are not very reactive. Therefore bond distances, pyramidalization angles or LUMOs shape cannot be used as a predictor of fullerene compounds reactivity, and as a consequence, all the possible additions should be investigated in order to give the correct picture of the reactivity of the considered compound. Even so, these tools are shown to be very useful for analyzing the different reactivity trends.

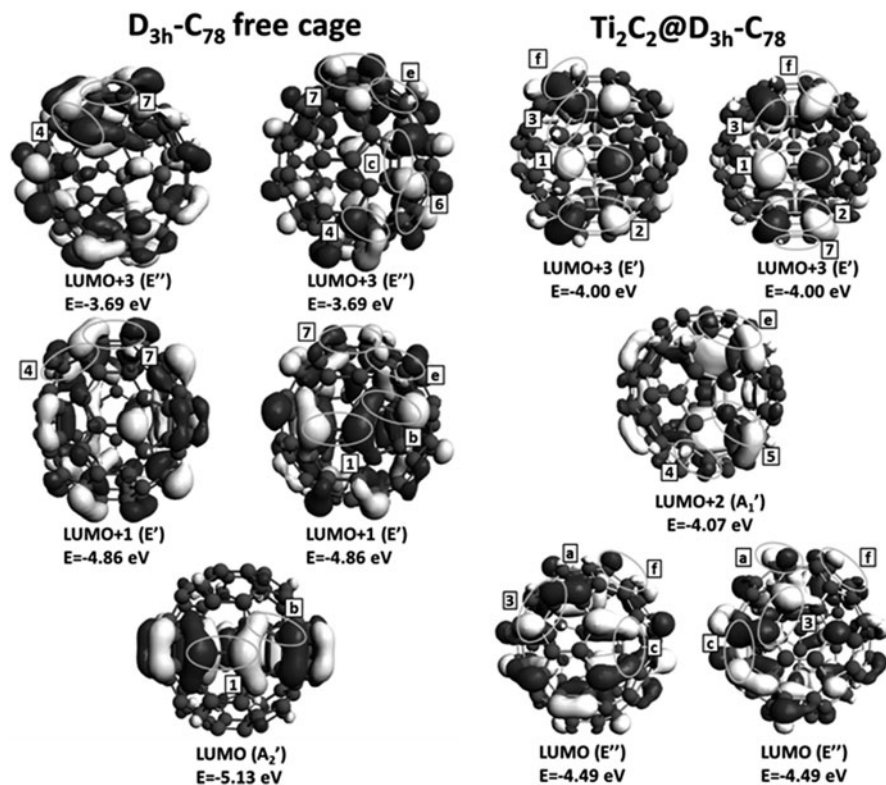
We have seen that the most reactive bonds in  $\text{Sc}_3\text{N}@D_{3h}\text{-C}_{78}$  exhibit short C–C bond distances with relatively high pyramidalization angles and situated far from the scandium atoms' influence. When the reaction takes place on  $\text{Y}_3\text{N}@D_{3h}\text{-C}_{78}$  the addition is basically favored over bond **d** having one of the yttrium atoms in close contact and one of the longest C–C bonds. The same situation is found for the **f** bond in the  $\text{Ti}_2\text{C}_2$  system. This preference for these bonds closer to the metal cluster is due to the fact that an addition there reduces the strain energy of the cage. We have to keep in mind that fullerene deformation energies for  $\text{Y}_3\text{N}$  and  $\text{Ti}_2\text{C}_2$  EMFs are much larger than the one found for the  $\text{Sc}_3\text{N}$  EMF. Thus, changes on the carbon cage



**Table 4.1** BP86/DZP bond lengths ( $R_{\text{full}}$ , Å) and pyramidalization angles ( $\theta_p$ , deg) for free  $C_{78}$ . The differences in bond lengths ( $\Delta R_{\text{full}}$ , Å) and pyramidalization angles ( $\Delta\theta_p$ , deg) between endofullerenes and free  $C_{78}$  cage are also presented for all non-equivalent bonds. Reported pyramidalization angles represent the average over the two atoms that constitute the bond under consideration. RMS values are calculated taking into account the total number of non-equivalent bonds

Bond	$D_{3h}-C_{78}^a$		$Sc_3N@D_{3h}-C_{78}^b$		$Y_3N@D_{3h}-C_{78}$ up		$Y_3N@D_{3h}-C_{78}$ down		$Ti_2C_2@D_{3h}-C_{78}$	
	$R_{\text{full}}$	$\theta_p$	$\Delta R_{\text{full}}$	$\Delta\theta_p$	$\Delta R_{\text{full}}$	$\Delta\theta_p$	$\Delta R_{\text{full}}$	$\Delta\theta_p$	$\Delta R_{\text{full}}$	$\Delta\theta_p$
1	1.369	10.46	0.071	3.340	0.094	3.570	0.094	3.570	0.019	0.560
2	1.465	8.58	0.001	-0.250	0.010	-0.120	0.009	-0.030	-0.009	0.340
3	1.432	9.62	0.018	-0.360	0.028	0.210	0.016	0.020	-0.019	0.090
4	1.415	9.60	0.011	-0.160	0.017	-0.380	0.020	-0.260	0.031	-0.945
5	1.418	9.53	0.014	-0.560	0.025	-0.970	0.025	-0.860	-0.002	0.215
6	1.420	9.44	-0.020	0.550	-0.024	0.220	-0.022	0.340	0.003	-0.765
7	1.388	11.64	0.012	-0.430	0.010	-0.470	0.013	-0.580	0.069	1.890
a	1.438	11.64	-0.001	-0.430	0.001	-0.470	0.002	-0.580	0.039	1.890
b	1.410	10.49	0.036	-0.760	0.045	-0.390	0.047	-0.600	0.037	0.165
c	1.465	10.32	-0.042	-1.050	-0.042	-1.300	-0.042	-1.300	-0.043	0.490
d	1.446	10.56	0.006	1.440	0.022	2.060	0.018	1.820	-0.015	0.200
e	1.438	10.38	0.011	0.540	0.016	0.220	0.015	0.320	-0.003	-1.745
f	1.442	11.13	-0.010	-0.250	-0.011	-0.550	-0.011	-0.540	0.010	-0.170
All bonds			0.022	0.858	0.033	1.163	0.032	1.127	0.027	0.918
RMS	[6, 6]		0.021	0.862	0.036	1.236	0.035	1.217	0.029	0.816
	[5, 6]		0.022	0.847	0.029	1.091	0.029	1.038	0.026	0.996



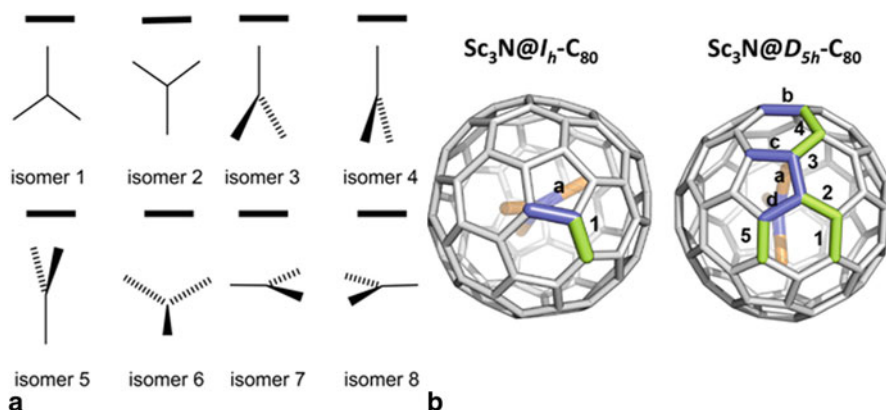


**Fig. 4.5** Representation of the  $D_{3h}$ - $C_{78}$  free cage LUMO, LUMO+1 and LUMO+3 (isosurface value 0.02 a.u.) in which only those bonds with favorable orbitals to interact with the HOMO of the diene are marked with *ellipses*. For comparison the same information is given for  $Ti_2C_2@D_{3h}$ - $C_{78}$ . (Reprinted with permission from (Garcia-Borràs et al. 2012a). Copyright 2012 Wiley)

due to the encapsulation of metallic clusters (fullerene strain, charge transfer, etc.) are much more important than the simplest rules based on the C–C bond distances, pyramidalization angles or LUMO orbitals shape. There exists not (yet) a predictive indicator of the most suitable addition sites, but we can rationalize the observed behavior based on the analysis of the metallic cluster effects.

#### 4.2.2 The Diels-Alder Cycloaddition on $I_h$ - $C_{80}$ versus $D_{5h}$ - $C_{80}$ Endohedral $M_3N$ ( $M = Sc, Lu, Gd$ ) Metallofullerenes

The computational exploration of the exohedral reactivity of EMFs has been shown to be a powerful tool to understand, predict and give support to the experimental addition sites (Osuna et al. 2011a). We decided to provide a detailed investigation of

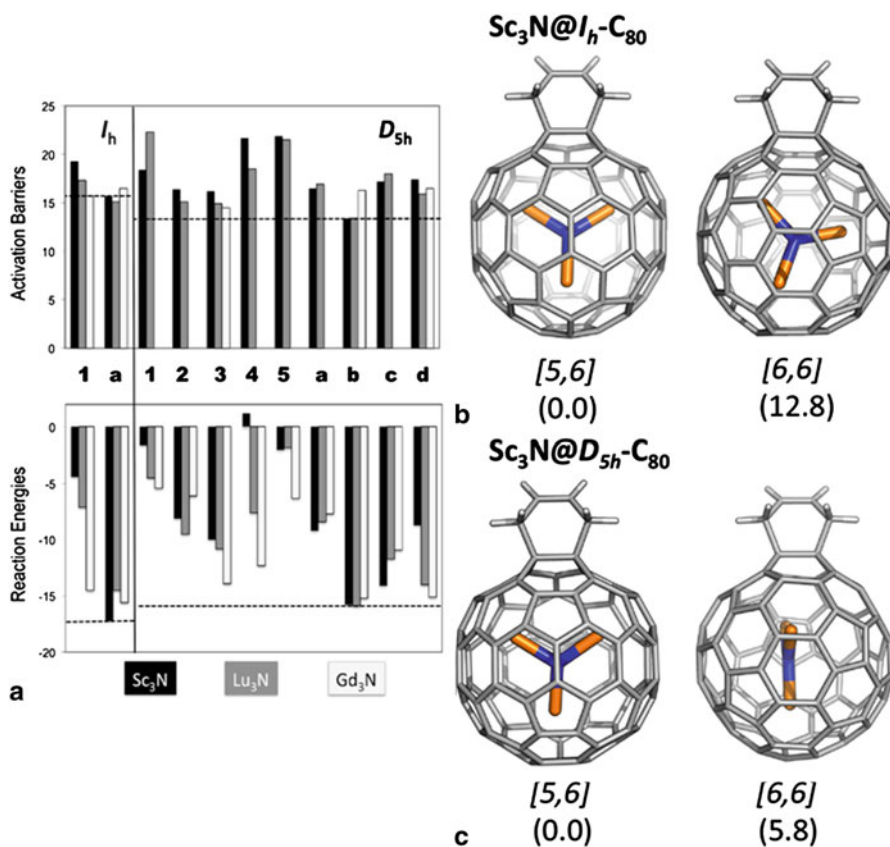


**Fig. 4.6** Representations of **a** the relative position of the metal nitride with respect to the attacked C–C bond of the fullerene cage; **b** non-equivalent bonds present in the  $I_h$  and  $D_{5h}$  cages

the exohedral reactivity of the most important and abundant EMFs, i.e. the Sc<sub>3</sub>N@I<sub>h</sub>-C<sub>80</sub> and its Sc<sub>3</sub>N@D<sub>5h</sub>-C<sub>80</sub> isomer, and the (bio)chemically relevant lutetium and gadolinium-based EMFs for both  $I_h$ -C<sub>80</sub> and  $D_{5h}$ -C<sub>80</sub> cages. As performed in previous studies, we analyze the thermodynamics and the kinetics of the DA cycloaddition of *s-cis*-1,3-butadiene on all different bonds of the  $I_h$ -C<sub>80</sub> and  $D_{5h}$ -C<sub>80</sub> cages.

The study of the reactivity on the M<sub>3</sub>N@C<sub>80</sub> EMFs is not straightforward since the metal nitride can rotate freely in the interior of the carbon cage cavity. This has been observed in NMR experiments (Duchamp et al. 2003; Stevenson et al. 1999; Yang et al. 2008) and has been confirmed by computational studies (Campanera et al. 2002; Popov and Dunsch 2008; Rodríguez-Fortea et al. 2006). In this study, we considered eight orientations of the M<sub>3</sub>N unit (see Fig. 4.6a) inside the  $I_h$ -C<sub>80</sub> cage, and five orientations (1, 2, 4, 5 and 8) for the  $D_{5h}$ -C<sub>80</sub> isomer. The lower number of orientations studied in the case of the  $D_{5h}$  cage is mainly due to the higher number of non-equivalent bonds present in the fullerene structure. In the case of  $I_h$ -C<sub>80</sub> only two different addition sites are possible: a type-D [5, 6] (corannulene) ring junction and a type-B [6, 6] junction. In contrast, the less symmetric  $D_{5h}$ -C<sub>80</sub> cage presents nine different C–C bonds: four [5, 6] bonds (type-D) and five [6, 6] bonds (one type-A, three type-B and one type-C, see Fig. 4.6b).

As observed in the previously studied Sc<sub>3</sub>N@D<sub>3h</sub>-C<sub>78</sub>, all EMFs are less reactive than their homologous hollow cages. Thus, for the pristine hollow  $I_h$ -C<sub>80</sub> fullerene, the Gibbs reaction energy for the addition on [5, 6] bond is  $-35.7 \text{ kcal mol}^{-1}$  while the corresponding value for the [6, 6] addition is  $-18.1 \text{ kcal mol}^{-1}$ . When the Sc<sub>3</sub>N is encapsulated inside  $I_h$ -C<sub>80</sub>, the lowest energy adduct corresponds to the [5, 6] addition (see Fig. 4.7) with a Gibbs reaction energy of  $-17.2 \text{ kcal mol}^{-1}$ . The addition is more stable than the [6, 6] one by more than  $12 \text{ kcal mol}^{-1}$ . The energy difference between the corresponding TSs is, however, notably smaller (*ca.*  $4 \text{ kcal mol}^{-1}$ ). Experimentally, the 1,3-dipolar cycloaddition of N-ethylazomethine



**Fig. 4.7** a Comparison of the reaction energies and activation barriers (in kcal mol<sup>-1</sup>) found for the Diels-Alder reaction over the nonequivalent bonds of  $M_3N@I_h-C_{80}$  and  $M_3N@D_{5h}-C_{80}$  ( $M = Sc$ , black; Lu, grey; Gd, white). Representation of the lowest-energy [5, 6] and [6, 6] regioisomers for the Diels-Alder cycloaddition between *s-cis*-1,3-butadiene and b  $Sc_3N@I_h-C_{80}$ , c  $Sc_3N@D_{5h}-C_{80}$ . The relative energies are expressed in kcal mol<sup>-1</sup> with respect to the lowest-energy isomer. The dotted lines indicate the lowest activation barriers and reaction energies for  $Sc_3N@I_h-C_{80}$  and  $Sc_3N@D_{5h}-C_{80}$ . (Adapted with permission from (Osuna et al. 2012b). Copyright 2012 Wiley)

ylide (Cardona et al. 2005b; Rodríguez-Forteza et al. 2006) and Diels-Alder addition of the diene generated from 6,7-dimethoxyisochroman-3-one (Lee et al. 2002) to  $Sc_3N@I_h-C_{80}$  occur regioselectively on the same [5, 6] bond of the fullerene cage. The lowest energy cycloadduct present the scandium atoms situated far away from the bond where the reaction has taken place. This observation is in line with the experimental findings and previous computational studies (Campanera et al. 2006; Osuna et al. 2008).

The theoretical evaluation of the exohedral reactivity of the less symmetric  $D_{5h}$  cage predicts bond  $D_{5h}$ -b, which is the most similar to the unique [5, 6] bond type in the icosahedral cage, as the most reactive bond. The activation barrier computed

for this bond is  $13.4 \text{ kcal mol}^{-1}$ , which is  $2.3 \text{ kcal mol}^{-1}$  lower than the barrier for the  $I_h$ -**a** bond. This lower activation barrier found for  $D_{5h}$ - $C_{80}$  cage indicates a higher reactivity towards Diels-Alder reaction than the parent  $I_h$  isomer, as observed recently by Dorn and co-workers (Cai et al. 2006b). This observation is also consistent with the smaller HOMO- LUMO gap for  $\text{Sc}_3\text{N}@D_{5h}\text{-}C_{80}$  ( $1.516 \text{ eV}$  and  $1.114 \text{ eV}$  for  $I_h$ - and  $D_{5h}\text{-}C_{80}$  cages, respectively) and a higher deformation energy of the  $D_{5h}$  cage ( $18.2$  and  $15.8 \text{ kcal mol}^{-1}$  for  $\text{Sc}_3\text{N}@D_{5h}\text{-}C_{80}$  and  $\text{Sc}_3\text{N}@I_h\text{-}C_{80}$ , respectively). The lowest energy regioisomer obtained, however, does not coincide with the regioisomer proposed experimentally from the  $^1\text{H}$  NMR spectra. Experimentally, it was proposed that the product under thermodynamic control for the Prato cycloaddition corresponded to the addition on the [6, 6] pyracylenic bond  $D_{5h}\text{-}5$ . But our calculations indicate that the  $D_{5h}\text{-}5$  regioisomer is not found among the lowest-energy regioisomers (its reaction energy is  $-2.0 \text{ kcal mol}^{-1}$  as compared to  $-15.8 \text{ kcal mol}^{-1}$  for the most stable  $D_{5h}\text{-}b$ ). Apart from that, it presents one of the larger reaction barriers ( $18.4$  and  $13.4 \text{ kcal mol}^{-1}$  for  $D_{5h}\text{-}5$  and  $D_{5h}\text{-}b$ , respectively). From our work, we propose regioisomer  $D_{5h}\text{-}b$  as the product under thermodynamic control for the Diels-Alder cycloaddition on  $\text{Sc}_3\text{N}@D_{5h}\text{-}C_{80}$ . Given that our study is focused on the Diels-Alder reaction with 1,3-*cis*-butadiene, and the experimental study on the Prato reaction with N-tritylazomethine ylide, we first investigated whether the 1,3-dipolar and Diels-Alder presented different regioselectivities (Osuna et al. 2012a). It should be emphasized that previous studies had shown that in general the 1,3-dipolar and Diels-Alder products behave similarly in related systems (Osuna and Houk 2009). As expected, the computational exploration of the 1,3-dipolar cycloaddition using N-tritylazomethine ylide yielded the same conclusions as for the DA reaction. The Prato reaction was found to be favored over corannulene [5, 6] bonds, and not over pyracylenic [6, 6] bonds as suggested by the experimental study. We therefore decided to compute the NMR chemical shieldings for the different adducts, which showed that the experimentally observed NMR spectra with a single peak at  $3.19 \text{ ppm}$  were incompatible with pyracylenic adducts. Instead, the computationally predicted lowest energy adduct was found to correspond to the experimental spectrum (Osuna et al. 2012a). This study highlights the importance of computations in helping to understand and predict the regioselectivity of the additions in EMFs.

We finally investigated the effect of the metal cluster on the reactivity of the cages (see Fig. 4.7).  $\text{Lu}_3\text{N}@C_{80}$  presents a similar reactivity to that of the scandium nitride homologue. However we observe that the regioselectivity of the DA reaction is somewhat smaller for both  $I_h$  and  $D_{5h}$  cages. The situation is more interesting for the  $\text{Gd}_3\text{N}$  cluster since  $\text{Gd}^{3+}$  ions are larger and more electropositive. For both lutetium and scandium-based EMFs, the lowest energy cycloaddition adducts present the metal atoms oriented far away from the functionalized C–C bond, but the nitride and the attacked C–C bond are coplanar. By increasing the size of the encapsulated metal atoms, those orientations presenting one M atom pointing towards the functionalized bond gain stability. In the case of  $\text{Gd}_3\text{N}$ , some [6, 6] regioisomers containing nitrides with the metal pointing towards the attacked bond become competitive. Calculations also show that for  $\text{Gd}_3\text{N}@I_h\text{-}C_{80}$  and  $\text{Gd}_3\text{N}@D_{5h}\text{-}C_{80}$  the product under kinetic control is not the same as the one under thermodynamic control. In a previous combined

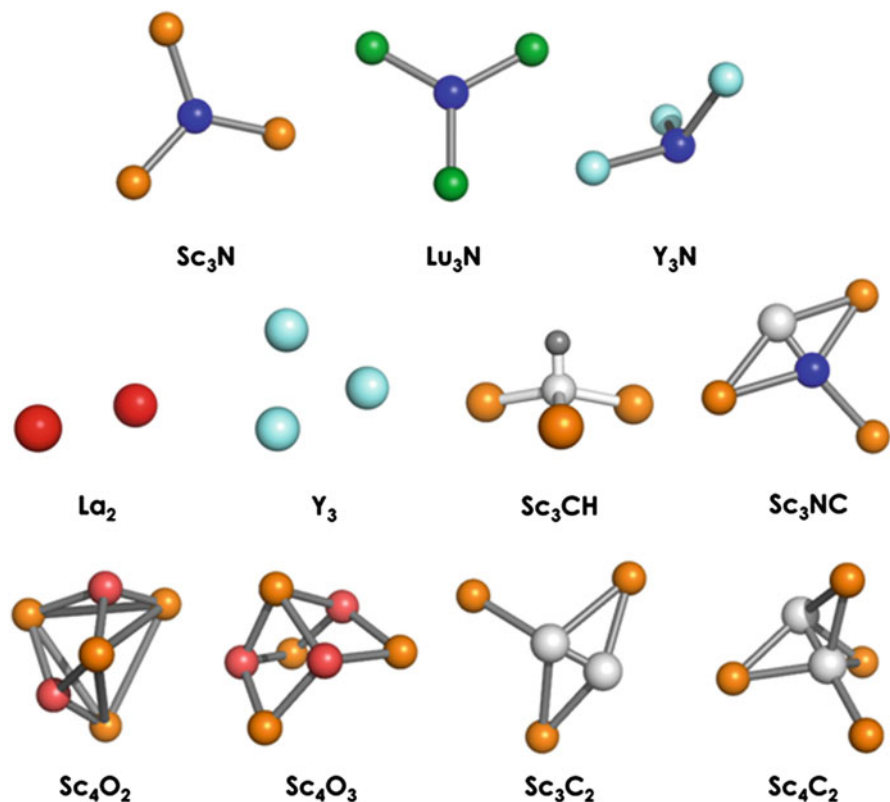
experimental/theoretical study the regioselectivity of the 1,3-dipolar cycloaddition reaction was compared for the mixed species  $\text{Sc}_x\text{Gd}_{3-x}\text{N}@I_h\text{-C}_{80}$  ( $x = 0-3$ ) (Chen et al. 2007). Experiments showed that the regioselectivity of the reaction was drastically changed as the [5, 6] regioisomer was obtained in the case of  $\text{Sc}_3\text{N}@I_h\text{-C}_{80}$ , whereas the [6, 6] one for  $\text{Gd}_3\text{N}@I_h\text{-C}_{80}$ . Our calculations indicate that the difference in reactivity observed experimentally is basically due to the *lower activation barrier* found for the  $\text{Gd}_3\text{N}@I_h\text{-C}_{80}$  [6, 6] addition ( $15.7 \text{ kcal mol}^{-1}$  for the [6, 6] addition as compared to  $16.5 \text{ kcal mol}^{-1}$  for the [5, 6] one). The kinetics of the Diels-Alder reaction at  $\text{Gd}_3\text{N}@I_h\text{-C}_{80}$  is therefore crucial to fully understand the experimental findings.

### 4.2.3 The Influence of Metal Clusters on the Diels-Alder Regioselectivity of $I_h\text{-C}_{80}$ Endohedral Metallofullerenes

In order to improve our understanding of the endohedral metallofullerene reactivity and the regioselectivity changes due to the different nature of the metal cluster encapsulated, we have systematically studied with density functional methods (ZORA-BLYP-dDsC/TZP//ZORA-BP86-D<sub>2</sub>/DZP) the Diels-Alder cycloaddition between *s-cis*-1,3-butadiene and practically all  $\text{X}@I_h\text{-C}_{80}$  synthesized up to date:  $\text{X} = \text{Sc}_3\text{N}$ ,  $\text{Lu}_3\text{N}$ ,  $\text{Y}_3\text{N}$ ,  $\text{La}_2$ ,  $\text{Y}_3$ ,  $\text{Sc}_3\text{C}_2$ ,  $\text{Sc}_4\text{C}_2$ ,  $\text{Sc}_3\text{CH}$ ,  $\text{Sc}_3\text{NC}$ ,  $\text{Sc}_4\text{O}_2$ , and  $\text{Sc}_4\text{O}_3$  (see Fig. 4.8). Using the Frozen Cage Model (FCM), which is a computationally cheap approach to accurately predict the exohedral regioselectivity of cycloaddition reactions in EMFs, (Garcia-Borràs et al. 2012b) we have studied both the thermodynamic and the kinetic regioselectivity of the process taking into account the free rotation of the metallic cluster inside the fullerene.

In Fig. 4.2 the two non-equivalent bonds for  $I_h\text{-C}_{80}$  fullerene are represented. Even though  $I_h\text{-C}_{80}$  fullerene has only two different non-equivalent bonds, the complexity of the theoretical study of  $\text{X}@I_h\text{-C}_{80}$  reactivity and regioselectivity arises from the free rotation that the inner metal clusters present (see for instance the previous 2.2 section). Indeed, the study presented here has only been made possible through the use of the FCM method, which in the first phase scans and finds the most stable products of a given reaction in EMFs at a low computational cost, which is followed in the second phase by a full (non-frozen) exploration of the reactivity for a small number of selected most reactive bonds.

In that sense, we have reported in Fig. 4.9 Gibbs reaction energies and Gibbs reaction barriers for all the studied systems considering the most favorable orientation of the inner metallic cluster. As said before, for the pristine hollow  $I_h\text{-C}_{80}$  fullerene, the Gibbs reaction energy for the addition on [5, 6] bond is  $-35.7 \text{ kcal mol}^{-1}$  while the corresponding value for the [6, 6] addition is  $-18.1 \text{ kcal mol}^{-1}$ . The reaction barriers are found to be 3.4 and 2.4  $\text{kcal mol}^{-1}$  for [5, 6] and [6, 6] additions at this level of theory. Thus, results indicate that the  $I_h\text{-C}_{80}$  empty cage is very reactive and thermodynamic and kinetic products are not the same.

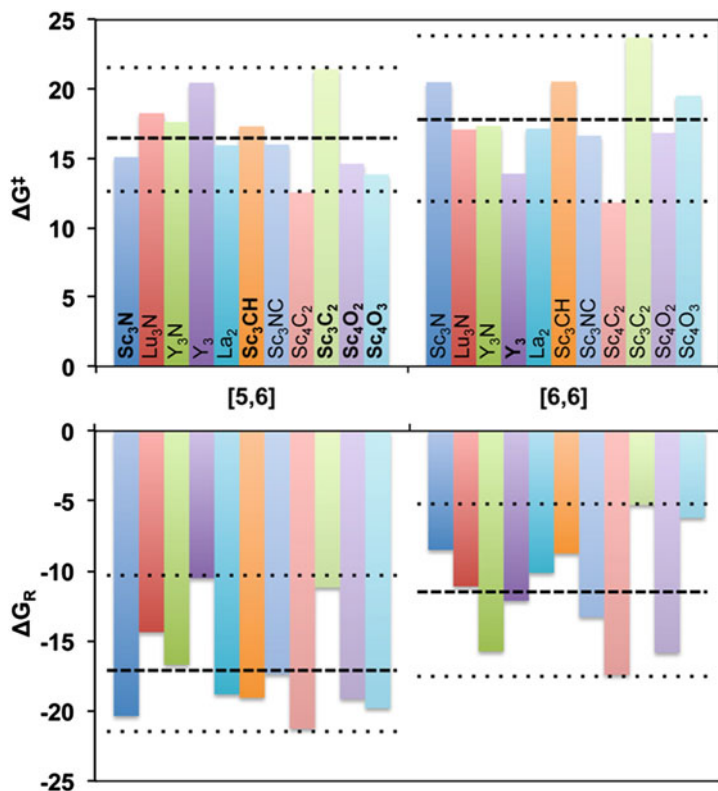


**Fig. 4.8** Representation of the  $Sc_3N$ ,  $Lu_3N$ ,  $Y_3N$ ,  $La_2$ ,  $Y_3$ ,  $Sc_3C_2$ ,  $Sc_4C_2$ ,  $Sc_3CH$ ,  $Sc_3NC$ ,  $Sc_4O_2$ , and  $Sc_4O_3$  metal cluster structures adopted inside the fullerene cage

When  $I_h-C_{80}$  EMFs are considered, our results show that the encapsulation of metal clusters inside the cage decreases its reactivity; there is a great increase in Gibbs reaction barriers and a decrease in Gibbs reaction energies. Here, we report a brief description of the reactivity and regioselectivity trends of all EMF families considered in this study:

**TNT Clusters ( $Sc_3N$ ,  $Lu_3N$ ,  $Y_3N$ )** Those systems that present a large HOMO-LUMO gap and a high charge transfer between the metallic cluster and the cage (see Table 4.2) exhibit a low reactivity (i.e. high activation barriers). The regioselectivity of the cycloaddition reaction depends strongly on the volume of the inner TNT and the related fullerene deformation energy. The larger the TNT (*or the more deformed the fullerene cage*), the smaller the energy difference between [6, 6] and [5, 6] additions, and the less regioselective the reaction. The preference for the [6, 6] addition increases for those systems that present a larger volume of the metal cluster and fullerene distortion energy.





**Fig. 4.9** Comparison of the Gibbs reaction barriers and reaction energies (in kcal mol<sup>-1</sup>) for the DA reaction over [5, 6] and [6, 6] bonds of X@I<sub>h</sub>-C<sub>80</sub> (X = Sc<sub>3</sub>N, Lu<sub>3</sub>N, Y<sub>3</sub>N, La<sub>2</sub>, Y<sub>3</sub>, Sc<sub>3</sub>C<sub>2</sub>, Sc<sub>4</sub>C<sub>2</sub>, Sc<sub>3</sub>CH, Sc<sub>3</sub>NC, Sc<sub>4</sub>O<sub>2</sub>, and Sc<sub>4</sub>O<sub>3</sub>) EMFs. Only energies for the lowest energy orientations of the metal cluster are considered. The *dotted* (*striped*) lines indicate the lowest and highest (average) Gibbs reaction barriers and reaction energies for each case. (Adapted with permission from (Garcia-Borràs et al. 2013c). Copyright 2013 Wiley)

*Classical Clusters (La<sub>2</sub>, Y<sub>3</sub>)* The charge transfer and HOMO- LUMO gaps are practically the same in the two considered cases as presented in Table 4.2. Therefore, the main factors that differentiate their reactivity are the volume of the cluster and the fullerene deformation energy. A larger volume of the inner cluster (and so a higher fullerene deformation energy) leads to an increase of the exohedral reactivity of the classical EMF. As observed in the TNT cases, the preference for the [6, 6] addition increases for those systems that have a larger cluster volume and fullerene deformation energy, which is the case for Y<sub>3</sub>.

*Metallic Carbide (Sc<sub>3</sub>C<sub>2</sub>, Sc<sub>4</sub>C<sub>2</sub>), hydrocarbide (Sc<sub>3</sub>CH), and carbonitride (Sc<sub>3</sub>NC)* For these types of I<sub>h</sub>-C<sub>80</sub> EMFs in general the reaction barriers decrease

**Table 4.2** Metallic cluster volumes, charge transferred to the fullerene cage, EMFs HOMO- LUMO gaps, and fullerene deformation energies in X@ $I_h$ - $C_{80}$  species

X	V <sup>a</sup>	Charge <sup>b</sup>	HOMO- LUMO <sup>c</sup>	$\Delta E_{\text{def.}}^{\text{d}}$
$Sc_3N$	453.1	1.279	2.294	6.9
$Lu_3N$	473.1	1.425	2.516	20.5
$Y_3N$	496.4	1.362	2.540	20.1
$Y_3$	491.4	1.570	1.236 <sup>e</sup>	13.9
$La_2$	369.5	1.542	1.287	5.5
$Sc_3CH$	471.3	1.253	2.520	8.5
$Sc_3NC$	473.9	1.189	2.294	14.9
$Sc_3C_2$	484.1	1.100	2.264 <sup>e</sup>	16.3
$Sc_4C_2$	571.2	1.044	2.021	13.8
$Sc_4O_2$	550.3	1.196	1.709	8.5
$Sc_4O_3$	562.1	1.126	2.294	9.4

<sup>a</sup> Volume measured by the GEPOL93(Pascual-Ahuir et al. 1994) procedure. Values given in  $\text{\AA}^3$

<sup>b</sup> Charge transferred from the metal cluster to the  $I_h$ - $C_{80}$  cage measured as the sum of Hirshfeld charges of all fullerene C atoms obtained at B3LYP-dDsC/TZP//BP86-D2/DZP. Values given in atomic units

<sup>c</sup> HOMO- LUMO gap of EMFs at B3LYP-dDsC/TZP//BP86-D2/DZP level. Values given in eV

<sup>d</sup> Fullerene deformation energy due to the presence of the inner metallic cluster, calculated as the energy difference between  $I_h$ - $C_{80}$  distorted geometry (the EMF cage) and the  $I_h$ - $C_{80}$  optimized one at B3LYP-dDsC/TZP//BP86-D2/DZP level. Values given in  $\text{kcal mol}^{-1}$

<sup>e</sup> For open-shell species, the HOMO-LUMO gap was calculated as the difference between the lowest  $\alpha$  non-occupied spinorbital and the highest  $\alpha$  occupied spinorbital

when the charge transferred to the cage decreases and the volume of the metallic cluster increases (see Table 4.2). This implies that also for these EMFs larger fullerene deformation energies decrease reaction barriers. The only exception for the latter observation is the  $Sc_4C_2@I_h-C_{80}$  EMF. Also for this type of EMFs the [6, 6] addition is preferred from a kinetic point of view for the EMF that has the larger metallic cluster encapsulated (i.e.  $Sc_4C_2$ ), while [5, 6] addition is the one preferred for the other cases. But under thermodynamic control, the most favored addition is the one corresponding to the [5, 6] position for all the present studied cases.

**Metallic Oxide ( $Sc_4O_2$ ,  $Sc_4O_3$ )** The spherical shape of the metallic oxide clusters makes this class of EMFs significantly different from the rest of the considered cases. The [5, 6] addition is preferred in all cases, especially for  $Sc_4O_3@I_h-C_{80}$ , from both thermodynamic and kinetic points of view. Moreover, by increasing the cluster size the reaction becomes more regioselective, and the EMF more reactive (lower reaction barriers and more negative reaction energies).

As a whole, our results show that the reactivity of EMFs is lower than the empty  $I_h$ - $C_{80}$  fullerene. The exothermicity of the reactions in EMFs tends to decrease when the charge transfer to the cage increases because the cage has less electron



affinity. In general, the [6, 6] addition becomes more favored as compared to the [5, 6] one when the size of the metallic cluster increases and the deformation of the fullerene cage is higher, and when the charge transfer to the cage is larger. This is the first reported study that provides an extended guideline for experimental and computational chemists to understand and predict the reactivity and regioselectivity of the Diels-Alder cycloaddition on the  $I_h$ - $C_{80}$  based EMFs.

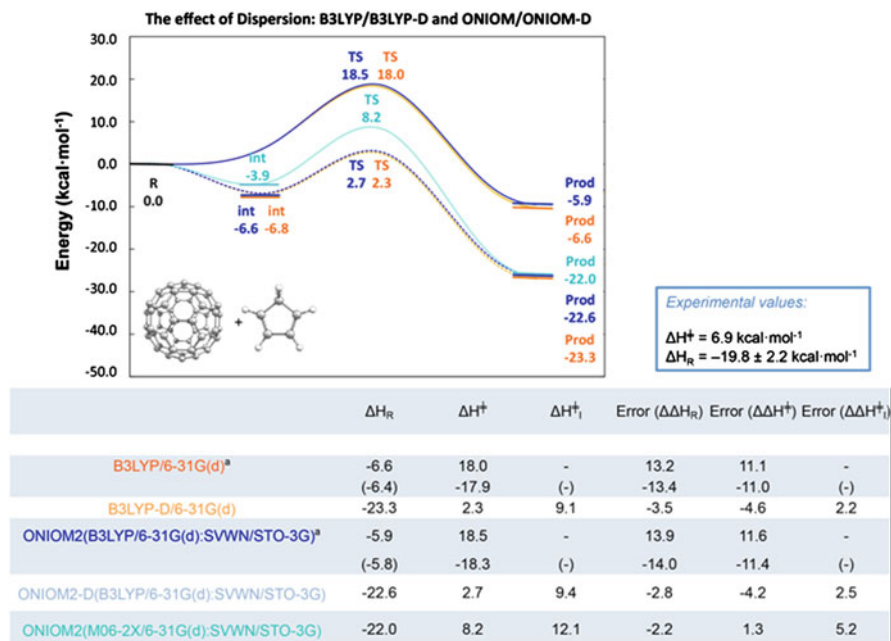
## 4.3 Dispersion Interactions

### 4.3.1 *The Importance of the Dispersion Corrections for the Study of Chemical Reactivity in Fullerenes*

The DA cycloaddition between cyclopentadiene and  $C_{60}$  for which experimental results on energy barriers and reaction energies were known was studied by some of us (Osuna et al. 2009b). It was found that the two-layered ONIOM2(B3LYP/6-31G(d):SVWN/STO-3G) method provides results very close to the full B3LYP/6-31G(d) ones. Unfortunately, the exothermicity of the reaction and also the energy barrier were clearly overestimated by these two methods compared to the experimental values (errors of ca. 12 kcal mol<sup>-1</sup>, see Fig. 4.10). Goerigk and Grimme (Goerigk and Grimme 2010) demonstrated that the B3LYP mean absolute deviation for an extensive benchmark was reduced by about 2 kcal mol<sup>-1</sup> when dispersion corrections were taken into account (B3LYP-D). Similarly, Grimme and coworkers (Kruse and Grimme 2009; Korona et al. (2009; Hesselmann and Korona 2011) pointed out the importance of London dispersion corrections to obtain good estimates of the interaction energy of  $C_{60}$  and  $C_{70}$  with encapsulated  $H_2$  and a noble gas molecule.

In light of the Grimme and Korona observations, we decided to investigate the effect of including dispersion interactions on the reaction and activation energies for the DA cycloaddition between cyclopentadiene and  $C_{60}$ . Our calculations including dispersion corrections indicate that the inclusion of London dispersion effects is mandatory to get an accurate description of the energy profile in the DA cycloaddition studied (see Fig. 4.10). B3LYP including Grimme dispersion corrections and also the hybrid meta exchange-correlation DFT functional M06-2X, (Zhao and Truhlar 2008) which includes medium-range correlation, yield reaction and activation energies close to the experimental values. ONIOM2 (M06-2X:SVWN) gives also accurate reaction energies (the reaction energy is overestimated by 2.2 kcal mol<sup>-1</sup>, see Fig. 4.10), but somewhat less accurate activation barriers (5.2 kcal mol<sup>-1</sup> higher than the experimental value).

We finally performed calculations both with and without dispersion corrections for the DA reaction of  $C_{60}$  and several dienes and for the DA cycloaddition of a (5,5) single walled carbon nanotube and 1,3-*cis*-butadiene. In all cases, large stabilizations are found which range from 15 to 22 kcal mol<sup>-1</sup> for the larger dienes presenting aromatic rings, such as anthracene. The results obtained in this study



**Fig. 4.10** Energy profile (in kcal mol<sup>-1</sup>) corresponding to the Diels-Alder reaction of C<sub>60</sub> with cyclopentadiene computed at B3LYP/6-31G(d) (represented in orange and continuous line), B3LYP-D/6-31G(d) (in orange, discontinuous line), ONIOM2(B3LYP/6-31G(d):SVWN/STO-3G) (in blue, continuous line), ONIOM2-D(B3LYP/6-31G(d):SVWN/STO-3G) (in blue, discontinuous line) and ONIOM2(M06-2X/6-31G(d):SVWN/STO-3G) (in cyan, continuous line). Comparison between the reaction energies  $\Delta H_R$  and activation barriers  $\Delta H^\ddagger$  (in kcal mol<sup>-1</sup>).  $\Delta H^\ddagger$  corresponds to the activation barrier calculated with respect to isolated reactants (i.e.  $H^{TS} - (H^{C60} + H^{diene})$ ) whereas  $\Delta H^\ddagger_1$  is referred to the optimized reactant complex (i.e.  $H^{TS} - H^{int}$ ). The difference between the computed energies and the experimental values is also indicated (the experimental reaction energy is  $-19.8 \pm 2.2$  kcal mol<sup>-1</sup> and the activation barrier is 6.9 kcal mol<sup>-1</sup>). In parentheses are given the relative enthalpies including solvent effects (PCM and toluene as the solvent)

indicate that inclusion of dispersion corrections is compulsory to accurately reproduce the experimental reaction and activation energies for the study of the chemical reactivity of fullerenes and nanotubes.

### 4.3.2 The Diels-Alder Regioselectivity and Different Product Stability of La@C<sub>2v</sub>-C<sub>82</sub> (1,2,3,4,5-Pentamethyl)cyclopentadiene

In the DA addition of cyclopentadiene (Cp) on La@C<sub>2v</sub>-C<sub>82</sub> the attack of Cp on bond **19** (see Fig. 4.11a) was proposed to be the major product of the reaction

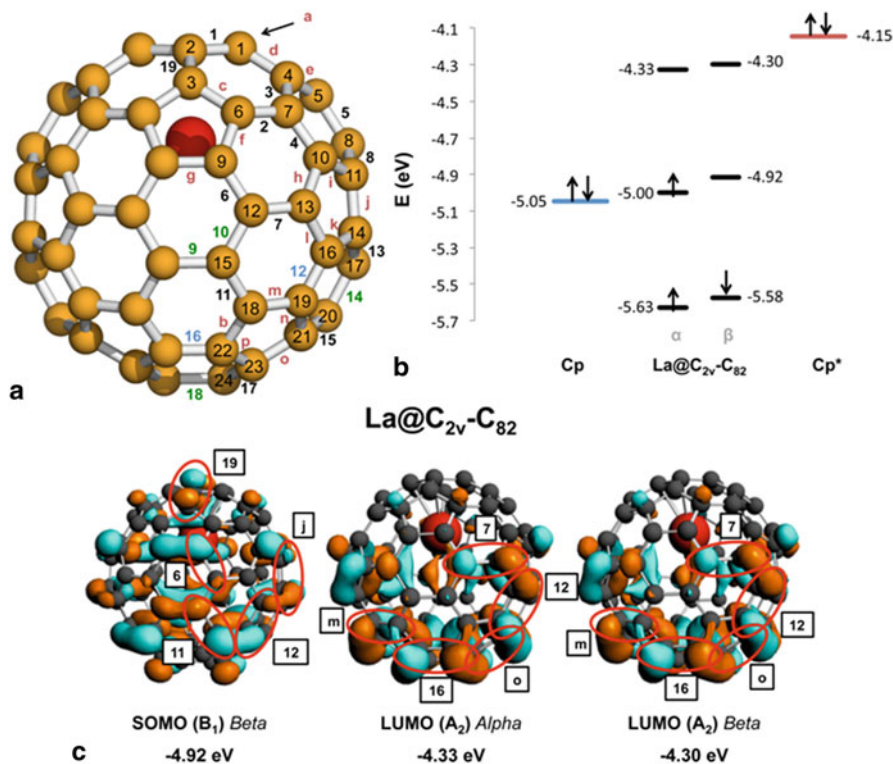
(Maeda et al. 2005). This proposal was based only on the shape of the SOMO orbital because the final  $\text{La}@C_{2v}\text{-}C_{82}\text{Cp}$  product was not isolated. In a posterior related work, 1,2,3,4,5-pentamethylcyclopentadiene ( $\text{Cp}^*$ ) was used as the diene in the DA reaction, where the final product could be isolated and characterized by X-ray crystallography indicating that the addition corresponded to the attack on bond **o** (Maeda et al. 2010). Thus, it was surprising that relatively similar dienes ( $\text{Cp}$  and  $\text{Cp}^*$ ) presented markedly different regioselectivities. Moreover, the final stabilities of both products were found to be largely different. At 298 K, only 36 % of  $\text{La}@C_{2v}\text{-}C_{82}\text{Cp}^*$  decomposes into  $\text{La}@C_{2v}\text{-}C_{82}$  and  $\text{Cp}^*$  after 12 h, (Maeda et al. 2010) while the half-life of  $\text{La}@C_{2v}\text{-}C_{82}\text{Cp}$  under the same conditions is only  $\tau = 1.8$  h (for comparison,  $\tau = 1800$  h for the decomposition of  $C_{60}\text{Cp}$ ). (Maeda et al. 2005)

In order to analyze and to give a rational explanation for these observations, we have performed a complete study on the regioselectivity of the process. We have considered the thermodynamics of the DA addition between  $\text{Cp}$  and  $\text{La}@C_{2v}\text{-}C_{82}$  for all 35 nonequivalent bonds, and for the 10 most favored cases, we have also studied the kinetics of the reaction (Garcia-Borràs et al. 2013a). For the  $\text{Cp}^*$  case, we have considered four different additions based on the previously reported experimental X-ray data (Maeda et al. 2010).

In Table 4.3, we report the electronic and Gibbs reaction energies and reaction (retro)-barriers for the DA addition of  $\text{Cp}$  and  $\text{Cp}^*$  on  $\text{La}@C_{2v}\text{-}C_{82}$ . Our results indicate that both cycloadditions present similar reactivities, with the thermodynamic most stable product being the one corresponding to the attack over bond **o** in the  $\text{Cp}^*$  case but also when the  $\text{Cp}$  is considered. In the present case, we have not found good correlations between the shape of the LUMO  $\text{La}@C_{2v}\text{-}C_{82}$  EMF orbitals and the final reactivity of the bonds (see Fig. 4.11 and Table 4.3), or even with the C–C bond distances or pyramidalization angles as expected from our previous studies (see previous subsections).

Nevertheless, we have to mention that from the kinetic point of view, the reaction barriers found for additions on bond **o** and bond **11** are very close in energy ( $\text{Cp}$ :  $\Delta G^\ddagger = 20.2$  kcal mol<sup>-1</sup> and  $\Delta G^\ddagger = 19.5$  kcal mol<sup>-1</sup> for bond **o** and **11**, respectively;  $\text{Cp}^*$ :  $\Delta G^\ddagger = 9.8$  kcal mol<sup>-1</sup> and  $\Delta G^\ddagger = 10.1$  kcal mol<sup>-1</sup> for bond **o** and **11**, respectively), presenting the addition on bond **11** with the lowest reaction barrier for the  $\text{Cp}$  case. However, the attack over bond **11** is very endergonic and, consequently, once product **11** is formed rapidly reverts back to the original reactants. Thus, the reaction presents a clearly regioselective formation of the **o** products for both  $\text{Cp}$  and  $\text{Cp}^*$  cases. Our results correct the previous wrong assignment for the  $\text{La}@C_{2v}\text{-}C_{82}\text{Cp}$  adduct, indicating that there exist no regioselective differences between the DA cycloaddition of both  $\text{Cp}$  and  $\text{Cp}^*$  over  $\text{La}@C_{2v}\text{-}C_{82}$  EMF.

Finally, we have investigated the different product stabilities. As mentioned previously, it was found experimentally that the stabilities of the  $\text{Cp}$  and  $\text{Cp}^*$  adducts were significantly different, with the decomposition of  $\text{La}@C_{2v}\text{-}C_{82}\text{Cp}$  being one order of magnitude faster than that of  $\text{La}@C_{2v}\text{-}C_{82}\text{Cp}^*$ . We have shown that electronic effects of the methyl substituents do not play a major role in the different  $\text{Cp}$  and  $\text{Cp}^*$  product stabilities. If we compare the retro reaction barriers ( $\Delta G^\ddagger\text{-retro} = 10.2$  kcal mol<sup>-1</sup> for  $\text{Cp}^*$  and  $\Delta G^\ddagger\text{-retro} = 12.4$  kcal mol<sup>-1</sup> for  $\text{Cp}$ , see Table 4.3), one could conclude



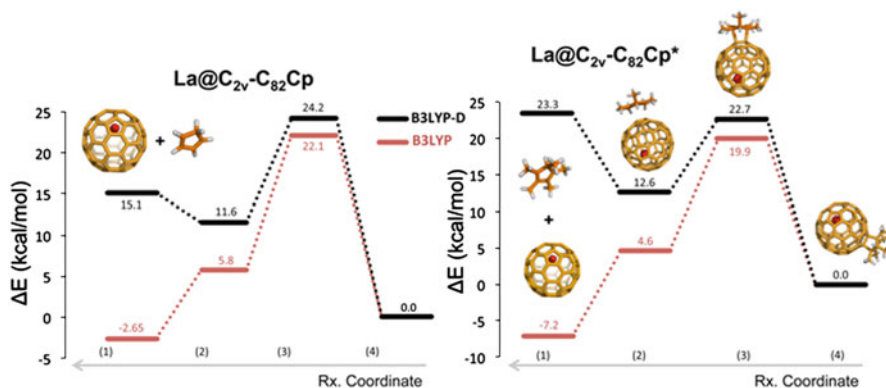
**Fig. 4.11** **a** Representation of the different non-equivalent bonds of  $\text{La@C}_{2v}\text{-C}_{82}$ ; numbers denote [6, 6] bonds and lower-case letters denote [5, 6] bonds. Different colors are used to label the different bond types (Fig. 4.1; type A: blue; type B: black; type C: green; type D: red). **b** Molecular-orbital levels of the frontier orbitals of  $\text{La@C}_{2v}\text{-C}_{82}$ , cyclopentadiene (Cp), and 1,2,3,4,5-pentamethylcyclopentadiene (Cp\*). **c** Representation of the SOMO (unoccupied *beta*) and LUMOs (*alpha* and *beta*) of  $\text{La@C}_{2v}\text{-C}_{82}$  (isosurface value 0.02 a.u.); only those bonds with favorable orbitals for interactions with the HOMO of the diene are marked with ellipses. Energy values of the levels are given in eV. (Reprinted with permission from (Garcia-Borràs et al. 2013a). Copyright 2013 Wiley)

that electronic effects of the methyl groups decrease the retro-barrier favoring the dissociation of  $\text{La@C}_{2v}\text{-C}_{82}\text{Cp}^*$ , which goes against experimental observations. In fact, we found that the higher stability of the  $\text{Cp}^*$  adduct arises from the long-range stabilizing dispersion interactions. If we analyze the effect of the dispersion-energy contribution on both reactions pathways (see Fig. 4.12), we can see that a lack of dispersion corrections completely changes the reaction energy profile.

The reaction pathways for Cp and  $\text{Cp}^*$  additions are quite similar when the initial reactant complex is considered. Thus, as discussed before, the electronic effects due to the methyl groups on  $\text{Cp}^*$  diene do not play a determinant role on the different half-life decomposition times of Cp and  $\text{Cp}^*$ . Hence, we can see that without considering

**Table 4.3** BLYP-D<sub>2</sub>/TZP//BLYP-D<sub>2</sub>/DZP reaction energies ( $\Delta E_R$ ) and Gibbs reaction energies ( $\Delta G_R$ ), reaction barriers ( $\Delta E^\ddagger$ ) and Gibbs reaction barriers ( $\Delta G^\ddagger$ ), and values for the retro-reaction barriers ( $\Delta E^\ddagger$ -retro) and Gibbs retro-barriers ( $\Delta G^\ddagger$ -retro) for the Diels-Alder cycloaddition reactions of Cp and Cp\* at the most favorable addition sites of the La@C<sub>2v</sub>-C<sub>82</sub> EMF at 298.15 K. Values in italics were obtained relative to the first reactant complex that was formed. Units are kcal mol<sup>-1</sup>

La@C <sub>2v</sub> -C <sub>82</sub> Cp Product	Bond type	$\Delta E_R$	$\Delta G_R$	$\Delta E^\ddagger$	$\Delta G^\ddagger$	$\Delta E^\ddagger$ -retro	$\Delta G^\ddagger$ -retro
11	B [6, 6]	-4.6	13.5	4.8	19.5	9.4	6.1
		<i>1.6</i>	<i>5.7</i>	<i>11.0</i>	<i>11.8</i>		
12	A [6, 6]	-5.5	12.6	6.9	22.1	12.4	10.8
		<i>0.5</i>	<i>3.1</i>	<i>12.9</i>	<i>12.6</i>		
16	A [6, 6]	-6.4	11.8	7.5	22.6	13.9	11.0
		<i>-0.5</i>	<i>2.5</i>	<i>13.4</i>	<i>13.3</i>		
19	B [6, 6]	-5.1	12.7	8.7	23.7	13.8	12.4
		<i>1.9</i>	<i>7.1</i>	<i>15.7</i>	<i>18.2</i>		
d	C [5, 6]	-6.2	11.7	10.2	24.1	16.4	10.3
		<i>0.3</i>	<i>4.1</i>	<i>16.7</i>	<i>16.5</i>		
e	C [5, 6]	-4.9	13.2	9.6	23.5	14.5	10.7
		<i>1.3</i>	<i>7.3</i>	<i>16.1</i>	<i>17.6</i>		
f	C [5, 6]	-5.3	12.9	8.8	23.6	14.1	10.8
		<i>0.2</i>	<i>3.4</i>	<i>14.4</i>	<i>14.1</i>		
h	C [5, 6]	-4.0	13.7	9.9	24.5	13.9	11.8
		<i>2.0</i>	<i>4.9</i>	<i>16.0</i>	<i>15.7</i>		
j	C [5, 6]	-7.1	10.9	8.6	22.7	15.7	12.4
		<i>-1.7</i>	<i>1.7</i>	<i>14.0</i>	<i>13.5</i>		
o	C [5, 6]	-10.5	7.8	5.6	20.2	16.0	12.4
		<i>-4.7</i>	<i>-1.5</i>	<i>11.3</i>	<i>10.9</i>		
11	B [6, 6]	-13.1	5.6	-5.3	10.1	7.8	10.2
		<i>1.8</i>	<i>7.3</i>	<i>9.6</i>	<i>11.8</i>		
16	A [6, 6]	-14.8	4.0	-3.7	10.3	11.1	6.3
		<i>-0.8</i>	<i>5.1</i>	<i>10.3</i>	<i>11.4</i>		
j	C [5, 6]	-15.5	2.9	-1.9	13.1	13.6	10.2
		<i>-1.7</i>	<i>3.6</i>	<i>12.0</i>	<i>13.9</i>		
o	C [5, 6]	-19.4	-0.7	-5.4	9.5	14.0	10.2
		<i>-5.1</i>	<i>0.5</i>	<i>8.9</i>	<i>10.8</i>		



**Fig. 4.12** Energy profiles at B3LYP-D/TZP//B3LYP-D/DZP level of theory of the Diels-Alder cycloaddition between La@C<sub>2v</sub>-C<sub>82</sub> and Cp and Cp\* for the attack on the most reactive bond (bond **o**), when dispersion effects were included (*black*) and not included (*red*). The stationary points represented are: (1) reactants, (2) reactant intermediate structure, (3) transition state, and (4) product. Relative energy values are given in kcal mol<sup>-1</sup>. (Reprinted with permission from (Garcia-Borràs et al. 2013a). Copyright 2013 Wiley)

dispersion corrections, the Cp monoadduct would be more stable than the Cp\* one. Nevertheless, when dispersion interactions are considered, this situation is inverted, with the Cp\* adduct being the one largely more stabilized. The reason is the higher stability of the Cp\* reactant complex due to dispersion interactions. This result confirms again that dispersion corrections are essential for analyzing the reactivity of fullerenes and related compounds.

## 4.4 Conclusions

In this chapter, we have presented several comprehensive computational investigations of the exohedral functionalization of endohedral metallofullerenes. The Diels-Alder (DA) cycloaddition is one of the most important and widely used reactions for the functionalization of fullerene compounds. First, we have focused our attention on the effect of different metallic clusters on the Diels-Alder cycloaddition. We have compared the Diels-Alder reactivity of the empty *D*<sub>3h</sub>-C<sub>78</sub> fullerene and Sc<sub>3</sub>N@*D*<sub>3h</sub>-C<sub>78</sub>, Y<sub>3</sub>N@*D*<sub>3h</sub>-C<sub>78</sub>, and Ti<sub>2</sub>C<sub>2</sub>@*D*<sub>3h</sub>-C<sub>78</sub> EMFs. Our results show that the encapsulation of the metal cluster reduces the DA reactivity of the fullerene cage, both from a thermodynamic and kinetic point of view. However, the three EMFs present very different regioselectivities. For instance, the most favorable adducts under kinetic control are for type A [6, 6] **1** bond for hollow *D*<sub>3h</sub>-C<sub>78</sub>, type B [6, 6] **6** bond for Sc<sub>3</sub>N@*D*<sub>3h</sub>-C<sub>78</sub>, type D [5, 6] **d** bond for Y<sub>3</sub>N@*D*<sub>3h</sub>-C<sub>78</sub>, and type D [5, 6] **c** bond for Ti<sub>2</sub>C<sub>2</sub>@*D*<sub>3h</sub>-C<sub>78</sub> EMFs. One key factor to explain the differences in the DA regioselectivity is the strain energy of the cage caused by the metallic cluster. Whereas for the large clusters (i.e. Y<sub>3</sub>N and Ti<sub>2</sub>C<sub>2</sub>) the DA attack occurs at the bonds

close to the metals to reduce the strain energy of the cage, for the  $\text{Sc}_3\text{N}@D_{3h}\text{-C}_{78}$  the most reactive bonds are far from the metals. Bond distances, pyramidalization angles or LUMOs shapes are also useful to analyze the DA regioselectivity of the fullerenes and EMFs. Nevertheless, our results clearly demonstrate that none of them alone predicts systematically the bond for which the attack is most favorable.

The enormous effect of the metal cluster on the DA regioselectivity is also clearly shown in the comparison of exohedral reactivity of  $\text{Sc}_3\text{N}$ ,  $\text{Lu}_3\text{N}$ , and  $\text{Gd}_3\text{N}$  encapsulated in both the  $D_{5h}\text{-C}_{80}$  and the  $I_h\text{-C}_{80}$  fullerene cage. This theoretical investigation presented the difficult handicap of taking into account the free rotation of the clusters inside the cage. Our calculations clearly show that the preference for the [6, 6] addition increases with the size of the metallic cluster. The origin of this regioselectivity change is found in the decrease of the DA [6, 6] activation barrier induced by the strain energy of the  $\text{Gd}_3\text{N}@I_h\text{-C}_{80}$  fullerene cage. Another very important result of this study is the correction of the wrong experimental assignment based on  $^1\text{H}$  NMR spectra of  $D_{5h}\text{-5}$  as the most stable thermodynamic Prato adduct. Both, the theoretical reaction energies and simulations of  $^1\text{H}$  NMR spectra clearly show that the most thermodynamically stable Prato cycloaddition product is the one obtained through attack to the [5, 6] **b** bond.

In order to have a complete guide on the influence of metal clusters on the DA regioselectivity of  $I_h\text{-C}_{80}$  EMFs we have studied the DA cycloaddition between *cis*-1,3-butadiene and  $\text{Sc}_3\text{N}$ ,  $\text{Lu}_3\text{N}$ ,  $\text{Y}_3\text{N}$ ,  $\text{La}_2$ ,  $\text{Y}_3$ ,  $\text{Sc}_3\text{C}_2$ ,  $\text{Sc}_4\text{C}_2$ ,  $\text{Sc}_3\text{CH}$ ,  $\text{Sc}_3\text{NC}$ ,  $\text{Sc}_4\text{O}_2$ , and  $\text{Sc}_4\text{O}_3$   $I_h\text{-C}_{80}$  EMFs. Taking into account the free rotation of the clusters, a rigorous study of the regioselectivity of these eleven EMFs was only possible because we used the Frozen Cage Model (FCM). In the first phase, the FCM determines the most stable adducts at a very low computational cost. In the second phase a number of selected adducts are optimized without any restriction. Our systematic study confirmed that the HOMO- LUMO gaps, the charge transfer, and the cluster volume are three key factors that rule the DA regioselectivity. The reactivity decrease when the HOMO-LUMO gaps and charge transfer increases. And the increase of the cluster volume decreases the regioselectivity, increasing the preference for the [6, 6] adducts. Nevertheless, as pointed above, none of these parameters has a general predictive power since there are always exceptions. For instance, opposing the general trend, the metallic oxide EMFs increase their regioselectivity when the cluster size increases.

A second main goal of this chapter was to remark the essential role of dispersion interactions to accurately reproduce the experimental reactivity of the EMFs. The inclusion of dispersion effects in the DFT simulations decrease the errors in the reaction enthalpy from  $13.2 \text{ kcal mol}^{-1}$  to only  $2.2 \text{ kcal mol}^{-1}$ . The dispersion corrections were also the key factor to correct the wrong assignment of the DA addition of cyclopentadiene on bond **19** of  $\text{La}@C_{2v}\text{-C}_{82}$ . Our results show that for both the cyclopentadiene and the 1, 2, 3, 4, 5-pentamethylcyclopentadiene, the most stable DA adduct is the attack on the **o** bond. Furthermore, our DFT study including the dispersion effects explain that the origin of the major stability of the  $\text{Cp}^*$  adduct is due to the larger dispersion interactions present in  $\text{Cp}^*$  as compared to  $\text{Cp}$ .

**Acknowledgments** We are grateful for financial support from the Spanish MICINN (projects CTQ2011-23156/BQU and CTQ2011-25086/BQU), the Catalan DIUE (projects 2009SGR637, 2009SGR528, and XRQTC), the FEDER fund for the grant UNGI08-4E-003. M.G.-B. thanks the Spanish MECD for a PhD fellowship (AP2010-2517) and S.O. thanks the European Community for a postdoctoral fellowship (PIOF-GA-2009-252856). Excellent service by the CIESCA is acknowledged. The authors are also grateful to the computer resources and assistance provided by the BSC-CNS. M. Solà thanks the Catalan DIUE for the ICREA Academia 2009 Award.

## Appendix: Computational Details

All Density Functional Theory (DFT) calculations were performed with the Amsterdam Density Functional (ADF) program (Baerends et al. 2010). The molecular orbitals (MOs) were expanded in an uncontracted set of Slater type orbitals (STOs) of double- $\zeta$  (DZP) and triple- $\zeta$  (TZP) quality containing diffuse functions and one set of polarization functions. In order to reduce the computational time needed to carry out the calculations, the frozen core approximation has been used (te Velde et al. 2001). In this approximation, the core density is obtained and included explicitly, albeit with core orbitals that are kept frozen during the SCF procedure. It was shown that the frozen core approximation has a negligible effect on the optimized equilibrium geometries (Swart and Snijders 2003). Scalar relativistic corrections have been included self-consistently using the Zeroth Order Regular Approximation (ZORA) (van Lenthe et al. 1993). An auxiliary set of  $s$ ,  $p$ ,  $d$ ,  $f$ , and  $g$  STOs was used to fit the molecular density and to represent the Coulomb and exchange potentials accurately for each SCF cycle (Baerends et al. 1973). Energies and gradients were calculated using the local density approximation (Slater exchange) with non-local corrections for exchange (Becke88) (Becke 1988) and correlation (Lee-Yang-Parr) (Lee et al. 1988) included self-consistently (i.e. the BLYP functional). In some cases, energies and gradients were calculated using the local density approximation (Slater exchange and VWN correlation) (Vosko et al. 1980) with non-local corrections for exchange (Becke 1988) and correlation (Perdew 1986) included self-consistently (i.e. the BP86 functional). Also in some studies, we performed single point energy calculations at the B3LYP-D<sub>2</sub>/TZP level of theory (Becke 1993; Lee et al. 1988; Stephens et al. 1994) (i.e., B3LYP-D<sub>2</sub>/TZP//BLYP-D<sub>2</sub>/DZP). Open-shell systems were treated with the unrestricted formalism.

Moreover, energy dispersion corrections were introduced using Grimme's methodology (Grimme 2006; Grimme et al. 2010) (D<sub>2</sub>/D<sub>3</sub>) implemented in ADF 2010.01 version (Baerends et al. 2010). All the structures were fully optimized using these corrections in each optimization step. It was shown that dispersion corrections are essential for a correct description of the thermodynamics and kinetics of fullerene and nanotube reactions (Osuna et al. 2010; Garcia-Borràs et al. 2012a).

The actual geometry optimizations and transition state (TS) searches were performed with the QUILD (Swart and Bickelhaupt 2008) (QUAntum-regions Interconnected by Local Descriptions) program, which functions as a wrapper around the ADF program. The QUILD program constructs all input files for ADF, runs ADF,



and collects all data; ADF is used only for the generation of the energy and gradients. Furthermore, the QUILD program uses improved geometry optimization techniques, such as adapted delocalized coordinates (Swart and Bickelhaupt 2006) and specially constructed model Hessians with the appropriate number of eigenvalues (Swart and Bickelhaupt 2006). The latter is particularly useful for TS searches. All TSs were characterized by computing the analytical (Wolff 2005) vibrational frequencies, to have one and only one imaginary frequency corresponding to the approach of the reacting carbons. In selected DA attacks, analytical Hessians were computed for all stationary points along the reaction coordinate to calculate unscaled zero-point energies (ZPEs) as well as thermal corrections and entropy effects using the standard statistical-mechanics relationships for an ideal gas (Atkins and De Paula 2006). These two latter terms were computed at 298.15 K and 1 atm to provide the reported relative Gibbs energies ( $\Delta G_{298}$ ). Pyramidalization angles, introduced by Haddon (Haddon 2001; Haddon and Chow 1998) as a measure of the local curvature in polycyclic aromatic hydrocarbons, were calculated using the POAV3 program (Haddon 1988).

In the case of the first study including dispersion corrections, full geometry optimizations were carried out with the hybrid B3LYP (Becke 1993; Lee et al. 1988; Stephens et al. 1994) density functional with the standard 6-31G(d) basis set (Hehre et al. 1972; Hariharan and Pople 1973). The two-layered ONIOM approach (ONIOM2) (Svensson et al. 1996; Dapprich et al. 1999; Vreven et al. 2006) were employed to perform geometry optimizations using a combination of the SVWN method (Slater 1974; Vosko et al. 1980) together with the standard STO-3G basis set (Hehre et al. 1969) for the low level calculations and the B3LYP methods with the standard 6-31G(d) basis set (Hehre et al. 1972; Hariharan and Pople 1973) for the high level part. In both cases, we performed the study including dispersion corrections following the Grimme's approach (B3LYP-D and ONIOM2-D) (Grimme 2004, 2006; Grimme et al. 2010). In selected cases, we carried out calculations with the M06-2X functional (Zhao and Truhlar 2008). Frequency calculations indicated that we obtained the correct stationary points, characterized by the number of imaginary eigenvalues of their analytic Hessian matrix. Solvent effects were estimated in some particular cases with single point calculations on the gas phase optimized structures using the polarizable continuous solvation model (PCM) and considering toluene as the solvent (Tomasi and Persico 1994). All calculations including Grimme's dispersion corrections (Grimme 2004, 2006) were performed using a locally modified version of the Gaussian 09 (revision A.02) program ("IOP(3/124 = 3)" for including the dispersion correction; the  $S_6$  value for B3LYP was set to 1.05). Apart from that, we adapted the program to allow the inclusion of dispersion effects within the ONIOM approach (the  $S_6$  value is set to 1.05 for the high level B3LYP-D and 1.0 for the low level SVWN-D).

## References

- Aihara J-I (2001) *Chem Phys Lett* 343:465–469
- Akasaka T, Nagase S (2002) *Endofullerenes: a new family of carbon clusters*. Kluwer Academic, Dordrecht
- Akasaka T, Nagase S, Kobayashi K, Wälchli M, Yamamoto K, Funasaka H, Kako M, Hoshino T, Erata T (1997) *Angew Chem Int Ed Engl* 36:1643–1645
- Atkins P, De Paula J (2006) *Physical chemistry*. Oxford University Press, Oxford
- Baerends EJ, Ellis DE, Ros P (1973) *Chem Phys* 2:41–51
- Baerends EJ, Ziegler T, Autschbach J, Bashford D, Bérces A, Bickelhaupt FM, Bo C, Boerrigter PM, Cavallo L, Chong DP, Deng L, Dickson RM, Ellis DE, Faassen MV, Fan L, Fischer TH, Fonseca Guerra C, Ghysels A, Giammona A, van Gisbergen SJA, Götz AW, Groeneveld JA, Gritsenko OV, Grüning M, Gusarov S, Harris FE, van den Hoek P, Jacob CR, Jacobsen H, Jensen L, Kaminski JW, van Kessel G, Kootstra F, Kovalenko A, Krykunov MV, van Lenthe E, McCormack DA, Michalak A, Mitoraj M, Neugebauer J, Nicu VP, Noodleman L, Osinga VP, Patchkovskii S, Philipsen PHT, Post D, Pye CC, Ravenek W, Rodriguez JI, Ros P, Schipper PRT, Schreckenbach G, Seldenthuis JS, Seth M, Snijders JG, Sola M, Swart M, Swerhone D, Te Velde G, Vernooijs P, Versluis L, Visscher L, Visser O, Wang F, Wesolowski TA, van Wezenbeek EM, Wiesenekker G, Wolff SK, Woo TK, Yakovlev AL (2010) *ADF2010*. ADF201001. ADF2010.01. SCM, Amsterdam
- Becke AD (1988) *Phys Rev A* 38:3098–3100
- Becke AD (1993) *J Chem Phys* 98:5648–5652
- Cai T, Slebodnick C, Xu L, Harich K, Glass TE, Chancellor C, Fettinger JC, Olmstead MM, Balch AL, Gibson HW, Dorn HC (2006a) *J Am Chem Soc* 128:6486–6492
- Cai T, Xu LS, Anderson MR, Ge ZX, Zuo TM, Wang XL, Olmstead MM, Balch AL, Gibson HW, Dorn HC (2006b). *J Am Chem Soc* 128:8581–8589
- Campanera JM, Bo C, Olmstead MM, Balch AL, Poblet JM (2002) *J Phys Chem A* 106:12356–12364
- Campanera JM, Bo C, Poblet JM (2005) *Angew Chem Int Ed* 44:7230–7233
- Campanera JM, Bo C, Poblet JM (2006) *J Org Chem* 71:46–54
- Cao B, Hasegawa M, Okada K, Tomiyama T, Okasaki T, Suenaga K, Shinohara H (2001) *J Am Chem Soc* 123:9679–9680
- Cardona CM, Kitaygorodskiy A, Echegoyen L (2005a) *J Am Chem Soc* 127:10448–10453
- Cardona CM, Kitaygorodskiy A, Ortiz A, Herranz MÁ, Echegoyen L (2005b) *J Org Chem* 70:5092–5097
- Cardona CM, Elliott B, Echegoyen L (2006) *J Am Chem Soc* 128:6480–6485
- Chai Y, Guo T, Jin C, Haufler RE, Chibante LPF, Fure J, Wang L, Alford JM, Smalley RE (1991) *J Phys Chem* 95:7564–7568
- Chaur MN, Melin F, Elliott B, Athans AJ, Walker K, Holloway BC, Echegoyen L (2007) *J Am Chem Soc* 129:14826–14829
- Chaur MN, Melin F, Ortiz AL, Echegoyen L (2009) *Angew Chem Int Ed* 48:7514–7538
- Chen N, Fan LZ, Tan K, Wu YQ, Shu CY, Lu X, Wang CR (2007) *J Phys Chem C* 111:11823–11828
- Dapprich S, Komáromi I, Byu KS, Morokuma K, Frisch MJ (1999). *J Mol Struct (Theochem)* 461–462:1–21
- Duchamp JC, Demortier A, Fletcher KR, Dorn D, Jezzi EB, Glass T, Dorn HC (2003) *Chem Phys Lett* 375:655–659
- Fatouros PP, Corwin FD, Chen ZJ, Broaddus WC, Tatum JL, Kettenmann B, Ge Z, Gibson HW, Russ JL, Leonard AP, Duchamp JC, Dorn HC (2006) *Radiology* 240:756–764
- Garcia-Borràs M, Osuna S, Luis JM, Swart M, Solà M (2012a) *Chem Eur J* 18:7141–7154
- Garcia-Borràs M, Romero-Rivera A, Osuna S, Luis JM, Swart M, Solà M (2012b) *J Chem Theory Comput* 8:1671–1683
- Garcia-Borràs M, Luis JM, Swart M, Solà M (2013a) *Chem Eur J* 19:4468–4479
- Garcia-Borràs M, Osuna S, Swart M, Luis JM, Solà M (2013b) *Angew Chem Int Ed*. doi:10.1002/anie.201303636

- Garcia-Borràs M, Osuna S, Swart M, Luis JM, Solà M (2013c) *Chem Eur J*. doi:10.1002/chem.201302220
- Goerigk L, Grimme S (2010) *J Chem Theory Comput* 6:107–126
- Grimme S (2004) *J Comput Chem* 25:1463–1473
- Grimme S (2006) *J Comput Chem* 27:1787–1799
- Grimme S, Antony J, Ehrlich S, Krieg H (2010) *J Chem Phys* 132:154104
- Guha S, Nakamoto K (2005) *Coord Chem Rev* 249:1111–1132
- Guldi DM, Feng L, Radhakrishnan SG, Nikawa H, Yamada M, Mizorogi N, Tsuchiya T, Akasaka T, Nagase S, Angeles Herranz M, Martin N (2010) *J Am Chem Soc* 132:9078–9086
- Haddon RC (1988) *QCPE 508/QCMP 044*. *QCPE Bull* 8
- Haddon RC (2001) *J Phys Chem A* 105:4164–4165
- Haddon RC, Chow SY (1998) *J Am Chem Soc* 120:10494–10496
- Hariharan PC, Pople JA (1973) *Theor Chim Acta* 28:213–222
- Heath JR, O'Brien SC, Zhang Q, Liu Y, Curl RF, Kroto HW, Tittel FK, Smalley RE (1985) *J Am Chem Soc* 107:7779–7780
- Hehre WJ, Stewart RF, Pople JA (1969) *J Chem Phys* 51:2657–2664
- Hehre WJ, Ditchfield R, Pople JA (1972) *J Chem Phys* 56:2257–2261
- Hesselmann A, Korona T (2011) *Phys Chem Chem Phys* 13:732–743
- Iezzi EB, Duchamp JC, Harich K, Glass TE, Lee HM, Olmstead MM, Balch AL, Dorn HC (2002) *J Am Chem Soc* 124:524–525
- Iiduka Y, Ikenaga O, Sakuraba A, Wakahara T, Tsuchiya T, Maeda Y, Nakahodo T, Akasaka T, Kako M, Mizorogi N, Nagase S (2005a) *J Am Chem Soc* 127:9956–9957
- Iiduka Y, Wakahara T, Nakahodo T, Tsuchiya T, Sakuraba A, Maeda Y, Akasaka T, Yoza K, Horn E, Kato T, Liu MTH, Mizorogi N, Kobayashi K, Nagase S (2005b) *J Am Chem Soc* 127:12500–12501
- Ishitsuka MO, Sano S, Enoki H, Sato S, Nikawa H, Tsuchiya T, Slanina Z, Mizorogi N, Liu MTH, Akasaka T, Nagase S (2011) *J Am Chem Soc* 133:7128–7134
- Iwasaki K, Hino S, Yoshimura D, Cao B, Okasaki T, Shinohara H (2004) *Chem Phys Lett* 397:169–173
- Jaffiol R, Débarre A, Julien C, Nutarelli D, Tchénio P, Taninaka A, Cao B, Okasaki T, Shinohara H (2003) *Phys Rev B* 68:014105
- Kobayashi K, Nagase S, Yoshida M, Ōsawa E (1997) *J Am Chem Soc* 119:12693–12694
- Korona T, Hesselmann A, Dodziuk H (2009) *J Chem Theory Comput* 5:1585–1596
- Krause M, Ziegls F, Popov AA, Dunsch L (2007) *Chem Phys Chem* 8:537–540
- Kroto HW (1987) *Nature* 329:529–531
- Kroto HW, Heath JR, O'Brien SC, Curl RF, Smalley RE (1985) *Nature* 318:162–163
- Kruse H, Grimme S (2009) *J Phys Chem C* 113:17006–17010
- Kurihara H, Iiduka Y, Rubin Y, Waelchli M, Mizorogi N, Slanina Z, Tsuchiya T, Nagase S, Akasaka T (2012) *J Am Chem Soc* 134:4092–4095
- Lee C, Yang W, Parr RG (1988) *Phys Rev B* 37:785–789
- Lee HM, Olmstead MM, Iezzi E, Duchamp JC, Dorn HC, Balch AL (2002) *J Am Chem Soc* 124:3494–3495
- Liu S, Sun S (2000) *J Organomet Chem* 599:74–86
- Lu X, Akasaka T, Nagase S (2011) *Chem Commun* 47:5942–5957
- Lu X, Feng L, Akasaka T, Nagase S (2012) *Chem Soc Rev* 41:7723–7760
- Lu X, Nikawa H, Nakahodo T, Tsuchiya T, Ishitsuka MO, Maeda Y, Akasaka T, Toki M, Sawa H, Slanina Z, Mizorogi N, Nagase S (2008) *J Am Chem Soc* 130:9129–9136
- Lukoyanova O, Cardona CM, Rivera J, Lugo-Morales LZ, Chancellor CJ, Olmstead MM, Rodriguez-Forte A, Poblet JM, Balch AL, Echegoyen L (2007) *J Am Chem Soc* 129:10423–10430
- Maeda Y, Miyashita J, Hasegawa T, Wakahara T, Tsuchiya T, Nakahodo T, Akasaka T, Mizorogi N, Kobayashi K, Nagase S, Kato T, Ban N, Nakajima H, Watanabe Y (2005) *J Am Chem Soc* 127:12190–12191

- Maeda Y, Sato S, Inada K, Nikawa H, Yamada M, Mizorogi N, Hasegawa T, Tsuchiya T, Akasaka T, Kato T, Slanina Z, Nagase S (2010) *Chem Eur J* 16:2193–2197
- Mercado BQ, Olmstead MM, Beavers CM, Easterling ML, Stevenson S, Mackey MA, Coumbe CE, Phillips JD, Phillips JP, Poblet JM, Balch AL (2010) *Chem Commun* 46:279–281
- Miertuš S, Scrocco E, Tomasi J (1981) *Chem Phys* 55:117–129
- Murata M, Murata Y, Komatsu K (2008) *Chem Commun* 6083–6094
- Nishibori E, Narioka S, Takata M, Sakata M, Inoue T, Shinohara H (2006) *ChemPhysChem* 7:345–348
- Osuna S, Houk KN (2009) *Chem Eur J* 15:13219–13231
- Osuna S, Swart M, Campanera JM, Poblet JM, Solà M (2008) *J Am Chem Soc* 130:6206–6214
- Osuna S, Swart M, Solà M (2009a) *J Am Chem Soc* 131:129–139
- Osuna SL, Morera J, Cases M, Morokuma K, Solà M (2009b) *J Phys Chem A* 113:9721–9726
- Osuna S, Swart M, Solà M (2010) *J Phys Chem A* 115:3491–3496
- Osuna S, Swart M, Solà M (2011a) *Phys Chem Chem Phys* 13:3585–3603
- Osuna SL, Swart M, Solà M (2011b) *J Phys Chem A* 115:3491–3496
- Osuna S, Rodríguez-Fortea A, Poblet JM, Solà M, Swart M (2012a) *Chem Commun* 48:2486–2488
- Osuna S, Valencia R, Rodríguez-Fortea A, Swart M, Solà M, Poblet JM (2012b). *Chem Eur J* 18:8944–8956
- Pascual-Ahuir JL, Silla E, Tuon I (1994) *J Comput Chem* 15:1127
- Perdew JP (1986) *Phys Rev B* 33:8822–8824
- Popov AA, Dunsch L (2008) *J Am Chem Soc* 130:17726–17742
- Popov AA, Zhang L, Dunsch L (2010) *ACS Nano* 4:795–802
- Rivera-Nazario DM, Pinzón JR, Stevenson S, Echegoyen LA (2013) *J Phys Org Chem* 26:194–205
- Rodríguez-Fortea A, Alegret N, Balch AL, Poblet JM (2010) *Nat Chem* 2:955–961
- Rodríguez-Fortea A, Campanera JM, Cardona CM, Echegoyen L, Poblet JM (2006) *Angew Chem Int Ed Engl* 45:8176–8180
- Rodríguez-Fortea A, Balch AL, Poblet JM (2011) *Chem Soc Rev* 40:3551–3563
- Shi Z-Q, Wu X, Wang C-R, Lu X, Shinohara H (2006) *Angew Chem Int Ed Engl* 45:2107–2111
- Slater JC (1974) *Quantum theory of molecules and solids*. McGraw-Hill, New York
- Stephens PJ, Devlin FJ, Chabalowski CF, Frisch MJ (1994) *J Phys Chem* 98:11623–11627
- Stevenson S, Rice G, Glass T, Harich K, Cromer F, Jordan MR, Craft J, Hadju E, Bible R, Olmstead MM, Maitra K, Fisher AJ, Balch AL, Dorn HC (1999) *Nature* 401:55–57
- Stevenson S, Phillips JP, Reid JE, Olmstead MM, Rath SP, Balch AL (2004) *Chem Commun* 2814–2815
- Stevenson S, Mackey MA, Stuart MA, Phillips JP, Easterling ML, Chancellor CJ, Olmstead MM, Balch AL (2008) *J Am Chem Soc* 130:11844–11845
- Suzuki T, Maruyama Y, Kato T, Kikuchi K, Nakao Y, Achiba Y, Kobayashi K, Nagase S (1995) *Angew Chem Int Ed Engl* 34:1094–1096
- Svensson M, Humbel S, Froese RDJ, Matsubara T, Sieber S, Morokuma K (1996) *J Phys Chem* 100:19357–19363
- Swart M, Bickelhaupt FM (2006) *Int J Quant Chem* 106:2536–2544
- Swart M, Bickelhaupt FM (2008) *J Comput Chem* 29:724–734
- Swart M, Snijders JG (2003) *Theor Chem Acc* 110:34–41
- Takano Y, Obuchi S, Mizorogi N, García R, Herranz MÁ, Rudolf M, Guldi DM, Martín N, Nagase S, Akasaka T (2012) *J Am Chem Soc* 134:19401–19408
- Tan K, Lu X (2005) *Chem Commun* 4444–4446
- Tan K, Lu X (2006) *J Phys Chem A* 110:1171–1176
- Tan K, Lu X, Wang C-R (2006) *J Phys Chem B* 110:11098–11102
- Te Velde G, Bickelhaupt FM, Baerends EJ, Fonseca Guerra C, van Gisbergen SJA, Snijders JG, Ziegler T (2001) *J Comput Chem* 22:931–967
- Tomasi J, Persico M (1994) *Chem Rev* 94:2027–2094
- Valencia R, Rodríguez-Fortea A, Poblet JM (2007) *Chem Commun* 4161–4163
- Valencia R, Rodríguez-Fortea A, Poblet JM (2008) *J Phys Chem A* 112:4550–4555

- Van Lenthe E, Baerends EJ, Snijders JG (1993) *J Chem Phys* 99:4597–4610
- Vosko SH, Wilk L, Nusair M (1980) *Can J Phys* 58:1200–1211
- Vreven T, Byun KS, Komáromi I, Dapprich S, Montgomery Jr JA, Morokuma K, Frisch MJ (2006) *J Chem Theory Comput* 2:815–826
- Wang C-R, Inakuma M, Shinohara H (1999) *Chem Phys Lett* 300:379–384
- Wang C-R, Kai T, Tomiyama T, Yoshida T, Kobayashi Y, Nishibori E, Takata M, Sakata M, Shinohara H (2001) *Angew Chem Int Ed Engl* 40:397–399
- Wang T, Wu J, Xu W, Xiang J, Lu X, Li B, Jiang L, Shu C, Wang C (2010a) *Angew Chem Int Ed* 49:1786–1789
- Wang T-S, Feng L, Wu J-Y, Xu W, Xiang J-F, Tan K, Ma Y-H, Zheng J-P, Jiang L, Lu X, Shu C-Y, Wang C-R (2010b) *J Am Chem Soc* 132:16362–16364
- Wolff SK (2005) *Int J Quantum Chem* 104:645–659
- Yamada M, Akasaka T, Nagase S (2010) *Acc Chem Res* 43:92–102
- Yamada M, Wakahara T, Nakahodo T, Tsuchiya T, Maeda Y, Akasaka T, Yoza K, Horn E, Mizorogi N, Nagase S (2006) *J Am Chem Soc* 128:1402–1403
- Yamada M, Someya C, Wakahara T, Tsuchiya T, Maeda Y, Akasaka T, Yoza K, Horn E, Liu MTH, Mizorogi N, Nagase S (2008) *J Am Chem Soc* 130:1171–1176
- Yamada M, Okamura M, Sato S, Someya CI, Mizorogi N, Tsuchiya T, Akasaka T, Kato T, Nagase S (2009) *Chem Eur J* 15:10533–10542
- Yang SF, Popov AA, Dunsch L (2008) *Angew Chem Int Ed* 47:8196–8200
- Yang S, Liu F, Chen C, Jiao M, Wei T (2011) *Chem Commun* 47:11822–11839
- Yumura T, Sato Y, Suenaga K, Iijima S (2005) *J Phys Chem B* 109:20251–20255
- Zhao Y, Truhlar DG (2008) *Acc Chem Res* 41:157–167
- Zheng H, Zhao X, Wang W-W, Yang T, Nagase S (2012) *J Chem Phys* 137:014308

# Chapter 5

## Cubic Silicon Carbide Nanowires

**Marco Negri, Francesca Rossi, Giovanni Attolini, Filippo Fabbri, Sathish Chander Dhanabalan, Francesco Boschi, Matteo Bosi, Marco Vittorio Nardi and Giancarlo Salviati**

**Abstract** Nowadays semiconductor nanowires (NWs) represent not only a field of great interest for the study of nanoscale new phenomena, but the technology has become increasingly mature insomuch as they are expected to give a fundamental contribution to electronic devices. Silicon carbide nanowires (SiC-NWs) embody a unique confluence of the well-known SiC chemical and mechanical peculiar properties with the size-dependent characteristics of quasi-one-dimensional structures. However, the synthesis of SiC nanostructures with tailored structure and their use in functional devices is still a challenge. In this chapter firstly a brief review on recent progress and the growth techniques used in literature to obtain SiC nanowires are introduced, then a survey of the growth mechanism of nanowires from vapour phase is presented. Some methods used to deposit catalysts for the growth are reviewed and the so called “dewetting” mechanism is analysed and studied with selected examples after a brief treatise of the thermodynamic of the phenomenon. The procedures for the synthesis of pure cubic silicon carbide nanowires by vapour phase epitaxy and core-shell SiC/SiO<sub>2</sub> nanowires by chemical vapour deposition are presented and the morphology and structure are investigated by means of electronic microscopy. Finally, for core-shell nanowires, X-ray photoelectron spectroscopy is presented as a powerful technique to analyse the chemical and electronic state of the core and cathodoluminescence measurements show the influence of the shell on the optical emission of the SiC core embedded in the wires.

---

M. Negri (✉) · F. Rossi · G. Attolini · F. Fabbri · S. C. Dhanabalan · F. Boschi  
· M. Bosi · G. Salviati

Istituto dei Materiali per l'Elettronica ed il Magnetismo,  
Consiglio Nazionale delle Ricerche, Parco Area delle Scienze 37/A, 43124 Parma, Italy  
e-mail: negri.ml@gmail.com

M. Negri · S. C. Dhanabalan · F. Boschi  
Facoltà di fisica, Università degli studi di Parma, via G.P. Usberti, 7/a, 43124 Parma, Italy

M. V. Nardi  
Institut für Physik, Humboldt-Universität zu Berlin, Newtonstrasse 15, 12489 Berlin, Germany

## 5.1 Introduction

Recently, many research groups focused on the preparation and characterisation of one-dimensional nanostructures such as nanowires based on oxides, nitrides, carbides, III-V's compounds, metals and silicon.

The aforementioned nanostructures present superior chemical, physical, electrical, optical and mechanical properties than their respective bulk materials. As a result, new opportunities for fundamental research and the fabrication of optoelectronic, electro-mechanical and sensor devices on a nanometer scale are achieved (Zheng et al. 2004; Koo et al. 2004; Fan et al. 2004; Johnson et al. 2002; Cui and Lieber 2001; Yang et al. 2002).

Silicon carbide (SiC) is a wide bandgap semiconductor used for high temperature, high power applications and radiation-hard environments, and gained importance both as a coating and a structural material for micro-electro-mechanical systems (MEMS) (Sarro 2000; Mehregany 2000).

The high Si-C bond energy confers a high Young's modulus and hence, mechanical toughness and a high fracture strength (Li and Bhushan 1999). In addition, it is chemically inert to the most corrosive and erosive chemicals and also biocompatible (Willander 2006; Casady and Johnson 1996; Yakimova 2007; Saddow 2012). More than 100 polytypes of SiC exist but the SiC cubic phase (3C-SiC or  $\beta$ -SiC) has drawn particular attention because it can be deposited on Si. Thanks to epitaxial techniques and dopant implantation, electronic devices such as metal-oxide-semiconductor-field-effect transistors (MOSFETs) or diodes can be fabricated from 3C-SiC/Si so that the integration between MEMS and 3C-SiC electronics is possible, enabling the fabrication of high temperatures, harsh environments, and radiation resistant devices (Zorman and Parro 2008; Wright and Horsfall 2007). 3C-SiC is also used as a high temperature gas sensor in the form of a Schottky diode with Pd contacts that catalyse  $H_2$  or other gases.

Moreover, hexagonal (4H- or 6H-) silicon carbide is the favourable material for electronic devices in bulk form grown by sublimation methods.

3C-SiC nanowires are interesting because of their good physical (mechanical, electrical, thermal) properties. This make them a promising material for devices operating in harsh environment (Young et al. (2004) due to the reason that their elasticity and strength greater than bulk, SiC-NWs are attractive for nanostructured composite materials (Wong et al. 1997; Yang et al. 2004).

Further, functionalized 3C-SiC nanowires have the potential to act as highly sensitive detector elements in bio-chemical field (Choi et al. 2006).

Cubic SiC nanowires are obtained by two main procedures, the bottom-up (B-U), which is mostly used, and the top-down (T-D).

Many procedures have been used in B-U methodology: one of the most important techniques to fabricate nanowires is chemical vapour deposition (CVD) and this method is used to grow both SiC-SiO<sub>2</sub> core-shell and SiC nanowires.

The CVD method can use carbon monoxide (CO) (Attolini et al. 2008), carbon tetrachloride (CCl<sub>4</sub>) (Attolini et al. 2009), silane, (SiH<sub>4</sub>) trimethylchlorosilane

( $\text{Si}(\text{CH}_3)_3\text{Cl}$ ), methytrichlorosilane (MTS), propane ( $\text{C}_3\text{H}_8$ ), as precursors and different metals as a catalyst (Attolini et al. 2014).

Carbothermal reduction involves a mixture of powders like  $\text{WO}_3$  with graphite (Park et al. 2004), at high temperatures (1050–1100 °) the reaction produces carbon monoxide (CO) which is carried by a carrier gas on the silicon substrate where it forms silicon carbide in the presence of catalyst with silicon vapour.

If we use as the starting material a target made of SiC under the action of laser (laser ablation), we have evaporation and condensation to form nanostructures on a cold finger (Shi et al. 2000).

Using arc discharge, it is possible to obtain SiC nanostructures with an hole anode made in graphite with inside silicon carbide powder and pure graphite as cathode to reach high temperature (Liu and Yao 2005).

There are also techniques which are less used: combustion process (Huczko et al. 2005), polymer pyrolysis (Gao et al. 2008) and microwave heating—assisted method (Sundaresan et al. 2007).

An interesting alternative method to obtain SiC nanowires is the surface conversion of silicon NWs through a carbon treatment (called carburization) by using a carbon source like propane or methane. The carburization process is similar to those in preparation of SiC layers on silicon substrate (Zhang et al. 2000; Xing et al. 2004; Ollivier 2013; Latu-Romain et al. 2013).

Instead of SiNWs, it is possible to use carbon nanotubes (CNTs) by reaction with SiO or  $\text{SiI}_2$  at high temperatures; transition occurs from CNTs to SiC NWs (Iijima 1991).

In literature, few publications occurs for the preparation of hexagonal SiC nanowires and are mainly related to 6H orientation.

The most important methods are polymer pyrolysis (Gao et al. 2008), arc-discharge procedure (Li et al. 2002) and microwave process (Wei et al. 2008).

The T-D method is not so common but SiCNWs with a diameter of 55 nm were fabricated by means of etching from 3C-SiC layers grown on silicon substrates with a thickness of 50 nm (Feng et al. 2010).

It is interesting to list the possible potential applications of silicon carbide nanowires due to their chemical and physical properties:

filler, reinforcing element of ceramic matrix to increase the mechanical performance

energy conversion

catalytic nanomaterials

hydrogen storage

field emission devices

coating

bio-applications



In this paper, we report the growth of SiC-SiO<sub>2</sub> core-shell nanowires on silicon substrate using carbon monoxide as precursor and iron as catalyst by CVD reactor and also pure SiC NWs grown in a vapour phase epitaxy (VPE) apparatus with propane and silane as precursors with nickel and iron as catalysts

The morphology and crystal habit of the grown nanowires were further investigated by Field Emission Gun Scanning Electron Microscopy (FEG-SEM) (Jeol—6400F) while Transmission Electron Microscopy (TEM) (Jeol—JEM 2200 FS) for High—Resolution Transmission Electron Microscopy (HR-TEM) studies and High Angle Dark Field imaging in Scanning mode (HAADF-STEM) and the Selected Area Electron Diffraction (SAED) patterns proved to be useful for detailing the nanowires structure. Optical properties have been investigated with SEM-Cathodoluminescence spectroscopy.

## 5.2 Growth Mechanisms of SiC Nanowires Synthesized from Vapour Phase

More than 250 polytypes of silicon carbide have been identified (Cheung 2006; Bechstedt et al. 1997), but only the cubic (3C or  $\beta$ , stacking sequence ABC) and two hexagonal (4H and 6H, both called  $\alpha$ , stacking sequence ABCB and ABCACB respectively) are the most common in literature for nanowires.

The polytype obtained in the final structure of the wires is strictly correlated to the growth parameters, both because the cubic polytype is the most stable at low growth temperature (Kimoto et al. 1997) and it is the most energetically favourite for nanowires with larger diameters (approximately more than 20 nm) (Zaima et al. 2006). That is due to the lower number of 4H-SiC dangling bonds per surface unit, which makes it the most stable polytype for smaller diameters. For large diameters the bulk energy contribution becomes preponderant and 3C polytype is then the most likely to be found. For these two reasons cubic polytype constitutes the majority of SiC nanowires that is possible to witness in literature.

Some growth mechanisms for the synthesis of silicon carbide need a catalyst in order to occur, like vapour-liquid-solid (VLS), vapour-solid-solid (VSS) and solid-liquid-solid (SLS); all of these are called catalytic growth mechanisms.

Frequently a catalytic growth mechanism is spotted by the presence of a catalytic particle either on the tip or at the bottom of the nanowire, but it would not be correct to exclude catalytic growth by the absence of it.

It is possible to make a distinction for two catalytic growth processes: float growth and root growth. In the former the particle remains at the top of the nanowire, while in the latter the particle stays at the bottom (Kolasinski 2006).

### 5.2.1 Vapour-Liquid-Solid Growth Mechanism

The vapour-liquid-solid mechanism, described by Wagner and Ellis in 1964, is the most exploited process for the synthesis of semiconductor nanowires and this is true in particular for silicon carbide synthesis; given that, this method was also used to

produce microstructures and bulk crystals (Krishna and Marshall 1971; Bootsma et al. 1971).

The process takes advantage of metal nanoclusters used as catalyst acting as preferential site on the substrate surface for the vapour deposition. The clusters are in liquid phase because the synthesis is carried out above the eutectic temperature of the metal-semiconductor system. The vapour is rapidly adsorbed by these liquid droplets until the solute supersaturates the eutectic until precipitation occurs, leading to the nucleation of a crystalline phase. The growth proceeds at the solid-liquid interface leading to an axial growth of an elongated structure. The metal nanoparticle has a larger sticking coefficient than the semiconductor surface, therefore this method allows lower growth temperature and a faster growth rate than direct growth on solid surface from gas phase.

The larger sticking coefficient of the nanoparticle can be due to many different reasons: liquid surface can have a large accommodation coefficient compared to an H-terminated silicon surface or even to a generic solid surface. Sometimes, like the case of silanes, metals have a catalytic action on the gas precursors, and that's the reason for a greater dissociation rate on the particle compared to that on the sidewalls (Kolasinski 2006). Often the energy barrier for new material incorporation in the crystalline wire is lower at the liquid-solid interface than on the solid-gas interface on the sidewalls. What appears to be critical is to have a lower nucleation energy barrier at the nanoparticle/wire interface in order to obtain an axial growth.

The size of the droplets has a direct influence on the final diameter of the nanowires (Gudixsen and Lieber 2000) and on growth kinetics as a manifestation of the Gibbs-Thompson effect (Biswas et al. 2013). This explains how the curvature of an interface can affect the chemical potential of a body:

$$\Delta\mu = \Delta\mu_0 - \frac{4\Omega\alpha}{d} \quad (5.1)$$

where  $\Delta\mu$  is the supersaturation, which is the growth driving force,  $\Delta\mu_0$  is the difference between the chemical potential of the precursor in vapour phase and in solid phase (inside the nanowire),  $\Omega$  is the atomic volume of the precursor specie,  $\alpha$  is the surface free energy of the wire and  $d$  is the diameter of the droplet. This means that the solubility of a specie in a catalyst particle becomes dependent of the particle size. As a general consequence, starting from bigger particles leads to faster kinetics in nanowires growth.

Since the first study of VLS by Wagner and Ellis (1964) researchers have been synthesizing silicon carbide wires or whiskers exploiting this growth mechanism (Krishna and Marshall 1971; Bootsma et al. 1971; Gudixsen and Lieber 2000; Biswas et al. 2013; Ryan et al. 1967) but only many years after some “nano” sized object were obtained (Saito et al. 1992; Zhou and Seraphin 1994).

The nanoscale size turns out to be critical for some structural characteristic of silicon carbide nanowires, such as the crystallographic orientation, strongly dependent on the nanowire diameter.

The most common growth direction for VLS growth mechanism in SiC literature is the nanowire axis parallel to  $\langle 111 \rangle$  crystallographic orientation, but in some cases also  $\langle 100 \rangle$  direction has been observed (Zhou et al. 1999). This is strongly dependent from the diameter, since crystallographic orientation of the nanowire is driven by the minimization of the total free energy. The contribution to the total free energy are the bulk energy of the nanowire, the surface energy of the interface between liquid catalyst and nanowire and finally the nanowire surface in vacuum (similar to that in gas atmosphere). With small nanowire diameters the surface energy of the NW in vacuum is dominating but, for bigger diameters, the contribution of the surface free energy of the interface between the semiconductor and the metal catalyst becomes predominant (Wagner 1970; Fortuna and Li 2010).

### 5.2.2 Vapour-Solid-Solid Growth Mechanism

In many cases nanowires growth was observed at temperatures far below the eutectic point of the semiconductor-metal system (Persson et al. 2004). Even if the melting point of a small body is smaller than the corresponding bulk (Buffat and Borel 1976), the temperature used and the size of the nanoparticles exclude the possibility for these particles to melt.

In some circumstances (Baker 1989) this phenomenon was explained with a growth mechanism very similar to the VLS, but presuming the solid state diffusion through the solid catalyst nanoparticle. In general, when an axial growth is nourished from gas phase and catalysed by a solid particle the growth mechanism is called vapour-solid-solid.

It is hard to find a strict borderline between VLS and VSS, since the catalyst nanoparticle act as a nucleation point in both cases and there are many examples in which the structure of the nanowires seems not to be affected by the catalyst phase (Kolasinski 2006).

### 5.2.3 Vapour-Solid Growth Mechanism

The presence of a catalytic specie isn't always necessary, since many other factors can induce an axial growth. The nucleation probability  $P_N$  on the surface of a whisker is related to thermodynamic variables and to crystallographic parameters:

$$P_N = B \exp \left( -\frac{\pi \gamma^2}{k^2 T^2 \ln \sigma} \right) \quad (5.2)$$

(after Dai et al. (2003) and Sears (1955))

where  $B$  is a constant related to the material,  $\gamma$  is the surface energy of the solid,  $k$  the Boltzmann constant,  $T$  is temperature and  $\sigma$  the supersaturation ratio:

$$\sigma = \frac{p}{p_0} \quad (5.3)$$

Where  $p$  is the actual partial pressure of the vapour specie and  $p_0$  is the equilibrium partial pressure at temperature  $T$ .

This means that the nucleation probability is related to  $\gamma$ , the surface energy of the solid, which can change for different crystallographic planes. An anisotropic growth can therefore be caused by a wide disparity between the surface energy of different crystallographic planes of the nanowire and the consequent surface energy minimization.

Furthermore, any irregularity such as defects or impurities on the substrate can act as a nucleation site for the nanowire growth (Yang and Lieber 2011) and, in particular, a screw dislocation can propagate and promote an axial growth (Burton et al. 1951) resulting in the formation of helical SiC nanowires (Zhang et al. 2002).

The possibility of growing catalyst free SiC nanowires (Yang et al. 2005) can be an advantage because the presence of a metal could be deleterious for device applications.

### 5.3 Substrate Preparation

The procedure for the growth of silicon carbide nanowires starts with the chemical cleaning of the substrate, then the metal catalyst is deposited onto it and finally the sample is inserted into the reactor chamber where the growth takes place.

In vapour phase epitaxy of semiconductor species the substrate plays a fundamental role, and the growth interface has a direct influence on the structure of the epi-layers. In addition, what produces the uniaxial elongation in a catalytic growth mechanism is the presence of nucleation points on the surface of the substrate, so, for nanowires synthesis, the presence and the arrangement of the catalyst holds sway on the final nanostructure morphology and organization. For that reason a peculiar attention must be paid to substrate preparation and catalyst deposition.

In this section, after a brief description of the substrate preparation procedure, different catalyst deposition techniques are illustrated and the dewetting process is studied with selected examples.

### 5.3.1 *Chemical Cleaning*

The preparation of the substrates prior to the deposition is critical for the result of the dewetting process. Since the catalyst has to form an alloy with the silicon of the substrate to transform to liquid phase, the presence of an interlayer between the metallic layer and the substrate may hinder the process. To avoid that, the substrate is prepared by removing impurities and clean the surface.

The first step is an ultrasonic bath in deionized water, then in acetone to dissolve organic molecules present on the surface.

Later RCA SC-1 and RCA SC-2 processes (Kern and Puotinen 1970) are performed to further remove organic and ionic contaminants. HF etchings are done between RCA SC-1 and RCA SC-2 and at the end to remove the silicon oxide layer formed by the chemical processes and exposition to air.

### 5.3.2 *Catalyst Deposition Methods*

Catalyst distribution stage has a pivotal role aiming to uniform and controlled growth. The essential step prior to VLS growth is to have uniform catalyst particles coverage of the substrate.

In order to obtain that, in our laboratory we followed two different approaches: it is possible to spread directly nanoparticles on a substrate or to deposit a thin film and then induce the so-called “dewetting” process.

For the growth of  $\beta$ -SiC nanowires in a vapour phase epitaxy reactor the deposition of the catalyst on the silicon substrate was carried out by two physical method (electron beam and sputtering) for nickel, iron and gold, by electrophoretic deposition for iron and by drop casting of a magnetite nanoparticles solution.

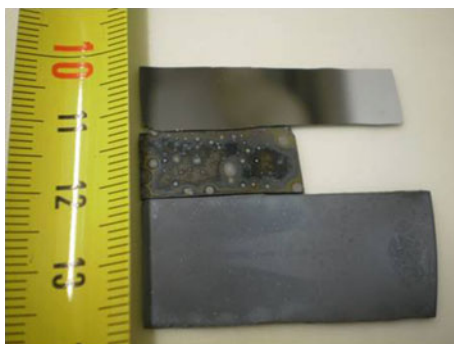
For the growth of core-shell SiC-SiO<sub>2</sub> nanowires the best and most straightforward method was found to be the drop casting of an ethanol solution of metal nitrates (Ni(NO<sub>3</sub>)<sub>2</sub> or Fe(NO<sub>3</sub>)<sub>3</sub>).

In order to acquire a uniform distribution we went through different routes: two physical methods and two chemical methods allowed us to obtain films of different metals with controlled thickness.

**Physical Methods and Electrophoretic Deposition** With e-beam evaporation deposition and radiofrequency sputtering, a 4 nm thick film was found to be the best candidate for SiC nanowires growth.

Electrophoretic deposition (EPD) (Van der Biest and Vandepierre 1999) proved to be an efficient method to obtain films for our aim, since it has high yield and it is easy to perform, but its drawbacks are correlated to the difficulty of reaching a good control over film thickness and uniformity.

The metal deposition rate can be controlled in a certain range by varying the electrical potential difference and deposition duration. For the present study iron was deposited starting from a ferrous sulphate (FeSO<sub>4</sub>) solution in water with a low electric field (potential used was 5 V) for a 30 min deposition time.



**Fig. 5.1** Photo comparison of a silicon substrate (*on top*) a core-shell nanowires sample synthesized without the use of surfactant (*in the mid-dle*) and a sample fully covered by nanowires with catalyst deposition carried out with the aid of an organic surfactant (*on the bottom*). The white stains in the middle sample are areas covered by nanowires bundles

**Nanoparticles** An excellent method to deposit catalyst was found to be the simple drop casting of a nanoparticles solution. For the aim of the present work it was used an acetone solution of magnetite ( $\text{Fe}_3\text{O}_4$ ) nanoparticles obtained by coprecipitation following the method proposed by Massart 1981.

The solution was spread over the surface of silicon substrate. The acetone drying process is fast compared to the aggregation kinetics of the nanoparticles (Velarde et al. 2007), so it is possible to obtain a uniform superficial distribution.

**Drop Casting of Nitrates** For the growth of core-shell nanowires, a very simple technique to obtain a metallic film on the substrate was found to be the drop casting of an ethanol solution of nickel (II) nitrate ( $\text{Ni}(\text{NO}_3)_2$ ) or Iron(III) nitrate  $\text{Fe}(\text{NO}_3)_3$ .

After HF treatment to remove native oxide, the surface of silicon is mainly composed of Si atoms bonded with 2 hydrogen atoms each (Ubara et al. 1984) and it has a low wettability with ethanol solution because it is non-polar. To enhance the hydrophobic surface wettability an organic surfactant (oleylamine) was added to the catalyst solution. The hydrophobic “tail” of oleylamine molecule is in contact with hydrophobic silicon surface, while hydrophilic “head” is facing the polar solution (Negri n.d).

The drying process is performed at  $40^\circ\text{C}$  for less than 20 min. to limit the formation of silicon oxide on the surface; as a result, a uniform layer of nitrate is obtained.

The uniformity of the nanowires bundle covering the whole substrate is visible with bare eye (Fig. 5.1).

### 5.3.3 Dewetting

A thin film deposited on a solid substrate is frequently a metastable phase and it agglomerates when the temperature is raised to the melting point of the metal or of

the alloy formed by the metal and the substrate. The result is the formation of an array of nanoscaled islands whose size can be controlled by varying the procedure parameters such as temperature and dewetting time or by starting from a different film thickness.

Surface energy minimization is the driving force of this process, since the surface to volume ratio of a nanoparticles array is smaller than that of a thin film (Thompson 2012).

As said before, the size of the islands demonstrated to be determinant for the final diameter of the wires (Gudiksen and Lieber 2000) and it is strictly correlated to the metal layer thickness (Kojima and Kato 2008) so, by varying this in the deposition stage, it is possible to obtain a certain control over the size of the islands and, consequently, over wires diameter.

According to equilibrium thermodynamics it is possible to calculate the minimum radius of a liquid metal cluster as

$$r_{\min} = \frac{2\gamma_{LV}V_L}{RT \ln \sigma} \quad (5.4)$$

where  $\gamma_{LV}$  is the liquid vapour surface free energy,  $V_L$  is the molar volume,  $R$  is the ideal gas constant,  $T$  is temperature and  $\sigma$  is the vapour phase supersaturation (Hu et al. 1999). Nevertheless droplets diameters smaller than those predicted by this formula have been frequently experimentally found (Kojima and Kato 2008) suggesting that this constraint from thermodynamics can be overcome out of equilibrium. Still this can be used as a general rule of thumb to know the dependence of droplets size from the thermodynamic conditions.

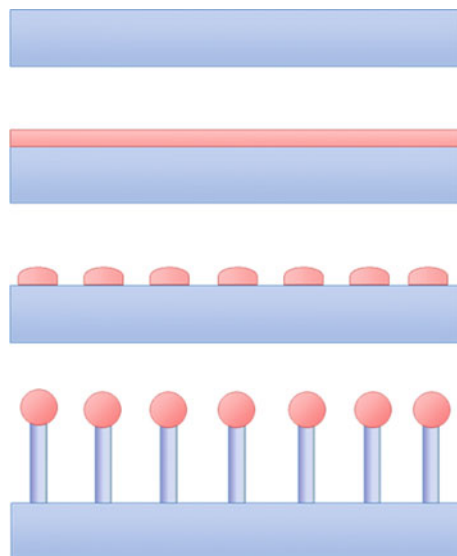
A scheme of a VLS growth mechanism with the dewetting of a solid-state film is represented in Fig. 5.2.

**Dewetting Procedure for Au, Fe, Ni Thin Films** The dewetting stage occurs in hydrogen atmosphere without the precursors at different temperatures for the various metals. The choice of the dewetting temperature is made basing on metal-catalyst phase diagram. The primary feature, is the eutectic temperature of the alloy because, for a liquid phase dewetting to occur it is necessary to exceed it but, if the film is thin enough, a solid-state dewetting can occur via surface diffusion even below the melting temperature (Thompson 2012).

The best temperatures for dewetting of Ni, Fe and Au films was found to be 1100°, 1250° and 600 °C respectively, while for nanoparticles no dewetting is needed. A summary of the eutectic temperatures of the alloys and the dewetting temperature used is reported in Table 5.1.

In Fig. 5.3 the dewetting of a nickel layer is reported, the size of the islands is mainly in between 10 nm and 1  $\mu$ m and the shape is generally squared.

**Fig. 5.2** Cartoon depicting SiC nanowires growth with a particular focus on the dewetting stage: (a) and (b) a uniform film of metal catalyst (in red) is deposited on the substrate (in blue), (c) after the eutectic temperature is reached and the catalyst is in liquid phase, the film forms liquid droplets all over substrate surface. (d) An axial growth takes place nucleated by the catalyst particles, which remain on the top of the wires



In semiconductor technology nickel silicides are finding increasing interest, therefore nickel diffusion in silicon is widely studied and it is possible to find many examples in literature of studies on nickel diffusion of Ni in silicon. The nickel diffusion through the bulk is faster than that on nickel diffusion in silicon surface and the transport to the surface is caused by the segregation when the solubility of nickel reduces owing to the temperature decrease. The shape and the state of the structures on surface is dependent on the cooling rate (Dolbak et al. 1989, 1991). The observation of square-shaped island is typical for the segregation of nickel on (100) surface of silicon.

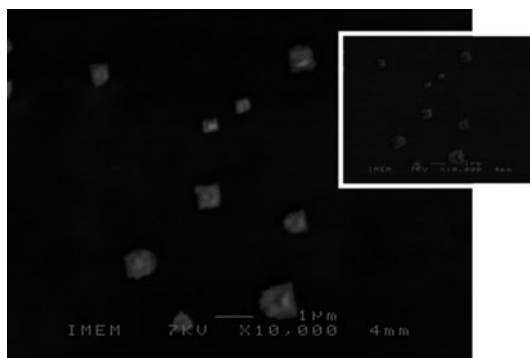
The dewetting of a 2 nm thick Au layer performed at 600 °C is shown in Fig. 5.4: the size of the islands here is much smaller because the eutectic temperature of silicon-gold system is lower (363 °C (Okamoto and Massalski 1983) and the cohesion forces are less.

**Table 5.1** Comparison between the alloy eutectic temperature reported in literature and the temperature set to obtain the dewetting of the samples

Metal Catalyst	Alloy eutectic temperature °C	Dewetting temperature °C
Ni	966 (Nash and Nash 1987)	1100
Fe	1200 (Massot et al. 2013)	1250
Au	363 (Okamoto and Massalski 1983)	600



**Fig. 5.3** Secondary electron SEM image of Ni film dewetting on silicon substrate. Backscattered electron SEM image (*in the inset*)

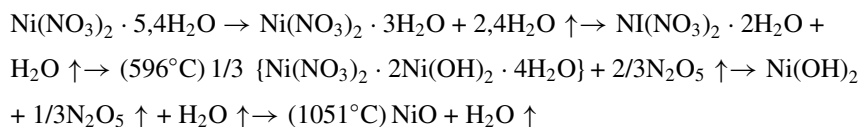


**Fig. 5.4** SEM image of 2 nm gold film dewetting

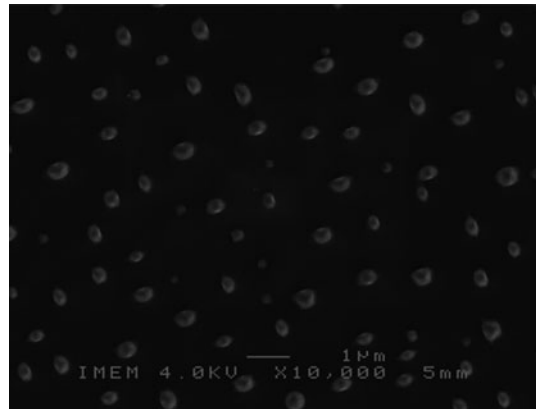


As said before, dewetting is driven by the minimization of elastic as well as surface energies and the competing process leading to island aggregation is the Ostwald ripening. The balance between these two tendencies varies with different temperatures and times (Bartelt 1996) and a clear example of that was observed for iron film dewetting. In Figs. 5.4 and 5.5 SEM images of two samples after 2 min. and 5 min. dewetting respectively show different distribution density and size of the islands demonstrating the evolution of the process with time.

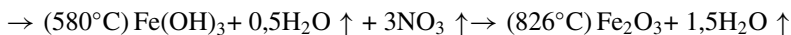
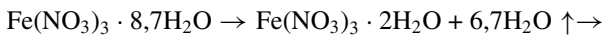
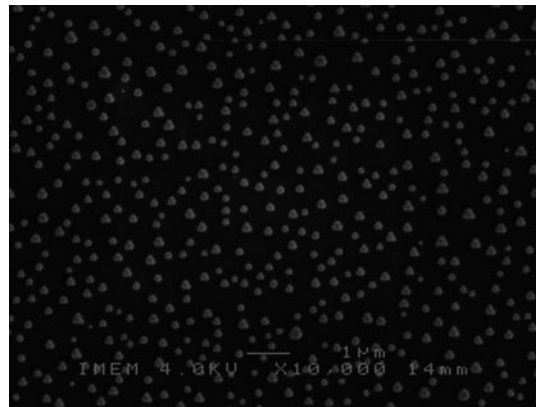
**Dewetting Procedure for Nitrates** Both ferrous nitrate and nickel nitrate undergo a dehydration and a thermal decomposition and the result is the formation of the corresponding oxide:



**Fig. 5.5** SEM image of iron film after 2 min dewetting



**Fig. 5.6** SEM image of iron film after 5 min dewetting



(after Elmasry et al. 1998)

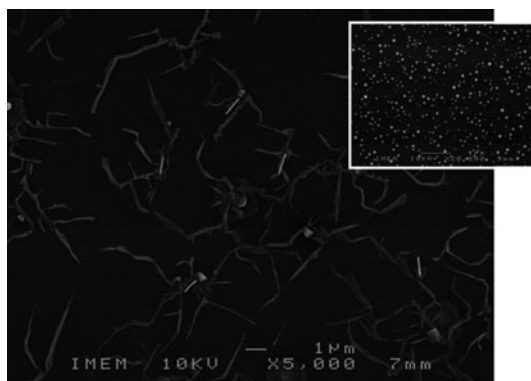
Gaseous species that are formed during heating are designated with  $\uparrow$  symbol and it means they drift apart.

After the introduction of carbon monoxide for nanowires growth (see following section) a reduction process of ferric oxide or nickel oxide takes place and it produces metallic iron or metallic nickel respectively through different reduction paths, depending on kinetics and thermodynamic conditions (Jozwiak et al. 2007; Szekely and Lin 1976).

Subsequently the metal forms an alloy with the silicon of the substrate and, after transformation into liquid phase, it creates a droplets array on the surface (Fig. 5.6).

From the SEM images the transition is clearly visible: the oxide forms islands whose elongated shape demonstrate that the liquid phase wasn't reached (Fig. 5.7),

**Fig. 5.7** SEM image of a sample covered by nickel nitrate catalyst after the decomposition to nickel oxide. Inset: SEM image of the same sample after 2 min exposition to carbon monoxide



but 1 minute after CO introduction in the chamber, the sample is covered with small droplets formed by a metal-silicon alloy (Fig. 5.7 inset).

## 5.4 Growth of Silicon Carbide Nanowires

The synthesis of pure  $\beta$ -SiC nanowires from vapour phase is here described.

The method, already widely used for thin films synthesis (Zorman et al. 1995), is based on the reaction at high temperature between silane and propane bringing to the formation of cubic silicon carbide on silicon substrate.

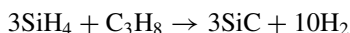
The process exploits the VLS growth mechanism; the use of different catalysts and their effect on the structure and morphology of the wires is discussed.

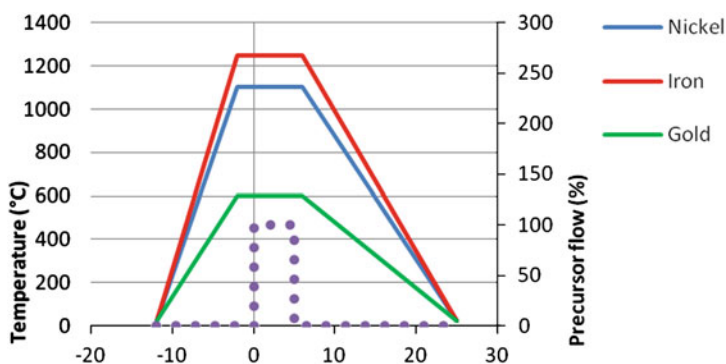
### 5.4.1 Experimental

Silicon carbide nanowires have been synthesized in a vapour phase epitaxy reactor using silane ( $\text{SiH}_4$ ) and propane ( $\text{C}_3\text{H}_8$ ) as precursors (both 3 % in  $\text{H}_2$ ) and hydrogen as carrier gas. The process is carried out at atmospheric pressure in a quartz chamber with (100) and (111) Si substrate placed on an induction-heated graphite susceptor.

The dewetting stage in hydrogen atmosphere, explained in the previous section, is performed not always at the same temperature as the growth, the thermalization between the two stages is carried out in hydrogen and it lasts less than one minute. After the set temperature is reached, the precursors are introduced into the growth chamber for a time of 5 min.

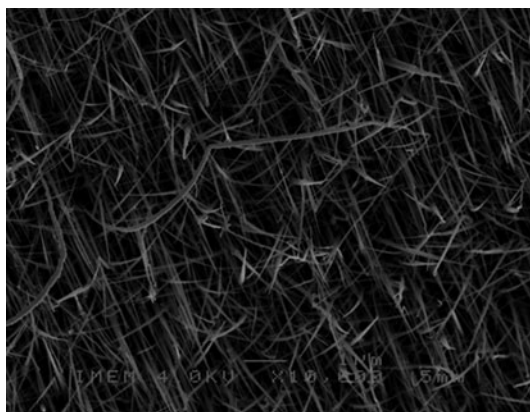
Hydrogen is used as carrier gas and it is one of the reaction products:





**Fig. 5.8** Scheme of the growth procedures for vapour phase epitaxy of SiC nanowires using different catalysts. “Nickel”, “Iron” and “gold” stands for nickel, iron and gold catalysed SiC nanowires. The flow of the precursors is indicated as percentage of the total flow

**Fig. 5.9** SEM image of a SiC nanowires array grown by means of Ni catalyst



The temperatures found to pledge the best results for nanowires synthesis by means of different catalyst were 1100 °C (for nickel), 1250 °C (for iron), 1150° (for gold) and 1100° for magnetite nanoparticles (Fig. 5.8).

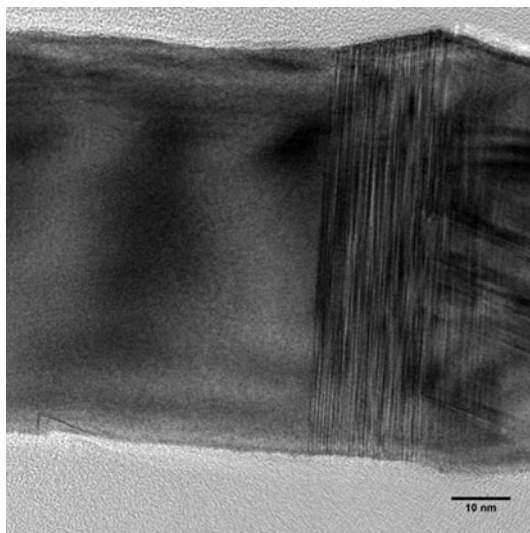
#### 5.4.2 Morphological and Structural Analysis

The growth kinetic is quite fast compared to traditional thin film epitaxy and after 5 min. it is possible to notice the formation of a dense nanowires network (Fig. 5.9).

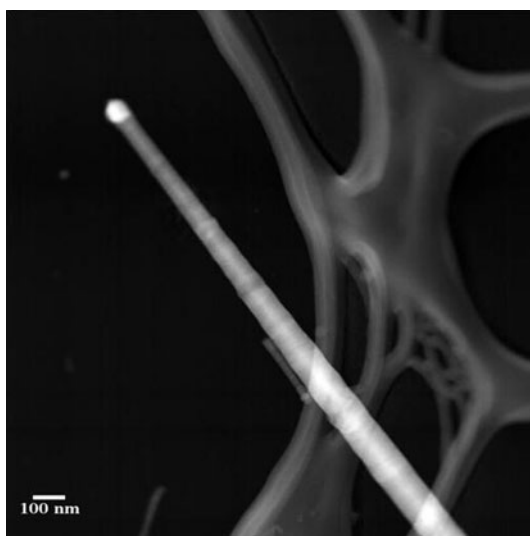
The wires have a circular cross section and the tapered shape is a clue of the VLS root growth because it can be caused either by catalyst consumption during the synthesis or by the radial growth, slower than the axial one, enlarging the base of each wire (60–100 nm diameter).

The length can vary in different parts of the sample from 1 to 10  $\mu\text{m}$ .

**Fig. 5.10** HRTEM image of a region of a Ni catalysed wire with planar defects



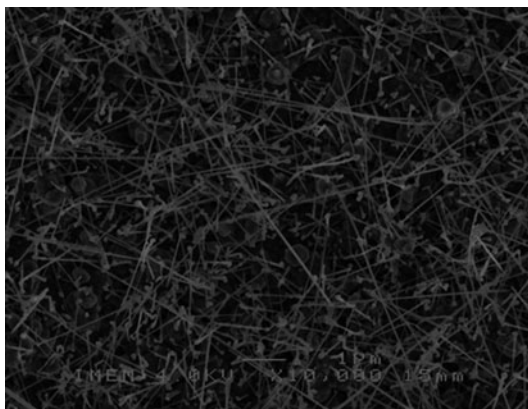
**Fig. 5.11** TEM- HAADF image of the region near to the tip. In this technique, called also z-contrast, high atomic number elements are highlighted by a lighter colour. In this case the tip is much brighter than the rest of the nanowire because it contains nickel ( $Z = 28$ ) instead of silicon ( $Z = 14$ ) and carbon ( $Z = 6$ )



TEM analysis (Fig. 5.10) shows a 3-C SiC structure with  $\langle 111 \rangle$  axis along the growth direction. Along the wire, it is possible to spot wide areas of good crystalline quality alongside of zones with stacking defects on (111) planes.

High Angle Annular Dark Field (HAADF) STEM Tomography (Fig. 5.11) highlight a particle on the tip of the nanowires. In the image the bright colour indicates the presence of high atomic number elements, in this case nickel, clue of a VLS type growth.

**Fig. 5.12** Top view SEM image of iron catalysed pure SiC nanowires



**Fig. 5.13** Side view SEM image of iron catalysed pure SiC nanowires



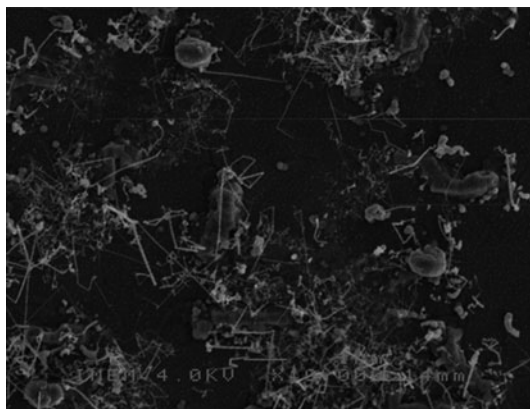
The morphology of the wires grown with iron catalyst (Figs. 5.12 and 5.13) is slightly different, possibly owing to the higher growth temperature (1250 °C), but the length and diameter are similar to those grown using nickel catalyst.

Some preliminary trials were done using gold as catalyst, the result was the formation of randomly oriented nanowires (Fig. 5.14), the gold was found also on nanowires walls (Fig. 5.15) owing to the high surface diffusivity of gold. This is due to the growth temperature, far above the eutectic temperature of the gold-silicon system.

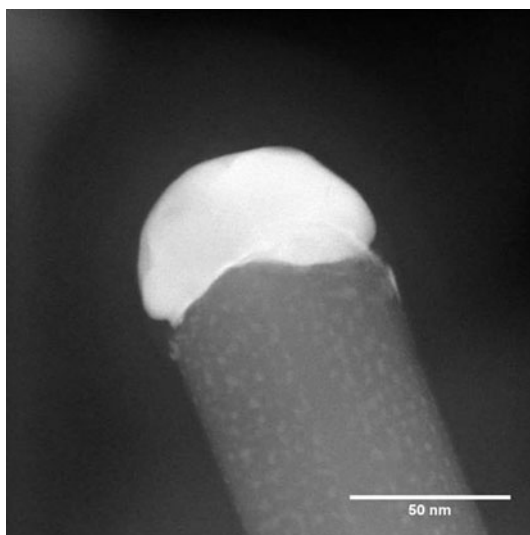
SiC nanowires were successfully synthesized using magnetite ( $\text{Fe}_3\text{O}_4$ ) nanoparticles prepared with a coprecipitation procedure (Massart 1981). From SEM images (Fig. 5.16) it was possible to observe a higher nanowires density. The average diameter of the wires is 55 nm, the length is more than 10 nm.

Nanoparticles synthesis via co-precipitation allows a good control over particles size and in principle this would result in a more accurate control over nanowires diameter. In our case we couldn't notice this because a coalescence of nanoparticles was observed prior to the growth during the heating stage. The final islands, even

**Fig. 5.14** SEM top view image of the nanowires ensemble grown using gold as catalyst



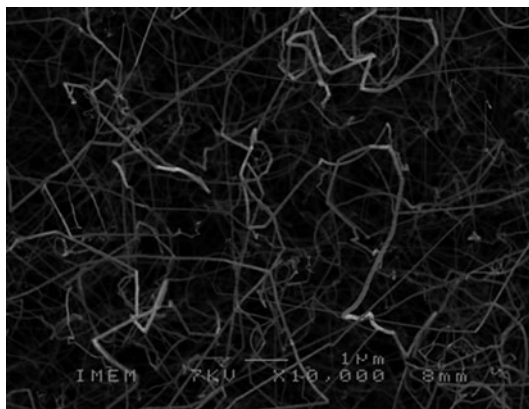
**Fig. 5.15** STEM image of the region near to the tip of the wire. The gold particle on the tip is clearly visible



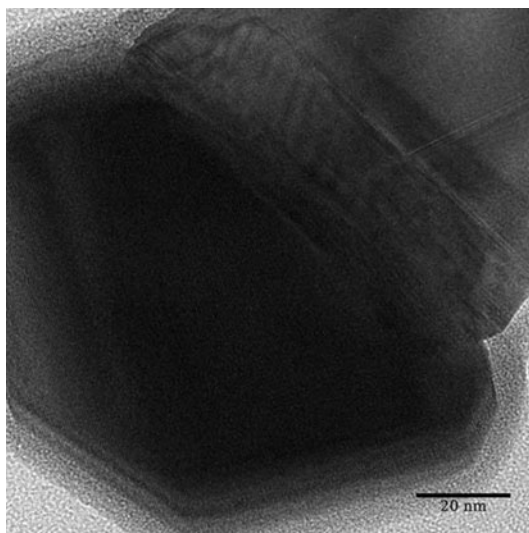
using nanoparticles with few nanometres diameter, were bigger owing to this phenomenon. This is evident from HR-TEM analysis (Fig. 5.17): the catalyst particle diameter (about 100 nm) is much bigger than the one of the initial nanoparticles used (6–10 nm).

The control over islands size using nanoparticles as a catalyst needs to be further investigated and improved.

**Fig. 5.16** SEM image of nanowires grown using magnetite nanoparticles as catalyst



**Fig. 5.17** HR-TEM magnification of the magnetite tip

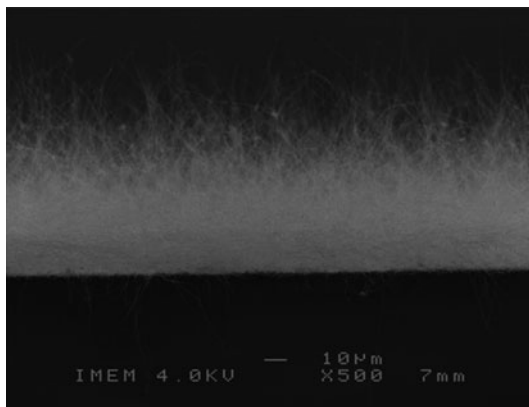


## 5.5 Growth of Core-Shell Silicon Carbide—Silicon Oxide Nanowires

Core-shell SiC-SiO<sub>2</sub> were synthesized from carbon monoxide in vapour phase and silicon coming from the substrate. This method allow to obtain core-shell nanowires in an easy and cheap way and it has high yield, since the growth procedure is quite fast (30 min.). The optical properties of the so-obtained nanostructure are peculiar because an enhancement of the core near-band-edge emission due to the presence of the amorphous silica shell has been demonstrated.



**Fig. 5.18** Side view SEM image of core-shell SiC-SiO<sub>2</sub> nanowires: It is hard to define the exact average length since nanowires form a dense bundle, but it exceeds 100  $\mu\text{m}$



### 5.5.1 Experimental Procedure

Experiments were carried out in an open tube reactor placed with a conventional horizontal tube furnace with a constant temperature region 10 cm long. (100) silicon is used as substrate as well as silicon source for the growth.

After catalyst deposition and drying (as explained before), the samples are placed in an open tube reactor purged with vacuum-nitrogen cycles to remove oxygen from the growth chamber.

The temperature is then raised to the synthesis setting (1100 °C) and CO is provided under a constant flow ( $4 \cdot 10^{-6} \text{ m}^3/\text{s}$ ) for 30 min. at atmospheric pressure in nitrogen carrier gas flow. Subsequently the sample is brought to ambient temperature during 10 min.

After the cooling step, the sample is covered with a white coloured deposit indicating the presence of a dense wires network all over the surface.

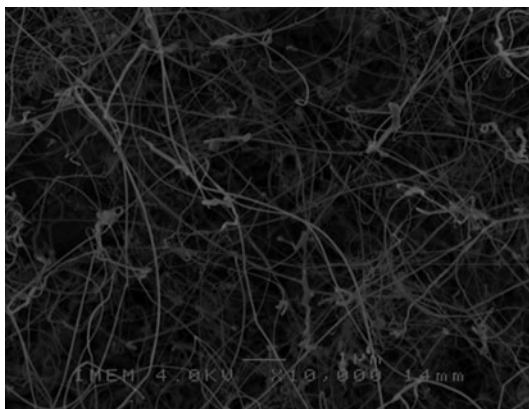
Using gaseous CO as precursor instead of a solid state reaction between C and WO<sub>3</sub> as proposed by Park et al. (2004) allows a continuous control over CO flow, so the concentration during the growth, and prevent tungsten contamination inside the chamber.

### 5.5.2 Morphological, Structural and Compositional Analysis

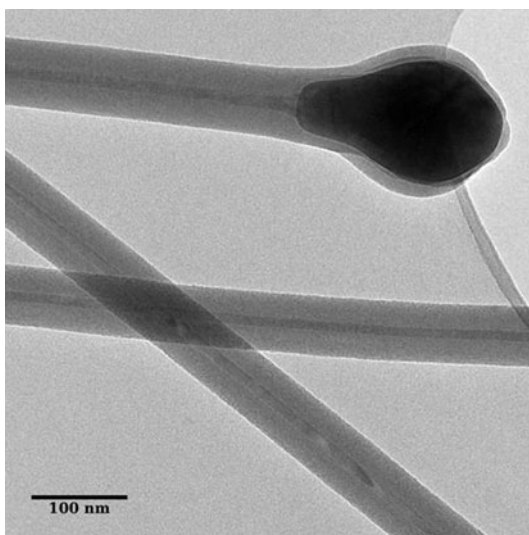
The shape of the wires is cylindrical, the average diameter is 60 nm and the length is more than 100  $\mu\text{m}$ .

From SEM observation it is possible to see the dense nanowire bundle forming a layer of about 100  $\mu\text{m}$  on the substrate (Fig. 5.18) the shape of the wires is curvilinear (Fig. 5.19) but it is rare to spot abrupt folds.

**Fig. 5.19** Top view SEM image of core-shell SiC-SiO<sub>2</sub> nanowires



**Fig. 5.20** TEM image of three different nanowires. It is possible to observe the core-shell structure. The wire ends with a particle with diameter bigger than that of the wire



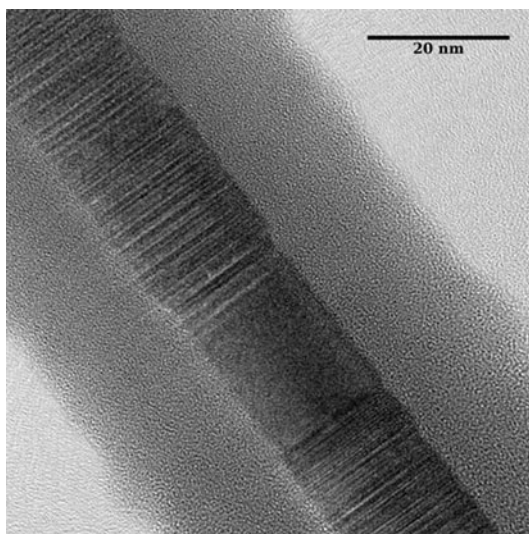
TEM analysis highlights the core-shell structure (Fig. 5.20); the core is continuous along the whole wire without interruption and it is connected to the particle on the tip of the wire.

The structure can be resolved by means of HRTEM (Fig. 5.21): the shell has an amorphous structure, while the symmetry and lattice spacings of the crystalline core correspond to 3C-SiC, with  $\langle 111 \rangle$  axis along the growth direction.

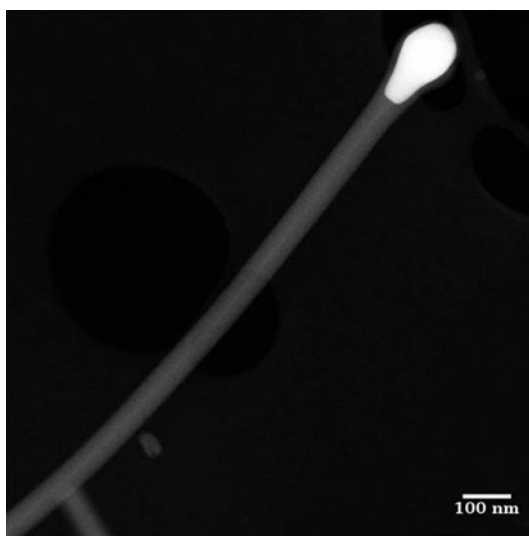
As in pure SiC nanowires (described before), quite long segments of the core are almost free of planar defects. In some other areas it is possible to observe the occurrence of (111) stacking faults with the manifestation of stacking sequences of 2H, 4H and 6H polytypes.

TEM- HAADF analysis (Fig. 5.22) shows a confirmation of core-shell structure: as said before, this technique, called also z-contrast discriminate elements with

**Fig. 5.21** HR-TEM magnification of a zone of the core-shell wire where good crystalline quality areas are near to planar defects



**Fig. 5.22** TEM-HAADF image of a core-shell nanowire. The particle on the tip is brighter because of the presence of higher atomic number elements (Iron,  $Z = 26$ )

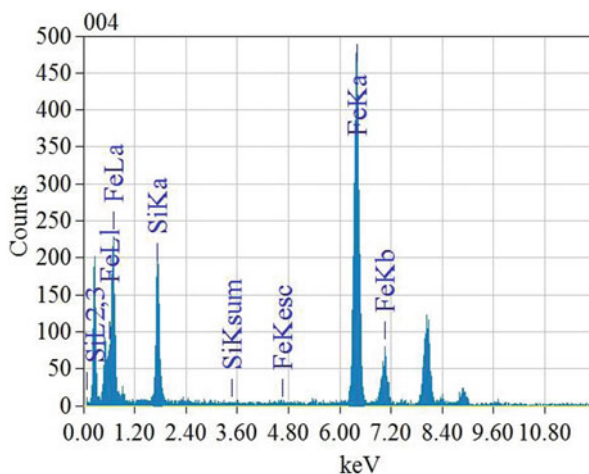


different atomic numbers ( $Z$ ) and highlights those with higher  $Z$ . In this case it shows the presence of iron in the particle on the tip, suggesting a mechanism of so called “float growth” (Kolasinski 2006) kind.

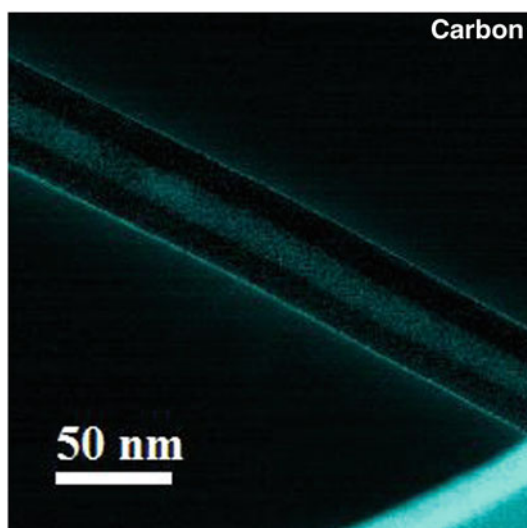
TEM-EDX analysis (Fig. 5.23) carried out on the particle reveals the presence of iron and silicon: this composition could suggest an iron-silicon alloy forming the particle.

The presence of a silicon carbide core and silicon oxide shell is confirmed by TEM-EDX elemental maps on the body of the nanowires (Figs. 5.24 and 5.25).

**Fig. 5.23** TEM- EDX spectrum of a region inside the particle on the tip of the nanowires showing the presence of silicon and iron. The peaks without label in the figure are ascribed to the presence of copper in the grid used as sample holder in TEM microscope



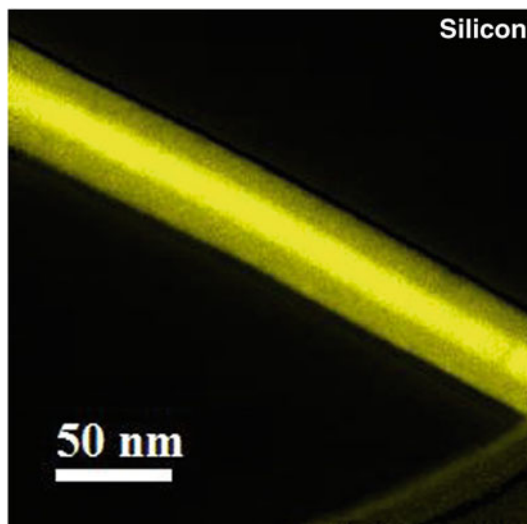
**Fig. 5.24** TEM- EDX map of the carbon presence. It is possible to spot the carbon forming SiC in the core. It is hard to state if the carbon on the surface of the shell is due to contaminations



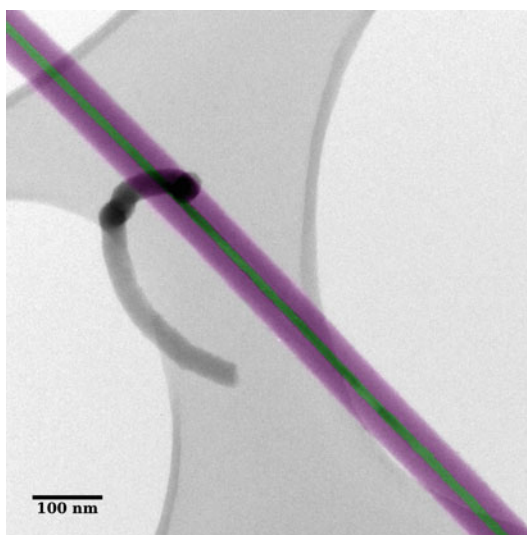
By varying growth parameters it is possible to achieve a certain control over nanowires structure and morphology, for example it was previously demonstrated that the carbon monoxide partial pressure in the reactor during the synthesis can have a direct influence over the core thickness (Dhanabalan et al. 2013). Figure 5.26 reports a TEM image of a typical wire synthesized with a smaller CO concentration (0,2 %). In this sample the average core diameter is 12,7 nm, while in nanowires grown with 0,4 % CO concentration the average core diameter is 20,1 (Choi et al. 2006).

Photoemission from core level of Si2p/C1s were analyzed with photon energy at 250 eV/400 eV, respectively, in order to have the better and same surface sensitivity (about 2–3 nm). The NWs have been previously etched by chemical treatments to remove the thick silicon oxide shell, in order to enable the analysis also of the

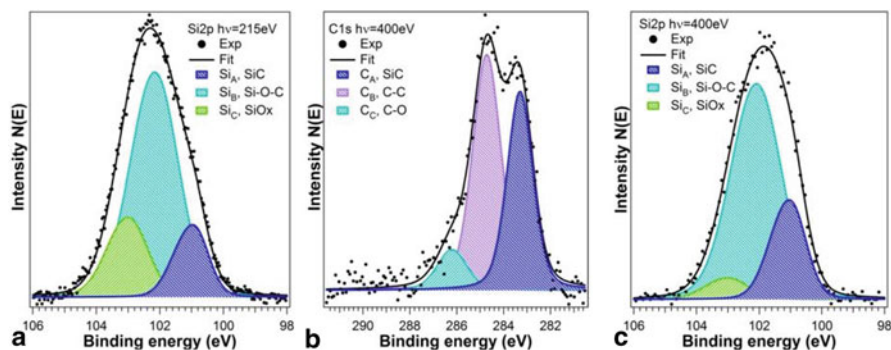
**Fig. 5.25** TEM-EDX map of the silicon presence



**Fig. 5.26** TEM image of a core-shell nanowire grown with a smaller CO partial pressure. The average core diameter shows a strong dependence from growth conditions, in particular from CO concentration (Dhanabalan et al. 2013)



embedded SiC NW core. The Si2p peak broadening and the C1s double peak line-shape shown in Fig. 5.27a and b respectively, clearly reveals the presence of several chemical components. The detailed lineshape analysis reveals the SiC related components (blue peaks in Fig. 5.27) Si<sub>A</sub> and C<sub>A</sub>, respectively at binding energies (BEs) of 101.0 eV and 283.3 eV, together with other features that can be generally ascribed to oxidized species. The Si<sub>A</sub>-C<sub>A</sub> energy distance is 182.3 eV, compatible with the presence of a cubic SiC (Mélinon et al. 1998).



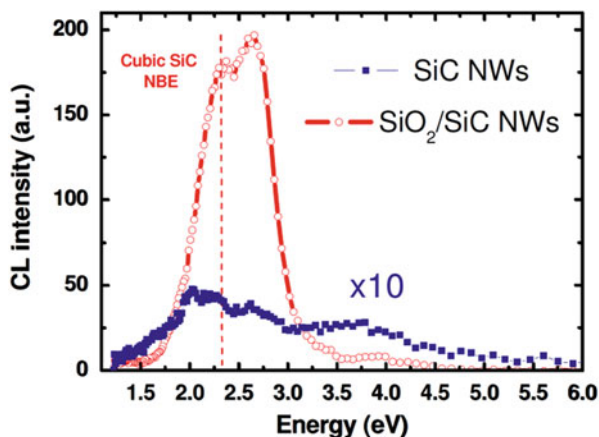
**Fig. 5.27** Core levels photoemission of Si2p (a, c) and C1s (b). Photon energies used are 215 eV (a) and 400 eV (b, c). Experimental data are shown as dots, the fit curves as black lines and the single deconvoluted components as colour lines

Regarding the Si2p core level analysis, the Si<sub>B</sub> peak at 102.1 eV falls into the typical BEs region of silicon oxycarbides (Önneby and Vac 1997; Sorarù et al. 1996), while the Si<sub>C</sub> peak at 103.0 eV is related to silicon oxides. In order to better identify the in depth distribution of the different chemical species, we analyzed the Si2p core level with a larger in-depth sensitivity of about 3–4 nm using a 400 eV photon (Fig. 5.27c). With respect to Fig. 5.27a, features showing the same BE but different relative intensities are present (the higher width is due to the different photon used). As a rule of thumb, by increasing the in-depth sensitivity the more external layers are depleted while the more internal ones are enhanced. In our case, we are dealing with a SiC core surrounded by a silicon oxycarbides structure and, finally, and external very thin SiO<sub>x</sub> layer. This also suggests that the chemical treatments have effectively etched only the more external shell, leaving a residual thin layer with a thickness  $\leq 0.5$  nm on a  $\leq 2$  nm thick silicon oxycarbide layer.

Regarding stoichiometry, the Si/C intensity ratio for the SiC components is  $0.85 \pm 0.05$ , with a slight carbon excess, while the overall Si/C intensity ratio is  $2.23 \pm 0.30$ , with a net silicon excess. This figures out an increasing silicon concentration gradient going from the NW core towards the surface, as well as a higher carbon stoichiometry located around the oxycarbides/SiC interface.

Both the C<sub>B</sub>/C<sub>C</sub> peaks at 284.7eV/286.2eV can be ascribed to C1s emission in oxycarbides, typically located in a BE range of 285–289eV. However, the C<sub>B</sub> component larger width suggests also the presence of sp<sup>2</sup>-sp<sup>3</sup> carbons aggregates, clusters, typically showing a C1s emission around 285eV. The wet chemical treatment did not remove this peak, evidencing that the carbon clusters are not surface contaminants. These carbon aggregates are responsible of the observed carbon excess, previously indeed located at the interface between the oxycarbide and the SiC layers.

**Fig. 5.28** CL spectra acquired at RT on core/shell NWs (red circles) and SiC NWs (blue squares)



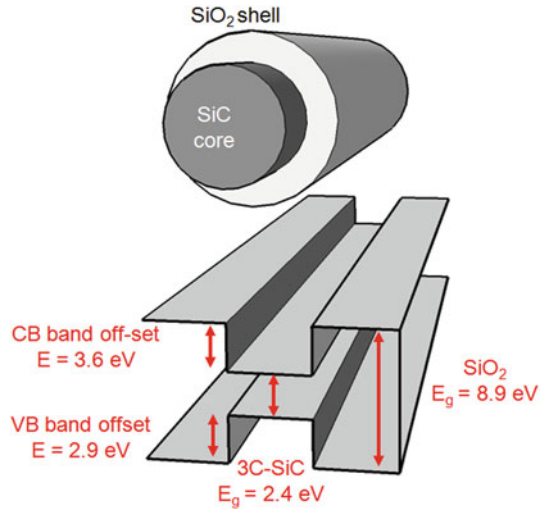
### 5.5.3 Optical Properties

The optical properties of the NWs, with and without the oxide shell, were studied by Cathodoluminescence (CL) spectroscopy. Figure 5.28 shows the comparison between typical room temperature CL spectra acquired on bundles of core/shell NWs (red curve in Fig. 5.28) and SiC NWs (blue curve,  $\times 10$  in Fig. 5.28). The comparison highlights that the emission from SiC NWs is very faint and broad, whereas the core/shell structure favours a more efficient luminescence emission, with quite sharp peaks at 2.3 eV due to the near-band-edge (NBE) recombination in the cubic SiC core and at 2.7 eV related to the SiO<sub>2</sub> shell (Fabbri et al. 2010, 2012).

To explain why the presence of the silicon dioxide shell increases the radiative recombination in the silicon carbide core, we can analyse the energy diagram of the nanosystem. A type I band alignment (Pistol and Pryor 2008) of 3C-SiC and SiO<sub>2</sub> can be hypothesized (Fig. 5.29). The conduction and valence band-offsets have been experimentally found in (Bechstedt et al. 1997) in the case of bulk material and they are equal to  $\delta E_c = 3.6$  eV and  $\delta E_v = 2.9$  eV respectively. In this framework, the carriers generated by the electron beam in the shell diffuse into the core, and here recombine according to the allowed transitions in 3C-SiC. The diffusion of the carriers could be considered as an energy transfer from the shell to the core, an effect that has been observed for semiconductor nanoparticles (Louis et al. 2006) but not yet in NWs. In our system, the amorphous shell results to be beneficial to enhance the luminescence intensity of the crystalline core, preferentially the SiC NBE radiative recombination. Besides the effectiveness as a carrier injector region, this could be partly related to the fact that the shell can act as a passivation layer to reduce the non-radiative recombination related to surface states, likewise in the case of entirely crystalline core/shell systems (e.g. GaAs-based NWs (Sköld et al. 2005; Jabeen et al. 2008).



**Fig. 5.29** Diagram of the type I band alignment between 3C-SiC and SiO<sub>2</sub>



**Acknowledgements** The research is partly supported by the FP7 MARIE CURIE ITN Project “Nanowiring” and by the Project “BioNiMed” funded by the bank foundation “Fondazione Cariparma”.

## References

- Attolini G, Rossi F, Bosi M, Watts BE, Salviati G (2008) *J Non Cryst Solids* 354:5227–5229
- Attolini G, Rossi F, Fabbri F, Bosi M, Watts BE, Salviati G (2009) *Mater Lett* 63:2581
- Attolini G, Rossi F, Negri M, Dhanabalan SC, Bosi M, Boschi F, Lagonegro P, Lupo P, Salviati G (2014) *Mater Lett* 124, 169
- Baker RTK (1989) *Carbon* NY 27:315
- Bartelt NC (1996) *Phys Rev B* 54:11741
- Bechstedt F, Käckell P, Zywietz A, Karch K, Adolph B, Tenelsen K, Furthmüller J (1997) *Phys Status Solidi* 202:35
- Biswas S, O’Regan C, Petkov N, Morris MA, Holmes JD (2013) *Nano Lett* 13:4044
- Bootsma GA, Knippenberg WF, Verspui G (1971) *J Cryst Growth* 11:297
- Buffat P, Borel J-P (1976) *Phys Rev A* 13:2287
- Burton WK, Cabrera N, Frank FC (1951) *Philos Trans R Soc A Math Phys Eng Sci* 243:299
- Casady JB, Johnson RW (1996) *Sol State Electron* 39:1409–1422
- Cheung R (2006) *Silicon carbide micro electromechanical systems for harsh environments*. Imperial College Press, p. 181
- Choi H, Lee CW, Lee GS, Oh MK, Ahn DJ, Kim J, Kim J-M, Ren F, Pearton SJ (2006) *Phys Status Sol* 203:R79
- Cui Y, Lieber CM (2001) *Science* 291, 851–853
- Dai ZR, Pan ZW, Wang ZL (2003) *Adv Funct Mater* 13:9
- Dhanabalan SC, Negri M, Rossi F, Attolini G, Campanini M, Fabbri F, Bosi M, Salviati G (2013) *Mater Sci Forum* 740–742:494
- Dolbak AE, Olshanetsky BZ, Stenin SI, Teys SA, Gavrilova TA (1989) *Surf Sci* 218:37
- Dolbak AE, Olshanetsky BZ, Stenin SI, Teys SA, Gavrilova TA (1991) *Surf Sci* 247:32
- Elmasry MAA, Gaber A, Khater EMH (1998) *J Therm Anal Calorim* 52:489



- Fabbri F, Rossi F, Attolini G, Salviati G, Iannotta S, Aversa L, Verucchi R, Nardi M, Fukata N, Dierre B, Sekiguchi T (2010) *Nanotechnology* 21:345702
- Fabbri F, Rossi F, Attolini G, Salviati G, Dierre B, Sekiguchi T, Fukata N (2012) *Mater Lett* 71:137
- Fan Z, Wang D, Chang P-C, Tseng W-Y, Lu JG (2004) *Appl Phys Lett* 85:5923–5925
- Feng XL, Matheny MH, Zorman CA, Mehregany M, Roukes ML (2010) *Nano Lett* 10:2891
- Fortuna SA, Li X (2010) *Semicond Sci Technol* 25:024005
- Gao F, Yang W, Wang H, Fan Y, Xie Z, An L (2008) *Cryst Growth Des* 8:1461
- Gudiksen MS, Lieber CM (2000) *J Am Chem Soc* 122:8801
- Hu J, Odom TW, Lieber CM (1999) *Acc Chem Res* 32:435
- Huczko A, Bystrzejewski M, Lange H, Fabianowska A, Cudzilo S, Panas A, Szala M (2005) *J Phys Chem B* 109:16244
- Iijima S (1991) *Nature* 354:56–58
- Jabeen F, Rubini S, Grillo V, Felisari L, Martelli F (2008) *Appl Phys Lett* 93:083117
- Johnson JC, Choi H-J, Knutsen KP, Schaller RD, Yang P, Saykally RJ (2002) *Nat Mater* 1:106–110
- Jozwiak WK, Kaczmarek E, Maniecki TP, Ignaczak W, Maniukiewicz W (2007) *Appl Catal A Gen* 326:17
- Kern W, Puotinen DA (1970) *RCA Rev* 187
- Kimoto T, Itoh A, Matsunami H (1997) *Phys Status Solidi* 202:247
- Kojima Y, Kato T (2008) *Nanotechnology* 19:255605
- Kolasinski KW (2006) *Curr Opin Sol State Mater Sci* 10:182
- Koo S-M, Fujiwara A, Han J-P, Vogel EM, Richter CA, Bonevich JE (2004) *Nano Lett* 4:2197
- Krishna P, Marshall RC (1971) *J Cryst Growth* 9:319
- Latu-Romain L, Ollivier M, Thiney V, Chaix-Pluchery O, Martin M (2013) *J Phys D Appl Phys* 46:092001
- Li X, Bhushan B (1999) *Thin Sol Films* 340:210–217
- Li Y, Xie S, Zhou W, Ci L, Bando Y (2002) *Chem Phys Lett* 356:325
- Liu X-M, Yao K-F (2005) *Nanotechnology* 16:2932
- Louis C, Roux S, Ledoux G, Dujardin C, Tillement O, Cheng BL, Perriat P (2006) *Chem Phys Lett* 429:157
- Massart R (1981) *IEEE Trans Magn* 17:1247
- Massot L, Bieber AL, Gibilaro M, Cassayre L, Taxil P, Chamelot P (2013) *Electrochim Acta* 96:97
- Mehregany M, Zorman CA, Roy S, Fleischman AJ, Rajan N (2000) *Int Mater Rev* 45:85–108
- Mélinon P, Kéghélian P, Perez A, Ray C, Lermé J, Pellarin M, Broyer M, Boudeulle M, Champagnon B, Rousset J (1998) *Phys Rev B* 58:16481
- Nash P, Nash A (1987) *Bull Alloy Phase Diagrams* 8:6
- Negri M, Dhanabalan SC, Attolini G, Rossi F, Campanini M, Fabbri F, Salviati G (n.d.) *To Be Publ*
- Okamoto H, Massalski TB (1983) *Bull Alloy Phase Diagrams* 4:190
- Ollivier M, Latu-Romain L, Martin M, David S, Mantoux A, Bano E, Soulière V, Ferro G, Baron T (2013) *J Cryst Growth* 363:158
- Önneby C (1997) *J Vac Sci Technol A Vac Surfaces Film* 15:1597
- Park B, Ryu Y, Yong K (2004) *Surf Rev Lett* 11:373
- Persson AI, Larsson MW, Stenström S, Ohlsson BJ, Samuelson L, Wallenberg LR (2004) *Nat Mater* 3:677
- Pistol M-E, Pryor C (2008) *Phys Rev B* 78:115319
- Ryan CE, Berman I, Marshall RC, Considine DP, Hawley JJ (1967) *J Cryst Growth* 1:255
- Saddow SE (2012) *Silicon carbide biotechnology: a biocompatible semiconductor for advanced biomedical devices and applications*. Elsevier, Waltham
- Saito M, Nagashima S, Kato A (1992) *J Mater Sci Lett* 11:373
- Sarro PM (2000) *Sens Actuators A Phys* 82:210–218
- Sears G (1955) *Acta Metall* 3:367
- Shi W, Zheng Y, Peng H, Wang N, Lee CS, Lee S-T (2000) *J Am Ceram Soc* 83:3228
- Sköld N, Karlsson LS, Larsson MW, Pistol M-E, Seifert W, Trägårdh J, Samuelson L (2005) *Nano Lett* 5:1943

- Sorarù GD, D'Andrea G, Glisenti A (1996) *Mater Lett* 27:1
- Sundaresan SG, Davydov AV, Vaudin MD, Levin I, Maslar JE, Tian Y-L, Rao MV (2007) *Chem Mater* 19:5531
- Szekely J, Lin CI (1976) *Metall Trans B* 7:493
- Thompson CV (2012) *Annu Rev Mater Res* 42:399
- Ubara H, Imura T, Hiraki A (1984) *Solid State Commun* 50:673
- Van der Biest OO, Vandeperre LJ (1999) *Annu Rev Mater Sci* 29:327
- Velarde MG, Dukhin AS, Dukhin SS, Goetz PJ (2007) *Adv Colloid Interfac Sci* 134:35
- Wagner RS (1970) *Whisker technology*. Wiley, New York
- Wagner RS, Ellis WC (1964) *Appl Phys Lett* 4:89
- Wei G, Qin W, Wang G, Sun J, Lin J, Kim R, Zhang D, Zheng K (2008) *J Phys D Appl Phys* 41:235102
- Willander M, Friesel M, Wahab Q, Straumal B, Mater J (2006) *Sci Mater Electron* 17:1
- Wong EW, Sheehan PE, Lieber CM (1997) *Science* 277:1971 (80)
- Wright NG, Horsfall AB (2007) *J Phys D Appl Phys* 40:6345
- Xing YM, Zhang JH, Yang WW, Yu YH, Song ZR, Lin ZX, Shen DS (2004) *Appl Phys Lett* 84:5461
- Yakimova R, Petoral RM, Yazdi GR, Vahlberg C, Lloyd Spetz A, Uvdal K (2007) *J Phys D Appl Phys* 40:6435
- Yang P, Lieber CM (2011) *J Mater Res* 12:2981
- Yang P, Yan H, Mao S, Russo R, Johnson J, Saykally R, Morris N, Pham J, He R, Choi H-J (2002) *Adv Funct Mater* 12:323
- Yang W, Araki H, Kohyama A, Thaveethavorn S, Suzuki H, Noda T (2004) *Mater Lett* 58:3145
- Yang W, Araki H, Thaveethavorn S, Suzuki H, Noda T (2005) *Appl Surf Sci* 241:236
- Young DJ, Du J, Zorman CA, Ko WH (2004) *IEEE Sens J* 4:464
- Zaima S, Miyazaki S, Takagi S, Miyao M, Murota J, Ito T, Sano K, Akiyama T, Nakamura K (2006) *Thin Solid Films* 508:243
- Zhang Y, Tang Y, Zhang Y, Lee C, Bello I, Lee S (2000) *Chem Phys Lett* 330:48
- Zhang H-F, Wang C-M, Wang L-S (2002) *Nano Lett* 2:941
- Zheng G, Lu W, Jin S, Lieber CM (2004) *Adv Mater* 16:1890
- Zhou D, Seraphin S (1994) *Chem Phys Lett* 222:233
- Zhou XT, Wang N, Lai HL, Peng HY, Bello I, Wong NB, Lee CS, Lee ST (1999) *Appl Phys Lett* 74:3942
- Zorman CA, Parro RJ (2008) *Phys Status Solidi* 245:1404
- Zorman CA, Fleischman AJ, Dewa AS, Mehregany M, Jacob C, Nishino S, Pirouz P (1995) *J Appl Phys* 78:5136

# Chapter 6

## Geometry and Topology of Nanotubes and Nanotori

Fatemeh Koorepazan-Moftakhar, Ali Reza Ashrafi,  
Ottorino Ori and Mihai V. Putz

**Abstract** A molecular graph is the graph of a molecule in which the vertices are atoms and edges are chemical bonds. We review the recent results on computing symmetry of series of armchair polyhex, zig-zag polyhex and  $C_4C_8(R/S)$  nanotubes and nanotori. The topological properties of these nanostructures are also investigated.

### 6.1 Introduction

A *graph*  $G$  is a pair  $(V, E)$  consisting of a set  $V = V(G)$  of vertices and a set  $E = E(G)$  of *unordered pairs*  $\{x, y\} = xy$  of distinct vertices of  $G$  called edges. Suppose  $M$  is a chemical system like a molecule (having dimensionality  $\Delta = 0$ ), a carbon nanotube ( $\Delta = 1$ ), a graphenic lattice ( $\Delta = 2$ ) or a diamond crystal ( $\Delta = 3$ ). The *molecular graph* of  $M$  is a simple graph such that *vertices are atoms* and *edges are chemical bonds*. The *degree*  $\delta$  of each vertex (the number of chemical bonds) in a molecular graph is assumed to be at most four. Taking into consideration  $sp^2$  carbon systems, we mention here that in the Hückel theory only pi electron molecular orbitals are included because these determine the general properties of these molecules and the sigma electrons are ignored. Thus, when we are talking about Hückel theory we need

---

F. Koorepazan-Moftakhar (✉) · A. R. Ashrafi  
Department of Nanocomputing, Institute of Nanoscience and Nanotechnology,  
University of Kashan, 87317-51167 Kashan, I. R. Iran  
e-mail: f.k.moftakhar@gmail.com

A. R. Ashrafi  
e-mail: alir.ashrafi@gmail.com

O. Ori  
Actinium Chemical Research, Via Casilina 1626/A, 00133 Rome, Italy  
e-mail: ottorino.ori@gmail.com

O. Ori · M. V. Putz  
Laboratory of Computational and Structural Physical-Chemistry for Nanosciences  
and QSAR, Department of Biology-Chemistry, West University of Timișoara,  
Pestalozzi Str. No. 16, Timișoara 300115, Romania

M. V. Putz  
e-mail: mv\_putz@yahoo.com

the molecule to have a pi network and therefore all molecular graphs should have max degree 3 or less—a vertex of degree 4 represents a saturated carbon atom that cannot be part of a pi system and which is typical of diamond-like bulk structures. The max degree 4 also holds for alkanes, which are not included in the present research.

Being this chapter devoted to the investigation of the structural and topological properties of some families of nanostructures, a few formal tools have to be shortly introduced here starting with a simple recap of the concept of *group*.

A *group* is a mathematical structure that is usually used to describe the symmetries characterizing a given set of mathematical objects. It is a set of elements  $G$  equipped with a binary operation of multiplication  $*$ :  $G \times G \rightarrow G$  such that:

- i) it is associative, e.g. for all  $x, y, z \in G$ ,  $x * (y * z) = (x * y) * z$ ;
- ii) there exists an element  $e \in G$  such that for an arbitrary element  $g$  in  $G$ ,  $g * e = e * g = g$ ;
- iii) and, for each  $x \in G$  there exists  $y \in G$  such that  $x * y = y * x = e$ .

A group is then called *finite* if the underlying set  $G$  is *finite*. The *symmetry* structure of  $G$  can be formalized by the notion of *finite group action*. To describe it, we assume  $G$  is a group and  $X$  is a set. We also assume that there is a map  $\phi : G \times X \rightarrow X$  with the following two properties:

- a. for each  $x \in X$ ,  $\phi(e, x) = x$ ,
- b. and, for all elements  $x \in X$  and  $g, h \in G$ ,  $\phi(g, \phi(h, x)) = \phi(gh, x)$ .

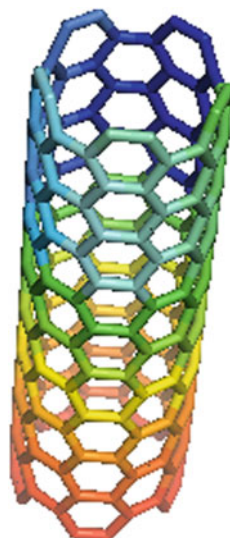
In this case,  $G$  and  $X$  are called a *transformation group* and a *G-set*, respectively. The mapping  $\phi$  is called a *group action*. For simplicity it is convenient to define  $gx = \phi(g, x)$ .

Suppose now  $G$  is a group and  $H$  is a non-empty subset of  $G$ .  $H$  is said to be a *subgroup* of  $G$ , if  $H$  is closed under group multiplication. A subgroup  $H$  of  $G$  is called to be *normal* in  $G$ , if for all  $g \in G$  we have  $g^{-1}Hg = H$ . When both  $H$  and  $K$  are subgroups of  $G$  such that  $H$  is normal in  $G$ ,  $H \cap K = 1$ , and  $G = HK$ , then  $G$  is called a semi-direct product of  $H$  by  $K$ . Here,  $HK$  is the set of all elements of  $G$  in the form of  $xy$  such that  $x \in H$  and  $y \in K$ .

An *automorphism* of  $G$  is a permutation  $g$  of  $V(G)$  such that  $g(u)$  and  $g(v)$  are adjacent if and only if  $u$  and  $v$  are adjacent, where  $u, v \in V(G)$ . It is well-known that the set of all automorphisms of  $G$ , with the operation of composition of permutations, is a permutation group on  $V(G)$ , denoted  $Aut(G)$ . The name *topological symmetry* is also used for this algebraic structure. Randić (1974, 1976) showed that a graph can be depicted in different ways such that its point group symmetry or even the 3D representation may differ, but its automorphism group symmetry remains the same. The *topological symmetry* of a molecular graph is not usually the same as its point group symmetry but it corresponds to the maximal symmetry the geometrical realization of a given topological structure may possess. This very important topological feature will play an instrumental role in the present investigations.

Computationally, several software packages are may be sourced on line for solving computational problems related to finite groups. GAP is an abbreviation for Groups,

**Fig. 6.1** The molecular graph of an armchair  $[p, 10]$  nanotube



Algorithms and Programming (The GAP Team 1995). Since all symmetry elements of a physical object is a group under composition of functions, the package is useful for this topic. Our calculations are based however on three other packages. These are *HyperChem* (HyperChem package Release 7.5 for Windows 2002), *TopoCluj* (Diudea et al. 2002) and *MAGMA* (Bosma et al. 1997).

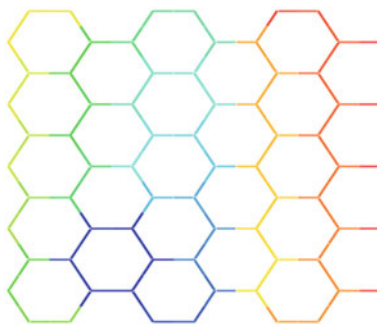
Calculations reported in this paper are done by using a combination of these packages. We first draw a nanotube or nanotorus by HyperChem. Then we will compute the adjacency matrix by TopoCluj. We then apply MAGMA and GAP for computing symmetry group. All notations are standard and taken from the standard book of group theory. We encourage to reader to consult the celebrated book of Trinajstić (1992) for more information on symmetry.

## 6.2 Nanotubes and Nanotori Topological Indices

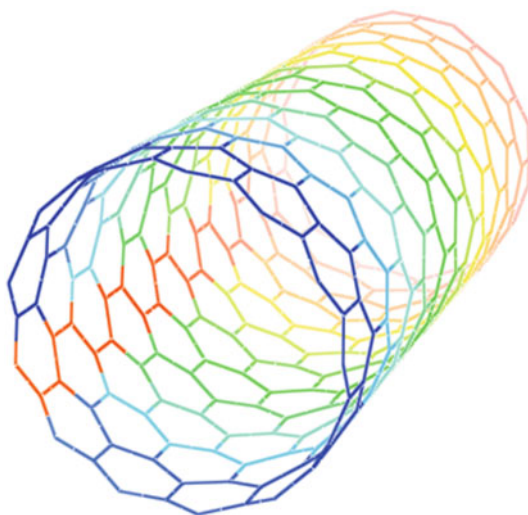
A *carbon nanotube* is a new allotrope of carbon with a tubular structure at the nanoscale. The molecular graphs of *armchair* and *zig-zag polyhex nanotubes* are depicted in Figs. 6.1 and 6.2, respectively. We associate two parameters  $[r, s]$  to each armchair and zig-zag polyhex nanotube as follows. In an armchair nanotube, Figs. 6.1 and 6.2, the parameter  $s$  denotes the number of vertical zig-zags, while in a zig-zag nanotube, Figs. 6.3 and 6.4,  $s$  denotes the number of horizontal zig-zags. On the other hand, the parameter  $r$  in an armchair polyhex is the number of rows and in a zig-zag nanotube it returns the number of hexagons in each row.

A  $C_4C_8$  net is a trivalent (atom degree 3) decoration made by *alternating* squares  $C_4$  and octagons  $C_8$ . Such a plane covering can be derived from square net by the

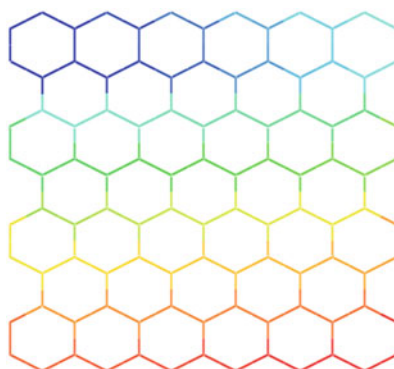
**Fig. 6.2** The 2D lattice of an armchair [11, 6] nanotube



**Fig. 6.3** The molecular graph of a zig-zag [13, 13] nanotube



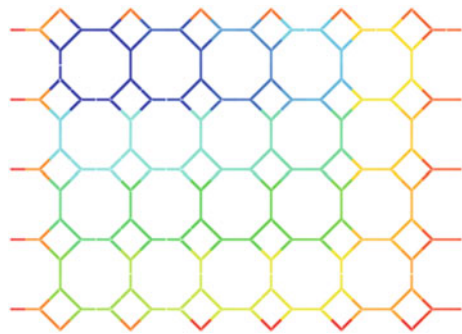
**Fig. 6.4** The 2D lattice of a zig-zag [6, 8] nanotube



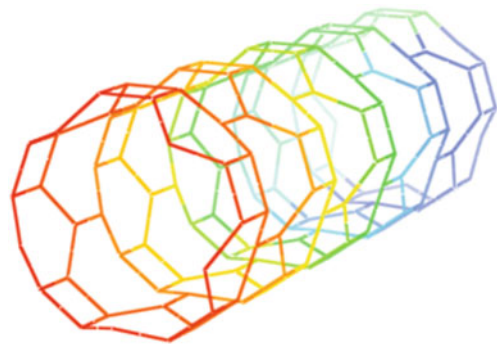
**Fig. 6.5** The molecular graph of a  $C_4C_8(R)$  nanotube



**Fig. 6.6** The 2D lattice of a  $C_4C_8(R)$  nanotube



**Fig. 6.7** The molecular graph of a  $C_4C_8(S)$  nanotube

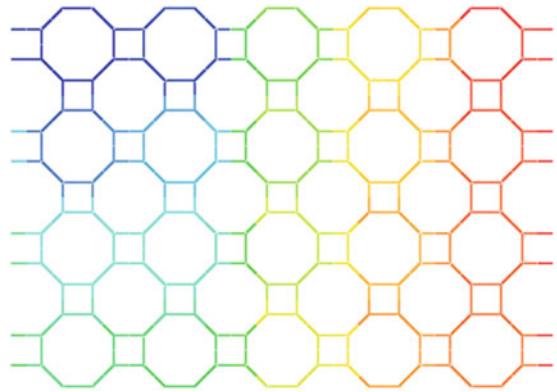


leapfrog operation, Figs. 6.5 and 6.6. A  $C_4C_8(R)$  nanotube is another beautiful mathematical object constructed by squares and octagons. An charming example is shown in Figs. 6.7 and 6.8. A *carbon nanotorus* is geometrically obtained by connecting the two ends of a carbon nanotube into a ring, Figs. 6.9, 6.10, 6.11 and 6.12.

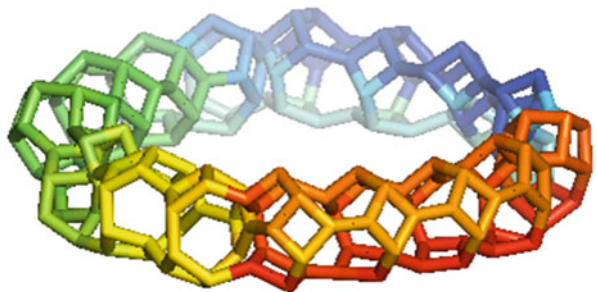
The symmetry properties of these nanostructures are one of the main subject of this study.

Suppose  $(G, \cdot_1)$  and  $(H, \cdot_2)$  are groups. The *cartesian product*  $G \times H$  is the set of all *ordered pairs*  $(a, b)$  where  $a \in G$  and  $b \in H$ , together with the following group

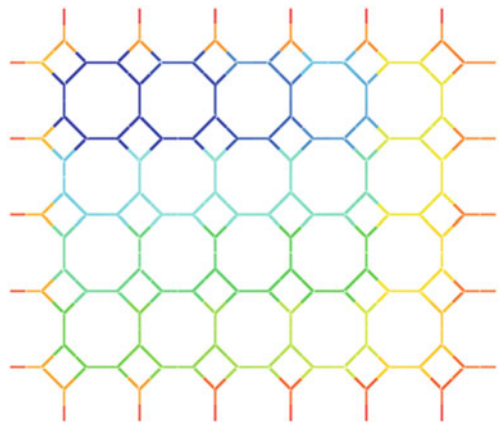
**Fig. 6.8** The 2D lattice of  $C_4C_8(S)$  nanotube



**Fig. 6.9** The molecular graph of a  $C_4C_8(R)$  nanotorus



**Fig. 6.10** The 2D Lattice of  $C_4C_8(R)$  Nanotorus



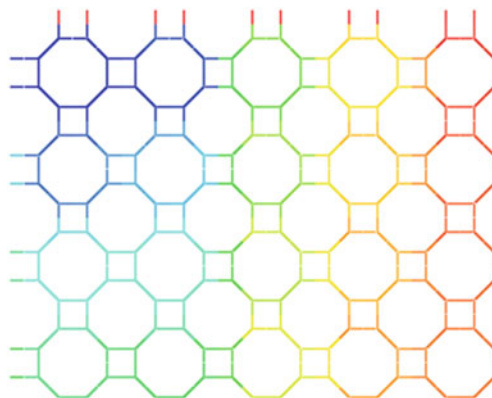
structure:

$$(a, b) * (x, y) = (a \cdot_1 x, b \cdot_2 y) \tag{6.1}$$

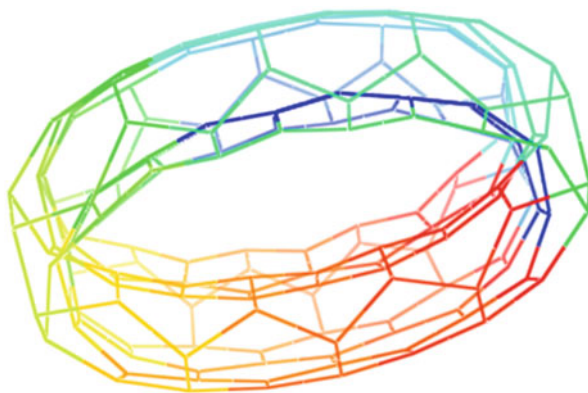
The concept of *semi-direct product* is a generalization of cartesian product. In the cartesian product of two groups, each component represents in fact a normal



**Fig. 6.11** The 2D lattice of  $C_4C_8(S)$  nanotorus



**Fig. 6.12** The molecular graph of a polyhex nanotorus



subgroup, their intersection is trivial and the components generate the whole group. In the *semi-direct product* instead we admit one of the subgroup to be non-normal. In mathematical exact phrasing: *in semi-direct product a group can be constructed from two subgroups, one of which is a normal subgroup, the intersection of two subgroups is trivial and they generate the group.*

It is easy to see that if  $N$  and  $H$  are groups and  $\varphi$  is a homomorphism of  $H$  into the automorphism group of  $N$  then the set  $N \times H$  by operation  $(n_1, h_1) \cdot (n_2, h_2) = (n_1 \varphi_{h_1}(n_2), h_1 h_2)$ ,  $n_1, n_2 \in N$  and  $h_1, h_2 \in H$ , has a group structure. This group is denoted by  $N \times_{\varphi} H$  and called the *semi-direct product* of  $N$  by  $H$ .

A *graph invariant* is a quantity that is *invariant under all graph automorphisms*. The *topological indices* are numerical *graph invariants* used in theoretical chemistry to encode molecules for the classification and design of chemical compounds with given physico-chemical properties or given pharmacological and biological activities (Trinajstić 1992) (MIHAI). Notice that the bond relations between atoms do not fully determine the molecular geometry and so, in general, topological indices cannot uniquely determine a chemical compound, but they are usually useful to obtain information on some physico-chemical properties of compounds.

We now recall some algebraic definitions used here. Suppose  $G$  is a simple graph and  $\{u, v\} \subseteq V(G)$ . A *path* connecting  $u$  and  $v$  in  $G$  is a sequence:

$$u = u_0, e_1, u_1, e_2, \dots, e_n, u_n = v \quad (6.2)$$

of distinct vertices  $u_1, \dots, u_n$  and distinct edges  $e_1, \dots, e_n$  such that  $e_i$  is an edge with end vertices  $u_{i-1}$  and  $u_i$ . The *distance*  $d(u, v)$  is defined to be the length of a minimal path connecting  $u$  and  $v$ . The half-summation of all distances between pairs of vertices in  $G$  is called the *Wiener index* of  $G$  which is denoted by  $W(G)$ . The Wiener index has been the first distance-based graph invariant and it was introduced by an American chemist Harold Wiener (1947). Suppose  $e = uv$  individuates an edge in  $G$ . Define quantities  $m_u(e)$  and  $m_v(e)$  as follows:  $m_u(e)$  is defined as the number of edges lying closer to the vertex  $u$  than the vertex  $v$ , and  $m_v(e)$  is defined analogously. The edges equidistant from both ends of the edge  $uv$  are not counted. In a similar way, we define  $n_u(e)$  to be the number of vertices lying closer to the vertex  $u$  than  $v$ . The *PI index* (Khadikar et al. 2001) of  $G$  is defined as

$$PI(G) = \sum_{e=uv} [m_u(e) + m_v(e)] \quad (6.3)$$

For acyclic molecular graphs  $G$ , Wiener discovered a remarkably simple algorithm for computing  $W(G)$ . To explain his method, we assume that  $e = ij$  is an edge of  $G$ ,  $N(i)$  is the number of vertices of  $G$  lying closer to  $i$  than to  $j$  and  $N(j)$  is defined analogously. Thus,

$$\begin{aligned} N(i) &= |\{u \in V(G) | d(u, i) < d(u, j)\}| \quad \text{and} \\ N(j) &= |\{u \in V(G) | d(u, j) < d(u, i)\}| \end{aligned} \quad (6.4)$$

Then the *Szeged index* of  $G$  is defined as the half-summation of all products  $N(i)N(j)$  over all graph edges  $e = ij$ . This generalization was conceived by Ivan Gutman (1994) at the Attila Jozsef University in Szeged, and so it was called the Szeged index. It is useful to mention here that Gutman in his 1994 paper proposed the existence of the cyclic index and abbreviated it by  $W^*$ . In that paper he has not given any name to this index. Khadikar et al. (1995) used the name ‘‘Szeged index’’ and abbreviated as Sz. According to a long-known result in the theory of graph distances, if  $G$  is a tree then  $Sz(G) = W(G)$ , reproducing Wiener’s original method.

Klavžar et al. (1996) proved that for every connected graph  $G$  we have  $W(G) \leq Sz(G)$ . So it is natural to ask about equality of these graph invariants. To find a characterization of graphs satisfy the equality, we need some notation. A maximal 2-connected subgraph of a connected graph  $G$  is called a *block* of  $G$ . The block graphs are those in which every block is a clique. Dobrynin and Gutman (1995) investigated the structure of a connected graph  $G$  featuring the property that  $Sz(G) = W(G)$ . They proved that  $Sz(G) = W(G)$  if and only if  $G$  is a block graph (Dobrynin et al. 1995). A new proof for this result is recently published (Khodashenas et al. 2011).

The Wiener, PI and Szeged indices are all distance based invariants of a graph. There are some other graph invariants based on degree sequence of the molecular

graph under consideration. The first such invariants are *Zagreb group indices*. The Zagreb indices have been introduced more than forty years ago by Gutman and Trinajstić (1972). They are defined as:

$$M_1(G) = \sum_{v \in V(G)} \text{deg}(v)^2 \quad \text{and} \quad M_2(G) = \sum_{uv \in E(G)} \text{deg}(u) \times \text{deg}(v) \quad (6.5)$$

where  $\text{deg}(u)$  is the degree of the vertex  $u$  of  $G$ . A historical background, computational techniques and mathematical properties of Zagreb indices can be found in papers (Gutman and Das 2004; Khalifeh et al. 2009; Zhou 2004; Zhou and Gutman 2005).

The *Randić molecular connectivity index*, Randić index for short, is a second degree-based topological invariant, introduced in (Randić 1975). It is defined as:

$$\chi(G) = \sum_{uv \in E(G)} (\text{deg}(u) \text{deg}(v))^{-1/2}. \quad (6.6)$$

It reflects molecular branching and has several applications in chemistry (Klarner 1997).

The *atom-bond connectivity (ABC) index* is another degree-based topological index introduced by Estrada et al. 1998 to study the stability of alkanes and the strain energy of cycloalkanes. This index is defined as follows:

$$ABC(G) = \sum_{uv \in E(G)} \sqrt{\frac{\text{deg}(u) + \text{deg}(v) - 2}{\text{deg}(u) + \text{deg}(v)}}. \quad (6.7)$$

Estrada (2008) presented a new topological approach which provides a good model for the stability of linear and branched alkanes as well as the strain energy of cycloalkanes. He also reported that the heat of formation of alkanes can be obtained as a combination of stabilizing effects coming from atoms, bonds and protobranches. Furtula et al. (2009) studied the mathematical properties of the ABC index of trees. They found chemical trees with extremal ABC values and proved that, among all trees, the star tree  $S_n$ , has the maximal ABC index. Das (2010) presented the lower and upper bounds on ABC index of graphs and trees, and characterize graphs for which these bounds are best possible. Fath-Tabar et al. (2011) obtained some inequalities for the atom-bond connectivity index of a series of graph operations and proved that the bounds are tight. They applied their result to compute the ABC indices of  $C_4$  nanotubes and nanotori.

The relationship between degree-based topological indices of graphs is an important problem in chemical graph theory. Das and Trinajstić (2010) compared the GA and ABC indices for chemical trees and molecular graphs and proved some results.

The *Balaban index* of a molecular graph  $G$  is defined by Balaban (1982, 1983) as:

$$j(G) = m / (\mu + 1) \sum_{e=uv} [d(u)d(v)]^{-0.5} \quad (6.8)$$

where  $m$  is the number of edges of  $G$ ,  $\mu(G) = |E(G)| - |V(G)| + 1$  is the cyclomatic number of  $G$  and for every vertex  $x$ ,  $d(x)$  is the summation of topological distances between  $x$  and all vertices of  $G$ .

In the end of this section the concept of *eccentric connectivity index* of molecular graphs is presented. Let  $G$  be a molecular graph (Sharma et al. 1997; Sardana and Madan 2001). The eccentric connectivity index  $\xi(G)$  is defined as:

$$\xi(G) = \sum_{u \in V(G)} \deg_G(u) \varepsilon_G(u) \quad (6.9)$$

where  $\deg_G(u)$  denotes the degree of vertex  $u$  and  $\varepsilon_G(u)$  is the largest distance between  $u$  and any other vertex  $v$  of the graph  $G$ .

### 6.3 Symmetry Considerations on Nanotubes and Nanotori

A *dihedral group* is the group of symmetries of a regular polygon, including both rotations and reflections. These groups play an important role in chemistry. Most of point group symmetry of molecules can be described by dihedral groups. It is easy to prove that a group generated by two involutions on a finite domain is a dihedral group. A dihedral group with  $2n$  symmetry elements is denoted by  $D_n$ . This group can be presented as follows:

$$D_n = \{x, y | x^n = y^2 = (xy)^2 = 1\} \quad (6.10)$$

We now consider the molecular graph of a zig-zag and armchair (achiral) polyhex nanotorus. Yavari and Ashrafi (2009) proved in some special cases that the symmetry group of armchair and zig-zag polyhex nanotorus is constructed from a dihedral group and a plane symmetry group of order 2.

Arezoomand and Taeri (2009) presented a generalization of this result. They proved that:

**Theorem 1 (Arezoomand and Taeri)** The symmetry group of the molecular graph of a zig-zag and armchair (achiral) polyhex nanotorus is isomorphic to  $D_{4m} \times Z_2$ , where  $Z_2$  denotes the cyclic group of order 2.

*Hypergraphs* are generalizations of graphs in which an edge can connect more than two vertices. In the graph theoretical language, a hypergraph consists of a set of vertices  $V$  and a set of hyper-edges  $E$  which is a collection of subsets in  $V$  in such a way that the union of hyper-edges are the whole vertices. A *k-hypergraph* is a hypergraph with the property that any edge connects exactly  $k$  vertices. The case of  $k = 2$  corresponds to the usual graphs considered so far. The best generalization of the mentioned result was introduced by Staic and Petrescu-Nita (2013). They studied the symmetry group of two special types of carbon nanotori by using the notion of *Cayley hypergraph*. To explain this concept, we assume that  $G$  is a group and  $S$  is a non-empty subset of  $G$  such that  $S = S^{-1}$  and  $G = \langle S \rangle$ . We define a graph  $\text{Cay}(G, S)$  as follows: (i)  $V(\text{Cay}(G, S)) = G$ , and, (ii) two vertices  $a$  and  $y$  are adjacent if and only if  $xy^{-1} \in S$ . The graph  $\text{Cay}(G, S)$  is called the *Cayley graph* of  $G$  constructed by  $S$ . If  $G$  is a group and  $T$  is a generator set for  $G$  containing elements of order 3 such that  $a \in T$  implies that  $a^{-1} \notin T$  then 3-hypergraph  $\text{Cay}_3(G, T)$  can be defined

as follows: take the set of vertices to be  $G$ . A cyclically ordered 3-subset  $\{g_1, g_2, g_3\}$  is a hyper-edge if there exists  $a \in T$  such that  $g_2 = g_1 a$  and  $g_3 = g_1 a$ . The main result of Staica and A. Petrescu-Nita is as follows:

**Theorem 2 (Staic and Petrescu-Nita)** Suppose  $T_n$  is a group presented as follows:

$$T_n = \{a; b | a^3 = 1; b^3 = 1; (ab)^3 = 1; (ab^2)^n = 1\} \tag{6.11}$$

Then  $T_n$  is a semi-direct product of  $Z_n \times Z_n$  by  $Z_3$ . Moreover, the Cayley hypergraph associated with the group  $T_n$  can be placed on a torus.

If  $SL(2,3)$  denotes the set of all  $2 \times 2$  matrices over a field of order 3 then a Cayley hypergraph associated with this group can be placed on a torus.

We end this section by a result on the symmetry group of nanotubes. Suppose  $A[p, q]$ ,  $B[p, q]$ ,  $C(R)[p, q]$  and  $C(S)[p, q]$  are zig-zag polyhex, armchair polyhex,  $C_4C_8(R)$  and  $C_4C_8(S)$  nanotubes with parameters  $p$  and  $q$ , respectively.

**Theorem 3** The symmetry groups of  $A[p, q]$ ,  $B[p, q]$ ,  $C(R)[p, q]$  and  $C(S)[p, q]$  are computed as follows:

1.  $\text{Aut}(A[p, q]) = \begin{cases} D_{4p} & p \neq q \\ C_2 \times D_{2p} & p = q \end{cases}$ ,
2. If  $q$  is even and  $p \neq 3$  then  $\text{Aut}(B[p, q]) = \begin{cases} D_{2q} & p \text{ is even} \\ D_{2q} & \frac{q}{2} \text{ is odd} \\ C_2 \times D_q & \frac{q}{2} \text{ is even} \end{cases}$   $p \text{ is odd}$
3. If  $p \neq 2$  then  $\text{Aut}(C(R)[p, q]) \cong \text{Aut}(C(S)[p, q]) \cong Z_2 \times D_{2p}$ . Moreover, if  $p = 2$  then  $\text{Aut}(C(S)[2, 1]) \cong Z_2 \times D_8$  and  $\text{Aut}(C(S)[2, q]) = C_2 \times C_2 \times C_2$ , when  $q \neq 1$ .

Previous theorems clearly illustrate the power of topological methods in predicting geometrical properties of carbon nanostructures.

### 6.4 Topology of Nanotubes and Nanotori

The history of computing topological indices of nanotubes and nanotori started by publishing two paper by Diudea and his co-workers (Diudea et al. 2004; John and Diudea 2004) about Wiener index armchair and zig-zag polyhex nanotubes. After publishing these seminal papers, several scientists focus on computing such numbers for the molecular graphs of nanostructures. For the sake of completeness we record the mentioned results of Diudea and his co-workers in Theorem 4.

**Theorem 4** Suppose  $A = A[p, q]$  and  $B = B[p, q]$  are zig-zag and armchair polyhex nanotubes, respectively. Then the Wiener index of these nanotubes can be computed by the following formulas:

$$1) \quad W(A) = \begin{cases} \frac{qp^2}{24}(4q^2 + 3qp - 4) + \frac{q^2p}{12}(q^2 - 1) & q \leq \frac{p}{2} + 1 \\ \frac{qp^2}{24}(8q^2 + p^2 - 6) - \frac{p^3}{192}(p^2 - 4) & q > \frac{p}{2} + 1 \end{cases},$$

$$2) \quad W(B) = \begin{cases} \frac{p}{12}[p^2(12q^2 - 2p^2 + 8) + 8pq(p^2 + q^2 - 2) + 3(-1 + (-1)^p)] & q \geq p \\ \frac{p}{12}[24p^2q^2 + 2q^4 - 8q^2 + 3(-1)^p(1 - (-1)^q)] & q \leq p \end{cases}.$$

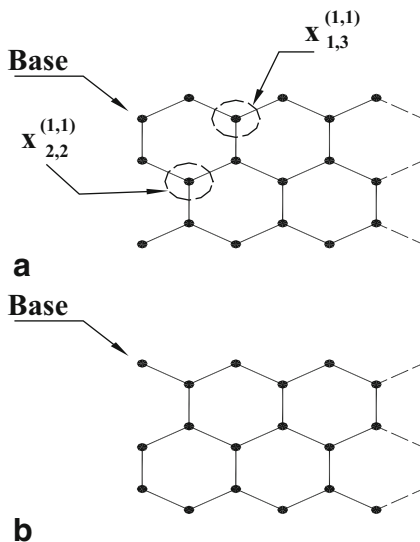
In a series of papers (Yousefi and Ashrafi 2006, 2007, 2008a, 2011; Yousefi et al. 2008c, d; Ashrafi and Yousefi 2007a, b) introduced a matrix method to recalculate the Wiener number of armchair, zig-zag polyhex nanotubes,  $C_4C_8(R/S)$  nanotube, polyhex nanotorus and  $C_4C_8(R/S)$  nanotorus. Choose a zig-zag polyhex nanotube  $T$ . The main idea of this matrix method is choosing a base vertex  $b$  from the 2-dimensional lattice of a  $T$  and then label vertices of hexagon by starting from the hexagon containing  $b$ . By computing distances between  $b$  and other vertices, we can obtain a distance matrix of nanotubes related to the vertex  $b$ . It is clear that by choosing different base vertices, one can find different distance matrices for  $T$ , but the summation of all entries will be the same. To explain, we assume that  $b$  is a base vertex from the 2-dimensional lattice of  $T$  and  $x_{ij}$  is the  $(i, j)^{\text{th}}$  vertex of  $T$ , Fig. 6.6. Define  $D_{m \times n}^{(1,1)} = [d_{ij}^{(1,1)}]$ , where  $d_{ij}^{(1,1)}$  is distance between  $(1,1)$  and  $(i, j)$ ,  $i = 1, 2, \dots, m$  and  $j = 1, 2, \dots, n$ . There are two separates cases for the  $(1,1)^{\text{th}}$  vertex, where in the first case  $d_{1,1}^{(1,1)} = 0, d_{1,2}^{(1,1)} = d_{2,1}^{(1,1)} = 1$  and in the second case  $d_{1,1}^{(1,1)} = 0, d_{1,2}^{(1,1)} = 1, d_{2,1}^{(1,1)} = 3$ . Suppose  $D_{m \times n}^{(p,q)}$  is distance matrix of  $T$  related to the vertex  $(p, q)$  and  $s_i^{(p,q)}$  is the sum of  $i^{\text{th}}$  row of  $D_{m \times n}^{(p,q)}$ . Then there are two distance matrix related to  $(p, q)$  such that  $s_i^{(p,2k-1)} = s_i^{(p,1)}$ ;  $s_i^{(p,2k)} = s_i^{(p,2)}$ ;  $1 \leq k \leq n/2$ ,  $1 \leq i \leq m$ ,  $1 \leq p \leq m$ . If  $b$  varies on a column of  $T$  then the sum of entries in the row containing base vertex is equal to the sum of entries in the first row of  $D_{m \times n}^{(1,1)}$ . On the other hand, one can compute the summation of all entries in other rows by distance from the position of base vertex. Therefore, if  $2 \mid (i + j)$  then

$$s_k^{(i,j)} = \begin{cases} s_{i-k+1}^{(1,1)} & 1 \leq k \leq i \leq m, \quad 1 \leq j \leq n \\ s_{k-i+1}^{(1,2)} & 1 \leq i \leq k \leq m, \quad 1 \leq j \leq n \end{cases}$$

and if  $2 \nmid (i + j)$  then we have  $s_k^{(i,j)} = \begin{cases} s_{i-k+1}^{(1,2)} & 1 \leq k \leq i \leq m, \quad 1 \leq j \leq n \\ s_{k-i+1}^{(1,1)} & 1 \leq i \leq k \leq m, \quad 1 \leq j \leq n \end{cases}$ .

We now describe our algorithm to compute distance matrix of a zig-zag polyhex nanotube. To do this, we define matrices  $A_{m \times (n/2+1)}^{(a)} = [a_{ij}]$ ,  $B_{m \times (n/2+1)} = [b_{ij}]$  and  $A_{m \times (n/2+1)}^{(b)} = [c_{ij}]$  as follows: (Fig. 6.13).

**Fig. 6.13** Two Basically Different Cases for the Vertex b



For computing distance matrix of this nanotube we must compute matrices  $D_{m \times n}^{(a)} = [d_{i,j}^a]$  and  $D_{m \times n}^{(b)} = [d_{i,j}^b]$ . By these calculations, one can see that

$$d_{i,j}^a = \begin{cases} \text{Max}\{a_{i,j}, b_{i,j}\} & 1 \leq j \leq n/2 \\ d_{i,n-j+2} & j > n/2 + 1 \end{cases} \text{ and } d_{i,j}^b = \begin{cases} \text{Max}\{a_{i,j}, c_{i,j}\} & 1 \leq j \leq n/2 \\ d_{i,n-j+2} & j > n/2 + 1 \end{cases}$$

By continuing this method, the mentioned authors proved that:

**Theorem 5** Suppose A and B are an armchair and zig-zag polyhex nanotube, respectively, with exactly m rows and n columns, Fig. 6.2. Moreover, we assume that C is a polyhex nanotorus with similar parameters. Then,

1. (Yousefi and Ashrafi 2007)

$$W(A) = \begin{cases} \frac{m^2 n}{12} (3n^2 + m^2 - 4) + \frac{n}{8} (-1)^{\frac{n}{2}} [1 - (-1)^n] & m \leq \frac{n}{2} + 1 \\ \frac{mn^2}{24} (n^2 + 4m^2 + 3mn - 8) - \frac{n^3}{192} (n^2 - 16) + \frac{n}{8} \left[ (-1)^{\frac{n}{2}} - 1 \right] & m > \frac{n}{2} + 1 \end{cases}$$

2. (Ashrafi and Yousefi 2007a)

$$W(B) = \begin{cases} \frac{mn^2}{24} (4m^2 + 3mn - 4) + \frac{m^2 n}{12} (m^2 - 1) & m \leq \frac{n}{2} + 1 \\ \frac{mn^2}{24} (8m^2 + n^2 - 6) - \frac{n^3}{192} (n^2 - 4) & m > \frac{n}{2} + 1 \end{cases}$$

3. Yousefi-Azari et al. (2008e)

$$W(C) = \begin{cases} \frac{pq^2}{24}(6p^2 + q^2 - 4) & q < p \\ \frac{p^2q}{24}(3q^2 + 3pq + p^2 - 4) & q \geq p \end{cases}$$

Suppose  $E = TUC_4C_8(R)[m, n]$ ,  $F = TUC_4C_8(S)[m, n]$  are two different types of  $C_4C_8$  nanotubes and  $G = TC_4C_8(R)[m, n]$  is a  $C_4C_8$  nanotorus in terms of the number of rhombs in a fixed row ( $m$ ) and column ( $n$ ). We have

**Theorem 6** The Wiener indices of  $E, F, G$  and  $H$  can be computed as follows:

1. (Yousefi and Ashrafi 2006)

$$W(E) = \begin{cases} \frac{2m}{3}(m^2 - 1) + mn(m + 3n) - k_1 & m < n \\ \frac{2n}{3}(n^2 - 1) + mn(3m + n) - k_2 & m > n \\ \frac{n}{3}(14n^2 - k_3) & m = n \end{cases}$$

$$\text{in which } k_1 = \begin{cases} 0 & 2|n \ \& \ 2|m \\ n - m & 2|n \ \& \ 2 \nmid m \\ m & 2 \nmid n \ \& \ 2|m \\ n & 2 \nmid n \ \& \ 2 \nmid m \end{cases} \quad k_2 = \begin{cases} 0 & 2|m \\ m & 2 \nmid m \end{cases} \quad k_3 = \begin{cases} 2 & 2|n \\ 5 & 2 \nmid n \end{cases}$$

2. (Ashrafi and Yousefi 2007b)

$$W(F) = \begin{cases} \frac{nm^2}{6}(6m^2 + 3nm + n^2 - 4) & n \leq m \\ \frac{mn^2}{6}(6n^2 + 3mn + m^2 - 4) & m < n \end{cases}$$

3. (Yousefi and Ashraf 2008b, 2011)

$$W(G) = \begin{cases} \frac{2mn^2}{3}(4m^2 + 9mn - 4) + \frac{m^2n}{6}[16m^2 - 7 + 3(-1)^n] & m \leq \frac{n+1}{2} \\ \frac{2mn^2}{3}(12m^2 + 3mn + 2n^2 - 5) - \frac{n^3}{6}(n^2 - 1) & \\ -\frac{n}{8}(8m^2 + n^2 - 4mn - 1)[1 - (-1)^n] & m > \frac{n+1}{2} \end{cases}$$

Suppose  $e = uv$  and  $M(e)$  denotes the number of edges that are equidistant to the vertices  $u$  and  $v$  (including the edge  $e$  itself), then evidently  $m_u(e) + m_v(e) + M(e) = m$ .



Therefore,  $PI(G) = m^2 - \sum_{e=uv} M(e)$ . Using this simple equation, it can be proved that if  $G$  is an acyclic graph containing  $n$  vertices then  $PI(G) = (n - 1)(n - 2)$ . In particular,  $PI = 0$ , for acyclic graphs when  $n = 1$  and  $2$ . Since every acyclic graph with  $n$  vertices has exactly  $m = n - 1$  edges, the previous result states that in every acyclic graph  $G$  with  $m$  edges  $PI(G) = m(m - 1)$ .

The notion of **PI partition** was introduced by Klavžar (2007) to find a formula for the PI index of product graphs. Suppose  $G$  is a graph and  $X$  is a subset of  $V(G)$ . The subgraph of  $G$  induced by  $X$  will be denoted  $\langle X \rangle$ . Moreover, let  $\partial X$  stands for the set of edges of  $G$  with one end vertex in  $X$  and the other not in  $X$ . For an edge  $e = uv$  of  $G$ , we define  $V_1(e)$  and  $V_2(e)$  as follows:

$$V_1(e) = \{x \in V(G) \mid d(x,u) < d(x,v)\} \text{ and } V_2(e) = \{x \in V(G) \mid d(x,u) > d(x,v)\}.$$

It is easily seen that if  $G$  is bipartite then for any edge  $e$  of  $G$ ,  $V_1(e)$  and  $V_2(e)$  form a partition of  $V(G)$ . We say that a partition  $E_1, \dots, E_k$  of  $E(G)$  is a PI-partition of  $G$  if for any  $i, 1 \leq i \leq k$ , and for any  $e, f \in E_i$  we have  $V_1(e) = V_1(f)$  and  $V_2(e) = V_2(f)$ . If  $e = uv$  is an edge a  $G$  then we define  $V_3(e)$  to be the set of all vertices that are at equal distance from  $u$  and  $v$ . Thus  $V(G) = V_1(e) \cup V_2(e) \cup V_3(e)$ . Klavžar (2007) proved that if  $E_1, \dots, E_k$  is a PI-partition of a graph  $G$  then  $PI(G) = |E(G)|^2 - \sum_{i=1}^k |E_i|(|E_i| + |E(\langle V_3(e) \rangle)| + |\partial V_3(e)|)$ . If  $G$  is bipartite then  $\partial V_3(e) = V_3(e) = \emptyset$ ; and consequently  $PI(G) = |E(G)|^2 - \sum_{i=1}^k |E_i|^2$ .

Using the mentioned method of Klavžar or a straightforward calculation by the mentioned simple equation, one can prove the following two results:

**Theorem 7** The PI index of armchair polyhex, zig-zag polyhex and polyhex nanotorus nanotubes can be computed as follows:

1. (Ashrafi and Loghman 2006a)

$$PI(B[2p, q]) = \begin{cases} \begin{cases} X - p & q \leq p + 1 \\ Y - p & q \geq p + 1 \end{cases} & 2|p \ \& \ 2|q - 1 \\ \begin{cases} X & q \leq p + 1 \\ Y & q \geq p + 1 \end{cases} & \text{Otherwise} \end{cases},$$

where  $X = 9p^2q^2 - 12p^2q - 5pq^2 + 8pq + 4p^2 - 4p$  and  $Y = 9p^2q^2 - 20p^2q - p^2 + 4pq + 4p^3 + 8p^2 - 4p$ .

2. (Ashrafi and Loghman 2006b)

$$PI(A[2p, q]) = \begin{cases} p^2(9q^2 - 7q + 2) - 4pq^2 & q \leq p \\ p^2(9q^2 - 15q + 4p - 2) + 4pq & q \geq p \end{cases}.$$

3. (Ashrafi and Rezaei 2007)

$$PI(C) = \begin{cases} 9p^2q^2 - pq^2 - 12p^2q + 4pq & q \geq 2p \\ 9p^2q^2 - 7pq^2 + 4pq & q < 2p \end{cases}$$

**Theorem 8** The PI index of  $TUC_4C_8(R/S)$  nanotubes and  $TC_4C_8(R/S)$  nanotori can be computed as follows:

1. (Ashrafi and Loghman 2008)

$$PI(E[p,q]) = \begin{cases} \begin{cases} 36p^2q^2 - 26pq^2 - 2p^2q + 8pq & q < p \\ 36p^2q^2 - 26p^2q - 2pq^2 + 8pq & q \geq p \end{cases} & \text{if } p \ \& \ q \text{ are even} \\ \begin{cases} 36p^2q^2 - 10pq^2 - 2p^2q & q < p \\ 36p^2q^2 - 10p^2q - 2pq^2 & q \geq p \end{cases} & \text{if } p \ \& \ q \text{ are odd} \\ \begin{cases} 36p^2q^2 - 18pq^2 - 2p^2q & q < p \\ 36p^2q^2 - 18p^2q - 2pq^2 + 8pq & q > p \end{cases} & \text{if } p \text{ is even } \ \& \ q \text{ is odd} \\ \begin{cases} 36p^2q^2 - 18p^2q - 2pq^2 & q > p \\ 36p^2q^2 - 18pq^2 - 2p^2q + 8pq & q < p \end{cases} & \text{if } p \text{ is odd } \ \& \ q \text{ is even} \end{cases}$$

2. (Ashrafi and Loghman 2006c)

$$PI(F[4p, q]) = \begin{cases} X & q \leq p \\ Y & q \geq p \end{cases},$$

where  $X = 36p^2q^2 - 28p^2q + 8p^2 - 8pq^2$  and  $Y = 36p^2q^2 - 36p^2q - 4pq^2 + 4pq + 4p^3 + 4p^2$ .

3. (Ashrafi et al. 2009)

$$PI(G[p, q]) = \begin{cases} 36p^2q^2 - 8p^2q - 10pq^2 + 4pq & q \leq 2p \\ 36p^2q^2 - 20p^2q - 4pq^2 + 4pq & q > 2p \end{cases}.$$

We are now ready to investigate the Szeged index of nanotubes and nanotori. Dobrynin and Gutman (1994) proved that if  $G$  is a connected bipartite graph with  $n$  vertices and  $m$  edges, then  $Sz(G) = \frac{1}{4} \left( n^2m - \sum_{e \in E(G)} (d(u) - d(v))^2 \right)$ . Using this result Yousefi et al. (2008d) proved that the Szeged index of a polyhex nanotorus is computed by  $Sz(C) = \frac{3}{8}p^3q^3$ . Another application of the mentioned result

of Dobrynin and Gutman is computing Szeged index of  $C_4C_8(S)$  nanotubes. In (Heydari and Taeri 2009) and (Manoochehrian et al. 2008) the Szeged index of  $TUC_4C_8(S)[p, q]$  and zig-zag polyhex nanotubes are computed as follows:

**Theorem 9** Suppose  $F$  denotes the  $TUC_4C_8(S)[p, q]$  nanotube. Then

1. If  $q \leq p$ , then the Szeged index of  $F$  is given by the following formula:

$$Sz(F) = \frac{pq}{3}(-2q^4 + (64p^2 + 2)q^2 - 16p^2).$$

2. If  $q > p$ , then Szeged index of long  $TUC_4C_8(S)$  nanotubes is given by

$$Sz(F) = \begin{cases} \frac{p}{15} (12p^5 - 80qp^4 + (160q^2 - 20)p^3 + 200q^3p^2 \\ + (20q^4 - 60q^2 + 8)p - 2q(q^4 - 5q^2 + 4)) & q \leq 2p \\ \frac{p^2}{15} (-52p^4 + 80qp^3 + 60p^2 + (280q^3 - 120q)p - 8) & q > 2p \end{cases} .$$

3. The Szeged index of zig-zag polyhex nanotube is as follows.

$$Sz(A[p, q]) = \begin{cases} \frac{8}{3}p^3q^3 - \frac{2}{3}p^3q + \frac{1}{6}pq^3 - \frac{1}{6}pq^5 & q \leq p \\ \frac{5}{2}p^6 + \frac{43}{6}p^5 + \frac{35}{6}p^4 + \frac{5}{6}p^3 - \frac{1}{3}p^2 & q = p + 1 \\ \frac{2}{3}p^3q^3 + \frac{2}{3}p^3q - \frac{2}{15}pq + \frac{2}{15}p^2 - \frac{1}{5}pq^5 + \frac{4}{3}p^2q^4 & \\ -\frac{5}{3}pq^3 + \frac{8}{3}p^2q^2 - \frac{1}{3}p^4 - \frac{4}{3}p^5q + \frac{1}{5}p^6 & p + 1 < q < 2p \\ \frac{89}{5}p^6 - \frac{5}{3}p^4 - \frac{1}{15}p^2 & q = 2p \\ 2p^3q^3 - \frac{4}{3}p^3q - \frac{2}{15}p^2 + \frac{4}{3}p^5q - \frac{13}{15}p^6 + p^4 & q > 2p \end{cases} .$$

Recently, (Farahani 2012) computed some degree-based topological indices of zig-zag and armchair polyhex nanotubes. His calculations shows that  $\chi(A[m, n]) = mn + 2m \left(\frac{\sqrt{6}-1}{3}\right)$ ,  $ABC(A[m, n]) = 2mn + 2m \left(\sqrt{2} - \frac{2}{3}\right)$ ,  $M_1(A[m, n]) = 18mn + 8$ ,  $M_2(A[m, n]) = 27mn + 6$ ,  $\chi(B[m, n]) = \left(n + \frac{\sqrt{6}-1}{3} + \frac{1}{2}\right)m$ ,  $ABC(B[m, n]) = \left(2n + \frac{3\sqrt{2}}{2} - \frac{2}{3}\right)m$ ,  $M_1(B[m, n]) = 18mn + 8$  and  $M_2(B[m, n]) = 27mn + 7m$ . Moreover, (Asadpour et al. 2011) proved that  $\chi(E[p, q]) = 4pq$ ,  $M_2(E[p, q]) = 108pq$ ,  $ABC(E[p, q]) = \frac{12\sqrt{2}}{\sqrt{3}}pq$ ,  $\chi(F[p, q]) = 6pq + \left(\frac{4}{\sqrt{6}} - 3\right)(p + q) + 4 - \frac{2}{\sqrt{6}}$ ,  $M_2(F[p, q]) = 16(3pq + p + q - 1)$  and  $ABC(F[p, q]) = \sqrt{2}(8pq - 3p - 3q + 4) + 4\sqrt{\frac{3}{5}}(p + q - 2)$ .

The Balaban index  $J$  which is defined as the average distance sum connectivity is the least degenerate single topological index proposed till now. The mathematical properties of this distance-based topological index in the classes of polyhex and  $TUC_4C_8(R/S)$  nanotori are investigated by (Iranmanesh and Ashrafi 2007). They proved that:

**Theorem 10** Suppose  $C[m, n]$ ,  $E[m, n]$  and  $F[m, n]$  are polyhex and  $TUC_4C_8(R/S)$  nanotori, respectively. Then,

$$a) \quad J(C[m, n]) = \begin{cases} \frac{12m^2n}{(mn + 4)(6m^2 + n^2 - 4)} & n < m \\ \frac{12mn^2}{(mn + 4)(3n^2 + 3mn + m^2 - 4)} & n \geq m \end{cases},$$

$$b) \quad J(E[m, n]) = \begin{cases} \frac{108m^3n^3}{(mn + 1)[2m(m^2 - 1) + 3mn(m + 3n) - 3k_1]} & m < n \\ \frac{108m^3n^3}{(mn + 1)[2n(n^2 - 1) + 3mn(3m + n) - 3k_2]} & m > n \\ \frac{108m^2n^3}{(n^2 + 1)(14n^2 - k_3)} & m = n \end{cases},$$

in which

$$k_1 = \begin{cases} 0 & \text{if } 2|n \quad \& \quad 2|m \\ n - m & \text{if } 2|n \quad \& \quad 2 \nmid m \\ m & \text{if } 2 \nmid n \quad \& \quad 2|m \\ n & \text{if } 2 \nmid n \quad \& \quad 2 \nmid m \end{cases}, \quad k_2 = \begin{cases} 0 & \text{if } 2|m \\ m & \text{if } 2 \nmid m \end{cases}, \quad k_3 = \begin{cases} 2 & \text{if } 2|n \\ 5 & \text{if } 2 \nmid n \end{cases},$$

and, “|” denotes the divisibility relation.

$$c) \quad J(F[m, n]) = \begin{cases} \frac{54mn^2}{(mn + 2)(6n^2 + 3nm + m^2 - 4)} & n \leq m \\ \frac{54mn^2}{(mn + 2)(6m^2 + 3mn + n^2 - 4)} & m < n \end{cases}$$

In the end of this chapter we report two recent results in computing eccentric connectivity index of nanotubes and nanotori.

**Theorem 11** The eccentric connectivity index of armchair and zig-zag polyhex nanotubes are computed as follows:

1. (Saheli and Ashrafi 2010a) The eccentric connectivity index of a zig-zag polyhex nanotube is as follows:

$$\xi(A[p, q]) = \begin{cases} -\frac{7}{2}pq + p + \frac{9}{2}pq^2 & p \leq q + 1 \\ -\frac{1}{2}pq + p + \frac{21}{4}pq^2 - 3p^2 + \frac{3}{4}p^3 - \frac{3}{2}qp^2 & \\ + \frac{1 - (-1)^q}{2} 3p \left( p - q - \frac{1}{4} \right) & q + 1 < p < 2q . \\ -4pq - 2p^2 + \frac{7}{4}p + \frac{9}{4}pq^2 + \frac{3}{2}qp^2 & \\ + \frac{1 - (-1)^q}{2} 3p(p + q + 1) & p \geq 2q \end{cases}$$

2. (Saheli and Ashrafi 2010b) The eccentric connectivity index of an armchair polyhex nanotube with parameters p and q is as follows:

$$\xi(B[p, q]) = \begin{cases} q^2(3p - 2) & p \leq \frac{q}{2} + 1 \\ \frac{3}{4}q^3 + \frac{1}{2}q^2 + 2q - 5qp + 3qp^2 & \frac{q}{2} + 1 < p \leq q . \\ \frac{9}{4}qp^2 - \frac{7}{2}qp + \frac{3}{2}q^2p - q^2 + \frac{5}{4}q & p \geq q + 1 \end{cases}$$

**Theorem 12** The eccentric connectivity index of  $TUC_4C_8(R/S)$  nanotubes and nanotori can be computed as follows:

1. The eccentric connectivity index of  $E[p, q]$  is given by

$$\xi(E[p, q]) = \begin{cases} (p + 1)[(9q^2 + 18pq + 15p + 22q + 10) + R(p, q)] & q < \left\lceil \frac{p}{2} \right\rceil \\ (p + 1)[6p^2 - (6pq + 33q^2 + 5p + 42q + 14) + R(p, q)] & \left\lceil \frac{p}{2} \right\rceil \leq q < p , \\ (p + 1)[(27q^2 + 6pq + 5p + 42q + 14) + R(p, q)] & q \geq p \end{cases}$$

where  $R[p, q] = \left[ (6q + 5) \frac{1 - (-1)^p}{2} + 3 \frac{1 - (-1)^q}{2} \right]$ .

2. The eccentric connectivity index of  $F[p, q]$  is given by

$$\xi(F[p, q]) = \begin{cases} 22pq + 8p^2 + 12p^2q + 18pq^2 & p \leq \left\lceil \frac{q+1}{2} \right\rceil \\ 28pq - 4p^2 + 12p^3 + 21pq^2 + 8p + 3p \frac{1 - (-1)^q}{2} & \left\lceil \frac{q+1}{2} \right\rceil < p \leq q + 1 . \\ 8pq + 16p^2 + 24p^2q + 9pq^2 + 3p + 3p \frac{1 - (-1)^q}{2} & p > q + 1 \end{cases}$$

3. The eccentric connectivity index of  $G[p, q]$  is given by

$$\xi(G[p, q]) = \begin{cases} 12p(q+1)(p+q+1) & p \leq \left\lceil \frac{q+1}{2} \right\rceil \\ \frac{4p+q}{2} + \frac{1-(-1)^q}{4} & p > \left\lceil \frac{q+1}{2} \right\rceil \end{cases}.$$

## 6.5 Conclusions

We have presented here a review of topological-based methods for evaluating the symmetry constraints and topological indices for carbon nanostructures such as nanotubes and nanotori. The first task, has been fulfilled by considering the *topological symmetry* of the graph of a given chemical system; such a symmetry just reflects the symmetry properties of the automorphism group of the graph providing *the upper limit—fully rooted in topology—on the geometrical symmetry* of the nanostructure. The second goal considers the application of topological indices in characterizing nanostructures. The reported theorems are very useful because they allow a fast computation of the topological indices for complex graphs (nanostructures) starting from their structural building elements, to derive exact algorithms easy to programme on the computer.

While the primary application concerns the description of carbon-networks in chemical compounds, other applications exist to rank for example proteins according to their degree of folding and topological invariants are useful in social-networks description.

**Acknowledgements** The first and second authors are partially supported by the university of Kashan under grant number 364988/99.

## References

- Arezoomand M, Taeri B (2009) The full symmetry and irreducible representations of nanotori. *Acta Cryst A* 65:249–252
- Asadpour J, Mojarad R, Safikhani L (2011) Computing some topological indices of nanostructures. *Dig J Nanomat Biostruct* 6:937–941
- Ashrafi AR, Loghman A (2006a) PI index of armchair polyhex nanotubes. *Ars Combin* 80:193–199
- Ashrafi AR, Loghman A (2006b) PI index of zig-zag polyhex nanotubes. *MATCH Commun Math Comput Chem* 55:447–452
- Ashrafi AR, Loghman A (2006c) Padmakar-Ivan index of  $TUC_4C_8(S)$  nanotubes. *J Comput Theor Nanosci* 3:378–381
- Ashrafi AR, Loghman A (2008) Computing Padmakar-Ivan index of a  $TC_4C_8(R)$  Nanotorus. *J Comput Theor Nanosci* 5:1431–1434
- Ashrafi AR, Rezaei F (2007) PI index of polyhex nanotori. *MATCH Commun Math Comput Chem* 57:243–250

- Ashrafi AR, Yousefi S (2007a) A new algorithm for computing distance matrix and Wiener index of zig-zag polyhex nanotubes. *Nanoscale Res Lett* 2:202–206
- Ashrafi AR, Yousefi S (2007b) Computing the Wiener index of a  $TUC_4C_8(S)$  nanotorus. *MATCH Commun Math Comput Chem* 57:403–410
- Ashrafi AR, Rezaei F, Loghman A (2009) PI index of the  $C_4C_8(S)$  nanotorus. *Revue Roum Chim* 54:823–826
- Ashrafi AR, Doššlić T, Saheli M (2011a) The eccentric connectivity index of  $TUC_4C_8(R)$  nanotubes. *MATCH Commun Math Comput Chem* 65:221–230
- Ashrafi AR, Saheli M, Ghorbani M (2011b) The eccentric connectivity index of nanotubes and nanotori. *J Comput Appl Math* 16:4561–4566
- Balaban AT (1982) Distance connectivity index. *Chem Phys Lett* 89:399–404
- Balaban AT (1983) Topological indices based on topological distances in molecular graphs. *Pure Appl Chem* 55:199–206
- Bosma W, Cannon J, Playoust C (1997) The Magma algebra system I: the user language. *J Symb Comput* 24:235–265
- Das KC (2010) Atom-bond connectivity index of graphs. *Discrete Appl Math* 158:1181–1188
- Das KC, Trinajstić N (2010) Comparison between first geometric-arithmetic index and atom-bond connectivity index. *Chem Phys Lett* 497:149–151
- Diudea MV, Ursu O, Nagy LCs (2002) TOPOCLUJ. Babes-Bolyai University, Cluj
- Diudea MV, Stefu M, Pârv B, John PE (2004) Wiener index of armchair polyhex nanotubes. *Croat Chem Acta* 77:111–115
- Dobrynin A, Gutman I (1994) On a graph invariant related to the sum of all distances in a graph. *Publ Inst Math (Beograd) (N.S.)* 56:18–22
- Dobrynin A, Gutman I (1995) Solving a problem connected with distances in graphs. *Graph Theor Notes NY* 28:21–23
- Dobrynin A, Gutman I, Domotor GA (1995) Wiener-type graph invariant for some bipartite graphs. *Appl Math Lett* 8(5):57–62
- Estrada E (2008) Atom-bond connectivity and the energetic of branched alkanes. *Chem Phys Lett* 463:422–425
- Estrada E, Torres L, Rodriguez L, Gutman I (1998) An atom-bond connectivity index: modelling the enthalpy of formation of alkanes. *Indian J Chem* 37A:849–855
- Farahani MR (2012) Some connectivity indices and Zagreb index of polyhex nanotubes. *Acta Chim Slov* 59:779–783
- Fath-Tabar GH, Vaez-Zadeh B, Ashrafi AR, Graovac A (2011) Some inequalities for the atom-bond connectivity index of graph operations. *Discret Appl Math* 159:1323–1330
- Furtula B, Graovac A, Vukičević D (2009) Atom-bond connectivity index of trees. *Discret Appl Math* 157:2828–2835
- Gutman I (1994) A formula for the Wiener number of trees and its extension to graphs containing cycles. *Graph Theor Notes NY* 27:9–15
- Gutman I, Das KC (2004) The first Zagreb index 30 years after. *Commun Math Comput Chem* 50:83–92
- Gutman I, Trinajstić N (1972) Graph theory and molecular orbitals. Total  $\phi$ -electron energy of alternant hydrocarbons. *Chem Phys Lett* 17:535–538
- Heydari A, Taeri B (2009) Szeged index of  $TUC_4C_8(S)$  nanotubes. *Eur J Combin* 30:1134–1141
- HyperChem package Release 7.5 for Windows (2002) Hypercube Inc., Florida, USA
- Iranmanesh A, Ashrafi AR (2007) Balaban index of an armchair polyhex,  $TUC_4C_8(R)$  and  $TUC_4C_8(S)$  nanotorus. *J Comput Theor Nanosci* 4:514–517
- John PE, Diudea MV (2004) Wiener index of zig-zag polyhex nanotubes. *Croat Chem Acta* 77:127–132
- Khadikar PV, Deshpande NV, Kale PP, Dobrynin A, Gutman I, Domotor G (1995) The Szeged index and an analogy with the wiener index. *J Chem Inf Compute Sci* 35:545–550
- Khadikar PV, Karmarkar S, Agrawal VK (2001) A novel PI index and its applications to QSPR/QSAR studies. *J Chem Inf Comput Sci* 41:934–949

- Khalifeh MH, Yousefi-Azari H, Ashrafi AR (2009) The first and second Zagreb indices of some graph operations. *Discret Appl Math* 157:804–811
- Khodashenas H, Nadjafi-Arani MJ, Ashrafi AR, Gutman I (2011) A new proof of the Szeged-Wiener theorem. *Kragujev J Math* 35:165–172
- Klarner DA (1997) Polyominoes. In: Goodman JE, O'Rourke J (eds) *Handbook of discrete and computational geometry*, CRC Press, Boca Raton, pp 225–242 (Chapter 12)
- Klavžar S (2007) On the PI index: PI-partitions and Cartesian product graphs. *MATCH Commun Math Comput Chem* 57:573–586
- Klavžar S, Rajapakse A, Gutman I (1996) The Szeged and the Wiener index of graphs. *Appl Math Lett* 9:45–49
- Manoochehrian B, Yousefi-Azari H, Ashrafi AR (2008) Szeged index of a zig-zag polyhex nanotube. *Ars Combin* 86:371–379
- Randić M (1974) On the recognition of identical graphs representing molecular topology. *J Chem Phys* 60:3920–3928
- Randić M (1975) On characterization of molecular branching. *J Am Chem Soc* 97:6609–6615
- Randić M (1976) On discerning symmetry properties of graphs. *Chem Phys Lett* 42:283–287
- Saheli M, Ashrafi AR (2010a) The eccentric connectivity index of zig-zag polyhex nanotubes and nanotori. *J Comput Theor Nanosci* 7:1900–1903
- Saheli M, Ashrafi AR (2010b) The eccentric connectivity index of armchair polyhex nanotubes. *Maced J Chem Chem Eng* 29:71–75
- Sardana S, Madan AK (2001) Application of graph theory: relationship of molecular connectivity index, Wiener's index and eccentric connectivity index with diuretic activity. *MATCH Commun Math Comput Chem* 43:85–98
- Sharma V, Goswami R, Madan AK (1997) Eccentric connectivity index: a novel highly discriminating topological descriptor for structure-property and structure-activity studies. *J Chem Inf Comput Sci* 37:273–282
- Staic MD, Petrescu-Nita A (2013) Symmetry group of two special types of carbon nanotori. *Acta Cryst A* 69:1–5
- The GAP Team (1995) *GAP, groups, algorithms and programming*. Lehrstuhl De für Mathematik, RWTH, Aachen
- Trinajstić N (1992) *Chemical graph theory*. CRC Press, Boca Raton
- Wiener H (1947) Structural determination of paraffin boiling points. *J Am Chem Soc* 69:17–20
- Yavari M, Ashrafi AR (2009) On the symmetry of a zig-zag and an armchair polyhex carbon nanotorus. *Symmetry* 1:145–152
- Yousefi S, Ashrafi AR (2006) An exact expression for the Wiener index a polyhex nanotoruse. *MATCH Commun Math Comput Chem* 56:169–178
- Yousefi S, Ashrafi AR (2007) An exact expression for the Wiener index of a  $TUC_4C_8(R)$  nanotorus. *J Math Chem* 42:1031–1039
- Yousefi S, Ashrafi, AR (2008a) Distance matrix and wiener index of armchair polyhex nanotubes. *Stud Univ Babes-Bolyai Chem* 53:111–116
- Yousefi S, Ashrafi AR (2008b) An algorithm for constructing Wiener matrix of  $TUC_4C_8(R)$  nanotubes. *Curr Nanosci* 4:161–165
- Yousefi S, Ashrafi AR (2011) 3-dimensional distance matrix of a  $TC_4C_8(R)$  nanotoruse. *MATCH Commun Math Comput Chem* 65:249–254
- Yousefi S, Yousefi-Azari H, Khalifeh MH, Ashrafi AR (2008c) Computing distance matrix and related topological indices of an achiral polyhex nanotube. *Int J Chem Mod* 1:149–156
- Yousefi S, Yousefi-Azari H, Ashrafi AR, Khalifeh MH (2008d) Computing Wiener and Szeged indices of a polyhex Nanotorus. *J Sci Univ Tehran* 33:7–11
- Yousefi-Azari H, Ashrafi AR, Khalifeh MH (2008e) Computing vertex-PI index of single and multiwalled nanotubes. *Dig J Nanomat Bios* 3:315–318
- Zhou B (2004) Zagreb indices. *MATCH Commun Math Comput Chem* 52:113–118
- Zhou B, Gutman I (2005) Further properties of Zagreb indices. *MATCH Commun Math Comput Chem* 54:233–239



# Chapter 7

## The First and Second Zagreb Indices of Several Interesting Classes of Chemical Graphs and Nanostructures

Ali Iranmanesh and Mahdieh Azari

**Abstract** Zagreb indices are among the oldest topological indices, and were introduced by Gutman and Trinajstić in 1972. In this chapter, we study the behavior of the first and second Zagreb indices under some graph decorations such as the bridge graphs, chain graphs and rooted product of graphs. Zagreb indices of the cluster of graphs and thorn graphs as two important special cases of rooted product are also determined. Using these results, the first and second Zagreb indices of several interesting classes of chemical graphs and nanostructures will be computed.

### 7.1 Introduction

In this chapter, we consider connected finite graphs without any loops or multiple edges. Let  $G$  be such a graph with the vertex set  $V(G)$  and the edge set  $E(G)$ . For  $u \in V(G)$ , we denote by  $N_G(u)$  the set of all neighbors of  $u$  in  $G$ . Cardinality of the set  $N_G(u)$  is called the degree of  $u$  in  $G$  and will be denoted by  $\deg_G(u)$ . We denote by  $\alpha_G(u)$ , the sum of degrees of all neighbors of the vertex  $u$  in  $G$ , i.e.,  $\alpha_G(u) = \sum_{a \in N_G(u)} \deg_G(a)$ . We denote by  $|S|$  the cardinality of a set  $S$ .

In theoretical chemistry, the physico-chemical properties of chemical compounds are often modeled by the molecular- graph-based structure-descriptors which are also referred to as topological indices (Gutman and Polansky 1986; Trinajstić 1992; Todeschini and Consonni 2000). The Zagreb indices are among the oldest topological indices, and were introduced as early as in 1972 (Gutman and Trinajstić 1972). For details on their theory and applications see (Gutman et al. 1975; Nikolić et al. 2003; Zhou 2004; Das and Gutman 2004; Azari and Iranmanesh 2011a; Réti 2012; Stevanović and Milanič 2012; Eliasi et al. 2012).

---

A. Iranmanesh (✉)

Department of Mathematics, Tarbiat Modares University,  
P.O. Box 14115-137, Tehran, Iran  
e-mail: iranmanesh@modares.ac.ir

M. Azari

Department of Mathematics, Kazerun Branch, Islamic Azad University,  
P.O. Box 73135-168, Kazerun, Iran  
e-mail: azari@kau.ac.ir

The first and second Zagreb indices of a graph  $G$  are denoted by  $M_1(G)$  and  $M_2(G)$ , respectively and are defined as follows:

$$M_1(G) = \sum_{u \in V(G)} \deg_G(u)^2 \quad \text{and} \quad M_2(G) = \sum_{uv \in E(G)} \deg_G(u)\deg_G(v).$$

The first Zagreb index can also be expressed as a sum over edges of  $G$ :

$$M_1(G) = \sum_{uv \in E(G)} [\deg_G(u) + \deg_G(v)].$$

Let  $P_n$ ,  $C_n$ , and  $S_n$  denote the path, cycle and star on  $n$  vertices. It is easy to that;

$$\begin{aligned} M_1(P_n) &= 4n - 6, & (n \geq 2), \\ M_2(P_2) &= 1, \quad M_2(P_n) = 4n - 8, & (n \geq 3), \\ M_1(C_n) &= M_2(C_n) = 4n, & (n \geq 3), \\ M_1(S_n) &= n(n - 1), \quad M_2(S_n) = (n - 1)^2, & (n \geq 2). \end{aligned}$$

We denote by  $K_1$ , the single vertex graph and assume that  $P_1 = S_1 = K_1$ . Clearly,  $M_1(K_1) = M_2(K_1) = 0$ .

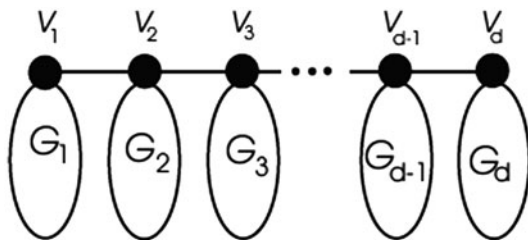
The fact that many interesting graphs are composed of simpler graphs that serve as their basic building blocks, prompted interest in the type of relationship that exists between topological indices of graph operations and their building blocks. For example see (Yeh and Gutman 1994; Sagan et al. 1996; Yan et al. 2007; Došlić 2008; Azari and Iranmanesh 2011b; Azari et al. 2010, 2012; Eliasi and Iranmanesh 2013). The corresponding relationships between Zagreb indices of some graph operations and their components were established in (Khalifeh et al. 2009; Arezoomand and Taeri 2013). In this chapter, this development is followed for Zagreb indices of some other classes of composite graphs. The chapter is organized as follows. In Sects. 7.2 and 7.3, we compute the first and second Zagreb indices for two kinds of bridge graphs. In Sect. 7.4, we present explicit formulae for the first and second Zagreb indices of the chain graphs. In Sect. 7.5, we study the behavior of the first and second Zagreb indices under the rooted product of graphs. At the end of each section, we also present some applications of our results in computing Zagreb indices of some chemical graphs and nano-structures.

## 7.2 Zagreb Indices of the Bridge Graph $B_1$

In this section, we compute the first and second Zagreb indices for the bridge graph  $B_1$ . All of the results of this section have been reported in (Azari et al. 2013). We start this section by definition of this class of composite graphs.

Let  $\{G_i\}_{i=1}^d$  be a set of finite pairwise disjoint graphs with distinct vertices  $v_i \in V(G_i)$ . The bridge graph  $B_1 = B_1(G_1, G_2, \dots, G_d; v_1, v_2, \dots, v_d)$  of  $\{G_i\}_{i=1}^d$  with

**Fig. 7.1** The bridge graph  
 $B_1 = B_1(G_1, G_2, \dots, G_d; v_1, v_2, \dots, v_d)$



respect to the vertices  $\{v_i\}_{i=1}^d$  is the graph obtained from the graphs  $G_1, G_2, \dots, G_d$  by connecting the vertices  $v_i$  and  $v_{i+1}$  by an edge for all  $i \in \{1, 2, \dots, d-1\}$ , as shown in Fig. 7.1.

First, we express the following simple lemma which is crucial in this section. Its proof follows immediately from the definition of  $B_1$ , so is omitted.

**Lemma 7.2.1** The degree of an arbitrary vertex  $u$  of the bridge graph  $B_1, d \geq 2$ , is given by:

$$\deg_{B_1}(u) = \begin{cases} \deg_{G_i}(u) & \text{if } u \in V(G_i) - \{v_i\}, 1 \leq i \leq d \\ v_1 + 1 & \text{if } u = v_1 \\ v_i + 2 & \text{if } u = v_i, 2 \leq i \leq d-1 \\ v_d + 1 & \text{if } u = v_d \end{cases},$$

where  $v_i = \deg_{G_i}(v_i)$ , for  $1 \leq i \leq d$ . ■

**Theorem 7.2.2** The first Zagreb index of the bridge graph  $B_1, d \geq 2$ , is given by:

$$M_1(B_1) = \sum_{i=1}^d M_1(G_i) + 2v_1 + 4 \sum_{i=2}^{d-1} v_i + 2v_d + 4d - 6,$$

where  $v_i = \deg_{G_i}(v_i)$ , for  $1 \leq i \leq d$ .

**Proof** Using the definition of the first Zagreb index, and Lemma 7.2.1, we have:

$$\begin{aligned} M_1(B_1) &= \sum_{i=1}^d \sum_{u \in V(G_i) - \{v_i\}} \deg_{G_i}(u)^2 + (v_1 + 1)^2 + \sum_{i=2}^{d-1} (v_i + 2)^2 + (v_d + 1)^2 \\ &= \sum_{i=1}^d M_1(G_i) - \sum_{i=1}^d v_i^2 + v_1^2 + 2v_1 + 1 + \sum_{i=2}^{d-1} v_i^2 + 4 \sum_{i=2}^{d-1} v_i \\ &\quad + 4(d-2) + v_d^2 + 2v_d + 1 \\ &= \sum_{i=1}^d M_1(G_i) + 2v_1 + 4 \sum_{i=2}^{d-1} v_i + 2v_d + 4d - 6. \end{aligned}$$
■

Suppose that  $v$  is a vertex of a graph  $G$ , and let  $G_i = G$  and  $v_i = v$  for all  $i \in \{1, 2, \dots, d\}$ . Using Theorem 7.2.2, we easily arrive at:

**Corollary 7.2.3** The first Zagreb index of the bridge graph  $B_1$ , ( $d \geq 2$  times), is given by:

$$M_1(B_1) = dM_1(G) + 4v(d - 1) + 4d - 6,$$

where  $v = \deg_G(v)$ . ■

**Theorem 7.2.4** If  $d = 2$ , the second Zagreb index of the bridge graph  $B_1$ , is given by:

$$M_2(B_1) = M_2(G_1) + M_2(G_2) + \alpha_{G_1}(v_1) + \alpha_{G_2}(v_2) + (v_1 + 1)(v_2 + 1),$$

and for  $d \geq 3$ ,

$$M_2(B_1) = \sum_{i=1}^d M_2(G_i) + \alpha_{G_1}(v_1) + \alpha_{G_d}(v_d) + 2 \sum_{i=2}^{d-1} \alpha_{G_i}(v_i) + \sum_{i=1}^{d-1} v_i v_{i+1} + 2(v_1 + v_d) - (v_2 + v_{d-1}) + 4 \sum_{i=2}^{d-1} v_i + 4(d - 2),$$

where  $v_i = \deg_{G_i}(v_i)$ , for  $1 \leq i \leq d$ .

*Proof* For the case  $d = 2$ , see the proof of Lemma 2.4 in (Ashrafi et al. 2011).

Now let  $d \geq 3$ . By definition of the second Zagreb index,  $M_2(B_1)$  is equal to the sum of  $\deg_{B_1}(a)\deg_{B_1}(b)$ , where summation is taken over all edges  $ab \in E(B_1)$ . From the definition of the bridge graph  $B_1$ ,  $E(B_1) = E(G_1) \cup E(G_2) \cup \dots \cup E(G_d) \cup \{v_i v_{i+1} | 1 \leq i \leq d - 1\}$ . In order to compute  $M_2(B_1)$ , we partition our sum into the four sums as follows:

The first sum  $S_1$  is taken over all edges  $ab \in E(G_1)$ . Using Lemma 7.2.1,

$$\begin{aligned} S_1 &= \sum_{ab \in E(G_1)} \deg_{B_1}(a)\deg_{B_1}(b) \\ &= \sum_{ab \in E(G_1); a, b \neq v_1} \deg_{G_1}(a)\deg_{G_1}(b) + \sum_{ab \in E(G_1); a \in V(G_1), b = v_1} \deg_{G_1}(a)[\deg_{G_1}(v_1) + 1] \\ &= M_2(G_1) + \alpha_{G_1}(v_1). \end{aligned}$$

The second sum  $S_2$  is taken over all edges  $ab \in E(G_d)$ . Using Lemma 7.2.1, we obtain:

$$\begin{aligned} S_2 &= \sum_{ab \in E(G_d)} \deg_{B_1}(a)\deg_{B_1}(b) \\ &= \sum_{ab \in E(G_d); a, b \neq v_d} \deg_{G_d}(a)\deg_{G_d}(b) + \sum_{ab \in E(G_d); a \in V(G_d), b = v_d} \deg_{G_d}(a)[\deg_{G_d}(v_d) + 1] \\ &= M_2(G_d) + \alpha_{G_d}(v_d). \end{aligned}$$

The third sum  $S_3$  is taken over all edges  $ab \in E(G_i)$  for all  $2 \leq i \leq d - 1$ . Using Lemma 7.2.1,

$$\begin{aligned} S_3 &= \sum_{i=2}^{d-1} \sum_{ab \in E(G_i)} \deg_{B_1}(a) \deg_{B_1}(b) \\ &= \sum_{i=2}^{d-1} \left\{ \sum_{ab \in E(G_i); a, b \neq v_i} \deg_{G_i}(a) \deg_{G_i}(b) + \sum_{ab \in E(G_i); a \in V(G_i), b = v_i} \deg_{G_i}(a) [\deg_{G_i}(v_i) + 2] \right\} \\ &= \sum_{i=2}^{d-1} M_2(G_i) + 2 \sum_{i=2}^{d-1} \alpha_{G_i}(v_i). \end{aligned}$$

Finally, the last sum  $S_4$  is taken over all edges  $v_i v_{i+1}, 1 \leq i \leq d - 1$ . Using Lemma 7.2.1, we get:

$$\begin{aligned} S_4 &= \sum_{i=1}^{d-1} \sum_{ab = v_i v_{i+1}} \deg_{B_1}(a) \deg_{B_1}(b) \\ &= (v_1 + 1)(v_2 + 2) + \sum_{i=2}^{d-2} (v_i + 2)(v_{i+1} + 2) + (v_{d-1} + 2)(v_d + 1) \\ &= v_1 v_2 + 2v_1 + v_2 + 2 + \sum_{i=2}^{d-2} v_i v_{i+1} + 2 \sum_{i=2}^{d-2} v_i + 2 \sum_{i=3}^{d-1} v_i + 4(d - 3) \\ &\quad + v_{d-1} v_d + v_{d-1} + 2v_d + 2 \\ &= \sum_{i=1}^{d-1} v_i v_{i+1} + 2(v_1 + v_d) - (v_2 + v_{d-1}) + 4 \sum_{i=2}^{d-1} v_i + 4(d - 2). \end{aligned}$$

Now the formula for  $M_2(B_1)$  is obtained by adding  $S_1, S_2, S_3, S_4$ . ■

Suppose that  $v$  is a vertex of a graph  $G$ , and let  $G_i = G$  and  $v_i = v$  for all  $i \in \{1, 2, \dots, d\}$ . Using Theorem 7.2.4, we can easily get the following result.

**Corollary 7.2.5** If  $d = 2$ , the first Zagreb index of the bridge graph  $B_1$ , is given by:

$$M_2(B_1) = 2M_2(G) + 2\alpha_G(v) + (v + 1)^2,$$

and for  $d \geq 3$ ,

$$M_2(B_1) = dM_2(G) + (d - 1)((v + 2)^2 + 2\alpha_G(v)) - 2(v + 2),$$

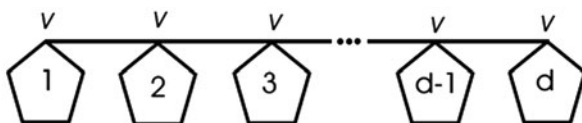
where  $v = \deg_G(v)$ . ■

Now, we apply our results to compute the first and second Zagreb indices of some chemical graphs.

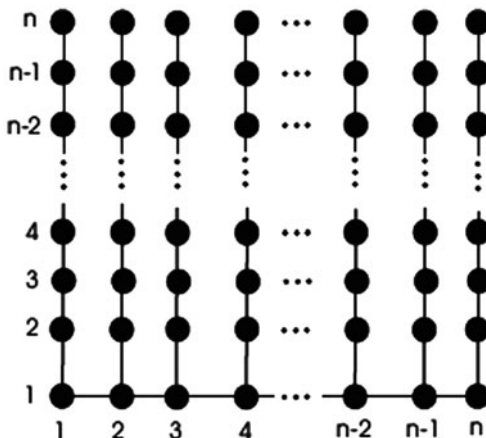
In the first example, we consider the bridge graph  $G = B_1(C_n, C_n, \dots, C_n; v, v, \dots, v)$ , ( $d$  times), where  $v$  is an arbitrary vertex of the  $n$ -cycle  $C_n$ , see Fig. 7.2 for the case  $n = 5$ .

Using Corollaries 7.2.3 and 7.2.5, we easily arrive at:

**Fig. 7.2** The bridge graph  $B_1(C_5, C_5, \dots, C_5; v, v, \dots, v)$ , ( $d$  times)



**Fig. 7.3** The square comb lattice graph with  $N = n^2$  vertices



**Corollary 7.2.6** The first and second Zagreb indices of the bridge graph  $G = B_1(C_n, C_n, \dots, C_n; v, v, \dots, v)$ , ( $d$  times), are given by:

1.  $M_1(G) = 4nd + 12d - 14$ ,
2.  $M_2(G) = \begin{cases} 8n + 17 & \text{if } d = 3 \\ 4nd + 24d - 32 & \text{if } d \geq 2 \end{cases}$ . ■

Our next example is about the square comb lattice graphs. Consider the square comb lattice graph  $Cq(N)$  with open ends, where  $N = n^2$  is the number of its vertices, see Fig. 7.3.

This graph can be represented as the bridge graph  $B_1(P_n, P_n, \dots, P_n; v, v, \dots, v)$ , ( $n$  times), where  $v$  is the first vertex (vertex of degree one) of the  $n$ -vertex path  $P_n$ . So we can apply Corollaries 7.2.3 and 7.2.5 to get the first and second Zagreb indices of  $Cq(N)$ .

**Corollary 7.2.7** The first and second Zagreb indices of  $Cq(N)$  are given by:

1.  $M_1(Cq(N)) = 4n^2 + 2n - 10, n \geq 2$ ,
2.  $M_2(Cq(N)) = \begin{cases} 8 & \text{if } n = 2 \\ 4n^2 + 5n - 19 & \text{if } n \geq 3 \end{cases}$ . ■

In our last example, we consider the van Hove comb lattice graph  $CvH(N)$  with open ends, where  $N = n^2$  is the number of its vertices, see Fig. 7.4.

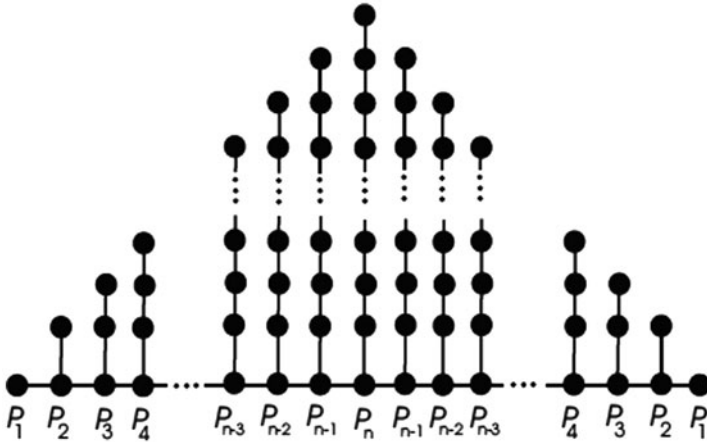


Fig. 7.4 The van Hove comb lattice graphs with  $N = n^2$  vertices

This graph can be represented as the bridge graph

$$B_1(P_1, P_2, \dots, P_{n-1}, P_n, P_{n-1}, \dots, P_2, P_1; v_{1,1}, v_{1,2}, \dots, v_{1,n-1}, v_{1,n}, v_{1,n-1}, \dots, v_{1,2}, v_{1,1}),$$

where for  $2 \leq i \leq n$ ,  $v_{1,i}$  is the first vertex (vertex of degree one) of the  $i$ -vertex path  $P_i$  and  $v_{1,1}$  is the single vertex (vertex of degree zero) of the singleton graph  $P_1$ . So by Theorems 7.2.2 and 7.2.4, the formulae for Zagreb indices of  $CvH(N)$  are obtained at once.

**Corollary 7.2.8** The first and second Zagreb indices of  $CvH(N)$  are given by:

1.  $M_1(CvH(N)) = 4n^2 + 4n - 12$ ,
2.  $M_2(CvH(N)) = \begin{cases} 9 & \text{if } n = 2 \\ 4n^2 + 10n - 28 & \text{if } n \geq 3 \end{cases}$ . ■

### 7.3 Zagreb Indices of the Bridge Graph $B_2$

In this section, we compute the first and second Zagreb indices for the bridge graph  $B_2$ . All of the results of this section have been reported in (Azari et al. 2013). We start this section by definition of this class of composite graphs.

Let  $\{G_i\}_{i=1}^d$  be a set of finite pairwise disjoint graphs with distinct vertices  $v_i, w_i \in V(G_i)$ . The bridge graph  $B_2 = B_2(G_1, G_2, \dots, G_d; v_1, w_1, v_2, w_2, \dots, v_d, w_d)$  of  $\{G_i\}_{i=1}^d$  with respect to the vertices  $\{v_i, w_i\}_{i=1}^d$  is the graph obtained from the graphs  $G_1, G_2, \dots, G_d$  by connecting the vertices  $w_i$  and  $v_{i+1}$  by an edge for all  $i \in \{1, 2, \dots, d - 1\}$ , as shown in Fig. 7.5.



Fig. 7.5 The bridge graph  $B_2 = B_2(G_1, G_2, \dots, G_d; v_1, w_1, v_2, w_2, \dots, v_d, w_d)$

First, we express the following simple lemma. It follows immediately from the definition of  $B_2$ .

**Lemma 7.3.1** The degree of an arbitrary vertex  $u$  of the bridge graph  $B_2, d \geq 2$ , is given by:

$$\deg_{B_2}(u) = \begin{cases} \deg_{G_1}(u) & \text{if } u \in V(G_1) - \{w_1\} \\ \deg_{G_d}(u) & \text{if } u \in V(G_d) - \{v_d\} \\ \deg_{G_i}(u) & \text{if } u \in V(G_i) - \{v_i, w_i\}, 2 \leq i \leq d - 1, \\ \omega_i + 1 & \text{if } u = w_i, 1 \leq i \leq d - 1 \\ v_i + 1 & \text{if } u = v_i, 2 \leq i \leq d \end{cases}$$

where  $v_i = \deg_{G_i}(v_i), \omega_i = \deg_{G_i}(w_i)$ , for  $1 \leq i \leq d$ , ■

**Theorem 7.3.2** The first Zagreb index of the bridge graph  $B_2, d \geq 2$ , is given by:

$$M_1(B_2) = \sum_{i=1}^d M_1(G_i) + 2 \sum_{i=1}^{d-1} \omega_i + 2 \sum_{i=2}^d v_i + 2d - 2,$$

where  $v_i = \deg_{G_i}(v_i), \omega_i = \deg_{G_i}(w_i)$ , for  $1 \leq i \leq d$ .

*Proof* Using the definition of the first Zagreb index, and Lemma 7.3.1, we have:

$$\begin{aligned} M_1(B_2) &= \sum_{u \in V(G_1) - \{w_1\}} \deg_{G_1}(u)^2 + \sum_{i=2}^{d-1} \sum_{u \in V(G_i) - \{v_i, w_i\}} \deg_{G_i}(u)^2 \\ &\quad + \sum_{u \in V(G_d) - \{v_d\}} \deg_{G_d}(u)^2 + \sum_{i=1}^{d-1} (\omega_i + 1)^2 + \sum_{i=2}^d (v_i + 1)^2 \\ &= M_1(G_1) - \omega_1^2 + \sum_{i=2}^{d-1} M_1(G_i) - \sum_{i=2}^{d-1} v_i^2 - \sum_{i=2}^{d-1} \omega_i^2 + M_1(G_d) - v_d^2 \\ &\quad + \sum_{i=1}^{d-1} \omega_i^2 + 2 \sum_{i=1}^{d-1} \omega_i + d - 1 + \sum_{i=2}^d v_i^2 + 2 \sum_{i=2}^d v_i + d - 1 \\ &= \sum_{i=1}^d M_1(G_i) + 2 \sum_{i=1}^{d-1} \omega_i + 2 \sum_{i=2}^d v_i + 2d - 2. \end{aligned}$$
■



Suppose that  $v$  and  $w$  are two vertices of a graph  $G$ , and let  $G_i = G$ ,  $v_i = v$ , and  $w_i = w$  for all  $i \in \{1, 2, \dots, d\}$ . Then Theorem 7.3.2 implies,

**Corollary 7.3.3** The first Zagreb index of the bridge graph  $B_2$ , ( $d \geq 2$  times), is given by:

$$M_1(B_2) = dM_1(G) + 2(d-1)(v + \omega + 1),$$

where  $v = \deg_G(v)$ ,  $\omega = \deg_G(w)$ . ■

**Theorem 7.3.4** The second Zagreb index of the bridge graph  $B_2$ ,  $d \geq 2$ , is given by:

$$\begin{aligned} M_2(B_2) &= \sum_{i=1}^d M_2(G_i) + \sum_{i=1}^{d-1} [\omega_i + \alpha_{G_i}(w_i)] + \sum_{i=2}^d [v_i + \alpha_{G_i}(v_i)] \\ &\quad + \sum_{i=1}^{d-1} \omega_i v_{i+1} + d + n - 1, \end{aligned}$$

where  $v_i = \deg_{G_i}(v_i)$ ,  $\omega_i = \deg_{G_i}(w_i)$ , for  $1 \leq i \leq d$  and  $n$  is the number of the graphs  $G_i$ ,  $2 \leq i \leq d-1$ , with the property that the vertices  $v_i$  and  $w_i$  are adjacent in them.

*Proof* From the definition of the bridge graph  $B_2$ ,  $E(B_2) = E(G_1) \cup E(G_2) \cup \dots \cup E(G_d) \cup \{w_i v_{i+1} \mid 1 \leq i \leq d-1\}$ . Using the same argument as in the proof of Theorem 7.2.4, we partition the sum in the formula of  $M_2(B_2)$  into the five sums as follows:

The first sum  $S_1$  is taken over all edges  $ab \in E(G_1)$ . Using Lemma 7.3.1, we have:

$$\begin{aligned} S_1 &= \sum_{ab \in E(G_1)} \deg_{B_2}(a) \deg_{B_2}(b) = \sum_{ab \in E(G_1); a, b \neq w_1} \deg_{G_1}(a) \deg_{G_1}(b) \\ &\quad + \sum_{ab \in E(G_1); a \in V(G_1), b = w_1} \deg_{G_1}(a) [\deg_{G_1}(w_1) + 1] \\ &= M_2(G_1) + \alpha_{G_1}(w_1). \end{aligned}$$

Analogously,

$$\begin{aligned} S_2 &= \sum_{ab \in E(G_d)} \deg_{B_2}(a) \deg_{B_2}(b) = \sum_{ab \in E(G_d); a, b \neq v_d} \deg_{G_d}(a) \deg_{G_d}(b) \\ &\quad + \sum_{ab \in E(G_d); a \in V(G_d), b = v_d} \deg_{G_d}(a) [\deg_{G_d}(v_d) + 1] \\ &= M_2(G_d) + \alpha_{G_d}(v_d). \end{aligned}$$

Suppose  $I = \{i \mid 2 \leq i \leq d-1, v_i w_i \in E(G_i)\}$ . The third sum  $S_3$  is taken over all edges  $ab \in E(G_i)$  for all  $i \in I$ . Using Lemma 7.3.1, we have:

$$S_3 = \sum_{i \in I} \sum_{ab \in E(G_i)} \deg_{B_2}(a) \deg_{B_2}(b)$$

$$\begin{aligned}
&= \sum_{i \in I} \left\{ \sum_{ab \in E(G_i); a, b \neq v_i, w_i} \deg_{G_i}(a) \deg_{G_i}(b) + \sum_{ab \in E(G_i); a \in V(G_i) - \{w_i\}, b = v_i} \deg_{G_i}(a) (\deg_{G_i}(v_i) + 1) \right. \\
&\quad \left. + \sum_{ab \in E(G_i); a \in V(G_i) - \{v_i\}, b = w_i} \deg_{G_i}(a) (\deg_{G_i}(w_i) + 1) + (\deg_{G_i}(v_i) + 1) (\deg_{G_i}(w_i) + 1) \right\} \\
&= \sum_{i \in I} (M_2(G_i) + \alpha_{G_i}(v_i) + \alpha_{G_i}(w_i) + 1).
\end{aligned}$$

Suppose  $\bar{I} = \{i \mid 2 \leq i \leq d-1, v_i w_i \notin E(G_i)\} = \{2, 3, \dots, d-1\} - I$ . The forth sum  $S_4$  is taken over all edges  $ab \in E(G_i)$  for all  $i \in \bar{I}$ . Using Lemma 7.3.1, we have:

$$\begin{aligned}
S_4 &= \sum_{i \in \bar{I}} \sum_{ab \in E(G_i)} \deg_{B_2}(a) \deg_{B_2}(b) \\
&= \sum_{i \in \bar{I}} \left\{ \sum_{ab \in E(G_i); a, b \neq v_i, w_i} \deg_{G_i}(a) \deg_{G_i}(b) + \sum_{ab \in E(G_i); a \in V(G_i), b = v_i} \deg_{G_i}(a) [\deg_{G_i}(v_i) + 1] \right. \\
&\quad \left. + \sum_{ab \in E(G_i); a \in V(G_i), b = w_i} \deg_{G_i}(a) (\deg_{G_i}(w_i) + 1) \right\} \\
&= \sum_{i \in \bar{I}} (M_2(G_i) + \alpha_{G_i}(v_i) + \alpha_{G_i}(w_i)).
\end{aligned}$$

Finally, the last sum  $S_5$  is taken over all edges  $w_i v_{i+1}, 1 \leq i \leq d-1$ . Using Lemma 7.3.1, we have:

$$\begin{aligned}
S_5 &= \sum_{i=1}^{d-1} \sum_{ab=w_i v_{i+1}} \deg_{B_2}(a) \deg_{B_2}(b) = \sum_{i=1}^{d-1} (\deg_{G_i}(w_i) + 1) (\deg_{G_{i+1}}(v_{i+1}) + 1) \\
&= \sum_{i=1}^{d-1} \omega_i + \sum_{i=2}^d v_i + \sum_{i=1}^{d-1} \omega_i v_{i+1} + d - 1.
\end{aligned}$$

Adding the quantities  $S_1, S_2, S_3, S_4, S_5$ , we can get the formula for  $M_2(B_2)$ . ■

Suppose that  $v$  and  $w$  are two vertices of a graph  $G$ , and let  $G_i = G, v_i = v$  and  $w_i = w$  for all  $i \in \{1, 2, \dots, d\}$ . Using Theorem 7.3.4 yields:

**Corollary 7.3.5** Let  $v = \deg_G(v)$  and  $\omega = \deg_G(w)$ . If  $v$  and  $w$  are adjacent in  $G$ , then

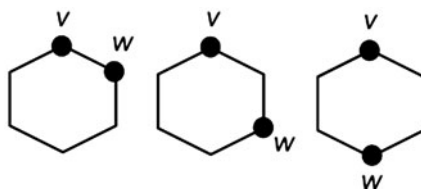
$$M_2(B_2) = dM_2(G) + (d-1)[v + \omega + v\omega + \alpha_G(v) + \alpha_G(w) + 2] - 1,$$

whereas otherwise;

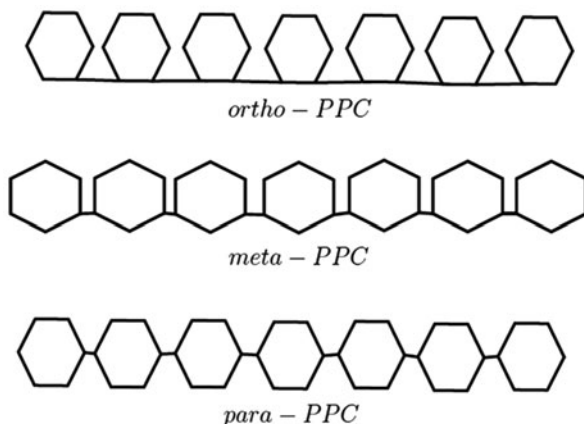
$$M_2(B_2) = dM_2(G) + (d-1)[v + \omega + v\omega + \alpha_G(v) + \alpha_G(w) + 1]. \quad \blacksquare$$

Now, we apply our results to compute the first and second Zagreb indices of some chemical graphs and nano-structures.

**Fig. 7.6** Ortho-, meta- and para-positions of vertices in hexagon



**Fig. 7.7** Ortho-, meta-, and para-polyphenyl chains with seven hexagons



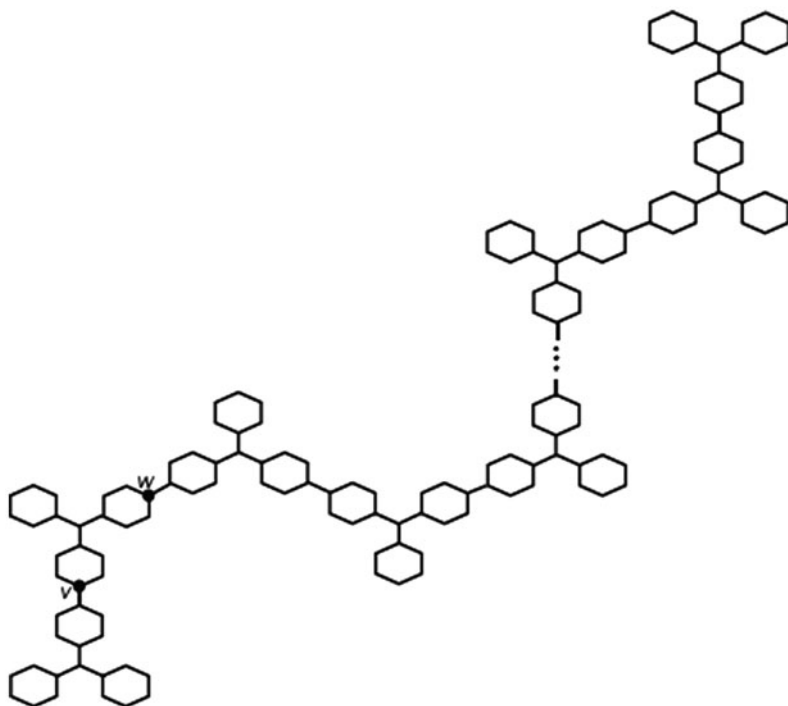
Our first example is about polyphenyl chains. Two vertices  $v$  and  $w$  of a hexagon  $H$  are said to be in ortho-position if they are adjacent in  $H$ . If two vertices  $v$  and  $w$  are at distance two, then they are said to be in meta-position, and if two vertices  $v$  and  $w$  are at distance three, then they are said to be in para-position. Examples of vertices in the above three types of positions are illustrated in Fig. 7.6.

An internal hexagon  $H$  in a polyphenyl chain is said to be an ortho-hexagon, meta-hexagon, or para-hexagon, respectively if two vertices of  $H$  incident with two edges which connect other two hexagons are in ortho-position, meta-position, para-position, respectively. A polyphenyl chain of  $h$  hexagons is ortho- $PPC_h$  and is denoted by  $O_h$ , if all its internal hexagons are ortho-hexagons. In a fully analogous manner, we can define meta- $PPC_h$  (denoted by  $M_h$ ) and para- $PPC_h$  (denoted by  $L_h$ ). See Fig. 7.7.

We may view the polyphenyl chains  $O_h$ ,  $M_h$ , and  $L_h$  as the bridge graph  $B_2(C_6, \dots, C_6; v, w, v, w, \dots, v, w)$ , ( $h$  times), where  $C_6$  is the cycle with six vertices and  $v$  and  $w$  are the vertices shown in Fig. 7.6. Since all vertices of  $C_6$  are of degree two, so  $M_1(C_6) = M_2(C_6) = 24$ ,  $v = \omega = 2$ , and  $\alpha_{C_6}(v) = \alpha_{C_6}(w) = 4$ . Note that  $v$  and  $w$  are adjacent in  $O_h$  but are not adjacent in  $M_h$  and  $L_h$ . Using Corollaries 7.3.3 and 7.3.5, we obtain the following result.

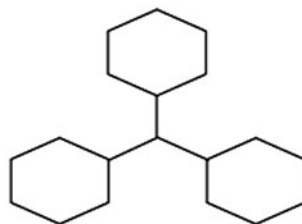
**Corollary 7.3.6** The first and second Zagreb indices of  $O_h$ ,  $M_h$ , and  $L_h$  are given by:

1.  $M_1(O_h) = M_1(M_h) = M_1(L_h) = 34h - 10$ ,
2.  $M_2(O_h) = 42h - 19$ ,  $M_2(M_h) = M_2(L_h) = 41h - 17$ . ■



**Fig. 7.8** The molecular graph of the nanostar dendrimer  $D_n$

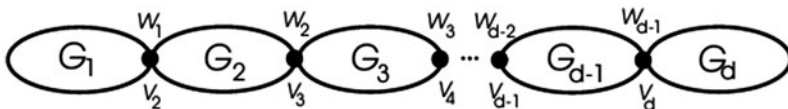
**Fig. 7.9** The graph of the nanostar dendrimer  $D_n$  for  $n = 1$



Our next example is about the molecular graph of the nanostar dendrimer  $D_n$  shown in Fig. 7.8. This graph can be represented as the bridge graph  $B_2(G, G, \dots, G; v, w, v, w, \dots, v, w)$ , ( $n$  times), where  $G$  is the graph depicted in Fig. 7.9,  $v$  and  $w$  are the vertices shown in Fig. 7.8 and  $n$  is the number of repetition of the fragment  $G$ .

It is easy to see that  $M_1(G) = 15 \times 4 + 4 \times 9 = 96$  and  $M_2(G) = 12(2 \times 2) + 6(2 \times 3) + 3(3 \times 3) = 111$ . Using Corollaries 7.3.3 and 7.3.5, we obtain the following result.

**Corollary 7.3.7** The first and second Zagreb indices of the nanostar dendrimer  $D_n$  are given by:



**Fig. 7.10** The chain graph  $C = C(G_1, G_2, \dots, G_d; v_1, w_1, v_2, w_2, \dots, v_d, w_d)$

1.  $M_1(D_n) = 106n - 10,$
2.  $M_2(D_n) = 128n - 17.$

■

### 7.4 Zagreb Indices of Chain Graphs

In this section, we compute the first and second Zagreb indices for chain graphs. All of the results of this section have been reported in (Azari et al. 2013). We start this section by definition of this class of composite graphs.

Let  $\{G_i\}_{i=1}^d$  be a set of finite pairwise disjoint graphs with distinct vertices  $v_i, w_i \in V(G_i)$ . The chain graph  $C = C(G_1, G_2, \dots, G_d; v_1, w_1, v_2, w_2, \dots, v_d, w_d)$  of  $\{G_i\}_{i=1}^d$  with respect to the vertices  $\{v_i, w_i\}_{i=1}^d$  is the graph obtained from the graphs  $G_1, G_2, \dots, G_d$  by identifying the vertices  $w_i$  and  $v_{i+1}$  for all  $i \in \{1, 2, \dots, d - 1\}$ , as shown in Fig. 7.10.

We first state a simple lemma which immediately follows from the definition of  $C$ .

**Lemma 7.4.1** The degree of an arbitrary vertex  $u$  of the chain graph  $C, d \geq 2$ , is given by:

$$\deg_C(u) = \begin{cases} \deg_{G_1}(u) & \text{if } u \in V(G_1) - \{w_1\} \\ \deg_{G_d}(u) & \text{if } u \in V(G_d) - \{v_d\} \\ \deg_{G_i}(u) & \text{if } u \in V(G_i) - \{v_i, w_i\}, 2 \leq i \leq d - 1, \\ \omega_i + v_{i+1} & \text{if } u = w_i = v_{i+1}, 1 \leq i \leq d - 1 \end{cases}$$

where  $v_i = \deg_{G_i}(v_i), \omega_i = \deg_{G_i}(w_i),$  for  $1 \leq i \leq d.$

■

**Theorem 7.4.2** The first Zagreb index of the chain graph  $C, d \geq 2$ , is given by:

$$M_1(C) = \sum_{i=1}^d M_1(G_i) + 2 \sum_{i=1}^{d-1} \omega_i v_{i+1},$$

where  $v_i = \deg_{G_i}(v_i), \omega_i = \deg_{G_i}(w_i),$  for  $1 \leq i \leq d.$

*Proof* Similar to the proof of Theorem 7.3.2 and by definition of the chain graph, we have:

$$\begin{aligned}
 M_1(C) &= \sum_{u \in V(G_1) - \{w_1\}} \deg_C(u)^2 + \sum_{i=2}^{d-1} \sum_{u \in V(G_i) - \{v_i, w_i\}} \deg_C(u)^2 + \sum_{u \in V(G_d) - \{v_d\}} \deg_C(u)^2 \\
 &\quad + \sum_{i=1}^{d-1} \sum_{u=w_i=v_{i+1}} \deg_C(u)^2 \\
 &= \sum_{u \in V(G_1) - \{w_1\}} \deg_{G_1}(u)^2 + \sum_{i=2}^{d-1} \sum_{u \in V(G_i) - \{v_i, w_i\}} \deg_{G_i}(u)^2 + \sum_{u \in V(G_d) - \{v_d\}} \deg_{G_d}(u)^2 \\
 &\quad + \sum_{i=1}^{d-1} (\omega_i + v_{i+1})^2 \\
 &= M_1(G_1) - \omega_1^2 + \sum_{i=2}^{d-1} M_1(G_i) - \sum_{i=2}^{d-1} v_i^2 - \sum_{i=2}^{d-1} \omega_i^2 + M_1(G_d) - v_d^2 \\
 &\quad + \sum_{i=1}^{d-1} \omega_i^2 + \sum_{i=2}^d v_i^2 + 2 \sum_{i=1}^{d-1} \omega_i v_{i+1} \\
 &= \sum_{i=1}^d M_1(G_i) + 2 \sum_{i=1}^{d-1} \omega_i v_{i+1}. \quad \blacksquare
 \end{aligned}$$

Suppose that  $v$  and  $w$  are two vertices of a graph  $G$ , and let  $G_i = G, v_i = v$ , and  $w_i = w$  for all  $i \in \{1, 2, \dots, d\}$ . Using Theorem 7.4.2, we can easily obtain the following result.

**Corollary 7.4.3** The first Zagreb index of the chain graph  $C$ , ( $d \geq 2$  times), is given by:

$$M_1(C) = dM_1(G) + 2(d - 1)v\omega,$$

where  $v = \deg_G(v), \omega = \deg_G(w)$ .

**Theorem 7.4.4** The second Zagreb index of the chain graph  $C, d \geq 2$ , is given by:

$$M_2(C) = \sum_{i=1}^d M_2(G_i) + \sum_{i=1}^{d-1} [\omega_i \alpha_{G_{i+1}}(v_{i+1}) + v_{i+1} \alpha_{G_i}(w_i)] + \sum_{i \in I} \omega_{i-1} v_{i+1},$$

where  $v_i = \deg_{G_i}(v_i), \omega_i = \deg_{G_i}(w_i)$ , for  $1 \leq i \leq d$  and  $I = \{i | 2 \leq i \leq d - 1, v_i w_i \in E(G_i)\}$ .

*Proof* In a similar manner as in the proof of Theorems 7.2.4 and 7.3.4, we can partition the sum in the formula of  $M_2(C)$  into the four sums as follows:

The first sum  $S_1$  is taken over all edges  $ab \in E(G_1)$ . Using Lemma 7.4.1, we get:

$$S_1 = M_2(G_1) + v_2 \alpha_{G_1}(w_1).$$

Further,

$$S_2 = M_2(G_d) + \omega_{d-1}\alpha_{G_d}(v_d),$$

where  $S_2$  is the sum over all edges  $ab \in E(G_d)$ .

The third sum  $S_3$  is taken over all edges  $ab \in E(G_i)$  for all  $i \in I$ . Using Lemma 7.4.1, we get:

$$S_3 = \sum_{i \in I} [M_2(G_i) + \omega_{i-1}\alpha_{G_i}(v_i) + v_{i+1}\alpha_{G_i}(w_i) + \omega_{i-1}v_{i+1}].$$

Similarly,

$$S_4 = \sum_{i \in \bar{I}} [M_2(G_i) + \omega_{i-1}\alpha_{G_i}(v_i) + v_{i+1}\alpha_{G_i}(w_i)],$$

where  $S_4$  is the sum over all edges  $ab \in E(G_i)$  for all  $i \in \bar{I}$ .

Adding the quantities  $S_1, S_2, S_3, S_4$ , we arrive at the expression for  $M_2(C)$  given in Theorem 7.4.4. ■

Suppose that  $v$  and  $w$  are two vertices of a graph  $G$ , and let  $G_i = G, v_i = v$ , and  $w_i = w$  for all  $i \in 1, 2, \dots, d$ . Then from Theorem 7.4.4 follows:

**Corollary 7.4.5** Let  $v = \deg_G(v)$  and  $\omega = \deg_G(w)$ . If  $v$  and  $w$  are adjacent in  $G$ , then

$$M_2(C) = dM_2(G) + (d-1)[\omega\alpha_G(v) + v\alpha_G(w)] + (d-2)v\omega,$$

whereas otherwise;

$$M_2(C) = dM_2(G) + (d-1)[\omega\alpha_G(v) + v\alpha_G(w)]. \quad \blacksquare$$

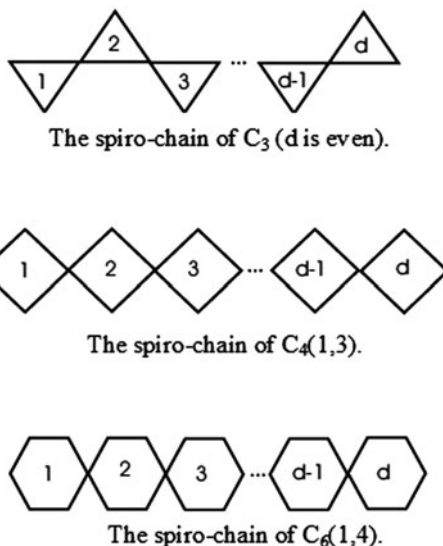
Now as an application of our results, we compute the first and second Zagreb indices of the spiro-chain of the cycle  $C_n$  for arbitrary  $n \geq 3$ . Choose a numbering for vertices of  $C_n$  such that the vertex  $v$  has number 1, the number  $i$  of the vertex  $w$  has to be in  $\{2, 3, \dots, n\}$ . However, due to the symmetry  $k \leftrightarrow n - k + 2$ , one can restrict  $i$  to  $\{2, 3, 4, \dots, \lfloor \frac{n}{2} \rfloor + 1\}$ . Denote the graph  $C_n$  by  $C_n(k, l)$ , where  $k$  and  $l$  are the numbers of the vertices  $v$  and  $w$ , respectively. The spiro-chain of the graph  $C_n(k, l)$  can be considered as the chain graph  $C(G, G, \dots, G; v, w, v, w, \dots, v, w)$ , where  $G = C_n(k, l)$ . The spiro-chains of  $C_3, C_4, C_6$  are shown in Fig. 7.11. We denote the spiro-chain containing  $d$  times the component  $C_n(k, l)$ , by  $S_d(C_n(k, l))$ .

Since all vertices of  $C_n(k, l)$  are of degree two, so  $M_1(C_n(k, l)) = M_2(C_n(k, l)) = 4n, v = \omega = 2$ , and  $\alpha_{C_n(k, l)}(v) = \alpha_{C_n(k, l)}(w) = 4$ . So using Corollaries 7.4.3 and 7.4.5, we easily arrive at:

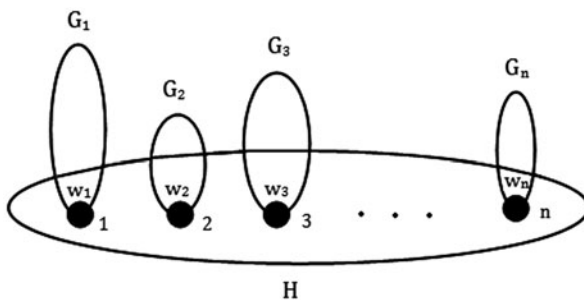
**Corollary 7.4.6** The first and second Zagreb indices of  $S_d(C_n(k, l))$  are given by:

1.  $M_1(S_d(C_n(k, l))) = 4nd + 8d - 8,$
2.  $M_2(S_d(C_n(1, l))) = \begin{cases} 4nd + 20d - 24 & \text{if } l \in \{2, n\} \\ 4nd + 16d - 16 & \text{if } l \in \{3, \dots, n-1\} \end{cases}.$

**Fig. 7.11** The spiro-chains of  $C_3, C_4, C_6$



**Fig. 7.12** The rooted product of  $H$  by  $G$ ,  $H(G) = H(G_1, G_2, \dots, G_n)$



### 7.5 Zagreb Indices of Rooted Product of Graphs

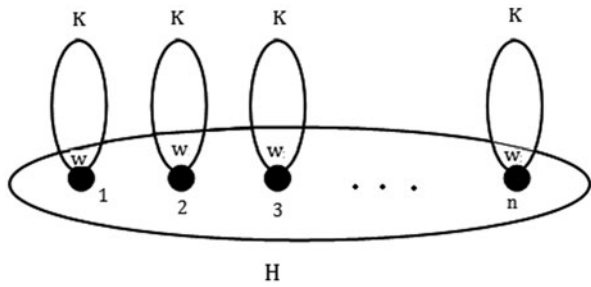
In this section, we compute the first and second Zagreb indices of rooted product of graphs. All of the results of this section have been reported in (Azari and Iranmanesh 2013a). We start this section by definition of the graph of rooted product.

Let  $H$  be a labeled graph on  $n$  vertices with the vertex set  $V(H) = \{1, 2, \dots, n\}$  and let  $G$  be a sequence of  $n$  rooted graphs  $G_1, G_2, \dots, G_n$ . According to (Godsil and McKay 1978), the rooted product of  $H$  by  $G$ , denoted by  $H(G) = H(G_1, G_2, \dots, G_n)$  is the graph obtained by identifying the root vertex of  $G_i$  with the  $i$ -th vertex of  $H$  for all  $i \in \{1, 2, \dots, n\}$ , see Fig. 7.12.

In the special case when the components  $G_i, i \in \{1, 2, \dots, n\}$ , are mutually isomorphic to a graph  $K$ , the rooted product of  $H$  by  $G$  is denoted by  $H\{K\}$  and is called the cluster of  $H$  and  $K$ , see Fig. 7.13. For more information on computing



**Fig. 7.13** The cluster of  $H$  and  $K$ ,  $H\{K\}$



topological indices of clusters see (Yeh and Gutman 1994; Došlić 2008; Azari and Iranmanesh 2013b).

In what follows, we denote the root vertex of  $G_i$  by  $w_i$  and the degree of  $w_i$  in  $G_i$  by  $\omega_i, i \in \{1, 2, \dots, n\}$ .

**Theorem 7.5.1** The first and second Zagreb indices of the rooted product  $H(G)$  are given by:

1.  $M_1(H(G)) = M_1(H) + \sum_{i=1}^n M_1(G_i) + 2 \sum_{i=1}^n \omega_i \deg_H(i),$
2.  $M_2(H(G)) = M_2(H) + \sum_{i=1}^n M_2(G_i) + \sum_{i=1}^n \deg_H(i) \alpha_{G_i}(w_i) + \sum_{ij \in E(H)} [\omega_j \deg_H(i) + \omega_i \deg_H(j) + \omega_i \omega_j].$

*Proof*

1. Using definition of the first Zagreb index, we have:

$$\begin{aligned} M_1(H(G)) &= \sum_{i=1}^n \left\{ [\deg_H(i) + \omega_i]^2 + \sum_{u \in V(G_i) - \{w_i\}} \deg_{G_i}(u)^2 \right\} \\ &= \sum_{i=1}^n \deg_H(i)^2 + \sum_{i=1}^n \left[ \omega_i^2 + \sum_{u \in V(G_i) - \{w_i\}} \deg_{G_i}(u)^2 \right] + 2 \sum_{i=1}^n \omega_i \deg_H(i) \\ &= M_1(H) + \sum_{i=1}^n M_1(G_i) + 2 \sum_{i=1}^n \omega_i \deg_H(i). \end{aligned}$$

2. Using definition of the second Zagreb index, we have:

$$\begin{aligned} M_2(H(G)) &= \sum_{ij \in E(H)} [\deg_H(i) + \omega_i][\deg_H(j) + \omega_j] + \sum_{i=1}^n \left\{ \sum_{uv \in E(G_i); u, v \neq w_i} \deg_{G_i}(u) \deg_{G_i}(v) + \sum_{uv \in E(G_i); u \in V(G_i), v = w_i} \deg_{G_i}(u) [\deg_H(i) + \omega_i] \right\} \\ &= \sum_{ij \in E(H)} \deg_H(i) \deg_H(j) + \sum_{ij \in E(H)} [\omega_j \deg_H(i) + \omega_i \deg_H(j) + \omega_i \omega_j] \end{aligned}$$

$$\begin{aligned}
 & + \sum_{i=1}^n \sum_{uv \in E(G_i)} \deg_{G_i}(u)\deg_{G_i}(v) + \sum_{i=1}^n \deg_H(i) \sum_{u \in N_{G_i}(w_i)} \deg_{G_i}(u) \\
 & = M_2(H) + \sum_{i=1}^n M_2(G_i) + \sum_{i=1}^n \deg_H(i)\alpha_{G_i}(w_i) \\
 & + \sum_{ij \in E(H)} [\omega_j \deg_H(i) + \omega_i \deg_H(j) + \omega_i \omega_j]. \quad \blacksquare
 \end{aligned}$$

Suppose that  $w$  is the root vertex of a rooted graph  $K$ , and let  $G_i = K$  and  $w_i = w$  for all  $i \in \{1, 2, \dots, n\}$ . Using Theorem 7.5.1, we easily arrive at:

**Corollary 7.5.2** The first and second Zagreb indices of the cluster  $H\{K\}$  are given by:

1.  $M_1(H\{K\}) = M_1(H) + nM_1(K) + 4m\omega$ ,
2.  $M_2(H\{K\}) = \omega M_1(H) + M_2(H) + nM_2(K) + m(\omega^2 + 2\alpha_K(w))$ ,

where  $\omega = \deg_K(w)$  and  $m = |E(H)|$ . \blacksquare

Let  $H$  be a labeled graph on  $n$  vertices. Choose a numbering for vertices of  $H$  such that its pendant vertices have numbers  $1, 2, \dots, k$  and its non-pendant vertices have numbers  $k + 1, \dots, n$ . Let  $G$  be a sequence of  $n$  rooted graphs  $G_1, G_2, \dots, G_n$  with  $G_i = K_1$  for  $i \in \{k + 1, k + 2, \dots, n\}$ . Using Theorem 7.5.1, we can easily get the following result.

**Corollary 7.5.3** The first and second Zagreb indices of the rooted product  $H(G) = H(G_1, G_2, \dots, G_k, K_1, K_1, \dots, K_1)$  are given by:

1.  $M_1(H(G)) = M_1(H) + \sum_{i=1}^k M_1(G_i) + 2 \sum_{i=1}^k \omega_i$ ,
2. If  $H \neq P_2$ , then  $M_2(H(G)) = M_2(H) + \sum_{i=1}^k M_2(G_i) + \sum_{i=1}^k \alpha_{G_i}(w_i) + \sum_{i=1}^k \omega_i \alpha_H(i)$ ,  
and  $M_2(P_2(G_1, G_2)) = M_2(G_1) + M_2(G_2) + \alpha_{G_1}(w_1) + \alpha_{G_2}(w_2) + (\omega_1 + 1)(\omega_2 + 1)$ ,

where for  $i \in \{1, 2, \dots, k\}$ ,  $w_i$  denotes the root vertex of  $G_i$  and  $\omega_i$  denotes its degree. \blacksquare

In the following corollary we consider a special case of Corollary 7.5.3, where the components  $G_i, i \in \{1, 2, \dots, k\}$ , are mutually isomorphic to a rooted graph  $K$ .

**Corollary 7.5.4** Let  $H$  be a labeled graph on  $n$  vertices whose pendant vertices have numbers  $1, 2, \dots, k$  and let  $K$  be a rooted graph with the root vertex  $w$ . Suppose  $G$  is a sequence of  $n$  rooted graphs  $G_1, G_2, \dots, G_n$  with  $G_i = K$  for  $i \in \{1, 2, \dots, k\}$ , and  $G_i = K_1$  for  $i \in \{k + 1, k + 2, \dots, n\}$ . Then

1.  $M_1(H(G)) = M_1(H) + kM_1(K) + 2k\omega$ ,
2. If  $H \neq P_2$ , then  $M_2(H(G)) = M_2(H) + k(M_2(K) + \alpha_K(w)) + \omega \sum_{i=1}^k \alpha_H(i)$ ,  
and  $M_2(P_2(G)) = 2M_2(K) + 2\alpha_K(w) + (\omega + 1)^2$ , where  $\omega = \deg_K(w)$ . \blacksquare

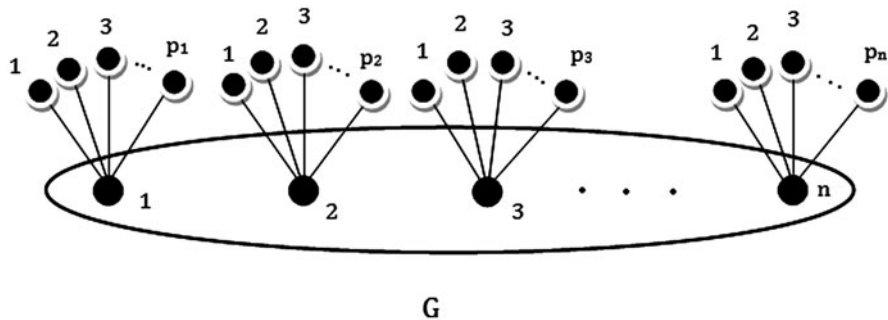


Fig. 7.14 The thorn graph  $G^*(p_1, p_2, \dots, p_n)$

Let  $G$  be a labeled graph on  $n$  vertices and let  $p_1, p_2, \dots, p_n$  be non-negative integers. The thorn graph  $G^*(p_1, p_2, \dots, p_n)$  of the graph  $G$ ,  $i \in \{1, 2, \dots, n\}$ , see Fig. 7.14.

The concept of thorny graphs was introduced in (Gutman 1998) and eventually found a variety of chemical applications (Bytautas et al. 2001; Vukićević and Graovac 2004; Walikar et al. 2006; Heydari and Gutman 2010). The thorn graph  $G^*(p_1, p_2, \dots, p_n)$  can be considered as the rooted product of  $G$  by the sequence  $\{S_{p_1+1}, S_{p_2+1}, \dots, S_{p_n+1}\}$ , where the root vertex of  $S_{p_i+1}$  is assumed to be in the vertex of degree  $p_i, i \in \{1, 2, \dots, n\}$ . So we can apply Theorem 7.5.1 to compute the first and second Zagreb indices of the thorn graph  $G^*(p_1, p_2, \dots, p_n)$ .

**Corollary 7.5.5** The first and second Zagreb indices of the thorn graph  $G^*(p_1, p_2, \dots, p_n)$  are given by:

1.  $M_1(G^*(p_1, p_2, \dots, p_n)) = M_1(G) + \sum_{i=1}^n p_i(p_i + 1) + 2 \sum_{i=1}^n p_i \deg_G(i)$ ,
2. If  $G \neq P_2$  then

$$M_2(G^*(p_1, p_2, \dots, p_n)) = M_2(G) + \sum_{i=1}^n p_i^2 + \sum_{i=1}^n p_i \deg_G(i) + \sum_{ij \in E(G)} [p_j \deg_G(i) + p_i \deg_G(j) + p_i p_j],$$

and  $M_2(P_2^*(p_1, p_2)) = p_1(p_1 + 1) + p_2(p_2 + 1) + (p_1 + 1)(p_2 + 1)$ . ■

**Remark 7.5.6** Let  $\{G_i\}_{i=1}^n$  be a set of finite pairwise disjoint graphs with distinct vertices  $w_i \in V(G_i), i \in \{1, 2, \dots, n\}$ . The bridge graph  $B_1 = B_1(G_1, G_2, \dots, G_n; w_1, w_2, \dots, w_n)$  can be considered as the rooted product of the  $n$ -vertex path  $P_n$  by the sequence  $\{G_1, G_2, \dots, G_n\}$ , where the root vertex of the graph  $G_i$  is assumed to be in the vertex  $w_i, i \in \{1, 2, \dots, n\}$ . So using Theorem 7.5.1, we can reproduce the results of the Theorem 7.2.2 and Theorem 7.2.4.

Now we consider several classes of molecular graphs constructed from rooted product and determine their Zagreb indices.

Our first example is about caterpillar trees. A caterpillar or caterpillar tree is a tree in which all the vertices are within distance one of a central path. If we delete all pendent vertices of a caterpillar tree, we reach to a path. So caterpillars are thorn graphs whose parent graph is a path, see Fig. 7.15.

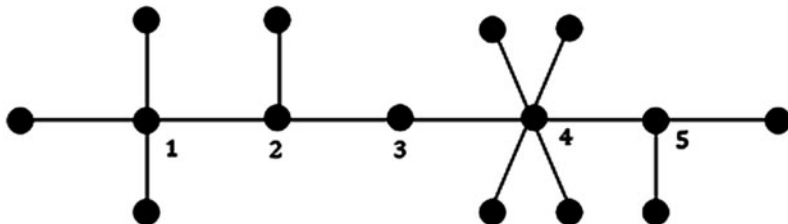


Fig. 7.15 The caterpillar tree  $P_5^*(3,1,0,4,2)$

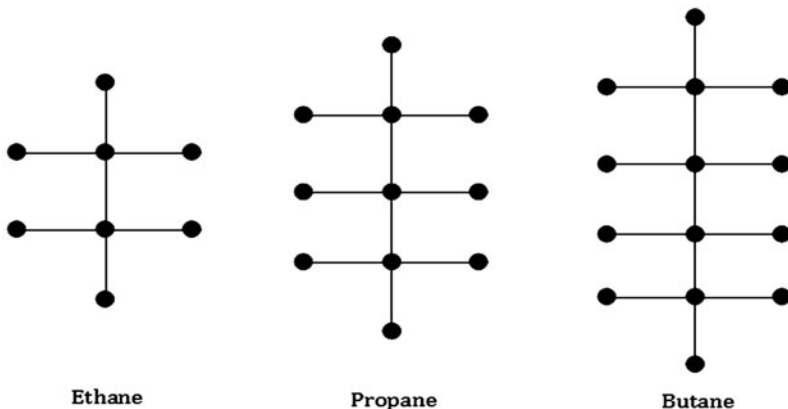


Fig. 7.16 The molecular graphs of Ethane, Propane and Butane

Using Corollary 7.5.5, we can easily get the formulae for the first and second Zagreb indices of caterpillar trees.

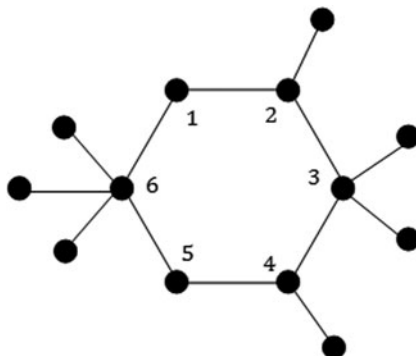
**Corollary 7.5.7** Let  $p_1, p_2, \dots, p_n$  be non-negative integers. The first and second Zagreb indices of the caterpillar tree  $P_n^*(p_1, p_2, \dots, p_n)$  are given by:

1.  $M_1(P_n^*(p_1, p_2, \dots, p_n)) = \sum_{i=1}^n p_i^2 + 5 \sum_{i=1}^n p_i - 2(p_1 + p_n) + 4n - 6, n \geq 2,$
2.  $M_2(P_n^*(p_1, p_2, \dots, p_n)) = \begin{cases} p_1(p_1 + 1) + p_2(p_2 + 1) + (p_1 + 1)(p_2 + 1) & \text{if } n = 2 \\ \sum_{i=1}^n p_i^2 + \sum_{i=1}^{n-1} p_i p_{i+1} + 6 \sum_{i=1}^n p_i & \\ -3(p_1 + p_n) - (p_2 + p_{n-1}) + 4n - 8 & \text{if } n \geq 3. \end{cases}$

■

Caterpillar trees are used in chemical graph theory to represent the structure of benzenoid hydrocarbon molecules. For example, for positive integer  $p \leq 3$ , the caterpillar tree  $P_n^*(p, 2, 2, \dots, 2, p)$  is the molecular graph of certain hydrocarbon. Specially,  $P_2^*(3,3), P_3^*(3,2,3), P_4^*(3,2,2,3)$ , are the molecular graphs of Ethane, Propane and Butane, respectively, see Fig. 7.16.

**Fig. 7.17** The cycle-caterpillar  $C_6^*(0,1,2,1,0,3)$



Using Corollary 7.5.7, we can get the formulae for the first and second Zagreb indices of  $P_n^*(p, 2, 2, \dots, 2, p)$ .

**Corollary 7.5.8** For positive integer  $p \leq 3$ , the first and second Zagreb indices of  $P_n^*(p, 2, 2, \dots, 2, p)$  are given by:

1.  $M_1(P_n^*(p, 2, \dots, 2, p)) = 2p^2 + 6p + 18n - 34$ ,
2.  $M_2(P_n^*(p, 2, \dots, 2, p)) = \begin{cases} 3p^2 + 4p + 1 & \text{if } n = 2 \\ 2p^2 + 10p + 24n - 56 & \text{if } n \geq 3 \end{cases}$ . ■

Specially, for Ethane, Propane and Butane, we easily arrive at:

**Corollary 7.5.9** The first and second Zagreb indices of Ethane, Propane and Butane, are given by:

1.  $M_1(P_2^*(3,3)) = 38, M_1(P_2^*(3,2,3)) = 56, M_1(P_2^*(3,2,2,3)) = 74$ ,
2.  $M_2(P_2^*(3,3)) = 40, M_2(P_2^*(3,2,3)) = 64, M_2(P_2^*(3,2,2,3)) = 88$ . ■

Our second example is about the cycle-caterpillars. A unicyclic graph is called cycle-caterpillar if deleting all its pendent vertices will reduce it to a cycle. So cycle-caterpillars are thorn graphs whose parent graph is a cycle, see Fig. 7.17. Using Corollary 7.5.5, we easily get the following formulae for Zagreb indices of cycle-caterpillars.

**Corollary 7.5.10** Let  $p_1, p_2, \dots, p_n$  be non-negative integers. The first and second Zagreb indices of the cycle-caterpillar  $C_n^*(p_1, p_2, \dots, p_n)$  are given by:

1.  $M_1(C_n^*(p_1, p_2, \dots, p_n)) = \sum_{i=1}^n p_i^2 + 5 \sum_{i=1}^n p_i + 4n$ ,
2.  $M_2(C_n^*(p_1, p_2, \dots, p_n)) = \sum_{i=1}^n p_i^2 + 6 \sum_{i=1}^n p_i + \sum_{i=1}^{n-1} p_i p_{i+1} + p_1 p_n + 4n$ . ■

Our next example is about sunlike graphs and starlike trees. Let  $G$  be a labeled graph on  $n$  vertices with the vertex set  $V(G) = \{1, 2, \dots, n\}$  and let  $k_1, k_2, \dots, k_n$  be positive integers. The sunlike graph  $G(k_1, k_2, \dots, k_n)$  is the graph obtained by identifying the root vertex of  $P_{k_i}$  with the  $i$ -th vertex of  $G$  for all  $i = 1, 2, \dots, n$ , see Fig. 7.18.

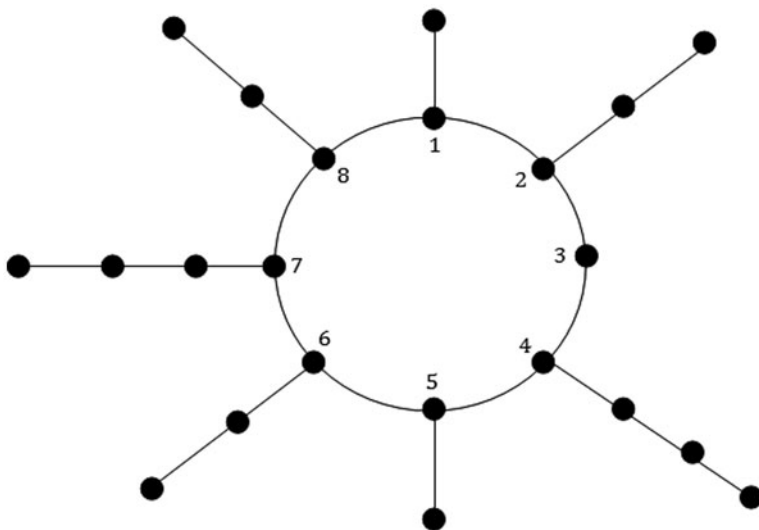


Fig. 7.18 The sunlike graph  $C_8(2,3,1,4,2,3,4,3)$

Note that in the case that  $k_i = 1$ , then  $P_{k_i} = P_1$  is a single vertex graph and for  $k_i > 1$  the root vertex of  $P_{k_i}$  is assumed to be in its pendant vertex. The sunlike graph  $G(k_1, k_2, \dots, k_n)$  can be considered as the rooted product of the graph  $G$  with the sequence  $\{P_{k_1}, P_{k_2}, \dots, P_{k_n}\}$ . So, we can apply Theorem 7.5.1 to compute the first and second Zagreb indices of the sunlike graph  $G(k_1, k_2, \dots, k_n)$ .

**Corollary 7.5.11** Let  $G$  be a labeled graph on  $n$  vertices with the vertex set  $V(G) = \{1, 2, \dots, n\}$  and let  $k_1, k_2, \dots, k_n$  be positive integers. Set  $I_1 = \{i | 1 \leq i \leq n, k_i = 1\}$ ,  $I_2 = \{i | 1 \leq i \leq n, k_i = 2\}$ , and  $I_3 = \{i | 1 \leq i \leq n, k_i \geq 3\}$  and let  $|I_1| = t$ ,  $|I_2| = r$ . The first and second Zagreb indices of the sunlike graph  $G(k_1, k_2, \dots, k_n)$  are given by:

1.  $M_1(G(k_1, k_2, \dots, k_n)) = M_1(G) + 2 \sum_{i \in I_2 \cup I_3} \deg_G(i) + 4 \sum_{i \in I_2 \cup I_3} k_i - 6(n - t)$ ,
2.  $M_2(G(k_1, k_2, \dots, k_n)) = M_2(G) + \sum_{i \in I_2} \deg_G(i) + 2 \sum_{i \in I_3} \deg_G(i) + \sum_{ij \in E(G); i, j \in I_2 \cup I_3} [\deg_G(i) + \deg_G(j) + 1] + \sum_{ij \in E(G); i \in I_1, j \in I_2 \cup I_3} \deg_G(i) + 4 \sum_{i \in I_3} k_i - 8n + 9r + 8t$ . ■

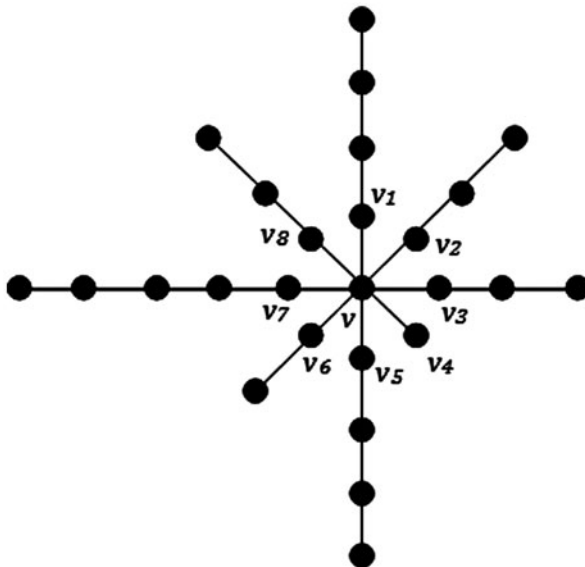
If for all  $1 \leq i \leq n, k_i \geq 2$ , then the formulae of Corollary 7.5.11 can be simplified as follows:

**Corollary 7.5.12** Let  $G$  be a labeled graph on  $n$  vertices and  $m$  edges with the vertex set  $V(G) = \{1, 2, \dots, n\}$  and let  $k_1, k_2, \dots, k_n$  be positive integers with  $k_i \geq 2$  for all  $1 \leq i \leq n$ .

1. The first Zagreb index of the sunlike graph  $G(k_1, k_2, \dots, k_n)$  is given by:

$$M_1(G(k_1, k_2, \dots, k_n)) = M_1(G) + 4 \sum_{i=1}^n k_i + 4m - 6n.$$

**Fig. 7.19** The starlike tree  $S(4,3,3,1,4,2,5,3)$  with vertex  $v$  of degree  $n = 8$



2. Suppose  $I = \{i | 1 \leq i \leq n, k_i = 2\}$  and  $I' = \{i | 1 \leq i \leq n, k_i \geq 3\}$  and let  $|I| = r$ . The second Zagreb index of the sunlike graph  $G(k_1, k_2, \dots, k_n)$  is given by:

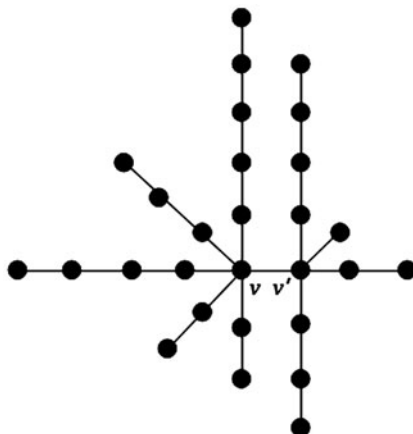
$$M_2(G(k_1, k_2, \dots, k_n)) = M_1(G) + M_2(G) - \sum_{i \in I} \deg_G(i) + 4 \sum_{i \in I'} k_i - 8n + 9r + 5m.$$

If in particular for all  $1 \leq i \leq n, k_i \geq 3$ , then

$$M_2(G(k_1, k_2, \dots, k_n)) = M_1(G) + M_2(G) + 4 \sum_{i=1}^n k_i + 5m - 8n.$$

A starlike tree is a tree with exactly one vertex having degree greater than two. We denote by  $S(k_1, k_2, \dots, k_n)$ , the starlike tree which has a vertex  $v$  of degree  $n \geq 3$  and has the property that  $S(k_1, k_2, \dots, k_n) - v = P_{k_1} \cup P_{k_2} \cup \dots \cup P_{k_n}$ , where  $k_1 \geq k_2 \geq \dots \geq k_n \geq 1$ . Clearly,  $k_1, k_2, \dots, k_n$  determine the starlike tree up to isomorphism and  $S(k_1, k_2, \dots, k_n)$  has exactly  $k_1 + k_2 + \dots + k_n + 1$  vertices. For  $1 \leq i \leq n$ , denote by  $v_i$ , the root vertex of  $P_{k_i}$  attached to the vertex  $v$ , see Fig. 7.19. Clearly, for  $k_i \geq 2$ ,  $\deg_{P_{k_i}}(v_i) = 1$ . Now consider the subtree  $T$  of  $S(k_1, k_2, \dots, k_n)$  with the vertex set  $V(T) = \{v, v_1, v_2, \dots, v_n\}$ . Clearly  $T$  is isomorphic to  $n + 1$ -vertex star,  $S_{n+1}$ . Choose a numbering for vertices of  $T$  such that the vertex  $v_i, 1 \leq i \leq n$ , has number  $i$  and the vertex  $v$  has number  $n + 1$ . So we can consider the starlike tree  $S(k_1, k_2, \dots, k_n)$  as the sunlike graph  $T(k_1, k_2, \dots, k_{n+1})$  where  $k_{n+1} = 1$  and we can apply Corollary 7.5.11 to compute the first and second Zagreb indices of the starlike tree  $S(k_1, k_2, \dots, k_n)$ .

**Fig. 7.20** The double starlike tree  $S(5,3,4,2,2;4,1,2,3)$



**Corollary 7.5.13** Let  $k_1, k_2, \dots, k_n$  be  $n$  positive integers. Set  $I_1 = \{i | 1 \leq i \leq n, k_i = 1\}$ ,  $I_2 = \{i | 1 \leq i \leq n, k_i = 2\}$  and  $I_3 = \{i | 1 \leq i \leq n, k_i \geq 3\}$  and let  $|I_1| = t$ ,  $|I_2| = r$ . The first and second Zagreb indices of the starlike tree  $S(k_1, k_2, \dots, k_n)$  are given by:

1.  $M_1(S(k_1, k_2, \dots, k_n)) = n^2 - 3n + 4t + 4 \sum_{i \in I_2 \cup I_3} k_i$ ,
2.  $M_2(S(k_1, k_2, \dots, k_n)) = 2n^2 - 6n + 8r - t(n - 6) + 4 \sum_{i \in I_3} k_i$ . ■

The starlike tree  $S(k_1, k_2, \dots, k_n)$  is said to be regular, if  $k_1 = k_2 = \dots = k_n = k$ . Clearly  $S(\underbrace{1, 1, \dots, 1}_{n \text{ times}}) = S_{n+1}$ . Using Corollary 7.5.13, we can get the following

formulae for Zagreb indices of regular starlike trees.

**Corollary 7.5.14** Let  $k$  be a positive integer. The first and second Zagreb indices of the regular starlike tree  $S(\underbrace{k, k, \dots, k}_{n \text{ times}})$  are given by:

1.  $M_1(S(\underbrace{k, k, \dots, k}_{n \text{ times}})) = n^2 - 3n + 4nk$ ,
2.  $M_2(S(\underbrace{k, k, \dots, k}_{n \text{ times}})) = \begin{cases} n^2 & \text{if } k = 1 \\ 2n^2 - 6n + 4nk & \text{if } k \geq 2 \end{cases}$ . ■

Let  $S(k_1, k_2, \dots, k_n)$  denote the starlike tree which has a vertex  $v$  of degree greater than two and has the property  $S(k_1, k_2, \dots, k_n) - v = P_{k_1} \cup P_{k_2} \cup \dots \cup P_{k_n}$ . Also let  $S(k'_1, k'_2, \dots, k'_{n'})$  denote the starlike tree which has a vertex  $v'$  of degree greater than two and has the property  $S(k'_1, k'_2, \dots, k'_{n'}) - v' = P_{k'_1} \cup P_{k'_2} \cup \dots \cup P_{k'_{n'}}$ . The graph  $S(k_1, k_2, \dots, k_n; k'_1, k'_2, \dots, k'_{n'})$  obtained by joining the vertex  $v$  of the graph  $S(k_1, k_2, \dots, k_n)$  to the vertex  $v'$  of the graph  $S(k'_1, k'_2, \dots, k'_{n'})$  by an edge is called double starlike tree, see Fig. 7.20. It has exactly two adjacent vertices  $v$  and  $v'$  of degree greater than three and has the property



$$S(k_1, k_2, \dots, k_n; k'_1, k'_2, \dots, k'_{n'}) - \{v, v'\} = P_{k_1} \cup P_{k_2} \cup \dots \cup P_{k_n} \cup P_{k'_1} \cup P_{k'_2} \cup \dots \cup P_{k'_{n'}}.$$

We can consider the double starlike tree  $S(k_1, k_2, \dots, k_n; k'_1, k'_2, \dots, k'_{n'})$ , as the bridge graph  $B_1(S(k_1, k_2, \dots, k_n), S(k'_1, k'_2, \dots, k'_{n'}); v, v')$ . So using Theorems 7.2.2, 7.2.4, and then Corollary 7.5.13, we can easily get the following result.

**Corollary 7.5.15** Let  $\{k_1, k_2, \dots, k_n\}$  and  $\{k'_1, k'_2, \dots, k'_{n'}\}$  be two sequences of positive integers. Set  $I_1 = \{i | 1 \leq i \leq n, k_i = 1\}$ ,  $I_2 = \{i | 1 \leq i \leq n, k_i = 2\}$ ,  $I_3 = \{i | 1 \leq i \leq n, k_i \geq 3\}$ ,  $I'_1 = \{i | 1 \leq i \leq n', k'_i = 1\}$ ,  $I'_2 = \{i | 1 \leq i \leq n', k'_i = 2\}$ , and  $I'_3 = \{i | 1 \leq i \leq n', k'_i \geq 3\}$ . Also let  $|I_1| = t, |I_2| = r, |I'_1| = t'$ , and  $|I'_2| = r'$ . The first and second Zagreb indices of the double starlike tree  $S(k_1, k_2, \dots, k_n; k'_1, k'_2, \dots, k'_{n'})$  are given by:

1.  $M_1(S(k_1, k_2, \dots, k_n; k'_1, k'_2, \dots, k'_{n'})) = 4 \left( \sum_{i \in I_2 \cup I_3} k_i + \sum_{i \in I'_2 \cup I'_3} k'_i \right) + n(n-1) + n'(n'-1) + 4(t+t') + 2,$
2.  $M_2(S(k_1, k_2, \dots, k_n; k'_1, k'_2, \dots, k'_{n'})) = 4 \left( \sum_{i \in I_3} k_i + \sum_{i \in I'_3} k'_i \right) + n(2n-t-3) + n'(2n'-t'-3) + 8(r+r') + 5(t+t') + nn' + 1.$  ■

If  $n = n'$  and  $k_i = k'_i$  for  $1 \leq i \leq n$ , then the double starlike tree  $S(k_1, k_2, \dots, k_n; k_1, k_2, \dots, k_n)$  is called symmetric double starlike. Using Corollary 7.5.15, we get the following formulae for the first and second Zagreb indices of symmetric double starlike trees.

**Corollary 7.5.16** Let  $k_1, k_2, \dots, k_n$  be positive integers. Set  $I_1 = \{i | 1 \leq i \leq n, k_i = 1\}$ ,  $I_2 = \{i | 1 \leq i \leq n, k_i = 2\}$ , and  $I_3 = \{i | 1 \leq i \leq n, k_i \geq 3\}$  and let  $|I_1| = t, |I_2| = r$ . The first and second Zagreb indices of the symmetric double starlike tree  $S(k_1, k_2, \dots, k_n; k_1, k_2, \dots, k_n)$  are given by:

1.  $M_1(S(k_1, k_2, \dots, k_n; k_1, k_2, \dots, k_n)) = 8 \sum_{i \in I_2 \cup I_3} k_i + 2n(n-1) + 8t + 2,$
2.  $M_2(S(k_1, k_2, \dots, k_n; k_1, k_2, \dots, k_n)) = 8 \sum_{i \in I_3} k_i + 5n^2 - 2n(t+3) + 16r + 10t + 1.$  ■

Now, we consider generalized Bethe trees. The level of a vertex in a rooted tree is one more than its distance from the root vertex. A generalized Bethe tree of  $k$  levels,  $k > 1$  is a rooted tree in which vertices at the same level have the same degree (Rojo 2007).

Let  $B_k$  be a generalized Bethe tree of  $k$  levels. For  $i \in \{1, 2, \dots, k\}$ , we denote by  $d_{k-i+1}$  and  $n_{k-i+1}$  the degree of the vertices at the level  $i$  of  $B_k$  and their number, respectively. Also, suppose  $e_k = d_k$  and  $e_i = d_i - 1$  for  $i \in \{1, 2, \dots, k-1\}$ . Thus,  $d_1 = 1$  is the degree of the vertices at the level  $k$  (pendent vertices) and  $d_k$  is the degree of the root vertex. On the other hand,  $n_k = 1$  is pertaining to the single vertex at the first level, the root vertex. For  $i \in \{1, 2, \dots, k-1\}$ , suppose  $\beta_{k-i+1}$  denotes the subtree of  $B_k$  which is also a generalized Bethe tree of  $k-i+1$  levels and its root is any vertex of the level  $i$  of  $B_k$ , as shown in Fig. 7.21 and let  $\beta_1 = K_1$ . Now consider the subtree of  $\beta_{k-i+1}, i \in \{1, 2, \dots, k-1\}$ , which is isomorphic to the star graph

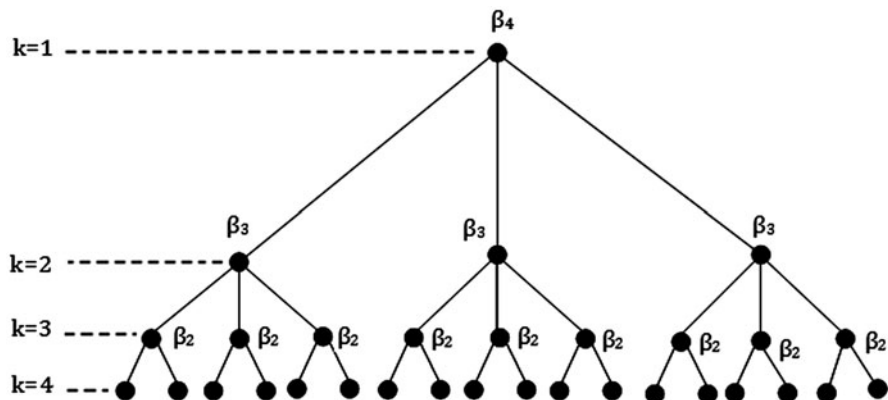


Fig. 7.21 A generalized Bethe tree of 4 levels with its subtrees  $\beta_2, \beta_3, \beta_4$

$S_{e_{k-i+1}+1}$  and choose a numbering for its vertices such that its  $e_{k-i+1}$  pendant vertices have numbers  $1, \dots, e_{k-i+1}$  and its vertex of degree  $e_{k-i+1}$  has number  $e_{k-i+1} + 1$ . We can consider the generalized Bethe tree  $\beta_{k-i+1}, i \in \{1, 2, \dots, k-1\}$  as the rooted product of  $S_{e_{k-i+1}+1}$  by the sequence  $\underbrace{\{\beta_{k-i}, \dots, \beta_{k-i}, K_1\}}_{e_{k-i+1} \text{ times}}$ , i.e.,

$$\beta_{k-i+1} = S_{e_{k-i+1}+1} \underbrace{\{\beta_{k-i}, \dots, \beta_{k-i}, K_1\}}_{e_{k-i+1} \text{ times}}, i \in \{1, 2, \dots, k-1\}.$$

Clearly,  $\beta_2 = S_{e_2} + 1, \beta_k = B_k$ .

So using Corollary 7.5.4, we can get the following recurrence relations for the first and second Zagreb indices of the generalized Bethe tree  $\beta_{k-i+1}, i \in \{1, 2, \dots, k-1\}$ .

**Corollary 7.5.17** The first and second Zagreb indices of the generalized Bethe tree  $\beta_{k-i+1}, i \in \{1, 2, \dots, k-1\}$ , are given by:

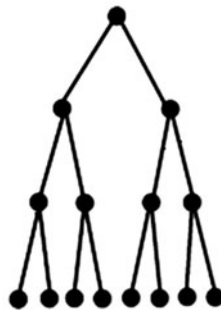
1.  $M_1(\beta_1) = 0, M_1(\beta_{k-i+1}) = e_{k-i+1}M_1(\beta_{k-i}) + e_{k-i+1}(e_{k-i+1} + 2e_{k-i} + 1), 1 \leq i \leq k-1,$
2.  $M_2(\beta_2) = e_2^2, M_2(\beta_{k-i+1}) = e_{k-i+1}M_2(\beta_{k-i}) + e_{k-i+1}^2d_{k-i} + e_{k-i+1}e_{k-i}d_{k-i-1}, 1 \leq i \leq k-2. \blacksquare$

Note that the formulae of Corollary 7.3.11 hold for all  $1 \leq i \leq k-1$ . So using Corollary 7.5.17, we can get the following explicit relations for computing the first and second Zagreb indices of the generalized Bethe tree  $B_k$ .

**Corollary 7.5.18** The first and second Zagreb indices of the generalized Bethe tree  $B_k$  are given by:

1.  $M_1(B_k) = \sum_{i=1}^k d_i^2 \prod_{j=i+1}^k e_j,$
2.  $M_2(B_k) = \sum_{i=1}^{k-1} e_{i+1}d_{i+1}d_i \prod_{j=i+2}^k e_j.$

**Fig. 7.22** The ordinary Bethe tree  $B_{2,4}$



The ordinary Bethe tree  $B_{d,k}$  is a rooted tree of  $k$  levels whose root vertex has degree  $d$ , the vertices from levels 2 to  $k - 1$  have degree  $d + 1$ , and the vertices at level  $k$  have degree 1, see Fig. 7.22.

Note that  $B_{1,k} = P_k$  and  $B_{d,2} = S_{d+1}$ . Using Corollary 7.5.18, we get the following relations for computing the first and second Zagreb indices of ordinary Bethe tree  $B_{d,k}$ .

**Corollary 7.5.19** The first and second Zagreb indices of the ordinary Bethe tree  $B_{d,k}$  are given by:

1.  $M_1(B_{d,k}) = d^2 + d^{k-1} + d(d + 1)^2 \sum_{s=0}^{k-3} d^s,$
2.  $M_2(B_{d,k}) = \begin{cases} d^2 & \text{if } k = 2 \\ 2d^2(d + 1) \sum_{s=0}^{k-3} d^s & \text{if } k \geq 3 \end{cases} .$  ■

Denote by  $C(d, k, n)$ , the unicyclic graph obtained by attaching the root vertex of  $B_{d,k}$  to the vertices of  $n$ -vertex cycle  $C_n$ , see Fig. 7.23. For more information about this graph, see (Rojo 2007).

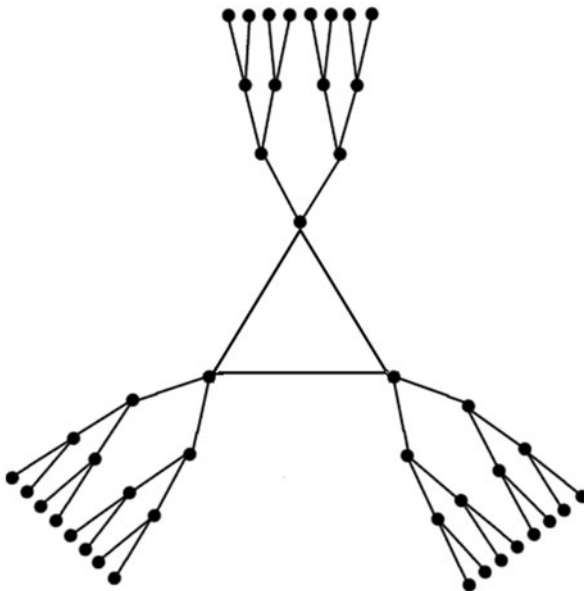
It is easy to see that  $C(d, k, n)$  is the cluster of  $C_n$  and  $B_{d,k}$ . So we can apply Corollary 7.5.2 and then Corollary 7.5.19, to get the formulae for the first and second Zagreb indices of  $C(d, k, n)$ .

**Corollary 7.5.20** The first and second Zagreb indices of  $C(d, k, n)$  are given by:

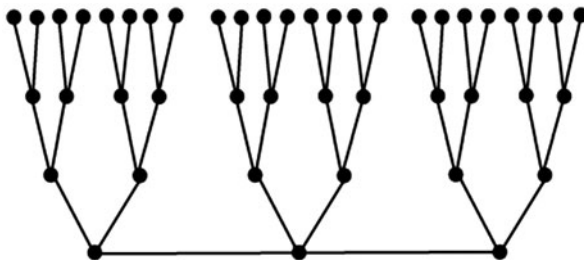
1.  $M_1(C(d, k, n)) = 4n(d + 1) + nd^2 + nd^{k-1} + nd(d + 1)^2 \sum_{s=0}^{k-3} d^s,$
2.  $M_2(C(d, k, n)) = \begin{cases} 2n(d^2 + 3d + 2) & \text{if } k = 2 \\ n(3d^2 + 6d + 4) + 2nd^2(d + 1) \sum_{s=0}^{k-3} d^s & \text{if } k \geq 3 \end{cases} .$  ■

Denote by  $P(d, k, n)$ , the tree obtained by attaching the root vertex of  $B_{d,k}$  to the vertices of  $n$ -vertex path  $P_n$ , see Fig. 7.24. For more information about this class of trees, see (Robbiano et al. 2008). The graph  $P(d, k, n)$  can be considered as the bridge graph  $B_1(B_{d,k}, B_{d,k}, \dots, B_{d,k}; w, w, \dots, w)$ , where  $w$  denotes the root vertex

**Fig. 7.23** The unicyclic graph  $C(2,4,3)$



**Fig. 7.24** The tree  $P(2,4,3)$



of  $B_{d,k}$ . So we can apply the Corollaries 7.2.3 and 7.2.5 and then Corollary 7.5.19, to get the formulae for the first and second Zagreb indices of the tree  $P(d,k,n)$ .

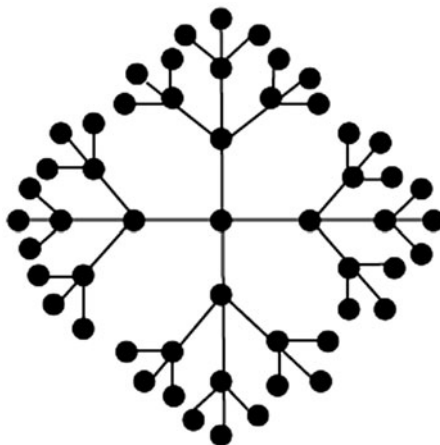
**Corollary 7.5.21** The first and second Zagreb indices of  $P(d,k,n)$  are given by:

1.  $M_1(P(d,k,n)) = 4d(n-1) + 4n - 6 + nd^2 + nd^{k-1} + nd(d+1)^2 \sum_{s=0}^{k-3} d^s,$
2.  $M_2(P(d,k,2)) = 3d^2 + 4d + 1 + 4d^2(d+1) \sum_{s=0}^{k-3} d^s,$  and

$$M_2(P(d,k,n)) = \begin{cases} (2n-1)d^2 + 6nd + 4n - 8d - 8 & \text{if } k = 2 \\ 3(n-1)(d+1)^2 + n - 2d - 5 + 2nd^2(d+1) \sum_{s=0}^{k-3} d^s & \text{if } k \geq 3 \end{cases} \blacksquare$$

Our last examples are about dendrimer trees and a class of dendrimer graphs. Dendrimers are hyperbranched molecules, synthesized by repeatable steps, either by

**Fig. 7.25** The dendrimer tree  $T_{4,3}$



adding branching blocks around a central core (thus obtaining a new, larger orbit or generation—the “divergent growth” approach) or by building large branched blocks starting from the periphery and then attaching them to the core (Diudea 1995). Details on dendrimers, an important and recently much studied class of nano-materials, and especially on their topological properties can be found in (Diudea 2006; Diudea and Nagy 2007; Iranmanesh and Gholami 2009; Iranmanesh and Dorosti 2011) and the references quoted therein.

A dendrimer tree  $T_{d,k}$  is a rooted tree such that the degree of its non-pendent vertices is equal to  $d$  and the distance between the rooted (central) vertex and the pendent vertices is equal to  $k$  (Dobrynin et al. 2001), see Fig. 7.25. So  $T_{d,k}$  can be considered as a generalized Bethe tree with  $k+1$  levels, such that whose non-pendent vertices have equal degrees. Note that  $T_{2,k} = P_{2k+1}$  and  $T_{d,1} = S_{d+1}$ . Using Corollary 7.5.18, we get the following relations for Zagreb indices of the dendrimer tree  $T_{d,k}$ .

**Corollary 7.5.22** The first and second Zagreb indices of the dendrimer tree  $T_{d,k}$  are given by:

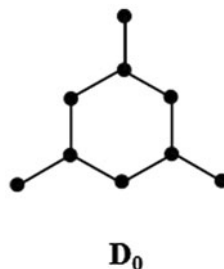
1.  $M_1(T_{d,k}) = d^2 + d(d-1)^{k-1} + d^3 \sum_{s=0}^{k-2} (d-1)^s,$
2.  $M_2(T_{d,k}) = d^2(d-1)^{k-1} + d^3 \sum_{s=0}^{k-2} (d-1)^s.$

Now we introduce a class of dendrimers for which Corollary 7.5.4 is applicable. This molecular structure can be seen in some of the dendrimer graphs such as tertiary phosphine dendrimers. Let  $D_0$  be the graph of Fig. 7.26.

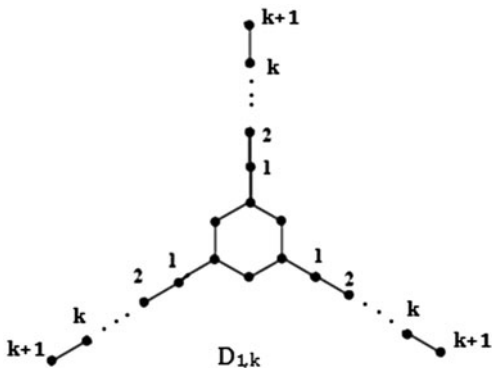
For positive integers  $d$  and  $k$ , suppose  $D_{d,k}$  be a series of dendrimer graphs obtained by attaching  $d$  pendent vertices to each pendent vertex of  $D_{d,k-1}$  and set  $D_{d,0} = D_0$ . Some examples of this class of dendrimer graphs are shown in Figs. 7.27 and 7.28.

It is easy to check that,  $M_1(D_0) = 42$  and  $M_2(D_0) = 45$ . Choose a numbering for vertices of  $D_0$  such that its pendant vertices have numbers 1, 2, 3 and its non-pendant

**Fig. 7.26** The dendrimer graph  $D_0$

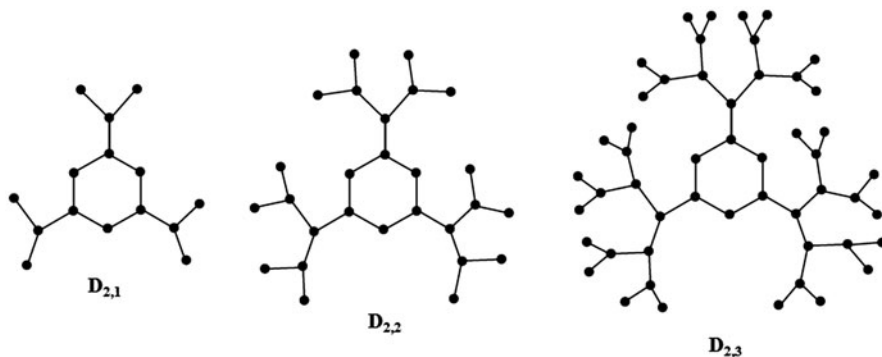


**Fig. 7.27** The dendrimer graph  $D_{1,k}$



vertices have numbers  $4, 5, \dots, 9$ . It is easy to see that,  $D_{d,k}$  is the rooted product of  $D_0$  by the sequence  $\{B_{d,k+1}, B_{d,k+1}, B_{d,k+1}, \underbrace{K_1, K_1, \dots, K_1}_{6 \text{ times}}\}$ . So by Corollary 7.5.4, we can get the following relations for the first and second Zagreb indices of the dendrimer graph  $D_{d,k}, k \geq 1$ ,

**Corollary 7.5.23** The first and second Zagreb indices of the dendrimer graph  $D_{d,k}, k \geq 1$ , are given by:



**Fig. 7.28** The dendrimer graphs  $D_{d,k}$ , for  $d = 2, k = 1, 2, 3$

1.  $M_1(D_{d,k}) = 42 + 3d(d + 3) \sum_{s=0}^{k-1} d^s$ ,
2.  $M_2(D_{d,k}) = 3d^2 + 12d + 45 + 6d^2(d + 1) \sum_{s=0}^{k-2} d^s$ . ■

**Acknowledgment** This work was partially supported by Center of Excellence of Algebraic Hyperstructures and its Applications of Tarbiat Modares University (CEAHA).

## References

- Arezoomand M, Taeri B (2013) MATCH Commun Math Comput Chem 69:131
- Ashrafi AR, Hamzeh A, Hosseinzadeh S (2011) J Appl Math Inf 29:327
- Azari M, Iranmanesh A (2011a) Studia Univ Babes-Bolyai Chemia 3:59
- Azari M, Iranmanesh A (2011b) Ars Combin 100:113
- Azari M, Iranmanesh A (2013a) MATCH Commun Math Comput Chem 70(3):901
- Azari M, Iranmanesh A (2013b) Discrete Appl Math 161(18):2827
- Azari M, Iranmanesh A, Tehranian A (2010) Studia Univ Babes-Bolyai Chemia 4:183
- Azari M, Iranmanesh A, Tehranian A (2012) Util Math 87:151
- Azari M, Iranmanesh A, Gutman I (2013) MATCH Commun Math Comput Chem 70(3):921
- Bytautas L, Bonchev D, Klein DJ (2001) MATCH Commun Math Comput Chem 44:31
- Das KC, Gutman I (2004) MATCH Commun Math Comput Chem 52:103
- Diudea MV (1995) MATCH Commun Math Comput Chem 32:71
- Diudea MV (ed.) (2006) Nanostructures: Novel Architecture. Nova, New York
- Diudea MV, Nagy CL (2007) Periodic nanostructures. Springer, Amsterdam
- Dobrynin AA, Entringer R, Gutman I (2001) Acta Appl Math 66:211
- Došlić, T (2008) Ars Math Contemp 1:66
- Eliasi M, Iranmanesh A (2013) MATCH Commun Math Comput Chem 69(1):111
- Eliasi M, Iranmanesh A, Gutman I (2012) MATCH Commun Math Comput Chem 68(1):217
- Godsil CD, McKay BD (1978) Bull Austral Math Soc 18:21
- Gutman I (1998) Publ Inst Math (Beograd) 63:31
- Gutman I, Polansky OE (1986) Mathematical concepts in organic chemistry. Springer, Berlin
- Gutman I, Trinajstić N (1972) Chem Phys Lett 17:535
- Gutman I, Ruscic B, Trinajstić N, Wilcox CF (1975) J Chem Phys 62:3399
- Heydari A, Gutman I (2010) Kragujevac J Sci 32:57
- Iranmanesh A, Dorosti N (2011) MATCH Commun Math Comput Chem 65(1):209
- Iranmanesh A, Gholami NA (2009) MATCH Commun Math Comput Chem 62(2):371
- Khalifeh MH, Yousefi-Azari H, Ashrafi AR (2009) Discrete Appl Math 157:804
- Nikolić S, Kovačević G, Miličević A, Trinajstić N (2003) Croat Chem Acta 76:113
- Réti T (2012) MATCH Commun Math Comput Chem 68:169
- Robbiano M, Gutman I, Jimenez R, San Martin B (2008) Bull Acad Serbe Sci Arts (Cl Sci Math Natur) 137:59
- Rojo O (2007) Lin Algebra Appl 420:490
- Sagan BE, Yeh YN, Zhang P (1996) Inter J Quantum Chem 60(5):959
- Stevanović D, Milanič M (2012) MATCH Commun Math Comput Chem 68:147
- Todeschini R, Consonni V (2000) Handbook of molecular descriptors. Wiley-VCH, Weinheim
- Trinajstić N (1992) Chemical graph theory. CRC Press, Boca Raton
- Vukičević D, Graovac A (2004) MATCH Commun Math Comput Chem 50:93
- Walikar HB, Ramane HS, Sindagi L, Shirakol SS, Gutman I (2006) Kragujevac J Sci 28:47
- Yan W, Yang BY, Yeh YN (2007) Appl Math Lett 20:290
- Yeh YN, Gutman I (1994) Discrete Math 135:359
- Zhou B (2004) MATCH Commun Math Comput Chem 52:113

# Chapter 8

## Exotic Allotropes of Carbon

Mircea V. Diudea, Beata Szefer, Csaba L. Nagy and Attila Bende

**Abstract** Carbon allotropes, including triple-, double-, and single periodic, and finite non-periodic, nanostructures have been designed by using map operations and their topological and energetic properties studied. Two allotropes of the diamond  $D_5$  are discussed in this chapter: the dense hyper-diamond, with an “anti”-diamantane structure, and a quasi-diamond, which is a five-fold symmetry quasicrystal with “syn”-diamantane structure. Some substructures of these allotropes are proposed as possible intermediates in the synthesis of some hyper-graphenes and their energetics evaluated at Hartree-Fock, DFT (B3LYP) and DFTB levels of theory. A topological description of  $D_5$ -anti network and derived hyper-graphenes, in terms of the net parameter and Omega polynomial, is also given.

### 8.1 Introduction

Nano-era, a period starting since 1985 with the discovery of the  $C_{60}$  fullerene, is marked by the scientific effort in finding novel applications, generically termed nanotechnology. Among the carbon structures, fullerenes (zero-dimensional), nanotubes (one dimensional), graphenes (two dimensional), diamonds and spongy nanostructures (three dimensional) were the most studied. Inorganic compounds also attracted the attention of scientists. Recent articles in crystallography promoted the idea of topological description and classification of crystal structures (Blatov et al. 2004, 2007, 2009; Delgado-Friedrichs and O’Keeffe 2005).

---

M. V. Diudea (✉) · C. L. Nagy

Faculty of Chemistry and Chemical Engineering, Babes-Bolyai University,  
Arany Janos street 11, 400028 Cluj-Napoca, Romania  
e-mail: diudea@chem.ubbcluj.ro

B. Szefer

Department of Physical Chemistry, Collegium Medicum, Nicolaus Copernicus University,  
Kurpińskiego 5, 85-950, Bydgoszcz, Poland

A. Bende

Molecular and Biomolecular Physics Department, National Institute for R&D  
of Isotopic and Molecular Technologies, Donath Street No. 65-103, 400293  
Cluj-Napoca, Romania  
e-mail: bende@itim-cj.ro

© Springer Science+Business Media Dordrecht 2015

M. V. Putz, O. Ori (eds.), *Exotic Properties of Carbon Nanomatter*,

Carbon Materials: Chemistry and Physics, DOI 10.1007/978-94-017-9567-8\_8



A crystal structure (Fig. 8.1, right-bottom corner), with pentagon/hexagon rings, of which 90 % pentagons, we call diamond  $D_5$ , is known as the clathrate II structure, or the *mtn* triple periodic, 3-nodal net, of point symbol net:  $\{5^5.6\}12\{5^6\}5$  and  $2[5^{12}]$ ;  $[5^{12}.6^4]$  tiling and belonging to the space group:  $Fd-3m$ . The clathrate II structure is also encountered silica synthetic zeolite ZSM-39 (Adams et al. 1994; Meier and Olson 1992; Böhme et al. 2007) and in germanium allotrope Ge(*cF*136) (Guloy et al. 2006; Schwarz et al. 2008) as real substances.

Four allotropes of the yet hypothetical diamond  $D_5$  have been discussed in ref (Nagy and Diudea 2013): a spongy net, a dense hyper-diamond  $D_5$ , with an “anti”-diamantane structure, the corresponding hyper-lonsdaleite and a quasi-diamond which is a five-fold symmetry quasicrystal with “syn”-diamantane structure. In this chapter, we will limit to the dense anti- $D_5$  and syn/quasi- $D_5$  and to some new “hyper-graphenes” conceived on the ground of the quasi-diamond, bringing new computational arguments in the favor of these new and exotic allotropes of carbon.

## 8.2 Allotropes of $D_5$

Substructures of  $D_5$  are related to the “seed”  $C_{17}$ . It can dimerize (probably by a cycloaddition reaction) to  $C_{34}$  (Fig. 8.1), a  $C_{20}$  derivative bearing  $2 \times 3$  pentagonal wings in the opposite polar disposition. Since this dimer is in fact the repeating unit of a triple-periodic structure, Benedek called this *fcc*- $C_{34}$ -network (*i.e.* face-centered cubic lattice—Benedek and Colombo 1996). The dimer can further form more complex substructures, such as adamantane-like Ada, diamantane-like Dia, and five-fold stars (see Fig. 8.1 and below).

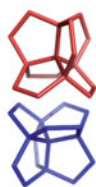
Energetic data (at the DFTB level of theory) for the structures in Fig. 8.1 are listed in Table 8.1.

The  $D_5\_ada$  units can self-arrange in the net of diamond  $D_5$  (Fig. 8.1). The network can be achieved starting either from  $C_{20}$  or  $C_{28}$  cages, so that pairs of substructures:  $D_5\_20\_ada\_156/ada\_28\_213$ ,  $D_5\_20\_dia\_226/D_5\_28\_dia\_292$ , etc. can be designed.

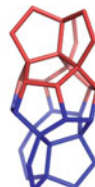
Domains of this diamond network, namely  $D_5\_20\_333\_860$  and  $D_5\_28\_333\_1022$  were optimized at the DFTB level of theory (Elstner et al. 1998). Hydrogen atoms were added to the external carbon atoms of the network structures in order to keep the charge neutrality and the  $sp^3$  character of the C-C bonds at the network surface. Energetically stable geometries were obtained in both cases. Identification of the equivalent carbon atoms in the neighboring units of the  $3 \times 3 \times 3$  super-cell along the main symmetry axes, envisaged a well-defined triclinic lattice, with the following parameters:  $a = b = c = 6.79 \text{ \AA}$ , and  $\alpha = 60^\circ$ ,  $\beta = 120^\circ$ ,  $\gamma = 120^\circ$ , even the most symmetrical structure is the *fcc*-one. Density of the  $D_5$  network was calculated to be around  $2.8 \text{ g/cm}^3$ .

Analyzing the C-C bond distances in these carbon networks, the values vary in a very narrow distance domain of  $1.50\text{--}1.58 \text{ \AA}$ , suggesting all carbon atoms are  $sp^3$  hybridized. Considering the one-electron energy levels of the HOMO and LUMO,

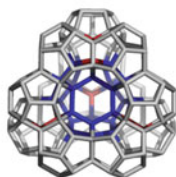
**Fig. 8.1** Diamond  $D_5$  and some of its substructures/allotropes



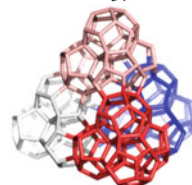
$2 \times C_{17}$



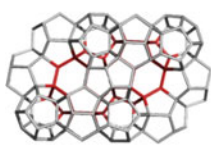
$C_{34}$



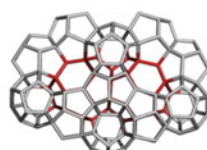
$D_5\_ada\_158$



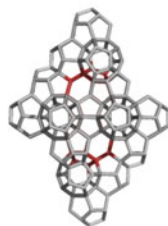
$D_5\_ada\_198$



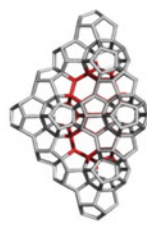
$D_5\_dia\_anti\_226$



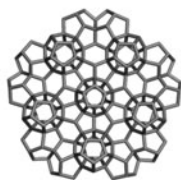
$D_5\_dia\_syn\_226$



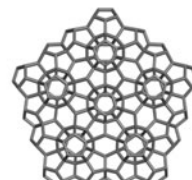
$D_5\_dia\_anti\_306$



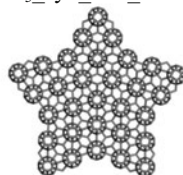
$D_5\_dia\_syn\_270$



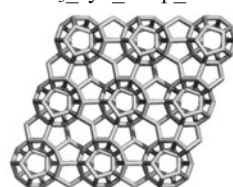
$D_5\_syn\_521\_315$



$D_5\_syn\_521p\_355$



$D_5\_syn\_531s\_1185$



$D_5\_20\_333\_860$

**Table 8.1** Energetic data (DFTB level of theory) for the Diamond  $D_5$  substructures in Fig. 8.1, (as hydrogenated species); reference structure was taken  $C_{60}H_{60}$ 

Structure	No C	$E_{tot}$ (au)	$E_{tot}/C$ (au)	GAP (eV)
$D_5\_ada\_156H_{84}$	156	- 305.340	- 1.957	8.812
$D_5\_ada\_198H_{100}$	198	- 380.717	1.923	8.725
$D_5\_dia\_anti\_226H_{108}$	226	- 432.311	- 1.913	8.584
$D_5\_dia\_syn\_226H_{108}$	226	- 432.264	- 1.913	8.514
$D_5\_dia\_anti\_306H_{140}$	306	- 583.049	- 1.905	8.482
$D_5\_dia\_syn\_270H_{122}$	270	- 513.845	- 1.903	8.448
$D_5\_521\_315H_{150}$	315	- 602.141	- 1.912	8.355
$D_5\_syn\_521p\_355H_{160}$	355	- 675.246	- 1.902	8.305
$D_5\_20\_333\_860H_{276}$	860	- 1595.702	- 1.855	8.055
$D_5\_531s\_1185H_{510}$	1185	- 2244.77	- 1.894	8.051
$C_{60}H_{60}$	60	- 125.584	- 2.093	10.412

**Table 8.2** Topological description of diamond  $D_5\_anti$  function of  $k$  ( $k = 1, 2, \dots$  the number of  $ada\_20$  units along the edge of a  $(k,k,k)$  triclinical domain

Formulas
$v(D_5\_anti) = -22 - 12k + 34k^3$
$Atoms(sp^3) = -10 - 36k^2 + 34k^3$
$Ring[5] = -18 - 6k - 18k^2 + 36k^3$
$Ring[6] = -1 + 6k - 9k^2 + 4k^3$
$R[5] + R[6] = -19 - 27k^2 + 40k^3$
$\lim_{k \rightarrow \infty} \frac{R[5]}{R[5]+R[6]} = 9/10$

a large energy gap could be observed for both  $D_5\_20\_860$  net ( $E_{HOMO} = -5.96$  eV,  $E_{LUMO} = +2.10$  eV,  $\Delta E_{HOMO-LUMO} = 8.06$  eV) and  $D_5\_28\_1022$  co-net ( $E_{HOMO} = -6.06$  eV,  $E_{LUMO} = +2.45$  eV,  $\Delta E_{HOMO-LUMO} = 8.51$  eV) structures, which indicates an insulating behavior for this carbon network.

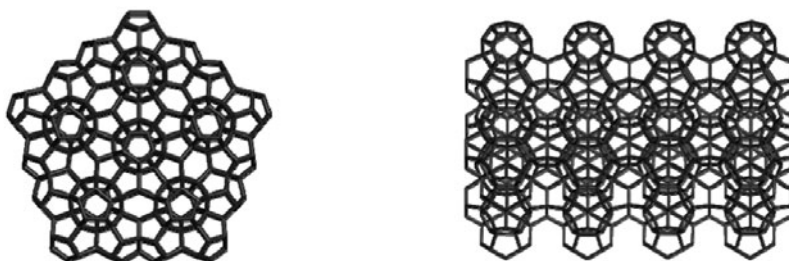
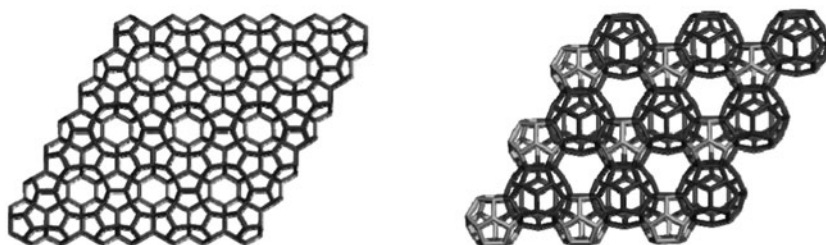
Structural stability of substructures related to the  $D_5$  diamond was evaluated both in static and dynamic temperature conditions by molecular dynamics MD (Kyani and Diudea 2012, Szeffler and Diudea 2012). Results show that  $C_{17}$  is the most temperature resistant fragment.

Topology of the diamond  $D_5\_anti$ , in a triclinical domain  $(k,k,k)$  (see Fig. 8.1) is presented in Table 8.2: formulas to calculate the number of atoms, number of rings  $R$  and the limits (at infinity) for the ratio  $R_5$ /all Rings are given function of  $k$  (i.e., the number of repeating units in the domain).

Considering the hexagons as the “window-faces” in the  $C_{28}$  hollows, we can evaluate the genus of the  $D_5$  net according to the theorem (Diudea and Szeffler 2012): In spongy structures, built up from  $u$  tube junction units, of genus  $g_u$ , the genus is calculated as:  $g = u(g_u - 1) + 1$ , irrespective of the unit tessellation. Data are given in Table 8.3.

**Table 8.3** Genus calculation in Diamond D5 substructures

Hollow structure	v	e	$g = 1 + u(g_u - 1)$	$g_u$	u
$(C_{20})_{12}C_{28\_ada\_158}$	158	274	3	1.5	4
$(C_{20})_{18}(C_{28})_2\_dia\_syn\_226$	226	398	5	2;1.5	3 + 2
$(C_{20})_{18}(C_{28})_2\_dia\_anti\_226$	226	398	5	1.5	8

**Fig. 8.2**  $D_5\_syn\_524\_1330$ —top view (*left*),  $D_5\_syn\_524\_1330$ —side view (*right*)**Fig. 8.3** “Exfoliation” of the hypothetical diamond  $D_5$  leading to hyper-graphenes:  $C_{20}Hex\_333\_506$  (a planar pure hexagonal  $C_{20}$  hyper-graphene—*left*);  $(C_{20}C_{28})Hex\_331\_327$  (a sheet of alternating  $C_{20}/C_{28}$  armchair hyper-hexagonal units—*right*)

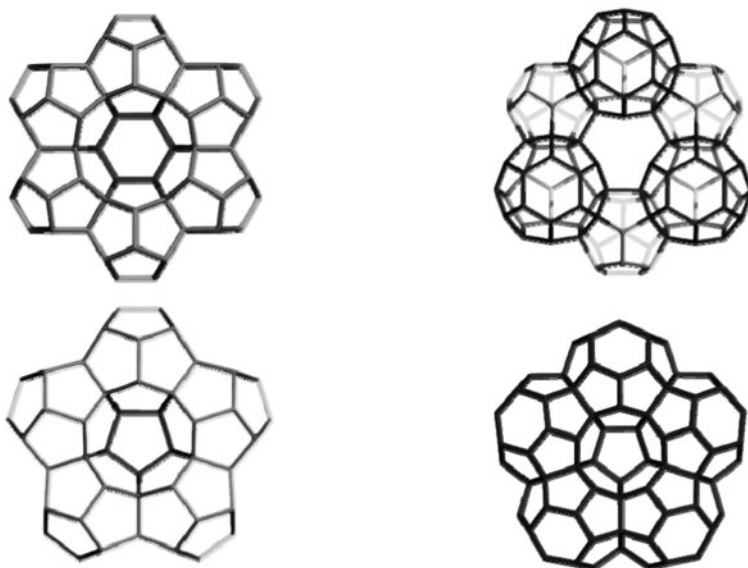
The quasi-diamond  $D_5\_syn$  can form a 1-periodic quasicrystal, *e.g.*  $D_5syn\_52n$ , of Amm2 space group; point symbol for net  $\{5^2.6\}6\{5^3\}4\{5^4.6.8\}5\{5^5.6\}7\{5^6\}3$ ; 12-nodal net 3,4-c (Fig. 8.2).

### 8.3 $D_5$ Substructures as Hyper-Graphenes

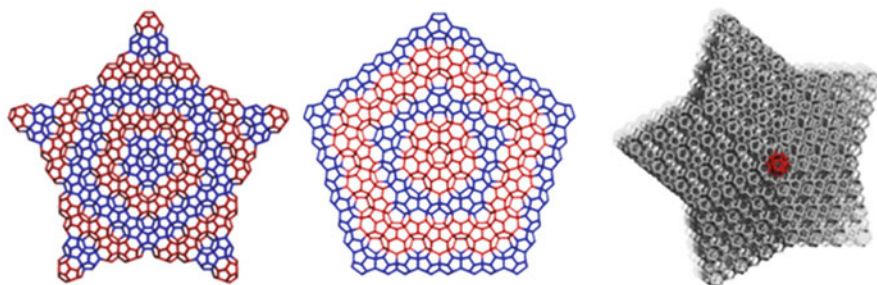
The small fullerenes  $C_{20}$  and  $C_{28}$ , filling the space in the frame of  $D_5$  can provide, by “exfoliation”, hyper-graphenes (Diudea MV, 2013), either as single-cages (Fig. 8.3, left) or mixed ones (Fig. 8.3, right).

The corresponding substructures of the hyper-graphenes in Fig. 8.3 are illustrated in Fig. 8.4 (top row).

Alternating  $C_{20}/C_{28}$  hyper-graphene domains with five-fold symmetry (Fig. 8.5) can result by sectioning a quasi-crystal (Fig. 8.5, right) by an electron beam (Diudea



**Fig. 8.4** Substructures of  $C_{20}/C_{28}$  hyper-graphenes; *Top row*:  $(C_{20})_{6\_90}$  (*right*);  $(C_{20}C_{28})_{3\_114}$  (*right*). *Bottom row*:  $(C_{20})_{5\_75}$  (*left*);  $(C_{28})_{5\_110}$  (*left*)



**Fig. 8.5** Five-fold symmetry hyper-graphene domains:  $C_{20}$ -centered ( $D_{5\_2028\_561s\_1345}$ , *left*);  $C_{28}$ -centered ( $D_{5\_2820\_541\_1170}$ , *middle*) and a  $D_5$ -quasicrystal ( $D_{5\_2028\_544s\_8160}$ , *right*)

MV 2013). Pentagonal hyper-rings appearing in the core of these stars are illustrated in Fig. 8.4, bottom.

Data for the above proposed hyper-graphenes are collected in Table 8.4. Data for some small fullerenes and corresponding 5-fold and 6-fold hyper-cycles are presented in Table 8.5.

A hyper-graphene could be conceived to appear when a thin layer of  $C_{60}$  is deposited on a (plane) surface. The polymerization process can start with  $[2 + 2]$

**Table 8.4** Energetic data (DFTB) for some C<sub>20</sub>-based hyper-graphenes HG (reference C<sub>60</sub>H<sub>60</sub>)

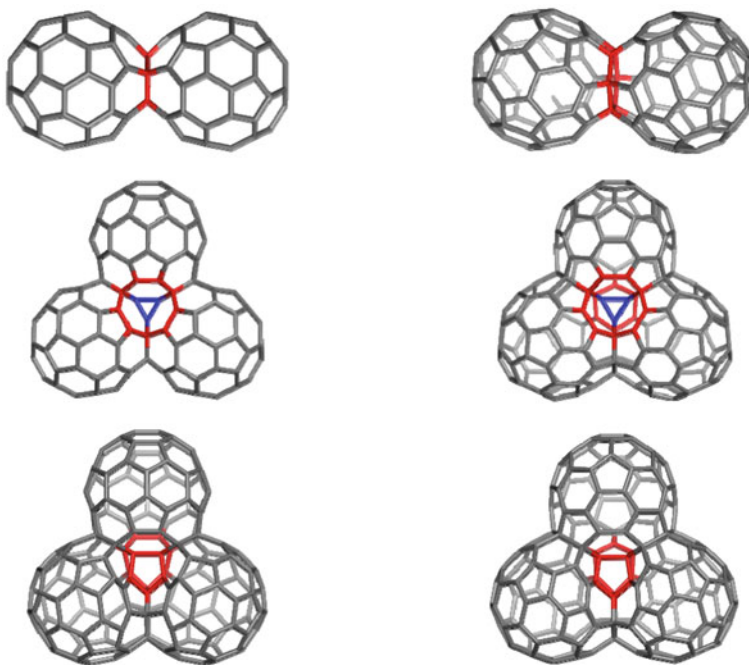
C <sub>20</sub> _hyper-graphene	C atoms	E <sub>tot</sub> (au)	E <sub>tot</sub> /C (au)	Gap (eV)
C <sub>20</sub> HG_11_90H <sub>60</sub> i.e. (C <sub>20</sub> ) <sub>6</sub> _90H <sub>60</sub>	90	- 178.393	- 1.982	8.992
C <sub>20</sub> HG_22_252H <sub>136</sub>	252	- 487.798	- 1.936	8.447
C <sub>20</sub> HG_44_780H <sub>360</sub>	780	- 1487.55	- 1.907	8.191
C <sub>20</sub> HGCor_621_384H <sub>192</sub>	384	- 737.736	- 1.921	8.307
C <sub>20</sub> HGCor_631_882H <sub>396</sub>	882	- 1678.02	- 1.903	8.155
C <sub>60</sub> H <sub>60</sub>	60	- 125.584	- 2.093	10.412

**Table 8.5** Energetic data (DFTB) for some small fullerenes and hyper-cycles

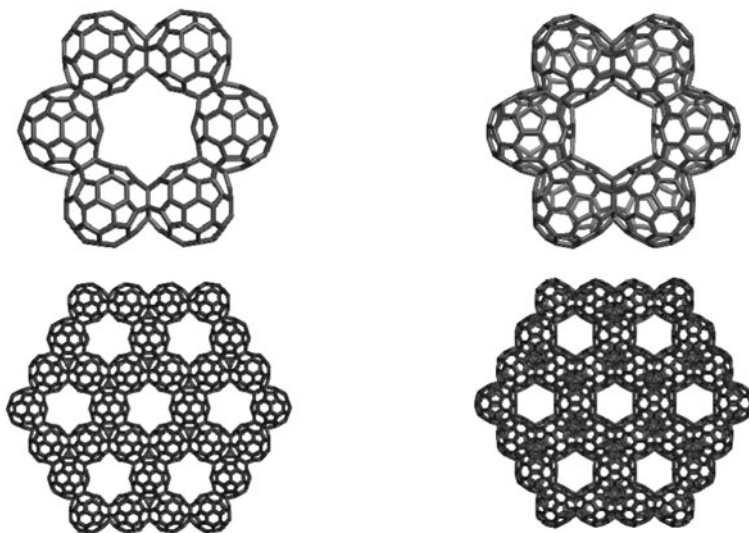
C <sub>20</sub> _hyper-graphene	C atoms	E <sub>tot</sub> (au)	E <sub>tot</sub> /C (au)	Gap (eV)
C <sub>60</sub>	60	- 102.185	- 1.703	1.930
C <sub>20</sub>	20	- 33.429	- 1.671	0.731
C <sub>24</sub>	24	- 40.142	- 1.673	1.667
C <sub>28</sub>	28	- 47.101	- 1.682	0.351
(C <sub>24</sub> ) <sub>5</sub> _90	90	- 152.998	- 1.700	1.634
(C <sub>20</sub> C <sub>28</sub> ) <sub>3</sub> _114	114	- 192.488	- 1.688	0.166
(C <sub>20</sub> ) <sub>5</sub> _75H <sub>50</sub>	75	- 146.956	- 1.959	9.969
(C <sub>24</sub> ) <sub>5</sub> _90H <sub>60</sub>	90	- 175.282	- 1.948	9.103
(C <sub>28</sub> ) <sub>5</sub> _110H <sub>80</sub>	110	- 220.185	- 2.002	9.270
(C <sub>20</sub> ) <sub>6</sub> _90H <sub>60</sub>	90	- 178.393	- 1.982	8.992
(C <sub>20</sub> C <sub>28</sub> ) <sub>3</sub> _114H <sub>84</sub>	114	- 226.346	- 1.985	10.278
C <sub>60</sub> H <sub>60</sub>	60	- 125.584	- 2.093	10.412
C <sub>20</sub> H <sub>20</sub>	20	- 41.659	- 2.083	12.295
C <sub>24</sub> H <sub>24</sub>	24	- 49.752	- 2.073	12.247
C <sub>28</sub> H <sub>28</sub>	28	- 58.301	- 2.082	12.384

cyclo-adducts but this is just the beginning of a more complex process that involves the coalescence of quasi-spherical units of C<sub>60</sub> to form oligomers and finally a polymer (see Figs. 8.6 and 8.7); Table 8.6 supports this idea.

Let us detail the structures participating to such a process. Two dimers with joint face for C<sub>60</sub> units can be designed (Fig. 8.6, top): C<sub>60</sub>P2J5\_115 (J5 meaning a pentagon identification) and C<sub>60</sub>P2J6\_114 (J6 representing a hexagon identification). These two dimers have the total energy per C atoms comparable to C<sub>60</sub>; the HOMO-LUMO gap of “J5”- dimer is larger than that of “J6”-dimer (even “J5” dimer has no Kekulé structures).



**Fig. 8.6**  $C_{60}$  oligomers. *Top row:*  $C_{60}P2J5_{115}$  (left) and  $C_{60}P2J6_{114}$  (right); *Middle row:*  $C_{60}P3J555_{165}$  (left) and  $C_{60}P3J666_{162}$  (right); *Bottom row:*  $C_{60}P3J556_{164}$  (left) and  $C_{60}P3J566_{163}$  (right)



**Fig. 8.7** Hyper-graphenes. *Top row:*  $\text{Hex}(C_{60}J5)_{330}$  (left);  $\text{Hex}(C_{60}J6)_{324}$ ; *Bottom row:*  $(\text{Le}(\text{Cor}(C_{20}))_{1560})$  (left);  $\text{Cor}(C_{60})_{1512}$  (right)



**Table 8.6** Energetic data (DFTB level of theory) for the C<sub>60</sub> oligomers

Structure	C atoms	E <sub>tot</sub> (au)	E <sub>tot</sub> /C	Gap(eV)
C <sub>60</sub>	60	-102.185	-1.703	1.930
C <sub>60</sub> P2J5_115	115	-195.708	-1.702	2.044
C <sub>60</sub> P2J6_114	114	-194.183	-1.703	1.444
C <sub>60</sub> P3J555_165	165	-280.787	-1.702	0.608
C <sub>60</sub> P3J556_164	164	-281.658	-1.717	0.333
C <sub>60</sub> P3_J566_163	163	-280.238	-1.719	0.391
C <sub>60</sub> P3J666_162	163	-278.935	-1.722	1.481
HypHex_165_330	330	-567.506	-1.710	0.179
HypHex_162_324	324	-557.737	-1.721	1.255
Le(Cor(C <sub>20</sub> ))_165_1560	1560	-2652.462	-1.700	0.021
Cor(C <sub>60</sub> )_162_1512	1512	-2603.270	-1.722	1.095

Next, among the four trimers (Fig. 8.6, middle and bottom) the most stable (see the total energy per carbon atom and gap values in Table x.5) appears to be C<sub>60</sub>P3J666\_162. The two highly distorted trimers (C<sub>60</sub>P3J556\_164 and C<sub>60</sub>P3J566\_163) are less stable and further will not be considered.

The “J555” trimer C<sub>60</sub>P3J555\_165 shows a lower gap probably because no Kekulé structure can be written. This could be not an argument since the “J5”-dimer also does not admit a Kekulé structure. At higher structures (see Fig. 8.6) the Kekulé structures are possible for the both J-type polymers and the J6-type joining appear the most stable. Is no matter which one of the oligomers will be formed, the hyper-graphene has a good chance to exist as areal structure. Note the hyper-graphene Le(Cor(C<sub>20</sub>))\_165\_1560 was designed by applying the leapfrog *Le* map operation (Diudea et al. 2006) on the coronene-like structure made from the C<sub>20</sub> smallest fullerene.

Comparative computations we made on small structures (see Table 8.7). One can see that, in general, the ordering in the three approaches is preserved, of course with some exceptions. The main drawback of DFTB is the underestimation of the gap values in case of *sp*<sup>2</sup> carbon-only structures (see Table 8.7). However, DFTB is useful in ordering series of rather large carbon nanostructures.

## 8.4 Omega Polynomial in Nanostructures

Let  $G(V, E)$  be a connected bipartite graph, with the vertex set  $V(G)$  and edge set  $E(G)$ . Two edges  $e = (x, y)$  and  $f = (u, v)$  of  $G$  are *codistant* (briefly: *e co f*) if

$$d(x, v) = d(x, u) + 1 = d(y, v) + 1 = d(y, u)$$



**Table 8.7** Comparative data for some small structures involved in hyper-graphenes at Hartree-Fock HF, DFT (B3LYP) and DFTB levels of theory

Structure	C atoms	Theory	$E_{\text{tot}}$ (au)	$E_{\text{tot}}/C$ (au)	Gap (eV)
C <sub>20</sub> _Cy5J5_75	75	HF	- 2838.062	- 37.841	4.158
C <sub>20</sub> _Cy6J5_90	90		- 3405.751	- 37.842	5.990
C <sub>28</sub> _Cy5J6_110	110		- 4163.361	- 37.849	5.533
C <sub>28</sub> _Cy6J6_132	132		- 4996.056	- 37.849	5.421
C <sub>60</sub> _HF	60		- 2271.830	- 37.864	7.418
C <sub>60</sub> P2J5_115	115		- 4354.333	- 37.864	7.597
C <sub>60</sub> P2J6_114	114		- 4316.491	- 37.864	6.270
C <sub>20</sub> _Cy5J5_75	75	DFT	- 2856.161	- 38.082	0.600
C <sub>20</sub> _Cy6J5_90	90		- 3427.462	- 38.083	0.900
C <sub>28</sub> _Cy5J6_110	110		- 4189.837	- 38.089	1.072
C <sub>28</sub> _Cy6J6_132	132		- 5027.845	- 38.090	1.059
C <sub>60</sub> _DFT	60		- 2286.174	- 38.103	2.760
C <sub>60</sub> P2J5_115	115		- 4381.797	- 38.103	2.907
C <sub>60</sub> P2J6_114	114		- 4343.730	- 38.103	1.908
C <sub>20</sub> _Cy5J5_75	75	DFTB	- 126.324	- 1.684	0.113
C <sub>20</sub> _Cy6J5_90	90		- 151.694	- 1.684	0.195
C <sub>28</sub> _Cy5J6_110	110		- 185.928	- 1.690	0.006
C <sub>28</sub> _Cy6J6_132	132		- 223.166	- 1.691	0.035
C <sub>60</sub> _DFTB	60		- 102.185	- 1.703	1.930
C <sub>60</sub> P2J5_115	115		- 195.708	- 1.702	2.044
C <sub>60</sub> P2J6_114	114		- 194.183	- 1.703	1.444

For some edges of a connected graph  $G$  there are the following relations satisfied (John et al. 2007):

$$e \text{ co } e$$

$$e \text{ co } f \Leftrightarrow f \text{ co } e$$

$$e \text{ co } f \& f \text{ co } h \Rightarrow e \text{ co } h$$

though the relation (11) is not always valid.

Let  $C(e) := \{f \in E(G); f \text{ co } e\}$  denote the set of edges in  $G$ , codistant to the edge  $e \in E(G)$ . If relation  $co$  is an equivalence relation (i.e.,  $C(e)$  obeys (4) to (6)), then  $G$  is called a *co-graph*. Consequently,  $C(e)$  is called an *orthogonal cut oc* of  $G$  and  $E(G)$  is the union of disjoint orthogonal cuts:  $C_1 \cup C_2 \cup \dots \cup C_k$  and  $C_i \cap C_j = \emptyset$  for  $i \neq j, i, j = 1, 2, \dots, k$ . Observe  $co$  is a  $\Theta$  relation, (Djoković 1973; Klavžar 2008; Winkler 1984).

A *quasi-orthogonal cut qoc* with respect to a given edge is the smallest subset of edges closed under taking opposite edges on faces. Since the transitivity relation (11) of the *co* relation is not necessarily obeyed, *qoc* represents a new concept within the cut methods. Any *oc* strip is a *qoc* strip but the reverse is not always true.

Let  $m(G, c)$  be the number of *qoc* strips of length  $c$  (i.e., the number of cut-off edges); for the sake of simplicity,  $m(G, c)$  can be written as  $m$ . The Omega polynomial is defined on the ground of *qoc* strips (Diudea 2006, 2010a–2010c; Diudea et al. 2008, 2011; Diudea and Ilić 2010; Diudea and Klavžar 2010):

$$\Omega(G, x) = \sum_c m(G, c) \cdot x^c$$

Its first derivative (in  $x = 1$ ) equals the number of edges in the graph:

$$\Omega'(G, 1) = \sum_c m \cdot c = e = |E(G)|$$

On Omega polynomial, the Cluj-Ilmenau<sup>32</sup> index,  $CI = CI(G)$ , was defined:

$$CI(G) = \{[\Omega'(G, 1)]^2 - [\Omega'(G, 1) + \Omega''(G, 1)]\}$$

It is easily seen that, for a single *qoc*, one calculates the polynomial:  $\Omega(G, x) = 1 \times x^c$  and the index  $CI(G) = c^2 - (c + c(c - 1)) = c^2 - c^2 = 0$ .

In tree graphs, the Omega polynomial simply counts the non-opposite edges, being included in the term of exponent  $c = 1$ . The coefficient of the term of exponent  $c = 1$  has found utility as a topological index, called  $n_p$ , the number of *pentagon fusions*, appearing in small fullerenes as a destabilizing factor. This index accounts for more than 90% of the variance in heat of formation HF of fullerenes  $C_{40}$  and  $C_{50}$ .<sup>38</sup>

Topology of diamond  $D_5$  in a cubic  $(k, k, k)$  domain, is presented in Tables 8.8, 8.9, 8.10, and 8.11 (see also Diudea et al. 2011). Formula to calculate Omega polynomial, number of atoms, number of rings and the limits (to infinity) for the ratio of  $sp^3$  C atoms over total number of atoms and also the ratio R[5] over the total number of rings as well as numerical examples are given. Tables 8.12, 8.13, 8.14, 8.15, 8.16, 8.17, 8.18, and 8.19 provides data for the topological analysis of  $C_{20}$ - and  $C_{60}$ -based hyper-graphenes.

## 8.5 Computational Methods

Geometry optimizations were performed at the at SCC-DFTB level of theory (Elstner et al. 1998) by using the DFTB + program (DFTB 2013; Aradi et al. 2007) with the numerical conjugated gradient method. We used this method because many structures have more than 100 atoms (or more than 1500 atoms).

The DFTB method can be combined with the self-consistent charge technique (SCC-DFTB) to provide more accurate results, comparable with some higher level theoretical methods.

**Table 8.8** Omega polynomial in diamond D<sub>5</sub>\_C<sub>20</sub> net function of  $k = \text{no. ada}_{C_{20}}$  units along the edge of a cubic  $(k, k, k)$  domain

	Omega(D <sub>5</sub> C <sub>20a</sub> ); R[6]; Formulas
1	$\Omega(D_5C_{20a}, x) = (32 - 54k + 36k^2 + 44k^3) \cdot x + (-3 + 18k - 27k^2 + 12k^3) \cdot x^2$
2	$\Omega'(1) = e(G) = -38 - 18k - 18k^2 + 68k^3$
3	$CI(G) = 1488 + 1350k + 1764k^2 - 4612k^3 - 2124k^4 - 2448k^5 + 4624k^6$
4	$v(D_5C_{20a}) = -22 - 12k + 34k^3$
5	$Atoms(sp^3) = -10 - 36k^2 + 34k^3$
6	$R[5] = -18 - 6k - 18k^2 + 36k^3$
7	$R[6] = -1 + 6k - 9k^2 + 4k^3$
8	$R[5] + R[6] = -19 - 27k^2 + 40k^3$
9	$\lim_{k \rightarrow \infty} \frac{R[5]}{R[6]} = 9; \lim_{k \rightarrow \infty} \frac{R[5]}{R[5]+R[6]} = 9/10$
10	$\lim_{k \rightarrow \infty} \left[ \frac{Atoms(sp^3)}{v(G)} = \frac{-10-36k^2+34k^3}{-22-12k+34k^3} = \frac{-\frac{10}{k^3} - \frac{36}{k} + 34}{-\frac{22}{k^3} - \frac{12}{k^2} + 34} \right] = 1$

**Table 8.9** Examples, Omega polynomial in the D<sub>5</sub>\_C<sub>20</sub> net

k	Omega (D <sub>5</sub> C <sub>20a</sub> ); R[6]	Atoms	sp <sup>3</sup> atoms (%)	Bonds	CI	R[5]	R[6]
2	$356x^1 + 21x^2$	226	118 (52.21)	398	157,964	186	7
3	$1318x^1 + 132x^2$	860	584 (67.91)	1582	2,500,878	774	44
4	$3144x^1 + 405x^2$	2106	1590 (75.50)	3954	15,629,352	1974	135
5	$6098x^1 + 912x^2$	4168	3340 (80.13)	7922	62,748,338	4002	304
6	$10,444x^1 + 1725x^2$	7250	6038 (83.28)	13,894	193,025,892	7074	575
7	$16,446x^1 + 2916x^2$	11,556	9888 (85.57)	22,278	496,281,174	11,406	972

**Table 8.10** Omega polynomial in D<sub>5</sub>\_C<sub>28</sub> co-net function of  $k = \text{no. ada}_{C_{20}}$  units along the edge of a cubic  $(k, k, k)$  domain

	Omega (D <sub>5</sub> C <sub>28a</sub> ); R[6]; Formulas
1	$\Omega(D_5C_{28a}, x) = (-26 - 12k - 6k^2 + 44k^3) \cdot x + (-18 + 9k^2 + 12k^3) \cdot x^2$
2	$\Omega'(1) = e(G) = -62 - 12k + 12k^2 + 68k^3$
3	$CI(G) = 3942 + 1500k - 1374k^2 - 8812k^3 - 1488k^4 + 1632k^5 + 4624k^6$
4	$v(D_5C_{28a}) = -40 - 6k + 18k^2 + 34k^3$
5	$Atoms(sp^3) = -4 - 6k - 30k^2 + 34k^3$
6	$R[5] = -18 - 18k^2 + 36k^3$
7	$R[6] = -1 + 6k - 9k^2 + 4k^3$
8	$\lim_{k \rightarrow \infty} \left[ \frac{Atoms(sp^3)}{v(G)} = \frac{-4-6k-30k^2+34k^3}{-40-6k+18k^2+34k^3} \right] = 1$

**Table 8.11** Examples, Omega polynomial in  $D_5C_{28}$  co-net

k	Omega ( $D_5C_{28a}$ ); R[6]	Atoms	sp <sup>3</sup> atoms (%)	Bonds	CI	R[5]	R[6]
2	$278x^1 + 114x^2$	292	136 (46.58)	506	255,302	198	38
3	$1072x^1 + 387x^2$	1022	626 (61.25)	1846	3,405,096	792	129
4	$2646x^1 + 894x^2$	2400	1668 (69.50)	4434	19,654,134	1998	298
5	$5264x^1 + 1707x^2$	4630	3466 (74.86)	8678	75,295,592	4032	569
6	$9190x^1 + 2898x^2$	7916	6224 (78.63)	14,986	224,559,414	7110	966
7	$14,688x^1 + 4539x^2$	12,462	10,146 (81.41)	23,766	564,789,912	11,448	1513

**Table 8.12** Omega polynomial in the  $C_{20}$ -based hypergraphene

	Omega( $D_5C_{20}HG$ ); R[6]: Formulas
1	$\Omega(D_5C_{20}HG) = (56k^2 + 100k - 12) \cdot x + 3k^2 \cdot x^2$
2	$\Omega'(1) = e(G) = 62k^2 + 100k - 12$
3	$CI(G) = 3844k^4 + 12400k^3 + 8444k^2 - 2500k + 156$
4	$v(D_5C_{20}HG) = 34k^2 + 60k - 4$
5	$R[5] = 30k^2 + 44k - 8$
6	$R[6] = k^2$
7	$No(C_{20}) = 3k^2 + 4k - 1$

**Table 8.13** Omega polynomial in the  $C_{60}$ -based hypergraphene

	Omega( $C_{60}Le(C_{20}HG)$ ); R[6]: Formulas
1	$\Omega(C_{60}Le(C_{20}HG)) = (36k^2 + 80k + 10) \cdot x^3 + (24k^2 + 20k - 20) \cdot x^5 + k^2 \cdot x^{12}$
2	$\Omega'(1) = e(G) = 240k^2 + 340k - 70$
3	$CI(G) = 57600k^4 + 163200k^3 + 80932k^2 - 48820k + 5310$
4	$v(C_{60}Le(C_{20}HG)) = 150k^2 + 220k - 40$
5	$Hyp[6] = k^2$
6	$R[3] = 2(k^2 - 1)$
7	$R[5] = 30k^2 + 44k - 8$
8	$R[6] = 60k^2 + 80k - 20$
9	$No(C_{60}) = (R[6])/20 = 3k^2 + 4k - 1$

Computations at a higher level of theory Hartree-Fock and DFT have been performed with the HF/6–31G(d, p) and B3LYP/6–31G(d, p) sets, on Gaussian 09 (Gaussian 09, 2009).

Topological data were calculated by our Nano Studio software (Nagy and Diudea 2009).

**Table 8.14** Examples, Omega polynomial in  $C_{20}$ -based hyper-graphene: R[6]

k	Omega ( $D_5C_{20}HG$ ); R[6]	CI	Atoms	Bonds	F[5]	F[6]
1	$144x + 3x^2$	22,344	90	150	66	1
2	$412x + 12x^2$	189,636	252	436	200	4
3	$792x + 27x^2$	714,816	482	846	394	9
4	$1284x + 48x^2$	1,902,924	780	1380	648	16
5	$1888x + 75x^2$	4,151,256	1146	2038	962	25

**Table 8.15** Examples, Omega polynomial in  $C_{60}$ -based hyper-graphene: R[6]

k	Omega ( $C_{60}Le(C_{20}HG)$ ); R[6]	CI	Atoms	Bonds	F[3]	F[5]	F[6]
1	$126x^3 + 24x^5 + 1x^{12}$	258,222	330	510	0	66	120
2	$314x^3 + 116x^5 + 4x^{12}$	2,458,598	1000	1570	6	200	380
3	$574x^3 + 256x^5 + 9x^{12}$	9,659,238	1970	3110	16	394	760
4	$906x^3 + 444x^5 + 16x^{12}$	26,295,342	3240	5130	30	648	1260

**Table 8.16** Omega polynomial in the  $C_{60}$ -based hypergraphene: R[6]

	Omega( $C_{60}J6HG$ ); R[6]: Formulas
1	$\Omega(C_{60}J6HG); R[6] = (36k^2 + 96k + 12) \cdot x^3 + (12k^2 + 12k - 6) \cdot x^4 + 2(k^2 - 1) \cdot x^{12} + 2(k^2 - 1) \cdot x^{27}$
2	$\Omega'(1) = e(G) = 234k^2 + 336k - 66$
3	$CI(G) = 54756k^4 + 157248k^3 + 79746k^2 - 45408k + 6090$
4	$v(C_{60}J6HG) = 144k^2 + 216k - 36$
5	$Hyp[6] = k^2$
6	$F[3] = R[3] = 2(k^2 - 1)$
7	$F[5] = R[5] = 36k^2 + 48k - 12$
8	$F[6] = 54k^2 + 76k - 16$
9	$No(C_{60}) = (F[5])/12 = 3k^2 + 4k - 1$

**Table 8.17** Examples, Omega polynomial in  $C_{60}$ -based hyper-graphene: R[6]

k	Omega ( $C_{60}J6HG$ ); R[6]:	CI	Atoms	Bonds	F[3]	F[5]	F[6]
1	$144x^3 + 18x^4$	252,432	324	504	0	72	114
2	$348x^3 + 66x^4 + 6x^{12} + 6x^{27}$	2,368,338	972	1542	6	228	352
3	$624x^3 + 138x^4 + 16x^{12} + 16x^{27}$	9,268,512	1908	3048	16	456	698
4	$972x^3 + 234x^4 + 30x^{12} + 30x^{27}$	25,181,802	3132	5022	30	756	1152

**Table 8.18** Omega polynomial in the C<sub>60</sub>-based hypergraphene: F[6]

	Omega(C <sub>60</sub> J6HG); F[6]: Formulas
1	$\Omega(C_{60}J6HG); F[6] = (54k^2 + 96k - 6) \cdot x^3 + (18k^2 + 12k - 12) \cdot x^4$
2	$\Omega'(1) = e(G) = 234k^2 + 336k - 66$
3	$CI(G) = 54756k^4 + 157248k^3 + 81234k^2 - 45408k + 4602$
4	$v(C_{60}J6HG) = 144k^2 + 216k - 36$
5	$Hyp[6] = k^2$
6	$F[3] = R[3] = 2(k^2 - 1)$
7	$R[5] = F[5] = 36k^2 + 48k - 12$
8	$F[6] = 54k^2 + 76k - 16$
9	$No(C_{60}) = (F[5])/12 = 3k^2 + 4k - 1$

**Table 8.19** Examples, Omega polynomial in C<sub>60</sub>-based hyper-graphene: F[6]

k	Omega(C <sub>60</sub> J6HG); F[6]	CI	Atoms	Bonds	F[3]	F[5]	F[6]
1	$144 x^3 + 18 x^4$	252,432	330	510	0	72	114
2	$402 x^3 + 84 x^4$	2,372,802	1000	1570	6	228	352
3	$768 x^3 + 186 x^4$	9,280,416	1970	3110	16	456	698
4	$1242 x^3 + 324 x^4$	25,204,122	3240	5130	30	756	1152

## 8.6 Conclusions

In this chapter we presented two allotropes of the diamond D<sub>5</sub>: the dense “anti”-diamond and the “syn”/quasi-diamond, which can form five-fold symmetry quasi-crystals. Some substructures of these allotropes are proposed as possible intermediates in the synthesis of hyper-graphenes and their energetics evaluated at Hartree-Fock, DFT (B3LYP) and DFTB levels of theory. A topological description of D<sub>5</sub>-anti network and derived hyper-graphenes, in terms of the net parameter and Omega polynomial, was also given.

**Acknowledgements** MVD acknowledges the financial support offered by project PN-II-ID-PCE-2011-3-0346. BSZ acknowledges the Grant no. 133 of PCSS (Poznań, Poland). Thanks are addressed to Professor Davide Proserpio, Università degli Studi di Milano, Italy, for crystallographic data.

## References

- Adams GB, O’Keeffe M, Demkov AA, Sankey OF, Huang Y-M (1994) Wide-band-gap Si in open fourfold-coordinated clathrate structures. *Phys Rev B* 49(12):8048–8053
- Aradi B, Hourahine B, Frauenheim T (2007) DFTB +, a sparse matrix-based implementation of the DFTB method. *J Phys Chem A* 111:5678–5684
- Benedek G, Colombo L (1996) Hollow diamonds from fullerenes. *Mater Sci Forum* 232:247–274

- Blatov VA, Carlucci L, Ciani G, Proserpio DM (2004) Interpenetrating metal-organic and inorganic 3D networks: a computer-aided systematic investigation. Part I. Analysis of the Cambridge structural database. *CrystEngComm* 6:377–395
- Blatov VA, Delgado-Friedrichs O, O’Keeffe M, Proserpio DM (2007) Three-periodic nets and tilings: natural tilings for nets. *Acta Crystallogr Sect A: Found Crystallogr* 63(5):418–25
- Blatov VA, O’Keeffe M, Proserpio DM (2009) Vertex-, face-, point-, Schläfli-, and Delaney-symbols in nets, polyhedra and tilings: recommended terminology. *CrystEngComm* 12(1):44–48
- Böhme B, Guloy A, Tang Z, Schnelle W, Burkhardt U, Baitinger M, Grin Yu (2007) Oxidation of  $M_4Si_4$  ( $M = Na, K$ ) to clathrates by HCl or H<sub>2</sub>O. *J Am Chem Soc* 129:5348–5349
- Delgado-Friedrichs O, O’Keeffe M (2005) Crystal nets as graphs: terminology and definitions. *J Solid State Chem* 178(8):2480–2485
- DFTB (2013) DFTB + 1.1 is a DFTB implementation, which is free for noncommercial use. <http://www.dftb-plus.info>. Bremen
- Diudea MV (2006) Omega polynomial. *Carpath J Math* 22:43–47
- Diudea MV (2010a) Nanomolecules and Nanostructures—Polynomials and Indices, MCM No. 10, University of Kragujevac
- Diudea MV (2010b) Counting polynomials and related indices by edge cutting procedures, *MATCH Commun Math Comput Chem* 64:569–590
- Diudea MV (2010c) Omega polynomial in all\_R[8] lattices. *Iran J Math* 1: 69–77
- Diudea MV (2013) Hyper-graphenes. *Int J Chem Model* 5: 211–220
- Diudea MV, Ilić A (2010) Omega polynomial in crystal-like single-type face/ring networks. *Int J Chem Model* 3: 65–71
- Diudea MV, Klavžar S (2010) Omega polynomial revisited. *Acta Chim Sloven* 57:565–570
- Diudea MV, Szeffler B (2012) Nanotube junctions and the genus of multi-tori. *Phys Chem Chem Phys* 14 (22):8111–8115
- Diudea MV, Štefu M, John PE, Graovac A (2006) Generalized operations on maps. *Croat Chem Acta* 79:355–362
- Diudea MV, Cigher S, John PE (2008) Omega and related counting polynomials. *MATCH Commun Math Comput Chem* 60:237–250
- Diudea MV, Ilić A, Medeleanu M (2011) Hyperdiamonds: a topological view. *Iran J Math Chem* 2:7–29
- Djoković DŽ (1973) Distance preserving subgraphs of hypercubes. *J Combin Theory Ser B* 14: 263–267
- Elstner M, Porezag D, Jungnickel G, Elsner J, Haugk M, Frauenheim T, Suhai S, Seifert G (1998) Self-consistent-charge density-functional tight-binding method for simulations of complex materials properties. *Phys Rev B* 58:7260–7268
- Frisch MJ, Trucks GW, Schlegel HB, Scuseria GE, Robb MA, Cheeseman JR, Scalmani G, Barone V, Mennucci B, Petersson GA, Nakatsuji H, Caricato M, Li X, Hratchian HP, Izmaylov AF, Bloino J, Zheng G, Sonnenberg JL, Hada M, Ehara M, Toyota K, Fukuda R, Hasegawa J, Ishida M, Nakajima T, Honda Y, Kitao O, Nakai H, Vreven T, Montgomery JA, Peralta JE, Ogliaro F, Bearpark M, Heyd JJ, Brothers E, Kudin KN, Staroverov VN, Kobayashi R, Normand J, Raghavachari K, Rendell A, Burant JC, Iyengar SS, Tomasi J, Cossi M, Rega N, Millam NJ, Klene M, Knox JE, Cross JB, Bakken V, Adamo C, Jaramillo J, Gomperts R, Stratmann RE, Yazyev O, Austin AJ, Cammi R, Pomelli C, Ochterski JW, Martin RL, Morokuma K, Zakrzewski VG, Voth GA, Salvador P, Dannenberg JJ, Dapprich S, Daniels AD, Farkas Ö, Foresman JB, Ortiz JV, Cioslowski J, Fox DJ (2009) *Gaussian 09 Rev. A.1*. Gaussian Inc, Wallingford
- Guloy A, Ramlau R, Tang Z, Schnelle W, Baitinger M, Grin Yu (2006) A quest-free germanium clathrate. *Nature* 443:320–323
- John PE, Vizitiu AE, Cigher S, Diudea MV (2007) CI index in tubular nanostructures. *MATCH Commun Math Comput Chem* 57:479–484
- Klavžar S (2008) Some comments on Co graphs and CI index. *MATCH Commun Math Comput Chem* 59: 217–222

- Kyani A, Diudea MV (2012) Molecular dynamics simulation study on the diamond  $D_5$  substructures. *Cent Eur J Chem* 10(4):1028–1033
- Meier WM, Olson DH (1992) *Atlas of Zeolite Structure Types*, vol 3E. Butterworth-Heineman, London
- Nagy CL, Diudea MV (2009) *Nano Studio*. Babes–Bolyai University, Cluj
- Nagy CL, Diudea MV (2013) Diamond  $D_5$ . In: Nagy CL, Diudea MV (eds) *Diamond and Related Nanostructures*. Springer, Dordrecht, 91–105
- Schwarz U, Wosylus A, Böhme B, Baitinger M, Hanfland M, Grin Yu (2008) A 3D network of four-bonded germanium: a link between open and dense. *Angew Chem Int Ed* 47:6790–6793
- Szeffler B, Diudea MV (2012) On molecular dynamics of the diamond  $D_5$  seed. *Struct Chem* 23(3):717–722
- Winkler PM (1984) Isometric embedding in products of complete graphs. *Discret Appl Math* 8: 209–212



# Chapter 9

## Web-based Computational Tools Used in Protein Surface Analysis and Characterization. Applications for Protein–Protein and Protein–Ligand Interactions

Adriana Isvoran

**Abstract** Proteins are a class of biological macromolecules involved in many cellular events and widely studied in our days. Conformation, size and chemical properties of protein surface are all important for its interaction with the specific substrate and with other macromolecules. In the last decade the surface-based approaches of proteins have been widely used for both analysis and characterization of proteins properties and interactions. Within this chapter, a few web-based tools concerning the proteins surface properties visualization and analysis are re-viewed and their applicability to the protein–ligand and protein–protein interactions prediction and/or characterization is revealed.

### 9.1 Introduction

Proteins play innumerable functions in all living organisms, their interactions governing the most cellular processes, including physiological and generating diseases events. The protein–protein and protein–ligands interactions are subjects widely considered in research works. Analysis of proteins complexes structures revealed that the bound form usually differs structurally from the unbound form and the binding caused from local changes in side chains to global changes of entire protein structure. Also, these studies emphasized that ligands interact with proteins in accessible regions usually forming well defined cavities or pockets at protein surfaces (Kauffman and Karypis 2010). Contrary, protein–protein interactions (PPIs) usually involve large interfacial surface areas, 350–1600 Å<sup>2</sup> (Janin and Chotia 1990; Ban et al. 2004; Fletcher and Hamilton 2006).

---

A. Isvoran (✉)

Department of Biology-Chemistry, West University of Timișoara,  
16 Pestalozzi, Timișoara 300115, Romania  
e-mail: adriana.isvoran@e-uvvt.ro

During the time, a few mechanisms for protein–ligand and protein–protein recognition and association have been proposed. The oldest and simplest is the “lock-and-key” mechanism (Fischer 1894) that is based on and emphasizes the chemical and shape complementarity of the involved molecules. This mechanism could not explain why a protein may bind more than one substrate and the scientists searched for other mechanisms. The induced fit mechanism has been proposed by Koshland (1958) and illustrated the importance of flexibility of both protein and ligand for optimization of binding and interaction. For allosteric proteins the Monod–Wyman–Changeux mechanism has been proposed (Monod et al. 1965). This mechanism considers that allosteric proteins present two conformational states in the unbound form, tense and relaxed, and the ligand binding causes the transition to the relaxed state. It also explains the positive cooperativity, but it cannot explain the negative cooperativity. In order to account for both positive and negative cooperativity, the Koshland–Nemethy–Filmer mechanism has been proposed (Koshland et al. 1966) considering that oligomeric proteins have some subunits in the weak binding state and others in the strong binding state. Another proposed mechanism of cooperative binding is the dynamic population shift mechanism (Freire 1999). It considers that protein exhibits a population of native conformations and upon ligand binding the probability distribution of this ensemble is redistributed changing the stability of certain residues and propagating a conformational change at specific residues.

The conformational selection mechanism (Ma et al. 1999; Tsai et al. 1999) is based on the concept of the funnel-like free energy landscape of protein folding (Karplus 1997) considering that the native state of a protein is an ensemble of co-existing conformers one of them binding the ligand. This mechanism has been validated by several experimental studies concerning the protein–ligand interactions (Berger et al. 1999; Foote and Milstein 1994; James et al. 2003; Goh et al. 2004; Levy et al. 2004; Tobi and Bahar 2005; Kuzu et al. 2012).

Complete deciphering and understanding of dynamic principles governing protein–ligand and protein–protein interactions is a challenge both for description and characterization of biological pathways and for designing of novel and efficient therapeutic agents. Also, in protein science, there is a large gap between the number of proteins with well characterized structures and biological functions (or malfunctions) and the proteins with unknown structures and/or functions. From these points of view, the computational approaches concerning the prediction and/or characterization of proteins structures, surfaces and interactions are increasingly needed and developed in life sciences.

Protein structures are better conserved than protein sequences and also protein structures contains more biological significant information. The biological functions of proteins rely on their interactions with other biomolecules, the wide variety of interactions being due to chemical and structural diversity observed at molecular surfaces level. Thus, to decipher biological processes at molecular level is crucial to accurately define the nature and shape of protein surfaces. It means to describe the surface in terms of atoms, residues, and surface curvature, patches, clefts and concavities or convexities and in order to do it the three-dimensional structure of protein is needed. The atomic structures of proteins and their complexes are publicly

available from the Protein Data Bank (PDB) archive (Berman et al. 2000). In October 8, 2013, this archive contained 94540 structures. Another important data bank in protein science is Universal Protein Resource (UniProt), a comprehensive resource for protein sequence and functional information (Jain et al. 2009).

Within this chapter, a few web-based tools concerning the proteins surface properties visualization and analysis are reviewed in correlation with their applicability to the protein–ligand and protein–protein interactions prediction, analysis and/or characterization. There also are illustrative examples presented in a didactic manner in order to allow to young scientists (students, PhD students) to reproduce the study and to facilitate the use of described computational tools.

## 9.2 Proteins Surface Analysis and Comparison

It is well known that interactions between macromolecules are usually determined by the properties of their surfaces. The surface of a protein is irregular and presents cavities and channels with different shapes, sizes and chemical properties that are crucial for many phenomena such as: molecular recognition and binding, diffusion and absorption of small molecules, enzyme catalysis, interactions with other macromolecules, etc.

There is not a generally accepted definition for protein surface but a few approaches are used to define it (Gerstein et al. 2001). The simplest is the van der Waals surface (VDWS), defined as the sum of exposed areas of the constituent atoms modeled as spheres with radii known from their van der Waals properties. Another approach, using the term of probe-sphere rolling around the surface, concerns the contact surface (CS). It is defined as the surface containing all contact points of the molecule and the probe particle. When this particle touches more than one atom we obtain the reentrant surface (RS). The sum between the contact and reentrant surfaces defines the molecular surface ( $MS = CS + RS$ ). The accessible solvent area (ASA) is defined as the surface generated by the centers of the probe particle rolling along the protein. When using the probe-sphere approach, the protein surfaces computation greatly depends on the value chosen for the probe-sphere radius that is frequently, but not always, set at a value considered to represent a water molecule, 1.4 Å, and there is not an agreement on what the proper radius should be. Table 9.1 shows the solvent accessible surface area computed for bovine recoverin (a calcium binding protein) for different probe-sphere radii using GETAREA software (Fraczkiewicz and Brown 1998). GETAREA is a web service provided by the University of Texas Medical Branch (<http://curie.utmb.edu/getarea.html>). The input file for GETAREA software is the protein three dimensional (3D) structure, in our case the bovine recoverin structural file that we have extracted from the Protein Data Bank (Berman et al. 2000), code entry IREC (Flaherty et al. 1993).

Depending on parameter setup, the output of GETAREA is the solvent accessible surface area in different formats (for the entire protein, per residue, per atom type or per individual atoms for non-hydrogen atoms) or solvation energy respectively.

**Table 9.1** Solvent accessible surface area of bovine recoverin computed with different probe-sphere radii

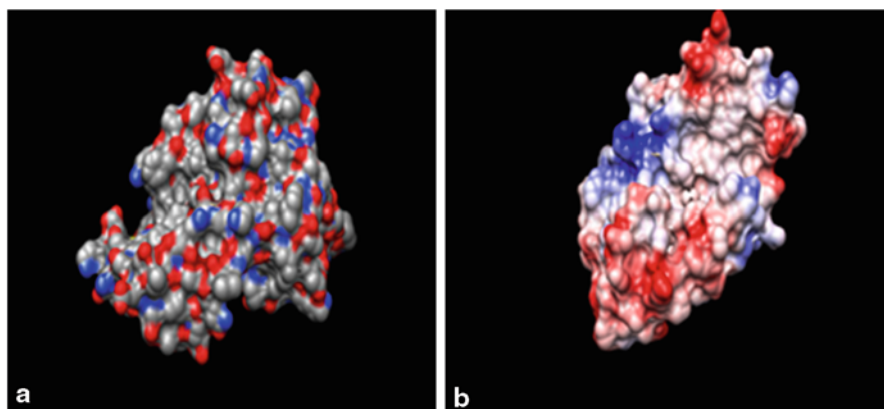
Probe sphere radius (Å)	Solvent accessible surface area (Å <sup>2</sup> )
1.0	10104.96
1.4	9470.86
1.8	9280.83
2.2	9290.03

Residue		Total	Apolar	Backbone	Sidechain	Ratio(%)	In/Out
LEU	9	71.41	45.53	26.14	45.26	31.0	
SER	10	14.48	8.95	1.98	12.50	16.1	i
LYS	11	62.41	59.60	3.88	58.53	35.6	
GLU	12	79.68	30.26	3.24	76.44	54.1	o
ILE	13	0.00	0.00	0.00	0.00	0.0	i
LEU	14	42.91	39.14	3.77	39.14	26.8	
GLU	15	110.01	37.09	10.60	99.41	70.4	o
GLU	16	90.59	37.34	33.16	57.43	40.7	
LEU	17	12.48	3.03	11.49	0.99	0.7	i
GLN	18	120.40	34.63	15.14	105.27	73.3	o
LEU	19	159.66	138.35	22.99	136.67	93.5	o
ASN	20	7.77	7.73	2.52	5.25	4.6	i
THR	21	42.14	24.91	17.23	24.91	23.5	
LYS	22	124.97	64.84	28.09	96.88	58.9	o
PHE	23	69.74	66.21	6.84	62.89	34.9	
THR	24	81.92	79.72	4.04	77.88	73.3	o
GLU	25	84.93	25.44	0.24	84.69	60.0	o
GLU	26	143.61	55.57	6.06	137.55	97.4	o
GLU	27	81.44	34.83	4.85	76.59	54.2	o
LEU	28	0.00	0.00	0.00	0.00	0.0	i
SER	29	44.42	33.45	0.80	43.62	56.4	o
SER	30	66.92	31.55	4.05	62.87	81.2	o

**Fig. 9.1** Fragment of solvent accessible surface area per residue computed for bovine recoverin using GETAREA webserver

When solvent accessible surface area per residue is computed, the contributions from backbone and side chain are emphasized and solvent exposed (o) and buried residues (i) are revealed, as it is presented in Fig. 9.1.

Residues are considered to be exposed or buried depending on the ratio of side-chain surface area to “random coil” value per residue. The “random coil” value is a constant computed for every residue as the average solvent-accessible surface area of this residue (X) in the tripeptide Gly-X-Gly in an ensemble of 30 random conformations (Fraczkiewicz and Brown 1998). If this ratio exceeds 0.5 the residue is considered to be exposed and if it is less than 0.2 the residue is considered to be buried. Information about exposed and/or buried residues is important when analyzing putative protein–ligand and protein–protein interactions.

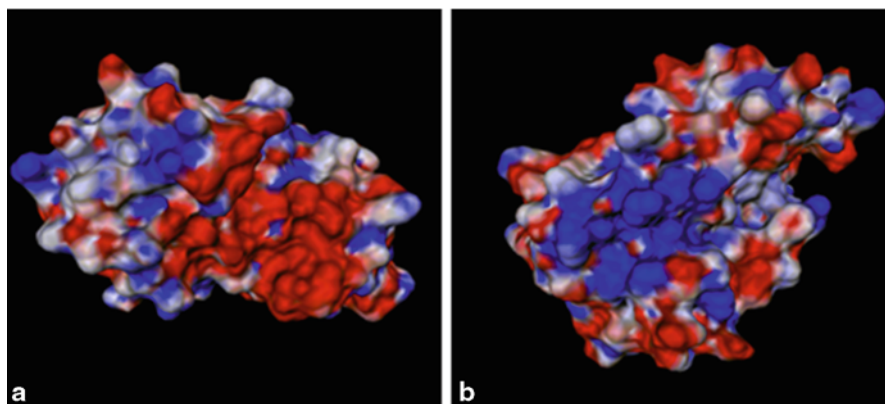


**Fig. 9.2** Visualization of bovine recoverin surface (PDB code 1REC) using Chimera software and two coloring possibilities: (a) by atom (carbon in grey, nitrogen in blue and oxygen in red) and (b) Coulombic Surface Coloring from  $-10$  (red) to  $+10$  (blue)

Numerous computational tools have been developed for protein structures and surfaces visualization and analysis. Usually, they allow surface representation and visualization, comparison of aligned protein surfaces, calculation of geometrical (area) and physicochemical (electrostatic potential and hydrophobicity) properties of surfaces and/or emphasizing PPIs. They also provide calculation of the geometrical properties of the entire protein, such as its volume and surface area. The protein volume computation informs about protein packing efficiency and small changes in packing efficiency due to ligand binding are significant and notifies about protein interactions (Tsai et al. 1999). Also, surface descriptors are provided: surface residues, surface patches, surface curvature (Albou et al. 2009). A few examples of such computational tools are: PyMol (DeLano 2002), Chimera (Pettersen et al. 2004), SURFACE (Ferre et al. 2004) and 3D-SURFER (Li et al. 2008).

Graphical surface representation and visualization allows a quick understanding and interpretation of protein shape, charge distribution and polarity, correlated to the protein possible interactions. All this information is useful in many areas of molecular modeling. A short illustration of the use of mentioned tools for protein surface analysis and characterization is provided further.

The specificity of protein–ligand, protein–DNA and PPIs is usually due to electrostatic and/or hydrophobic interactions. Qualitative analysis of the electro-static properties of the protein surface provides information on the local charge density. It reveals how positive, negative or neutral a region of the protein surface is relative to the rest of the protein. The local charge density may influence how and where various ligands bind. If these ligands are also charged, the binding might be significantly increased. Figure 9.2 depict the surface of bovine recover-in visualized using Chimera software (Pettersen et al. 2004): the surface is colored by atom type (Fig. 9.2a, the carbon is grey, nitrogen is blue and oxygen is red) and also using Coulombic Surface Coloring (Fig. 9.2b). Chimera software also allows calculation of the protein volume

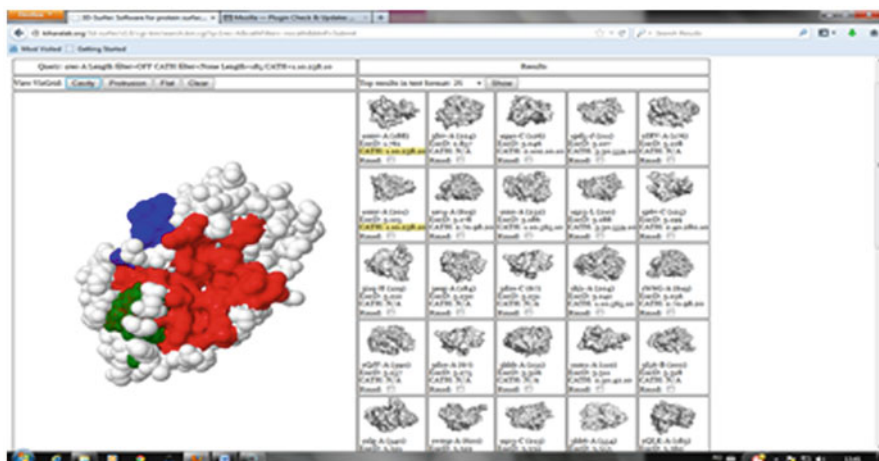


**Fig. 9.3** Images of the electrostatic potential mapped on the molecular surface of the bovine recoverin (PDB code 1REC) obtained using PCE tool: view of two regions of protein from  $-2.0$  kcal/mol/e (red) to  $+2.0$  kcal/mol/e (blue)

and surface area, for bovine recoverin the surface area is  $8609 \text{ \AA}^2$  and the volume is  $23,660 \text{ \AA}^3$ .

Another possibility to analyze the electrostatic properties of the protein surface is the electrostatic potential mapping on molecular surface using Protein Continuum Electrostatics (PCE) tool (Miteva et al. 2005). PCE server (<http://bioserv.rpbs.jussieu.fr/cgi-bin/PCE-Pot>) allows calculation of electrostatic potential (PCE-pot) and pKa values of titratable groups in proteins (PCE-pKa). When using PCE-pot tool, electrostatic potentials are displayed on the molecular surface using a color-code: blue regions are positively charged, red ones are negatively charged and white regions are neutral. When using PCE-pKa tool, the pKint, pK1/2 and pH-dependent protonation curves of all titratable groups, estimated isoelectric points (pI) and electrostatic interaction energy in kcal/mole between titratable groups are provided. The use of PCE-pot tool with default parameters for bovine recoverin is presented in Fig. 9.3. It illustrates the charge distribution on the bovine recoverin and we may identify the balance of regions with negative charge in good correlation to known data concerning other calcium binding proteins (Mouawad et al. 2009).

Analysis and comparison of protein surfaces may be done using 3D-SURFER computational tool (Li et al. 2008). 3D-SURFER is a web-based tool (<http://dragon.bio.purdue.edu/3d-surfer/>) used for protein surface comparison and analysis. It allows a high throughput screening and visualization of a protein surface comparison against all protein structures in the Protein Data Bank. The web interface renders additional important information: animated protein rotations, protein structure classification codes, structure alignment calculations and identification of pocket regions on a given structure (Li et al. 2008). An example of using this tool in order to analyze and compare the surface properties of bovine recoverin is presented in the Fig. 9.4. This picture also illustrates that this web-based tool allows identification, visualization and characterization of local geometric features of surface such as cavities



**Fig. 9.4** Illustration of 3D-SURFER tool utilization to characterize and compare the bovine recoverin surface

(Fig. 9.4, red—first largest cavity, green—second largest cavity, blue—third largest cavity), protrusions and flat regions that may represent potential ligand binding sites of bovine recoverin. The characteristics of identified geometric features are also provided, including areas and volumes for these regions and the list of the residues forming the three largest groups (Fig. 9.5). A large number of these residues are known to be functionally important, see further. This tool also allows comparison of surface of considered protein to all protein structures in the PDB and retrieves PDB structures that have similar surface shapes giving the opportunity to identify functionally related proteins that, due to distant evolutionary relationship, cannot be emphasized otherwise.

For bovine recoverin, the result of using 3D-SURFER for identification of similar surfaces in PDB is presented in Table 9.2. The comparison is based on the Euclidean distance between the descriptor vectors representing the proteins (Li et al. 2008). We have considered the default value of 25 for selection of the number of entries to be listed and we also performed structural alignment of considered structures expressed by root-mean-square distance (RMSD) between equivalent atom pairs (Carugo and Eisenhaber 1997). Identical structures have zero value for the RMSD and it increases for dissimilar structures. Results display also includes the CATH codes (Orengo et al. 1997) that reflect the structural topology of proteins. The result illustrated in Table 9.2 indicates 1OMV, chain A (Ames et al. 2002) as a structural file of a protein having high surface similarity with bovine recoverin. 1OMV is the structural file of E85Q mutant of bovine recoverin, so it is expected the two files share high structural and surface similarity and this information is not relevant for biological interpretation. It is not the case of 3FXV that is the structural file of the ligand binding domain (residues 248–475) of NR1H4 (nuclear receptor subfamily 1, group H, member 4) protein (Feng et al. 2009) that also shares structural and surface similarity to bovine recoverin and this information could be meaningful.



**CAVITIES****RED:**

1st Largest Cavity Residues: (Surface Area = 2030.359, Volume = 6181.758):

22 31 51 52 53 55 56 57 59 90 91 93 94 95 98 99 132 133 134 137 183 184 187 189 190 191 192  
194 196

**GREEN:**

2nd Largest Cavity Residues: (Surface Area = 713.147, Volume = 1506.678):

126 129 130 141 151 184 185 187 193 196 197

**BLUE:**

3rd Largest Cavity Residues: (Surface Area = 883.861, Volume = 2060.317):

16 17 18 19 20 92 99 100 102 103 104 173

**PROTRUSIONS****RED:**

1st Largest Protrusion Residues: (Surface Area = 3703.735, Volume = 16599.465):

11 15 18 19 24 25 26 27 30 33 34 37 38 40 41 46 47 48 55 56 58 59 67 84 135 136 139 140 191  
197 198

**GREEN:**

2nd Largest Protrusion Residues: (Surface Area = 456.149, Volume = 554.706):

168 170 174 177 178 180

**BLUE:**

3rd Largest Protrusion Residues: (Surface Area = 217.494, Volume = 179.704):

112 113 114 120

**FLAT REGIONS****YELLOW:**

Flat Region Residues: (Surface Area = 1017.031, Volume = 2407.870):

16 70 71 72 73 79 80 81 82 84 85 88 104 107 110 111 113

**Fig. 9.5** Characterization of the largest cavities of bovine recoverin surface and identification of residues involved in their formation

Binding sites of proteins are usually associated to structural cavities and/or pockets situated on protein surface and it becomes important not only to identify but also to characterize these cavities. The scientific literature is abundant in computational tools allowing characterization of cavities and pockets situated at protein surface. One of these tools is Computed Atlas of Surface Topography of proteins (CASTp) that can be used to study surface features and functional regions of proteins (Dundas et al. 2006). It provides an online resource (<http://sts.bioengr.uic.edu/castp/>) for locating and characterizing concave surface regions (pockets located on protein surfaces and voids buried in the interior) on three-dimensional structures of proteins and allows the measurement of the area and volume of pocket or void and identification of all residues and even atoms participating in their formation. For bovine recoverin, CASTp tool identifies 23 cavities, the measured areas and volumes for the largest cavities being presented in Table 9.3. The largest cavity identified by CASTp involves the residues TRP31, PHE35, GLU38, CIS39, ILE44, GLU48, THR51,



**Table 9.2** Structural files of proteins presenting similar surfaces to bovine recoverin

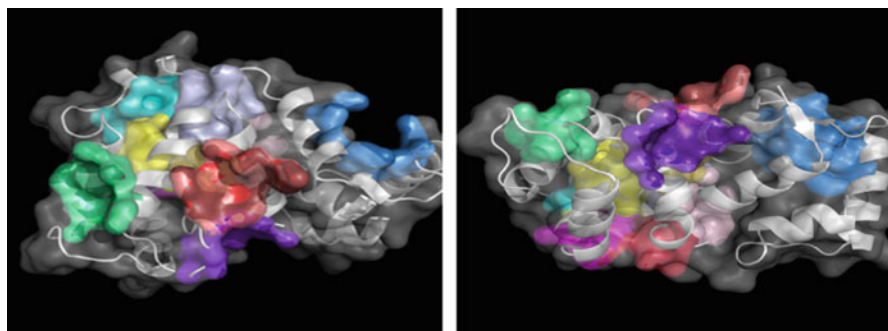
PDB ID	Euclidian distance	CATH	RMSD (Å <sup>2</sup> )
1omv-A	1.761	1.10.238.10	0.28
3fxv-A	2.857	Unassigned	3.26
1q90-C	3.046	2.102.10.10	5.28
1pd5-J	3.107	3.30.559.10	4.28
2irv-A	3.108	Unassigned	3.99
1omr-A	3.125	1.10.238.10	0.33
1av4-A	3.178	2.70.98.20	4.24
1xnx-A	3.186	1.10.565.10	7.33
1q23-L	3.188	3.30.559.10	4.43
1p6v-C	3.199	2.40.280.10	5.47
3i1q-H	3.212	Unassigned	4.24
3esg-A	3.23	Unassigned	5.44
3d2s-C	3.231	Unassigned	5.54
1hj1-A	3.242	1.10.565.10	4.90
1w6 g-A	3.256	2.70.98.20	4.25
2qjf-A	3.257	Unassigned	4.86
3d2s-A	3.275	Unassigned	5.56
3kkk-A	3.306	Unassigned	4.91
1um1-A	3.311	2.30.42.10	4.91
3f56-B	3.318	Unassigned	6.68
1nlg-A	3.321	Unassigned	7.43
1wmp-A	3.322	2.70.98.20	4.32
1q23-C	3.33	3.30.559.10	4.29
3kk6-A	3.353	Unassigned	5.27

ILE52, LYS55, PHE56, TYR86, LEU90. Comparison of this result to residues identified by 3D-SURFER as forming the largest cavity of bovine recoverin (Fig. 9.5) emphasizes some common residues and also the areas and volumes of identified cavities by the two tools are strongly different. It illustrates that the two computational tools use distinct detection algorithms for identification of cavities.

Another online available resource for locating and characterization of protein potent binding sites is Fpocket (Le Guilloux et al. 2009). Fpocket is a fast open source protein pocket detection algorithm that can be used on-line (<http://fpocket.sourceforge.net/>) or downloaded from the web page. The input of Fpocket is a PDB file containing the receptor and cofactors and not the ligands, if

**Table 9.3** Geometric characteristics of pockets of bovine recoverin identified using CASTp tool

Pocket ID	Area ( $\text{\AA}^2$ )	Volume ( $\text{\AA}^3$ )
23	168.4	306.1
22	174.0	258.4
21	185.1	139.8
20	164.1	142.4
19	61.70	67.40
18	138.0	112.1



**Fig. 9.6** Pockets snapshots for bovine recoverin identified using Fpocket. The protein is presented in *grey* and identified pocket are colored

there is the case. The output of Fpocket returns different files containing information about the identified pockets ranked upon their putative capacity to bind a small molecule. One of this output files is a PDB file containing all atoms used for pocket detection. Another output file provides statistics about each pocket listing different characteristics and scores of pockets identified on the surface of the protein. The results may be visualized using PyMol or VMD software. Fpocket identifies 11 pockets for bovine recoverin, as presented in Fig. 9.6.

Pocket characterization includes the computation of numerous descriptors, the most important from my point of view being the following (Le Guilloux et al. 2009): (i) hydrophobicity score measuring the hydrophobic character of the pocket, (ii) polarity score that, contrary to hydrophobicity score, measures the hydrophilic character of the pocket, (iii) charge score taking into account the charge for all amino acids in the pocket, (iv) local hydrophobic density score identifying if the binding pocket contains local parts that are rather hydrophobic and (v) the volume of the binding pocket computed using a Monte-Carlo algorithm that summarize the full volume occupied by all alpha sphere in the given pocket. A pocket score is assigned for every pocket tacking into account the values of all the descriptor used for computation. Table 9.4 contains the mentioned above descriptors for the 11 pockets identified by Fpocket for bovine recoverin.

**Table 9.4** Characteristics of bovine recoverin's pockets identified using Fpocket tool

Pocket score	Hydrophobicity score	Polarity score	Charge score	Local hydrophobic density score	Volume	Residues
42.84	11.64	14	0	27.60	718.87	TRP31, SER34, PHE35, GLU38, CIS39, ILE44, GLU48, THR51, ILE52, LYS55, PHE56, TYR86
17.58	22.17	6	2	13.00	443.50	LYS180, GLU181, LEU183, ARG184, GLN187, LYS196
40.96	18.15	14	0	35.29	289.68	LYS119, ASN120, VAAL122, LEU123, GLU149, GLU153, TRP156, ASN163
35.00	48.97	8	4	25.53	255.76	TYR109, VAL126, ILE129, PHE130, ILE133, LEU141, ARG151, ARG184, GLN187, LYS192, VAL193, LYS196, LEU197
31.26	17.16	16	8	13.00	496.79	GLY96, LYS97, THR98, N99, K180, LEU183, LYS192, GLU195, LYS196
30.49	38.49	10	0	24.81	200.97	PHE57, GLU59, ALA60, TYR65, ILE129, MET132, ILE133, SER134, ASP137, PHE188, PRO190, GLN191, VAL193, LYS194
23.17	20.13	12	2	17.43	173.42	ILE133, ASP137, THR138, LEU141, PRO142, GLU145, ARG151, VAL193, LYS194, LYS196, LEU197
23.17	20.13	12	2	17.43	173.42	ILE133, ASP137, THR138, LEU141, PRO142, GLU145, ARG151, ARG1584, VAL193, LYS194, LYS196, LEU197
23.15	17.60	12	-2	13.87	255.68	PHE57, THR93, SER94, ALA95, GLY96, GLU189, PRO190, GLN191, LYS192
23.02	3.96	14	-2	1.00	564.99	ARG71, SER72, PHE73, PHE106, SER107, ASP110, VAL111, GLY113, GLY115, GLU169
20.85	48.64	6	-2	28.93	110.90	ARG46, ALA64, ASN67, H68, R71, VAL111, GLU124

Fpocket tool has been used to analyze the properties of the alpha-helix binding pockets belonging to different proteins and reflected that the hydrophobicity was not uniformly distributed inside these pockets (Isvoran et al. 2013). This result indicated that Fpocket tool can be also used to identify key hydrophobic hot spots.

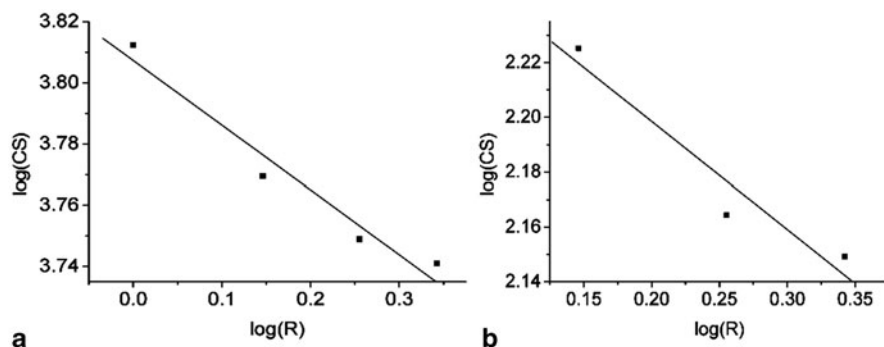
The interacting residues in protein–protein, protein–DNA and protein–ligand complexes can be identified by using ContPro (Firoz et al. 2010) web-based tool (<http://procarb.org/contpro/>).

The interacting residues are identified by calculating the distance between the atoms of protein and ligand and comparing this distance to a cutoff value lying from 3.5 to 6 Å. The interacting residues of the bovine recoverin with rhodopsin kinase (PDB code entry 2I94) has been identified using ContPro and are the following: LYS22, TRP31, PHE35, GLU38, PHE49, ILE52, TYR53, LYS55, PHE56, PHE57, TYR86, LEU90, THR93, SER94, MET132, PHE188, GLU189.. It can be noticed that most all of them belong to one detected cavity and/or pocket. There also are a few experimental data supporting the functional importance of residues identified as belonging to the largest surface cavity of bovine recoverin The hydrophobic cavity involving aromatic residues PHE23, TRP31, TYR53, PHE56, PHE83, and TYR86 has been identified by X-ray crystallography (Flaherty et al. 1993) and also by nuclear magnetic resonance studies of a myristoylated E85Q recoverin mutant (Gray-Keller et al. 1993; Ames et al. 2002). It was found that the myristoyl group is located within this cavity and it is important for calcium-myristoyl switch and modulates recoverin activity (Tanaka et al. 1995).

Comparison of the largest pocket identified by Fpocket with the largest cavity identified by 3D-SURFER reflects strong differences but it is in reasonable agreement to predictions made by CASTp tool. Once again, I need to underline that these tools use distinct approaches for identifying and characterizing cavities and pockets. Indeed, 3D-SURFER tool uses grid based approach for cavity detection and CASTp and Fpocket use alpha sphere approach. Usually, in my research work I use more than one tool for pockets/cavities identification, I compare the results and I take into account those cavities predicted by almost all used tools.

### 9.3 Fractal Aspects of Protein Surfaces

It was already shown that the protein surface is irregular presenting cavities, pockets and channels with different sizes and shapes. It means that the protein surface is heterogeneous and rough and its roughness may be quantitatively described by surface fractal dimension (Lewis and Rees 1985). The calculation of surface fractal dimension is based on computation of the contact surface (CS) of protein for probe molecules with different radii  $R$  and taking into account the scaling law between the two quantities,  $CS \sim R^{2-D_s}$ , with  $D_s$  the surface fractal dimension (Lewis and Rees 1985). There are numerous published studies revealing fractal aspects of protein surface with fractal dimensions between 2.18 and 2.56, a review has been published



**Fig. 9.7** Illustration of global (entire protein—**a**) and local (the biggest cavity—**b**) surface fractal dimension calculation for bovine recoverin

by Craciun et al. (2009). These studies revealed strong correlations between the surface fractal dimension and the macromolecule size (Goetze and Brickman 1992), the molecular and cellular function of proteins (Stawiski et al. 2000; Pitulice et al. 2008a) and their catalytic activity (Stawiski et al. 2002). Also, such studies emphasized that surface roughness does not depend on the composition of protein in secondary structure elements (Pitulice et al. 2008b) but it strongly depends on the properties of the protein environment such as pH, electrolyte concentration and temperature (Vreeker et al. 1992; Petit and Bowie 1999) being always higher for proteins in solution than for proteins in crystal (Craciun et al. 2012). Moreover, there are published papers illustrating that protein surfaces reveal both global and local surface fractal dimensions, usually cavities and pockets presenting a higher roughness than the global surface (Avnir and Farin 1990; Pettit and Bowie 1999; Ciorsac et al. 2011; Isvoran et al. 2013). This finding is important because it is known that the rate of substrate trapping by the active sites is largest when the protein surface has a dimension close to 2.2 (Aon et al. 2000). Also, the presence of hydrophobic cavities at the protein surface with a complex shape, expressed by a higher surface fractal dimension, has been shown to be an important property related to the ability of proteins to bind alpha-helical peptides (Isvoran et al. 2013).

Figure 9.7 illustrate the determination of the surface fractal dimension for bovine recoverin, both at global (a) and local (b) levels. The contact surface for the entire protein is computed using GETAREA server and the contact surface for the biggest identified cavity is computed using CASTp web-server respectively. For these calculations, distinct values for the probe-sphere radii are used, from 1.4 to 3.0 Å. Every computed contact surface is plotted against the probe sphere radius in double logarithmical scale and the surface fractal dimensions are extracted from the slopes of the lines:  $D_{sg} = 2.21 \pm 0.03$  for the global surface and  $D_{sl} = 2.40 \pm 0.09$ . These values are in good agreement with other published data (Craciun et al. 2009).

It seems that the distribution pattern of atoms on the protein surface is fractal and has determinant contribution to the biological function. Moreover, the surface fractal dimension seems to be a quantitative parameter that can be used to describe the complexity of the shape of protein surface.

## 9.4 Computational Analysis of Protein–Ligand Interactions

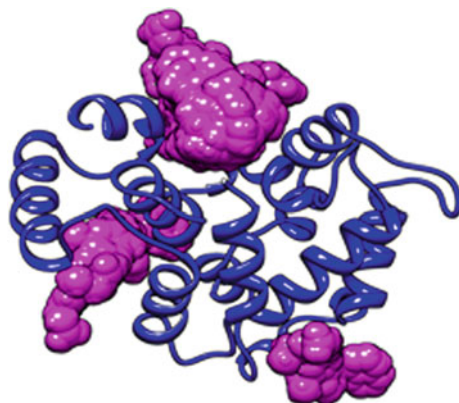
The last decade is characterized by intensive studies concerning the complex interactions between proteins and ligands (usually small organic molecules) because they play key roles in many biological and therapeutic processes including drug activities. In previous subchapter, a few web-based tools used to identify and characterize the potent ligand binding regions in proteins have been considered. The aim of this subchapter is to refer to molecular docking as a computational tool able to predict the structure of the intermolecular complex formed by the protein and ligand. Molecular docking explores the binding modes of the two interacting molecules (protein and ligand in our case) and asks known 3D structures of both protein and ligand. The docking procedure can be summarized as the search for the precise ligand conformations and orientations within the protein (posing) and prediction of the binding affinity using scoring functions, i.e. mathematical methods used to predict the strength of the non-covalent interaction between the two molecules, in this case the protein and the ligand (Sousa et al. 2006).

There are two approaches used for molecular docking. One approach is shape-based and implies the existence of molecular surface complementarity between the ligand and its receptor protein (Goldman and Wipke 2000). The second approach takes into account the interaction energies (Morris et al. 1998; Meng et al. 2004). As it is common to consider that the shape of a molecule is described by its surface, application of the shape-based approach means a rigid docking involving the use of surface descriptors: the molecular surface or solvent-accessible surface area for the protein and matching surface for the ligand (Morris et al. 2005). The complementarity between the two surfaces allows finding the pose. Docking methods based on this approach are fast and robust, but they do not allow taking into account the flexibility of protein and ligand. The energetic approach used in molecular docking supposes to search at the protein surface areas with favorable energy change when buried upon protein–ligand association (Fernandez-Recio et al. 2005) and it allows flexible docking.

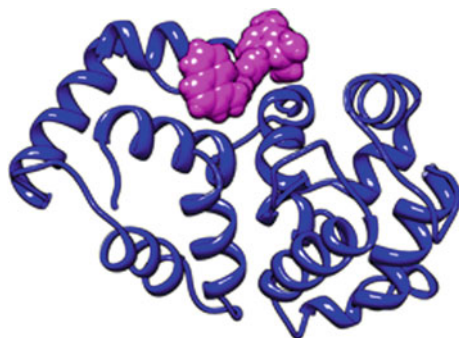
There are three possibilities for applying docking methods: (i) both the protein and ligand are considered rigid, (ii) the protein is rigid and the ligand is flexible and (iii) both the protein and ligand are flexible. The rigid docking is fast and robust, but introducing the degrees of freedom for ligand and/or protein becomes slow and complex.

Both free available and commercial software for performing molecular docking are developed by various groups. Examples of free software are AutoDock (Goodsell and Olson 1990), UCSF DOCK (Moustakas et al. 2006), SwissDock (Grosdidier et al. 2011), ODA (Fernandez-Recio et al. 2005) and commercial ones are GOLD (Verdonk et al. 2003), FlexX (Sousa et al. 2006) and Surflex (Tripos Company). The use of SwissDock server (<http://www.swissdock.ch/>) is provided further. SwissDock tool is based on the docking software EADock (Grosdidier et al. 2011) and its implementation consists of the following steps: (i) many binding modes are generated either in the vicinity of all target cavities, (ii) their CHARMM (Brooks et al. 1983)

**Fig. 9.8** Predicting binding poses of therphenyl (viewed as magenta surface) into bovine recoverin (viewed as blue ribbon). There are 57 almost superposed poses concerning the same region of the target protein, *magenta* region on the top of figure



**Fig. 9.9** The best scored pose for therphenyl 2 (viewed as *magenta* surface) binding into bovine recoverin (viewed as *blue* ribbon)



energies are estimated on a grid, (iii) the binding modes with the most favorable energies are evaluated and clustered and (iv) the most favorable clusters can be visualized online or/and downloaded by user.

An illustration of using molecular docking technique under SwissDock server to investigate a protein–ligand interaction is provided here for the putative therphenyl binding into bovine recoverin. Therphenyl is a small hydrophobic molecule mimicking one face of an alpha-helical peptide, i.e. the side chains of three key residues occupying positions  $i$ ,  $i + 3$  and  $i + 7$  (Fairlie et al. 1998, Maity and König 2008) or  $i$ ,  $i + 4$  and  $i + 7$  (Yin et al 2005) of the bound helix. Therphenyl was found to interact to other calcium binding proteins: calmodulin (Orner et al. 2001), centrin 2 (Isvoran et al. 2011) and troponin C (Isvoran et al. 2013). The target, i.e. bovine recoverin, has been prepared as input for docking experiments by using DockPrep tool of CHIMERA software (Pettersen et al. 2004) and default parameters of accurate dock under SwissDock server (Grosdidier et al. 2011) are considered for calculations. There are 60 predicted therphenyl binding poses to bovine recoverin (Fig. 9.8), 57 of them concerning the same region of protein but with distinct orientations of the ligand. The best scored docking pose is given in Fig. 9.9.

The predicted interaction energy of the best scored pose of therphenyl 2 to bovine recoverin is  $-8.96$  kcal/mol and it is in very good agreement with the predicted

interaction energies of  $-7.98$  and  $-8.18$  kcal/mol for terphenyl binding in calmodulin (Isvoran et al. 2011) and troponin C respectively (Isvoran et al. 2013). All these energies suggest favorable interactions of terphenyl with the three proteins and this result may be used to gain insights into the underlying molecular mechanisms of selectivity of these proteins.

Web-based tools used in protein–ligand interaction analysis also take into account several databases of domain–peptide interactions. One of these databases is DOMINO, an open-access database (<http://mint.bio.uniroma2.it/domino/>) comprising more than 3900 annotated experiments describing interactions mediated by protein–interaction domains (Ceol et al. 2006). BindingDB is another web-accessible and public database containing measured binding affinities and focusing on the interactions of protein considered to be drug–targets with small, drug-like molecules (Liu et al. 2007). Binding DB also allows validation of computational chemistry and molecular modeling approaches such as docking, scoring and free energy methods.

## 9.5 Computational Analysis of Protein–Protein Interactions

Protein–protein interactions play crucial roles in all cellular processes and numerous computational methods to infer proteins interactions networks have been proposed in the last decade. The aim of protein–protein interactions study concerns both a better understanding of the biochemical pathways and the PPIs disruption from therapeutic reasons. PPIs result in the formation of protein interfaces and molecular surface complementarity is a concept that also applies in these cases.

The general physicochemical features found in PPIs are based on computational analysis of crystallographic structures of the protein–protein complexes. A general description reveals that protein–protein interfaces are typically large having average areas between 350 and 1600 Å<sup>2</sup> and a hydrophobic character (Janin and Chotia 1990; Ban et al. 2004; Fletcher and Hamilton 2006). They also often are featureless in comparison to well defined ligand binding pockets and/or cavities.

There two categories of protein–protein interactions: stable or transient interactions, and both types of interactions can be either strong or weak (Byrum et al. 2012). Stable interactions are those associated with proteins forming multi-chain complexes, homo- or hetero-multimers, for example hemoglobin that is a homotetramer. Transient interactions are temporary in nature requiring a set of conditions that promote the interaction: conformational changes of the involved proteins, phosphorylation, methylation, glycosylation or localization to discrete areas of the cell (Ngounou et al. 2013). Transient interactions can be fast or slow and usually are reversible. Transiently interacting proteins are involved in a wide range of cellular processes, including protein modification, transport, folding, signaling, and cell cycling.

There are many approaches applying for PPIs studies (Ngounou et al. 2013): biochemical (cross-linking and chemical modification, combined fractionation during chromatography and coimmunoprecipitation, electrophoresis), biophysical (fluorescence resonance-energy transfer, analytical ultracentrifugation, microscopy, mass spectrometry), genetic and computer-based approaches. Computer-based methods



use available information on the structure of genes, proteins, and functional relationships between them. Investigation of PPIs by means of computer-based methods allows verification or confirmation of experimental results to avoid false-positive and/or false-negative conclusions and it can serve to assess the validity of possible interacting partners.

There are many computer-based tools and algorithms for prediction of PPIs allowing identification of interface residues and assignment of protein functions to genes are also possible. Investigation of PPIs through computer-based methods involves a few basic steps: (i) the retrieval of the amino acid sequences of the proteins of interest, (ii) generation of three-dimensional models of the proteins of interest, (iii) models optimization and validation.

For the estimation of PPIs we must take into account the genomic sequence analysis and associated physicochemical properties of amino acids (Pazos et al. 1997), and recognition of specific residue motifs (Kini and Evans 1996).

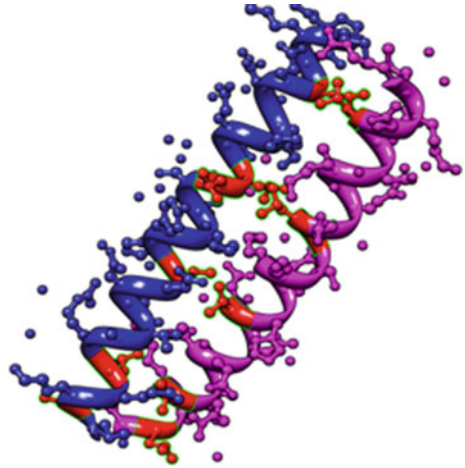
Today, there are numerous databases of PPI data such as: database of interacting proteins—DIP (Xenarios et al. 2002), biomolecular interaction network database—BIND (Bader et al. 2003), general repository for interaction datasets—GRID (Breitkreutz et al. 2003), *Saccharomyces* genome dataset-SGD (Christie et al. 2004), and human protein reference database—HPRD (Peri et al. 2004).

Proteins bind together through a combination of physicochemical interactions: hydrophobic bonding, van der Waals forces and salt bridges. There also are specific binding domains on each interacting protein. These domains are either binding clefts and can be a few peptides long, either large surface spanning hundreds of amino acids. The size of the binding domains is very important as it influences the strength of the binding.

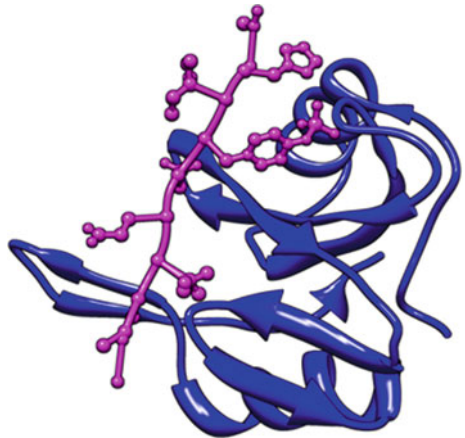
There are several typical protein–protein interaction motifs. Such a motif is the leucine zipper, which consists of  $\alpha$ -helices on each protein that bind to each other in a parallel fashion through the hydrophobic bonding of regularly-spaced leucine residues on each  $\alpha$ -helix interdigitating into the adjacent helix, forming a stable coiled-coil (Phizicky and Fields 1995). Figure 9.10 illustrates the leucine zipper structural motif for the dimer of general control protein GCN4 from *Saccharomyces Cerevisiae*, PDB code entry 1ZIK (Gonzales et al. 1996) visualized using Chimera software. Leucine zippers provide a tight and stable molecular binding for multi-protein complexes and also for protein–DNA complexes.

Another motif involved in protein–protein interactions is the SH2 domain. It is a motif of about 100 amino acids belonging to Src-protein and also found in many other proteins being involved in the recognition of proteins and peptides containing phosphorylated tyrosines (Phizicky and Fields 1995). This motif is presented in Fig. 9.11 for the SH2-domain of human cytoplasmic protein NCK2 (blue ribbon) in complex with a decaphosphopeptide (magenta, atoms ball and sticks), PDB code entry 1CIA (Frese et al. 2006). Src protein also contains a SH3 binding motif, a noncatalytic domain which is involved in protein–protein interactions and is found in many proteins. Its length varies between about 55 and 75 amino acids, and its structure contains antiparallel sheets, as it is illustrated in Fig. 9.12 for the SH3 domain of human Lyn-tyrosine kinase, PDB code entry 1WIF (Bauer et al. 2005).

**Fig. 9.10** The leucine zipper structural motif for the dimer of general control protein GCN4 from *Saccharomyces Cerevisiae* (PDB code entry 1ZIK). The monomer A is presented in *blue* and the monomer B in *magenta*. Leucine residues belonging to both monomers are presented in *red*



**Fig. 9.11** SH2 structural motif for the human cytoplasmic protein NCK2 (*blue* ribbon) in complex with a decaphosphopeptide (*magenta*, atoms ball and sticks), PDB code entry 1CIA



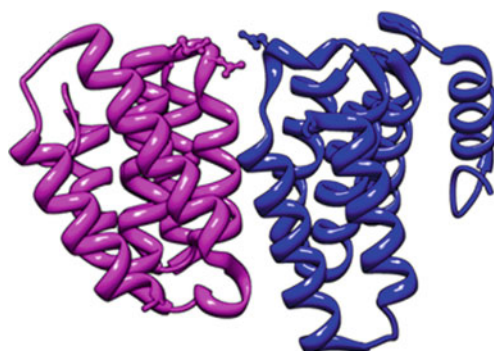
A structural motif found in numerous proteins is the tetratricopeptide repeat (TPR) that facilitates specific interactions with a partner protein (Blatch and Lassle 1999). Three-dimensional structural data revealed that a TPR motif contains antiparallel alpha-helices with an amphipathic channel that might accommodate the complementary region of a target protein, as it is shown in Fig. 9.13 for human dual specificity protein kinase MPS1 dimer, PDB code entry 4H7X (Thebault et al. 2012).

The WW motif is one of the smallest protein domains, composed of 40 amino acids, which mediates specific protein–protein interactions with short proline-rich or proline-containing motifs (Chen and Sudol 1995). The name of this motif comes from the two tryptophan residues spaced 20–23 amino acids apart and it binds to proteins with particular proline-motifs and/or phosphoserine-phos-phothreonine-containing motifs.

**Fig. 9.12** SH3 structural motif for the human Lyn-tyrosine kinase, PDB code entry 1WIF



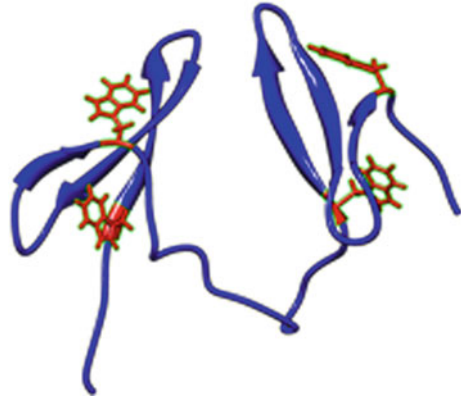
**Fig. 9.13** TPR structural motif for the dimer of the human dual specificity protein kinase MPS1, PDB code entry 4H79. One monomer is colored in *blue* and the other in *magenta*



The PDZ motif is a common structural domain of 80–90 amino-acids found in the signaling proteins (Boxus et al 2008). This domain is used to anchor trans-membrane proteins to the cytoskeleton and bring together signaling complexes (Ranganathan and Ross 1997). Figure 9.14 illustrates the two WW motifs of the human WW domain binding protein 4, PDB code entry 2JXW (Huang et al. 2009) and Fig. 9.15 illustrates the PDZ structural motif of the human multiple PDZ domain protein, PDB code entry 2IWO (Elkins et al. 2007).

The presence of such structural motifs in numerous proteins reveals that interacting amino acids in proteins are often part of conserved motifs. Even if coverage and sensitivity of experimental techniques used in studying protein interactions increased, elucidating the interacting residues is still experimentally difficult. In most cases, all that is known in PPIs is the identity of the two interacting proteins with little information about the binding site. On the other hand, detailed knowledge of interaction specificity is important for understanding the molecular mechanisms of protein functions. From this point of view, the last decade is characterized by the increase of number of computational tools able to predict PPIs.

**Fig. 9.14** Two WW structural motifs of the human WW domain binding protein 4, PDB code entry 2JXW. The four tryptophan residues (two for each WW motif) are shown in full and colored in *red*



**Fig. 9.15** PDZ structural motifs of the human multiple PDZ domain protein, PDB code entry 2IWO



Several computational prediction methods exploit the conservation of protein-binding interfaces by identifying domain pairs that constantly co-occur in interacting proteins and use them to predict new interactions (Deng et al. 2002; Ng et al. 2003; Guimaraes et al. 2006; Betel et al. 2007). There is a library of 3-D structures of protein complexes containing a detailed description of the binding interfaces between interacting proteins (Salama et al. 2001). Such a library is used by structure-based prediction methods to model interactions between proteins that are homologous in structure to the complex components (Aloy et al. 2004; Hou et al. 2006). Other prediction methods use integrative approaches incorporating experimentally proved interaction and additional functional information: correlated expression level, common functional annotation, cross-species comparisons (Li et al. 2004; Betel et al. 2007).

**Table 9.5** Predicted functional partners of bovine recoverin using STRING database

Protein name	Experiments	Databases	Textmining	Homology	Score
Rhodopsin kinase precursor	X	X	X		0.999
Rhodopsin;			X		0.967
Retinol-binding protein 3	X				0.962
G protein-coupled receptor kinase 7		X	X		0.915
Tubulin beta-2B chain	X				0.911
Tubulin alpha-4A chain	X				0.911
Guanylate cyclase 2C			X		0.758
Phosducin			X		0.758
Calbindin			X		0.615
Retinal pigment epithelium-specific 65 kDa protein			X		0.577
Retinaldehyde-binding protein 1			X		0.544
Gag protein			X		0.540
Elongation factor 2			X		0.540
Beta-adrenergic receptor kinase 1			XC		0.501

Web-based resources to analyze PPIs include protein–protein interaction data bases, predicted PPI databases, structural PPI databases, PPI prediction servers and interaction network visualization software. Examples of PPI databases are: Search Tool for the Retrieval of Interacting Genes/Proteins-STRING (Franceschini et al. 2013; <http://string.embl.de/>) and DOMINE (Yellaboina et al. 2011; <http://domine.utdallas.edu/cgi-bin/Domine>). DOMINE database contains a total of 26,219 known and predicted protein domain (domain-domain) interactions. STRING is a database of known and predicted protein interactions including direct (physical) and indirect (functional) associations derived from four sources (genomic context, high-throughput experiments, co-expression and previous knowledge), integrated for a large number of organisms and transferring information between these organisms. Table 9.5 illustrates the predicted interaction partners of bovine recoverin using STRING database and choosing only those prediction having a score higher than 0.5.

We notice that predicted functional partners of bovine recoverin using STRING database are based on experimental data, information contained in other databases and textmining methods. There is not structural homology between these proteins.

**Table 9.6** Fragment of the result of SH2 domain search using 3DID server

PDB	Chains
1a07	A, B
1a08	A, B
1a1a	A, B
1a1b	A, B
1a1c	A, B
1a1e	A, B
1a81	A, C, E, G, . . .
1ab2	A
1ad5	A, B
1aot	F
1aou	F
1a1a	A, B

3DID is a database of high-resolution three-dimensional structural templates for domain-domain interactions. It contains templates for interactions between two globular domains as well as novel domain-peptide interactions (Mosca et al. 2013). Table 9.6 presents a fragment of the result obtained using 3DID server for the SH2 domain search, i.e. the PDB entries that contain the SH2 domain (the total is 285 structures).

Several other web servers for PPI prediction are: JENA PPI server (<http://www.imb-jena.de/jcb/ppi/>), meta-PPISP (<http://pipe.scs.fsu.edu/meta-ppisp.html>), SPPIDER (<http://sppider.cchmc.org/>), SNAPPI (<http://www.compbio.dundee.ac.uk/SNAPPI/inde9.jsp>), hotPOINT (<http://prism.cccb.ku.edu.tr/hotpoint/>), PINUP (<http://sparks.informatics.iupui.edu/PINUP/>) and InterPreTS (<http://www.russelllab.org/cgi-bin/tools/interprets.pl>).

## 9.6 Conclusion

This chapter summarizes and illustrates several on-line tools which are publicly available in the context of protein surface analysis and comparison, protein–ligand and protein–protein interactions respectively giving an overview of the most versatile and efficient webservers. Web-based computational tools allow investigation and comparison of protein sequences and structures, predictions and characterization of their interactions with small molecules or other proteins. Integration of all these data concerning protein sequences, structures and interactions permits to decipher the mechanisms of cellular both physiological and generating diseases events.

## References

- Albou LP, Schwarz B, Poch O, Wurtz JM, Mora D (2009) *Proteins* 76:1
- Aloy P, Bottcher B, Ceulemans H, Leutwein C, Mellwig C, Fischer S, Gavin AC, Bork P, Superti-Furga G, Serrano L, Russell RB (2004) *Science* 303:2026
- Ames JB, Hamasaki N, Molchanova T (2002) *Biochemistry* 41:5776
- Aon MA, Cortassa S, Lloyd D (2000) *Cell Biol Int* 24:581
- Avnir D, Farin D (1990) *New J Chem* 14:197
- Bader GD, Betel D, Hogue CW (2003) *Nucl Acids Res* 31:248
- Ban YEA, Edelsbrunner H, Rudolph J (2004) RECOMB'04, San Diego
- Bauer F, Schweimer K, Meiselbach H, Hoffmann S, Roesch P, Sticht H (2005) *Protein Sci* 14:2487
- Berger C, Weber-Bornhauser S, Eggenberger J, Hanes J, Pluckthun A, Bosshard HR (1999) *FEBS Lett* 450:14
- Berman HM, Westbrook J, Feng Z, Gilliland G, Bhat TN, Weissig H (2000) *Nucl Acids Res* 28:235
- Betel D, Breitkreuz KE, Isserlin R, Dewar-Darch D, Tyers M, Hogue CWV (2007) *PLoS Comput Biol* 3:e182
- Blatch GL, Lässle M (1999) *Bioessays* 21:932
- Boxus M, Twizere JC, Legros S, Dewulf JF, Kettmann R, Willems L (2008) *Retrovirology* 5:76
- Breitkreuz BJ, Stark C, Tyers M (2003) *Genome Biol* 4:R23
- Brooks BR, Bruccoleri RE, Olafson BD, States DJ, Swaminathan S, Karplus M (1983) *J Comp Chem* 4:187
- Byrum S, Smart SK, Larson S, Tackett AJ (2012) *Methods Mol Biol* 833:143
- Carugo O, Eisenhaber F (1997) *J Appl Crystallogr* 30:547
- Ceol A, Chatrarrayamtri A, Santonico E, Sacco R, Castagnoli L, Cesareni G (2006) *Nucl Acids Res* 35:D557
- Chen HI, Sudol M (1995) *Proc Natl Acad Sci U S A* 92:7819
- Christie KR, Weng S, Balakrishnan R, Costanzo MC (2004) *Nucl Acids Res* 32:D311
- Ciorsac AA, Craciun D, Ostafe V, Isvoran A (2011) *Rom Biotech Lett* 16:6473
- Craciun D, Pitulice L, Isvoran A (2009) *Int J Cheml Mod* 2:33
- Craciun D, Pitulice L, Ciorsac A, Ostafe V, Isvoran A (2012) *Rom Rep Phys* 64:116
- DeLano WL (2002) The PyMOL Molecular Graphics System, DeLano Scientific, San Carlos
- Deng M, Mehta S, Sun F, Chen T (2002) *Genome Res* 12:1540
- Dundas J, Ouyang Z, Tseng J, Binkowski A, Turpaz Y, Liang J (2006) *Nucl Acids Res* 34:W116
- Elkzys JM, Papagrigoriou E, Berridge G, Yang X, Phillips C, Gileadi C, Savitsky P, Doyle DA (2007) *Protein Sci* 16: 683
- Fairlie DP, West ML, Wong AK (1998) *Curr Med Chem* 5:29
- Feng S, Yang M, Zhang Z, Wang Z, Hong D, Richter H, Benson GM, Bleicher K, Grether U, Martin RE, Plancher J-M, Kuhn B, Rudolph MG, Chen L (2009) *Bioorg Med Chem Lett* 19: 2595
- Fernandez-Recio J, Totrov M, Skorodumov C, Abagyan R (2005) *Proteins* 58:134
- Ferre F, Ausiello G, Zanzoni A, Helmer-Citterich M (2004) *Nucl Acids Res* 32:D240
- Firoz A, Malik A, Afzal O, Jha V (2010) *Bioinformation* 5:55
- Fischer E (1894) *Ber Dtsch Chem Ges* 27: 2984
- Flaherty KM, Zozulya S, Stryer L, McKay DB (1993) *Cell* 75:709
- Flatcher S, Hamilton AD (2006) *J R Soc Interface* 3:215
- Foote J, Milstein C (1994) *PNAS* 91:10370
- Fraczkiewicz R, Braun W (1998) *J Comp Chem* 19:319
- Franceschini A, Szklarczyk D, Frankild S, Kuhn M, Simonovic M, Roth A, Lin J, Minguez P, Bork P, von Mering C, Jensen LJ (2013) *Nucl Acids Res* 41:D808–15
- Freire E (1999) *PNAS* 96:10118
- Frese S, Schubert WD, Findeis AC, Marquardt T, Roske YS, Stradal TEB, Heinz DW (2006) *J Biol Chem* 281:18236

- Gerstein M, Richards FM, Chapman MS, Connolly ML (2001) Protein surfaces and volumes: measurement and use. In: Rossmann MG, Arnold E (eds) *International tables for crystallography crystallography of biological macromolecules*, Vol F. Kluwer, Dordrecht, pp 531–545
- Goetze T, Brickman J (1992) *Biophys J* 61:109
- Goh CS, Milburn D, Gerstein M (2004) *Curr Opin Struct Biol* 14:104
- Goldman BB, Wipke WT (2000) *Proteins* 38:79
- Gonzalez LJ, Woolfson DN, Alber T (1996) *Nat Struct Biol* 3:1011
- Goodsell DS, Olson AJ (1990) *Proteins: Struct Funct Genet* 8:234
- Gray-Keller MP, Polans AS, Palczewski K, Detwiler PB (1993) *Neuron* 10:523
- Grosdidier A, Zoete V, Michielin O (2011) *Nucl Acids Res* 39:W270–7
- Guimaraes KS, Jothi R, Zotenko E, Przytycka TM (2006) *Genome Biol* 7:R104
- Hou T, Chen K, McLaughlin WA, Lu B, Wang W (2006) *PLoS Comput Biol* 2:e1
- Huang X, Beullens M, Zhang J, Zhou Y, Nicolaescu E, Lesage B, Hu Q, Wu J, Bollen M, Shi Y (2009) *J Biol Chem* 284:25375
- Isvoran A, Badel A, Craescu CT, Miron S, Miteva MA (2011) *BMC Struct Biol* 11:24
- Isvoran A, Craciun D, Martiny V, Sperandio O, Miteva MA (2013) *BMC Pharmacol Toxicol* 14:31
- Kini RM, Evans HJ (1996) *FEBS Lett* 385:81
- Le Guilloux V, Schmidtke P, Tuffery P (2009) *BMC Bioinformatics* 10:168
- Lewis M, Rees DC (1985) *Science* 230:1163
- Li H, Li J, Tan SH, Ng SK (2004) *Pac Symp Biocomput* 312
- Li B, Turuvekere S, Agrawal M, La D, Ramani K, Kihara D (2008) *Proteins: Struct Funct Bioinform* 71:670
- Liu T, Lin Y, Wen X, Jorissen RN, Gilson MK (2007) *Nucl Acids Res* 35:D198
- James LC, Roversi P, Tawfik DS (2003) *Science* 299:1362
- Karplus M (1997) *Fold Des* 2:S69
- Kauffman C, Karypis G (2010) In: Rangwala H, Karypis G (eds) *Introduction to protein structure prediction*, Wiley, New Jersey, p. 343
- Koshland DEJ (1958) *PNAS* 44:98
- Koshland DEJ, Nemethy G, Filmer D (1966) *Biochemistry* 5:365
- Kuzu G, Keskin O, Gursoy A, Nussinov R (2012) *Methods Mol Biol* 819:59
- Jain E, Bairoch A, Duvaud S, Phan I, Redaschi N, Suzek BE, Martin MJ, McGarvey P, Gasteiger E (2009) *BMC Bioinformatics* 10:136
- Janin J, Chotia C (1990) *J Biol Chem* 265:16027
- Levy Y, Wolynes PG, Onuchic JN (2004) *PNAS* 101:511
- Ma B, Kumar S, Tsai CJ, Nussinov R (1999) *Protein Eng* 12:713
- Maity P, König B (2008) *Org Lett* 10:1473
- Meng EC, Shoichet BK, Kuntz ID (2004) *J Comp Chem* 13:505
- Miteva MA, Tufféry P, Villoutreix BO (2005) *Nucl Acids Res* 33:W372
- Monod J, Wyman J, Changeux J (1965) *J Mol Biol* 12:88
- Morris GM, Goodsell DS, Halliday RS, Huey R, Hart WE, Belew RK, Olson AJ (1998) *J Comp Chem* 19:1639
- Morris RJ, Najmanovich RJ, Kahraman A, Thornton JM (2005) *Bioinformatics* 21:2347
- Mosca R, Ceol A, Stein A, Olivella R, Aloy P (2013) *Nucl Acids Res* doi:10.1093/nar/gkt887
- Mouawad L, Isvoran A., Quiniou E, Craescu CT (2009) *FEBS J* 276:1082
- Moustakas DT, Lang PT, Pegg S, Pettersen E, Kuntz ID, Brooijmans N, Rizzo RC (2006) *J Comput Aided Mol Des* 20:601
- Ng SK, Zhang Z, Tan SH, Lin K (2003) *Nucl Acids Res* 31:251
- Ngounou Wetie AG, Sokolowska I, Woods AG, Roy U, Loo JA, Darie CC (2013) *Proteomics* 13:538
- Orengo CA, Michie AD, Jones S, Jones DT, Swindells MB, Thornton JM (1997) *Structure* 5:1093
- Orner BP, Ernst JT, Hamilton AD (2001) *J Am Chem Soc* 123:5382
- Pazos F, Helmer-Citterich M, Ausiello G, Valencia A (1997) *J Mol Biol* 271:511
- Peri S, Navarro JD, Kristiansen TZ, Amanchy R (2004) *Nucl Acids Res* 32:D497



- Pettersen EF, Goddard TD, Huang CC, Couch GS, Greenblatt DM, Meng EC, Ferrin TE (2004) *J Comput Chem* 25:1605
- Pettit FK, Bowie JU (1999) *J Mol Biol* 285:1377
- Phizicky EM, Fields S (1995) *Microbiol Rev* 59:94
- Pitulice L, Isvoran A, Craescu CT, Chiriac A (2008a) *Chaos Solitons Fractals* 35:960
- Pitulice L, Isvoran A, Chiriac A (2008b) *J Serb Chem Soc* 73:805
- Ranganathan R, Ross E (1997) *Curr Biol* 7:R770
- Salama JJ, Donaldson I, Hogue CW (2001) *Biopolymers* 61:111
- Sousa SF, Fernandes PA, Ramos MJ (2006) *Proteins: Struct Funct Bioinformat* 65:15
- Stawiski EW, Baucom AE, Lohr SC, Gregoret LM (2000) *PNAS* 97:3954
- Stawiski EW, Mandel-Gutfreund Y, Lowenthal AC, Gregoret LM (2002) *Pac Symp Biocomput* 7:637
- Tanaka T, Ames JB, Harvey TS, Stryer L, Ikura M (1995) *Nature* 376:444
- Thebault P, Chirgadze DY, Dou Z, Blundell TL, Elowe S, Bolanos-Garcia VM (2012) *Biochem J* 448:321
- Tobi D, Bahar I (2005) *PNAS* 102:18908
- Tsai CJ, Kumar S, Ma B, Nussinov R (1999) *Protein Sci.* 8:1181
- Verdonk ML, Cole JC, Hartshorn MJ, Murray CW, Taylor RD (2003) *Protein: Struct Funct Genet* 52:609
- Vreeker R, Hoekstra LL, den Boer DC, Agterol WGM (1992) *Food Hydrocolloid* 6:423
- Xenarios I, Salwinski L, Duan XJ, Higney P (2002) *Nucl Acids Res* 30:303
- Yellaboina S, Tasneem A, Zaykin DV, Raghavachari B, Jothi R (2011) *Nucl Acids Res* 39: D730
- Yin H, Lee G, Park HS, Payne GA, Rodriguez JM, Sebti SM, Hamilton AD (2005) *Angew Chem* 117:2764

# Chapter 10

## Bondonic Chemistry: Physical Origins and Entanglement Prospects

Mihai V. Putz and Ottorino Ori

**Abstract** The predicted quantum particles of the chemical bonding, the *bondons*, are searched for their ontological bosonic existence and frontier inter-disciplinary applications. To this end, special theoretical methodology and measuring setups are needed in order to find the bondons through entangled experiments on cold nanosystems as graphenic layers with optically-induced topological (Stone-Wales) defects, such that the emergence of the associated bondons is caused by teleportation of defective chemical bonds corresponding to the long-range topological propagation of defective information on the nano-carbon sheet(s). The entangled control of the chemical bonding by bondons, once established, is further implemented providing quantum eigen-energy by quantum phase iterative computations for aromatic chemicals designed *in situ* on graphene by optical lattice with controlling gates accounting for specific molecular Hamiltonians. Moreover, the bondons' existence is also employed to develop the green quantum effector—biological activity determinations (q-EC50) on graphenic optical lattices, highly considered (e.g. by Organisation for Economic Co-operation and Development, along European Commission—Joint Research Center) for global welfare, health and consumer protection due to their toxicological prediction of chemical-biological interactions in organisms and environment; while recognizing the Stone-Wales topological-like walls' propagation mechanism (as on graphene) in cellular homeostasis and morphogenesis, the specific q-EC50 for chemicals acting on a biological system is resolved against recording and fitting the entanglement purity degree curve of teleportation of SMILE (simplified molecular-input line-entry system) molecules to the Hypermolecule form superimposed in a series of congeners (anti-HIV and aromatic compounds are targeted) by counting the “emitted” bondons detected with appropriate optical lattice SWAP protocol(s).

---

M. V. Putz (✉) · O. Ori

Laboratory of Computational and Structural Physical-Chemistry for Nanosciences and QSAR,  
Department of Biology-Chemistry, Faculty of Chemistry, Biology, Geography,  
West University of Timișoara, Pestalozzi Str. No. 16, 300115 Timișoara, Romania  
Tel.: +40-256-592638  
e-mail: mv\_putz@yahoo.com; mvputz@cbg.uvt.ro

O. Ori

Actinium Chemical Research, Via Casilina 1626/A, 00133 Rome, Italy  
e-mail: ottorino.ori@gmail.com

© Springer Science+Business Media Dordrecht 2015

M. V. Putz, O. Ori (eds.), *Exotic Properties of Carbon Nanomatter*,

Carbon Materials: Chemistry and Physics, DOI 10.1007/978-94-017-9567-8\_10

## 10.1 Introduction

“Sometimes it seems to me that a bond between two atoms has become so real, so tangible, so friendly that I can almost see it. And then awake with a little shock: for a chemical bond is not real thing: it does not exist; no-one has ever seen it: no-one ever can. It is a figment of our own imagination.”—as such conveyed the visionary theoretical chemist Coulson in 1951 in the midst of molecular orbital (MO) electronic revolution of chemical structure description. His mixed feeling about chemical bonding is legitimate due to the plethora of unicorns (a mythical creature bringing law, health and fortune in an otherwise chaotic universe) in the world of physical-chemistry of atoms in molecules, on three inter-related directions of nowadays developments:

(i) It starts with the Lewis’ (1916) cornerstone paper advancing the model of cubic atoms in molecule (despite the orbital model of Bohr available from 1913): it allows introducing the octet rule, much employed then by influential Langmuir (1919) works that advanced the hypervalent (e.g.  $\text{PF}_5$ ) and hypovalent (e.g.  $\text{BF}_3$ ) molecules, to end-up in the Linnett’s (1961) double quartet theory; along this, the electron pair concept was able to explain the shared pair of electrons as the benchmark of chemical bond, then rationalized by the Pauling repulsion, to what latter become the variational covalent bonding by equilibrating the molecular energy of wave-function changes among polarization, sharing and contraction (orbital breathing and distortion included) towards achieving the virial  $\frac{1}{2}$  ratio for electronic kinetic energy vs. inter-electronic and electron-nuclei potentials in chemical bonding process (Ruedenberg and Schmidt 2007), which also resembles much of the Bader’s atoms-in-molecule (AIM) theory based on virial forces (Bader et al. 2007); The octet and electron pairing rules in bonding eventually let to the geometrically intuitive valence shell electron pair repulsion—VSEPR (Gillespie and Popelier 2001) and ultimately to the electron localization function (ELF) models (Becke and Edgecombe 1990; Putz 2005); however, according with Roald Hoffman’s (2008) perspective: “AIM and ELF are analytical and descriptive. They are not predictive nor productive”; nevertheless, at this point one should emphasis that Lewis let the subtle bold legacy by his insight according which *the Coulomb law changes its nature in electronic pairs of chemical bonding*, i.e. at very short distances between electrons: in some way the quantum Pauli (spin) repulsion was anticipated.

(ii) On other side, since the ionic and covalent (overlapping) characters should be also equilibrated in chemical gauge bonding ( $A \cdot \cdot B \leftrightarrow A^- : B^+ \leftrightarrow A^+ : B^-$ ) the concept of *resonance structures* using localized pairs modeling valence bond firstly emerged by the Pauling (1939) insight; although criticized since introducing large amount of structures even for describing small molecules (e.g. about 4 millions of mesomers for the simple ion as  $\text{SO}_4^-$ ), it entered the revival due to the modern works of Shaik and Hiberty (2008) who identified the so called “no-pair bonds” through their concept of charge-shift bonding (Shaik et al. 2009) by which chemical bonding may also occur when each atom has a single valence electron of the same spin (i.e. apparently violating the Pauli exclusion principle); this was further verified for

cluster atoms like  $\text{Li}_{12}$  or  $\text{Cu}_{14}$  (the so called ferromagnetic bonding, since achieving a plateau of about 19 kcal/mol where the van der Waals bonding is excluded) as based on covalent-ionic resonance interaction in two atoms (by a triplet-state electronic pair, i.e. for anti-bonding state in molecular orbital theory terms); we thus remain with the message that by mimicking the covalent bonding (as in  $\text{H}_2$ ) the *ionic-covalent bonds* (as in  $\text{F}_2$ ) *may be viewed as a realization of distance interaction of parallel spins in triplet (valence) states.*

(iii) The “polyphonic culture” of chemical bonding is completed by the molecular orbital (MO) approach initiated by the seminal work of Heitler and London (1927) introducing the *mathematical term of resonance* through overlapping and exchange integrals of bonding of atomic orbitals in molecule, having  $\text{H}_2$  as a paradigmatic covalent system; it opened the way of physical, mathematical and computationally tracking the molecular structure by mean-field and beyond approaches of many-body (fermionic) systems by the celebrated method of Hartree-Fock (Löwdin 1955) then augmented to include correlations by delocalization symmetry adapted, towards the (less intuitive) Complete Active Space of Self Consistent Field (CAS-SCF) calculation (Jensen 2007) and multi-reference (by multi-configuration) systems including static (“left-right”) correlation based on near-degeneracy correlation, along the dynamic (“in-out”) correlation based on local fluctuation in charge due to chemical environment—viewed merely as fluctuation in Hilbert space rather than in time (Truhlar 2007); the lesson is paradoxically: *dealing with the molecular orbitals’ delocalization in modeling of size increasingly systems* is like “building a larger and larger pyramid from smaller and smaller stones” (Malrieu et al. 2007) *so losing the chemical bonding intuition*; this way, we face with high demand in searching for alternative quantum chemistry theory and allied computation schemes for electronically delocalized and correlated structures by necessary complex-intuitive picture of chemical bonding.

There is therefore understandable why “Coulson’s dream” is populated by emerged unicorns like resonance, conjugation, hyperconjugation, frontier orbitals, bonding-antibonding, donor-acceptor bond,  $\pi$ -bonding, aromaticity, and many others. On the other side, Hoffman (2008) firmly advice: “push the chemical bonding concept to its limits. Be aware of the different experimental and theoretical measures out there. Accept that (at the limits) a bond will be a bond by some criteria, maybe not others, respect chemical tradition, relax, and . . . have fun with the fuzzy richness of the idea.”

Along this line, our project proceeds with the recent frontier idea of chemical bonding, till now a non observable quantum object simply because wave-functions do not possess an observable nature (Scerri 2000). What is traditionally missing in the molecular orbital approach so far is the proper focus on the quantum (quasi)particle associated to the chemical bond wave function. Basal quantum mechanics adopts the *dual-picture* by associating to each particle (say an electron) its dual wave-function, and vice-versa, i.e. any field (say electromagnetic) may be quantized by particles in the second quantization.

The chemical bonding scenario remained till now incomplete from the quantum perspective: atomic electrons (eventually in valence states) were represented by their

wave-functions and combined in the molecular wave-function which is a chemical field representing all bonding particles. By applying the dual-pictures, one should then consider the existence of a quasi-particle corresponding to the chemical field of bonding, the so-called *bondons* (Putz 2010, 2012a). In short: electrons  $\rightarrow$  wave functions  $\rightarrow$  interference (resonance, exchange and correlation) resulting in *chemical bonding wave function*  $\rightarrow$  *the bondon as associated quantum quasi-particle*. The bondon, emerging as the new boson representing the chemical bond, nowadays prompts researchers for the complete theoretical characterization and for the prediction of its observable features and practical applications. This idea is at the background of the actual project and will be jointly unfolded on the fundamental and experimental objectives and methods.

## 10.2 Bondons by Dirac Theory of Chemical Field (Putz 2010)

The search for the bondons follows the algorithm:

1. Considering the de Broglie-Bohm electronic wave-function/spinor  $\Psi_0$  formulation of the associated quantum Schrödinger/Dirac equation of motion.
2. Checking for recovering the charge current conservation law

$$\frac{\partial \rho}{\partial t} + \nabla \cdot \vec{j} = 0 \quad (10.1)$$

that assures for the circulation nature of the electronic fields under study.

3. Recognizing the (Bohmian) quantum potential  $V_{qua}$  and its equation, if it eventually appears.
4. Reloading the electronic wave-function/spinor under the augmented U(1) or SU(2) group form

$$\Psi_G(t, x) = \Psi_0(t, x) \exp\left(\frac{i e}{\hbar c} \aleph(t, x)\right) \quad (10.2)$$

with the standard abbreviation  $e = e_0^2/4\pi\epsilon_0$  in terms of the chemical field  $\aleph$  considered as the inverse of the fine-structure order:

$$\aleph_0 = \frac{\hbar c}{e} \sim 137.03599976 \left[ \frac{\text{Joule} \times \text{meter}}{\text{Coulomb}} \right] \quad (10.3)$$

since upper bounded, in principle, by the atomic number of the ultimate chemical stable element ( $Z = 137$ ). Although apparently small enough to be neglected in the quantum range, the quantity (10.3) plays a crucial role for chemical bonding where the energies involved are around the order of  $10^{-19}$  Joules (electron-volts)! Nevertheless, for establishing the physical significance of such chemical bonding quanta, one can proceed with the chain equivalences

$$\begin{aligned}
 \aleph_{\#} &\sim \frac{\text{energy} \times \text{distance}}{\text{charge}} \\
 &\sim \frac{\left( \text{charge} \times \frac{\text{potential}}{\text{difference}} \right) \times \text{distance}}{\text{charge}} \\
 &\sim \left( \frac{\text{potential}}{\text{difference}} \right) \times \text{distance}
 \end{aligned} \tag{10.4}$$

revealing that the chemical bonding field carries *bondons* with unit quanta  $\hbar c/e$  along the distance of bonding within the potential gap of stability or by tunneling the potential barrier of encountered bonding attractors.

5. Rewriting the quantum wave-function/spinor equation with the group object  $\Psi_G$ , while separating the terms containing the real and imaginary  $\aleph$  chemical field contributions.
6. Identifying the chemical field charge current and term within the actual group transformation context.
7. Establishing the global/local gauge transformations that resemble the de Broglie-Bohm wave-function/spinor ansatz  $\Psi_0$  of steps (1)–(3).
8. Imposing invariant conditions for  $\Psi_G$  wave function on pattern quantum equation respecting the  $\Psi_0$  wave-function/spinor action of steps (1)–(3).
9. Establishing the chemical field  $\aleph$  specific equations.
10. Solving the system of chemical field  $\aleph$  equations.
11. Assessing the stationary chemical field

$$\frac{\partial \aleph}{\partial t} \equiv \partial_t \aleph = 0 \tag{10.5}$$

that is the case in chemical bonds at equilibrium (ground state condition) to simplify the quest for the solution of chemical field  $\aleph$ .

12. The manifested bondonic chemical field  $\aleph_{\text{bondon}}$  is eventually identified along the bonding distance (or space).
13. Checking the eventual charge flux condition of Bader within the vanishing chemical bonding field (Bader 1990)

$$\aleph_{\#} = 0 \Leftrightarrow \nabla \rho = 0 \tag{10.6}$$

14. Employing the Heisenberg time-energy relaxation-saturation relationship through the kinetic energy of electrons in bonding

$$v = \sqrt{\frac{2T}{m}} \sim \sqrt{\frac{2\hbar}{m t}} \tag{10.7}$$

15. Equate the bondonic chemical bond field with the chemical field quanta (10.3) to get the bondons' mass

$$\aleph_{\mathcal{B}}(m_{\mathcal{B}}) = \aleph_0. \quad (10.8)$$

This algorithm will be next unfolded both for non-relativistic as well as for relativistic electronic motion to quest upon the bondonic existence, eventually emphasizing their difference in bondons' manifestations.

In treating the quantum relativistic electronic behavior, the consecrated starting point stays the Dirac equation for the scalar real valued potential  $w$  that can be seen as a general function of  $(tc, \vec{x})$  dependency (Dirac 1928)

$$i\hbar\partial_t\vec{\Psi}_0 = \left[ -i\hbar c \sum_{k=1}^3 \hat{\alpha}_k \partial_k + \hat{\beta} m c^2 + \hat{\beta} w \right] \vec{\Psi}_0 \quad (10.9)$$

with the spatial coordinate derivative notation  $\partial_k \equiv \partial/\partial x_k$  and the special operators assuming the Dirac 4D representation

$$\hat{\alpha}_k = \begin{bmatrix} 0 & \hat{\sigma}_k \\ \hat{\sigma}_k & 0 \end{bmatrix}, \hat{\beta} = \begin{bmatrix} \hat{1} & 0 \\ 0 & -\hat{1} \end{bmatrix} \quad (10.10a)$$

in terms of bi-dimensional Pauli and unitary matrices

$$\hat{\sigma}_1 = \begin{bmatrix} 0 & 1 \\ 1 & 0 \end{bmatrix}, \hat{\sigma}_2 = \begin{bmatrix} 0 & -i \\ i & 0 \end{bmatrix}, \hat{\sigma}_3 = \begin{bmatrix} 1 & 0 \\ 0 & -1 \end{bmatrix}, \hat{1} \equiv \hat{\sigma}_0 = \begin{bmatrix} 1 & 0 \\ 0 & 1 \end{bmatrix} \quad (10.10b)$$

Written within the de Broglie-Bohm framework, with the  $R$ -amplitude and  $S$ -phase action factors given, respectively, as

$$R(t, x) = \sqrt{\Psi_0(t, x)^2} = \rho^{1/2}(x) \quad (10.11a)$$

$$S(t, x) = px - Et \quad (10.11b)$$

in terms of electronic density  $\rho$ , momentum  $p$ , total energy  $E$ , and time-space  $(t, x)$  coordinates the spinor solution of Eq. (10.9) looks like

$$\begin{aligned} \vec{\Psi}_0 &= \frac{1}{\sqrt{2}} R(t, x) \begin{bmatrix} \varphi \\ \phi \end{bmatrix} \\ &= \frac{1}{\sqrt{2}} R(t, x) \left[ \begin{array}{c} \exp \left\{ \frac{i}{\hbar} [S(t, x) + s] \right\} \\ \exp \left\{ -\frac{i}{\hbar} [S(t, x) + s] \right\} \end{array} \right]^{s=\pm\frac{1}{2}} \end{aligned} \quad (10.12a)$$

that from the beginning satisfies the necessary electronic density condition

$$\vec{\Psi}_0^* \vec{\Psi}_0 = R^* R = \rho \quad (10.12b)$$

Going on, aiming for the separation of the Dirac Eq. (10.9) into its real/imaginary spinorial contributions, one firstly calculates the terms

$$\partial_t \vec{\Psi}_0 = \frac{1}{\sqrt{2}} \partial_t R \begin{bmatrix} \varphi \\ \phi \end{bmatrix} + \frac{1}{\sqrt{2}} R \frac{i}{\hbar} \partial_t S \begin{bmatrix} \varphi \\ -\phi \end{bmatrix} \quad (10.13a)$$

$$\partial_k \vec{\Psi}_0 = \frac{1}{\sqrt{2}} \partial_k R \begin{bmatrix} \varphi \\ \phi \end{bmatrix} + \frac{1}{\sqrt{2}} R \frac{i}{\hbar} \partial_k S \begin{bmatrix} \varphi \\ -\phi \end{bmatrix} \quad (10.13b)$$

$$\begin{aligned} & \sum_{k=1}^3 \hat{\alpha}_k \partial_k \vec{\Psi}_0 \\ &= \frac{1}{\sqrt{2}} \sum_{k=1}^3 \partial_k R \begin{bmatrix} 0 & \hat{\sigma}_k \\ \hat{\sigma}_k & 0 \end{bmatrix} \begin{bmatrix} \varphi \\ \phi \end{bmatrix} + \frac{1}{\sqrt{2}} R \frac{i}{\hbar} \sum_{k=1}^3 \partial_k S \begin{bmatrix} 0 & \hat{\sigma}_k \\ \hat{\sigma}_k & 0 \end{bmatrix} \begin{bmatrix} \varphi \\ -\phi \end{bmatrix} \\ &= \frac{1}{\sqrt{2}} \begin{bmatrix} \phi \sum_k (\partial_k R) \hat{\sigma}_k \\ \varphi \sum_k (\partial_k R) \hat{\sigma}_k \end{bmatrix} + \frac{1}{\sqrt{2}} R \frac{i}{\hbar} \begin{bmatrix} -\phi \sum_k (\partial_k S) \hat{\sigma}_k \\ \varphi \sum_k (\partial_k S) \hat{\sigma}_k \end{bmatrix} \end{aligned} \quad (10.13c)$$

$$\hat{\beta} m c^2 \vec{\Psi}_0 = \frac{m c^2}{\sqrt{2}} R \begin{bmatrix} \hat{1} & 0 \\ 0 & -\hat{1} \end{bmatrix} \begin{bmatrix} \varphi \\ \phi \end{bmatrix} = \frac{m c^2}{\sqrt{2}} R \begin{bmatrix} \varphi \\ -\phi \end{bmatrix} \quad (10.13d)$$

$$\hat{\beta} w \vec{\Psi}_0 = \frac{w}{\sqrt{2}} R \begin{bmatrix} \varphi \\ -\phi \end{bmatrix} \quad (10.13e)$$

to be then combined in (10.9) producing the actual de Broglie-Bohm-Dirac spinorial Equation

$$\begin{aligned} & \begin{bmatrix} i \hbar \varphi \partial_t R - R \varphi \partial_t S \\ i \hbar \phi \partial_t R + R \phi \partial_t S \end{bmatrix} \\ &= \begin{bmatrix} -i \hbar c \phi \sum_k (\partial_k R) \hat{\sigma}_k - R c \phi \sum_k (\partial_k S) \hat{\sigma}_k + (m c^2 + w) R \varphi \\ -i \hbar c \varphi \sum_k (\partial_k R) \hat{\sigma}_k + R c \varphi \sum_k (\partial_k S) \hat{\sigma}_k - (m c^2 + w) R \phi \end{bmatrix} \end{aligned} \quad (10.14)$$

When equating the imaginary parts of (10.14) one yields the system

$$\begin{cases} \varphi \partial_t R + \phi c \sum_k (\partial_k R) \hat{\sigma}_k = 0 \\ \varphi c \sum_k (\partial_k R) \hat{\sigma}_k + \phi \partial_t R = 0 \end{cases} \quad (10.15)$$



that has non-trivial spinorial solutions only by canceling the associate determinant, *i.e.*, by forming the Equation

$$(\partial_t R)^2 = c^2 \left[ \sum_k (\partial_k R) \hat{\sigma}_k \right]^2 \quad (10.16)$$

of which the minus sign of the squared root corresponds with the electronic conservation charge, while the positive sign is specific to the relativistic treatment of the positron motion. For proving this, the specific relationship for the electronic charge conservation (10.1) may be unfolded by adapting it to the present Bohmian spinorial case by the chain equivalences

$$\begin{aligned} 0 &= \partial_t \rho + \nabla \vec{j} \\ &= \partial_t (R^2) + \sum_k \partial_k j_k \\ &= 2R \partial_t R + \sum_k \partial_k (c \hat{\Psi}_0^* \hat{\alpha}_k \hat{\Psi}_0) \\ &= 2R \partial_t R + \frac{c}{2} \sum_k \partial_k R^* R \begin{bmatrix} e^{-\frac{i}{\hbar}(S+s)} & \\ & e^{\frac{i}{\hbar}(S+s)} \end{bmatrix} \begin{bmatrix} 0 & \hat{\sigma}_k \\ \hat{\sigma}_k & 0 \end{bmatrix} \begin{bmatrix} e^{\frac{i}{\hbar}(S+s)} \\ \\ \\ e^{-\frac{i}{\hbar}(S+s)} \end{bmatrix} \\ &= 2R \partial_t R + \frac{c}{2} \sum_k \hat{\sigma}_k \left( \underbrace{\phi^2}_1 + \underbrace{\varphi^2}_1 \right) \partial_k R^2 \\ &= 2R \partial_t R + 2Rc \sum_k \hat{\sigma}_k (\partial_k R) \end{aligned} \quad (10.17a)$$

The result

$$\partial_t R = -c \sum_k \hat{\sigma}_k (\partial_k R) \quad (10.17b)$$

indeed corresponds with the squaring root of (10.16) with the minus sign, certifying, therefore, the validity of the present approach, *i.e.*, being in accordance with the step (2) in the above bondonic algorithm.

Next, let us see what information is conveyed by the real part of Bohmian decomposed spinors of Dirac Eq. (10.14); the system (10.18) is obtained

$$\begin{cases} \phi (\partial_t S + mc^2 + w) - \phi c \sum_k (\partial_k S) \hat{\sigma}_k = 0 \\ \phi c \sum_k (\partial_k S) \hat{\sigma}_k - (\partial_t S + mc^2 + w) \phi = 0 \end{cases} \quad (10.18)$$

that, as was previously the case with the imaginary counterpart (10.15), has no trivial spinors solutions only if the associate determinant vanishes, which gives the Equation

$$c^2 \left[ \sum_k (\partial_k S) \hat{\sigma}_k \right]^2 = (\partial_t S + mc^2 + w)^2 \quad (10.19)$$

Now, considering the Bohmian momentum-energy (10.17) equivalences, the Eq. (10.19) further becomes

$$\begin{aligned} c^2 \left[ \sum_k p_k \hat{\sigma}_k \right]^2 &= (-E + mc^2 + w)^2 \\ \Leftrightarrow c^2 (\vec{p} \cdot \hat{\sigma})^2 &= (-E + mc^2 + w)^2 \\ \Leftrightarrow c^2 p^2 &= (-E + mc^2 + w)^2 \end{aligned} \quad (10.20)$$

from where, while retaining the minus sign through the square rooting (as prescribed above by the imaginary spinorial treatment in relation with charge conservation), one recovers the relativistic electronic energy-momentum conservation relationship

$$E = cp + mc^2 + w \quad (10.21)$$

thus confirming in full the reliability of the Bohmian approach over the relativistic spinors.

Moreover, the present Bohmian treatment of the relativistic motion is remarkable in that, except in the non-relativistic case, it does not produce the additional quantum (Bohm) potential in (10.15)–responsible for entangled phenomena or hidden variables. This may be justified because within the Dirac treatment of the electron the entanglement phenomenology is somehow included throughout the Dirac Sea and the positron existence. Another important difference with respect to the Schrödinger picture is that the spinor equations that underlie the total charge and energy conservation do not mix the amplitude (10.2) with the phase (10.3) of the de Broglie-Bohm wave-function, whereas they govern now, in an independent manner, the flux and the energy of electronic motion. For these reasons, it seems that the relativistic Bohmian picture offers the natural environment in which the chemical field and associate bondons particles may be treated without involving additional physics.

Let us see, therefore, whether the Dirac-Bohmian framework will reveal (or not) new insight in the bondon (Schrödinger) reality. This will be done by reconsidering the working Bohmian spinor (10.12a) as transformed by the internal gauge symmetry SU(2) driven by the chemical field  $\aleph$  related phase—in accordance with Eq. (10.2) of the step (4) of bondonic algorithm

$$\begin{aligned} \tilde{\Psi}_G(t, x) &= \tilde{\Psi}_0(t, x) \exp \left( \frac{i}{\hbar} \frac{e}{c} \aleph(t, x) \right) \\ &= \frac{1}{\sqrt{2}} R(t, x) \begin{bmatrix} \varphi_G \\ \phi_G \end{bmatrix} = \frac{1}{\sqrt{2}} R(t, x) \begin{bmatrix} \exp \left\{ \frac{i}{\hbar} \left[ S(t, x) + \frac{e}{c} \aleph(t, x) + s \right] \right\} \\ \exp \left\{ -\frac{i}{\hbar} \left[ S(t, x) + \frac{e}{c} \aleph(t, x) + s \right] \right\} \end{bmatrix} \end{aligned} \quad (10.22)$$

Here it is immediate that expression (10.22) still preserves the electronic density formulation (10.2) as was previously the case with the gaugeless field (10.12a)

$$\tilde{\Psi}_G^* \tilde{\Psi}_G = R^* R = \rho \quad (10.23)$$

However, when employed for the Dirac equation terms, the field (10.22) modifies the previous expressions (10.13a)–(10.13c) as follows

$$\partial_t \tilde{\Psi}_G = \frac{1}{\sqrt{2}} \partial_t R \begin{bmatrix} \varphi_G \\ \phi_G \end{bmatrix} + \frac{1}{\sqrt{2}} R \frac{i}{h} \left( \partial_t S + \frac{e}{c} \partial_t \aleph \right) \begin{bmatrix} \varphi_G \\ -\phi_G \end{bmatrix} \quad (10.24a)$$

$$\partial_k \tilde{\Psi}_0 = \frac{1}{\sqrt{2}} \partial_k R \begin{bmatrix} \varphi_G \\ \phi_G \end{bmatrix} + \frac{1}{\sqrt{2}} R \frac{i}{h} \left( \partial_k S + \frac{e}{c} \partial_k \aleph \right) \begin{bmatrix} \varphi_G \\ -\phi_G \end{bmatrix} \quad (10.24b)$$

$$\begin{aligned} & \sum_{k=1}^3 \hat{\alpha}_k \partial_k \tilde{\Psi}_G \\ &= \frac{1}{\sqrt{2}} \sum_k (\partial_k R) \hat{\sigma}_k \begin{bmatrix} \phi_G \\ \varphi_G \end{bmatrix} + \frac{1}{\sqrt{2}} R \frac{i}{h} \sum_k \left( \partial_k S + \frac{e}{c} \partial_k \aleph \right) \hat{\sigma}_k \begin{bmatrix} -\phi_G \\ \varphi_G \end{bmatrix} \end{aligned} \quad (10.24c)$$

while producing the gauge spinorial Equation

$$\begin{aligned} & \begin{bmatrix} i\hbar\varphi_G \partial_t R - R\varphi_G \left( \partial_t S + \frac{e}{c} \partial_t \aleph \right) \\ i\hbar\phi_G \partial_t R + R\phi_G \left( \partial_t S + \frac{e}{c} \partial_t \aleph \right) \end{bmatrix} \\ &= \begin{bmatrix} -i\hbar c\phi_G \sum_k (\partial_k R) \hat{\sigma}_k - Rc\phi_G \sum_k \left( \partial_k S + \frac{e}{c} \partial_k \aleph \right) \hat{\sigma}_k + (mc^2 + w) R\varphi_G \\ -i\hbar c\varphi_G \sum_k (\partial_k R) \hat{\sigma}_k + Rc\varphi_G \sum_k \left( \partial_k S + \frac{e}{c} \partial_k \aleph \right) \hat{\sigma}_k - (mc^2 + w) R\phi_G \end{bmatrix} \end{aligned} \quad (10.25)$$

Now it is clear that since the imaginary part in (10.25) was not at all changed with respect to Eq. (10.14) by the chemical field presence, the total charge conservation (10.1) is naturally preserved; instead the real part is modified, respecting the case (10.14), in the presence of the chemical field (by internal gauge symmetry). Nevertheless, in order that chemical field rotation does not produce modification in the total energy conservation, it imposes that the gauge spinorial system of the chemical field must be as

$$\begin{cases} \varphi_G \partial_t \aleph - \phi_G c \sum_k (\partial_k \aleph) \hat{\sigma}_k = 0 \\ \varphi_G c \sum_k (\partial_k \aleph) \hat{\sigma}_k - \phi_G \partial_t \aleph = 0 \end{cases} \quad (10.26)$$

According to the already custom procedure, for the system (10.26) having no trivial gauge spinorial solution, the associated vanishing determinant is necessary, which brings to light the chemical field Equation

$$c^2 \left[ \sum_k (\partial_k \aleph) \hat{\sigma}_k \right]^2 = (\partial_t \aleph)^2 \quad (10.27a)$$

equivalently rewritten as

$$c^2[\nabla\aleph \cdot \hat{\sigma}]^2 = (\partial_t\aleph)^2 \quad (10.27b)$$

that simply reduces to

$$c^2(\nabla\aleph)^2 = (\partial_t\aleph)^2 \quad (10.27c)$$

through considering the Pauling matrices (10.10b) unitary feature upon squaring.

At this point, one has to decide upon the sign of the square root of (10.27c); this was previously clarified to be minus for electronic and plus for positronic motions. Therefore, the electronic chemical bond is modeled by the resulting chemical field equation projected on the bonding length direction

$$\frac{\partial\aleph}{\partial X_{bond}} = -\frac{1}{c} \frac{\partial\aleph}{\partial t} \quad (10.28)$$

The Eq. (10.28) is of undulatory kind with the chemical field solution having the general plane wave form

$$\aleph_{\mathcal{B}} = \frac{\hbar c}{e} \exp[i(kX_{bond} - \omega t)] \quad (10.29)$$

that agrees with both the general definition of the chemical field (10.3) as well as with the relativistic “traveling” of the bonding information. In fact, this is the paradox of the Dirac approach of the chemical bond: it aims to deal with electrons in bonding while they have to transmit the chemical bonding information—as waves—propagating with the light velocity between the bonding attractors. This is another argument for the need of bondons reality as a specific existence of electrons in chemical bond is compulsory so that such a paradox can be solved.

Note that within the Dirac approach, the Bader flux condition (10.6) is no more related to the chemical field, being included in the total conservation of charge; this is again natural, since in the relativistic case the chemical field is explicitly propagating with a percentage of light velocity (see the Discussion in Sect. 10.4 below) so that it cannot drive the (stationary) electronic frontiers of bonding.

Further on, when rewriting the chemical field of bonding (10.29) within the de Broglie and Planck consecrated corpuscular-undulatory quantifications

$$\aleph_{\mathcal{B}}(t, X_{bond}) = \frac{\hbar c}{e} \exp\left[\frac{i}{\hbar}(pX_{bond} - Et)\right] \quad (10.30)$$

it may be further combined with the unitary quanta form (10.3) in the Eq. (10.8) of the step (xv) in the bondonic algorithm to produce the phase condition

$$1 = \exp\left[\frac{i}{\hbar}(pX_{bond} - Et)\right] \quad (10.31)$$

that implies the quantification

$$pX_{bond} - Et = 2\pi n\hbar, n \in \mathbb{N} \quad (10.32)$$

By the subsequent employment of the Heisenberg time-energy saturated indeterminacy at the level of kinetic energy abstracted from the total energy (to focus on the motion of the bondonic plane waves)

$$E = \frac{\hbar}{t} \quad (10.33a)$$

$$p = mv = \sqrt{2mT} \rightarrow \sqrt{\frac{2m\hbar}{t}} \quad (10.33b)$$

the bondon Eq.(10.32) becomes

$$X_{bond} \sqrt{\frac{2m\hbar}{t}} = (2\pi n + 1)\hbar \quad (10.34)$$

that when solved for the bondonic mass yields the expression

$$m_{\mathcal{B}} = \frac{\hbar t}{2} \frac{1}{X_{bond}^2} (2\pi n + 1)^2, n = 0, 1, 2 \dots \quad (10.35)$$

which appears to correct the previous non-relativistic Schrödinger expression (Putz 2010) with the full quantification. However, the Schrödinger bondon mass is here recovered from the Dirac bondonic mass (10.35) in the ground state, *i.e.*, by setting  $n = 0$ . Therefore, the Dirac picture assures the complete characterization of the chemical bond through revealing the bondonic existence by the internal chemical field symmetry with the quantification of mass either in ground or in excited states ( $n \geq 0, n \in N$ ).

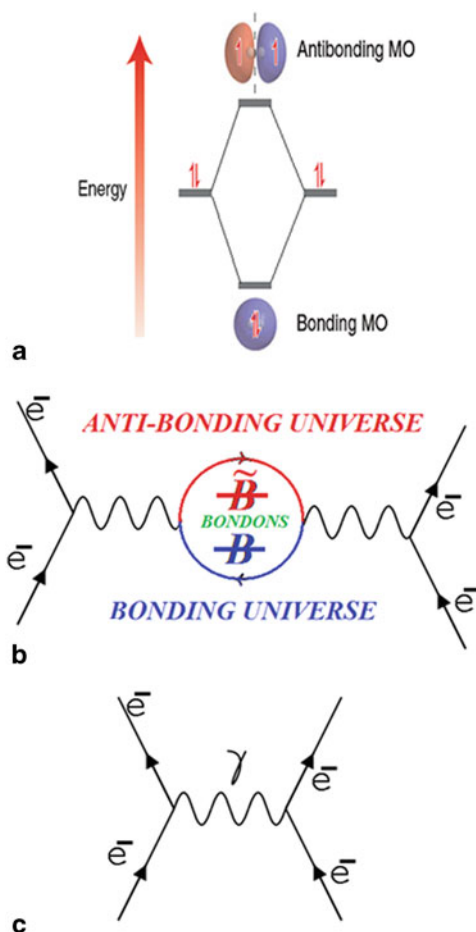
Moreover, as always happens when dealing with the Dirac equation, the positronic bondonic mass may be immediately derived as well, for the case of the chemical bonding is considered also in the anti-particle world; it emerges from reloading the square root of the Dirac chemical field—Eq. (10.27c) with a plus sign that will be propagated in all the subsequent considerations, *e.g.*, with the positronic incoming plane wave replacing the departed electronic one of (10.29), until delivering the positronic bondonic mass

$$\tilde{m}_{\mathcal{B}} = \frac{\hbar t}{2} \frac{1}{X_{bond}^2} (2\pi n - 1)^2, n = 0, 1, 2 \dots \quad (10.36)$$

It nevertheless differs from the electronic bondonic mass (10.35) only in the excited spectrum, while both collapse in the non-relativistic bondonic mass (10.38) for the ground state of the chemical bond.

Remarkably, for both the electronic and positronic cases, the associated bondons in the excited states display heavier mass than those specific to the ground state, a behavior once more confirming that the bondons encompass all the bonding information, *i.e.*, have the excitation energy converted in the mass-added-value in full agreement with the mass-energy relativistic custom Einstein equivalence (Einstein 1905).

**Fig. 10.1** The phenomenological representation of the bonding-antibonding molecular orbital (MO) picture of chemical bonding (a) vis-à-vis the two bosonic bondonic-antibondonic ( $B$  vs.  $\tilde{B}$ ) states by associated Feynman diagram picture of chemical bonding interaction (b), respecting the physical repelling interaction of electrons by  $\gamma$ -photon (c) (see the text for further details and references)



### 10.3 Entangled Chemistry: Objectives

Having the electrons participating into the chemical bond all “merged” in the new bondon—which is a bosonic particle—induces a de-facto *bosonization of the electrons* in the resulting chemical field. Qualitatively, this is depicted by the side-by-side diagrams of Fig. 10.1 “translating” the MOs of bonding in the actual bosonic-bondonic picture.

Quantitatively, the bosonization transforms the fermionic field  $\psi$  into the bosonic one  $F \exp(-i\aleph)$  with  $F$  being the Klein factor (Schönhammer 2002) and  $\aleph$  the bosonic field, and was introduced by the (observational) necessity to correctly quantify the (quasi) one-dimensional systems. It roots in the breaking down of the Fermi liquid theory for 1D-excitations of electrons with linear dispersion (Tomonaga 1950) while developing into the Luttinger liquid (Mattis and Lieb 1965),

**Table 10.1** Ratios for the bondon-to-electronic mass ( $m_0$ ) and charge ( $e$ ) and for the bondon-to-photon velocity ( $c$ ) percent, along the associated bondonic life-time for selected chemical bonds in terms of their basic characteristics such as the bond length ( $X_{bond}$ ) and energy ( $E_{bond}$ ) for the bondonic ground states, respectively. (Putz 2010, 2012a)

Bond type	$X_{bond}$ (Å)	$E_{bond}$ (kcal/mol)	$\zeta_m = \frac{m_{\#}}{m_0}$	$\zeta_v = \frac{v_{\#}}{c}$ [%]	$\zeta_e = \frac{e_{\#}}{e}$ [ $\times 10^3$ ]	$t_{\#}$ [ $\times 10^{15}$ ] (seconds)
H–H	0.60	104.2	2.34219	3.451	0.3435	9.236
F–F	1.28	37.6	1.42621	2.657	0.264	25.582
Cl–Cl	1.98	58	0.3864	6.330	0.631	16.639
C–C	1.54	81.2	0.45624	6.890	0.687	11.894
C–H	1.09	99.2	0.7455	5.961	0.594	9.724
C=C	1.34	147	0.33286	10.816	1.082	6.616
C≡C	1.20	194	0.31451	12.753	1.279	5.037

with the subsequent fundamental description of the 1D organic conductors (Heeger et al. 1988; Keiss 1992), semiconductor quantum wires (Tarucha et al. 1995) and carbon nanotubes (Bockrath et al. 1999). Since fermions in 1D systems cannot pass each other (akin to chemical bonding modeling in conjugated carbon systems with primary methodological interest in the present project), their interaction is “strong” and dramatically changes the physics of the spin-charged separation specific to Pauli repulsion, so that the bosonic-bondonic carrier of such interaction is created. Moreover, the actual bosonic-bondonic picture is supported by the relativistic Dirac-de Broglie-Bohm framework employing the chemical field bosonization by the gauge transformation of (10.12a and b) (Putz 2010, 2012a).

By considering this mixed fermionic-bosonic form as an ansatz solution of Dirac equation, with the probability current density equation fulfilled, one recovers the unitary wave-particle phase transformation leaving with the subsequent bosonic-bondonic/antibondonic mass quantification (10.35) and (10.36) (Putz 2010)

$$m_{(\#)} = \frac{\hbar^2 (2\pi n \pm 1)^2}{2 E_{bond} X_{bond}^2}, n = 0, 1, 2, \dots, \quad (10.37)$$

resembling the qualitative picture of Fig. 10.1b. The bondonic mass is then complemented with the bondonic velocity ( $v_{\#}$ ), bondonic charge ( $e_{\#}$ ), and bondonic life-time ( $t_{\#}$ ) for a given ( $X_{bond}$ ,  $E_{bond}$ ) couple information, as illustrated for basic chemical bonds in Table 10.1.

One may see from Table 10.1 that the actual bosonic-bondonic model provides the top  $H_2$  bondonic mass in the actual series consecrating this way the main criteria for covalent bonding; by contrast,  $F_2$  molecule associates with the top life-time (in femto-seconds!) so indicating the charge-shift character by ionic interaction inclusion requiring larger time for bondon carrying the bonding information between adducts, since posing the lowest velocity in the series too; the quite opposite bondonic behavior of  $H_2$  and  $F_2$  widely agrees with the charge-shift phenomenology

in bonding (Shaik et al. 2009); moreover, the  $F_2$  slightly different bonding hierarchy versus  $Cl_2$  in terms of the higher velocity and less life-time for the latter also certifies the correct modeling of bondonic picture. Interesting results are revealed also for carbon-bonding systems; bondonic properties display systematically trends from single to triple bonding: mass and life-time decreasing, velocity and charge increasingly associate with mixed character of ionicity (in terms of low velocity and higher time-life) and covalent higher mass for single C-bond, while the more covalent character is emphasized for double and triple C-bonds in terms of lower bondonic life-time in chemical bonding. However, peculiar closeness in C-C and C-H bondonic characteristics (especially for velocity, charge and life-time) fully justifies the bosonization of saturated nanocarbon tubes and further advocates for their use enlightening the bondonic effects. As such, bondons can be further considered as part of (quasi) Bose-Einstein Condensation–BEC (Greiner et al. 2003; Pethick and Smith 2004) in chemical bonding and chemical aggregates, while being appropriately implemented in the density functional theory—DFT (Argaman and Band 2011) with which it shares the two main features: the total conservation of particles' number

$$N = \int \rho(\mathbf{r})d\mathbf{r} = \int |\psi(\mathbf{r})|^2 d\mathbf{r} \quad (10.38)$$

and inclusion of correlation effects (Putz 2011a, b, 2012b, c).

In this combined DFT-BEC context, the general bosonic-fermionic mixed heteropolar Heitler-London Hamiltonian combines with the nonlinear Gross-Pitaevsky equation for bosonic condensation, to recover the singlet (bonding) and triplet (anti-bonding) states as in general chemical covalency, while obtaining a richer related spectra of energies involved, appropriately classified in two pairs,  $E_{bond-BEC-I}^{\pm}$  and  $E_{bond-BEC-II}^{\pm}$ , see Fig. 10.2a (Putz 2011a, 2012a, b).

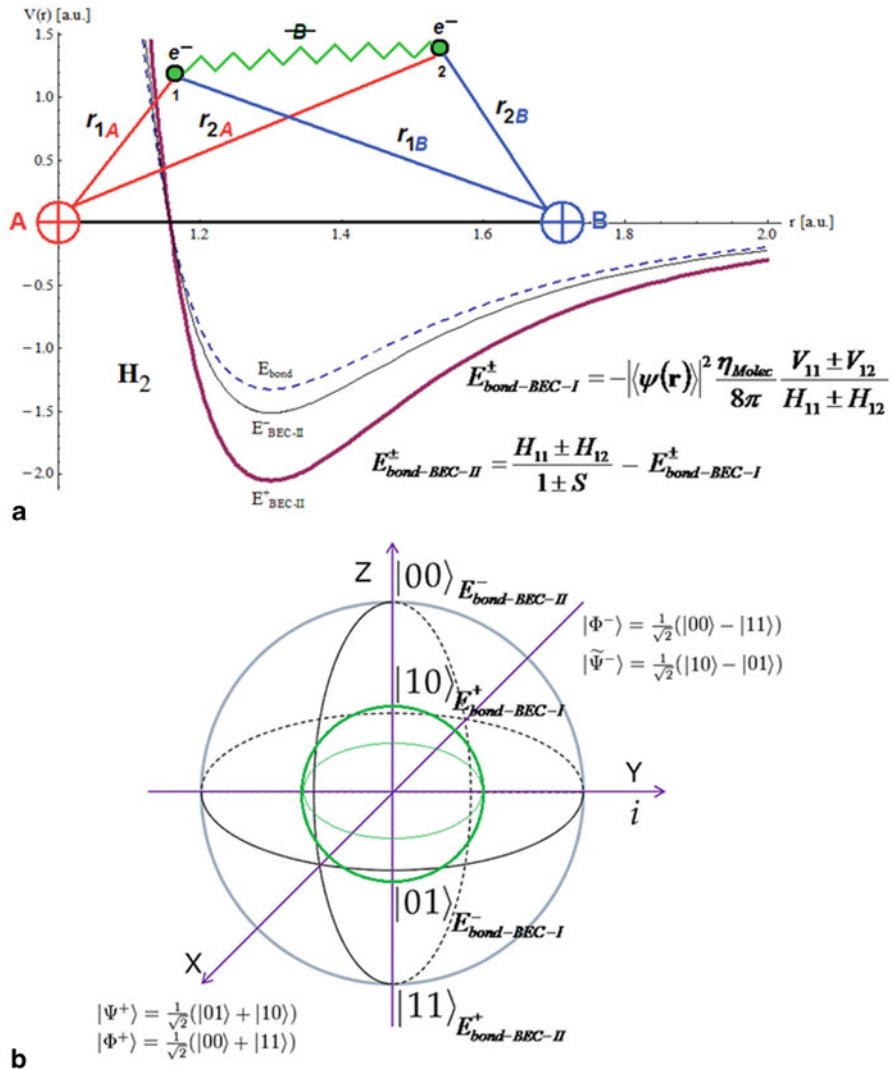
The general results of Fig. 10.2a open exciting perspectives of treating chemical bonding through entangled bondons; this because there is revealed that the chemical bonding consists, in the bosonization picture, by two related sets of bonding-anti bonding states: those arising from “chemical” BEC-II correspond to the fashioned states  $|11\rangle$ ,  $|00\rangle$  superimposed into the two-level system for MO chemical bonding paradigm, while the additional “physical” (higher and inversed respecting BEC-II hence the name) BEC-I energies provide additional  $|01\rangle$ ,  $|10\rangle$  bonding and anti-bonding states, respectively (Fig. 10.2b). Most interestingly, while combining these 4 states obtained from treatment of chemical bonding as bosonic condensate of bondons, one may form the Bell states (Williams 2011) depicted in Fig. 10.2b; one observes that the actual mixed bonding-antibonding state

$$|\tilde{\Psi}^{-}\rangle = 1/\sqrt{2}(|10\rangle - |01\rangle) \quad (10.39)$$

is asymmetrical respecting the corresponding Bell state

$$|\Psi^{-}\rangle = 1/\sqrt{2}(|01\rangle - |10\rangle); \quad (10.40)$$





**Fig. 10.2** **a** Illustration of the bi-atomic chemical bond through the bondonic-bosonic contribution at inter-electronic interaction; the model is overlapped with the states of the molecular hydrogen; the highlighted BEC-II levels of bonding (“+”thick line) and antibonding (“-”thin line) are both placed below the level of “normal” bonding of the H<sub>2</sub> molecule in gaseous state, after Putz (2012b); **b** The entangled chemical bonding states in the 2-qubits space (BEC-I, and BEC-II, each with “+” & “-” bonding realizations) projected on the two centered Bloch spheres with the actually resulted Bell states

This behavior may be view as specific for bosonization of fermions, i.e. different from the original Bell treatments of bosonic photons. With this finding a completely new physics is advanced in treating the *chemical bond by entangled*

*bondonic model*, here resumed as: (i) electrons in chemical bonding bosonize to form bondons and antibondons; (ii) the resulted bonding and anti-bonding states further interact and lift their degeneracy to provide pairs of physical-chemical entangled states  $\{|00\rangle, |11\rangle, |01\rangle, |10\rangle\}$  so forming a 2-qubit system; (iii) the entangled bondonic-antibondonic states interfere in the resulted entangled chemical bonding Bell states  $\{\Phi^+, \Psi^+, \Phi^-, \tilde{\Psi}^-\}$  (iv) the electronic specificity is noted by the manifested fermionic antisymmetry for the fourth bosonic-bondonic Bell state respecting the bosonic-photonic one ( $\tilde{\Psi}^- = -\Psi^-$ ). Worth remarking that when replacing the terms: “entanglement” for “correlation”, “interference” for “overlapping”, and “antisymmetry” for “exchange” the actual bosonic-bondonic picture of chemical bonding truly triggers what we can call *the entangled quantum chemistry* (ENTA-QUA-CHEM).

In this context we arrive to the first major objective of the present project: ENTA-QUA-CHEM-1: *REVEALING THE ONTOLOGICAL EVIDENCE OF CHEMICAL BONDONS AS THE QUANTUM QUASI-PARTICLES OF CHEMICAL BONDING*.

At this stage of comprehension we are on the right way for fulfilling the first two main criteria for a reliable model of universal chemical bonding (Poater et al. 2006; Frenking and Krapp 2007): (i) rooted in quantum mechanics; (ii) the used terms must be mathematically unambiguously defined. Although just these two criteria already finely accord with the Coulson (1960) impetus (“gives us inside not numbers”), they should be balanced by applications and accuracy in knowledge and control as wisely remarked by Kutzelnigg (2007): “understanding without models is impossible; however, a model is useful only if one understands its scope and limitations”. To this aim we are also targeting to accomplish the remaining three conditions, namely: (iii) the numerical counterpart of used terms must not significantly change at different levels of theory; (iv) the terms provide insights in a plausible interpretable way; (v) the model and terms used showcase predictive power in structure and reactivity with a wide range of applicability for electronic ground and excited states.

The numerical prediction of the entangled bondonic model is particularly related to the hot topic of performing quantum chemistry by quantum information/computer; among the most spectacular achievements in this regard are: the molecular spectra determination by a quantum algorithm (Wang et al. 2008), the simulation of a chemical dynamics (Kassal et al. 2008); predicting the lattice protein conformation (Perdomo et al. 2008); modeling the photosynthesis harvesting by quantum transport phenomena with special enhancement while some noise in the quantum system is present (Rebentrost et al. 2009). However, what is particularly interesting for quantum chemistry is the *eigen-values*’ quantum computing for chemical systems, given the fact that accurate computation by ordinary computers involve, for instance 1.3 billion of configurations just for Cr<sub>2</sub> molecule (Dachsel et al. 1999) or about 10<sup>17</sup> configurations for full CI calculation with 6–31G\* for methanol/CH<sub>3</sub>OH (10.18 electrons and 50 basis functions). In this regard, for a given quantum chemical eigen-value problem

$$\hat{H} |\psi_\lambda\rangle = \lambda |\psi_\lambda\rangle \quad (10.41)$$

one employs the associated propagator's unitary operator

$$U = e^{i\hat{H}} \quad (10.42)$$

so that dealing with the transformed phase-equation

$$U |\psi_\lambda\rangle = e^{i\lambda} |\psi_\lambda\rangle \quad (10.43)$$

allowing to set the phase as

$$\lambda = 2\pi\phi \quad (10.44)$$

and expressing the new phase with n-bits precision

$$\phi = 0.x_1x_2\dots x_n \quad (10.45)$$

which helps in synthesizing the phase state, e.g. over the above bondonic Bell states, say

$$\Theta = 1/\sqrt{2^n} \sum_{y=0}^{2^n-1} e^{2\pi i(0.x_1x_2\dots x_n)y} |y\rangle, \quad (10.46)$$

ending to the phase estimation by the Quantum Fourier Transformation

$$QFT^{-1}\Theta = |x_1x_2\dots x_n\rangle \quad (10.47)$$

which practically solves the initial eigen-problem by a exponential speedup quantum algorithm (Abrams and Lloyd 1999; Aspuru-Guzik et al. 2005). With this we arrived to the second major objective of the present project: *ENTA-QUA-CHEM-2: PERFORMING ENTANGLED QUANTUM CHEMICAL COMPUTATION, ESPECIALLY EIGEN-VALUES ESTIMATIONS, FOR COMPLEX MOLECULES THROUGH EMPLOYING THE BONDONIC BELL STATES INFORMATION.*

At last but not at least, one likes making even further advancement of the present approach in the direction of quantum/green evaluation of the biological activities (toxicities) by performing entangled quantum chemistry determinations *without* involving any organisms or species. Such possibility is sustained since the development of the so called *biological field theory* (Fröhlich 1968; Glauber 1963; Popp 1992), turning the biological coding and computing as the heart of biological organization modeling having biological nesting codes, biocodes and error-correcting codes as the basic tools explaining the macroevolution (Barbieri 1998, 2008; Battail 2007); illustrative example are the coexistence of triplet code in protein synthesis (Trifonov 1989), or the arithmetic generator of the genetic code (Shcherbak 1994); for instance, the nucleon number (nn), an atomic intensive quantity eventually driving the electrons on the outer shells too, balances for the canonical DNA base pairing (T = A, C ≡ G) as well as for RNA base U since furnishing the uniquely related 037 coding:

$$nn(T, A) = 125 + 134 = 259 = 7 \times 037, \quad (10.48)$$

$$\text{nn}(\text{C}, \text{G}) = 110 + 150 = 260 = 7 \times 037 + 1, \quad (10.49)$$

$$\text{nn}(\text{U}) = 111 = 3 \times 037; \quad (10.50)$$

many analogues combinations involve  $0 \bmod 037$  and  $1 \bmod 037$  as the binary 0&1 pairs (suitable for information computing) so controlling the forming of biomolecules by blocks + chains analogue rules (Shcherbak 2003). It appears therefore that cellular structure and evolution, so accustomed with information terms such as self-similarity, coding, copying, transcription, sequence, etc. (Hameroff and Penrose 2003) are indeed the major playground for any chemical bonding theory seeking verifiable predictions. In this context, what is among the forefront interest for applicative science in environmental, population protection and health safety (EC 2006, EU 2008) regards the green determination of the 50 %-effective concentration ( $EC_{50}$ ) dose of a given chemical compound targeting biological/toxicological activity

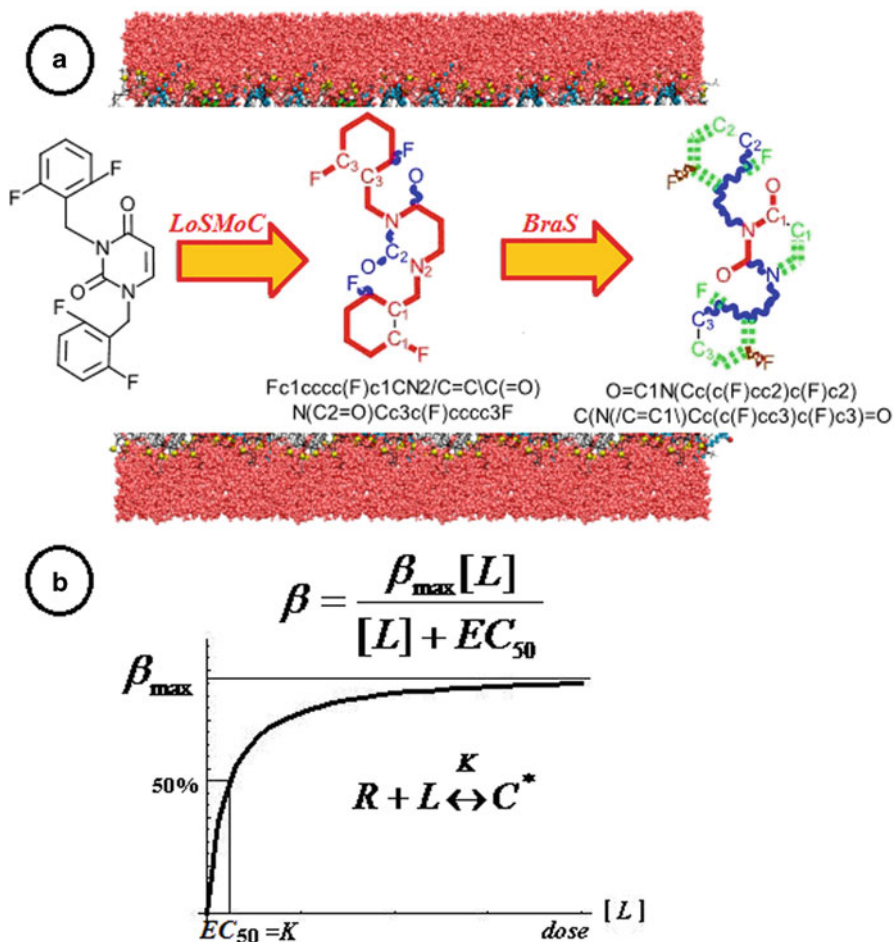
$$A = \ln(1/EC_{50}) \quad (10.51)$$





for certain species, according with Organisation for Economic Co-operation and Development (OECD 2005).

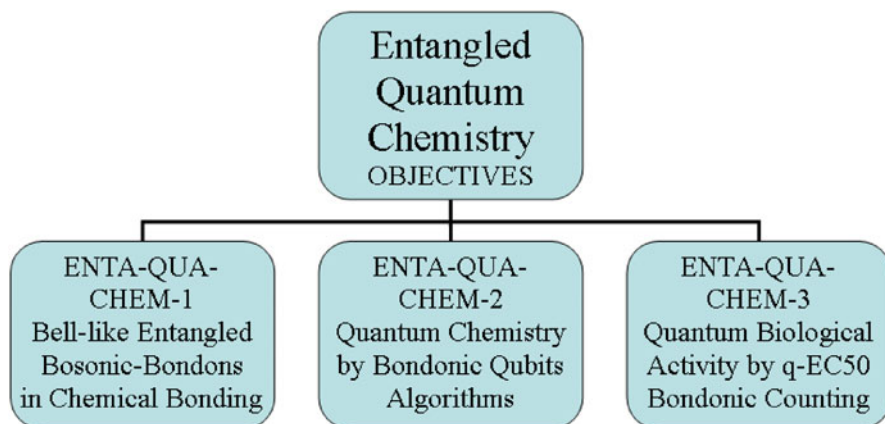
While this aim is in general assigned to “classical” statistical computational task, involving high throughput tedious screenings among large (under developing unified international) databases, including those of European Joint Research Center (OECD QSAR Toolbox 2012), eventually involving the celebrated quantitative structure-activity relationships (QSAR) analysis (OECD 2007, Putz 2012d).

The present project proposes the alternative determination of  $EC_{50}$  by using the bondonic de-coding information for a molecule as it would pass a cellular hydrophobic wall targeting a specific organismal receptor. This can be done once realizing that the molecules during the transduction of the cellular walls suffer selective bonding breakages (Putz and Dudaş 2013a, b), according to their simplified molecular-input line-entry system = SMILES form (Weininger 1988; Drefahl 2011), see Fig. 10.3a; worth noting that SMILES formalism avoids double and superior bonding breakage, in accordance with the actual bonding prescriptions of Table 10.1 since associated with smaller bondonic mass and life-time, i.e. bearing more photonic nature than the bondon of the single carbon bonding.

Accordingly, the counting of breaking bonds in SMILES passages through cellular walls by detecting the maximum output of bondons (e.g. from LoSMoC to BraS molecular forms in Fig. 10.3a) would correspond with the ligand-receptor saturation kinetics or maximum uptake ( $\beta_{\max}$ ): it eventually provides the direct reading of the so formed  $q-EC_{50}$  by appropriately fitting with the hyperbolic kinetics, e.g. of Michaelis-Menten type (Putz and Putz 2013), as illustrated in Fig. 10.3b for the observed bondons “emitted” from the chemical systems on/from a surface mimicking the cellular walls. This way, the main third objective of the actual project states as: ENTA-QUA-CHEM-3: *DETERMINING QUANTUM CHEMICAL-BIOLOGICAL GREEN MEASURE OF 50 % EFFECTIVE CONCENTRATION ( $q-EC_{50}$ ) OF A CHEMICAL COMPOUND TRANSDUCTING SPECIFIC CELLULAR LIPIDIC WALLS.*



**Fig. 10.3** **a** Illustration of the cellular lipidic wall's penetration, after Volinsky et al. (2011) for the anti-HIV molecule of 1,3-Bis-(10,2,6-difluoro-benzyl)-1H-pyrimidine-2,4-dione (*left side*) through the two SMILES generated states, after Putz and Dudaş (2013a, b) as obtained by two different chemical bonding breakage algorithms: the first one (*middle*) based on the longest SMILES molecular chain (LoSMoC) along the principal chain ([  ]) with few branches ([  ]); and the second one (*in right*) based on branching SMILES (BraS) containing a shorter (or shortest) principal chain with branches of superior orders ([  ], [  ]); **b** The ligand-receptor (L-R) saturated kinetics with the biological uptake ( $\beta$ ) relating its maximal value ( $\beta_{\max}$ ) with the 50 % effective concentration ( $EC_{50}$ ) of the ligand dose, after Putz and Putz (2013)



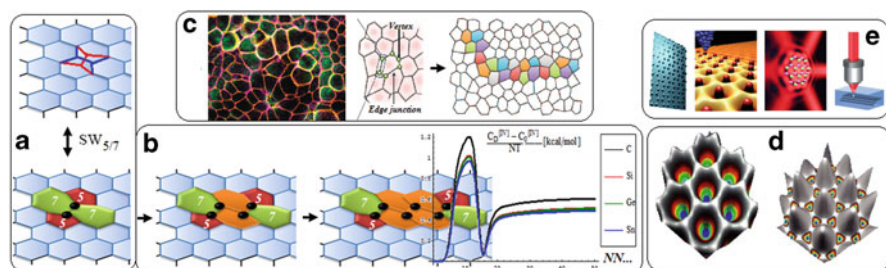
**Fig. 10.4** Synopsis of the entangled quantum chemistry (ENTA-QUA-CHEM) objectives

All in all, the three main related objectives of the present proposal are resumed in Fig. 10.4.

## 10.4 Entangled Chemistry: Methodology

Again we start quoting a master of modern Chemistry, Roald Hoffmann (1971): “Experimental trends are noted. A Theory is constructed that does not merely rationalize but makes verifiable predictions. When these predictions fail the theory can be enriched by re-examination. Chemistry advances”. Also the present frontier project requires in its great extend the experimental parts using two of the latest tools and equipment: graphene nanosystems and (ultra)cold 2D optical lattices (OL) combined in unique setups towards the ENTA-QUA-CHEM fulfilling objectives of Fig. 10.4. Before unfolding one-by-one the original methodology for each objective, we firstly like motivating the use of the graphene and OL in the context of current advanced entangled quantum chemistry project:

(a) *Graphene* is the thinnest (one atom thick) and the strongest known material, made by carbon atoms arranged in a honeycomb lattice supporting (in principle) the 2D infinite extension (Novoselov et al. 2012), and represents the best substrate for the low-dimensional physics (Geim and Novoselov 2007), there where the bosonization of bonding electrons may acquire observable reality (see the previous section). Beside structural features, graphene carriers exhibit high conductivity and almost zero effective mass for relativistic electrons at Fermi velocity of about  $10^6$  m/s (Novoselov et al. 2005), falling just in the range of bosonic-bondons, see Table 10.1, with mobility weakly depending by temperature. Moreover, graphene metal/semiconductor double-behavior (Neto et al. 2009) opens the road for electronic nano-devices directly built over the carbon honeycomb, controlling the “active” hexagonal units by



**Fig. 10.5** The main conceptual and experimental tools of entangled quantum chemistry: **a** graphene and its 5/7 Stone-Wales (SW) bonding transformation, after Ori et al. (2011); Putz and Ori (2012, 2014); **b** the SW wave propagation on honeycomb group-IV systems with bondonic raised signal (best for C-graphene) starting from the next and beyond nearest neighboring (NN...) steps as revealed by pristine-to-topological defect phase transition in terms of caloric capacity in fourth order quantum path integral, after Putz and Ori (2014); **c** the cellular-vertex junction dynamics in tissue homeostasis and morphogenesis closely following the SW waves on graphenic lattice, after Guillot and Lecuit (2013); **d** trigonal/hexagonal tunable optical lattice, after Becker et al. (2010); **e** the associated graphenic artificial synthesis with honeycomb nanopatterning, after Polini et al. (2013)

molecular deposition/zippering/synthesis, exploring at the same time, the bondonic linkage/breakage mechanisms (ENTA-QUA-CHEM-2, 3).

Additionally, from the topological point of view, graphenic lattices manifest also subtle and significant isomerization phenomena such as the creation and the *wave-like* propagation of the Stone-Wales topological defects (Ori et al. 2011), see Fig. 10.5a, 10.5b, which in turn originate countless *isomeric re-tessellations* of the hexagonal mesh, like the pentagon-octagon-pentagon defect whose pure topological nature has been recently demonstrated (Ori and Putz 2014). Structural isomeric transformations of pristine honeycomb lattices may be viewed as a topological expression of bondonic entanglement among the involved bonding's junctions and allows employing the associate bondons of the involved breaking/transformed bonds in teleporting experiments aiming the detecting the specific bondons of SW cell at certain distance on graphene sheet (ENTA-QUA-CHEM-1); such "reality" was already predicted by recent studies modeling the bondonic "pulses" of the SW junction propagating on graphene nanoribbons (Putz and Ori 2012, 2014) offering the theoretical expectation for experiments with entangled bondons on graphenic lattices (Fig. 10.5b). Remarkably, the bondonic "emission" from the SMILES molecular forms on graphene (ENTA-QUA-CHEM-3) while mimicking the cellular walls' transduction is further advocated by the recently discovered SW-like junction dynamics for epithelial cells' division and propagation during tissue homeostasis and morphogenesis (Guillot and Lecuit 2013), Fig. 10.5c.

Quite relevant for the current methodology of entangled quantum chemistry, especially in its quantum computation part (ENTA-QUA-CHEM-2), is that the graphene can be modeled by the tight-binding model, also related with the optical lattice description and the Hückel valence model for bondons in chemical bonding (Kutzelnigg



2007). It associates with the Hamiltonian in the second quantization, i.e. in accordance with bondonic quantum particle description as quantification of the chemical field of bonding over graphene lattice:

$$H_{G(0)} = -t \sum_{\langle i,j \rangle} (a_i^+ b_j + h.c.) - t' \sum_{\langle\langle i,j \rangle\rangle} (a_i^+ a_j + b_i^+ b_j) \quad (10.52)$$

where the summations are made over electronic creation ( $a_i^+, b_i^+$ ) and annihilation ( $a_j, b_j$ ) operators over nearest neighbors  $NN$ :  $\langle i, j \rangle$  and next-nearest neighbors  $NNN$ :  $\langle\langle i, j \rangle\rangle$  while emphasizing on chemical bonding (bondonic formation and its driving hopping term  $t \sim 2.8$  eV) for the first Hamiltonian term, and the propagation of chemical bonding information by long-range hopping propagation (driven by  $t' \sim 0.1$  eV) for the latter, respectively (Band and Avishai 2013); noteworthy, this framework is consistent with the most recent (Putz and Ori 2014) theoretical prediction of bondonic signals of SW waves over limited  $NNN$ ... steps for graphenic nanoribbons, see Fig. 10.5b.

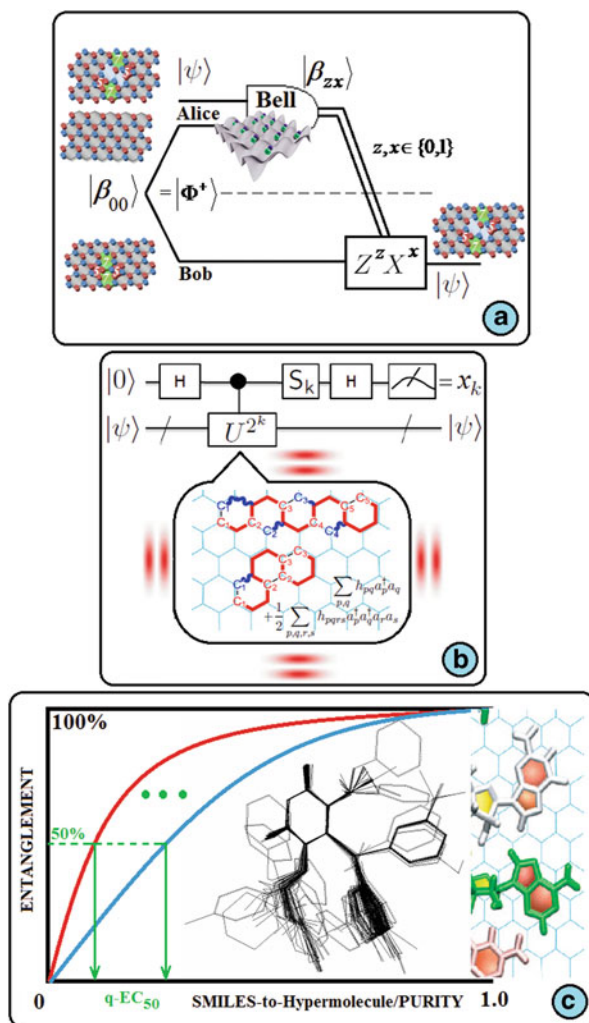
(b) *Optical lattices*, on the other hand, are obtained by superimposing counter-propagating laser beams with an optical standing wave effect (Fig. 10.5d), and were consecrated as modern advanced tool for controlling of correlated matter with the occasion of studying the (supersolid/superfluid) phase transition in Bose-Einstein condensates (Greiner et al. 2002); however, its relation with graphene may be achieved by recognizing the 2D lattice monolayer extended Bose-Hubbard picture in the presence of the long-range interaction, modeled by the (equally working for bondons) Hamiltonian (Baranov et al. 2012)

$$H_B = -t \sum_{\langle i,j \rangle} (a_i^+ b_j + h.c.) + V \sum_{i < j} n_i n_j / r_{ij}^3 - \mu \sum_i n_i \quad (10.53)$$

with  $V$  the tuning potential such that for large enough  $t/V$  ratio the low energy phase is superfluid, for overall (floating) particles' chemical potential  $\mu$ ; Moreover, since the optical lattices serve for optically trapping of cold atoms or molecules, their operational dressing for particles along nearest neighboring sites as well as over long-range flowing exciting particle states (Bloch 2008) is also functioning for entangled bondons in ENTA-QUA-CHEM-1 and "emitted" bondons in ENTA-QUA-CHEM-3, and allows considering them as a hardware candidate for quantum cellular automata (Brennen et al. 1999; Deutsch et al. 2000) in the view of realizing ENTA-QUA-CHEM-2. To this aim triangular/hexagonal optical lattices are to be employed (Becker et al. 2010), such that to finely correspond the honeycomb lattice of graphene (Sun et al. 2012), or even artificially creating it (Polini et al. 2013) so offering a flexible nanopatterning for the 2D-anyons (Freedman et al. 2002; Camino et al. 2005; Stern 2010) by controlling the electronic-to-bondonic graphenic states and their entangled evolution.

With graphene and optical lattices tools, the three main objectives of entangled quantum chemistry (Fig. 10.4) may be achieved, respectively, upon the following frontier conceptual setups (Fig. 10.6).





**Fig. 10.6** The main conceptual setups in achieving entangled quantum chemistry main objectives (see text for details); **a** ENTA-QUA-CHEM-1: teleportation of the bondonic 5/7 SW graphenic topological defects; **b** ENTA-QUA-CHEM-2: bondonic qubits' quantum phase estimation aiming eigen-value computations of working aromatics synthesized on graphene driven by optical lattice modulation; **c** ENTA-QUA-CHEM-3: q-EC50 determination for anti-HIV (and/or ecotoxicological) molecules by counting the "emitted" entangled-teleporting bondons by their SMILES-to-Hypermolecule on graphene under light crystal dressing (see the text for further details and references)

**ENTA-QUA-CHEM-1:** the bondonic evidence is aimed by quantum teleportation (Bennett et al. 1993) of a given bondonic state for a topological Stone-Wales state of graphene, say  $|\psi\rangle$  in Fig. 10.6a, as the second ( $NN$ ) step in bondonic propagation of

Fig. 10.5b, for the first time proposed under optical lattices and laser specific modulation (Putz 2013) as following: the entangled bondonic states are prepared between pristine (Alice) and first 5/7 Stone-Wales (Bob) topological states of graphene, both entangled by the bondonic ground state

$$|\Phi^+\rangle \equiv |\beta_{00}\rangle \quad (10.54)$$

of Fig. 10.2b, and controlled by the Heisenberg-like bondonic relationship (Putz 2010; Putz and Ori 2012)

$$\langle X_{Bond} \rangle [\text{\AA}] \times \langle E_{bond} \rangle [\text{kcal/mol}] = 182,019 \quad (10.55)$$

then, Alice state is (completely) Bell measured by employing the optical lattice dressing so being projected into the Bell transformed quantum state

$$|\beta_{zx}\rangle = 1/2(|0x\rangle + (-1)^z |1\bar{x}\rangle), \quad (10.56)$$

while retaining two classical bits  $z, x \in \{0,1\}$ ; the optical lattice action actually performs the electrons-in-bondons (qubits) rotations according with Pauli matrices

$$Z = \sigma^z, X = \sigma^x \quad (10.57)$$

such that the obtained measured Bell states equivalently write as

$$|\beta_{zx}\rangle = (I \otimes X^x Z^z) |\beta_{00}\rangle; \quad (10.58)$$

Finally, Alice send to Bob the Bell measurement result by the dense coding  $\{|\psi\rangle, |\beta_{zx}\rangle\}$ , along the classical 2-bits information such that Bob can further apply the correct decoding by X-Z rotation-optical lattice protocol to decrypt the teleported state  $|\psi\rangle$  respecting the entangled rooted state:

$$|\psi\rangle \otimes |\beta_{00}\rangle = 1/2 \sum_{z,x \in \{0,1\}} |\beta_{zx}\rangle \otimes X^x Z^z |\psi\rangle. \quad (10.59)$$

This way, the Stone-Wales propagation of 5/7 topological defects on graphene under optical lattices Heisenberg-entangled control may provide the proper quantum environment for realizing the first time teleporting scheme of a chemical bond by its associate quasi-particle bondon, so completing the teleporting list of photons (Boschi et al. 1998), trapped ions (Riebe et al. 2004; Barret et al. 2004) and the composite 2-qubits systems (Zhang et al. 2006).

**ENTA-QUA-CHEM-2:** once the ontological existence of bondons being established (ENTA-QUA-CHEM-1) the teleportation protocol of entangled bondons on graphene under optical lattice and control is further extended for quantum chemical computation by quantum information: chemical working aromatics' compounds (Putz et al. 2013) are *in situ* synthesized with optical lattice by appropriately tuning the  $(NV\dots)$  hopping and the applied potential while working-out the specific second quantized molecular Hamiltonian (Whitfield et al. 2011); for each such molecular

structure designed on pristine graphenic optical lattice the previous bondonic teleporting scheme is generalized (Fig. 10.6b) by  $k$ -iterations until the desired accuracy for solving the eigen-value by phase estimation of the quantum Hamiltonian propagator ( $U$ ); actually, the Alice-Bell operation is now realized by the controlled- $U$  quantum gate

$$|\beta_{zx}\rangle = (\text{controlled} - U) \cdot (H \otimes I) |z, x\rangle \quad (10.60)$$

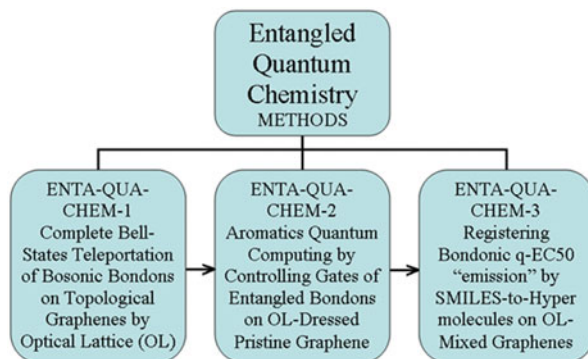
with

$$(\text{controlled} - U) = |1\rangle \langle 1| \otimes U + |0\rangle \langle 0| \otimes I, \quad (10.61)$$

and with  $H$  corresponding to Hadamard transformation of basis  $X$  into  $Z$  (Figs. 10.2b, 10.6b); the general  $H - U^{2^k}$  operation is supplemented by the electrons-in-bondon entangled counter-rotation ( $S_k$ ) by quantum Fourier transformation ( $S_k - H$ ) such that the  $k$ -decimal of eigen-value phase is accurately decoded. This procedure may be applied for genuine molecules as well as for their SMILES forms (as in Fig. 10.6b suggested), being the latter involved in chemical-biological interaction, see Fig. 10.3a. This way, the actual teleporting approach may provide the first hardware prototype for a quantum computer for quantum chemistry (Lanyon et al. 2010) by driving the entangled bondons from real-time (artificially) synthesized complex molecules on graphenic optical lattice.

**ENTA-QUA-CHEM-3:** finally, one combines the previous two protocols (ENTA-QUA-CHEM-1&2) aiming to deal with teleportation of bondons from a synthesized series of molecules on entangled pristine with a Stone-Wales graphenic optical lattice setup; in this case one deals with entanglement teleportation applied to mixed graphenic states, technically corresponding to the SWAP quantum gate (Żukowski et al. 1993; Bouwmeester et al. 1997; Brassard et al. 2004) involved in controlled- $U$  gate and for the propagation on mixed (Werner/noisy) states (Bennett et al. 1996), so executing the most general teleportation protocol to date; remarkable, since the mixed graphenic pristine, Stone-Wales in first, second, . . . neighboring states are involved (Fig. 10.5b), the experiment mimics also the transduction of cellular walls or the cellular dynamics under chemical interaction (Fig. 10.5c) being so suitable for quantum—biological (q-EC<sub>50</sub>) activity recordings for a given molecule. Thus, the ligand-receptor kinetics maps into the entanglement experiment of Fig. 10.3b and is realized as following: a target molecule in a homological series is considered to be q-EC<sub>50</sub> characterized; it is synthesized on an entangled graphenic optical lattice; then, one tunes the light crystal such that the molecule to pass from the genuine (as in environmentally hazardous) state into its SMILE (LoSMoC to BraS) molecular forms (Fig. 10.3a) till teleporting the entangled hyper-molecular structure (with “purity 1”) eventually obtained by superposition of all molecules in the homological series of interest; the “emitted”/recorded/breaking bondons’ signals by such procedure will generate the fitted graph of Fig. 10.6c; the searched q-EC<sub>50</sub> directly reads. The protocol is envisaged for molecules with anti-HIV activity (Duda-Seiman et al. 2006; Putz and Dudaş 2013a, b) and with the inter-species toxicological potential (Chicu

**Fig. 10.7** Synopsis of the entangled quantum chemistry (ENTA-QUA-CHEM) methods



and Putz 2009); while bio-molecular kinetics was recently unzipped on graphene by quantum simulation (Mogurampelly et al. 2012), the actual SWAP-Werner design advances for the first time the determination of EC<sub>50</sub> with quantum computing (of entangled-teleporting) accuracy for ligand green-dynamics on mixed graphenic (receptor) states by bondonic optical lattice control.

All in all, the methods envisaged for fulfilling the objectives of Fig. 10.4 are resumed in Fig. 10.7.

## 10.5 Conclusions

While passing from the Lewis point-like ansatz to the undulatory modeling of electrons in bonding, the reverse passage was still missing in a systematic formulation. Only recently the first attempt was formulated, based on the broken-symmetry approach of the Schrödinger Lagrangian with the electronegativity-chemical hardness parabolic energy dependency, showing that a systematical quest for the creation of particles from the chemical bonding fields is possible (Putz 2008).

Following this line, the present work makes some steps forward by considering the gauge transformation of the electronic wave-function and spinor over the de Broglie-Bohm augmented non-relativistic and relativistic quantum pictures of the Schrödinger and Dirac electronic (chemical) fields, respectively. As a consequence, the reality of the chemical field in bonding was proved in either framework, while providing the corresponding bondonic particle with the associate mass and velocity in a full quantization form, see Eqs. (10.37) and (10.72). In fact, the Dirac bondon (10.35) was found to be a natural generalization of the Schrödinger one, while supplementing it with its anti-bondon particle (10.36) for the positron existence in the Dirac Sea.

However, one of the most important consequences of bondonic existence is that the chemical bonding may be described in a more complex manner than relying only on the electrons, but eventually employing the fermionic (electronic)-bosonic (bondonic) mixture: the first preeminent application is currently on progress, that is,

exploring the effect that the Bose-Einstein condensation has on chemical bonding modeling (Putz 2011a, b). Yet, such possibility arises due to the fact that whether the Pauli principle is an independent axiom of quantum mechanics or whether it depends on other quantum description of matter is still under question (Kaplan 2002), as is the actual case of involving hidden variables and the entanglement or non-localization phenomenology that may be eventually mapped onto the delocalization and fractional charge provided by quantum chemistry over and on atomic centers of a molecular complex/chemical bond, respectively.

Concluding, we firmly believe that the actual project, while implemented will materialize the prophetic words of Primas (1981): “We have an enormous amount of scientific data but we have not yet found simple words for great ideas.” So we are here for tomorrow: advancing the *entangled quantum chemistry by bosonic-bondonic information and teleportation of chemical bonding on (extended) nano- (carbon) systems, as are topological Stone-Wales defects on graphene*, to green (optical) controlling the chemical -synthesis, -computing and complex (bio) -interactions.

**Acknowledgements** This work is abstracted from the Project Proposal ETA-QUA-CHEM (Entangled Quantum Chemistry: Bondons in Search of Chemical Bonding and Complex Interactions) submitted by MVP to European Commission within ERC-2014-CoG call as a part of Excellent Science/Pillar I of European Union HORIZON 2020 framework. Although not currently financed, the actual project was appreciated as: “A very profound and potentially high-impact proposal; An interdisciplinary aspect to this proposal in that it combines general chemistry with the most theoretical and arcane end of quantum physics; The proposed research direction is intriguing. There are several highly innovative ideas, e.g. teleportation of chemical bonding. This is a very good quantum chemistry project, which could advance the field.” OO kindly thanks Biology-Chemical Department of West University of Timișoara for hospitality during his visit on spring of 2014 at Laboratory of Computational and Structural Physical-Chemistry for Nanosciences and QSAR.

## References

- Abrams DS, Lloyd S (1999) Quantum algorithm providing exponential speed increase for finding eigenvalues and eigenvectors. *Phys Rev Lett* 83:5162–5165
- Argaman N, Band YB (2011) Finite-temperature density-functional theory of Bose-Einstein condensates. *Phys Rev A* 83:023612
- Aspuru-Guzik A, Dutoi AD, Love PJ, Head-Gordon M (2005) Simulated quantum computation of molecular energies. *Science* 309:1704–1707
- Bader RFW (1990) *Atoms in molecules-A quantum theory*. Oxford University Press, Oxford
- Bader RFW, Hernández-Trujillo J, Cortés-Guzmán F (2007) Chemical bonding: from Lewis to atoms in molecules. *J Comput Chem* 28:4–14
- Band YB, Avishai Y (2013) *Quantum mechanics with application to nanotechnology and information science*. Academic Press, Oxford
- Baranov MA, Dalmonte M, Pupillo G, Zoller P (2012) Condensed matter theory of dipolar quantum gases. *Chem Rev* 112:5012–5061
- Barbieri B (1998) The organic codes. The basic mechanism of macroevolution. *Riv Biol-Biol Forum* 91:481–514
- Barbieri B (2008) The mechanisms of evolution: natural selection and natural conventions. In: Barbieri M (ed) *The codes of life. The rules of macroevolution*. Springer, pp 15–35

- Barrett MD, Chiaverini J, Schaetz T, Britton J, Itano WM, Jost JD, Knill E, Langer C, Leibfried D, Ozeri R, Wineland DJ (2004) Deterministic quantum teleportation of atomic qubits. *Nature* 429:737–739
- Battail G (2007) Information theory and error correcting codes in genetics and biological evolution. In: Barbieri M (ed) *Introduction to biosemiotics: the new biological synthesis*. Springer, pp 299–345.
- Becke AD, Edgecombe KE (1990) A simple measure of electron localization in atomic and molecular systems. *J Chem Phys* 92:5397–5403
- Becker C, Soltan-Panahi P, Kronjäger J, Dörscher S, Bongs K, Sengstock K (2010) Ultracold quantum gases in triangular optical lattices. *New J Phys* 12:065025
- Bennett CH, Brassard G, Crépeau C, Jozsa R, Peres A, Wootters W (1993) Teleporting an unknown quantum state via dual classical and EPR channels. *Phys Rev Lett* 70:1895–1899
- Bennett CH, Brassard G, Popescu S, Schumacher B, Smolin J, Wootters W (1996) Purification of noisy entanglement and faithful teleportation via noisy channels. *Phys Rev Lett* 76:722–725
- Bloch I (2008) Quantum coherence and entanglement with ultracold atoms in optical lattices. *Nature* 453:1016–1022
- Bockrath M, Cobden DH, Lu J, Rinzler AG, Smalley RE, Balents T, McEuen PL (1999) Luttinger-liquid behaviour in carbon nanotubes. *Nature (London)* 397:598
- Boschi D, Branca S, De Martini F, Hardy L, Popescu S (1998) Experimental realization of teleporting an unknown pure quantum state via dual classical and Einstein-Podolsky-Rosen channels. *Phys Rev Lett* 80:1121–1125
- Bouwmeester D, Pan JW, Mattle K, Eibl M, Weinfurter H, Zeilinger A (1997) Experimental quantum teleportation. *Nature* 390:575–579
- Brassard G, Horodecki P, Mor T (2004) TelePOVM—A generalized quantum teleportation scheme. *IBM J Res Dev* 48:87–97
- Brennen GK, Caves C, Jessen PS, Deutsch IH (1999) Quantum logic gates in optical lattices. *Phys Rev Lett* 82:1060–1063
- Camino F, Zhou W, Goldman V (2005) Realization of a Laughlin quasiparticle interferometer: observation of fractional statistics. *Phys Rev B* 72:075342
- Chicu SA, Putz MV (2009) Köln-Timișoara molecular activity combined models toward interspecies toxicity assessment. *Int J Mol Sci* 10:4474–4497
- Coulson CA (1960) After-dinner speech at the Conference on Molecular Quantum Mechanics, Boulder-Colorado
- Dachsel H, Harrison RJ, Dixon DA (1999) Multireference configuration interaction calculations on  $\text{Cr}_2$ : passing the one billion limit in MRCI/MRACPF calculations. *J Phys Chem A* 103:152–155
- Deutsch IH, Brennen GK, Jessen PS (2000) Quantum computing with neutral atoms in an optical lattice. *Fortsch Phys* 48:925–943
- Dirac PAM (1928) The quantum theory of the electron. *Proc Roy Soc (London) A* 117:610–624.
- Drefahl A (2011) CurlySMILES: a chemical language to customize and annotate encodings of molecular and nanodevice structures. *J Cheminform* 3:1
- Duda-Seiman C, Duda-Seiman D, Dragos ȚD, Medeleanu M, Careja V, Putz MV, Lăcrămă AM, Chiriac A, Nutiu R, Ciubotariu D (2006) Design of anti-HIV ligands by means of minimal topological difference (MTD) method. *Int J Mol Sci* 7:537–555
- EC (2006) Regulation (EC) No 1907/2006 of The European Parliament and of The Council of 18 December 2006 concerning the Registration, Evaluation, Authorisation and Restriction of Chemicals (REACH), establishing a European Chemicals Agency, amending Directive 1999/45/EC and repealing Council Regulation (EEC) No 793/93 and Commission Regulation (EC) No 1488/94 as well as Council Directive 76/769/EEC and Commission Directives 91/155/EEC, 93/67/EEC, 93/105/EC and 2000/21/EC
- Einstein A (1905) Does the inertia of a body depend upon its energy content? *Ann Physik (Leipzig)* 18:639–641
- EU (2008) Green Paper on the management of bio-waste in the European Union, COM (2008) 811 final, Brussels, 3.12.2008 [[http://ec.europa.eu/green-papers/index\\_en.htm](http://ec.europa.eu/green-papers/index_en.htm)]

- Freedman M, Kitaev A, Larsen M, Wang Z (2002) Topological quantum computation. *Bull Am Math Soc* 40:31–38
- Frenking G, Krapp A (2007) Unicorns in the world of chemical bonding models. *J Comput Chem* 28:15–24
- Fröhlich H (1968) Long-range coherence and energy storage in biological systems. *Int J Quantum Chem* 2:641–649
- Geim AK, Novoselov KS (2007) The rise of graphene. *Nat Mater* 6:183–191
- Gillespie RJ, Popelier PLA (2001) *Chemical bonding and molecular geometry*. Oxford University Press, New York
- Glauber RJ (1963) Coherent and incoherent states of radiation field. *Phys Rev* 131:2766–2788
- Greiner M, Mandel O, Esslinger T, Hänsch TW, Bloch I (2002) Quantum phase transition from a superfluid to a Mott insulator in a gas of ultracold atoms. *Nature* 415:39–44
- Greiner M, Regal CA, Jin DS (2003) Emergence of a molecular Bose–Einstein condensate from a Fermi gas. *Nature* 426:537–540
- Guillot C, Lecuit T (2013) Mechanics of epithelial tissue homeostasis and morphogenesis. *Science* 340:1185–1189
- Hameroff S, Penrose R (2003) Conscious events as orchestrated space-time selections. *NeuroQuantology* 1:10–35
- Heeger AJ, Kivelson S, Schrieffer JR, Su WP (1988) Solitons in conducting polymers. *Rev Mod Phys* 60:781–850
- Heitler W, London F (1927) Wechselwirkung neutraler atome und homöopolare bindung nach der quantenmechanik. *Z Phys* 44:455–472
- Hoffmann R (1971) In: Daudel R, Pullman A (eds) *Aspects de la chimie quantique contemporaine*. CNRS: Paris, pp 133–164
- Hoffmann R (2008) All the ways to have a bond. *Powell Lectures Series*. University of Richmond
- Jensen F (2007) *Introduction to computational chemistry*. Wiley, Chichester
- Kaplan IG (2002) Is the Pauli exclusive principle an independent quantum mechanical postulate? *Int J Quantum Chem* 89:268–276
- Kassal I, Jordan SP, Love PJ, Mohseni M, Aspuru-Guzik A (2008) Polynomial-time quantum algorithm for the simulation of chemical dynamics. *PNAS* 105:18681–18686
- Keiss HG (1992) *Conjugated conducting polymers*. Springer, Berlin
- Kutzelnigg W (2007) What I like about Hückel theory. *J Comput Chem* 28:25–34
- Langmuir I (1919) The arrangement of electrons in atoms and molecules. *J Am Chem Soc* 41:868–934; *ibid.* Isomorphism, isosterism and covalence. *J Am Chem Soc* 41:1543–1559
- Lanyon BP, Whitfield JD, Gillett GG, Goggin ME, Almeida MP, Kassal I, Biamonte JD, Mohseni M, Powell BJ, Barbieri M, Aspuru-Guzik A, White AG (2010) Towards quantum chemistry on a quantum computer. *Nat Chem* 2:106–111
- Lewis GN (1916) The atom and the molecule. *J Am Chem Soc* 38:762–785
- Linnett JW (1961) A modification of the Lewis–Langmuir octet rule. *J Am Chem Soc* 83:2643–2653
- Löwdin PO (1955) Quantum theory of many-particle systems. III. Extension of the Hartree–Fock scheme to include degenerate systems and correlation effects. *Phys Rev* 97:1509–1520
- Malrieu JP, Guihéry N, Jiménez-Calzado C, Angeli C (2007) Bond electron pair: its relevance and analysis from the quantum chemistry point of view. *J Comput Chem* 28:35–50
- Mattis DC, Lieb EH (1965) Exact solution of a many-fermion system and its associated boson field. *J Math Phys* 6:304–312.
- Mogurampelly S, Panigrahi S, Bhattacharyya D, Sood AK, Maiti PK (2012) Unraveling siRNA unzipping kinetics with graphene. *J Chem Phys* 137:054903
- Neto AC, Peres NMR, Novoselov KS, Geim AK (2009) The electronic properties of graphene. *Rev Mod Phys* 81:109–162
- Novoselov KS, Geim AK, Morozov SV, Jiang D, Katsnelson MI, Grigorieva IV, Dubonos SV, Firsov AA (2005) Two-dimensional gas of massless Dirac fermions in graphene. *Nature* 438:197–200
- Novoselov KS, Falco VI, Colombo L, Gellert PR, Schwab MG, Kim K (2012) A roadmap for graphene. *Nature* 490:192–200

- OECD (2005) Guidance document on the validation and international acceptance of new or updated test methods for hazard assessment, series on testing and assessment, No. 34. OECD, Paris, p 96
- OECD (2007) Guidance document on the validation of (Quantitative) structure-activity relationship [(Q)SAR] models, series on testing and assessment, No. 69. OECD, Paris, p 154
- OECD QSAR Toolbox (2012) Guidance document for using the (Q)SAR application toolbox to develop chemical categories according to the OECD guidance on grouping of chemicals [<http://www.oecd.org/env/ehs/risk-assessment/theoecdqsartoolbox.htm>]
- Ori O, Putz MV (2014) Isomeric formation of 51815 defects in graphenic systems. Fuller Nanotub Carbon Nanostructures 22(10):887–900. doi:10.1080/1536383X.2012.749454
- Ori O, Cataldo F, Putz MV (2011) Topological anisotropy of stone-wales waves in graphenic fragments. Int J Mol Sci 12:7934–7949
- Pauling L (1939) The nature of the chemical bond and the structure of molecules and crystals. Cornell University Press, Ithaca
- Perdomo A, Truncik C, Tubert-Brohman I, Rose G, Aspuru-Guzik A (2008) Construction of model hamiltonians for adiabatic quantum computation and its application to finding low-energy conformations of lattice protein models. Phys Rev A 78:012320
- Pethick CJ, Smith H (2004) Bose-Einstein condensation in dilute gases. Cambridge University Press, Cambridge
- Poater J, Solà M, Bickelhaupt FM (2006) A model of the chemical bond must be rooted in quantum mechanics, provide insight, and possess predictive power. Chem Eur J 12:2902–2905
- Polini M, Guinea F, Lewenstein M, Manoharan HC, Pellegrini V (2013) Artificial honeycomb lattices for electrons, atoms and photons. Nat Nanotechnol 8:625–633
- Popp FA (1992) Some essential questions of biophoton research and probable answers. In: Popp FA, Li KH, Gu Q (eds) Recent advances in biophoton research and its applications. World Scientific, pp 1–46
- Primas H (1981) Chemistry, quantum mechanics and reductionism. Springer, Berlin, pp 1–2
- Putz MV (2005) Markovian approach of the electron localization functions. Int J Qua Chem 105: 1–11
- Putz MV (2008) The chemical bond: spontaneous symmetry-breaking approach. Symmetr Cult Sci 19:249–262
- Putz MV (2010) The bondons: the quantum particles of the chemical bond. Int J Mol Sci 11: 4227–4256
- Putz MV (2011a) Hidden side of chemical bond: the bosonic condensate. In: Taylor JC (ed) Advances in chemistry research, vol 10. NOVA Science, New York, pp 261–298
- Putz MV (2011b) Conceptual density functional theory: from inhomogeneous electronic gas to Bose-Einstein condensates. In Putz MV (ed) Chemical information and computational challenges in 21<sup>st</sup> century. NOVA Science, New York, pp 1–60
- Putz MV (2012a) Quantum theory: density, condensation, and bonding. Apple Academics, Toronto
- Putz MV (2012b) Density functional theory of Bose-Einstein condensation: road to chemical bonding quantum condensate. Struct Bond 149:1–50
- Putz MV (2012c) From Kohn-Sham to Gross-Pitaevsky equation within Bose-Einstein condensation  $\psi$ -theory. Int J Chem Model 4:1–11
- Putz MV (ed) (2012d) QSAR & SPECTRAL-SAR in computational ecotoxicology. Apple Academics, Toronto
- Putz MV (2013) Quantum and optical dynamics of matter for nanotechnology. IGI Global, Pasadena
- Putz MV, DudaşNA (2013a) Variational principles for mechanistic quantitative structure-activity relationship (QSAR) studies: application on uracil derivatives' anti-HIV action. Struct Chem 24:1873–1893
- Putz MV, DudaşNA (2013b) Determining chemical reactivity driving biological activity from SMILES transformations: the bonding mechanism of anti-HIV pyrimidines. Molecules 18:9061–9116
- Putz MV, Ori O (2012) Bondonic characterization of extended nanosystems: application to graphene's nanoribbons. Chem Phys Lett 548:95–100



- Putz MV, Ori O (2014) Bondonic effects in group-IV honeycomb nanoribbons with Stone-Wales topological defects. *Molecules* 19:4157–4188
- Putz MV, Putz AM (2013) DFT chemical reactivity driven by biological activity: applications for the toxicological fate of chlorinated PAHs. *Struct Bond* 150:181–232
- Putz MV, Tudoran MA, Putz AM (2013) Structure properties and chemical-bio/ecological of PAH interactions: from synthesis to cosmic spectral lines, nanochemistry, and lipophilicity-driven reactivity. *Curr Org Chem* 17:2845–2871
- Rebentrost P, Mohseni M, Kassal I, Lloyd S, Aspuru-Guzik A (2009) Environment-assisted quantum transport. *New J Phys* 11:033003
- Riebe M, Häffner H, Roos CF, Hänsel W, Benhelm J, Lancaster GPT, Körber TW, Becher C, Schmidt-Kaler F, James DFV, Blatt R (2004) Deterministic quantum teleportation with atoms. *Nature* 429:734–737
- Ruedenberg K, Schmidt MW (2007) Why does electron sharing lead to covalent bonding? A variational analysis. *J Comput Chem* 28:391–410
- Scerri ER (2000) Have orbitals really been observed? *J Chem Edu* 77:1492–1494
- Schönhammer K (2002) Canonically conjugate pairs and phase operators. *Phys Rev A* 66:014101
- Shaik S, Hiberty PC (2008). *A chemist's guide to valence bond theory*. Wiley-Interscience, New Jersey
- Shaik S, Danovich D, Wu W, Hiberty P (2009) Charge-shift and its manifestations in chemistry. *Nat Chem* 1:443–449
- Shcherbak VI (1994) Sixty-four triplets and 20 canonical amino acid of the genetic code: the arithmetical regularities. Part II. *J Theor Biol* 166:475–477
- Shcherbak VI (2003) Arithmetic inside the universal genetic code. *BioSystems* 70:187–209
- Stern A (2010) Non-Abelian states of matter. *Nature* 464:187–193
- Sun K, Liu WV, Hemmerich A, Sarma SD (2012) Topological semimetal in a fermionic optical lattice. *Nat Phys* 8:67–70
- Tarucha S, Honda T, Saku T (1995) Reduction of quantized conductance at low temperatures observed in 2–10  $\mu\text{m}$ -long quantum wires. *Solid State Commun* 94:413–418
- Tomonaga S (1950) Remarks on Bloch's method of sound waves applied to many-fermion problems. *Prog Theor Phys* 5:544–569
- Trifonov EN (1989) The multiple codes of nucleotide sequences. *Bull Math Biol* 51:417–432
- Truhlar DG (2007) Valence bond theory for chemical dynamics. *J Comput Chem* 28:73–86
- Volinsky R, Cwiklik L, Jurkiewicz P, Hof M, Jungwirth P, Kinnunen PKJ (2011) Oxidized phosphatidylcholines facilitate phospholipid flip-flop in liposomes. *Biophys J* 111:1376–1384
- Wang H, Kais S, Aspuru-Guzik A, Hoffmann MR (2008) Quantum algorithm for obtaining the energy spectrum of molecular systems. *Phys Chem Chem Phys* 10:5388–5393
- Weininger D (1988) SMILES, a chemical language and information system. 1. Introduction to methodology and encoding rules. *J Chem Inf Comput Sci* 28:31–36
- Whitfield JD, Biamonte J, Aspuru-Guzik A (2011) Simulation of electronic structure hamiltonians using quantum computers. *Mol Phys* 109:735–750
- Williams CP (2011) *Explorations in quantum computing* (2nd edn). Springer, London
- Zhang Q, Goebel A, Wagenknecht C, Chen YA, Zhao B, Yang T, Mair A, Schmiedmayer J, Pan JW (2006) Experimental quantum teleportation of a two-qubit composite system. *Nat Phys* 2:678–682
- Żukowski M, Zeilinger A, Horne MA, Ekert AK (1993) “Event-ready-detectors” Bell experiment via entanglement swapping. *Phys Rev Lett* 71:4287–4290

# Chapter 11

## Bondonic Chemistry: Non-classical Implications on Classical Carbon Systems

Mihai V. Putz, Laura Pitulice, Daniela Dascălu and Delia Isac

**Abstract** The present chapter illustrates our pursuits to correlate the structure and the reactivity of some aliphatic and aromatic compounds making use of quantum-mechanic calculations, while emphasizing the peculiar properties of bondonic influence in driving the chemical bonding in various realizations and respecting various chemical variables. The studied compounds, aromatic amines and their derivatives and also hydroxiarenes, have been chosen to reveal their usage in diazotization and coupling reactions in order to obtain azoic colorants. For didactic purposes, the results obtained by both Hückel (MO -molecular orbitals) and DFT (density functional theory) models have been correlated considering some aspects of bondonic chemistry. From the bondonic side, the quantum computational information, always relating regarding the bonding energy is projected on the length radii or action, bondonic mass and gravitational effects, all without eigen-equations in “classical” quantum mechanics, although being of observable nature, here discussed and compared for their realization and predictions.

### 11.1 Introduction

This chapter is addressed in many parts to college and undergraduate studies teachers as well as to freshman chemistry (i.e. students from the first university cycle). It aims at enhancing the perception and comprehension of aliphatic and aromatic concepts

---

M. V. Putz (✉)

Laboratory of Computational and Structural Physical-Chemistry for Nanosciences and QSAR,  
Department of Biology-Chemistry, Faculty of Chemistry, Biology, Geography,  
West University of Timișoara, Pestalozzi Str. No. 16, 300115 Timișoara, Romania  
Tel.: + 40-256-592638  
e-mail: mv\_putz@yahoo.com; mvputz@cbg.uvt.ro

L. Pitulice · D. Dascălu · D. Isac

Department of Biology-Chemistry, Faculty of Chemistry, Biology, Geography,  
West University of Timișoara, Pestalozzi Str. No. 16, 300115 Timișoara, Romania  
Tel.: + 40-256-592621  
e-mail: laura.pitulice@cbg.uvt.ro

D. Dascălu

e-mail: dana\_denisa\_2005@yahoo.com

© Springer Science+Business Media Dordrecht 2015

M. V. Putz, O. Ori (eds.), *Exotic Properties of Carbon Nanomatter*,

Carbon Materials: Chemistry and Physics, DOI 10.1007/978-94-017-9567-8\_11

(Truhlar 2007; Rzepa 2007) and in relation with advanced/exotic characterization of chemical bonding by the associated quantum quasi-particle called *bondon*.

The chapter unfolds the correlation of some accessible quantum mechanics results with the physicochemical properties of different compounds. Some of the compounds are used to obtain azoic colorants. Other studied compounds are molecules contributing to the formation of the skeleton of some natural products of vital importance (Avram 1994, Chap. 19, 1995, Chaps. 22, 31, 32).

From the structural point of view, the  $\pi - \pi$ ,  $\sigma - \pi$ , and  $n - \pi$  electronic interactions are the basis when interpreting the chemical reactivity of hydrocarbons, nitrogen heterocycles and organic functions. The behavior of aromatic hydrocarbons is compared with that of nitrogen heterocycles. Mono- and polyhydroxy arens are analyzed within the class of hydroxo compounds. The character of some aromatic amines as substrates is put into evidence in diazotization and coupling reactions. The thermal and photochemical stability of aromatic diazonium salts, both as diazotization products and electrophilic reactants, certainly dictate their stability.

The aromaticity characterization of the investigated organic structures is undertaken in order to compare their chemical reactivity. In order to do so, common and recent aromaticity indicators are employed against compounds chemical hardness, computed by the modern density functional theory and the classical Hückel one. On the one hand, the values of the energetic indices calculated by the two methods are in good agreement with other data presented in the literature and with the experimental behavior of the studied compounds. On the other hand, the chemical hardness scale determined by Hückel method is in accordance either with the potential contour maps for the sites susceptible for electrophilic attack or with the computed global values or chemical hardness calculated by DFT method. However, all these “classical cases” of carbon systems will be systematically enriched by the bondonic effects at the level of action length in molecule, i.e. predicting on the localization/delocalization degree the chemical bond is spreading over the molecule and surrounding it encountering the reactivity, along the associated mass and gravitational effects that makes the structure stable or prepared to be engaged in further chemical reactions.

## 11.2 Chemical Bonding by Nonrelativistic Bondons (Putz 2010a)

The general physical origins of bondons and of quantum information implication were extensively exposed in the previous chapter (Putz and Ori 2015) as based on quantum chemical field built within the Dirac-Bohm theory of electronic existence in chemical bonding. In what follows we actually redo the bondonic analytical discovering by following the classical quantum mechanical way, i.e. as based on Schrodinger formalism combined with the Bohmian characterization of non-locality (for accounting for entangled effects of bondons in chemical bonding).

The starting point resides in considering the de Broglie-Bohm electronic wavefunction (de Broglie and Vigier 1953; Bohm and Vigier 1954),

$$\Psi_{BB}(x, t) = R(x, t) \exp\left(i \frac{S(x, t)}{\hbar}\right) \quad (11.1)$$

with the  $R$ -amplitude and  $S$ -phase factors given respectively as:

$$R(x, t) = \sqrt{\Psi(x, t)^2} = \rho^{1/2}(x) \quad (11.2a)$$

$$S(x, t) = px - Et = S_0 - Et \quad (11.2b)$$

in terms of electronic density  $\rho$ , momentum  $p$ , total energy  $E$ , and space-time  $(x, t)$  coordinates, without spin. In these conditions, since one perfumes the wavefunction partial derivatives respecting space and time,

$$\frac{\partial^2 \Psi_{BB}}{\partial x^2} = \left[ \frac{\partial^2 R}{\partial x^2} + 2 \frac{i}{\hbar} \frac{\partial R}{\partial x} \frac{\partial S}{\partial x} + \frac{i}{\hbar} R \frac{\partial^2 S}{\partial x^2} - \frac{R}{\hbar^2} \left( \frac{\partial S}{\partial x} \right)^2 \right] \exp\left(\frac{i}{\hbar} S\right) \quad (11.3a)$$

$$\frac{\partial \Psi_{BB}}{\partial t} = \left[ \frac{\partial R}{\partial t} + \frac{i}{\hbar} R \frac{\partial S}{\partial t} \right] \exp\left(\frac{i}{\hbar} S\right) \quad (11.3b)$$

the conventional Schrödinger equation (Schrodinger 1926)

$$i \hbar \frac{\partial \Psi_{BB}}{\partial t} = - \frac{\hbar^2}{2m} \frac{\partial^2 \Psi_{BB}}{\partial x^2} + V \Psi_{BB} \quad (11.4)$$

takes the real and imaginary forms:

$$\frac{\partial R}{\partial t} = - \frac{1}{2m} \left[ 2 \frac{\partial R}{\partial x} \frac{\partial S}{\partial x} + R \frac{\partial^2 S}{\partial x^2} \right] \quad (11.5a)$$

$$-R \frac{\partial S}{\partial t} = - \frac{\hbar^2}{2m} \frac{\partial^2 R}{\partial x^2} + \frac{R}{2m} \left( \frac{\partial S}{\partial x} \right)^2 + VR \quad (11.5b)$$

that can be further arranged as:

$$\frac{\partial R^2}{\partial t} + \frac{\partial}{\partial x} \left[ \frac{R^2}{m} \frac{\partial S}{\partial x} \right] = 0 \quad (11.6a)$$

$$\frac{\partial S}{\partial t} - \frac{\hbar^2}{2m} \frac{1}{R} \frac{\partial^2 R}{\partial x^2} + \frac{1}{2m} \left( \frac{\partial S}{\partial x} \right)^2 + V = 0 \quad (11.6b)$$

Worth noting that the first Eq. (11.6a) recovers in 3D coordinates the charge current (j) conservation law,

$$\frac{\partial \rho}{\partial t} + \nabla \cdot \mathbf{j} = 0, \quad \mathbf{j} = (R^2/m) \overline{\nabla S} \quad (11.7a)$$

while the second Eq. (11.6b) in 3D,

$$\frac{\partial S}{\partial t} - \frac{\hbar^2}{2m} \frac{\nabla^2 R}{R} + \frac{1}{2m} (\nabla S)^2 + V = 0 \quad (11.7b)$$

extends the basic Schrödinger Eq. (11.4) to include further quantum complexity. It may be clearly seen since recognizing that:

$$(\nabla S)^2 = p^2 \Rightarrow \frac{1}{2m} (\nabla S)^2 = \frac{p^2}{2m} = T; \quad \frac{\partial S}{\partial t} = -E \quad (11.8)$$

one gets from (11.7b) the total energy expression:

$$E = T + V + V_{qua} \quad (11.9a)$$

in terms of newly appeared so called quantum (or Bohm) potential

$$V_{qua} = -\frac{\hbar^2}{2m} \frac{\nabla^2 R}{R} \quad (11.9b)$$

Exploring the consequences of the existence of the Bohm potential (11.9b) reveals most interesting features of the fundamental nature of electronic quantum behavior. We will survey some of them in what follows.

Since the chemical bonding is carried by electrons only, one can see the basic de Broglie-Bohm wavefunction (11.1) as belonging to gauge U(1) group transformation:

$$\begin{aligned} \Psi_{U(1)}(x, t) &= \Psi_{BB}(x, t) \exp\left(\frac{i}{\hbar} \frac{e}{c} \aleph(x, t)\right) \\ &= R(x, t) \exp\left[\frac{i}{\hbar} \left(S(x, t) + \frac{e}{c} \aleph(x, t)\right)\right], \quad e = \frac{e_0^2}{4\pi \epsilon_0} \end{aligned} \quad (11.10)$$

where the *chemical field*  $\aleph$  should account through of variational principle (Schrödinger equation here) by the electronic bond, eventually being quantified by associate corpuscle.

As such, one employs the gauge wavefunction (11.10) to compute the actual Schrödinger partial derivative terms as:

$$\frac{\partial \Psi_{U(1)}}{\partial x} = \left[ \frac{\partial R}{\partial x} + \frac{i}{\hbar} R \left( \frac{\partial S}{\partial x} + \frac{e}{c} \frac{\partial \aleph}{\partial x} \right) \right] \exp\left[\frac{i}{\hbar} \left(S + \frac{e}{c} \aleph\right)\right] \quad (11.11a)$$

$$\begin{aligned} \frac{\partial^2 \Psi_{U(1)}}{\partial x^2} &= \left\{ \begin{aligned} &\frac{\partial^2 R}{\partial x^2} + 2 \frac{i}{\hbar} \frac{\partial R}{\partial x} \left( \frac{\partial S}{\partial x} + \frac{e}{c} \frac{\partial \aleph}{\partial x} \right) + \frac{i}{\hbar} R \left( \frac{\partial^2 S}{\partial x^2} + \frac{e}{c} \frac{\partial^2 \aleph}{\partial x^2} \right) \\ &- \frac{R}{\hbar^2} \left[ \left( \frac{\partial S}{\partial x} \right)^2 + \left( \frac{e}{c} \frac{\partial \aleph}{\partial x} \right)^2 \right] - 2 \frac{e}{\hbar^2 c} R \frac{\partial S}{\partial x} \frac{\partial \aleph}{\partial x} \end{aligned} \right\} \quad (11.11b) \\ &\times \exp\left[\frac{i}{\hbar} \left(S + \frac{e}{c} \aleph\right)\right] \end{aligned}$$

$$\frac{\partial \Psi_{U(1)}}{\partial t} = \left[ \frac{\partial R}{\partial t} + \frac{i}{\hbar} R \left( \frac{\partial S}{\partial t} + \frac{e}{c} \frac{\partial \aleph}{\partial t} \right) \right] \exp \left[ \frac{i}{\hbar} \left( S + \frac{e}{c} \aleph \right) \right] \quad (11.11c)$$

leading with the decomposition of the corresponding Schrödinger U(1) equation on the imaginary and real parts respectively:

$$-\frac{\partial R}{\partial t} = \frac{1}{m} \left( \frac{\partial R}{\partial x} \frac{\partial S}{\partial x} + \frac{R}{2} \frac{\partial^2 S}{\partial x^2} \right) + \frac{e}{mc} \left( \frac{\partial R}{\partial x} \frac{\partial \aleph}{\partial x} + \frac{R}{2} \frac{\partial^2 \aleph}{\partial x^2} \right) \quad (11.12a)$$

$$\begin{aligned} -R \frac{\partial S}{\partial t} - R \frac{e}{c} \frac{\partial \aleph}{\partial t} = & -\frac{\hbar^2}{2m} \frac{\partial^2 R}{\partial x^2} + \frac{R}{2m} \left[ \left( \frac{\partial S}{\partial x} \right)^2 + \left( \frac{e}{c} \frac{\partial \aleph}{\partial x} \right)^2 \right] \\ & + \frac{e}{mc} R \frac{\partial S}{\partial x} \frac{\partial \aleph}{\partial x} + V R \end{aligned} \quad (11.12b)$$

that can be further rearranged as:

$$-\frac{\partial R^2}{\partial t} = \frac{1}{m} \frac{\partial}{\partial x} \left( R^2 \frac{\partial S}{\partial x} \right) + \frac{e}{mc} \frac{\partial}{\partial x} \left( R^2 \frac{\partial \aleph}{\partial x} \right) \quad (11.13a)$$

$$\begin{aligned} -\left( \frac{\partial S}{\partial t} + \frac{e}{c} \frac{\partial \aleph}{\partial t} \right) = & -\frac{\hbar^2}{2m} \frac{1}{R} \frac{\partial^2 R}{\partial x^2} + \frac{1}{2m} \left[ \left( \frac{\partial S}{\partial x} \right)^2 + \left( \frac{e}{c} \frac{\partial \aleph}{\partial x} \right)^2 \right] \\ & + \frac{e}{mc} \frac{\partial S}{\partial x} \frac{\partial \aleph}{\partial x} + V \end{aligned} \quad (11.13b)$$

Equations (11.13) reveal some interesting features of the chemical bonding to be in next discussed.

The Eq. (11.13a) provides the conserving charge current with the form:

$$\mathbf{j}_{U(1)} = \frac{R^2}{m} \left( \overrightarrow{\nabla S} + \frac{e}{c} \overrightarrow{\nabla \aleph} \right) = \mathbf{j}_S + \mathbf{j}_\aleph \quad (11.14)$$

leaving with idea that additional current is responsible for the chemical field to be activated, namely:

$$\mathbf{j}_\aleph = \frac{e}{mc} R^2 \overrightarrow{\nabla \aleph} \quad (11.15)$$

which vanishes when the *global gauge* condition is considered, i.e. when

$$\frac{\partial \aleph}{\partial x} = 0 \quad (11.16)$$

Therefore, in order the chemical bonding be created the *local gauge* transformation should be used that is

$$\frac{\partial \aleph}{\partial x} \neq 0 \quad (11.17)$$

In these conditions, the chemical field current (11.15) carries specific bonding particles that can be appropriately called as *bondons*, closely related with electrons, in fact with the those electrons involved in bonding, either as single, lone pair or delocalized, and having an oriented direction of moving, with an action depending on chemical field itself  $\aleph$ .

Nevertheless, another important idea abstracted from above discussion is that going to search the chemical field  $\aleph$  no global gauge condition as (11.16) should be used. Worth noting as well that the presence of the chemical field do not change the Bohm quantum potential (11.9b) which is recovered untouched in (11.13b) thus preserving the entanglement of interaction. With his there follows that in order the de Broglie-Bohm-Schrödinger formalism and Eq. (11.6) to be invariant under gauge U(1) transformation (11.10) a couple of gauge conditions the chemical field has to fulfilled out of Eq. (11.13); they are respectively:

$$\frac{e}{mc} \frac{\partial}{\partial x} \left( R^2 \frac{\partial \aleph}{\partial x} \right) = 0 \quad (11.18a)$$

$$\frac{e}{c} \frac{\partial \aleph}{\partial t} + \frac{1}{2m} \left( \frac{e}{c} \frac{\partial \aleph}{\partial x} \right)^2 + \frac{e}{mc} \frac{\partial S}{\partial x} \frac{\partial \aleph}{\partial x} = 0 \quad (11.18b)$$

Now, the chemical field  $\aleph$  is found through combining its spatial-temporal information contained in Eqs. (11.18). From condition (11.18a) is getting that:

$$\vec{\nabla} \aleph = -R \frac{\vec{\nabla}^2 \aleph}{\vec{\nabla} R \cdot \vec{j}} \vec{j} \quad (11.19)$$

where the vectorial feature of the chemical field gradient was emphasized on the direction of its associated charge current (11.15) fixed by the versor  $\vec{j}$  ( $j^2=1$ ). We will maintain such procedure whenever necessary for avoiding scalar to vector ratios and preserving the physical sense of the whole construction as well.

Next, the gradient (11.19) is replaced in (11.18b) to obtain a single equation for the chemical field:

$$\frac{e}{2mc} \frac{R^2}{(\nabla R)^2} (\nabla^2 \aleph)^2 - \frac{R}{m} \frac{\vec{\nabla} \aleph \cdot \vec{\nabla} \aleph}{\vec{\nabla} R \cdot \vec{\nabla} \aleph} (\nabla^2 \aleph) + \frac{\partial \aleph}{\partial t} = 0 \quad (11.20)$$

that can be further rewritten as

$$2 \frac{e}{mc} \frac{\rho^2}{(\nabla \rho)^2} (\nabla^2 \aleph)^2 - 2 \frac{\rho \vec{\nu} \cdot \vec{j}}{\vec{\nabla} \rho \cdot \vec{j}} (\nabla^2 \aleph) + \frac{\partial \aleph}{\partial t} = 0 \quad (11.21)$$

since calling the relations:

$$R = \rho^{1/2}; \vec{\nabla} \aleph = \vec{p} \Rightarrow \left\{ \begin{array}{l} \nabla R = \frac{1}{2} \frac{\nabla \rho}{\rho^{1/2}}; \quad (\nabla R)^2 = \frac{1}{4} \frac{(\nabla \rho)^2}{\rho} \\ \frac{\vec{\nabla} \aleph \cdot \vec{\nabla} \aleph}{\vec{\nabla} R \cdot \vec{\nabla} \aleph} = \frac{2\rho^{1/2} \vec{p} \cdot \vec{j}}{\vec{\nabla} \rho \cdot \vec{j}} \end{array} \right. \quad (11.22)$$

Equation (11.21) can be solved for the Laplacian of the chemical field with general solutions:

$$(\nabla^2 \aleph)_{1,2} = \frac{2 \frac{\rho \vec{v} \cdot \vec{j}}{\nabla \rho \cdot \vec{j}} \pm \sqrt{\frac{4 \rho^2 v^2}{(\nabla \rho)^2} - 4 \frac{2e}{mc} \frac{\rho^2}{(\nabla \rho)^2} \frac{\partial \aleph}{\partial t}}}{\frac{4e}{mc} \frac{\rho^2}{(\nabla \rho)^2}} \quad (11.23)$$

Equation (11.23), is a special propagation equation for the chemical field since it links the spatial Laplacian  $\nabla^2 \aleph = \Delta \aleph$  with temporal evolution of the chemical field  $(\partial \aleph / \partial t)^{1/2}$ ; however, it may be considerable be simplified if assuming the stationary chemical field, i.e. chemical field as not explicitly depend on time,

$$\frac{\partial \aleph}{\partial t} = 0 \quad (11.24)$$

in agreement with the fact that once established the chemical bonding should be manifested stationary in order to preserve the stability of the structure it applies.

With condition (11.24) we may still have two solutions for the chemical field.

One corresponds with the *homogeneous* chemical bonding field

$$\Delta \aleph = 0 \Rightarrow \aleph_h = \frac{mc}{e} v_{\vec{j}} X_{bond} \quad (11.25)$$

with the constant determined such that the field (11.25) to be of the same nature as the Bohm phase action S in (11.10).

The second solution of (11.23) looks like

$$\Delta \aleph = \frac{mc}{e} \frac{v \cdot \nabla \rho}{\rho} \quad (11.26)$$

Finally, Eq. (11.26) may be integrated to primarily give:

$$\vec{\nabla} \aleph = \frac{mc}{e} \vec{v} \int_{\infty}^r \frac{\vec{\nabla} \rho \cdot \vec{j}}{\rho} dx = \frac{mc}{e} \vec{v} \left[ \int_{\infty}^0 \frac{\vec{\nabla} \rho \cdot \vec{j}}{\rho} dx + \int_0^r \frac{\vec{\nabla} \rho \cdot \vec{j}}{\rho} dx \right] \quad (11.27)$$

that can be projected on *bondonic* current direction  $\vec{j}$  and then further integrated as:

$$\aleph - \aleph_0 = \frac{mc}{e} v_{\vec{j}} X_{bond} \left( \int_{\infty}^0 \frac{\vec{\nabla} \rho \cdot \vec{j}}{\rho} dl \right) + \frac{mc}{e} v_{\vec{j}} \int_0^{x(t)} \left( \int_0^r \frac{\vec{\nabla} \rho \cdot \vec{j}}{\rho} dl \right) dr \quad (11.28)$$

from where there is identified both the so called *manifested* chemical bond field:

$$\aleph_0 = \frac{mc}{e} v_{\vec{j}} X_{bond} \left( \int_0^{\infty} \frac{\vec{\nabla} \rho \cdot \vec{j}}{\rho} dl \right) \quad (11.29a)$$



for a given inter-nuclear distance  $X_{bond}$ , as well as the *delocalized* chemical bond field:

$$\aleph(x(t)) = \frac{mc}{e} v_{\vec{j}} \int_0^{x(t)} \int_0^r \frac{\vec{\nabla}\rho \cdot \vec{j}}{\rho} dr dl \quad (11.29b)$$

which is the most general stationary chemical bonding field without spin. Worth commenting on the integrand of above chemical bonding fields, since it accounts for the entangled distance concerned; as such, the expression (11.29b) converges to (11.29a) when  $x(t) \rightarrow \infty$  and  $r \rightarrow X_{bond}$  meaning that the  $X_{bond}$  is (locally) manifested in the infinite bath of nonlocal (entangled) interactions. Relation (11.25) may be as well recovered from (11.29b) when the density gradient becomes  $\nabla\rho \rightarrow \rho/X_{bond}$  and  $x(t) \rightarrow r \rightarrow X_{bond}$  revealing that the electronic system is completely isolated and with a uniform charge distribution along bonding (no no-local interactions admitted).

Another interesting point regards the general density gradient dependency of the chemical field (11.29b), a feature that finely resembles two important results of quantum chemistry:

- The gradient expansion when chemical structure and bonding is described in the context of density functional theory (Bader 1990, 1994, 1998a, b, Bader and Austin 1997);
- The Bader zero flux condition for defining the basins of bonding (Parr and Yang 1989; Putz 2003) that in the present case is represented by the zero chemical boning fields, viz.:

$$\aleph = 0 \Leftrightarrow \vec{\nabla}\rho \cdot \vec{j} = 0 \quad (11.30)$$

It is this last feature the decisive reason that the aleph function in gauge transformation (11.10) is correctly associated with chemical bonding!

Last issue addresses the range values of the chemical bonding field as well as its physical meaning. For the typical values enough observing that from the gauge U(1) transformation (11.10) that the chemical bonding field has to be in relation with the inverse order of the fine-structure constant:

$$\aleph_{bondon} \sim \frac{\hbar c}{e} \sim 137.03599976 \frac{Joule \times meter}{Coulomb} \quad (11.31)$$

an enough small quantity, in quantum range, to be apparently neglected, however with crucial role for chemical bonding where the energies involved are about orders of  $10^{-19}$  J (electron-volts)! Nevertheless, for establishing the physical significance of the chemical bonding quanta field (11.31) one can proceed with the chain equivalences:

$$\langle \aleph \rangle \sim \left( \frac{\text{potential}}{\text{difference}} \right) \times \text{distance} \quad (11.32)$$

The combined phenomenology of the results (11.31) and (11.32) states that: the chemical bonding field carries *bondons* with unit quanta (11.31) along the distance

of bonding within the potential gap of stability or by tunneling the potential barrier of encountered bonding attractors.

Alternatively, from the generic form (11.25) for the chemical field, if one replaces the velocity by the kinetic energy and making then use by Heisenberg relationship, viz.

$$v = \sqrt{\frac{2T}{m}} \sim \sqrt{\frac{2\hbar}{m t}} \quad (11.33a)$$

the space-chemical bonding field dependence is simply achieved as:

$$\varkappa \sim \left( \frac{c\hbar}{e} \sqrt{\frac{2m}{\hbar t}} \right) X_{bond} \sim 4.28715 \cdot 10^{13} X_{bond} \quad (11.33b)$$

where we can assume various instantaneous times according with the studied phenomena. At one extreme, when the ration of the first Bohr radius ( $a_0 = 0.52917 \cdot 10^{-10}m$ ) to the speed velocity is assumed,  $t \rightarrow t_0 = a_0/c = 1.76512 \cdot 10^{-19} < \text{seconds} >$ , the two numerical relations for the chemical bonding field, namely (11.31) and (11.33b), are equated to give the typical lengths of the entanglement bond  $X_{bond} \in (0, 3.19643 \cdot 10^{-12}) < \text{meters} >$  with an observable character in the fine-structure phenomena ranges. On the other side, on a chemically femto-second scale, i.e.  $t_{bonding} \sim 10^{-12}s$ , one finds  $X_{bond} \sim 10^{-8}m$  thus widely recovering the custom length of the chemical bonding phenomena at large distance. Further studies may be envisaged from this point concerning the chemical reactivity, times of reactions, i.e. of tunneling the potential barrier between reactants, at whatever chemical scale.

Lastly but not at last, the relations (11.31) and (11.33) may be further used in determining the *mass of bondons* carried by the chemical field on a given distance:

$$m_{bondons} = \frac{\hbar t}{2} \frac{1}{X_{bond}^2} \quad (11.34)$$

For instance, considering the above typical chemical bond length,  $t_{bonding} \sim 10^{-12}s$  and  $X_{bond} \sim 10^{-8}m$ , one gets the bondon mass about  $m_{bondons} \sim 5.27286 \cdot 10^{-31}kg$ , of electronic mass order, of course, but not necessary the same since in the course of reaction, due to the inner undulatory nature of electron and of the wave-function based phenomena of bonding, the electronic specific mass may decrease. Note that the bondon mass decreases faster by broader the bond distance than the time providing a typical quantum effect without a macroscopic rationalization. In fact as increases the entangled distance to be covered by the chemical interaction not only the time is larger but also the quantum mass carried by the field decreases in order the phenomena be unitary, non-separated, and observable! Most remarkably, the higher limit of bondonic mass correctly stands the electronic mass  $m_0 \sim 9.1094 \cdot 10^{-31}kg$  as easily verified when the first Bohr radius and associated time are replaced in (11.34) formula.

In this context, the bondons ( $\mathcal{B}$ ) represents (Putz 2010a, b, 2012) the bosonic counterpart of the bonding electrons' wave function carrying the quantized mass

related with the bonding length and the energy, with Eq. (11.34) rewritten in the ground state as:

$$m_B = \frac{\hbar^2}{2E_{bond} X_{bond}^2} \quad (11.35)$$

At this point one may further inquire on the elementary time-space-gravitation consequences of having the energy-mass form of Eq. (11.35). To unfold this route in a ‘‘Fermi calculation’’ way one may, *mutatis-mutandis*, considering the macro-micro unification of particle nature, in the same way the early Planck universe is characterized (Putz 2014). Actually, one employs the inertial gravity Newtonian equation with the de Broglie relationship:

$$\begin{cases} a = G \frac{m}{r^2} \\ p\lambda = h \end{cases} \quad (11.36a)$$

into the working parameter bondonic space:

$$\begin{cases} G_B = \frac{X_B c^2}{m_B} \\ (m_B c) X_B = h \end{cases} \quad (11.36b)$$

Note that unlike the Planck constant ( $h$ ) and light speed in vacuum ( $c$ ) that intervened already in derivation of the bondonic mass (11.35) the gravitation constant ( $G$ ) behaves here as free-parameter, being this the reason it was considered as bondonic-dependent in (11.36b); it opens also the insight into evaluating the gravitational effects for the chemical bonding phenomenology. This is not surprising due to the fact such gravitational effects should be present and act towards chemical bonding formation against the inter-electronic electrostatic repulsion; accordingly, like in the ‘‘early birth of universe in the Planck era’’ the chemical bonding should compensate the electronic repelling by gravitational nano-effects sustaining chemical binding; the system (11.36b) nevertheless assures the macroscopic gravitational equation is scaled at the quantum level by corresponding de Broglie equation applied to the same bondon; the price is that we have to assume the bondon as moving with light velocity in bonding (i.e. linking the pairing electrons)—a picture which we can assume at the orbital bonding and which will be avoided for cases the bondon is delocalized over the entire molecule, see the Chaps. 12 and 13 of the same book (Putz et al. 2015a, b). Worth remembering that the bonding-fermionic and condensing-bosonic properties are unified by Bohmian/entangled quantum field quantized by the bondon quasi-particle (Putz 2012) carrying the electronic elementary charge (like a fermion) with almost velocity of light (like a light boson) in the femtoseconds range of observation (Martin et al. 1993) either along bonds (pairing electrons) or networks (connecting many-atoms in nanosystems), respectively (Putz and Ori 2012).

However, the orbitalic treatment of the bondon being of photonic-like nature, is partly justified by the fact the bondon is a boson, like photons, while rooting in the inter-electronic interaction so inheriting some of the fermionic features too.

This way, assuming the bonding energy is given, for a given orbitalic (bonding) state,  $E_{bond}$ , one can combine the Eq. (11.35) with the second one in (11.36) to result in the actual bondonic “action radii”

$$X_B = \frac{\hbar c}{4\pi E_{bond}}. \quad (11.36c)$$

With this, the corresponding bondonic mass takes the form:

$$m_B = \frac{8\pi^2 E_{bond}}{c^2} \quad (11.36d)$$

which displays the bondonic realization of the Einstein’s mass-energy relationship within the special relativity theory. However, the most exciting consequence here is to evaluate/estimate the Gravitational constant modification or variation in the bondonic universe due to the chemical bonding “attractive” space; with (11.36c) and (11.36d) back in the first equation of (11.36b) one finds the parametric dependency of the gravitational parameter in the bondonic universe:

$$G_B = \frac{\hbar c^5}{32\pi^3 E_{bond}^2} \quad (11.36e)$$

One notes that all bondonic measures (radii, mass, gravitation) directly depend on the bonding-energy so making suitable link with quantum chemistry computations in whatever framework of approximation. However, for numerical analysis they will correspond with actual [kcal/mol] implementation for custom chemical energies:

- The absolute photonic-like bondonic radii of action:

$$X_B (\text{\AA}) = \frac{3621.14}{E_{bond} (kcal/mol)}. \quad (11.37a)$$

Qualitatively, for the chemical range of bonding energies about few tens of kcal/mol the resulted hundred of Angstroms for bondonic radii or action conceptually accords with molecular systems, say carbon systems about and over ten carbon atoms in a chemical bonding compound; this confirm the present approach for the “classical” carbon systems characterization in non-classical (quantum, bondonic) manner.

- The relative photonic-like bondonic motion mass relative to electronic rest mass:

$$\zeta_m = \frac{m_B}{m_0} = \frac{8\pi^2 E_{bond}}{m_0 c^2} = 6.7004 \times 10^{-6} \times E_{bond} (kcal/mol). \quad (11.37b)$$

Qualitatively, the generic bondonic mass is naturally below the electronic value, thus confirming its photonic-like nature here assumed; the other way around, one needs to deal with chemical compound with bonding energies of mega-kcal/mol for that bondons (of photonic-like nature) with an electronic mass be observed in the range of gamma-ray spectroscopy (thousands of electron-volts), however consistent with the

present Bohmian (matter-antimatter) treatment of bondons, see also the Chap. 10 of the present book (Putz and Ori 2015a, b); in this line of analysis, for tens of kcal/mol for bonding energy (say 10 kcal/mol) may be found in infra-red (IR) spectra of chemical compounds, see Chap. 13 of the present book (Putz et al. 2015b).

- The relative photonic-like bondonic gravitational influence relative to universal gravitation constant:

$$\zeta_G = \frac{G_{\#}}{G} = \frac{\hbar c^5}{32\pi^3 G E_{bond}^2} = \frac{79895.4 \times 10^{53}}{[E_{bond} (kcal/mol)]^2} \quad (11.37c)$$

Qualitatively, this is the most exciting result: it proves that indeed the gravitation manifestation is huge “inside the chemical bond” so that the chemical bond being created despite the electrostatic repulsion; the gravitation arrives to be of such order of magnitude it certainly curve the space-time in chemical bonding: this may also justifying the orbitals existence in chemical bonding as rooting in the gravitational effect that curved the electronic pairing existence in a closed space of bonding; this phenomenology is at the nano-scale of the level of “black hole” for macro-gravity, of course with the specific adjustments of electronic delocalization nature, etc. Nevertheless, the attractors in chemical bonding behave like “nano-cosmic-systems” such that electrons are the “universe-galactic” particles traveling in between them depending on the gravitation balance manifested at short and long distance in a chemical compound. Such ideas should be further investigated in a more profound manner, eventually involving the space-time metrics itself relating the gravitational-cause-effects of chemical bonding by bondons. Such studies are in the purview of the main author and will be reported in further communications.

However, Eqs. (11.37a–11.37c) are the main bondonic quantities to be evaluated for various instances of chemical bonding as resulted from various carbon systems and quantum computation environments, as following.

### 11.3 Aliphatic Nature of Symmetric and Asymmetric Hydrocarbons

The quantum mechanical calculations made by the Hückel molecular method have led to the energetic indices and molecular orbital diagrams for ethene, butadiene, propene, allyl, their structural indices being correlated with the chemical reactivity of the atoms of these molecules. Thus, the higher the bond order ( $p_{rs}$ ), the higher the reactive capacity of the bonds (multiple bond); the homolytic attack prefers the sublayer atoms with high free valence index ( $F_r$ ), and the electrophile, unlike the nucleophile, prefers the atoms with high electronic charge density ( $q_r$ ) (Simon 1973, pp. 29–53).

By applying the Woodward-Hoffmann rule of the conservation of orbital symmetry, we have built the correlation diagrams of the molecular orbitals for ethene

hydrogenation and Diels-Alder cycloaddition (4 + 2). Thus, it was possible to anticipate when the reaction occurs thermally and when it would take place under light action (Woodward and Hoffmann 1970, pp. 8–28, 52–75).

In the Hückel approximation for ethene and butadiene the parametric schemes are built (Streitwieser 1961):



The homogenous equation systems and the normalization conditions for the two molecules are the following:

$$c_1^2 + c_2^2 = 1 \quad (11.38c)$$

$$c_1^2 + c_2^2 + c_3^2 + c_4^2 = 1 \quad (11.38d)$$

Considering the abbreviation

$$\frac{\alpha - \varepsilon}{\beta} = K \quad (11.39)$$

the Hückel secular determinants result as:

$$\begin{vmatrix} K & 1 \\ 1 & K \end{vmatrix} = 0 \quad (11.40a)$$

$$\begin{vmatrix} K & 1 & 0 & 0 \\ 1 & K & 1 & 0 \\ 0 & 1 & K & 1 \\ 0 & 0 & 1 & K \end{vmatrix} = 0. \quad (11.40b)$$

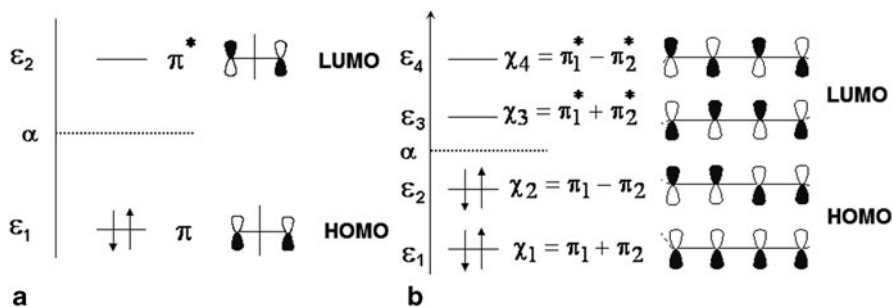
Subsequent to their solving, the following equations are obtained. For ethene  $K^2 - 1 = 0$ , and for butadiene  $K^4 - 3K^2 + 1 = 0$ , which, by grouping the terms, it becomes  $(K^2 - K - 1)(K^2 + K - 1) = 0$ . The K values lead to the energies ( $\varepsilon$ ) and the coefficient sets of molecular orbitals for the two aliphatic hydrocarbons (Table 11.1).

The values calculated for the energy of the highest occupied molecular orbital ( $\varepsilon_{\text{HOMO}}$ ) and the energy of the lowest free molecular orbital ( $\varepsilon_{\text{LUMO}}$ ) are correlated with the butadiene oxidizing character and reducing one, which is stronger than that of ethene. The graphical and mathematical models of the molecular orbitals corresponding to the calculated energies are shown in Fig. 11.1.

The bondonic information for molecules of Table 11.1 is reported in Table 11.2 and graphically represented in Fig. 11.2. It provides the specific behavior:

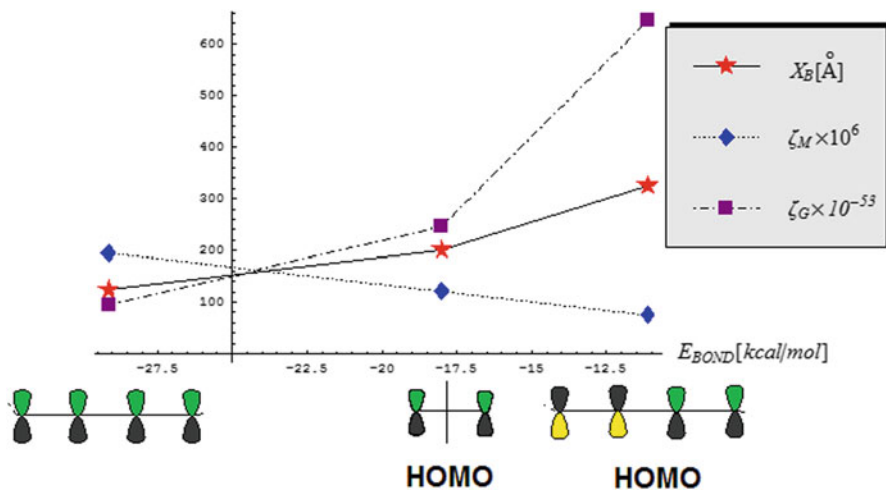
**Table 11.1** Energies and coefficients of the atomic orbitals contributions to the molecular orbitals of ethene and butadiene

Hydrocarbon	K	$\varepsilon$	$c_1$	$c_2$	$c_3$	$c_4$
C <sub>2</sub> H <sub>4</sub>	-1.0000	$\varepsilon_1 = \varepsilon_{\text{HOMO}} = \alpha + \beta$	$\frac{1}{\sqrt{2}}$	$\frac{1}{\sqrt{2}}$	-	-
	1.0000	$\varepsilon_2 = \varepsilon_{\text{LUMO}} = \alpha - \beta$	$\frac{1}{\sqrt{2}}$	$-\frac{1}{\sqrt{2}}$	-	-
C <sub>4</sub> H <sub>6</sub>	-1.6180	$\varepsilon_1 = \alpha + 1.6180\beta$	0.3717	0.6015	0.6015	0.3717
	-0.6180	$\varepsilon_2 = \varepsilon_{\text{HOMO}} = \alpha + 0.6180\beta$	0.6015	0.3717	-0.3717	-0.6015
	0.6180	$\varepsilon_3 = \varepsilon_{\text{LUMO}} = \alpha - 0.6180\beta$	0.6015	-0.3717	-0.3717	0.6015
	1.6180	$\varepsilon_4 = \alpha - 1.6180\beta$	0.3717	-0.6015	0.6015	-0.3717

**Fig. 11.1** Energetic diagrams for ethene (a) and butadiene (b)**Table 11.2** Absolute bonding energies in kcal/mol ( $\alpha = 0$ ,  $\beta = -18$  kcal/mol) for the Hückel orbital HOMO-like levels for molecules of Table 11.1, along the related bondic radii of action, mass ratio respecting the electronic unit, and the bondic gravitational ratio respecting the universal gravitational unit, according with Eqs. (11.37a, 11.37b, 11.37c), respectively

Hydrocarbon	$E_{\text{bond}}(\text{kcal/mol})$	$X_B(\text{\AA})$	$\zeta_m \times 10^6$	$\zeta_G \times 10^{-53}$
C <sub>2</sub> H <sub>4</sub>	$\varepsilon_1 = \varepsilon_{\text{HOMO}} = -18$	201.174	120.607	246.591
C <sub>4</sub> H <sub>6</sub>	$\varepsilon_1 = -29.124$	124.335	195.142	94.1932
	$\varepsilon_2 = \varepsilon_{\text{HOMO}} = -11.124$	325.525	74.5352	645.654

- The bondic radii and gravitational actions are parallel increasing, while somehow anti-parallel with the bondic mass variation as the bonding energy decreases from more to less bonding nature, i.e. from inner molecular orbital to the frontier HOMO;
- For larger system the HOMO level is less bound so having less bondic mass and higher radius of action that determine also a higher gravitational influence (in order to keep the bond to a longer range of action).



**Fig. 11.2** The graphical plot for the bondonic features of ethene and *butadiene* as computed in Table 11.2 for their lowest orbitals of Fig. 11.1

However, worth noticing that the parallel variation of bondonic radius of action and gravitational influence is a specific quantum manifestation, apparently in contradiction with classical inverse relationship, here interpreted as a Bohmian entangled effect by which to a larger distance the quantum information remains bound under an increasing gravitational action too. The present behavior offers also a subtle way in unifying the quantum with gravitational effects at the chemical bonding level, since at shorter distance gravitation effects should prevail the electrostatic electronic inter-repulsion in order to achieve bonding itself. Further considerations are given in Conclusions section of the present chapter, while more sophisticated geometrical Riemannian quantum-space-time quaternion approach is let for further approach and communication.

Returning to the data in Table 11.1, we can find the *energetic* and *structural indices* (Table 11.3).

We consider the presentation of the calculation methods for the total energy ( $E_\pi$ ) and conjugation or resonance energy ( $E_R$ ) of the two molecules to be of particular interest.

- For ethene:

$$E_\pi = 2(\alpha + \beta) = 2\alpha + 2\beta; E_R = 0 \quad (11.41a)$$

- For butadiene:

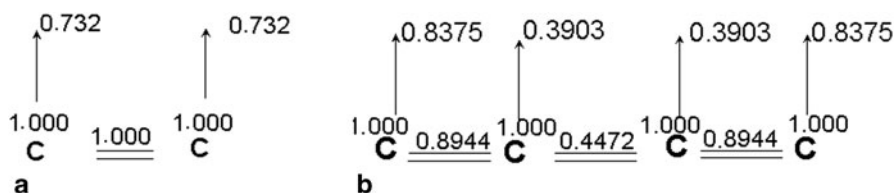
$$E_\pi = 2(\alpha + 1.6180\beta) + 2(\alpha + 0.6180\beta) = 4\alpha + 4.4720\beta \quad (11.41b)$$

$$\begin{aligned} E_R &= 4\alpha + 4.4720\beta - 2(2\alpha + 2\beta) = 0.4720\beta \\ &= 8.4960 \text{ kcal} \cdot \text{mol}^{-1} (-\beta = 18 \text{ kcal} \cdot \text{mol}^{-1}) \end{aligned} \quad (11.41c)$$



**Table 11.3** Structural indices calculated for ethene and butadiene by the Hückel molecular orbital method

Hydrocarbon	$\rho_r = \sum_i 2c_{ri}^2$	$P_{rs} = \sum_i 2c_{ri} \cdot c_{si}$	$F_r = 1.732 - \sum_{s\text{-adjacency}-r} P_{rs}$
$C_2H_4$	$\rho_1 = \rho_2 = 2\left(\frac{1}{\sqrt{2}}\right)^2 = 1$	$P_{12} = 2 \cdot \frac{1}{\sqrt{2}} \cdot \frac{1}{\sqrt{2}} = 1$	$F_1 = F_2 = 1.732 - 1 = 0.732$
$C_4H_6$	$\rho_1 = \rho_2 = \rho_3 = \rho_4 = 2(0.3717^2 + 0.6015^2) = 1$	$P_{12} = P_{34} = 2(0.3717 \cdot 0.6015 + 0.6015 \cdot 0.3717) = 0.8944$ $P_{23} = 2(0.6015^2 - 0.3717^2) = 0.4472$	$F_1 = F_4 = 1.732 - 0.8944 = 0.8375$ $F_2 = F_3 = 1.732 - (0.4472 + 0.8944) = 0.3903$

**Fig. 11.3** Molecular diagrams for ethene (a) and butadiene (b)

Using experimental data, we can calculate the butadiene conjugation energy as being the difference between the value of its hydrogenation heat ( $\Delta H = -57.1 \text{ kcal mol}^{-1}$ ) and the value calculated from the double hydrogenation heat of ethene ( $\Delta H = -32.8 \text{ kcal mol}^{-1}$ ):

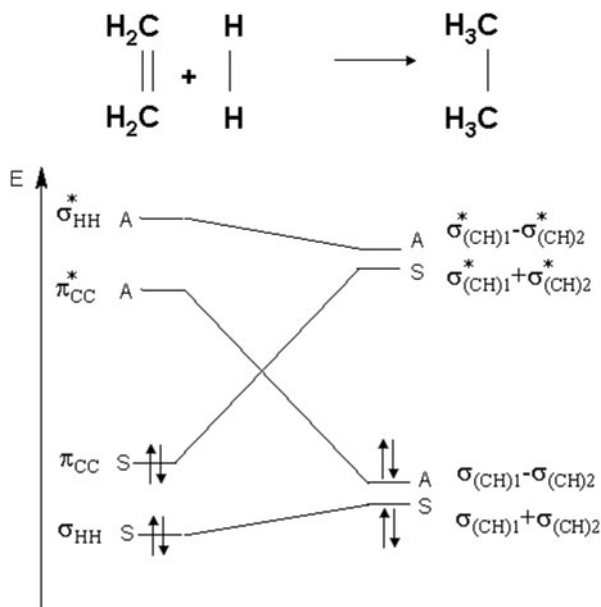
$$E_{\text{conjugation}} = -57.1 - 2(-32.8) = 8.5 \text{ kcal} \cdot \text{mol}^{-1} \quad (11.41d)$$

When we compare the butadiene hydrogenation heat with that of 1-butene ( $-30.3 \text{ kcal mol}^{-1}$ ) or with the mean value of an alkene hydrogenation with a marginal double bond, we see a significant difference of  $5 \text{ kcal mol}^{-1}$  with respect to our calculations. Anyway, the butadiene conjugation energy is much lower than the one in benzene ( $22 \text{ kcal mol}^{-1}$ ) (Avram 1994, pp. 239–241; Nenitzescu 1966, pp. 288–293). The distribution of the density charge, bond orders and free valences of the two hydrocarbons is a component of the molecular diagrams (Fig. 11.3).

One can see that the carbon atoms in ethene have relatively high free valences, so that the homolytic addition to the  $C=C$  bond has free atoms and radicals as intermediates. During this type of reactions, the alkene is transformed into a free radical that is then stabilized through one of the characteristic ways of free radicals.

Hydrogenation with metals and proton donors is not possible, considering the very weak reducing and oxidizing character of ethene. The addition of molecular hydrogen

**Fig. 11.4** The Woodward-Hoffmann correlation diagram for the reaction of  $C_2H_4$  with  $H_2$



is made in the presence of transition metals such as Ni, Pd, Pt, Rh (heterogeneous catalysis) at normal or increased temperature and pressure (Avram 1994, pp. 162–166; Nenitzescu 1966, pp. 130–132).

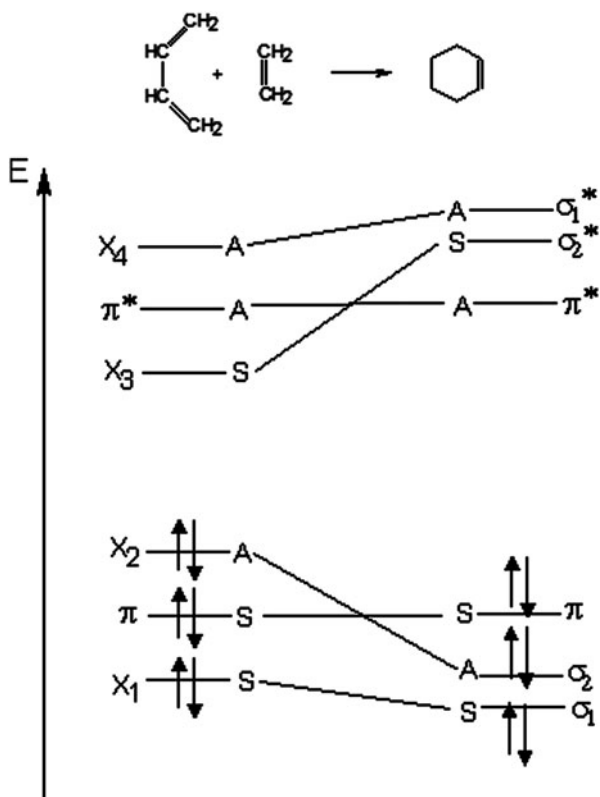
The Woodward-Hoffmann correlation diagram of the molecular orbitals of ethene hydrogenation is shown in Fig. 11.4. The preserved symmetry element is a symmetry plane perpendicular on the middle of the two reacting molecules (Woodward and Hoffmann 1970, pp. 52–75; Simon 1973, pp. 29–53).

According to this Woodward-Hoffmann correlation diagram, ethene hydrogenation does not take place through a molecular mechanism (see Fig. 11.4). This is due to the fact that the symmetry correlations between the involved molecular orbitals of the reactants and product attest the existence of a potential barrier to the reaction. Instead, the hydrogenation of ethene with atomic hydrogen takes easily place with  $E_{\text{activation}} \cong 0$  (Simon 1973, pp. 29–53).

The chemical reactivity of butadiene, in correlation with the calculated structural indices and the reaction mechanisms, is found in its chemical properties (Avram 1994, pp. 349–353; Nenitzescu 1966, pp. 288–293):

- the bond orders ( $p_{12} = p_{34}$ ) >  $p_{23}$  indicate the attaching degree of the double bonds but also the possibility of electrophilic additions of halogens, hydric acids in 1,2 and 1,4 positions of diene;
- the radicalic additions of  $CCl_4$  or  $Cl_3CBr$  in the presence of benzoyl peroxide and the catalytic hydrogenation prefer the 1 and 4 positions in butadiene, with higher free valence index ( $F_1 = F_4$ ) > ( $F_2 = F_3$ );

**Fig. 11.5** Correlation diagram of molecular orbitals for the cycloaddition of ethene at butadiene

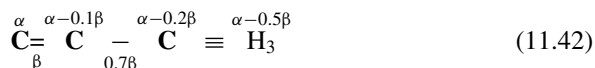


- the conjugated double bonds of butadiene are easily polarizable, thus offering it the capacity of being reduced with sodium or sodium amalgam as electron donors, and alcohol, water or acids as proton donors;
- the enhanced reactivity of the 1 and 4 positions with higher free valence is also attested by the diene synthesis. Applying the Woodward-Hoffmann rule of conservation of the orbital symmetry with respect to the symmetry plane, which passes through the centre of the butadiene molecule between  $C_2$ – $C_3$ , the correlation diagram is obtained; see Fig. 11.5 (Woodward and Hoffmann 1970, pp. 52–75).

In this cycloaddition (4 + 2), the binding levels of the reactants are correlated with the binding levels of the product. There are no correlations intersecting high-energy intervals between the bonding and antibonding levels. The ground state levels are directly correlated with one another. The diagram shows that, from the symmetry point of view, the thermal process should take place without activation energy. Consequently, there is no barrier conditioned by symmetry, even though experimentally there is found  $E = 20 \text{ kcal mol}^{-1}$ . The activation energy is not directly related to the conservation of the orbital symmetry, but it is determined by rehybridization, increase or decrease of the bond length, or deformation of the valence angles. Therefore, the reaction of butadiene with ethene is slightly thermic, because there are no

great electron transitions from the low-energy levels to the higher-energy ones. This diene synthesis can also take place photochemically, but the process is energetically disadvantaged (Simon 1973, pp. 29–53; Avram 1994, pp. 349–353).

In the case of propene with  $\sigma - \pi$  conjugation (hyperconjugation) the following parametric scheme is chosen (Nenitzescu 1966, p. 70; Streitwieser 1961):



The algorithm related to quantum-mechanics calculations leads to the system of homogeneous equations beside the normalization condition of the molecular orbitals:

$$\left\{ \begin{array}{l} c_1(\alpha - \varepsilon) + c_2\beta = 0 \\ c_1\beta + c_2(\alpha - 0.1\beta - \varepsilon) + c_30.7\beta = 0 \\ c_20.7\beta + c_3(\alpha - 0.2\beta - \varepsilon) + c_42\beta = 0 \\ c_32\beta + c_4(\alpha - 0.5\beta - \varepsilon) = 0 \\ c_1^2 + c_2^2 + c_3^2 + c_4^2 = 1 \end{array} \right. \quad (11.43)$$

Considering abbreviation as in (11.43) we obtain the Hückel secular determinant:

$$\begin{vmatrix} \text{K} & 1 & 0 & 0 \\ 1 & (\text{K} - 0.1) & 0.7 & 0 \\ 0 & 0.7 & (\text{K} - 0.2) & 2 \\ 0 & 0 & 2 & (\text{K} - 0.5) \end{vmatrix} = 0 \quad (11.44)$$

which is successively rewritten till obtaining the simple equation:

$$\begin{aligned} & (\text{K}^2 - 0.1\text{K})[(\text{K} - 0.2)(\text{K} - 0.5) - 4] - 0.7\text{K}[0.7(\text{K} - 0.5)] - \\ & [(\text{K} - 0.2)(\text{K} - 0.5) - 4] = 0 \\ & \text{K}^4 - 0.8\text{K}^3 - 5.32\text{K}^2 + 1.335\text{K} + 3.9 = 0 \end{aligned} \quad (11.45)$$

Using the standard algebraic computational analysis, we obtain the solution values of the secular equation and of the coefficient sets of the molecular orbitals (Table 11.4).

Based on Table 11.4 data, the structural indices are calculated as follows:

- charge densities

$$\begin{aligned} \rho_1 &= 2[0.1878^2 + 0.7073^2] = 1.0709 \\ \rho_2 &= 2[0.3475^2 + 0.5938^2] = 0.9465 \\ \rho_3 &= 2[0.6996^2 + (-0.2135)^2] = 1.0699 \\ \rho_4 &= 2[0.5954^2 + (-0.3188)^2] = 0.9122 \end{aligned} \quad (11.46)$$

**Table 11.4** Molecular orbitals energies of propene and the coefficients of the atomic orbitals contributions to them

K	$\varepsilon$	$c_1$	$c_2$	$c_3$	$c_4$
-1.84989	$\alpha + 1.84989\beta$	0.18784	0.34748	0.69959	0.59543
-0.83949	$\alpha + 0.83949\beta$	0.70728	0.59376	-0.21350	-0.31878
1.01488	$\alpha - 1.01488\beta$	0.67450	-0.68454	-0.06893	0.26777
2.47451	$\alpha - 2.47451\beta$	0.09740	-0.24102	0.67840	-0.68716

**Table 11.5** Bonding energies in kcal/mol ( $\alpha = 0$ ,  $\beta = -18$  kcal/mol) for the Hückel eigen-orbital levels for *propene* of Table 11.4, along the related bondonic features of absolute action radii, mass and gravitation effect, as in Table 11.2 reported, according with Eqs. (11.37a, 11.37b, 11.37c), respectively

Orbital Energy	$E_{bond}(kcal/mol)$	$X_B(\text{\AA})$	$\zeta_m \times 10^6$	$\zeta_G \times 10^{-53}$
$\varepsilon_1 = 1.84989\beta$	-33.298	108.748	223.11	72.05
$\varepsilon_2 = 0.83949\beta$	-15.1108	239.639	101.249	349.901
$\varepsilon_3 = -1.01488\beta$	18.2678	198.225	122.402	239.413
$\varepsilon_4 = -2.47451\beta$	44.5412	81.2987	298.444	40.2715

- bond orders

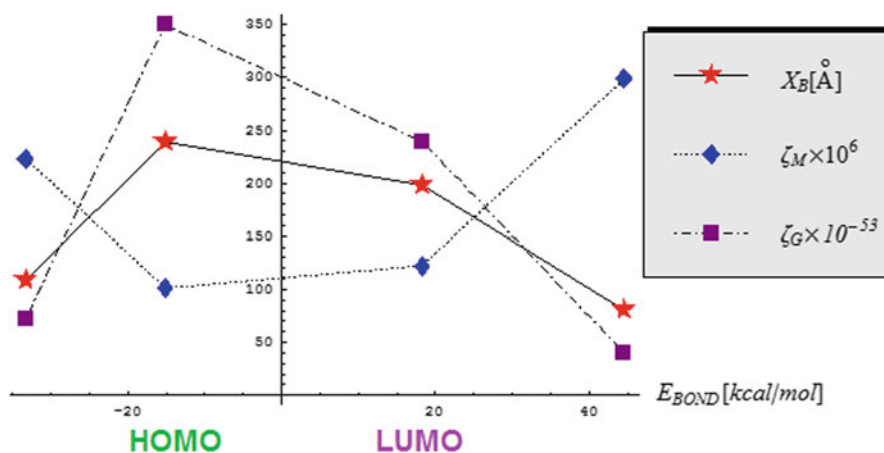
$$\begin{aligned}
 p_{12} &= 2(0.1878 \times 0.3475 + 0.7073 \times 0.5938) = 0.9704 \\
 p_{23} &= 2[0.3475 \times 0.6996 + 0.5938 \times (-0.2135)] = 0.2326 \\
 p_{34} &= 2[0.6996 \times 0.5954 + (-0.2135) \times (-0.3188)] = 0.9690 \quad (11.47)
 \end{aligned}$$

- free valences

$$\begin{aligned}
 F_1 &= 1.732 - p_{12} = 0.7616 \\
 F_2 &= 1.732 - (p_{12} + p_{23}) = 0.5290 \\
 F_3 &= 1.732 - (p_{23} + p_{34}) = 0.5304 \\
 F_4 &= 1.732 - p_{34} = 0.7630 \quad (11.48)
 \end{aligned}$$

The bondonic information for molecules of Table 11.4 is reported in Table 11.5 and graphically represented in Fig. 11.6. It provides the specific behavior:

- The bondonic radii and gravitational actions are confirmed as parallel in variation, yet increasing for HOMO frontier and decreasing for LUMO excited frontier, with inverse bondonic mass variation as the bonding energy varies from HOMO to LUMO levels;
- The variation shape of bondonic information seems to display an optimum value, under a parabolic form, with maximum/minimum placed on HOMO frontier rather than on LUMO one, for bondonic radius/gravitational action and mass, respectively; this behavior is nevertheless quite relevant for consecrating the parabolic



**Fig. 11.6** The graphical plot for the bondonic features vs. orbital energies of propene as computed in Table 11.5

**Table 11.6** Coefficients of atomic orbitals contribution to the molecular orbitals in HBr

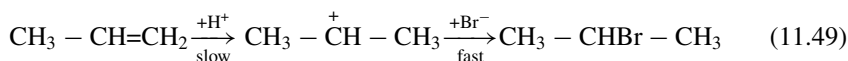
Bond	$\bar{X}_{\text{Br}} - \bar{X}_{\text{H}}$ after Pauling	Ionic character(%)	Bonding molecular orbital		Antibonding molecular orbital	
			$c_{\text{Br}}$	$c_{\text{H}}$	$c_{\text{Br}}$	$c_{\text{H}}$
H-Br	$2.8 - 2.1 = 0.7$	12	0.55	0.45	0.45	0.55

orbitalic bondonic shape and overall on molecular reactivity respecting the orbital occupancy, a matter still being in the middle of debates, without a definite proof (Putz 2011).

Back to “classical” chemical structure-reactivity analysis, for the chemical reactivity of propene we have chosen its reactions with HBr through electrophilic addition and radicalic addition mechanisms, as well as thermal- or photochemical chlorination with radicalic substitution and radicalic addition mechanisms.

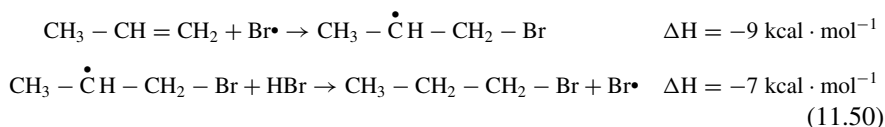
The analysis of propene reactivity as substrate also implies a presentation of the HBr reactant with its structural properties in the isolated state, see Table 11.6 (Bătcă 1981, pp. 115).

In the case of electrophilic addition mechanism of hydrobromic acid addition, the electrophilic reactant attacks the propene secondary carbon atom with higher charge density ( $q_1 = 1.0709$ ), being thus in accordance with Markovnikov’s rule

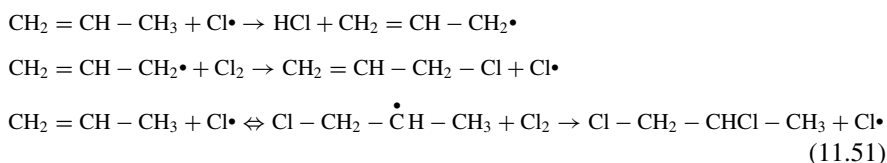


In the presence of organic peroxides at high temperature or peroxides and light at low temperature, the Kharash addition takes place (Avram 1994, pp. 170–171). In other words, the hydrobromic acid addition occurs contrary to Markovnikov’s rule. This is

explained by the fact that the Br· radical prefers the propene secondary carbon atom with high free valence ( $F_1 = 0.7616$ ). The propagation stage of the (RA) mechanism is:



The hydrobromic acid addition is possible only as described above, because the two stages of the propagation reaction are exothermic and have low activation energy. The fact that the HCl and HI addition does not take place homolitically is due to the unfavourable energetics of the two stages of propagation. In the case of HI, the first elementary reaction is endothermic ( $\Delta H = +6 \text{ kcal mol}^{-1}$ ) and the second exothermic ( $\Delta H = -24 \text{ kcal mol}^{-1}$ ). In the case of HCl, the first reaction is exothermic ( $\Delta H = -22 \text{ kcal mol}^{-1}$ ) and the second, endothermic ( $\Delta H = +8 \text{ kcal mol}^{-1}$ ). When propene reacts with chlorine at 500–600 °C, the substitution of the allylic hydrogen takes place. The reaction is industrially used for the synthesis of the allyl chloride through a chained homolytic mechanism (radicalic substitution). The 1,2-dichloropropane (RA mechanism) is obtained as a by-product. In both cases, during the propagation stages, the radicalic attack occurs at atoms with high free valence.



The allyl molecule ( $\text{C}_3\text{H}_5$ ), as intermediate in the reaction mechanism presented here, may be an example of the application of the algorithm related to the structure-properties correlation for polyatomic molecules (Chiriac et al. 2003, pp. 92–93).

- Hydrogen (H) has 1 atomic orbital;  $1 e^-$
- Carbon (C) has 4 atomic orbitals;  $4 e^-$
- $N = 5 \cdot 1 + 3 \cdot 4 = 17$  atomic orbitals  $\Rightarrow$  17 molecular orbitals
- $\sum e^- = 5 \cdot 1 + 3 \cdot 4 = 17e^- \Rightarrow 8.5$  pairs.

Even when populated by a single electron, an energy level becomes occupied. As a result, the analysed system present 9 occupied energy levels ( $8.5 \rightarrow 9$  pairs).

- $N_1 = N - p = 17 - 9 = 8$  antibonding molecular orbitals  $\Rightarrow$  8 bonding molecular orbitals.
- $N_2 = N - 2N_1 = 17 - 2 \cdot 8 = 1$  nonbonding molecular orbital.

As the molecule has 8 atoms, the system should have:

- $N_3 = 8 - 1 = 7$   $\sigma$ -bonding molecular orbitals (7  $\sigma^*$ -antibonding molecular orbitals).

The system has a  $\pi$ -symmetry molecular orbital because

- $N_4 = N_1 - N_3 = 8 - 7 = 1$

This one is certainly tricentrically delocalized. It is formed by the linear combination of three p pure atomic orbitals, one from each atom. The independent linear combinations of the three atomic orbitals result in three molecular orbitals with different energies.

- $\pi = p_1 + p_2 + p_3$ ; the combination corresponds to a bonding molecular orbital, because it has no nodal plane.
- $\pi^* = p_1 - p_2 + p_3$ ; the combination corresponds to an antibonding molecular orbital, because it has two nodal planes.

Nonbonding molecular orbital  $\pi = (p_1 + p_2) - (p_2 + p_3) = p_1 - p_3$ ; the combination has one nodal plane that passes through the central atom. Its energy is intermediate between  $\pi$  and  $\pi^*$  molecular orbitals.

The bond order between the carbon atoms is:  $1 \sigma + 1 \frac{\pi}{2} = 1.5$ .

As the  $\pi$ -nonbonding tricentric molecular orbital is semi-occupied (the 17th electron), the allyl molecule is paramagnetic.

## 11.4 On Aromaticity Character of Organic Compounds (Putz et al. 2010)

The aromaticity concept has been recently extended not only to the inorganic systems (Chattaraj et al. 2007; Mandado et al. 2007), but also to zones and molecular fragments, using models, like HOMA (Harmonic Oscillator Model of Aromaticity) (Kruszewski and Krygowski 1972; Krygowski 1993), CRCM (Conjugated Ring Circuits Model) (Mracec and Mracec 2003) and TOPAZ (Topological Path and Aromatic Zones) (Tarko 2008). Even to the transition state of the pericyclic reactions which are constructed within Hückel or Möbius cyclic systems (Rzepa 2007; Putz et al. 2013) one can apply the aromaticity.

The aromaticity of different systems has been assessed using new developed software capable of performing high accuracy calculations, but despite that, as teachers, we could see that our students encounter difficulties in interpreting the obtained results. In order to overcome this inconvenient, the reactivity of some aromatic hydrocarbons and heteroaromatic compounds were explained using a comparison between Hückel molecular orbital theory (HMO), as a highly didactical impact approach, and the new developed density functional theory (DFT).

Due to the fact that Hückel method is a simple one, it is often used as the basis reference in understanding other methods. Worth notice the fact that, when the static parameters of reactivity are computed with the HMO method, the Coulomb energy ( $\alpha_r = \alpha + \delta_r \beta$ ) is assumed for the atomic orbital "r" and the exchange energy ( $\beta_{rs} = \eta_{rs} \beta$ ) for the bond between the atomic orbital "r" and "s", as determined from experimental results.



The standard values of both  $\alpha$  and  $\beta$  are benchmarked to the atomic orbital  $2p_z$  of the  $sp^2$  C and to a  $\pi$  bond for the benzene molecule. The accuracy of this method is high enough; and despite its simplifications it correctly gives the variation of the electronic densities and the energetic levels applied to a series of molecules that slightly differ.

However, DFT is still the most popular and versatile methods available in computational chemistry (Kohn et al. 1996), and the calculations they provide are reflecting the electronic density influence of a chemical structure towards its reactivity (Kohn and Sham 1965), while the electronic energy is approximated by various density functional forms (Putz 2008a)

$$E[\rho] = \underbrace{T[\rho]}_{\text{KINETIC}} + \underbrace{J[\rho]}_{\text{COULOMB}} + \underbrace{E_{\text{XC}}[\rho]}_{\text{EXCHANGE-CORRELATION}} + \underbrace{\int V(\mathbf{r})\rho(\mathbf{r})d\mathbf{r}}_{\text{CHEMICAL ACTION}} \quad (11.52)$$

This expression is the most general to be used in defining electronegativity and chemical hardness indices as its first and second functional derivatives, respectively (Putz 2008b)

$$\chi \equiv -\left(\frac{\delta E}{\delta \rho}\right)_{V(\mathbf{r})} \quad (11.53)$$

$$\eta = \left(\frac{\delta^2 E}{\delta \rho^2}\right)_{V(\mathbf{r})} \quad (11.54)$$

having an important role in assessing the chemical stability and reactivity propensity through the associate principles, especially those referring to the electronegativity equalization and the maximum chemical hardness (Putz 2008c).

The actual working systems presented were selected according to their industrial significance: hydrocarbons (aromatic annulenes), amines, molecules, ions, hydroxyarenes, and heterocycles with nitrogen (e.g. the obtained azo dyes from the aromatic amines and phenols through diazotization and coupling reactions). The heterocyclic compounds are nevertheless vital in some natural product as being part in building up their skeleton (Avram 1994, Chap. 19; Avram 1995, Chaps. 22, 31, 32).

Remember that the planar molecules of interest, with  $(4n+2)\pi$  electrons are displaying high stability, low magnetic susceptibility (diamagnetism), and affinity for substitution reactions rather than for addition (Chattaraj et al. 2007; Hendrickson et al. 1976, Chaps. 5, 8). There are several molecules which are fitting to the aromatic (Ar) model  $\text{Ar-Y}$  ( $Y = \text{OH}, \text{NH}_2, \text{NR}_2, \overset{+}{\text{N}}\text{H}_3$ ), and they are highly correlated with the substituent constants and the related inductive ( $\sigma$  and  $\pi$ ) effects (Katritzky and Topson 1971).

The considered aromatic compounds are: Benzene, Aniline, Phenol, Naphthalene,  $\alpha$ -Naphthol,  $\beta$ -Naphthol,  $\alpha$ -Naphthylamine,  $\beta$ -Naphthylamine, Pyridine, Pyrimidine, 4-N, N'-dimethylaminoaniline, and monochlorohydrate of 4-N, N'-dimethylaminoaniline. Some of those molecules present symmetry, an important

**Table 11.7** The parameters values considered for the conjugated systems by Hückel molecular orbital (HMO method); the number of points indicates the  $\pi$  electrons/atom. (Putz et al. 2010)

$\delta_r$	$\eta_{rs}$
$\delta_{\overset{\bullet}{\underset{ }{\text{C}}^-}} = 0.0$	$\eta_{\text{C}-\overset{\bullet}{\text{O}}^-} = 0.8$
$\delta_{\overset{\bullet}{\underset{ }{\text{N}}^-}} = 0.5$	$\eta_{\text{C}-\overset{\bullet}{\text{N}}^-} = 0.8$
$\delta_{\overset{\bullet}{\text{C}}(\overset{\bullet}{\text{N}}^-)} = 0.5$	$\eta_{\text{C}^{\bullet\bullet}\text{C}} = 1.0$
$\delta_{\overset{\bullet}{\text{N}}-\overset{\bullet}{\text{C}}\text{H}_3} = 1.1$	$\eta_{\text{C}^{\bullet\bullet}\text{N}} = 1.0$
$\delta_{\overset{\bullet}{\text{N}}-\text{H}} = 1.5$	–
$\delta_{\overset{\bullet}{\text{O}}^-} = 2.0$	–

item in lowering the degree of the secular determinant which is obtained following the Hückel molecular orbital (HMO) method (Hückel 1930, 1931; Mandado et al. 2007) in joint using the data from Table 11.7.

In this computational framework several parameter were calculated: the Hückel matrices, the eigenvectors, the  $\pi$  levels of energy, the total ground state energy ( $E_\pi$ ), the delocalization energy/ $\pi$  electrons ( $\bar{\pi}$ ), the charge densities ( $\rho_r$ ), the bond orders ( $p_{rs}$ ) and the free valence ( $F_r = 1.732 - \sum p_{rs}$ ).

On the other side, the present-based molecular computations employ for the DFT computational framework, the exchange sum and the correlation contributions in the mixed functional of Eq. (11.52)

$$E_{\text{XC}}[\rho] = \underbrace{K[\rho]}_{\text{EXCHANGE}} + \underbrace{E_{\text{c}}[\rho]}_{\text{CORRELATION}} \quad (11.55)$$

under the for of hybrid B3-LYP functional proposed by Becke through empirical comparisons made against very accurate experimental results, containing the exchange contribution (20 % Hartree Fock + 8 % Slater + 81 % Becke88) which was added to the correlation energy (81 % Lee-Yang-Parr + 19 % Vosko-Wilk-Nusair). Nevertheless, the Becke's functional *via* the so-called semiempirical (SE) modified ( $\beta, \gamma$ )-parameterized gradient-corrected functional (Becke 1986) was use for the considered 81 % contribution in the *exchange* term:

$$\begin{aligned} K^{\text{SE}} &= K_0 - \beta \sum_{\sigma} \int \rho_{\sigma}^{4/3} \frac{x_{\sigma}^2(r)}{1 + \gamma x_{\sigma}^2(r)} dr, \\ K_0 &= -\frac{3}{2} \left( \frac{3}{4\pi} \right)^{1/3} \int \rho^{4/3}(r) dr, \\ x_{\sigma}(r) &= \frac{|\nabla \rho_{\sigma}(r)|}{\rho_{\sigma}^{4/3}(r)}, \end{aligned} \quad (11.56)$$

so producing the working single-parameter density functional (Becke 1988):

$$K^{\text{B88}} = K_0 - \beta \sum_{\sigma} \int \rho_{\sigma}^{4/3}(r) \frac{x_{\sigma}^2(r)}{1 + 6\beta x_{\sigma}(r) \sinh^{-1} x_{\sigma}(r)} dr \quad (11.57)$$

where the value  $\beta = 0.0042[\text{a.u.}]$  has assessed as the best fit among the noble gases (He to Rn atoms) exchange energies. However, for the counter-side 81 % of the correlation part of energy the *Lee, Yang, and Parr* (LYP) functional considered the Colle-Salvetti approximation (Lee et al. 1988):

$$E_c^{\text{LYP}} = -a_c b_c \int dr \gamma(r) \xi(r) \left( \begin{array}{c} \sum_{\sigma} \rho_{\sigma}(r) \sum_i |\nabla \phi_{i\sigma}(r)|^2 \\ -\frac{1}{4} \sum_{\sigma} \rho_{\sigma}(r) \Delta \rho_{\sigma}(r) \\ -\frac{1}{4} |\nabla \rho(r)|^2 \\ +\frac{1}{4} \rho(r) \Delta \rho(r) \end{array} \right) - a_c \int dr \frac{\gamma(r)}{\eta(r)} \rho(r) \quad (11.58)$$

with

$$\begin{aligned} \gamma(r) &= 4 \frac{\rho_{\uparrow}(r) \rho_{\downarrow}(r)}{\rho(r)^2}, \\ \eta(r) &= 1 + d_c \rho(r)^{-1/3}, \\ \xi(r) &= \frac{\rho(r)^{-5/3}}{\eta(r)} \exp[-c_c \rho(r)^{-1/3}] \end{aligned} \quad (11.59)$$

and where the involved constants are given as:  $a_c = 0.04918$ ,  $b_c = 0.132$ ,  $c_c = 0.2533$ ,  $d_c = 0.349$ .

The simple Hückel method and the advanced DFT one are both adapted for the chemical hardness “frozen core” approximation of Eq. (11.54) (Koopmans 1934) and used in this study to ordering the reactivity of the 12 compounds (among both mononuclear and polynuclear forms)

$$\eta = \left( \frac{\partial^2 E_N}{\partial N^2} \right)_{V(r)} \cong E_{N+1} - 2E_N + E_{N-1} = IP - EA \cong LUMO - HOMO \quad (11.60)$$

in terms of ionization potential  $IP$  and electron affinity  $EA$  so related (the effective Koopmans’ approximation, see Putz 2013) with the lowest unoccupied molecular orbital (*LUMO*) and highest occupied molecular orbital (*HOMO*) energies.

The aromaticity of benzene (6 annulene) and its derivatives are here to be employed with quantum chemistry DFT and Hückel (1930, 1931) and approximations of quantum mechanics, with the results interpreted with the bondonic chemistry (Putz 2010a, b, 2012; Putz and Ori 2015) as well as by the many valence theories (Saltzman 1974).

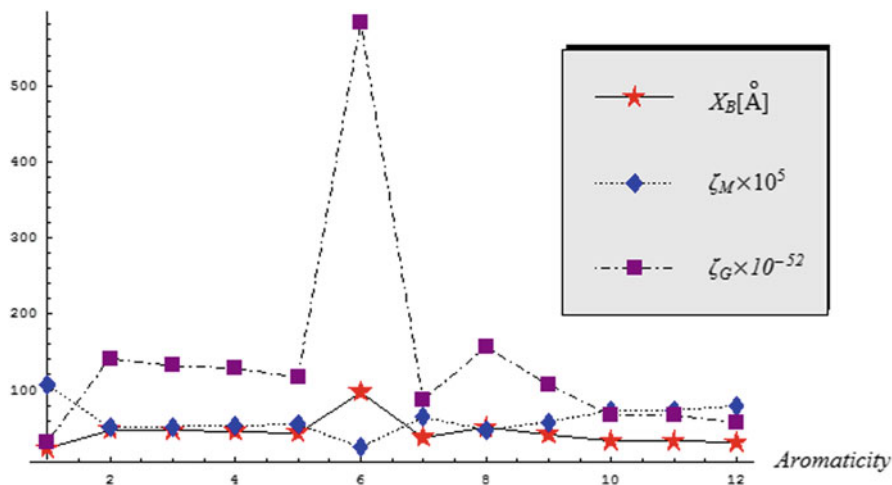
The DFT HOMO /LUMO and Hückel numerical results are presented in Tables 11.8 and 11.10, while the bondonic analysis are presented in the Tables 11.9 and

**Table 11.8** Energetic indices for the organic molecules under study as computed within the density functional theory (DFT) with B3-LYP exchange-correlation, according with Hypercube, Inc. (2002); all values in electron-volts (eV). (Putz et al. 2010)

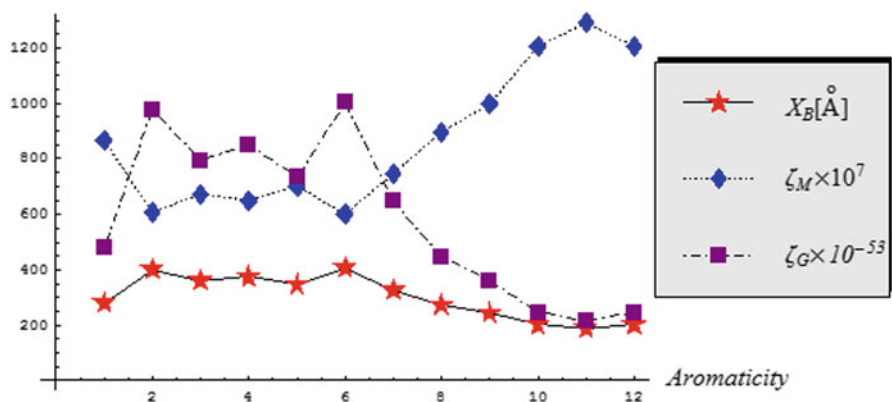
Compound	No. Aroma.	$\epsilon_{LUMO}^{DFT}$	$\epsilon_{HOMO}^{DFT}$	$\eta^{DFT}$
monochlorohydrate of 4-N, N'-dimethylaminoaniline	A01	- 2.230419	- 6.886414	4.656
$\alpha$ - Naphthylamine	A02	1.538881	- 3.264623	4.8035
$\beta$ - Naphthylamine	A03	1.524541	- 3.370884	4.89543
$\alpha$ -Naphthol	A04	1.534517	- 3.422596	4.95711
$\beta$ -Naphthol	A05	1.426792	- 3.5884	5.01519
4-N, N'-dimethylaminoaniline	A06	3.450884	- 1.606443	5.05733
Naphthalene	A07	1.29009	- 4.156888	5.44698
Aniline	A08	2.96429	- 3.097193	6.06148
Phenol	A09	2.597031	- 3.760442	6.35747
Pyridine	A10	1.622078	- 4.751688	6.37377
Pyrimidine	A11	0.9239021	- 4.744836	7.34187
Benzene	A12	2.523545	- 5.132959	7.6565

**Table 11.9** Bonding energies in kcal/mol (1 eV = 23.06035 kcal/mol) for the highest occupied orbital levels (DFT- HOMOs) for molecules of Table 11.8, along the related bondonic features of absolute action radii, mass and gravitation effect, as in Table 11.2 reported, according with Eqs. (11.37a, 11.37b, 11.37c), respectively

Aromatic compound	$E_{bond}(kcal/mol)$	$X_B(\text{\AA})$	$\zeta_m \times 10^5$	$\zeta_G \times 10^{-52}$
A01	- 158.803	22.8027	106.404	31.6814
A02	- 75.2833	48.1001	50.4429	140.969
A03	- 77.7338	46.5839	52.0847	132.222
A04	- 78.9263	45.88	52.8838	128.256
A05	- 82.7498	43.7601	55.4456	116.678
A06	- 35.0451	97.7494	24.8217	582.183
A07	- 95.8593	37.7756	64.2296	86.9467
A08	- 71.4224	50.7004	47.8558	156.622
A09	- 86.7172	41.7581	58.1039	106.246
A10	- 109.576	33.047	73.42	66.5417
A11	- 109.418	33.0947	73.3142	66.7341
A12	- 118.368	30.5923	79.3112	57.0236



**Fig. 11.7** The graphical plot for the bondonic features of aromatic molecules in Table 11.8 for their HOMO energy orbitals of Table 11.9



**Fig. 11.8** The graphical plot for the bondonic features of molecules in Table 11.10 for their HOMO energy orbitals of Table 11.11

11.11, respectively. The bondonic information for molecules of Table 11.9 and 11.11 are reported in graphically represented in Figs. 11.7 and 11.8 with the actual specific behavior:

- For DFT shape (Fig. 11.7) the bondonic distribution follow the Gaussian for radii and gravitational actions and with anti-parallel variation for bondonic mass; the extreme behavior is recorded for A06 (4-N, N<sup>2</sup>-dimethylaminoaniline) aromatics of Table 11.8 which is nevertheless not the most aromatic compound in the series

**Table 11.10** Energetic indices for compounds of Table 11.8, supplemented with the delocalization energy per  $\pi$  electrons ( $\bar{\pi}$ ) as computed within the Hückel theory (HT) or calibrated with the density functional counterparts from Table 11.8 (Putz et al. 2010)

Compound	No. Aroma.	$\epsilon_{LUMO}^{HT}$	$\epsilon_{HOMO}^{HT}$	$\eta^{HTa}$	$\bar{\pi}^{HTa}$	$-\alpha^b$	$-\beta^b$	$\eta_{DFT}^{HTc}$	$\bar{\pi}_{DFT}^{HTc}$
Monochlorohydrate of 4-N, N'-dimethylaminoaniline	A01	$\alpha-0.9415\beta$	$\alpha+0.7178\beta$	1.6593	0.4304	4.8723	2.806	4.656	1.2077
$\alpha$ -naphthylamine	A02	$\alpha-0.6698\beta$	$\alpha+0.5022\beta$	1.1720	0.4522	1.2063	4.0986	4.8036	1.8534
$\beta$ -naphthylamine	A03	$\alpha-0.6363\beta$	$\alpha+0.5573\beta$	1.1936	0.4515	1.0852	4.1014	4.8954	1.8518
$\alpha$ -naphthol	A04	$\alpha-0.6606\beta$	$\alpha+0.5382\beta$	1.1988	0.4906	1.1971	4.1351	7.6499	2.0287
$\beta$ -naphthol	A05	$\alpha-0.6332\beta$	$\alpha+0.5807\beta$	1.2139	0.4901	1.1893	4.1315	5.0152	2.0248
4-N, N'-dimethylaminoaniline	A06	$\alpha - \beta$	$\alpha+0.4962\beta$	1.4962	0.3089	-0.071	3.3801	5.0573	1.0441
Naphthalene	A07	$\alpha-0.6180\beta$	$\alpha+0.6180\beta$	1.2360	0.3680	1.4334	4.4069	5.4469	1.6217
Aniline	A08	$\alpha - \beta$	$\alpha+0.7437\beta$	1.7437	0.4665	0.5119	3.4762	6.0614	1.6216
Phenol	A09	$\alpha-0.9999\beta$	$\alpha+0.8274\beta$	1.8273	0.5246	0.8818	3.8283	6.9954	2.0083
Pyridine	A10	$\alpha-0.8410\beta$	$\alpha + \beta$	1.8410	0.4243	1.2896	3.4621	6.3737	1.4690
Pyrimidine	A11	$\alpha-0.7800\beta$	$\alpha+1.0700\beta$	1.8500	0.5156	1.4662	3.0642	5.6688	1.5799
Benzene	A12	$\alpha - \beta$	$\alpha + \beta$	2.0000	0.3333	1.3047	3.8282	7.6564	1.2759

<sup>a</sup>In  $[-\beta]$  units

<sup>b</sup>In electron-Volts [eV], obtained by HT with DFT calibrations of LUMO and HOMO energies

<sup>c</sup>In electron-Volts [eV], obtained from  $\eta^{HT}$  and  $\bar{\pi}$  by multiplication with corresponding calibrated  $[-\beta]$  (in eV) value

**Table 11.11** Bonding energies in kcal/mol ( $\alpha = 0$ ,  $\beta = -18$  kcal/mol) for the Hückel eigen-orbital HOMO levels for molecules of Table 11.10, along the related bondonic features of absolute action radii, mass and gravitation effect, as in Table 11.9 reported, according with Eqs. (11.37a, 11.37b, 11.37c), respectively

No. Aroma.	$E_{bond}(kcal/mol)$	$X_B(\text{Å})$	$\zeta_m \times 10^7$	$\zeta_G \times 10^{-53}$
A11	-19.26	188.013	1290.5	216.382
A10	-18.0	201.174	1206.07	246.591
A12	-18.0	201.174	1206.07	246.591
A09	-14.8932	243.14	997.904	360.202
A08	-13.3866	270.505	896.956	445.842
A01	-12.9204	280.265	865.718	478.597
A07	-11.124	325.525	745.352	645.645
A05	-10.4526	346.434	700.366	731.262
A03	-10.0314	360.981	672.144	793.96
A04	-9.6876	373.791	649.108	851.313
A02	-9.0396	400.586	605.689	977.74
A06	-8.9316	405.43	598.453	1001.53

(according with the chemical hardness ordering); this may open further subtle approaches and new definitions for aromaticity itself;

- The Hückel shape (Fig. 11.8) the Gaussian bondonic form of DFT framework is dissolved and another peak appears for the A02 ( $\alpha$ -Naphthylamine) aromatics of Table 11.8 which is now the less aromatic according with HT-chemical hardness of Table 11.10, see also the ordering of Eq. (11.62); this leads with the idea that although not as refined in computation as DFT the Hückel theory appears to be consistent with bondonic description, a finding which favors both theories towards their degree of observability, despite the inherent approximations to the first and the entanglement information for the last.
- In both approaches (DFT and Hückel) the higher aromaticity the higher the bondonic mass (however with lighter Hückel bondon so stronger gravitational action), which confirms the inertia in chemical reactivity associated with aromaticity, here physically represented by the bondonic mass.

Continuing with aromatic-chemical hardness connections, from Tables 11.8 and 11.10 the following aromaticity hierarchies are obtained.

DFT hierarchy of aromaticity of Table 11.8:

$$\begin{aligned}
 & \eta^{DFT}(A12) > \eta^{DFT}(A11) \\
 & > \eta^{DFT}(A10) > \eta^{DFT}(A09) \\
 & > \eta^{DFT}(A08) > \eta^{DFT}(A07) \\
 & & > \eta^{DFT}(A06) \\
 & > \eta^{DFT}(A05) > \eta^{DFT}(A04) \\
 & > \eta^{DFT}(A03) > \eta^{DFT}(A02) \\
 & & > \eta^{DFT}(A01)
 \end{aligned} \tag{11.61}$$

HT hierarchy of aromaticity according to the chemical hardness values of Table 11.10 (fourth column), for universal Hückel [- $\beta$ ] integral:

$$\begin{aligned}
 & \eta^{HT}(A12) > \eta^{HT}(A11) \\
 & > \eta^{HT}(A10) > \eta^{HT}(A09) > \eta^{HT}(A08) \\
 & & > \eta^{HT}(A01) \\
 & > \eta^{HT}(A06) > \eta^{HT}(A07) > \eta^{HT}(A05) \\
 & > \eta^{HT}(A04) > \eta^{HT}(A03) > \eta^{HT}(A02)
 \end{aligned} \tag{11.62}$$

HT hierarchy of aromaticity according to the chemical hardness values of Table 11.10 (eighth column), for calibrated Hückel-DFT [- $\beta$ ] integral:

$$\begin{aligned}
 & \eta_{DFT}^{HT}(A12) > \eta_{DFT}^{HT}(A04) \\
 & > \eta_{DFT}^{HT}(A09) > \eta_{DFT}^{HT}(A10) > \eta_{DFT}^{HT}(A08) \\
 & & > \eta_{DFT}^{HT}(A11) > \eta_{DFT}^{HT}(A07) \\
 & & > \eta_{DFT}^{HT}(A06) > \eta_{DFT}^{HT}(A05) \\
 & & > \eta_{DFT}^{HT}(A03) > \eta_{DFT}^{HT}(A02) \\
 & & > \eta_{DFT}^{HT}(A01)
 \end{aligned} \tag{11.63}$$

HT hierarchy of aromaticity according to the  $\bar{\pi}$  values of Table 11.10 (fifth column), for universal Hückel [- $\beta$ ] integral:

$$\begin{aligned}
 & \bar{\pi}^{HT}(A09) > \bar{\pi}^{HT}(A11) \\
 & > \bar{\pi}^{HT}(A04) > \bar{\pi}^{HT}(A05) > \bar{\pi}^{HT}(A08) \\
 & & > \bar{\pi}^{HT}(A02) > \bar{\pi}^{HT}(A03) \\
 & & > \bar{\pi}^{HT}(A01) > \bar{\pi}^{HT}(A10) \\
 & > \bar{\pi}^{HT}(A07) > \bar{\pi}^{HT}(A12) > \bar{\pi}^{HT}(A06)
 \end{aligned} \tag{11.64}$$



HT hierarchy of aromaticity according to the  $\bar{\pi}$  values of Table 11.10 (ninth column), for calibrated Hückel-DFT [- $\beta$ ] integral:

$$\begin{aligned}
 & \bar{\pi}_{DFT}^{HT}(A04) > \bar{\pi}_{DFT}^{HT}(A05) \\
 & > \bar{\pi}_{DFT}^{HT}(A09) > \bar{\pi}_{DFT}^{HT}(A02) \\
 & > \bar{\pi}_{DFT}^{HT}(A03) > \bar{\pi}_{DFT}^{HT}(A07) \\
 & > \bar{\pi}_{DFT}^{HT}(A08) > \bar{\pi}_{DFT}^{HT}(A11) \\
 & > \bar{\pi}_{DFT}^{HT}(A10) > \bar{\pi}_{DFT}^{HT}(A12) \\
 & > \bar{\pi}_{DFT}^{HT}(A01) \\
 & > \bar{\pi}_{DFT}^{HT}(A06)
 \end{aligned} \tag{11.65}$$

The principal points which arise from the aromaticity scale are:

- There is an agreement between the DFT and Hückel chemical hardness scales, (except for the case of the displacement and the inversion of the 4-N, N'-dimethylaminoaniline/A06 and monochlorohydrate of 4-N, N'-dimethylaminoaniline/A01 in the HT scheme), and also with the aromaticity/stability/reactivity scale for the molecules of interest, using experimental or other presented theoretical methods;
- Unlike the DFT counterpart scale of aromaticity, the mixed DFT-Hückel chemical hardness scale of aromaticity further inverts and departs the two forms of Naphtol (A04 & A05) and the Pyridine & Pyrimidine (A10 & A11) pairs considered;
- The inversion of the Phenol/A09 and Naphtalene/A07 with Benzene/A12 structural inertia in reactivity (aka aromaticity), as an effect of the delocalization energy per pi electrons is present in both realizations as HT and HT-DFT scales;
- Only the  $A_{\text{Phenol}} > A_{\text{Aniline}}$  ordering is appearing to be the only invariant across above aromaticity.

Overall, the chemical hardness although custom to be considered a versatile tool in assessing reactivity and aromaticity, conceptually superior to the classical delocalization energy per pi electrons index, it is currently challenged by the bondonic chemistry insight, especially regarding the bondonic mass and gravity production that can reshape the aromaticity concept itself.; however, the DFT approach parallels remarkably well with the simple Hückel quantum picture of organic molecules, which nevertheless appears to be more "spectroscopically reach" in bondonic peaks of information.

## 11.5 On Reducing Character of Mono- and Polyhydroxy Arens

Selected for their usage to obtain artificial resins, medicines and azo dyes, hydroxyarenes has properties of both hydroxyl groups and the aromatic rings (Avram 1995, Chap. 32). Hückel and DFT specific calculations were performed for these systems in which the conjugation between non participating electrons of oxygen of the

hydroxyl groups and  $\pi$  electrons of the aromatic rings takes place (Avram 1994, Chap. 19). Using the Streitwieser parameters (Table 11.7) standardized based on experimental results using computational technique (of the secular determinant and its diagonalization on the irreducible representations of the symmetry group associated to the corresponding molecules) results allowing the correlation with their chemical reactivity have been obtained.

The presence of the ( $-\text{SO}_3\text{H}$ ) group does not disturb the electronic state of the carbon atom to which it is linked and it does not participate in conjugation with the aromatic ring (Streitwieser 1961).

The delocalization energy (DE),  $\varepsilon_{\text{HOMO}}$  and  $\varepsilon_{\text{LUMO}}$  enable the estimation of aromaticity, reducing or oxidizing character of these compounds (Table 11.12).

Regarding the absorption bands in visible and ultraviolet domains, the first band ( $\lambda_{\text{max}}$ ) corresponds to either the transition between  $\varepsilon_{\text{LUMO}}$  and  $\varepsilon_{\text{HOMO}}$  of the large conjugated system or the transition from a non participating atomic orbital to  $\varepsilon_{\text{LUMO}}$  (Simon 1973, Chap. 2, 1964).

The internal consistency of the data in Table 11.12 is checked with the following relationship by determining the resonance integral parameter for each analyzed system obtaining the results reported in the last column of Table 11.12. Their striking similarity proves the reliability of the used data and the undertaken calculations.

$$\beta[\text{eV}] = \frac{2\pi c\hbar}{\lambda[\varepsilon_{\text{LUMO}}(\beta) - \varepsilon_{\text{HOMO}}(\beta)]} \quad (11.66)$$

Moreover, the common value  $\beta = -2.3877 \text{ eV} = -55.0819 \text{ kcal/mol}$  predicts the localization of this constant for cyclic aromatic systems under the range of linear polyenes, of approximately  $-60 \text{ kcal/mol}$ ,  $-70 \text{ kcal/mol}$ .

The obtained results lead us to the following hierarchy on the chemical reactivity of the eight hydroxyl arenes:

- According with  $\varepsilon_{\text{HOMO}}$  and  $\varepsilon_{\text{LUMO}}$  values, the  $\text{C}_{10}\text{H}_7\text{OH}$  compounds show superior tendency to oxidation or reduction processes than the corresponding  $\text{C}_6\text{H}_5\text{OH}$   $\pi$ —systems. Unlike the more stable phenol, the less aromatic naphthols participate in some chemical reactions under tautomeric form (Avram 1994, Chap. 19).
- Phenol (I), more reactive than benzene ( $\text{DE} = 8\beta$ ) (Simon 1973, Chap. 2), is more sensitive against oxidizing agents ( $\text{FeCl}_3$ ). It easily participates at reactions with SE mechanisms. In contrast to the (II-VIII) compounds, it does not present prototropic tautomerism (Nenitzescu 1966, Part II, Chap. 2).
- Our calculations are consistent with the physico-chemical behavior of diphenols. Thus, 1,2-dihydroxy phenol (II) with 1,2-benzoquinone form an electrochemically reversible redox system. The value of the quinone redox potential is small, therefore this compound is a strong oxidant and consequently the corresponding diphenol is a weaker reductant (Avram 1995, Chap. 25). However, the diphenol is oxidated by the ammoniacal solution of silver at low temperature and by the Fehling reagent at high temperature, while 1,3-dihydroxy phenol (III) only reacts with the Tollens reagent at high temperature (Nenitzescu 1966, Part II, Chap. 2).

Table 11.12 Energetic indices calculated by HMO method for aromatic hydroxo compounds

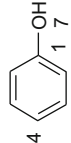
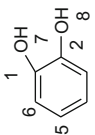
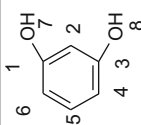
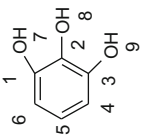
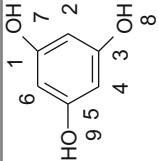
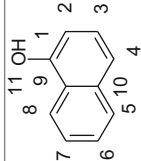
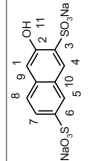
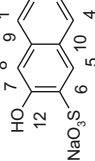
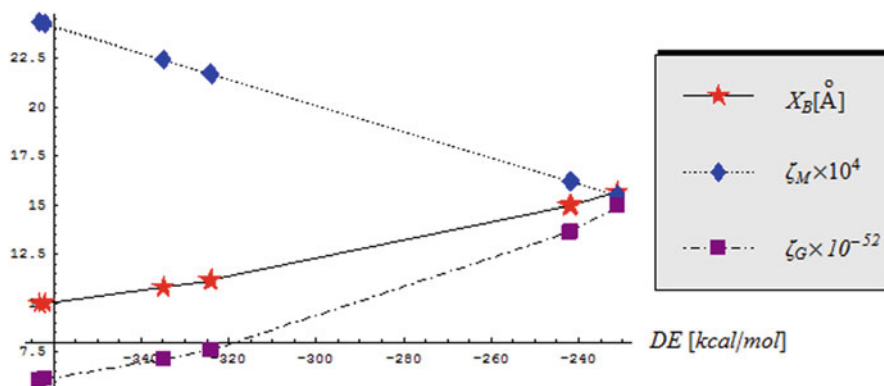
Compound	DE ( $\beta$ )	$\varepsilon_{LUMO}$	$\varepsilon_{HOMO}$	$\lambda_{max}$ (nm)	$-\beta$ (eV)
 5 6 4 3 2 1 OH 7	(I) 4.1973	$\alpha - 0.9999\beta$	$\alpha + 0.8274\beta$	284.39	2.3877
 6 5 4 3 1 OH 7 OH 2 8	(II) 4.3856	$\alpha - 1.0379\beta$	$\alpha + 0.7260\beta$	294.61	2.3877
 6 5 4 3 1 OH 7 OH 2 8	(III) 4.3950	$\alpha - 1.0340\beta$	$\alpha + 0.7726\beta$	287.65	2.3877
 6 5 4 3 1 OH 7 OH 2 8 OH 9	(IV) 6.5736	$\alpha - 1.0945\beta$	$\alpha + 0.7048\beta$	288.81	2.3877

Table 11.12 (continued)

Compound	DE ( $\beta$ )	$\varepsilon_{LUMO}$	$\varepsilon_{HOMO}$	$\lambda_{max}$ (nm)	$-\beta$ (eV)
 <chem>Oc1cc(O)c(O)cc1</chem>	(V)	$\alpha - 1.1082\beta$	$\alpha + 0.7727\beta$	276.28	2.3877
 <chem>Oc1cccc2ccccc12</chem>	(VI)	$\alpha - 0.6606\beta$	$\alpha + 0.5382\beta$	433.49	2.3877
 <chem>Oc1ccc(S(=O)(=O)O)cc1</chem>	(VII)	$\alpha - 0.6332\beta$	$\alpha + 0.5807\beta$	428.10	2.3877
 <chem>Oc1ccc(S(=O)(=O)O)cc1</chem>	(VIII)	$\alpha - 0.6505\beta$	$\alpha + 0.5552\beta$	431.00	2.3877

**Table 11.13** Bonding delocalization energies in kcal/mol ( $\beta = -55.0819$  eV) for the aromatic hydroxo compounds of Table 11.12, along the related bondonic radii of action, mass ratio respecting the electronic unit, and the bondonic gravitational ratio respecting the universal gravitational unit, according with Eqs. (11.37a, 11.37b, 11.37c), respectively

Compound	$DE_{bond}(kcal/mol)$	$X_B(\text{\AA})$	$\zeta_m \times 10^4$	$\zeta_G \times 10^{-52}$
(V)	-363.155	9.97134	24.3328	6.05812
(IV)	-362.086	10.0008	24.2612	6.09393
(VIII)	-334.909	10.8123	22.4402	7.12309
(VI)	-324.317	11.1654	21.7305	7.59597
(VII)	-323.981	11.177	21.708	7.61173
(III)	-242.085	14.9581	16.2207	13.6328
(II)	-241.567	14.9902	16.186	13.6913
(I)	-231.195	15.6627	15.491	14.9473



**Fig. 11.9** The graphical plot for the bondonic features of molecules in Table 11.13 for their delocalization energies of Table 11.12

The bondonic information for molecules of Table 11.12 is reported in Table 11.13 and graphically represented in Fig. 11.9. It provides the specific behavior:

- The bondonic information goes now with delocalization energy, which is in fact an energy difference driving reactivity; accordingly, the bondonic actions as radii, mass and gravitational effects display a monotonic variation, rather than a parabolic one, while maintaining, nevertheless their already established parallel and anti-parallel relationships, respectively;
- The decreasing in delocalization energy (in energy difference) actually free the bondon to a higher radii and gravitational action, whereas less bondonic mass is accumulated or distributed in between the bonding centers defining the bonding area.

Back to the “classical” quantum structure-reactivity interpretations, among phenols, pyrocatechol (II) and pyrogallol (IV) are the most reducing ones. Consequently, they are used as photographic developer. The alkaline solution of the 1,2,3-trihydroxy phenol (IV) quickly and quantitatively absorbs oxygen, serving for gas analysis (Nenitzescu 1966, Part II, Chap. 2). Phloroglucinol (V), resorcinol (III) and naphthols (VI-VIII) have the practical and theoretical support in their tendency to ketolyse (Avram 1994, Chap. 19). Along with the extension of the conjugated bonds system, the maximum absorption bands moves toward visible (bathochromic effect) (Hendrickson et al. 1976, Chap. 7). In this respect, naphthols are more suitable as coupling agents (Avram 1995, Chap. 22; Nenitzescu 1966, Part II, Chap. 5). The structural indices calculated for different atoms in hydroxy arenes (Table 11.14) allow us to establish some structure-property correlations in organic chemical reactions.

The values  $\rho_O > \rho_C$ ;  $F_O > F_C$  correlate with the higher oxygen electronegativity than that of the carbon atom (Putz 2006, 2007) and also with the potential contours presented in Fig. 11.10.

The reactions occurring at nucleus with electrophilic substitution mechanism: halogenation, nitrosation, sulfonation, nitration, alkylation, and coupling take place preferentially at carbon atoms possessing the highest electron density. Therefore, the electrophilic reagents turn to C(2) and C(4) of phenol, C(1) of 2-naphthol-3,6-sodium disulfonate, C(4) of 1-naphthol. The 1,3,5-trihydroxybenzene carbon atoms are favored by high electron densities, but certainly in substitution reactions they experience steric hindrance (Avram 1994, Chap. 19). The high free valences of some atoms in these molecules indicate their increased reactivity in reactions with both ionic and radicalic mechanisms. The low free valences of the carbon atoms to which hydroxyl groups are bounded confirm that, opposed to alcohols, hydroxyarenes do not participate to reaction during which carbon-oxygen bond is broken (Nenitzescu 1966, Part II, Chap. 2).

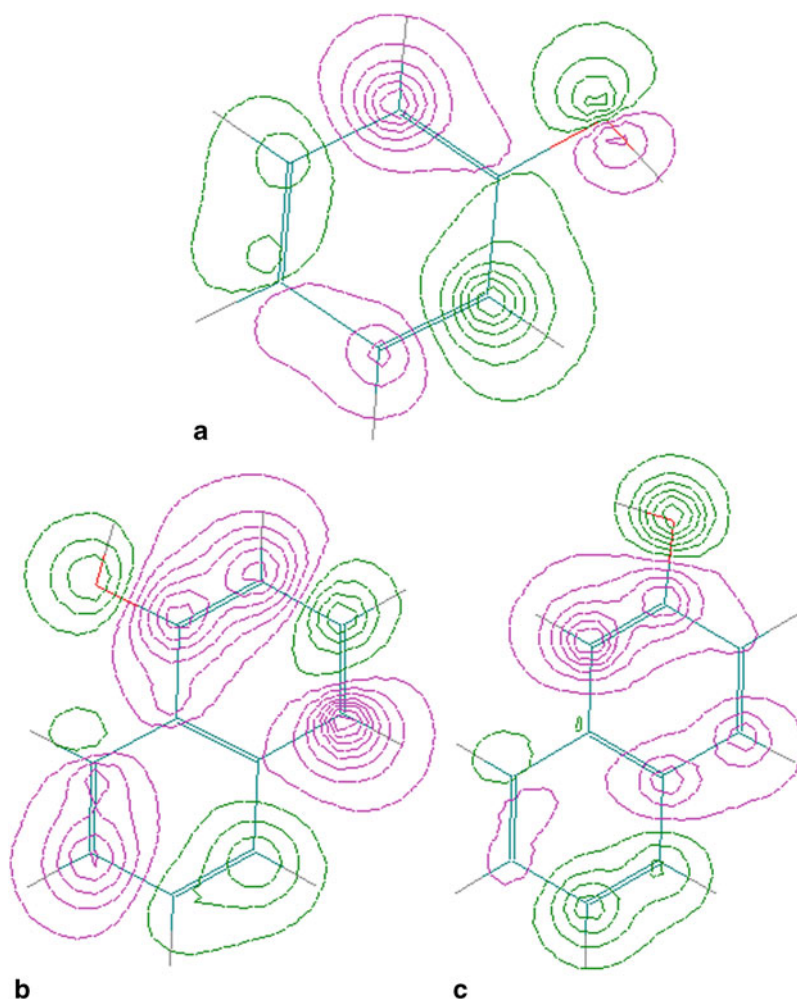
Increased reactivity of the hydroxyl group of these compounds show the heterolytic cleavage of the bond during neutralization, etherification, esterification, and also colligation of some intermediary formed radicals (Avram 1994, Chap. 19; Nenitzescu 1966, Part II, Chap. 2).

## 11.6 Structure and Reactivity of Aromatic Compounds Involved in Azo Dyes Synthesis

Our interest for such compounds resides in their participation to diazotisation and coupling reactions, both as substrates and electrophilic reactants. The aromatic amines and mononuclear/polynuclear hydroxyarenes undergo electrophilic substitution reactions with a higher rate than their reference compounds, benzene and naphthalene, respectively:  $k_{Ar-Y}/k_{ArH} > 1$  ( $Y = OH, NH_2$ ) (Nenitzescu 1968, Part IV). This behavior is due to the ring activation by conjugation of the non-participating electrons of nitrogen and oxygen atoms with the  $\pi$  electrons of the aromatic ring (Avram 1994, Chap. 19). In this respect, the aromaticity of these molecules can be

**Table 11.14** Electron repartition indices calculated by HMO method for different phenols and naphthols atoms

No.	Electronic densities ( $\rho_r$ )							Free valences ( $F_r$ )						
	$\rho_1$	$\rho_2$	$\rho_3$	$\rho_4$	$\rho_7$	$\rho_{11}$	$F_1$	$F_2$	$F_3$	$F_4$	$F_7$	$F_{11}$		
I	0.9547	1.0400	0.9980	1.0292	1.9400	–	0.1936	0.4162	0.3971	0.4038	1.4836	–		
V	0.9513	1.1087	0.9513	1.1087	1.9400	–	0.1899	0.4390	0.1899	0.4390	1.4829	–		
VI	0.9442	1.0561	0.9958	1.0407	1.0095	1.9346	0.2400	0.4259	0.4010	0.4583	0.4055	1.4751		
VII	1.0566	0.9530	1.0259	0.9957	1.0000	1.9391	0.4721	0.1982	0.4195	0.4504	0.4043	1.4819		



**Fig. 11.10** The potential contour maps for phenol (a), 1-naphthol (b), 2-naphthol-3,6-sodium disulfonate (c) under discussion on their HOMO state. A higher density of contours indicates that the site is susceptible for electrophilic attack either for positive (*green*) or negative (in *cyan*) molecular electrostatic potential

discussed using the energetic and  $\pi$  electron density distribution indices calculated by HMO and DFT methods.

The structure and reactivity in diazotization reaction electronic spectra (200–800 nm) are recorded for sulphanilic acid and sulphanilamide, the corresponding hydrochlorides, diazonium salts and hydrolysis products. Molecular orbital calculations by the HMO method are performed for the above molecules (Isac et al. 1981a).



The diazonium salts were obtained through diazotization in acidic solution with sodium nitrite, the nitrous acid excess was destroyed with ammonium sulphamate. The concentrations and the preparation technique were those described in literature (Ciuhandu and Mracec 1968).

Solid sulphanilic acid can also be treated with gaseous NOCl, to give solid diazonium chloride in 100% yield. The water produced by the reaction is removed in situ reaction with excess of NOCl (Kaupp et al. 2002).

Diazonium salts both as diazotization products and electrophilic reactants in azocoupling processes are also involved in thermal decompositions (Simon and Bădilescu 1967).

The kinetics of thermal decompositions in solution of diazonium salts of sulphanilic acid and sulphanilamide were followed spectrophotometrically. The following activation energies ( $E$ ) and preexponent ( $A$ ) were obtained for thermal decompositions of benzenediazonium salts: for the sulphanilic acid derivative  $E = 127.19 \text{ kJ mol}^{-1}$ ,  $A = 6.0 \cdot 10^{15} \text{ s}^{-1}$ , for the sulphanilamide derivatives  $E = 124.20 \text{ kJ mol}^{-1}$ ,  $A = 4.0 \cdot 10^{15} \text{ s}^{-1}$  (Isac et al. 1981b).

For these quick reactions of breaking the C–N bonds,  $A > 10^{14} \text{ s}^{-1}$  indicates that within the activated complex the interaction of  $\pi$  electrons between the nitrogen atoms and those of the molecule residue is weakened or even cancelled (Simon 1966a).

The correlation diagram of molecular orbitals and the correlation diagram of electronic states for the decomposition reaction of the benzenediazonium cation were established, using Hückel molecular orbital calculations (Isac et al. 1985). The activation energy of the thermal decomposition must be of purely thermodynamic nature, without a certain barrier, as the diazonium cation is more stable than the decomposition products (Simon and Bădilescu 1967).

The following activation enthalpies ( $\Delta H^\ddagger$ ) and activation entropies ( $\Delta S^\ddagger$ ) were obtained for thermal decompositions of benzenediazonium salts: for the sulphanilic acid derivative  $\Delta H^\ddagger = 124.683 \text{ kJ mol}^{-1}$ ,  $\Delta S^\ddagger = 48.116 \text{ J K}^{-1} \text{ mol}^{-1}$  for the sulphanilamide derivatives  $\Delta H^\ddagger = 121.336 \text{ kJ mol}^{-1}$ ,  $\Delta S^\ddagger = 44.350 \text{ J K}^{-1} \text{ mol}^{-1}$  (Isac et al. 1981b). The activation enthalpies were quite high, and in contrast, the corresponding activation entropies have high positive values.

The experimental data indicate that the stability of substituted diazonium ions, precipitated as diazoniumfluoroborates, can be increased by complexation with crown ethers (Bräse et al. 2004). Diazonium cations are not strong electrophilic reactants because of their positive charge delocalization. Increased reactivity is found in those diazonium cations containing electron attractive substituents in para position (Nenişescu 1966, Part II, Chap. 5, pp. 590–593).

The azocoupling of these compounds may occur only with strong nucleophiles such as phenolates, naphtholates, and free aromatic amines. In this case the reaction selectivity is high (Nenitzescu 1968, Part IV, Chap. 5, pp. 430–436). This behavior makes the azocoupling processes to occur almost unitary into positions of highest electron density ( $\rho_r$ ) of the coupling agents (Simon 1973, Chap. 2, pp. 35–50). The reactivity of coupling components variously substituted in the same position falls within the series  $-\text{O}^- > -\text{NH}_2 > -\text{OH}$ .

**Table 11.15** The parameters values considered for the conjugated systems (HMO method)

	$\delta_r$		$\eta_{rs}$
$(-\overset{+}{\text{N}}\equiv)$	1.25	$\text{Ar}-\text{N}=\equiv$	1.00
$(\equiv\text{N})$	1.25	$-\overset{+}{\text{N}}\equiv\text{N}$	1.00
		$\text{Ar}-\text{COOH}$	0.90
$(=\text{O})$	1.00	$-\overset{\text{O}}{\underset{ }{\text{C}}}=\text{O}$	1.00

The bondonic information for molecules of Table 11.16 is reported in Table 11.17 and graphically represented in Fig. 11.11 with the actual peculiarity:

- The monotonic bondonic behavior vs. delocalization energy is maintained, as in the Fig. 11.9 recorded, however, here with a smooth non-linear effect, which somehow extends and generalizes the earlier linear shapes of Fig. 11.9, probably due to the actual ionic/radicalic character of the considered compounds; accordingly, there appears that the bondonic treatment is indeed sensitive, even when about of gravitational effects, by the ionicity character which superimposes the highly covalent (hydrocarbon) compounds.

Back on the “classical” chemical interpretation of structure-reactivity relationship, the orientation of substitution at polyfunctional components is governed by pH through protolytic equilibrium involving hydroxyl and amino groups (Panchartek and Sterba 1969). Selecting the Streitwieser parameters (Table 11.7) and data of Table 11.15 (Streitwieser 1961) the chemical reactivity indices of conjugated systems containing a number of electrons ( $n_\pi$ ) are calculated.

The values obtained by HMO calculations sustain the chemical reactivity of those 15 investigated organic molecules (Table 11.16).

- The hydrochlorides of sulfanilic acid and sulfanilamide (IX), (X), and also their diazonium salts (XI), (XII) present low values of delocalization energy (DE), as these compounds are double substituted in para positions with electron attractive groups. The hydrolysis products of sulfanilic acid and sulfanilamide diazonium salts (XIII), (XIV), and also the salicylic acid (XV) are more aromatic than N, N-dimethyl aniline (XVI) and m-phenylene diamine (XVII), in accordance with TOPAZ aromaticity. Moreover, it can be seen that 1-naphthol (VI) and 2-naphthol (XVIII) are more stable than 1-naphthyl ethylenediamine (XIX) and 2-naphthyl amine (XX), and the (XIII), (XIV) compounds are more aromatic than (XVI) molecule. The favorable effect that first order substituents bring on aromaticity is in accordance with TOPAZ modeling for these compounds, such as  $A(\text{XVI}) \cong 90\% A[(\text{XIII}), (\text{XIV})]$  relationship (Tarko 2008).
- Based on HOMO- LUMO gap criteria for aromaticity (Table 11.10), the (XIX) and (XX) molecules are less aromatic than (XVI) compound showing properties intermediary to those of pure aromatic amines and aliphatic ones (Nenitzescu 1966/Part I). The monochlorhydrate of 4-N, N-dimethylamino aniline (XXII), one

**Table 11.16** Energetic indices calculated by HMO method for the organic compound used in diazotization and coupling reactions

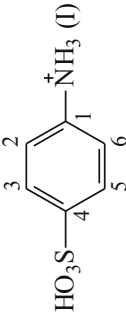
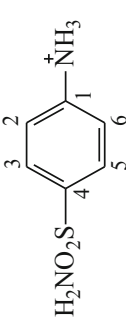
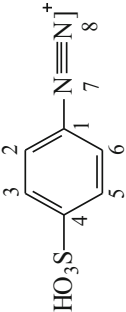
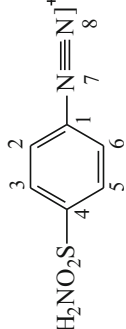
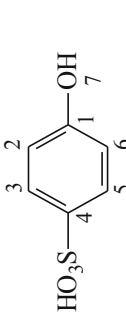
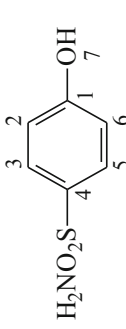
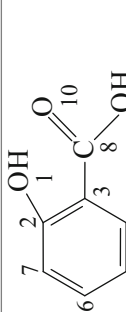
Compound	$n_{\pi}$	DE ( $\beta$ )	$\epsilon_{\text{LUMO}}$	$\epsilon_{\text{HOMO}}$	$\lambda_c$ (nm)
 (IX)	6	2.0490	$\alpha - 0.8409 \beta$	$\alpha + \beta$	282
 (X)	6	2.0490	$\alpha - 0.8409 \beta$	$\alpha + \beta$	282
 (XI)	8	2.6073	$\alpha + 0.1786 \beta$	$\alpha + \beta$	633
 (XII)	8	2.6073	$\alpha + 0.1786 \beta$	$\alpha + \beta$	633
 (XIII)	8	4.1968	$\alpha - 0.9999 \beta$	$\alpha + 0.8274 \beta$	284
 (XIV)	8	4.1968	$\alpha - 0.9999 \beta$	$\alpha + 0.8274 \beta$	284
 (XV)	12	5.1408	$\alpha - 0.5351 \beta$	$\alpha + 0.8386 \beta$	378

Table 11.16 (continued)

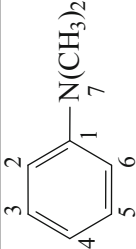
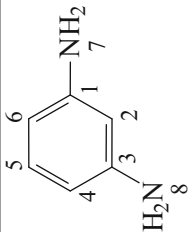
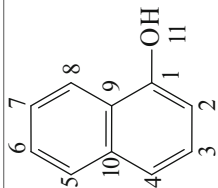
Compound	$n_{\pi}$	DE ( $\beta$ )	$\epsilon_{\text{LUMO}}$	$\epsilon_{\text{HOMO}}$	$\lambda$ (nm)
 (XVI)	8	3.7320	$\alpha - \beta$	$\alpha + 0.7437 \beta$	298
 (XVII)	10	3.4650	$\alpha - 1.0404 \beta$	$\alpha + 0.6824 \beta$	302
 (VI)	12	5.8872	$\alpha - 0.6606 \beta$	$\alpha + 0.5382 \beta$	434

Table 11.16 (continued)

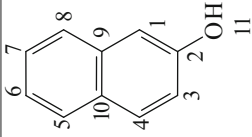
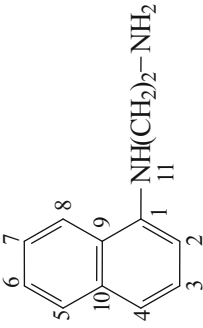
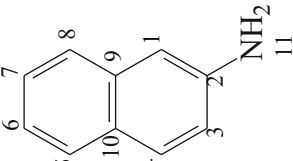
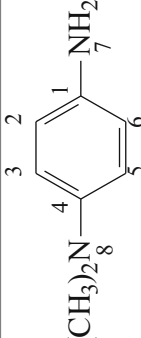
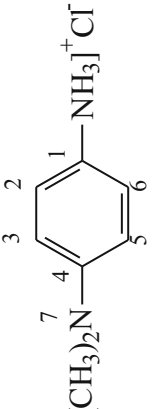
Compound	$n_{\pi}$	DE ( $\beta$ )	$\epsilon_{\text{LUMO}}$	$\epsilon_{\text{HOMO}}$	$\lambda$ (nm)
 <p>(XVIII)</p>	12	5.8812	$\alpha - 0.6332 \beta$	$\alpha + 0.5807 \beta$	428
 <p>(XIX)</p>	12	5.4264	$\alpha - 0.6698 \beta$	$\alpha + 0.5022 \beta$	444

Table 11.16 (continued)

Compound	$n_{\pi}$	DE ( $\beta$ )	$\epsilon_{\text{LUMO}}$	$\epsilon_{\text{HOMO}}$	$\lambda$ (nm)
 (XX)	12	5.4180	$\alpha - 0.6363 \beta$	$\alpha + 0.5573 \beta$	435
 (XXI)	10	3.0890	$\alpha - \beta$	$\alpha + 0.4962 \beta$	347
 (XXII)	8	3.0890	$\alpha - 0.9415 \beta$	$\alpha + 0.7178 \beta$	313

**Table 11.17** Bonding delocalization energies in kcal/mol ( $\beta = -55.0819$  eV) for the compounds of Table 11.16, along the related bondonic radii of action, mass ratio respecting the electronic unit, and the bondonic gravitational ratio respecting the universal gravitational unit, according with Eqs. (11.37a, 11.37b, 11.37c), respectively

Compounds	$DE_{bond}(kcal/mol)$	$X_B(\text{\AA})$	$\zeta_m \times 10^4$	$\zeta_G \times 10^{-52}$
(VI)	-324.278	11.1668	21.7279	7.59777
(XVIII)	-323.948	11.1782	21.7058	7.61328
(XIX)	-298.896	12.115	20.0273	8.94294
(XX)	-298.434	12.1338	19.9963	8.97069
(XV)	-283.165	12.7881	18.9732	9.9642
(XIII, XIV)	-231.168	15.6646	15.4892	14.9509
(XVI)	-205.566	17.6155	13.7737	18.9069
(XVII)	-190.859	18.9729	12.7883	21.933
(XXI, XXII)	-170.148	21.2823	11.4006	27.5974
(XI, XII)	-143.615	25.2142	9.62278	38.7366
(IX, X)	-112.863	32.0844	7.56226	62.722

of the amine form in HCl solution, is more aromatic than 4-N, N-dimethylamino aniline (XXI) as predicted by the values of TOPAZ aromaticity (Tarko 2008).

- The  $\varepsilon_{LUMO}$  and  $\varepsilon_{HOMO}$  values indicate that (IX), (X), (XI), (XII) compounds are the most resistant to oxidation, and the (XVI), (XVII), (XXI) molecules are the most resistant to reduction. The (XI), (XII) compounds should be stronger oxidizing agents, and the (XIX), (XXI) compounds should be stronger reducing agent.
- For the (IX), (XI), (XIII) compounds that are present in the acidic solution when sulfanilic acid diazotization occurs, and also the (X), (XII), (XIV) compounds present in the medium when sulfanilamide is diazotized, the correlations between  $\lambda_{calculated}$  and spectral measurements  $\lambda_{exp}$  are satisfactory (Isac et al. 1981a).

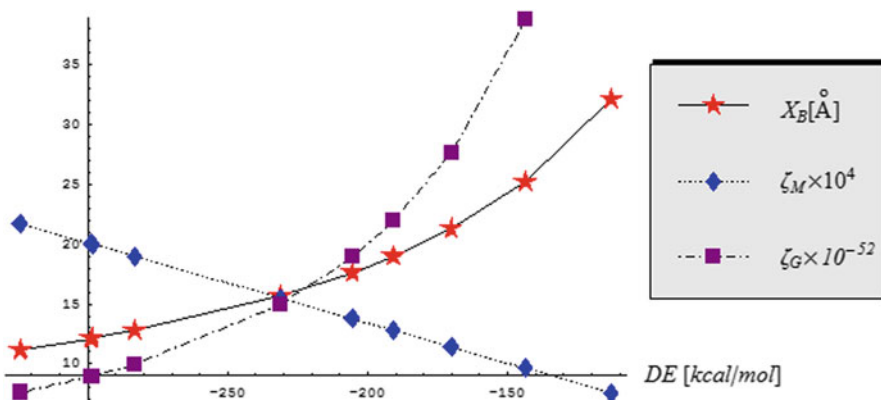
Regarding the electronic densities ( $\rho_r$ ) calculated by HMO method (Table 11.18) correlated with the results obtained by DFT method (Fig. 11.12), it should be mentioned that their relative values are more important than their absolute ones within this series of similar compounds, or for different atoms of the same substance.

The atoms electronic densities follow the  $\rho_O > \rho_N > \rho_C$  relationship being in good agreement with the known electronegativity tendency (Putz 2006, 2007). The usage of phenolates and naphtholates, strong nucleophiles, in azo coupling reactions is based on the fact that the oxygen atom in the  $-O^-$  anion is less electronegative than in the  $-OH$  group due to its negative charge (Simon 1973, Chap. 2, pp. 35–50).

The calculated values in Table 11.18 place the coupling components upon reactivity as follow:

$$(XVII) > (XVI) > (XIII) \quad (11.67a)$$

$$(XIV) > (XV) \quad (11.67b)$$



**Fig. 11.11** The graphical plot for the bondonic features of molecules in Table 11.17 for their delocalization energies of Table 11.16

**Table 11.18** Electronic densities ( $\rho_r$ ) calculated by HMO method for atoms of some coupling components of sulfanilic acid and sulfanilamide diazonium salts

No.	$\rho_1$	$\rho_2$	$\rho_3$	$\rho_4$	$\rho_5$	$\rho_6$	$\rho_7$	$\rho_8$	$\rho_9$	$\rho_{10}$	$\rho_{11}$
XIII, XIV	0.9547	1.0400	0.9980	1.0292	0.9980	1.0400	1.9400	–	–	–	–
XV	1.9306	0.9035	1.0572	0.9523	1.0288	0.9574	1.0417	0.6394	1.8953	1.5939	–
XVI	0.9538	1.0484	0.9977	1.0367	0.9977	1.0484	1.9172	–	–	–	–
XVII	0.9521	1.0989	0.9521	1.0835	0.9953	1.0835	1.9173	1.9173	–	–	–
VI	0.9442	1.0561	0.9958	1.0407	1.0071	0.9983	1.0095	0.9934	1.0210	0.9993	1.9346
XVIII	1.0566	0.9530	1.0259	0.9957	0.9983	1.0097	1.0000	1.0096	0.9984	1.0138	1.9399
XIX	0.9418	1.0685	0.9952	1.0514	1.0092	0.9980	1.0127	0.9923	1.0248	0.9993	1.9076
XX	1.0695	0.9516	1.0305	0.9951	0.9980	1.0124	1.0000	1.0122	0.9982	1.0177	1.9154

$$(XIX) > (VI) \quad (11.67c)$$

$$(XVIII) > (VI) \quad (11.67d)$$

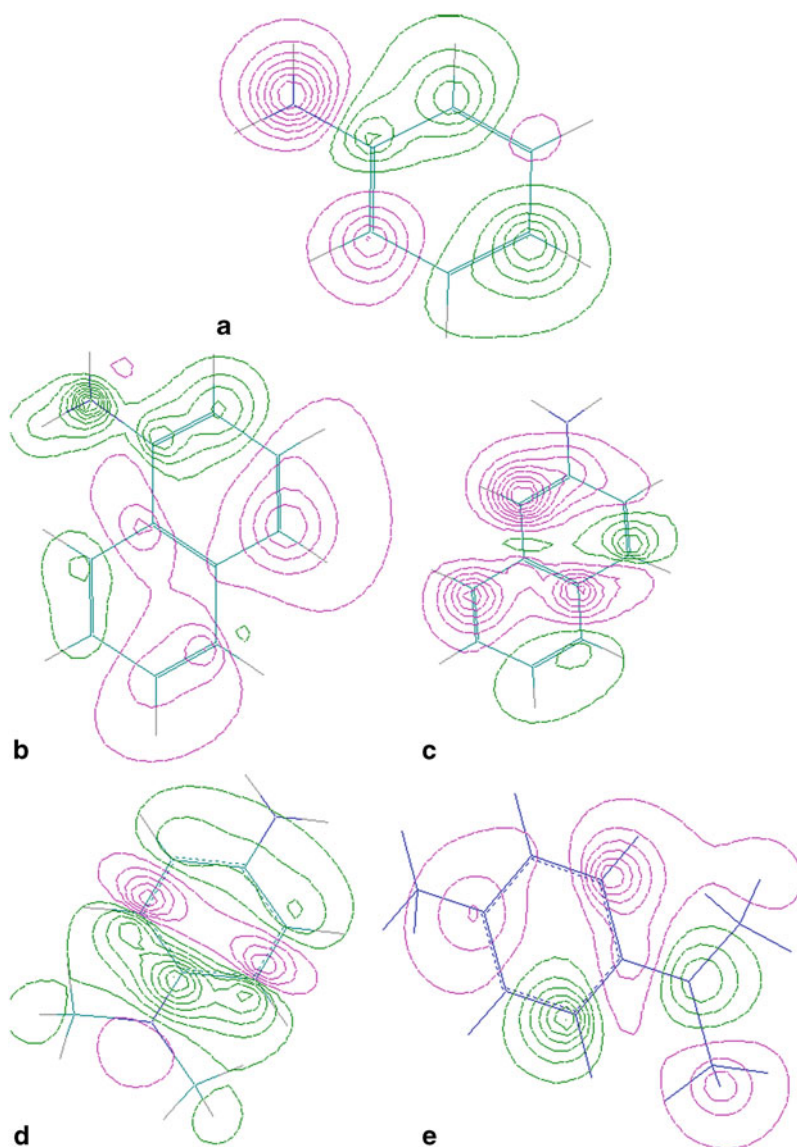
$$(XX) > (XIX) \quad (11.67e)$$

$$(XX) > (XVIII) \quad (11.67f)$$

according to their experimental behavior.

The diazonium cations (XI), (XII) perform electrophilic attacks to the following atoms: C(4) of (XIII), (XIV), (XVI), (XVII), (VI), (XIX), C(5) of (XV) and C(1) of (XVIII), (XX) coupling components. It should be mentioned that the ( $-\text{SO}_3\text{H}$ )





**Fig. 11.12** The potential contour maps for N, N-dimethylaniline (a), 1-naphthylethylenediamine (b), 2-naphthylamine (c), 4-N, N-dimethylamino aniline (d), monochlorohydrate of 4-N, N-dimethylamino aniline (e) under discussion on their HOMO state. A higher density of contours indicates that the site is susceptible for electrophilic attack either for positive (green) or negative (in cyan) molecular electrostatic potential

**Table 11.19** Aromatic amines, hydroxy arenes and corresponding azo dyes. (Nenițescu 1968, Part IV, Chap. 5, pp. 430–436)

Diazotable components	Coupling components	Azo dye
IX	XVI	Methyl orange
IX	XVIII	Beta-naphthol orange
IX	VI	Alpha-naphthol orange
IX	XVII	SFD
IX	XV	Chromable acid yellow (or azo salicylic dye)
IX	XIX	SNED
X	XVII	Red prontosil

group of (XIII) molecule and the ( $-\text{SO}_2\text{NH}_2$ ) group of (XIV) molecule are removed through these reactions (Nenitzescu 1966, Part II, Chap. 5, pp. 590–593). Even though the C(2) atoms of (XIII), (XIV), (XVI), (XVII), (VI), (XIX) compounds and C(7) atom of (XV) molecule are positions with the highest electronic density, the electrophilic attacks do not occur at these atoms due to steric impediments. The structural indices ( $p_{rs}$ ) and ( $F_r$ ) calculated by HMO method for the atoms of these molecules, in turn, are correlated with aromaticity, and their basic or acidic character.

Considering the monosubstituted aromatic compounds: (XIII), (XIV), (XVI); (VI), (XIX); (XVIII), (XX), it can be observed the correlation between the decrease of the aromaticity and the increase of the  $p_{C-O}$ ,  $p_{C-N}$ , values (Streitwieser 1961), which is in good agreement with the results of TOPAZ model (Tarko 2008).

The elevated values of the free valences calculated for nitrogen ( $F_N = 1.42 - 1.44$ ) of the aromatic amines and oxygen ( $F_O = 1.47 - 1.48$ ) of the hydroxyarenes are reflected in the chemical properties of the corresponding functional groups. Thus, the phenols and naphthols are week acids ( $p_{K_a} = 9 - 10$ ) and the aromatic amines are week bases with stronger conjugated acids ( $p_{K_a} = 4 - 5$ ) (Avram 1994, Chap. 19, 1995, Chap. 22). The rationale of choosing the molecules investigated within this study is mainly linked to the azo dyes that can be synthesized from these compounds (Table 11.19).

Among other applications, diazotization and coupling reactions are especially suited for measuring nitrites concentration in water samples. In comparison to potentiometric methods (Vlascici et al. 2007), the Aquaquant Kit 1.14408, by Merck KGaA Germany, is based on a colorimetric method which correlates the color intensity of SNED compound obtained from (IX) and (XIX) molecules (see Table 11.19) with the dosed anion concentration (Negreanu-Pirjol et al. 2012).

**Table 11.20** Rate constants for thermal decomposition of some diazonium cations in diluted solution at four different temperature values. (De Tar and Kwong 1956; Isac et al. 1981b)

$C_6H_5-N\equiv N]^+$		$4-HO_3S-C_6H_4-N\equiv N]^+$		$4-H_2NO_2S-C_6H_4-N\equiv N]^+$	
T (K)	$k \cdot 10^5 (s^{-1})$	T (K)	$k \cdot 10^3 (s^{-1})$	T (K)	$k \cdot 10^3 (s^{-1})$
317.26	73.24	348.16	38.80	348.16	37.90
312.29	36.91	343.16	29.60	343.16	15.60
309.51	24.89	333.16	7.00	333.16	3.50
301.61	7.89	323.16	2.00	323.16	1.00

## 11.7 The Kinetics of Thermal and Photochemical Decomposition of Some Aromatic Diazonium Salts

Our investigations have been focused on the kinetics and mechanisms of thermal and photochemical decompositions of some diazonium salts, as well as on spectral studies and molecular orbitals in fundamental or excited state.

The HMO calculations of the molecular orbitals have allowed the correlation of thermal and photochemical characteristics with structural parameters. The sulphanilic acid and sulphanilamide diazonium salts, which are used in azo dyes industry, are photochemically stable but thermo-unstable conducting to a rapid decomposition with a high preexponential coefficient.

The ability to form dyes with coupling compounds and the loss of this capacity by exposure to light, encourage the use of diazonium salt of 4-N, N'-dimethylaminoaniline in diazotization processes.

The thermal and photochemical decompositions of the aromatic diazonium salts formally take place according to the same radical or ionic mechanism, depending on the medium and the reacting substances (Boudreaux and Boulet 1958; Simon and Bădilescu 1967; Simon 1966b).

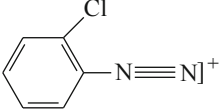
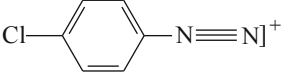
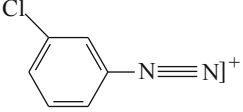
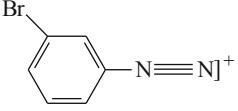
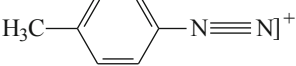
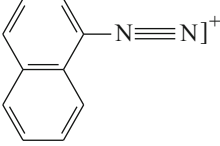
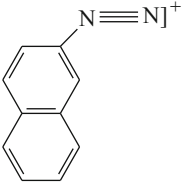
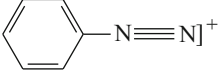
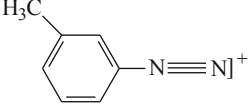
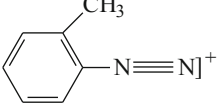
A homolotic process has been reported for basic medium, in buffer alcoholic solutions, or in organic solvents as mixtures (benzene-tetramethylsulphone, or nitrobenzene-tetramethylsulphone) when the decomposition of the diazonium salts leads to the formation of an arylether.

In acidic medium water solutions, the thermal or photochemical decompositions follow a heterolytic mechanism with the formation of the phenol. The first determining rate step is the monomolecular dissociation of the C-N bond with the formation of  $N_2$  and of the phenylcarbonium ion. In the rapid second step, the carbonium ion is saturated owing to the attack of a nucleophilic agent (Avram 1995, pp. 65).

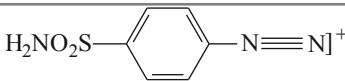
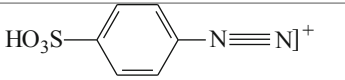
The decomposition reaction rate is practically independent of the concentration and nature of the acids present in solution (De Tar and Kwong 1956). The temperature favors the decomposition of the diazonium salts (Table 11.20) (Isac et al. 1981b).

The bondionic information for molecules of Table 11.21 is reported in Table 11.22 and graphically represented in Fig. 11.13. It provides the specific behavior as:

**Table 11.21** Arrhenius parameters for thermal decomposition of some diazonium salts (DS) in diluted solutions. (Crossley et al. 1940; Simon 1966a; Isac et al. 1985)

Compound	No.	LogA	Ea (kJ mol <sup>-1</sup> )	Log k <sup>a</sup>
	DS1	14.4149	128.7440	- 7.8500
	DS2	14.2041	132.0880	- 6.8000
	DS3	16.3222	126.2360	- 5.5200
	DS4	16.2304	124.1460	- 5.2427
	DS5	15.9810	122.0062	- 5.1200
	DS6	15.5051	117.4580	- 4.8112
	DS7	15.5910	117.4580	- 4.7253
	DS8	15.5162	113.2696	- 4.0700
	DS9	15.0452	107.0355	- 3.4700
	DS10	15.1760	107.4200	- 3.3800

**Table 11.21** (continued)

Compound	No.	lg A	E <sub>a</sub> (kJ mol <sup>-1</sup> )	Log k <sup>a</sup>
	DS11	15.6020	124.2647	- 1.8300
	DS12	15.7781	127.1936	- 1.7100

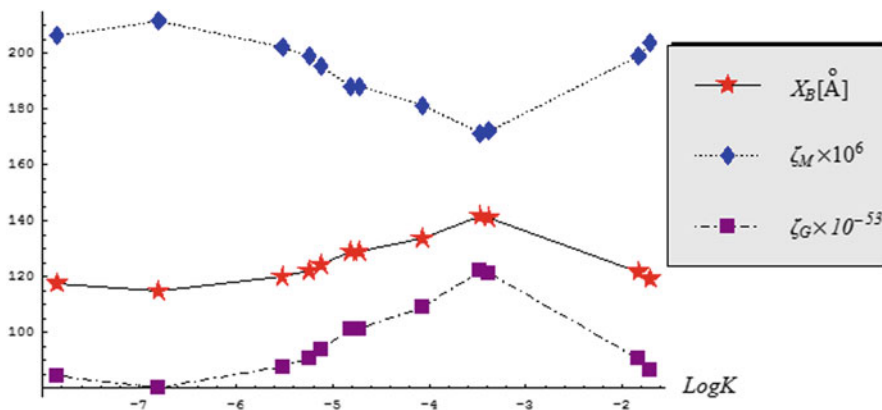
<sup>a</sup>log k (or logK) refers to the rate constant k at 25 °C; for the cases without determinations at this temperature, the k values at 25 °C were calculated from Arrhenius equation

**Table 11.22** Bonding activation energies in kcal/mol (Energy Units Converter 2014) for diazonium salts (DS) of Table 11.21, along the related bondonic radii of action, mass ratio respecting the electronic unit, and the bondonic gravitational ratio respecting the universal gravitational unit, according with Eqs. (11.37a, 11.37b, 11.37c), respectively

Compound	E <sub>a</sub> (kcal/mol)	X <sub>B</sub> (Å)	ζ <sub>m</sub> × 10 <sup>6</sup>	ζ <sub>G</sub> × 10 <sup>-53</sup>
DS1	30.7705545	117.682	206.175	84.3823
DS2	31.5697897	114.703	211.53	80.1638
DS3	30.1711281	120.02	202.159	87.7685
DS4	29.6716061	122.041	198.812	90.7485
DS5	29.1601816	124.181	195.385	93.9596
DS6	28.0731358	128.99	188.101	101.377
DS7	28.0731358	128.99	188.101	101.377
DS8	27.0720841	133.759	181.394	109.013
DS9	25.5820985	141.55	171.41	122.081
DS10	25.6739962	141.043	172.026	121.209
DS11	29.6999761	121.924	199.002	90.5753
DS12	30.4	119.116	203.692	86.4519

- The bondonic information shape is presenting the extreme points for all bondonic radii paralleling gravitational and anti-paralleling mass actions: the minimum/maximum point for para and high logK molecular realization in Table 11.21 (DS2), and the maximum/minimum points for meta/ortho and lower rate reaction logK for the diazonium salts of Table 11.21 (DS9 and DS10), respectively;
- The chemical reactivity may be indeed modeled by chemical bondonic information vs. rate reaction, since this going like a molecular potential itself—see the bondonic mass curve.

Back to the general-chemical structural analysis, the effect of electronegative substituents on the photochemical stability of the diazo compounds is inverted as compared to their effect upon thermal stability. The thermal stability of the 4-amino



**Fig. 11.13** The graphical plot for the bondonic features of Table 11.22 in respecting the rate of reaction (LogK) at 25 °C for molecules of Table 11.21

and N substituted 4-aminophenyldiazonium salts at room temperature is relatively high and the photochemical effects can be easily distinguished (Isac et al. 1981b). The sulphanilic acid, the sulphanilamide and 4-N, N'-dimethylaminoaniline were diazotized according to an analytical method (Ciuhandu and Mracec 1968).

The thermal and photochemical stability of the obtained diazonium salts was verified by a spectrometric method. The diazonium salts of sulphanilic acid and sulphanilamide are photochemically stable up to 353 K, but thermally instable; that is why the kinetics of their decomposition could be followed in the UV domain.

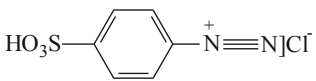
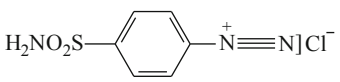
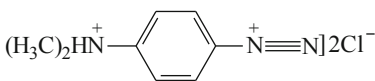
The diazonium salt of 4-N, N'-dimethylaminoaniline is thermally stable, but very sensitive photochemically, which allows the qualitative study of its photodecomposition in the UV and visible domain. There is a surprising effect of substituents upon kinetics of thermal and photochemical decomposition of aromatic diazonium salts (Table 11.21) (Isac et al. 1981b; Simon 1966a).

The substituents with – M and – I effect in meta or para positions decrease the reaction rates. Electron donor substituents in meta position increase the reaction rates, but the same substituents in para position strongly decrease the reaction rates. It is supposed that this stabilization is due to a resonance effect that increases the C–N bond order (Barraclough et al. 1972).

Table 11.23 shows a satisfactory correlation between the positions of experimental absorption maxima and the transition energies calculated by the HMO method (Isac et al. 1981a).

Although the first calculated transition energies for the diazonium salts are too low, the relative order of the calculated transitions corresponds to the experimental one. Based on experimental data and reactivity indices calculated by HMO method we proposed structure-reactivity correlations for some diazonium cations (Table 11.24) (Isac et al. 1981a, 1985).

**Table 11.23** Electronic transitions (nm) and molar extinction coefficients for the diazonium salts of sulphanilic acid, sulphanilamide and 4-N, N'-dimethylaminoaniline

Compound	Solvent	$\lambda_{\text{exp}}$ (nm)	$\lambda_{\text{calc}}$ (nm)	$\Delta\lambda^a$ (nm)	$\log \epsilon_M$
$\text{HO}_3\text{S}-\text{C}_6\text{H}_4-\text{N}^+\equiv\text{N}]\text{Cl}^-$ 	water	303 (sh)	633	320	3.27
		269	586	317	4.28
$\text{H}_2\text{NO}_2\text{S}-\text{C}_6\text{H}_4-\text{N}^+\equiv\text{N}]\text{Cl}^-$ 	water	313 (sh)	633	320	3.10
		269	586	317	4.27
$(\text{H}_3\text{C})_2\text{HN}^+-\text{C}_6\text{H}_4-\text{N}^+\equiv\text{N}]\text{Cl}^-$ 	water	377	672	295	
		248	(818) <sup>b</sup>	(301)	4.61
			539	291	
			(585) <sup>b</sup>	(197)	3.79

<sup>a</sup> $\Delta\lambda = \lambda_{\text{calc}} - \lambda_{\text{exp}}$  (nm);

<sup>b</sup>The values in parentheses are calculated for monocation

The results indicate a good correlation between the wave numbers ( $\nu'_{\text{exp}}$ ) and the calculated  $\epsilon$  transition.

- The bond orders values obtained from calculations are correlated with the compounds structure, considering the single, double and triple character of the bond between the considered atoms. The molecular diagrams of diazonium salts suggest a triple bond character for the N-N bond and explain the fact that the diazo group is the well-known electron withdrawing substituent. The diazo group is a strong perturber of the aromatic system and in this respect it may be compared with the nitro group (Evleth and Cox 1967).
- The  $\pi$  charge densities of the atoms from the diazonium groups are favored by the electron repulsive substituent ( $-\text{N}(\text{CH}_3)_2$ ), but disadvantaged by the electron attractive groups ( $-\text{SO}_3\text{H}$ ,  $-\text{SO}_2\text{NH}_2$ ,  $-\text{HN}^+(\text{CH}_3)_2$ ).
- The high photochemical reactivity of 4-N, N'-dimethylaminobenzenediazonium cation can be explained as follows: even though present in small fraction, the monocation will have the absorption maximum significantly shifted to red (visible domain of diffuse light) due to the extended conjugated system. Moreover, the monocation has the highest value  $\epsilon_{\text{LUMO}} = \alpha + 0.1111\beta$  among the diazonium salts. In this case, the pre dissociation mechanism (the transition from the potential curve of the excited state ( $\pi\pi^*$ ) to the triple repulsive curve ( $\pi\sigma^*$ )) would become preponderant (Simon and Bădilescu 1967).

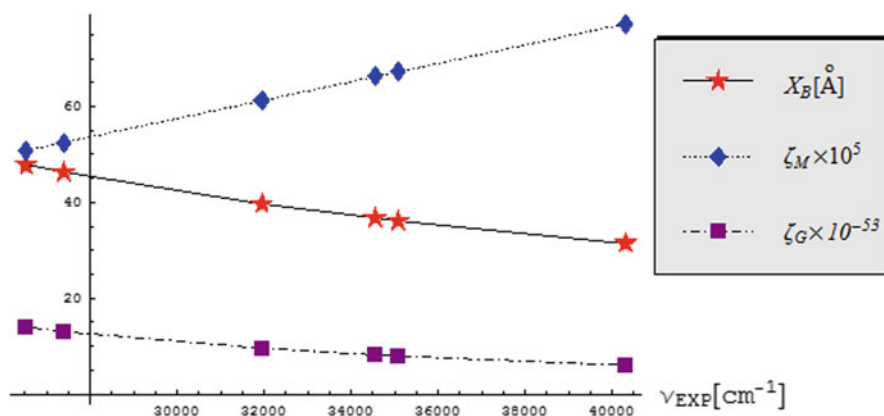






**Table 11.25** Transition energies in kcal/mol for the experimental wave-numbers (Energy Units Converter 2014) for the diazonium cations of Table 11.24 (taken as averages for DC1 and DC2 and lower value for lower LUMO and higher value for higher LUMO energies for DC3 and DC4), along the related bondonic radii of action, mass ratio respecting the electronic unit, and the bondonic gravitational ratio respecting the universal gravitational unit, according with Eqs. (11.37a, 11.37b, 11.37c), respectively

Compound	$\nu_{\text{exp}} (\text{cm}^{-1})$	$\Delta E_{\text{exp}} (\text{kcal/mol})$	$X_B (\text{\AA})$	$\zeta_M \times 10^5$	$\zeta_G \times 10^{-53}$
DC3	26,525	75.8388	47.7479	50.815	13.8912
DC5	27,397	78.332	46.2281	52.4856	13.021
DC6	31,949	91.3468	39.6417	61.206	9.57492
DC2	34,561	98.8149	36.6457	66.2099	8.18233
DC1	35,088.5	100.32308	36.0948	67.2205	7.93816
DC4	40,322	115.286	31.4101	77.2462	6.0113



**Fig. 11.14** The graphical plot for the bondonic features of diazonium cations of Table 11.24 respecting the related transition wave numbers of Table 11.25

Finally, the bondonic information for molecules of Table 11.24 is reported in Table 11.25 and graphically represented in Fig. 11.14 with the following characteristic:

- The bondonic quasi-linear monotonic shape of radii/gravitational and mass actions of associated bondons is again displayed since (i) the variation is respecting the experimental wave-number that is a frequency that is quantum mechanically related with an energy difference accounting for the quantum transition modeled—so again being driven by an energy difference in the same manner as was the case with bondonic vs. delocalization energy (where also an energy difference was assumed as independent variable), see Figs. 11.10 and 11.11; also the smooth

non-linear effect is present since dealing with cations of Table 11.24 as were the ionic information present by the same effect in Fig. 11.11 too.

- The difference with Fig. 11.11 comes from the non-convergence of the radii and gravitational curves, here remaining indeed parallel, while both being in inverse variation with respect with bondonic mass, nevertheless still consistent with the phenomenology they represent: e.g. for higher wave-number/frequency a higher energy difference is measured so a heavier bondonic mass is associated; instead, restrained bondonic radii is manifested (due to higher accumulated inertia in bonding) that corresponds with even lower gravitational values since resuming to the chemical localization it encompasses.

## 11.8 Conclusions

In this chapter we have applied both the Hückel and DFT theory, but mostly the first one in order to describe the physico-chemical properties of some aromatic hydrocarbons and their derivatives with the aim of describing by the structure (valence) properties their reactivity as substrates and reactants involved in addition and substitution reactions with homolytic and ionic mechanisms, including aromaticity effects (Nenitzescu 1968, Part V). These two approaches have provided good correlations among the energetic indices calculated with regard to the substitution reactions in which these compounds are involved and the acidity and basicity of their functional groups, although the Huckel method seems to provide, in spite of their inherent approximation, more insight regarding the frontier electronic behavior and about the delocalization electronic features. This feature was tested also by the vanguardist approach of bondonic chemistry, by which the chemical bond is described with the help of the associated quantum quasi-particle called as *bondon*, see also the previous chapter (Putz and Ori 2015). By combining the Schrödinger with Bohmian description of electronic motion the main feature of bondonic particle were derived, having in the first site its predicted mass in terms of radii of action and of the binding energy (in kcal/mol); most interestingly, since of bosonic nature, when assuming the bondon as behaving like the photon in communicating the bonding information between the electrons of bonding, interesting features are emerging so that the gravitational effects are involved and predicted such that to overcome the “classical” electrostatic inter-repulsion among electrons in bonding; this approach follows the Fermi-Planck description of the early universe (the so called Planck Universe), however here adapted at the level of quantum nanochemistry; in this context also the related bondonic action radii emerges as paralleling the gravitational effect: higher the bondonic action radii higher the gravitational influence need in order to keep bound such extended system; also the bondonic mass is reshaped, with gravitational effects, yet spherically correcting the Einstein basic mass-energy relationship, see Eq. (11.37b), due to the gravitational influence at the distance. However, apart of the new insight provided by bondon in the nature of the chemical bond, i.e. by considering its combined features of bosonating fermionic particle with the photonic

properties and variable gravity parameter in chemical bonding, the actual bondonic triplet (*radii, mass, and gravity*) =  $(X_{\mathbf{B}}, m_{\mathbf{B}}, G_{\mathbf{B}})$  actions were specialized for all “classical” carbon systems considered, in order to explore various shape of information they contain as depending of various energetic representations. Accordingly, one represented the actual bondonic triplet: (i) respecting orbital energies and found the parabolic shape behavior confirming the chemical reactivity ansatz so disputed in conceptual DFT chemistry; (ii) respecting aromaticity (at its turn driven by chemical hardness) and found the bondonic behavior with peaks (of Gaussian type in DFT approach and by double-well potential for Hückel approximation) however different than those provided by chemical hardness driving aromaticity, so opening new perspective of aromaticity aka inertia in chemical reactivity by bondonic insight; (iii) respecting delocalization energies and by energy differences in general when the bondonic information display monotonic variation in chemical bonding, including also non-linear effects for the case of ionicity (salts, cations) present in chemical bonds/compounds; (iv) respecting the chemical reactivity feature as the reaction rate ( $\log K$ ) when the bondonic information unfolds similar variation with the molecular interaction potential as a whole, so making it most reliable in capturing the very mechanism of chemical bonding at the nano-yet-entangled (long range with memory effects) level, all due to the present gravitational effects. At this point, one readily feels the need to finally re-discuss some consequences of having included gravitational arguments in chemical bonding by bondons, since being of striking interest for the present and future conceptual and predictive quantum chemistry. In this regard, say one likes to calculate the “classical” mechanical work  $L_G = Gm_0^2/r$  produced by two attractive electrons in a chemical bond separated at the long range nano-distance  $r = 100[\text{\AA}]$ : that gives about  $L_G \cong G \times 10^{-52}[\text{Joule}] \cong G \times 10^{-33}[\text{eV}]$ ; next, when further considering the custom kcal/mol conversion and the bondonic representation of the gravitation by the specific transformation (11.37c) one arrives to the actual work function in terms of bonding energy  $L_G \cong 10^{16}/E_{bond}^2[\text{kcal/mol}]$ , while not forgetting this expression has inside the electronic origin ( $m_0$ ) as the base of gravitational work; accordingly, when equating the last gravitational work with the bondonic Einstein energy ( $L_{\mathbf{B}} = m_{\mathbf{B}}c^2$ ) one gets the bondonic/electronic mass ratio  $m_{\mathbf{B}}/m_0 \sim [10E_{bond}^2(\text{kcal/mol})]^{-1}$  so that generally achieving, e.g. for  $E_{bond} \sim 100[\text{kcal/mol}]$  the correct fraction of  $\zeta_m = m_{\mathbf{B}}/m_0 \sim 10^{-5}$  as recorded in Table 11.9 for the specific aromatic compounds of Table 11.8 so confirming the correct and meaningful of the actual numerics as starting from the gravitational work between electrons in keeping/forming/stabilizing the chemical bonding by the bosonic bondon. Finally, worth addressing also the range of prediction for such bondonic information as based on gravitational effects in bonding: when going to thousands of [kcal/mol] in bonding energy, i.e. when dealing with larger molecules, say polymers or fragments of them thereof, one actually deals with bonding-gravitational work in the range of  $L_{G/\mathbf{B}} \sim 10^9[\text{kcal/mol}] \sim 10^7[\text{MeV}]$  that is specific to Gama (Y) rays spectroscopy, so experimentally achievable! Moreover, while having present that 1MeV accounts for double the rest energy of an electron  $1[\text{MeV}] = 1.602 \times 10^{-13}[\text{Joule}] \sim 2 \times (m_0c^2)$ , there is immediate that

the present prediction should correlate also with the number of bonds created or supported/involved in the observed bonding energy, thus giving the information also about the so called “active core” of the chemical compound—that that is activated by the bondonic action range associated with the bond energy detected. We are confident that all these issues will be on the frontline in the XXI structural physical-chemistry in general and in the description of the chemical bonding in special, while being further extended in analytical, conceptual, computational and experimental parts, within the bondonic chemistry.

**Acknowledgement** MVP thanks Romanian Ministry of Education and Research for supporting the present work through the CNCS-UEFISCDI project <Quantification of The Chemical Bond Within Orthogonal Spaces of Reactivity. Applications on Molecules of Bio-, Eco- and Pharmacological Interest>, Code PN-II-RU-TE-16/2010-2013.

## References

- Avram M (1994) Organic chemistry (In Romanian), vol. I. Zecasin Publishing House, Bucharest
- Avram M (1995) Organic chemistry (In Romanian), vol. II. Zecasin Publishing House, Bucharest
- Bader RFW (1990) Atoms in molecules—a quantum theory. Oxford University Press, Oxford
- Bader RFW (1994) Principle of stationary action and the definition of a proper open system. *Phys Rev B* 49:13348
- Bader RFW (1998a) A bond path—a universal indicator of bonded interactions. *J Phys Chem A* 102:7314–7323
- Bader RFW (1998b) Why are there atoms in chemistry? *Can J Chem* 76:973–988
- Bader RFW, Austen MA (1997) Properties of atoms in molecules: atoms under pressure. *J Chem Phys* 107:4271–4285
- Barracough R, Jones F, Patterson D, Tetlow A (1972) *J Soc Dyers Colour* 88:22
- Bâtcă A. (1981) Modern inorganic chemistry by answers and questions (in Romanian). Scientific and Encyclopedic Publishing House, Bucharest, p 115
- Becke AD (1986) *J Chem Phys* 84:4524
- Becke AD (1988) *Phys Rev A* 38:3098
- Bohm D, Vigier JP (1954) Model of the causal interpretation of quantum theory in terms of a fluid with irregular fluctuations. *Phys Rev* 96(1):208–216
- Boudreaux EA, Boulet E (1958) *J Am Chem Soc* 80:1588
- Bräse S, Dahmen S, Popescu C, Schroen M, Wartmann F-J (2004) The structural influence in the stability of polymer-bound diazonium salts. *Chem Eur J* 10(21):5285–5296
- Chattaraj PK, Sarkar U, Roy DR (2007) *J Chem Edu* 84:354
- Chiriac V, Chiriac VA, Dascălu D, Isac D (2003) Course of General Chemistry (in Romanian). Mirton Publishing House, Timișoara
- Ciuhandu G, Mracec M (1968) *Z Anal Chem* 238:104
- Crossley ML, Kienle RH, Benbrook CH (1940) *J Am Chem Soc* 62:1400
- de Broglie L, Vigier MJP (1953) La physique quantique restera-t-elle indéterministe? Gauthier-Villars, Paris
- De Tar DF, Kwong S (1956) *J Am Chem Soc* 78:3916–3921
- Energy Units Converter (2014) <http://www.colby.edu/chemistry/PCChem/Hartree.html>. Accessed July 2014
- Evleth EM, Cox RJ (1967) *J Phys Chem* 71:4082
- Hendrickson JB, Cram DJ, Hammond GS (1976) Organic chemistry (Romanian edition). Didactic and Pedagogic Publishing House, Bucharest

- Hückel E (1930) *Z Physik* 60:423
- Hückel E. (1931) *Z Physik* 70:204
- Hypercube, Inc (2002) HyperChem 7.01 [Program package]
- Isac D, Mracec M, Simon Z (1981a) Structure and reactivity in diazotization reaction. *Rev Roum Chim* 26(3):341–348
- Isac D, Mracec M, Proșteanu N, Simon Z (1981b) The kinetics of thermal and photochemical decomposition of aromatic diazonium salts. *Rev Roum Chim* 26(1):29–35
- Isac D, Mracec M, Simon Z (1985) Thermal and photochemical stability of diazoderivatives. *Rev Roum Chim* 30(6):473–481
- Katritzky AR, Topson RD (1971) *J Chem Edu* 48:427
- Kaupp G, Herrmann A, Schmeyers J (2002) *Chem Eur J* 8(6):1395–1406
- Kohn W, Sham LJ (1965) *Phys Rev* 140:1133
- Kohn W, Becke AD, Parr RG (1996) *J Phys Chem* 100:12974
- Koopmans T (1934) *Physica* 1:104
- Kruszewski J, Krygowski TM (1972) *Tetrahedron Lett* 13:3839
- Krygowski TM (1993) *J Chem Inf Comput Sci* 33:70
- Lee C, Yang W, Parr RG (1988) *Phys Rev B* 37:785
- Mandado M, Moa MJG, Mosquera RA (2007) Exploring basic chemical concepts with the quantum theory of atoms in molecules: aromaticity. In: Hoffman EO (ed) *Progress in quantum chemistry research*. Nova Science Publishers Inc., New York (Chapter 1)
- Martin J-L, Migus A, Mourou GA, Zewail AH (eds) (1993) *Ultrafast phenomena VIII*. Springer, Berlin
- Mracec M, Mracec M (2003) Elements of quantum chemistry. In: Chiriac A, Mracec M, Oprea TI, Kuruncki L, Simon Z (eds) *Quantum biochemistry and specific interaction*. Mirton Publishing House, Timișoara (Chapter 2)
- Negreanu-Pirjol B, Negreanu-Pirjol T, Zagan S, Paraschiv GM, Zagan R, Sirbu R (2012) Study regarding dynamic of groundwater quality after some unusual meteorological phenomena, *J Chem (Revista de Chimie (Bucharest))* 63(1):110–115
- Nezitescu CD (1966) *Organic chemistry (in Romanian)*, vol. I, 6th edn. Didactic and Pedagogic Publishing House, Bucharest
- Nezitescu CD (1968) *Organic chemistry (in Romanian)*, vol. II. Didactic and Pedagogic Publishing House, Bucharest
- Panchartek J, Sterba V (1969) *Collect Czech Chem Commun* 34:2971
- Parr RG, Yang W (1989) *Density functional theory of atoms and molecules*. Oxford University Press, Oxford
- Putz MV (2003) Contributions within density functional theory with applications to chemical reactivity theory and electronegativity. *Disertation.Com, Parkland*
- Putz MV (2006) *Int J Quantum Chem* 106:361
- Putz MV (2007) *J Theor Comp Chem* 6:33
- Putz MV (2008a) *Int J Mol Sci* 9:1050
- Putz MV (2008b) *Absolute and chemical electronegativity and hardness*. Nova Publishers Inc., New York
- Putz MV (2008c) *MATCH Commun Math Comput Chem* 60:845
- Putz MV (2010a) Beyond quantum nonlocality: chemical bonding field. *Int J Environ Sci* 1:25–31
- Putz MV (2010b) The bondons: the quantum particles of the chemical bond. *Int J Mol Sci* 11(11):4227–4256
- Putz MV (2011) Quantum Parabolic Effects of Electronegativity and Chemical Hardness on Carbon  $\pi$ -Systems. In: Putz MV (ed) *Carbon bonding and structures: advances in physics and chemistry*. Springer, Dordrecht, pp 1–32 (Chapter 1)
- Putz MV (2012) *Quantum theory: density, condensation, and bonding*. Apple Academics & CRC Press, Toronto
- Putz MV (2013) Koopmans' analysis of chemical hardness with spectral like resolution. *Sci World J*. Article ID 348415, 14 p. doi:10.1155/2013/348415

- Putz MV (2014) Nanouniverse expanding macrouniverse: from elementary particles to dark matter and energy. In: Putz MV (ed) *Quantum nanosystems: structure, properties and interactions*. Apple Academic Press & CRC Press, Toronto, pp 1–57 (Chapter 1)
- Putz MV, Ori O (2012) Bondonic characterization of extended nanosystems: application to graphene's nanoribbons. *Chem Phys Lett* 548:95–100
- Putz MV, Ori O (2015) Bondonic chemistry: physical origins and entanglement prospects. In: Putz MV, Ori O (eds) *Exotic properties of carbon nanomatter*. *Advances in physics and chemistry*. Springer, Dordrecht (Chapter 10)
- Putz MV, Putz AM, Pitulice L, Chiriac V (2010) On chemical hardness assessment of aromaticity for some organic compounds. *Int J Chem Model* 2(4):343–354
- Putz MV, De Corato M, Benedek G, Sedlar J, Graovac A, Ori O (2013) Topological invariants of moebius-like graphenic nanostructures. In: Ashrafi AR, Cataldo F, Iranmanesh A, Ori O (eds) *Topological modeling of nanostructures and extended systems*. Springer, Dordrecht pp 229–244 (Chapter 7)
- Putz MV, Duda-Seiman C, Duda-Seiman M, Bolcu C (2015a) Bondonic chemistry: consecrating silanes as metallic precursors for silicenes materials. In: Putz MV, Ori O (eds) *Exotic properties of carbon nanomatter*. *Advances in physics and chemistry*. Springer, Dordrecht, Chapter 12
- Putz MV, Dudaş NA, Putz AM C (2015b) Bondonic chemistry: Predicting ionic liquids' (IL) bondons by Raman-IR Spectra. In: Putz MV, Ori O (eds) *Exotic properties of carbon nanomatter*. *Advances in physics and chemistry*. Springer, Dordrecht, Chapter 13
- Rzepa HS (2007) *J Chem Edu* 84:1535
- Saltzman MD (1974) *J Chem Edu* 51:498
- Schrodinger E (1926) An undulatory theory of the mechanics of atoms and molecules. *Phys Rev* 28(6):1049–1070
- Simon Z (1964) *Stud Res Chem* (in Romanian: Studii și cercetări de Chimie) 13(10):697–724
- Simon Z (1966a) *Stud Res Chem* (in Romanian: Studii și cercetări de Chimie) 14(3):173
- Simon Z. (1966b) *Stud Res Chem* (in Romanian: Studii și cercetări de Chimie) 14(6):437
- Simon Z (1973) *Quantum biochemistry and specific interactions* (in Romanian). Scientific Publishing House, Cluj
- Simon Z, Bădilescu I (1967) *Rev Roum Chimie* 12(3):243–261
- Streitwieser A (1961) *Molecular orbital theory for organic chemists*. Wiley, New York
- Tarko L (2008) *ARKIVOC* xi:24
- Truhlar DG (2007) *J Chem Edu* 84:781
- Vlascici D, Pică EM, Făgădar-Cosma E, Bizerea O, Cosma V (2007) *J Chem* (Revista de Chimie (Bucharest)) 58(2):186–190
- Woodward RB, Hoffmann R (1970) *The conservation of orbital symmetry*. Chemie Verlag, Weinheim

# Chapter 12

## Bondonic Chemistry: Consecrating Silanes as Metallic Precursors for Silicenes Materials

Mihai V. Putz, Corina Duda-Seiman, Daniel M. Duda-Seiman and Constantin Bolcu

**Abstract** Evidence-based medicine needs targeted therapy approaches challenging all pathophysiological chains. Modern drug delivery systems have been imagined starting from concepts of macrochemistry and nanoparticles. In this paper, while succinctly reviewing physico-chemical features of new silicenes materials with applicability in bio-medicine with their most important role in medicine, the recent vanguardistic bondonic chemistry is employed with the striking result all the actual silanes presursors behave as a metallic conductors for the bondons, so highly supporting the switch from the graphene to silicene nanotechnology since basically displaying the upper extreme limits of pairing electronic information by bosonic bondon.

### 12.1 Introduction

Along human history, progress and technological development with implications in almost every aspect of life were possible through a tremendous effort of human mind. A fragment of progress was to imagine a solution in order to make possible

---

M. V. Putz (✉) · C. Duda-Seiman

Laboratory of Computational and Structural Physical-Chemistry for Nanosciences and QSAR,  
Department of Biology-Chemistry, Faculty of Chemistry, Biology, Geography,  
West University of Timișoara, Pestalozzi Str. No. 16, 300115 Timișoara, Romania  
Tel.: +40-256-592638  
e-mail: mv\_putz@yahoo.com; mvputz@cbg.uvt.ro

C. Duda-Seiman · C. Bolcu

Laboratory of Organic Chemistry, Department of Biology-Chemistry,  
Faculty of Chemistry, Biology, Geography, West University of Timișoara,  
Pestalozzi Str. No. 16, 300115 Timișoara, Romania  
Tel.: + 40-256-592638  
e-mail: cori\_mam@yahoo.com

D. M. Duda-Seiman

Department of Medical Ambulatory, Medical Emergencies, University of Medicine  
and Pharmacy “Victor Babes”, B-dul C.D. Loga nr. 49, 300020 Timișoara, Romania  
e-mail: duda.seiman@cardiologie.ro; dannymduda@yahoo.com

C. Bolcu

e-mail: bolcu@cbg.uvt.ro; constantinbolcu@yahoo.com

© Springer Science+Business Media Dordrecht 2015

M. V. Putz, O. Ori (eds.), *Exotic Properties of Carbon Nanomatter*,

Carbon Materials: Chemistry and Physics, DOI 10.1007/978-94-017-9567-8\_12



to hold together two or more materials of different types. Organofunctional silanes were found to contribute to adhesion between interfaces of various kinds (e.g., organic and inorganic substrates), with respect to their chemical and physical properties (Plueddemann 1982). Alkoxysilanes (e.g., tetramethoxysilane, tetraethoxysilane) are silicon precursors used in obtaining of materials with several applications (Belton et al. 2012). It has been shown that alkali metals determine reduction of methoxy or phenoxy silicon compounds (with obtaining of methyl or phenyl silicon compounds), being an important way to obtain carbon-silicon bonds (reduction reactions) (Ryan 1962).

Since the middle of the past century, organofunctional silanes were widely used as adhesion promoters or crosslinkers because of their capacity to form chemical bonds to different substrates (both organic and inorganic) (Altmann and Pfeiffer 2003). Alkoxysilanes are a family of monomers with the capacity to form where silica, or chains of alkylpolysiloxanes by hydrolization with water (Öztürk 1992). Silanes, by means of chemical structure, have a silicon skeleton, and, in order to be classified as alkoxysilanes, this skeleton has to be bounded directly to alkyl and/or alkoxy groups via a silicon-carbon link or an ester link (Öztürk 1992).

On the other side, although not among the first ten great mysteries of the Universe (Putz 2010a, b), the chemical bond nature seems to subsist in many of them, especially in relation with the existence in a quantum world. As such, as far as the quantum mechanics opens the way for an entangled non-local picture of interaction between, in principle, all things in Universe the Chemistry—through its bonding level of manifestation—makes things discernable, observable and at the end measurable. In supporting this view, the de Broglie-Bohm wavefunction was transformed, actually rotated in the complex space of phases with a quantity that was later shown to account for the chemical bonding field  $\chi$  by means of consequences raised by Schrödinger invariance condition under such U(1) transformation. There is remarkable that despite U(1) gauge transformation is well noted in the Yang-Mills transformation of fields that helps in explaining the symmetry broken by creation of elementary particle, this is the first study that addresses nonlocal gauge transformation on de Broglie-Bohm-Schrödinger wave fields, however leading with impressive result of identifying the chemical bonding field with observable quantity as electronic density and its gradients (Putz 2012a, b). Moreover, the existence of chemical  $\chi$  fields implies that the entangled interaction in bonding is carried by associate elementary particles called as bondons; they have lower mass than electrons for typical chemical bonding length having the electronic mass as the superior limit when the first Bohr radius is set as the bonding length (Putz et al. 2015a, b/Chapters 11 and 13 of this book). This way, the present work opens the possibility of unifying the chemical interactions through chemical bonding fields and associate bondons (Putz 2010a, b; Putz and Ori 2012, 2014, 2015 /Chapter 10 of this book).

The present chapter unfolds, for the first time the bondonic study on silanes, as precursors of highly regarded nowadays silicenes materials (Putz and Ori 2014; De Padova et al. 2014) through the following chapter organization: in Sect. 12.2 extends the bondonic chemistry exposed in previous chapters of the present volume (Putz and Ori 2015 /Chapter 10 of this book; Putz et al. 2015a, b Chapters 11 and 13 of

this book) towards achieving the observable characteristic of mass, charge, velocity and life-time in relation with the standard electronic information (Putz 2010b; Putz 2012a, b); Sect. 12.3 reviews the main features of the silanes in the sol-gel processes context and with bio-medical applications, while in Sect. 12.4 one performs the bondonic quantum features for a representative series of silanes and draw essential conclusion on their reliability as precursors fro silicenes for future smart materials by quantum nanotechnology.

## 12.2 Bondonic Hierarchy of Chemical Bonding (Putz 2010b)

The chemical bond, perhaps the greatest challenge in theoretical chemistry, has generated many inspiring theses over the years, although none definitive. Few of the most preeminent regard the orbitalic based explanation of electronic pairing, in valence shells of atoms and molecules, rooted in the hybridization concept (Pauling 1931) then extended to the valence-shell electron-pair repulsion (VSEPR) (Gillespie 1970). Alternatively, when electronic density is considered, the atoms-in-molecule paradigms were formulated through the geometrical partition of forces by Berlin (1951), or in terms of core, bonding, and lone-pair lodges by Daudel (1980), or by the zero local flux in the gradient field of the density  $\nabla\rho$  by Bader (1990), until the most recent employment of the chemical action functional in bonding (Putz 2009a, b).

Yet, all these approaches do not depart significantly from the undulatory nature of electronic motion in bonding, either by direct wave-function consideration or through its probability information in electronic density manifestation (for that is still considered as a condensed—observable version—of the undulatory manifestation of electron).

In other words, while passing from the Lewis point-like ansatz to the undulatory modeling of electrons in bonding, the reverse passage was still missing in an analytical formulation. Only recently the first attempt was formulated, based on the broken-symmetry approach of the Schrödinger Lagrangean with the electronegativity-chemical hardness parabolic energy dependency, showing that a systematical quest for the creation of particles from the chemical bonding fields is possible (Putz 2008).

Following this line, the present work makes a step forward and considers the gauge transformation of the electronic wave-function and spinor over the de Broglie-Bohm augmented non-relativistic and relativistic quantum pictures of the Schrödinger and Dirac electronic (chemical) fields, respectively. As a consequence, the reality of the chemical field in bonding was proved in either framework, while providing the corresponding bondonic particle with the associate mass and velocity in a full quantization form, see below. In fact, the Dirac bondon (Putz 2010b; Putz and Ori 2015 /Chapter 10 of this book) was found to be a natural generalization of the Schrödinger one (Putz 2010a, b; Putz et al. 2015a, b Chapters 11 and 13 of this book), while supplementing it with its anti-bondon particle for the positron existence in the Dirac Sea.

The bondon is the quantum particle corresponding to the superimposed electronic pairing effects or distribution in chemical bond; accordingly, through the values of its mass and velocity it may be possible to indicate the type of bonding (in particular) and the characterization of electronic behavior in bonding (in general).

However, one of the most important consequences of bondonic existence is that the chemical bonding may be described in a more complex manner than relying only on the electrons, but eventually employing the fermionic (electronic)-bosonic (bondonic) mixture: the first preeminent application is currently on progress, that is, exploring the effect that the Bose-Einstein condensation has on chemical bonding modeling (Putz 2011a, b; 2012a, b, c, d). Yet, such possibility arises due to the fact that whether the Pauli principle is an independent axiom of quantum mechanics or whether it depends on other quantum description of matter is still under question (Kaplan 2002), as is the actual case of involving hidden variables and the entanglement or non-localization phenomenology that may be eventually mapped onto the delocalization and fractional charge provided by quantum chemistry over and on atomic centers of a molecular complex/chemical bond, respectively.

On the other side, the mass, velocity, charge, and life-time properties of the bondons may be employed for analyzing some typical chemical bonds, with the respective working formulae as following.

The bondonic mass, having the quantization form

$$m_B = \frac{\hbar^2 (2\pi n + 1)^2}{2 E_{bond} X_{bond}^2}, n = 0, 1, 2, \dots \quad (12.1)$$

is more practical than the traditional characterization of bonding types in terms of length and energy of bonding; it may further assume the numerical ground state ratio form

$$S_m = \frac{m_B}{m_0} = \frac{87.8603}{(E_{bond}[kcal/mol]) \left(X_{bond}^0 [A]\right)^2} \quad (12.2)$$

when the available bonding energy and length are considered (as is the custom for chemical information) in kcal/mol and Angstrom, respectively. Note that having the bondon's mass in terms of bond energy implies the inclusion of the electronic pairing effect in the bondonic existence, without the constraint that the bonding pair may accumulate in the internuclear region (Berlin 1951).

Moreover, since the bondonic mass general formulation (12.1) resulted within the relativistic treatment of electron, it is considering also the companion velocity of the bondonic mass that is reached in propagating the bonding information between the bonding attractors. As such, when the Einstein type relationship (Einstein 1905a)

$$\frac{mv^2}{2} = h\nu \quad (12.3)$$

is employed for the relativistic bondonic velocity-mass relationship (Einstein 1905b, c)

$$m = \frac{m_B}{\sqrt{1 - \frac{v_B^2}{c^2}}} \quad (12.4)$$

and for the frequency of the associate bond wave

$$\nu = \frac{v_B}{X_{bond}} \quad (12.5)$$

it provides the quantified searched bondon to light velocity ratio

$$\frac{v_B}{c} = \frac{1}{\sqrt{1 + \frac{1}{64\pi^2} \frac{\hbar^2 c^2 (2\pi n + 1)^4}{E_{bond}^2 X_{bond}^2}}}, n = 0, 1, 2 \dots \quad (12.6)$$

or numerically in the bonding ground state as

$$\zeta_v = \frac{v_B}{c} = \frac{100}{\sqrt{1 + \frac{3.27817 \times 10^6}{(E_{bond}[\text{kcal/mol}])^2 (X_{bond}[\text{\AA}])^2}}} [\%] \quad (12.7)$$

Next, dealing with a new matter particle, one will be interested also on its charge, respecting the benchmarking charge of an electron. To this end, one re-employs the chemical bonding field closure by hyperfine structure of bondonic algorithm (Putz 2010b; Putz and Ori 2015 /Chapter 10 of this book), in the form emphasizing the bondonic charge appearance, namely

$$\aleph_B(e_B) = \aleph_0 \quad (12.8)$$

Next, when considering for the left-hand side of (12.8), the form provided by Equation (Putz 2010b)

$$\aleph_B = \frac{mc}{e} v X_{bond} \quad (12.9)$$

and for the right-hand side of (12.8), the fundamental hyperfine value

$$\aleph_0 = \frac{\hbar c}{e} \sim 137.03599976 \left[ \frac{\text{Joule} \times \text{meter}}{\text{Coulomb}} \right] \quad (12.10)$$

one gets the working Equation

$$c \frac{m_B v_B}{e_B} X_{bond} = 137.036 \left[ \frac{\text{Joule} \times \text{meter}}{\text{Coulomb}} \right] \quad (12.11)$$

from where the bondonic charge appears immediately, once the associate expressions for mass and velocity are considered from Eqs. (12.1) and (12.6), respectively, yielding the quantified form

$$e_B = \frac{4\pi\hbar c}{137.036} \frac{1}{\sqrt{1 + \frac{64\pi^2 E_{bond}^2 X_{bond}^2}{\hbar^2 c^2 (2\pi n + 1)^4}}}, n = 0, 1, 2 \dots \quad (12.12)$$

However, even for the ground state, and more so for the excited states, one may see that when forming the practical ratio respecting the unitary electric charge from (12.12), it actually approaches a referential value, namely

$$\zeta_e = \frac{e_B}{e} = \frac{4\pi}{\sqrt{1 + \frac{(E_{bond}[kcal/mol])^2 (X_{bond}[A])^2}{3.27817 \times 10^6 (2\pi n + 1)^4}}} \cong 4\pi \quad (12.13)$$

for, in principle, any common energy and length of chemical bonding. On the other side, for the bondons to have different masses and velocities (kinetic energy) as associated with specific bonding energy but an invariant (universal) charge seems a bit paradoxical. Moreover, it appears that with Eq. (12.13) the predicted charge of a bonding, even in small molecules such as H<sub>2</sub>, considerably surpasses the available charge in the system, although this may be eventually explained by the continuous matter-antimatter balance in the Dirac Sea to which the present approach belongs. However, to circumvent such problems, one may further use the result (12.13) and map it into the Poisson type charge field Equation

$$e_B \cong 4\pi \times e \leftrightarrow \nabla^2 V \cong 4\pi \times \rho \quad (12.14)$$

from where the bondonic charge may be reshaped by appropriate dimensional scaling in terms of the bounding parameters ( $E_{bond}$  and  $X_{bond}$ ) successively as

$$e_B \sim \frac{1}{4\pi} [\nabla_X^2 V]_{X=X_{bond}} \rightarrow \frac{1}{4} \frac{E_{bond} X_{bond}}{\aleph_0} \quad (12.15)$$

Now, Eq. (12.15) may be employed towards the working ratio between the bondonic and electronic charges in the ground state of bonding

$$\zeta_e = \frac{e_B}{e} \sim \frac{1}{32\pi} \frac{(E_{bond}[kcal/mol]) (X_{bond}[A])}{\sqrt{3.27817 \times 10^3}} \quad (12.16)$$

With Eq. (12.16) the situation is reversed compared with the previous paradoxical situation, in the sense that now, for most chemical bonds (Putz 2010b; Putz and Ori 2015 /Chapter 10 of this book), the resulted bondonic charge is small enough to be not yet observed or considered as belonging to the bonding wave spreading among the binding electrons.

Instead, aiming to explore the specific information of bonding reflected by the bondonic mass and velocity, the associated ratios of Eqs. (12.2) and (12.7) for some typical chemical bonds (Oelke 1969; Findlay 1955) are computed (Putz 2010b; Putz and Ori 2015 /Chapter 10 of this book). They may be eventually accompanied by the predicted life-time of corresponding bondons, obtained from the bondonic mass and velocity working expressions (12.2) and (12.7), respectively, throughout the basic time-energy Heisenberg relationship—here restrained at the level of kinetic energy

**Table 12.1** Phenomenological classification of the chemical bonding types by bondonic (mass, velocity, charge and life-time) properties abstracted from Table 12.1; the used symbols are: > and >> for ‘high’ and ‘very high’ values; < and << for ‘low’ and ‘very low’ values; ~ and ~> for ‘moderate’ and ‘moderate high and almost equal’ values in their class of bonding (Putz 2010b)

Property	$\zeta_m$	$\zeta_v$	$\zeta_e$	$t_B$
Chemical bond				
Covalence	>>	<<	<<	>>
Multiple bonds	<	>	>	<
Metallic	<<	>	>	<
Ionic	~>	~	~	~>

only for the bondonic particle; this way one yields the successive analytical forms

$$\begin{aligned}
 t_B &= \frac{\hbar}{T_B} = \frac{2\hbar}{m_B v_B^2} = \frac{2\hbar}{(m_0 \zeta_m)(c \zeta_v \cdot 10^{-2})^2} \\
 &= \frac{\hbar}{m_0 c^2} \frac{2 \cdot 10^4}{\zeta_m \zeta_v^2} = \frac{0.0257618}{\zeta_m \zeta_v^2} \times 10^{-15} [s]_{SI}
 \end{aligned}
 \tag{12.17}$$

and the specific values for various bonding types that are to be computed for a given chemical bonding in a molecular structure. Note that defining the bondonic life-time by Eq. (12.17) is the most adequate, since it involves the basic bondonic (particle!) information, mass and velocity; instead, when directly evaluating the bondonic life-time by only the bonding energy one deals with the working formula

$$t_{bond} = \frac{\hbar}{E_{bond}} = \frac{1.51787}{E_{bond}[kcal/mol]} \times 10^{-14} [s]_{SI}
 \tag{12.18}$$

that usually produces at least one order lower values than those computed upon employing the more complex Eq. (12.17). This is nevertheless reasonable, because in the last case no particle information was considered, so that the Eq. (12.18) gives the time of the associate *wave* representation of bonding; this departs by the case when the time is computed by Eq. (12.17) where the information of bonding is contained within the *particle* (bondonic) mass and velocity, thus predicting longer life-times, and consequently a more susceptible timescale in allowing the bondonic observation. Therefore, as far as the chemical bonding is modeled by associate bondonic particle, the specific time of Eq. (12.17) rather than that of Eq. (12.18) should be considered.

Overall, the present study likes to challenge the chemical bonding classification upon bondons in terms of the above observable quantities, for a given series of silanes (see Sect. 12.4); they will be nevertheless judged against the fuzzy classification of chemical bonding types in terms of the bondonic-to-electronic mass and charge ratios  $\zeta_m$  and  $\zeta_e$ , and of the bondonic-to-light velocity percent ratio  $\zeta_v$ , along the bondonic observable life-time,  $t_B$  respectively—as summarized in Table 12.1.

These rules are expected to be further refined through considering the new paradigms of special relativity in computing the bondons’ velocities, especially

within the modern algebraic chemistry (Whitney 2007). Yet, since the bondonic masses of chemical bonding ground states seem untouched by the Dirac relativistic considerations over the Schrödinger picture, it is expected that their analytical values may make a difference among the various types of compounds, while their experimental detection is hoped to be some day completed (Putz 2010a, b; 2012a, b, c, d; Putz and Ori 2012, 2014, 2015 /Chapter 10 of this book), see also the next Chapter of this book (Putz et al. 2015b).

## 12.3 From Sols, Gels, and Sol-Gel Processes to Silanes and Bio-Medicine

*Sols* are generally referred to stable suspensions comprising colloidal solid particles, denser than the surrounding liquid (Pierre 1998), their diameter being ranged between 2 nm and 0.2  $\mu\text{m}$ , corresponding to  $10^3$ – $10^9$  atoms/particle. (Livage and Lemerle 1982).

*Gels* are three-dimensional interconnected solid networks with the ability to have a space-limited expansion in a liquid environment (Pierre 1998). When drying methods at low temperatures (25–100 °C) are applied to gels, it is possible to obtain porous solid matrices (*xerogels*) (Brinker and Scherer 1990).

*Sol-Gel processes* have the capacity to obtain inorganic oxides, starting from colloidal dispersions, or from metal alkoxydes (Segal 1984). Nowadays, nitrides and sulfides are included in these processes, being used in the synthesis of hybrid organic-inorganic materials (Pierre 1998). Perhaps one of the most important issue concerning sol-gel processes is that it is possible to obtain solid (e.g., ceramic) materials at low temperatures (room temperature). In this way, soft materials (dopants) can be incorporated in solid materials (such as glasses) (Brinker and Scherer 1990). The hydrolysis-condensation reactions of metal alkoxide precursors determine the integration of organic or biological active molecules within an inorganic network obtaining new hybrid organic-inorganic materials (Sanchez et al. 2000).

Sol-gel processes are able to cover a demanding aspect of contemporary technological requirements: development and practical applicability of new and performing organic/inorganic hybrid materials. Furthermore, composite and nanocomposite materials can be obtained by combining the sol-gel method with organic polymers synthesis. These new "clever" materials may improve physical and chemical properties of classical used materials (e.g., coatings that increase the resistance to scratching) (Pandey and Mishra 2011).

Silica shows several advantages, like strength, thermal stability and high modulus. By incorporating silica and organic polymers (polymers show less thermal stability), a new material with improved properties can be obtained (mechanical properties). This may be an important condition for achieving biocompatibility with direct implications in development of biomedical compounds or devices (Jeon et al. 2009).

The combination of organic and inorganic parts into a hybrid material provides the possibility to model especially physical properties of this new hybrid material

(mechanical, electrical, optical properties), enlarging its area of utilities. Coating of different materials is one of the broadest application ranges, preventing substrates from mechanical abrasion, corrosion, or permeation. Considering the integration of new and “sophisticated” dopants (nanoparticles, polymers, nanocomposites), materials can develop also optical functions, with applicability in electronics, media, etc. (Schottner 2001). Organic nanocrystals embedded in sol-gel thin films show interesting optical features, like luminescence, photochromism and non-linear optical properties (Monnier et al. 2008).

In his very recent paper, Minami (2013) emphasized the benefit of sol-gel techniques applicable as coating materials in various situations: coatings on metals (for protective purposes), antireflective coatings on lenses and glasses, coatings on glasses for easier recycling purposes, etc. Coating hardness can be increased even with a low number of crosslinks of trimethoxysilane groups to siloxane (He et al. 2012).

Ionic liquids can be widely used as electrolyte membranes after their integration and immobilization within organic or inorganic matrices. This is because ionic liquids have high ionic conductivity, wide electrochemical potential window. Also, they can function as solvents both for organic and inorganic substrates, being categorized as *green solvents* due to the very low rate of vaporization, chemical stability and high possibilities to be recycled. Ionogels may be used as fuel and solar cells, as well as electrolyte membranes within lithium batteries (Vioux et al. 2010).

Membranes on silicophosphate basis are considered nanocomposites with an increased number of mesopores, which contain P–OH groups ensuring protonic conductivity with a maximum in those nanocomposites resistant to dehydration at high temperatures (over 200 °C) (Tsvetkova et al. 2008). Silica membranes with tetraethyl orthosilicate as precursor have type IV isotherms and H1 hysteresis loop, corresponding to cylindrical mesopores (Kuznetsova and Eremenko 2013).

Biosensors and bioreactors can be developed when proteins, poly-saccharides, phospholipids can be encapsulated in mineral hosts. This may be the precursor of artificial organ growth, achieved by encapsulation of whole cells, assuring their survival and controlling their multiplication rate (Avnir et al. 2006). Modified sol-gel derived silica coatings may be good environments for cell proliferation, and, in support of this idea, methyl-modified coating proved to be an excellent substrate for cell proliferation (Beganskiene et al. 2007).

Aqueous silicates are biocompatible, have neutral or very low influence on the environment and are very suitable for development of materials with direct applicabilities in bio-medicine (Coradin and Livage 2007).

Silica glasses seen as photonic materials find applicability beyond classical optical systems also in biology and medicine. To accomplish this, monodispersity in size of the building blocks is necessary, spherical particles being proper for this aim (Chiappini et al. 2011).

On the other side, modern medicine employs a tremendous effort to implement diagnosis techniques that confer accuracy in order to lead to the best choices of treatment for a given pathological condition. Medicines have a long course from identifying (inclusively through drug design techniques) potentially bioactive molecules, to synthesis, all testing stages, and, finally, approval for treatment. Efficiency of



treatment is a matter of formulation and of delivery, taking into account all factors that may interact with the bioactive molecule.

Drug delivery systems refer to a formulation or a device that ensures the administration of a bio-active compound (medicine), and ensures as well an enhancement of the therapeutic effect with respect to the safety of administration. A competitive drug delivery system covers all essential aspects of pharmacokinetics and pharmacodynamics: rate, time and place of release of the bio-active compound according to host factors (pH, etc.) and formulation factors (Asadujjaman and Mishuk 2013).

It is very well known that interactions between cells and external substrates happen at microscale levels. To serve this scope, an ideal drug delivery system has to facilitate this type of interactions. Thereby, inter- and trans-disciplinary research focused on development of micro- and nano-devices with applicability in drug and gene delivery systems, as well as in biosensors and tissue engineering. Most used materials for these purposes are polymers because of their adjustment ability to cells and molecules (Caldorera-Moore and Peppas 2009). Already classic examples are silicon or polymeric micro-membranes designed to obtain implantable biocapsules which produce the immunoisolation of pancreatic islet cells with intention to control pancreatic hormonal secretion intervening in diabetes management (Tao and Desai 2003). Establishing a good glycemic equilibrium means to assure a good state of health, and a good quality of life. Biosensors are already used to assess different biological parameters (traditional ones are tetraethoxysilane derived sol-gel composite). A new glucose biosensor based on covalent immobilization of enzyme in sol-gel composite showed an improved electrochemical and biosensing stability (Fu et al. 2011).

Self-aggregates of amphiphilic prodrugs define the so-called self-assembled drug delivery systems. Antiviral nucleoside analogues were processed in order to obtain amphiphilic prodrugs, then liposome-like self-aggregates in water were obtained. These systems have affinity for immunocompetent cells (e.g., macrophages), thus being highly effective in viral infections, inclusively HIV infections (Jin et al. 2008).

Ajami and Aguey-Zinsou (2012) imagined a new system for active bio-molecules delivery, by modifying the surface of titanium with self-assembled mono-layers. The technological process implied the electropolishing of the titanium surface in order to obtain the above mentioned mono-layers containing OctadecylTrichloroSilane at low temperature (10 °C). This surface showed an increased capacity to immobilize and release antibiotics over a consistent period of time (up to 26 days). This technology shows high potentiality to release active therapeutic agents from implant surfaces. Amoxicillin (hydrophilic antibiotic) was studied by means of drug delivery and efficiency using a new carrier, namely SBA-15 particles (Sevimli and Yilmaz 2012): loading efficiency with amoxicillin was monitored using the UV spectrophotometry. Release profiles are sustained and not so prolonged, but amoxicillin release can be controlled.

Naproxen (important and significant non-steroidal anti-inflammatory drug) was loaded both in the amine-modified and unmodified mesoporous silica SBA-15 (Halamová et al. 2010). The release of naproxen was made in a faster manner from the unmodified carrier, but, in time, the amount of released naproxen was larger from

the amine-modified carrier because this system has the ability to be loaded with a larger amount of the drug.

A modern technique called *molecular imprinting technique (MIT)* makes possible to create binding-sites with memory of the template molecule regarding shape, size and functional groups. In a recent work (Zhou et al. 2013), imprinted polymers (semi-covalent imprinting sol-gel materials) were developed for selective uptake of target molecules, demonstrating that this technology has excellent selective adsorption capacity for the target molecule (in the discussed study, ibuprofen was taken as target molecule).

Cancer therapy remains the most important challenge for scientists. Mesoporous silica nanoparticles are part of a new technology, in which, combining both supramolecular chemistry and mechanostereochemistry, they determined the appearance of a new category of materials, namely mechanized mesoporous silica nanoparticles. They are better known as “nanoscale bombs” that can enter within the cancerous tissues and more specifically, within each cancerous cell, having the capacity to destroy these cells by releasing a cytotoxin (Coti et al. 2009).

Silica nanoparticles have a significant disadvantage by their non-biodegradability and their low biocompatibility. These reasons have motivated to find new carriers for bio-active molecules, especially in cancer treatment. Cerasomes (comprised by a liposomal bilayer and an atomic layer of inorganic polyorganosiloxane) meet the criteria to be good carriers for bio-active molecules: good mechanical and thermal stability and, low rigidity and decreased possibilities to precipitate in aqueous solutions. Cholesteryl succinyl silane particles loaded with doxorubicin showed improved effectiveness in cancer treatment, especially in leukemia, decreasing the exposure of healthy cells to the drug, thus minimizing potential side effects (Ma et al. 2011).

ZnO nanorods loaded with daunorubicin showed also an increased anti-tumor activity. Through immunochemistry techniques, it has been shown that cytotoxic activity of daunorubicin is mediated by reactive oxygen species. There is also a direct increase of the anti-tumor activity of daunorubicin (Zhang et al. 2011).

Li et al. (2011) developed two types of novel nanogels (using shell cross-linking of Pluronic F127 micelles with polyethylenimine (PEI), and penetrating network of poly(butylcyanoacrylate) (PBCA) in Pluronic F127 micelles), capable to deliver low soluble anticancer drugs, in this case paclitaxel and 10-hydroxycamptothecin. Their study demonstrated that the anticancer activity of the mentioned drugs can be enhanced *in vitro* when these types of nanogels are used as carriers and delivery systems.

A variety of drug delivery systems for cytotoxic drugs was imagined. A challenge is to incorporate and to prolong the time of activity in those bio-active molecules with short half-life time. 10-hydroxycamptothecin was incorporated in iron-polysaccharide multilayered microcapsules in an efficient manner and with quite a high encapsulation rate (about 60 %). These kinds of systems have an increased drug release rate, proportionally with the number of the deposited bilayers (Guo et al. 2011).

In another recent paper (Larsen et al. 2009), the authors observed that PEGylated magnetic nanoparticles of a larger size (40 nm) had a better yield of accumulation in

murine tumors then smaller particles, improving the MRI contrast, thus the quality of this imaging method. This may be a viable approach for early MRI detections of various neoplasias. Detection of cancer has to be as early as possible, in order to take all necessary therapy measures for cure and prolonged free-cancer survival. Nanoparticles comprised from alginate and folic acid-conjugated chitosan loaded with 5-aminolevulinic acid are suitable carriers for 5-aminolevulinic acid in colorectal tumor cells with the possibility of detection through fluorescent endoscopy (Yang et al. 2011).

Cellular interactions are important to be understood, and to be predicted in order to draw comprehensive pathophysiological chains of morbid conditions and to improve therapy choices. It was demonstrated that protein adsorbed to nanoparticle surfaces can bind to endothelial cells, regardless of their size, underlying that the capacity of adsorption is a good predictor of intercellular interactions in terms of amount (Ehrenberg et al. 2009).

A very promising field is that of organ repair and regeneration.

Heart failure is a wide-spread condition, leading to disabilities and finally to death. Myocardial infarction, if untreated or not properly treated, leads to heart failure. Due to bioengineering techniques, it was possible to imagine several possibilities to correct the structure and functionality of the heart after myocardial infarction. Biomaterials containing keratin (the hydrogel forms itself when water is added to lyophilized keratin powder) are characterized by a porous configuration that is able to penetrate myocardial and endothelial cells, having pro-angiogenesis properties (Shen et al. 2011).

In dentistry, there is the need that material to be friendly to be modeled, durable in time, without negative interactions with adjacent tissues or systemic side effects. Silane coupling agents promote durability of the adhesion between resin and ceramics. Current dental treatment protocols recommend as standard measure silanation, especially in dental restorations and reconstructions (Lung and Matinlinna 2012).

## 12.4 Bondons' Observables for Silanes

One can made predictions regarding the values of bonding energy and length required for a bondon to acquire either the unity of electronic charge or its mass (with the consequence in its velocity fraction from the light velocity) on the ground state, by setting Eqs. (12.2) and (12.16) to unity, respectively. These predictions are summarized in Table 12.2 (Putz 2010b, 2012a, b, c, d).

From Table 12.2, one note is that the situation of the bondon having the same charge as the electron is quite improbable, at least for the common chemical bonds, since in such a case it will feature almost the light velocity (and almost no mass—that is, however, continuously decreasing as the bonding energy decreases and the bonding length increases). This is natural since a longer distance has to be spanned by lower binding energy yet carrying the same unit charge of electron while it is transmitted with the same relativistic velocity! Such behavior may be regarded as the present *zitterbewegung* (trembling in motion) phenomena, here at the bondonic level. However one records the systematic increasing of bondonic life-time towards being

**Table 12.2** Predicted basic values for bonding energy and length, along the associated bondonic lifetime and velocity fraction from the light velocity for a system featuring unity ratios of bondonic mass and charge, respecting the electron values, through employing the basic formulas (12.17), (12.7), (12.2), and (12.16), respectively (Putz 2010b, 2012)

$X_{bond}$ [Å]	$E_{bond}$ [kcal/mol]	$t_{\#}$ [ $\times 10^{15}$ ] (seconds)	$\zeta_v = \frac{v_{\#}}{c}$ [%]	$\zeta_m = \frac{m_{\#}}{m_0}$	$\zeta_e = \frac{e_{\#}}{e}$
1	87.86	10.966	4.84691	1	$0.4827 \times 10^{-3}$
1	182019	53.376	99.9951	$4.82699 \times 10^{-4}$	1
10	18201.9	533.76	99.9951	$4.82699 \times 10^{-5}$	1
100	1820.19	5337.56	99.9951	$4.82699 \times 10^{-6}$	1

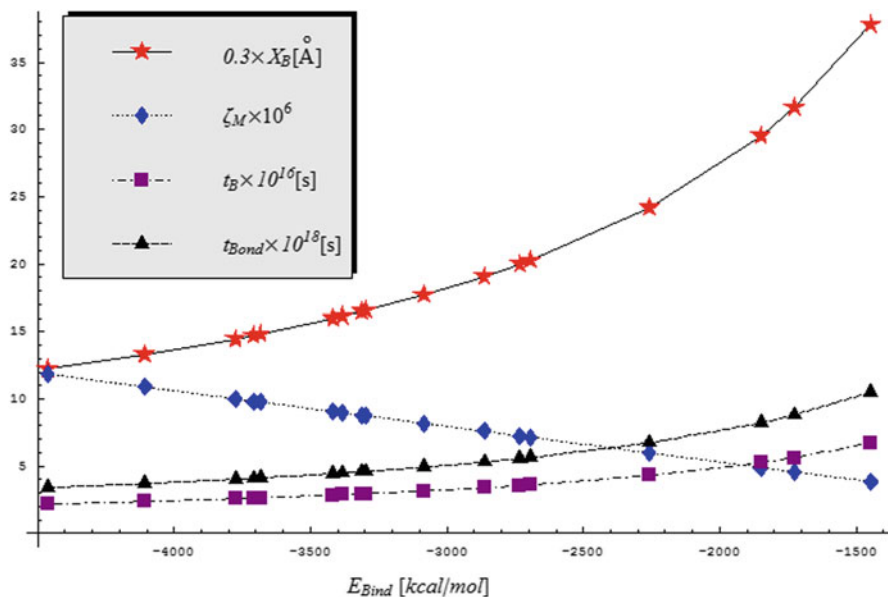
observable in the femtosecond regime for increasing bond length and decreasing the bonding energy—under the condition the chemical bonding itself still exists for certain  $\{ X_{bond}, E_{bond} \}$  combinations (Putz 2010b, 2012b);

On the other side, the situation in which the bondon will weigh as much as one electron may be assumed as the custom case (Putz 2010b, 2012b); nevertheless, it is accompanied by quite reasonable chemical bonding length and energy information that it can carry at a low fraction of the light velocity, however with very low charge as well. Nevertheless, the discovered bonding energy-length relationship from Table 12.2, based on Eq. (12.16), namely (Putz 2010b, 2012a, b, c, d)

$$E_{bond}[\text{kcal/mol}] \times X_{bond}[\text{Å}] = 182,019 \quad (12.19)$$

should be used in setting appropriate experimental conditions in which the bondon particle  $\mathcal{B}$  may be observed as carrying the unit electronic charge yet with almost zero mass. In this way, *the bondon is affirmed as a special particle of Nature, that when behaving like an electron in charge it is behaving like a photon in velocity and like neutrino in mass, while having an observable (at least as femtosecond) lifetime for nanosystems having chemical bonding in the range of hundred of Angstroms and thousands of kcal/mol!* Such a peculiar nature of a bondon as the quantum particle of chemical bonding, the central theme of Chemistry, is not as surprising when noting that Chemistry seems to need both a particle view (such as offered by relativity) and a wave view (such as quantum mechanics offers), although nowadays these two physics theories are not yet fully compatible with each other, or even each fully coherent internally. Maybe the concept of ‘bondons’ will help to improve the situation for all concerned by its further conceptual applications (Putz 2010b, 2012a, b, c, d).

For instance, Eq. (12.19) prescribes that a nano-system with hundred atoms that comprise an energy about 1,000 kcal/mol may have a spanned maximum bonding for 182.019 Å that it can be detected across the ends of a nanotube of length 18 nm, while a bonding system may support along 100 Å (e.g. along a nanotube of length 10 nm) maximum of 1,820 kcal/mol due to bosonic condensation of bondons (Putz and Ori 2012).



**Fig. 12.1** The graphical plot for the bondonic features as of absolute action radii, mass ratio vs. electronic mass, bondonic time-life and bonding time life for silane molecules in Table 12.3

However, when focusing on silanes, the molecular compounds and their optimized structures are considered in Table 12.3, with the bondonic information respecting the custom electronic ones, along the percentage ratio respecting the light velocity, and the estimated life-time through employing the basic formulas (12.2), and (12.16), (12.7), and (12.17) are reported and in the Fig. 12.1 represented, respectively. The main found characteristics display as following:

- The binding energies in the range of thousands of kcal/mol qualifies such structures to be investigated from their experimental bondonic identification with the aid of Gamma ray ( $\gamma$ ) spectroscopy, see the conclusion of the previous chapter (Putz et al. 2015a);
- The related bondonic radii of action, according with the Heisenberg like Eq. (12.19), is placed in the range 40–126 [Å], so being in they range of tenth of Carbon atom influences, or, more general in the above illustrated nano-tube regime; nevertheless the Si-atom presence actually capture the main electrostatic influence around its center—according with the electrostatic maps for molecules of Table 12.3; combining these two ideas one arrives to the condensed phase of bondons around the Si-center of bonding for the whole generic silane’s molecular structure—a further impetus for further experimental spectra identification;
- The actual mass values of bondons in silanes’ compounds are generally with an order of magnitude lower than the for the “classical” carbon systems, see (Putz et al. 2015a), which places by this information the dominant chemical bonding

in being decided between the multiple bonds and metallic bond, according with the Table 12.1 synopsis;

- The most striking result is provided by the velocity and charge bondon-to-electron ratios,  $\zeta_v$  and  $\zeta_e$ , which for all silanes considered achieve in Table 12.3 their maximum values, 99.9951 [%] and 1, respectively, and identically with those generally prescribed in Table 12.2 (last row) corresponding with the generic realization of the actual silanes bondonic radii and bonding energy, although in various realizations above and below of those values; nevertheless, the highest velocity and the identity of the bondonic charge with the electron one, although the bondon is a bosonization of an electronic pair, strongly suggest the actual silanes chemical bond as being of metallic nature according with the appropriate columns prescriptions of Table 12.1;
- Finally, the bondonic life time as computed with the specific Eq. (12.7) results in two order of magnitude higher (i.e. longer times) than the predicted spectroscopically times of Eq. (12.18); this has two important consequences: one is that the silanes chemical bonding by bondon is this way definitely consecrated as being of metallic nature since also the last column condition of Table 12.1 is fulfilled; the second consequence is of experimental nature and gives high hopes that under appropriate time-resolved spectroscopy investigation the longer bondonic lifetime than the spectroscopic (fluctuation) levels times may lead with the real observation of the bondonic signal itself so different by that of electronic transition or chemical bonding vibrations, see also next chapter (Putz et al. 2015b).

All these bondonic features were unitarily represented in Fig. 12.1 for the silanes molecules of Table 12.3: it has a shape classifying it in the class of bondonic variations with delocalization energy, or with inverse of the transition frequencies for their (HOMO-LUMO) frontier levels, or among the carbon-based systems with intermediate reaction rate at room temperature, see the previous chapter (Putz et al. 2015a); all of these highly predicting the silanes compounds as the reliable nano-structures with high nano-extended properties, by both their metallic and reactivity behavior; they are therefore recommended as ideal candidate for silicene smart materials, at their turn replacing in the near future the actual celebrated graphene structures.

**Table 12.3** Predicted bondonic observables for bondonic information under the form of ratios for bondonic mass and charge to the custom electronic ones, along the percentage ratio respecting the light velocity, and the estimated life-time through employing the basic formulas (12.2), and (12.16), (12.7), and (12.17), respectively, for a series of silanes optimized with the HyperChem (Hypercube 2002) environment (PolakRibiere Geometry optimization, SemiEmpirical, AM1), featuring also the resulted electrostatic potential superimposed on the 3D optimized structure, and employing the overall molecular bondonic action radii  $X_{bond}$  relating the computed absolute (positive) binding energy  $E_{bind}$  by the Eq. (12.19), while the bondonic information comments (respecting the general prescriptions of Table 12.2) are in text exposed, respectively

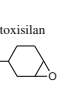
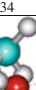

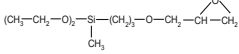
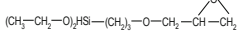
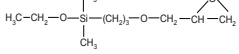
Molecule Chemical Structure	$E_{bind}$ [kcal/mol]	$X_{bond}$ [Å]	$\zeta_m = \frac{m_B}{m_0} \times 10^6$	$\zeta_v = \frac{v_B}{c} [\%]$	$\zeta_e = \frac{e_B}{e}$	$t_B [\times 10^{16}]$ (100 atto- seconds)	$t_{bond} [\times 10^{18}]$ (atto- seconds)
<b>I.</b> $\beta$ -(3,4-Epoxiciclohexil)etiltriotosilano <chem>(CH2-CH2-O)3Si-CH2-CH2-</chem> 	-4462.2278084	40.7911	11.8334	99.9951	1	2.17725	3.4016
<b>II.</b> N-Fenil- $\gamma$ -aminopropiltriotosilano <chem>(CH2-O)3Si-(CH2)3-NH-C6H5</chem>	-4107.8103525	44.3105	10.8936	99.9951	1	2.3651	3.69508
<b>III.</b> $\gamma$ -Glicidopropiltriotosilano <chem>(CH2-CH2-O)3Si-(CH2)3-O-CH2-CH-</chem> 	-4106.4344813	44.3253	10.8899	99.9951	1	2.36589	3.69632
<b>IV.</b> $\beta$ -(3,4-Epoxiciclohexil)etildietotosilano <chem>(CH2-CH2-O)2-SH-CH2-CH2-</chem> 	-3775.0975922	48.2157	10.0112	99.9951	1	2.57354	4.02074

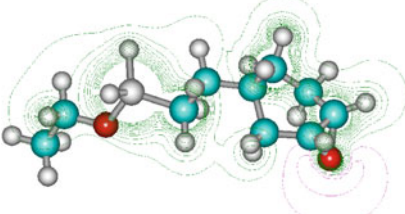
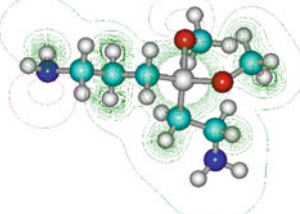

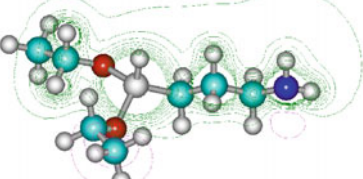
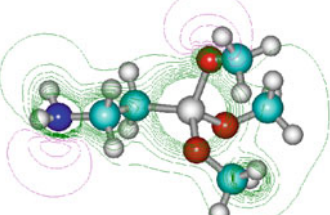


Table 12.3 (continued)

<p>V.  <math>\gamma</math>-Glicidoxipropilmetildietoxisilan  <math>(\text{CH}_2-\text{CH}_2-\text{O})_2-\text{Si}-\text{CH}_2-\text{O}-\text{CH}_2-\text{CH}-\text{CH}_2</math>  </p>	-3709.1865438	49.0725	9.83644	99.9951	1	2.61928	4.09219
<p>VI.  N-Fenil-<math>\gamma</math>-aminopropildimetoxisilan  <math>(\text{CH}_3-\text{O})_2\text{SiH}-\text{CH}_2-\text{CH}_2-\text{NH}-\text{C}_6\text{H}_5</math></p>	-3684.1600465	49.4058	9.77007	99.9951	1	2.63707	4.11999
<p>VII.  <math>\gamma</math>-Glicidoxipropildietoxisilan  <math>(\text{CH}_2-\text{CH}_2-\text{O})_2\text{HSi}-\text{CH}_2-\text{O}-\text{CH}_2-\text{CH}-\text{CH}_2</math>  </p>	-3417.1609375	53.2661	9.06201	99.9951	1	2.84312	4.4419
<p>VIII.  <math>\gamma</math>-Aminopropiltrietoxisilan  <math>(\text{CH}_3-\text{CH}_2-\text{O})_3\text{Si}-\text{CH}_2-\text{CH}_2-\text{NH}_2</math></p>	-3383.2045823	53.8008	8.97196	99.9951	1	2.87165	4.4864
<p>IX.  <math>\gamma</math>-Glicidoxipropildimetilmonoetoxisilan    <math>\text{H}_3\text{C}-\text{CH}_2-\text{O}-\text{Si}-\text{CH}_2-\text{O}-\text{CH}_2-\text{CH}-\text{CH}_2</math></p>	-3311.4052728	54.9673	8.78156	99.9951	1	2.93392	4.58376
<p>X.  N-Fenil-<math>\gamma</math>-aminopropilmonometoxisilan  <math>\text{H}_3\text{C}-\text{O}-\text{SiH}_2-\text{CH}_2-\text{CH}_2-\text{NH}-\text{C}_6\text{H}_5</math></p>	-3295.7993739	55.2276	8.74017	99.9951	1	2.94781	4.60547



**Table 12.3** (continued)

<p><b>XI.</b>  <math>\beta</math>-(3,4-Epoxycyclohexyl)ethylmonoethoxisilan  <math>\text{H}_3\text{C}-\text{CH}_2-\text{O}-\text{SiH}_2-\text{CH}_2-\text{CH}_2-</math> </p>	-3084.5951157	59.009	8.18008	99.9951	1	3.14965	4.92081
<p><b>XII.</b>  <i>N</i>-<math>\beta</math>-(aminoethyl)-<math>\gamma</math>-aminopropildimethoxisilan  <math>\text{H}_2\text{N}-(\text{CH}_2)_3-</math>   <math>\begin{array}{c} \text{O}-\text{CH}_3 \\   \\ \text{Si}-\text{O}-\text{CH}_3 \\   \\ \text{CH}_2-\text{CH}_2-\text{NH}_2 \end{array}</math></p>	-2863.4012319	63.5674	7.59349	99.9951	1	3.39295	5.30093
<p><b>XIII.</b>  <math>\gamma</math>-Glicidoxipropilmonoethoxisilan  <math>\text{H}_3\text{C}-\text{CH}_2-\text{O}-\text{SiH}_2-(\text{CH}_2)_3-\text{O}-\text{CH}_2-</math> </p>	-2732.0961951	66.6225	7.24528	99.9951	1	3.55602	5.5557
<p><b>XIV.</b>  <math>\gamma</math>-Aminopropildietoxisilan  <math>(\text{CH}_3-\text{CH}_2-\text{O})_2\text{HSi}-(\text{CH}_2)_3-\text{NH}_2</math>  </p>	-2694.1224148	67.5615	7.14458	99.9951	1	3.60614	5.63401
<p><b>XV.</b>  <math>\beta</math>-Aminoethyltrimethoxisilan  <math>\text{H}_2\text{N}-\text{CH}_2-\text{CH}_2-\text{Si}-(\text{O}-\text{CH}_3)_3</math>  </p>	-2257.1584360	80.6408	5.98579	99.9951	1	4.30425	6.72469

**Table 12.3** (continued)

<p><b>XVI.</b>  <math>\beta</math>-Aminoetildimetoxisilan  <math>\text{H}_2\text{N}-\text{CH}_2-\text{CH}_2-\text{SiH}(\text{---O---CH}_3)_2</math></p>	-1849.6915020	98.4051	4.90522	99.9951	1	5.25243	8.20607
<p><b>XVII.</b>  <math>\gamma</math>-Aminopropilmonotoxisilan  <math>\text{H}_3\text{C}-\text{CH}_2-\text{O}-\text{SiH}_2-(\text{CH}_2)_3-\text{NH}_2</math></p>	-1726.1090449	105.45	4.57749	99.9951	1	5.62849	8.79359
<p><b>XVIII.</b>  <math>\beta</math>-Aminoetilmonometoxisilan  <math>\text{H}_2\text{N}-\text{CH}_2-\text{CH}_2-\text{SiH}_2-\text{O}-\text{CH}_3</math></p>	-1445.1272742	125.954	3.83235	99.9951	1	6.72286	10.5034

## 12.5 Conclusions

Silanes are suitable precursors to obtain new materials with high potentiality to be used in bio-medicine. Drug delivery systems based on silanes and nanotechnologies are highly efficient in modern therapies, inclusively in cancer therapies. Obtaining methods are relatively cheap, requiring low temperatures, applicable at industrial level, reducing therapy costs and improving therapy effectiveness. However, establishing the chemical nature of silanes compounds as a whole, i.e. as unities in more complex silicene materials, is crucial in order to properly predict and control the resulted physicochemical properties in terms of reactivity, toxicity, stability/aromaticity, etc. To this aim, the bondonic chemistry analysis was performed by assessing the bondon to the electronic localized/delocalized chemical bonding of a given series of silicenes; the computed chemical bonding energy rooted in the bondonic radii of action by a Heisenberg-like relationship, Eq. (12.19), and with their help the further observables as the associated bondonic mass, velocity, charge and life time were obtained with most interesting interpretation: as such, while the first three properties (mass, velocity and charge) placed the specific chemical bond of silanes as being of metallic nature, according with the general chemical bonding classification of Table 12.1, which confirm its ceramic and material properties, while promoting it also for an extended silicene network with specific properties otherwise

accessible only to graphenic materials (i.e. very high conductivity and electronic velocities approaching the light limit, widely here confirmed); whereas the bondonic lifetime was found with two order of magnitude larger than the custom spectroscopically level fluctuation times so predicting the silanes bondons as truly approached by the pulsed lasers in time resolved spectroscopy ( $10^{-16}$  [s]). Such bondonic detection and then bondonic control by nano-photonics direction may be readily achieved on the medium term laboratory experimentation (Putz and Ori 2015). and is envisaged for further research and subsequent communications.

**Acknowledgements** Authors thank Dr. Ottorino Ori for important stimulus and support of the present study of silanes as silicenes' precursors, on which he made constructive comments with occasion of his visit as scientific secretary of the "Laboratory of Computational and Structural Physical-Chemistry for Nanosciences and QSAR" recently accredited by West University of Timișoara, Faculty of Chemistry, Biology, Geography, at Biology-Chemistry Department, which are equally acknowledged for working and research facilities provided therefore.

## References

- Ajami E, Aguey-Zinsou KF (2012) Functionalization of electropolished titanium surfaces with silane-based self-assembled monolayers and their application in drug delivery. *J Colloid Interface Sci* 385(1):258–267
- Altmann S, Pfeiffer J (2003) The hydrolysis/condensation behaviour of Methacryloyloxyalkylfunctional Alkoxysilanes: structure-reactivity relations. *Chem Mon* 134:1081–1092
- Asadujjaman M, Mishuk AL (2013) Novel approaches in lipid based drug delivery systems. *J Drug Deliv Therapeutics* 3(4):124–130
- Avnir D, Coradin T, Lev O, Livage J (2006) Recent bio-applications of sol-gel materials. *J Mater Chem* 16:1013–1030.
- Bader RFW (1990) *Atoms in molecules-A Quantum theory*. Oxford University Press, Oxford
- Beganskiene A, Raudonis A, Jokhadar SZ, Batista U, Kareiva A (2007) Modified sol-gel coatings for biotechnological applications. *J Phys Conf Ser* 93. doi: 10.1088/1742-6596/93/1/012050
- Belton DJ, Deschaume O, Perry CC (2012) An overview of the fundamentals of the chemistry of silica with relevance to biosilicification and technological advances. *FEBS J* 279(10):1710–1720
- Berlin T (1951) Binding regions in diatomic molecules. *J Chem Phys* 19:208–213
- Brinker CJ, Scherer GW (1990) *Sol-gel science—The physics and chemistry of sol-gel processing*. Academic, San Diego
- Caldorera-Moore M, Peppas NA (2009) Micro- and nanotechnologies for intelligent and responsive biomaterial-based medical systems. *Adv Drug Deliv Rev* 61:1391–1401
- Chiappini A, Chiasera A, Berneschi S, Armellini C, Carpentiero A, Mazzola M, Moser E, Varas S, Righini GC, Ferrari M (2011) Sol-gel-derived photonic structures: fabrication, assessment, and application. *J Sol-Gel Sci Technol* 60:408–425
- Coradin T, Livage J (2007) Aqueous silicates in biological sol-gel applications: new perspectives for old precursors. *Acc Chem Res* 40:819–826
- Coti KK, Belowich ME, Liong M, Ambrogio MW, Lau YA, Khatib HA, Zink JL, Khashab NM, Stoddart JF (2009) Mechanised nanoparticles for drug delivery. *Nanoscale* 1:16–39
- Daudel R (1980) In electron and magnetization densities in molecules and crystals. In: Becker P (ed) *NATO ASI, Series B-Physics, Vol 40*. Plenum Press, New York
- De Padova P, Ottaviani C, Quaresima C, Olivieri B, Imperatori P, Salomon E, Angot T, Quagliano L, Romano C, Vona A, Muniz-Miranda M, Generosi A, Paci B, Le Lay G (2014) 24h stability of thick multilayer silicene in air, *2D Materials* 1:021003

- Ehrenberg MS, Friedman AE, Finkelstein AE, Oberdörster G, McGrath JL (2009) The influence of protein adsorption on nanoparticle association with cultured endothelial cells. *Biomaterials* 30:603–610
- Einstein A (1905a) On a Heuristic viewpoint concerning the production and transformation of light. *Ann Physik (Leipzig)* 17:132–148
- Einstein A (1905b) On the electrodynamics of moving bodies. *Ann Physik (Leipzig)* 17:891–921
- Einstein A (1905c) Does the inertia of a body depend upon its energy content? *Ann Physik (Leipzig)* 18:639–641
- Findlay A (1955) *Practical physical chemistry*. Longmans, London
- Fu G, Yue X, Dai Z (2011) Glucose biosensor based on covalent immobilization of enzyme in sol-gel composite film combined with Prussian blue/carbon nanotubes hybrid. *Biosens Bioelectron* 26(9):3973–3976
- Gillespie RJ (1970) The electron-pair repulsion model for molecular geometry. *J Chem Educ* 47:18–23
- Guo S, Zheng J, Dong J, Guo N, Jing L, Yue X, Wang Y, Dai Z (2011) Iron/dextran sulfate multilayered microcapsules for controlled release of 10-hydroxycamptothecin. *Int J Biol Macromol* 49(3):409–415
- Halamová D, Badaničová M, Zelenák V, Gondová T, Vainio U (2010) Naproxen drug delivery using periodic mesoporous silica SBA-15. *Appl Surf Sci* 256(22):6489–6494
- He J, Chisholm BJ, Mayo BA, Bao H, Risan J, Christianson DA, Rafferty CL (2012) Hybrid organic/inorganic coatings produced using a dual-core mechanism. *J Coat Technol Res* 9(4):423–431
- Hypercube, Inc (2002) *HyperChem 7.01* [Program package]
- Jeon YS, Lei J, Chung DJ, Kim JH (2009) Sol-gel derived organic/inorganic hybrid gels based on poly(2-hydroxyethyl aspartamide) and silica. *J Ind Eng Chem* 15(4):544–549
- Jin Y, Xin R, Ai P, Chen D (2008) Self-assembled drug delivery systems 2. Cholesteryl derivatives of antiviral nucleoside analogues: synthesis, properties and the vesicle formation. *Int J Pharmaceut* 350:330–337
- Kaplan I.G. (2002) Is the Pauli exclusive principle an independent quantum mechanical postulate? *Int J Quantum Chem* 89:268–276
- Kuznetsova TF, Eremenko SI (2013) Properties of Sol-Gel Derived Silica Membranes. *Inorg Mater* 49(2):159–164
- Larsen EKV, Howard KA, Kjems J, Nielson T, Wittenborn T, Birkedal H, Vorup-Jensen T, Jakobsen MH, Ostergaard L, Horsman MR, Besenbacher F (2009) Size-Dependent accumulation of PEGylated silane-coated magnetic Iron Oxide Nanoparticles in Murine Tumors. *ACS Nano* 3:1947–1951
- Li N, Wang J, Yang X, Li L (2011) Novel nanogels as drug delivery systems for poorly soluble anticancer drugs. *Colloids Surf B Biointerfaces* 83(2):237–244
- Livinge J, Lemerle J (1982) *Transition Metal Oxide Gels and Colloids*. *Ann Rev Matter Sci* 12:103–122
- Lung CYK, Matinlinna JP (2012) Aspects of silane coupling agents and surface conditioning in dentistry: An overview. *Dent Mater* 28(5):467–477
- Ma Y, Dai Z, Zha Z, Gao Y, Yue X (2011) Selective antileukemia effect of stabilized nanohybrid vesicles based on cholesteryl succinyl silane. *Biomaterials* 32(35):9300–9307
- Minami T (2013) Advanced sol-gel coatings for practical applications. *J Sol-Gel Sci Technol* 65:4–11
- Monnier V, Dubuisson E, Sanz N, Ibanez A (2008) Organic nanocrystals in sol-gel matrices: new hybrid organic-inorganic materials for optics. *Res Chem Intermed* 34(2–3):155–167
- Oelke WC (1969) *Laboratory physical chemistry*. Van Nostrand Reinhold Company, New York
- Óztürk I (1992) Alkoxysilanes consolidation of stone and earthen building material. Thesis for the degree of Master of Science, University of Pennsylvania
- Pandey S, Mishra SB (2011) Sol-gel derived organic-inorganic hybrid materials: synthesis, characterizations and applications. *J Sol-Gel Sci Technol* 59:73–94
- Pauling L (1931) The nature of the chemical bond II. The one-electron bond and the three-electron bond. *J Am Chem Soc* 53:3225–3237

- Pierre AC (1998) *Introduction to Sol-Gel Processing*. Kluwer Academic Publishers, Boston
- Plueddemann EP (1982) *Silane coupling agents*. Plenum Press, New York
- Putz MV (2008) The chemical bond: spontaneous symmetry-breaking approach. *Symmetr Cult Sci* 19:249–262
- Putz MV (2009a) Chemical action and chemical bonding. *J Mol Struct (THEOCHEM)* 900:64–70
- Putz MV (2009b) Levels of a unified theory of chemical interaction. *Int J Chem Model* 1:141–147
- Putz MV (2010a) Beyond quantum nonlocality: chemical bonding field. *Int J Environ Sci* 1:25–31
- Putz MV (2010b) The bondons: the quantum particles of the chemical bond. *Int J Mol Sci* 11(11):4227–4256
- Putz MV (2011a) Conceptual density functional theory: from inhomogeneous electronic gas to Bose-Einstein condensates. In: Putz MV (ed), *Chemical Information and Computational Challenges in 21st Century*. NOVA Science Publishers, Inc., New York, Chapter 1, pp. 1–60
- Putz MV (2011b) Hidden side of chemical bond: the bosonic condensate. In *Advances in Chemistry Research*, vol 10, Taylor J.C. (ed.), NOVA Science Publishers, Inc., New York, Chapter 8, pp. 261–298
- Putz MV (2012a) *Quantum theory: density, condensation, and bonding*. Apple Academic Press, Toronto
- Putz MV (2012b) Chemical orthogonal spaces, in *mathematical chemistry monographs*, vol. 14. Faculty of Science, University of Kragujevac
- Putz MV (2012c) From Kohn-Sham to Gross-Pitaevsky equation within Bose-Einstein condensation  $\psi$ -theory. *Int J Chem Model* 4(1):1–11
- Putz MV (2012d) Density functional theory of Bose-Einstein condensation: road to chemical bonding quantum condensate. *Struct Bonding* 149:1–50
- Putz MV (2015) *Quantum Nanochemistry. Vol. II (Quantum Molecules and Reactivity) & Vol IV (Quantum Solids and Orderability)*. Apple Academic Press, Toronto
- Putz MV, Ori O (2012) Bondonic characterization of extended nanosystems: application to graphene's nanoribbons. *Chem Phys Lett* 548:95–100
- Putz MV, Ori O (2014) Bondonic effects in group-iv honeycomb nanoribbons with Stone-Wales topological defects. *Molecules* 19(4):4157–4188
- Putz MV, Ori O (2015) Bondonic chemistry: physical origins and entanglement prospects. In: Putz MV, Ori O (eds), *Exotic properties of carbon nanomatter. Advances in physics and chemistry*. Springer, Dordrecht-London (Chapter 10)
- Putz MV, Pitulice L, Dascălu D, Isac D (2015a) Bondonic chemistry: non-classical implications on classical carbon systems. In: Putz MV, Ori O (eds) *Exotic properties of carbon nanomatter. Advances in physics and chemistry*. Springer, Dordrecht-London (Chapter 11)
- Putz MV, Dudaş NA, Putz AM (2015b) Bondonic chemistry: predicting ionic liquids' (IL) bondons by Raman vs. IR Spectra. In: Putz MV, Ori O (eds) *Exotic properties of carbon nanomatter. Advances in physics and chemistry*. Springer, Dordrecht-London (Chapter 13)
- Ryan JW (1962) Redistribution and reduction reactions of Alkoxysilanes. *J Am Chem Soc* 84(24):4730–4734
- Sanchez C, Lebeau B, Ribot F, In M (2000) Molecular design of sol-gel hybrid organic-inorganic nanocomposites. *J Sol-Gel Sci Technol* 19:31–38
- Schottner G (2001) Hybrid sol-gel derived polymers: applications of multifunctional materials. *Chem Mater* 13(10):3422–3435
- Segal DL (1984) Sol-gel processing: routes to oxide ceramics using colloidal dispersions of hydrous oxides and alkoxide intermediates. *J Non-Crystalline Solids* 63:183–191
- Sevimli F, Yilmaz A (2012) Surface functionalization of SBA-15 particles for amoxicillin delivery. *Microporous Mesoporous Mater* 158:281–291
- Shen D, Wang X, Zhang L, Li J, Cheng K, Zhang J (2011) The amelioration of cardiac dysfunction after myocardial infarction by the injection of keratin biomaterials derived from human hair. *Biomaterials* 32(35):9290–9299
- Tao SL, Desai TA (2003) Microfabricated drug delivery systems: from particles to pores. *Adv Drug Deliv Syst* 55(3):315–328

- Tsvetkova IN, Shilova OA, Voronkov MG, Gomza YP, Sukhoy KM (2008) Sol-Gel synthesis and investigation of proton-conducting hybrid organic-inorganic Silicophosphate materials. *Glas Phys Chem* 34(1):68–76
- Vioux A, Viau L, Volland S, Bideau JL (2010) Use of ionic liquids in sol-gel; ionogels and applications. *Comptes Rendus Chimie* 13(1–2):242–255
- Whitney CK (2007) Relativistic dynamics in basic chemistry. *Found Phys* 37:788–812
- Yang SJ, Lin FH, Tsai HM, Lin CF, Chin HC, Wong JM, Shieh MJ (2011) Alginate-folic acid-modified chitosan nanoparticles for photodynamic detection of intestinal neoplasms. *Biomaterials* 32:2174–2182
- Zhang H, Chen B, Jiang H, Wang C, Wang H, Wang X (2011) A strategy for ZnO nanorod mediated multi-mode cancer treatment. *Biomaterials* 32:1906–1914
- Zhou L, Kong Y, Zhong S, Zhou X (2013) Preparation and characterization of molecularly imprinted organic-inorganic hybrid materials by sol-gel processing for selective recognition of ibuprofen. *J Sol-Gel Sci Technol* 66:59–67

# Chapter 13

## Bondonic Chemistry: Predicting Ionic Liquids' (IL) Bondons by Raman-IR Spectra

Mihai V. Putz, Nicoleta A. Dudaş and Ana-Maria Putz

**Abstract** The notable nowadays physical-chemical structures as ionic liquids (ILs) are, due to their versatility properties adjusted by changing either the anion or cation sides, with spread applications as solvents (viz. organic reaction, bio- and nano-catalysis, polymerization), electrolytes (viz. fuel cells, batteries and sensors), lubricants and additives (including fuel additives), or in chemical engineering including separation (gas chromatography/GC-head space solvents, gas separation, membranes extraction, extractive distillation), heat storage (as thermal fluids), till the nano-technology (protein crystallization, liquids crystals and their use in monitor displays, robotics and artificial muscles), just to name few, are in the present chapter reviewed from the scientific generations created with their structural consequences; they are then used as the compounds for which the recently predicted bondon as the quantum quasi-particle of chemical bonding may be identified in the allied Raman/IR spectra through a specific algorithm involving the bondonic quantum numbers prediction in spectra and of their most tangible quantum appearance; this because the invariable four-levels for bondonic formations confirms the quantum entangled states associated with their existences, as just noted by Putz and Ori (2015), see Chap. 10 of the same monograph, while the objective realization associates either with IR or Raman of IL computed spectra; connection with experimental recorded IR spectra is also presented with encouragement perspective for bondonic observation, while correlation with eco-toxicological data (EC50) is equally presented and interpreted from a bondonic sub-atomic perspective.

---

M. V. Putz (✉) · N. A. Dudaş · A.-M. Putz

Laboratory of Computational and Structural Physical-Chemistry for Nanosciences and QSAR,  
Department of Biology-Chemistry, Faculty of Chemistry, Biology, Geography,  
West University of Timișoara, Pestalozzi Str. No. 16, 300115 Timișoara, Romania  
Tel.: +40-256-592638

e-mail: mv\_putz@yahoo.com; mvputz@cbg.uvt.ro;

N. A. Dudaş

e-mail: nicole\_suceveanu@yahoo.com

A.-M. Putz

Institute of Chemistry, Timișoara of the Romanian Academy,  
24 Mihai Viteazul Bld., 300223 Timișoara, Romania  
Tel.: +40-256-491-818

e-mail: putzanamaria@yahoo.com

### 13.1 Introduction: A Survey on IL Challenges

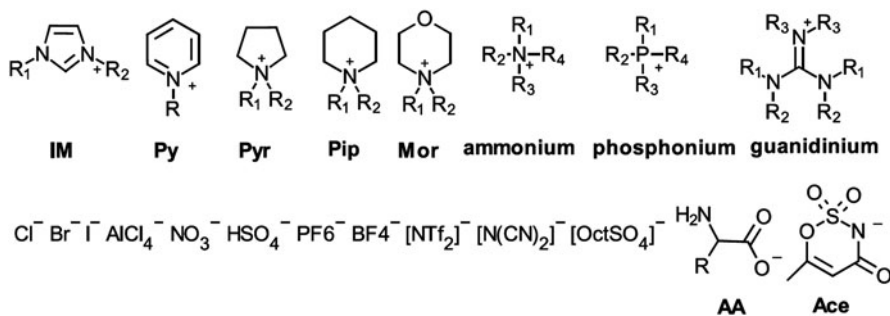
In 1914 the first ionic liquid (IL) was mentioned as the ethyl ammonium nitrate (Walden 1914). Research in this area went diffident, since in 1948 the physical and chemical properties of pyridinium aluminium tetrachloride have been investigated, and the first review in more detail about IL based on tetraalkylammonium cation with chloroaluminate anions appeared only in 1983 (Hussey 1983). In 1990's came the first reports of ILs based on imidazolium cation, stable in air and water, which predict some possible uses of these salts (Wilkes and Zaworotko 1992). Thus was sparked the interest of researchers, it is actually the start for future intensive research of ILs, with more surprising results, ILs offering unexpected opportunities in numerous fields (Zhang et al. 2009; Mallakpour and Rafiee 2011a, b).

Ionic liquids are salts, peculiar organic molten salts, stable in air and water, completely composed of ions, and generally exhibit melting temperatures below 100 °C (Stark and Seddon 2007). Their remarkable characteristics such as: melting point, their preservation state as liquids within a broad temperature as large as 300 °C, dielectric constant, viscosity, density, polarity, water-miscibility, they are able to dissolve a wide range of organic, inorganic, organometallic compounds and polymers, low toxicity, negligible vapor pressure, non-flammable, non-explosive, non-coordinating, non-solvating, not very corrosive, high ion conductivity, the electrochemical window, excellent thermal and chemical stability, ILs have become a very interesting topic to research, with applications in many branches of chemistry and chemical technology and many other areas. (Wei and Ivaska 2008; Zhang et al. 2009; Mallakpour and Rafiee 2011a, b).

Usually ILs consist of a organic cation associated with a (poly)atomic anion that may be either organic or inorganic. Because the symmetrical species tend to pack more effectively in the solid state, and tend to form salts with higher melting points, the cations are ordinarily designed with a reduced symmetry, limiting their packing in a crystal and giving a low melting point (Zhang et al. 2009; Coleman and Gathergood 2010). The structure of ILs which is modular nature, and afford structural modifications that can be made either to the anionic or the cationic component thus may be obtained a wide diversity of possible ILs with different physicochemical properties (Zhang et al. 2009; Coleman and Gathergood 2010). By modifying the structural factors of cations and anions: size, symmetry, charge density, chain length, functional groups, etc., physicochemical properties are fine-tuned (Zhang et al. 2009; Coleman and Gathergood 2010; Pham et al. 2010). According to the choice of cation are determine the principal physical properties (e.g., melting point, viscosity, density, solubility, hydrofobicity, etc.), whilst the choice of the anion affects more the chemistry (Mallakpour and Rafiee 2011a, b). Special ILs can be designed by changing cations and anions to meet the specific physical/chemical properties required for each specific application, in this way can be made task-specific ILs (TSIL) for a certain application (Wei and Ivaska 2008; Pham et al. 2010; Carrera et al. 2010).

Generally ILs are classified by type cation into: ILs containing aromatic head groups cation and ILs containing acyclic head groups cation (Petkovic et al. 2011) or for being more specific in ILs based on the: imidazolium (IM), pyridinium (Py),





**Fig. 13.1** Examples of the cationic and anionic structures that may be found in the ionic liquids' constitution

quinolinium (Quin), pyrrolidinium (Pyr), piperidinium (Pip), morpholinium (Mor), quaternary ammonium (N), quaternary phosphonium (P), guanidinium (G), sulfonium, and other cations (Fig. 13.1) (Zhang et al. 2009; Pham et al. 2010; Frade and Afonso 2010; Carrera et al. 2010; Zhao et al. 2007). This cations can be found in combination with different anions such as:  $\text{Cl}^-$ ,  $\text{Br}^-$ ,  $\text{I}^-$ ,  $\text{AlCl}_4^-$ ,  $\text{NO}_3^-$ ,  $\text{HSO}_4^-$ ,  $\text{PF}_6^-$ ,  $\text{BF}_4^-$ ,  $[\text{CF}_3\text{COO}]^-$ ,  $[\text{CF}_3\text{SO}_3]^-$  or  $[\text{TfO}]^-$ ,  $[\text{N}(\text{CF}_3\text{SO}_2)_2]^-$  or  $[\text{NTf}_2]^-$ ,  $[\text{N}(\text{C}_2\text{F}_5\text{SO}_2)_2]^-$  or  $[\text{P}_2\text{N}]^-$ ,  $[\text{N}(\text{CN})_2]^-$ ,  $[\text{OctSO}_4]^-$ , and others (Fig. 13.1), see Wei and Ivaska (2008); Frade and Afonso (2010); Petkovic et al. (2011).

By incorporating carboxylic acids, glucose, non-nutritive sweeteners as acesulfamate  $[\text{Ace}]^-$  and saccharinate  $[\text{Sac}]^-$ , amino acids (AA) scientists are trying to obtain biocompatible ILs (Petkovic et al. 2011; Imperato et al. 2007) Because amino acids have in their molecule both a carboxylic residue and an amino group, they can be used either as anions or cations (e.g. from glycine  $[\text{Gly}]^-$  as anion or from proline  $[\text{Pro}]^+$  as cation) so obtaining amino acid ionic liquids (AAILs) (Fig. 13.1) (Fukumoto et al. 2005; Ohno and Fukumoto 2007; Gao et al. 2010; Rahman et al. 2010; Mohajeri and Ashrafi 2011; Mu et al. 2012). Also by trying to reduced the number of additional chemicals required per application, the combination [cation][anion] of ILs, wich can include two active chemicals as a single moiety has become very attractive, so was made the design of herbicidal ionic liquids—HILs, with herbicidal anions such as 2,4-D (2,4-dichlorophenoxyacetic acid) or MCPA (4-chloro-2-methylphenoxyacetic acid) (Pernak et al. 2011; Praczyk et al. 2012).

Another classification of ILs can be done according to generation they belong to: *first generation of ILs*, researchers focused mainly on their special physicochemical properties (density, viscosity, conductivity, solubility, and high thermal and chemical stability); *second generation of ILs*, researchers explore the potential to tune some of physicochemical properties, allowing the formation of TSIL, more environmentally friendly (greener); *third generation of ILs*, researchers involve active pharmaceutical ingredients (API), which are being used to produce ILs with biological activity (Ferraz et al. 2011; Hough et al. 2007).

The acronyms used in the literature for ILs are slightly differing from one author to another. For ILs mentioned in this article we have used abbreviations that

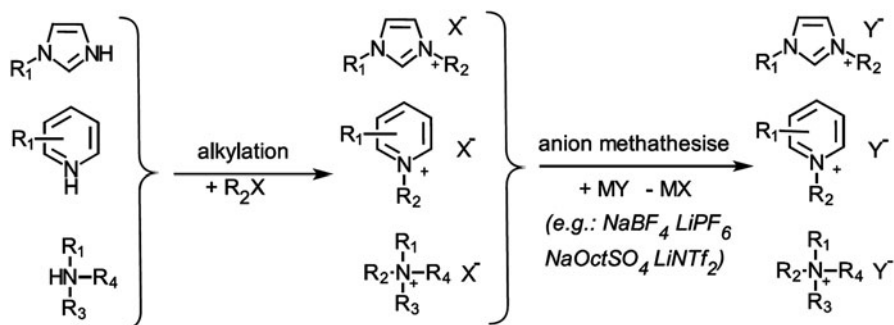


Fig. 13.2 Schematization of two-steps synthesis of ILs

appear to be most frequently used in literature, as those adapted from (Ranke et al. 2007a). In this way, the cation head groups were abbreviated as stated above, and the alkyl chains attached to the head group are given as numbers corresponding to the number of carbon in the alkyl residues, with the exception of pyridinium cation which abbreviation was made by noting the position of attachment and a symbol for the attached group (e.g. Py4-3Me-4Me BF<sub>4</sub> for 1-butyl-3,4-dimethylpyridinium tetrafluoroborate) (Ranke et al. 2007a; Pham et al. 2010).

ILs are usually obtained in a two step synthesis, which involves the preparation of cation in the first step and anion exchange in the second step (Fig. 13.2) (Zhang et al. 2009; Scammells et al. 2005). Synthesis method obviously may suffer small variations depending on the type of ILs (Zhang et al. 2009; Carrera et al. 2010; Ohno and Fukumoto 2007; Pernak et al. 2011; Zhao et al. 2007; Scammells et al. 2005; Harjani et al. 2009; Papaiconomou et al. 2007, 2010). Commonly the cations are prepared essentially by protonation with a free acid, or by quaternization of an amine or an phosphine. This involves the alkylation of an organic substrate (e.g., pyridine, imidazole, trialkylamine, etc.)—reaction of a Lewis-basic nucleophile heteroatom with an alkyl halide, the mixture being stirred and heated (Fig. 13.2) (Zhang et al. 2009; Pernak et al. 2011; Zhao et al. 2007; Scammells et al. 2005; Harjani et al. 2009; Papaiconomou et al. 2007, 2010). In the second step, the precursor obtained in the first step is used for anion metathesis with Lewis acids or metal salts of the desired anions finally obtaining a mixture which contain the desired IL (Fig. 13.2) (Zhang et al. 2009; Pernak et al. 2011; Zhao et al. 2007; Scammells et al. 2005; Harjani et al. 2009; Papaiconomou et al. 2007, 2010). The resulting mixtures can form either a biphasic system or a homogeneous phase with water, which depends on the IL solubility in water (Zhang et al. 2009; Scammells et al. 2005). From these mixtures the IL must be separated very carefully because the impurities may have a drastic effect on the physicochemical properties (Zhang et al. 2009; Scammells et al. 2005).

From the desire to obtain ILs in just one reactor and also to avoid separation and purification processes of the intermediate chemical compounds, the researchers have been able to realize one-pot synthesis of a part of ILs (Zhang et al. 2009; Allen et al. 2006).

Impurities that can be found in ILs are: water, halides, unreacted organic starting materials and compounds from the incomplete metathesis reaction, this are affecting the physicochemical properties of ILs (e.g.: density, viscosity, their decomposition, etc.) (Zhang et al. 2009; Scammells et al. 2005). In some cases they do not have a very big impact, such as the Heck reaction that is unaffected by the presence of impurities. But in other cases or in the case of certain very sensitive chemical applications (catalysis, electrochemical and spectroscopic application), the ILs must be of high purity (Scammells et al. 2005; Zhang et al. 2009).

As mentioned above the *physical properties* of ILs can be tailored by a variation in the cationic and the anionic precursor.

Usually when an IL is heated from the solid state cannot pass directly in liquid state, is going through several phase change points such as glass transition point ( $T_g$ ), melting point ( $T_m$ ) and clearing point ( $T_c$ ) (Zhang et al. 2009). ILs can exhibit the supercooled phenomena, and may form supercooled liquids when the freezing point ( $T_f$ ) is not consistent with melting point ( $T_m$ ) and the gap between them is as wide as 40–90 K (Zhang et al. 2009).

For a low *melting points*, the cations are typically unsymmetric (Zhang et al. 2009; Coleman and Gathergood 2010) and also we should take account that ILs with shorter alkyl chains are ruled by electrostatic forces and ILs with longer alkyl chains are ruled by the short-range van der Waals interactions (Zhang et al. 2009). Papaiconomou et al. (2007, 2010) find that in many cases the melting point is higher for the imidazolium or pyridinium cations substituted with methyl substituents than those ionic liquids containing no alkyl substituents. Also they find that some pyridinium-based ILs containing iodine anions are solid at room temperature (e.g. [Py8-3Me-5Me][I]) and for ILs containing [TfO]<sup>-</sup> anions, the addition of an extra methyl group on pyridine ring increases melting temperature; ILs containing butyl chains and [NTf<sub>2</sub>]<sup>-</sup> anions exhibited  $T_g$  and no  $T_m$ , whatever the alkyl chain or cation ring was used (Papaiconomou et al. 2007, 2010) and for the same anion and pyridinium ring, the ionic liquids containing butyl chains exhibit lower  $T_g$  values than those containing octyl chains (Papaiconomou et al. 2007, 2010). The melting points of ILs generally increase with the decreasing of anion size  $Cl^- > Br^- > [PF_6]^- > [BF_4]^- > [TfO]^- > [TFSI]^-$  (Zhang et al. 2009).

ILs usually have good *thermal stability* which is a little bit influenced by the organic nature of the cations/anions that restricts their upper stability temperature, defined by the decomposition point ( $T_d$ ) (Zhang et al. 2009). The thermal stability of ILs is dominated by the charge density, acidic proton, and expansionary force of cations and anions. The influence of the pyridinic cation on thermal stability is not so clear, and it has been observed that imidazolium ILs are more stable than the corresponding ammonium and pyridinium ILs (Zhang et al. 2009; Papaiconomou et al. 2007, 2010). Degradation of ionic liquids is mostly influenced by the nature of the anion, its nucleophilicity (Scammells et al. 2005; Papaiconomou et al. 2007, 2010). ILs containing weakly coordinating anions are mostly stable to high-temperature decomposition (Zhang et al. 2009). For any pyridine cation studied by Papaiconomou et al. (2007), the decomposition temperatures of the ionic liquids are in the following anion order: [I] < [SCN] < [N(CN)<sub>2</sub>] < [NTf<sub>2</sub>] ≤ [TfO] < [BF<sub>4</sub>] (Papaiconomou et al.

2007, 2010) and also was showed that pyridinium salts exhibit rather low thermal decomposition temperatures (Scammells et al. 2005; Patrascu et al. 2004).

*Densities* of ILs is strongly depend on the temperature, water content of ILs, and the structures of cations and anions. In general, the densities of ILs decrease with the increase in alkyl chain length and the increase of cation size (Zhang et al. 2009; Papaiconomou et al. 2007, 2010). It was show that because of the absence of trifluoromethyl groups on the anion, pyridinium-based ILs containing dicyanamide or thiocyanate anions exhibit low densities ( $\approx 1 \text{ g/cm}^3$ ) and ILs with  $[\text{NTf}_2]$  anions exhibit the highest densities (Papaiconomou et al. 2007, 2010).

*The refractive indices* (Papaiconomou et al. 2007, 2010) for pyridinium-based ILs are range from 1.4 to 1.6, are higher than those for corresponding imidazolium-based ILs. The influence of the cation is not very clear, anions have the most important influence on the refractive index: the refractive index increase with the decrease of the anion. For the same cation, refractive indices increase in the following anion order:  $n(\text{NTf}_2) < n(\text{TfO}) < n(\text{N}(\text{CN})_2) < n(\text{SCN}) < n(\text{I})$  (Papaiconomou et al. 2007, 2010).

The *viscosities* are very sensitive to impurities, water content and temperatures: the water and organic solvents will decrease the viscosity of ILs, while the presence of chloride increases it (Zhang et al. 2009; Wei and Ivaska 2008; Seddon et al. 2000). Presence of cosolvents in ILs reduces the viscosity, with the effect on being stronger with the higher the dielectric constant of the cosolvent is (Seddon et al. 2000). The viscosity at room temperature of ILs are in range from 10 to 500 cP, ILs being more viscous than molecular solvents. The viscosities of imidazolium ILs have the same trends to those of the pyridinium IL: increase with an increase in cation alkyl chain length and also with the number of methyl that are added onto the pyridine ring (Zhang et al. 2009; Papaiconomou et al. 2007, 2010). Presence of ester or hydroxyl groups in ILs based on the pyridinium or ammonium cations increases the viscosity, ester functions having a bigger effect than the hydroxyl functionalities (Deng et al. 2011).

Commonly lattice energy and ion solvation of salts determine their *water solubility* (Ranke et al. 2009). For ILs the lattice energy is irrelevant and differences in hydrophobicity account more for differences in their water solubility (Ranke et al. 2009). According to their *solubility in water* ILs can generally be divided into *water-immiscible (hydrophobic)* and *water-miscible (hydrophilic) ILs* (Wei and Ivaska 2008; Ranke et al. 2009). *Water-immiscible ILs* form non-polarizable interfaces in contact with water and they can be easily prepared in aqueous solution. They can also be obtained in very dry state and they are especially suitable for applications in electrochemical systems (Wei and Ivaska 2008; Ranke et al. 2009). *Water-miscible (hydrophilic) ILs* have been considered unstable in aqueous solutions but recently was found that they also can form films with active electrochemical properties on glassy carbon electrode (Wei and Ivaska 2008; Ranke et al. 2009).

The miscibility of ILs in water is strongly dependent on the anions (Wei and Ivaska 2008; Seddon et al. 2000; Anthony et al. 2001). Anions like  $\text{Cl}^-$ ,  $\text{Br}^-$ ,  $\text{I}^-$ ,  $\text{NO}_3^-$ ,  $\text{CH}_3\text{COO}^-$  and  $\text{CF}_3\text{COO}^-$  are making the ILs miscible with water, while anions such as  $\text{PF}_6^-$  and  $\text{Tf}_2\text{N}^-$  are making them immiscible with water. For ILs containing anions as  $\text{BF}_4^-$  and  $\text{CF}_3\text{SO}_3^-$  ( $\text{TfO}^-$ ) the miscibility with water depend on the structure of the cations (in general are miscible with water) (Wei and Ivaska 2008;

Seddon et al. 2000; Anthony et al. 2001). The increase in the cation chain length decrease the miscibility with water of ILs (Wei and Ivaska 2008). Other study underline that the solubility parameter for ILs is influence by the anion and increases in the following order:  $[\text{Cl}]^- < [\text{NTf}_2]^- < [\text{TfO}]^- < [\text{OctSO}_4]^- < [\text{PF}_6]^- < [\text{BF}_4]^- < [\text{TOS}]^- < [\text{SCN}]^- < [\text{MDEGSO}_4]^- < [\text{TFA}]^-$ , being higher for the ILs with less aliphatic character (Marciniak 2010).

ILs containing octylpyridinium (Py8) cation are hydrophobic, the hydrophobicity increases with the number of alkyl substituents on the cation ring, so Py8 di- or tri-substituted with methyl group have limited solubilities in water (Papaiconomou et al. 2007, 2010). Comparing the solubilities of ILs containing Py4 and Py8 (substituted or not) cations, was observed a decrease in the solubility of ILs in water (Papaiconomou et al. 2007, 2010). Pyridinium ILs with  $[\text{NTf}_2]^-$  anion has been shown the lowest solubility in the water and the influence of the trialkyl- or tetraalkylpyridinium cation on the solubility is small, while that containing  $\text{I}^-$  anion are found to be hydrophobic (for the first time reported in literature) (Papaiconomou et al. 2007, 2010). Moreover, there was found that the *surface tensions* of the ILs increased with the increasing cation chain length (Wei and Ivaska 2008). *Interfacial tensions* of the ILs with aqueous solutions were found to decrease with the length of the cation chain due to the increased surface activity of the longer chain cations (Wei and Ivaska 2008). It was observed that HILs exhibit a low contact angle of droplets and low surface tension (Praczyk et al. 2012).

It was observed that even the hydrophobic ILs can present hygroscopic capacities (Seddon et al. 2000), and even if ILs containing  $[\text{SCN}]^-$  and  $[\text{N}(\text{CN})_2]^-$  exhibit higher solubilities in water are hygroscopic, ILs containing  $[\text{SCN}]^-$  are more hygroscopic than their  $[\text{N}(\text{CN})_2]^-$  homologues (Papaiconomou et al. 2007, 2010). The *water content* (i.e., *hygroscopicity*) of ILs is linked to the nature of the anion and for pyridinic ILs follows the trend  $w(\text{NTf}_2) < w(\text{TfO}) < w[\text{N}(\text{CN})_2] < w(\text{SCN})$  (Papaiconomou et al. 2007, 2010). The longer the attached chain or the substituted pyridine ring is, the more lower water content is, and a more hydrophilic anion such as  $[\text{SCN}]^-$  or  $[\text{N}(\text{CN})_2]^-$  is used, the water contents is higher (Papaiconomou et al. 2007, 2010).

By increasing the length of the alkyl chain there is a large decrease of *ionic conductivity* of ILs, being higher for ILs composed of 1-alkyl-3-methylimidazolium cations or for tetraethylammonium-based amino acids ILs (chiral ionic liquids—CILs) (Rahman et al. 2010; Yoshida et al. 2007). By varying the alkyl chain length or the anion the ionic conductivity of ILs can be changed in controllable manner (Wei and Ivaska 2008).

*Electrochemical window* of ILs can be as wide as 4.5 V compared with 1.2 V in most aqueous electrolytes (Wei and Ivaska 2008; Suarez et al. 1997). Electrochemical windows for ILs with di- or tri-substituted Py8, Py4-CN and  $[\text{NTf}_2]^-$  as counter anion are at around 4 V (Papaiconomou et al. 2010; Zhang et al. 2007).  $[\text{NTf}_2]^-$  anion it is a well-known anion exhibiting increased electrochemical stability, and ILs containing long linear alkyl chains has been reported to be slightly less subject to reduction than those containing shorter alkyl chains (Wei and Ivaska 2008; Papaiconomou et al. 2010; Appetecchi et al. 2009). Pyridinium-based ILs in generally exhibit high

reduction potentials, high oxidation and thermal stability (Papaiconomou et al. 2007, 2010). For an IL the *reduction potential* is mostly influenced to the type of the cation: ILs containing saturated heterocyclic cations such as pyrrolidinium (Pyr) or piperidinium (Pip) are subject to reduction at much more negative potentials ( $-3$  V versus Ag/AgCl electrode) than ILs containing unsaturated heterocycles as imidazolium heterocycles which are reduced below  $-2$  V or di- or tri-substituted Py8 that are reduced around  $-1.2$  to  $-1.3$  V; (Papaiconomou et al. 2010; Appetecchi et al. 2009; Zhang et al. 2007). *Oxidation potentials* is related to the electrochemical stability of the anion, whatever the cation used. (Papaiconomou et al. 2010; Appetecchi et al. 2009; Ohno et al. 2005). It was reported that presence (of more than two) methyl groups on pyridinium cations, reduction occurs at lower potentials and increases the oxidation potential of the IL (Papaiconomou et al. 2010; Zhang et al. 2007).

ILs can *solubilize* various gases (e.g. CO<sub>2</sub>—the most significant greenhouse gas, which can be seen as a non-toxic C1 resources, and he have many applications in the production of valuable products and materials) (Zhang et al. 2009; Carrera et al. 2010; Deng et al. 2011). In particular, Deng et al. (2011) reported that introduction of oxygen functionalities or chemical modification of the alkyl side chain in imidazolium-based ILs does not lead to significant changes of the solubility of different families of gases, while the nitrile or vinyl groups in the cation of the IL, can lead to ILs with interesting solvation properties (Deng et al. 2010; Muldoon et al. 2007; Costa Gomes 2007; Anthony et al. 2002). Also they showed that the presence of the ester and hydroxyl groups in the cation of the pyridinium- or ammonium-based ILs not influenced the CO<sub>2</sub> solubility, except for the case of functionalized-pyridinium-based ILs in which the gas is much less soluble (Deng et al. 2011). According to the structural features and fixation/absorption mechanisms, the ILs can be classified into: *conventional ILs*—can absorb/fix less CO<sub>2</sub> because of the physical interactions between CO<sub>2</sub> and ILs (e.g. IM14 PF<sub>6</sub> that can solubilize CO<sub>2</sub> in much higher quantities than other gases such as CO, CH<sub>4</sub>, H<sub>2</sub>, N<sub>2</sub>, and ethane) and *task-specific ILs* with alkaline groups ( $-\text{NH}_2$ )—because of the chemical interactions or reactivity between CO<sub>2</sub> and the alkaline groups of the ILs they can sequester larger amounts of CO<sub>2</sub> than the conventional ILs (e.g. P<sub>4444</sub> AA). (Zhang et al. 2009; Carrera et al. 2010; Anthony et al. 2002). Poly-ILs (PILs) have good CO<sub>2</sub> sorption capacities which are depending on the type of cation and anion, decreasing in the following order: ammonium > pyridinium > phosphonium > imidazolium when we discuss the cations, and  $[\text{Cl}]^- > [\text{BF}_4]^- > [\text{PF}_6]^- \gg [\text{NTf}_2]^-$  when we discuss the anions (Mallakpour and Rafiee 2011a, b).

Due to their special properties ILs have gained attention for a wide variety of applications such as: *solvent and catalyst* for many chemical synthesis, polymerization reactions, nanostructures and nanomaterial technologies, enzymatic reactions and biocatalysis; *extraction and separation*—extraction of CO<sub>2</sub> and metal ions (and also media to store gases), gas or liquid chromatography and capillary electrophoresis; *electroanalytical applications and electrochemical devices*—lithium batteries, fuel or solar cells, different types of (super)capacitors, electrodeposition of metals, electropolishing of stainless steel; *sensors*—electrochemical sensors, optical sensors and biosensors; *biopolymers; matrices* for matrix-assisted laser desorption/ionization



(MALDI) mass spectrometry; *active pharmaceutical ingredients* (APIs) (Zhang et al. 2009; Mallakpour and Rafiee 2011a, b; Wei and Ivaska 2008; Petkovic et al. 2011; Carrera et al. 2010; Rahman et al. 2010; Mohajeri and Ashrafi 2011; Mu et al. 2012; Pernak et al. 2011; Praczyk et al. 2012; Ferraz et al. 2011; Hough et al. 2007; Papaiconomou et al. 2010; Calvano et al. 2012; Li et al. 2012; Yang et al. 2012; Florindo et al. 2013; Marrucho et al. 2014). There are several books and reviews on the applications, properties and synthesis of ILs part of them are listed by (Mallakpour and Rafiee 2011a, b).

It is true that imidazolium and ammonium ILs occupy a leading position in many applications of ILs but also other classes ILs like pyridinium-based ILs, find their place in these applications. N-alkylpyridinium ILs was used as solvent for cycloaddition of CO<sub>2</sub> to propylene oxide, Py1-3-BuOCO NTf<sub>2</sub> as the reaction solvent in Diels–Alder reactions and Py4 Cl as catalyst for catalytic cracking of polyethylene (Zhang et al. 2009; Mallakpour and Rafiee 2011a, b); Py4 Cl, [Pd(bi-Py)<sub>2</sub>][PF<sub>6</sub>]<sub>2</sub>, Py1-3-BuOCO [NTf<sub>2</sub>] and Py1-2-EtOCO [NTf<sub>2</sub>]—solvents for different types of polymerization (Mallakpour and Rafiee 2011a, b); Py8 PF6 increase the electrolytic activity of the electrode and have been used to construct a potentiometric ion sensor, pasting binder in conventional carbon paste electrodes to simultaneously determine dopamine, ascorbic acid and uric acid; Py4 PF6 was used as binder to immobilize the hemoglobin (Wei and Ivaska 2008); 4-acetyl-N-butyl pyridinium hexafluorophosphate was conjugated with nanospheres forming a new kind of fluorescent core–shell ellipsoidal (RBITC@SiO<sub>2</sub>-IL) nanoparticle that can enter into HeLa cells and induce the cells to condense, split and decrease the oxygen consumption (Yang et al. 2012), pyridinium-based ILs have been tested as HILs and as active pharmaceutical ingredients (Praczyk et al. 2012; Florindo et al. 2013).

Usually it is said that ILs are green solvent, but research in recent years have shown that they are not so green.

For a rigorous evaluation of the *toxicity* of ILs the testes should be made on all Kingdoms in the classification of living organisms (bacteria, fungi, crustaceans, algae, plants, mammalian cell lines and animals), each organisms gives a different answer in the presence of ILs (Petkovic et al. 2011). It was observed that freshwater crustacean *Daphnia magna* seemed to produce the lowest EC<sub>50</sub> within the aquatic models together with IPC-81 cell line that looked to be the most vulnerable to the ionic liquids within the experimented cell line models, this would be why these models should be used in the first stage for a preliminary screening (Frade and Afonso 2010).

Also are very necessary to establish if an IL and its metabolites persist or do not persist in the environment, and this can be made by *biodegradation*, *mineralization* and *bioaccumulation* studies (Coleman and Gathergood 2010). The molecular features of compounds that delay biodegradability and mineralization have been identified as following (Howard et al. 1991; Boethling 1994): presence of halogens (especially chlorine and fluorine), chain branching (in particular problems associated with quaternary carbons), tertiary amines, polycyclic systems or heterocycles, aliphatic ethers (Coleman and Gathergood 2010; Pham et al. 2010; Petkovic et al. 2011) and the molecular features that increase biodegradability are presence of esters, amides, hydroxyl, aldehyde, carboxylic acid groups, or linear alkyl chains (Coleman and Gathergood 2010; Pham et al. 2010; Petkovic et al. 2011).

The *biodegradability of ILs* depends on the structure of the cation—especially on the length of the alkyl side chain (the longer is alkyl side chain (> C6) the better the biodegradability is) with the exception of octyl side chain which have a disputable effect on biodegradation (Coleman and Gathergood 2010; Pham et al. 2010; Petkovic et al. 2011; Abrusci et al. 2011; Stolte et al. 2008; Gathergood and Scammells 2002; Romero et al. 2008). But with increasing alkyl side chain length it is also increasing the toxicity to microorganisms, effect that can be attenuated by introduction of ester functional groups into the alkyl side chain of imidazolium and pyridinium based ILs (Coleman and Gathergood 2010; Pham et al. 2010; Petkovic et al. 2011; Abrusci et al. 2011; Gathergood et al. 2004; Garcia et al. 2005). The biodegradability of ILs also depends on the structure of anion: organic anions are usually biodegradable (e.g.  $[\text{OctSO}_4]^-$ ,  $[\text{CH}_3\text{COO}]^-$ ) (Coleman and Gathergood 2010; Pham et al. 2010; Petkovic et al. 2011; Abrusci et al. 2011; Yu et al. 2008), and for inorganic anions, the biodegradability 18 decreased in the order  $\text{PF}_6^- > \text{BF}_4^- > \text{Br}^- > \text{Cl}^-$  (Coleman and Gathergood 2010; Pham et al. 2010; Petkovic et al. 2011; Abrusci et al. 2011; Ranke et al. 2007). The presence of functional oxygenated moieties reduce the lipophilicity of ILs (including pyridine) leading to a decrease in the risk of bioaccumulation in environment (Denga et al. 2012). A warning sign is that in general the most common ILs shown to be not readily biodegradable (Petkovic et al. 2011; Abrusci et al. 2011).

Every ionic liquid is unique and has a distinct individual toxicity and biodegradability (Coleman and Gathergood 2010). In general ILs are more toxic than many traditional solvents to aquatic organisms and an increase hydrophobicity (lipophilicity) and toxicity correspond to an increase in alkyl chain length of the substituted groups, ILs with longer alkyl chains possess more lipophilic properties, the shorter the chain length(s) of side chain(s), the lower the cytotoxicity (Zhang et al. 2009; Coleman and Gathergood 2010; Pham et al. 2010; Petkovic et al. 2011; Frade and Afonso 2010; Ranke et al. 2004; Jastorff et al. 2005; Stepnowski et al. 2004). Jastorff and coworkers observed a good correlation between the cations lipophilicity and the toxicity of the corresponding halide ILs but there are some exceptions of very lipophilic cations or anions (side chains > C10), that exhibited lower toxicity than that predicted (Stolte et al. 2007a, b). Aquatic toxicity can be the result from disruption of the membrane by the compounds (Scammells et al. 2005). This can be made by a hydrophobic/ionic adsorption at the cell membrane/water interface, since this hydrophobic molecules tend to accumulate at this interface probably toxicity will increase with the increase of hydrophobicity (Scammells et al. 2005).

ILs toxicity seems to be influenced mainly by the characteristics of the cation which can be explained by intercalation of the lipophilic part of the molecules into the membrane, whereas the ionic headgroup is at least partially solvated in the aqueous solution (Zhang et al. 2009; Ranke et al. 2004), also toxicity being dependent on the incubation time (Cho et al. 2008).

A theoretical study predicted that expected toxicity should increase in the order ammonium < pyridinium < imidazolium < triazolium < tetrazolium, with increasing the number of nitrogen atoms in an aromatic cation ring (Couling et al. 2006). Toxicity of the ILs cations to IPC-81 seems to increase in the order: [Mor] < [Pip] < [Py] < [Pyr] < [IM] < [Quin] < [N<sub>4444</sub>] < [P<sub>4444</sub>], and in MCF-7 cells increase in a



little bit different order: [Pip] < [IM] < [Pyr] < [Py] (Frade and Afonso 2010). Toxicity of ILs tested on freshwater organisms: the cladoceran *Daphnia magna*, the green alga *Pseudokirchneriella subcapitata* (*Selenastrum capricornutum*), and the fish *Danio rerio* (zebrafish) reveal that long-chain ammonium salts showed higher toxicity to all organism and that ILs are not toxic for *D. rerio* if they do not have a surfactant-like structure (Pretti et al. 2009). Toxicity to *D. magna* and *P.subcapitata* increase from non-aromatic cyclic and acyclic compounds (pyrrolidinium, ammonium, and morpholinium) to aromatic heterocyclic nitrogen-containing compounds (pyridinium and imidazolium) (Pretti et al. 2009).

The anion toxicity trend varies with the cation and seems to have a bigger impact for shorter alkyl chain lengths, lipophilicity and chemical reactivity of anions might be responsible for the observed toxicity of ILs (Zhang et al. 2009; Frade and Afonso 2010). For the model with more collected data (*Vibrio fischeri*), anion toxicity seems to increase in the order [Br] < [DCA] < [Cl] < [BF<sub>4</sub>] < [PF<sub>6</sub>] < [NTf<sub>2</sub>] (Pham et al. 2010; Frade and Afonso 2010; Ranke et al. 2004). Some studies concluded that the cytotoxicity of ionic liquids cannot be systematically estimated by a summation of the independent effects of the cation and anion (Petkovic et al. 2011; Papaiconomou et al. 2010; Torrecilla et al. 2010; Palomar et al. 2010). The use of biocompatible anions (e.g. amino acids, non-nutritive sweeteners) may decrease the toxicity and biological activity, but may increase biodegradability (Pham et al. 2010; Petkovic et al. 2011; Stasiewicz et al. 2008).

As was shown in a recent study that water salinity influence the toxicity of ILs—higher chloride concentrations prevent cations from interacting with the molecules in the cell wall structures (Frade and Afonso 2010; Latala et al. 2010). Also was observe that sensitivity of the marine microorganisms decrease in the following order cyanobacterium > diatoms > green algae (Frade and Afonso 2010; Latala et al. 2010).

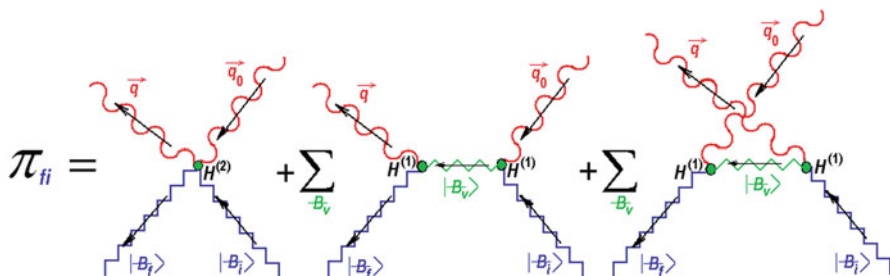
Usually pyridinium-based ILs obey general rules toxicity and biodegradability of pyridinium-based ILs. They are more environmental friendly than imidazolium ILs but have been found some examples that are more toxic than the corresponding imidazolium, pyrrolidinium-, piperidinium-based ILs (Coleman and Gathergood 2010; Papaiconomou et al. 2007, 2010; Stolte et al. 2007b; Docherty and Kulpa 2005). Their toxicity increase with the alkyl chain length, and also increase with increasing the length of both alkyl and alkoxyethyl (Petkovic et al. 2011; Papaiconomou et al. 2007, 2010). Position of the methyl group on pyridinium cation it is questionable, some authors said that has limited influence on toxicity, while by adding an extra substituent (methyl group) leads to an increase in toxicity (Petkovic et al. 2011; Papaiconomou et al. 2010; Stasiewicz et al. 2008). Ranke et al. (2007) reported that an additional methyl group in positions R2 or R3 reduce toxicity (IPC-81 cells) and in position R4 increased toxicity (IPC-81 cells), whereas Kumar et al. (2009) reported that presence of an methyl group in any position lead to a minor reduction of toxicity (MCF7 cells). Stolte et al. (2007a) concluded that the 4-(dimethylamino)pyridinium cation and the ethoxymethyl side chain exhibit higher cytotoxicities. With increasing of alkoxy chain lengths (C3–C18) toxicity increased, while for 1-alkoxymethyl-3-hydroxypyridinium and 1-alkoxymethyl-3-dimethylaminopyridinium chlorides have

been reported null/weak and strong biocidal effects (Petkovic et al. 2011). The nature of substituents in position R3 in the pyridine ring has a very big influence on the toxicity (Petkovic et al. 2011). Presence of an ester group into long alkyl chains reduced toxicity and improved ecotoxicity of pyridine ILs (Pham et al. 2010). Bis(pyridinium) ILs are only slightly toxic to the microorganisms and showed extremely poor mineralization (Ford et al. 2010). Pyridinium ILs with a C4 alkyl chain at the one-position gave poor biodegradabilities, and the introduction of a methyl group to the three-position of the pyridinium core do not increased biodegradation (Coleman and Gathergood 2010; Petkovic et al. 2011; Harjani et al. 2008, 2009). Docherty et al. (2007) found that Py4-3Me Br is metabolized by the activated sludge community (Pham et al. 2010; Docherty et al. 2007). Full mineralization was achieved for specifically designed ILs as those constituted by pyridinium rings with longer alkyl side chains or hydroxyl groups combined with biodegradable anions as saccharinate or octylsulfate (Coleman and Gathergood 2010; Stasiewicz et al. 2008; Abrusci et al. 2011; Stolte et al. 2008). Presence of a 1-(2-hydroxyethyl) side chain showed high levels of biodegradation while methyl or ethyl ether side chains showed significantly lower levels of biodegradability, acetal and carbamate functionalities also showing low levels of mineralization (Ford et al. 2010). Ester group in the side chain of pyridinium ILs improved the primary biodegradability of the cation (Coleman and Gathergood 2010; Petkovic et al. 2011; Harjani et al. 2009). Pyridine ILs with ester group in position "1" or an ester linkage from the 3-carboxy group on pyridine ring are classified as readily biodegradable, while amide linkage from the 3-carboxy group form a IL with poor biodegradability (Coleman and Gathergood 2010). In case of pyridine ILs the acesulfamate derivatives gave better biodegradation than the saccharinates (Coleman and Gathergood 2010; Pham et al. 2010; Stasiewicz et al. 2008). Recently was propose for Py4-3Me Br (1-butyl-3-methylpyridinium bromide) two degradation pathway (Coleman and Gathergood 2010; Pham et al. 2010; Petkovic et al. 2011): one by Pham et al. (2009), which implies the hydroxylation of the side chain, and the second pathway involve unsaturation of the alkyl side chain and hydroxylation of the aromatic ring (Docherty et al. 2010).

Being the exposed structural reaches of ILs a representative class of them will be in this study employed for the quantum bondons search by the aid of computed spectra in the Raman/IR regimes, while establishing the associate rules for their experimental identification.

### 13.2 Bondonic Information with Raman Scattering (Putz 2010a)

Just to give a conceptual glimpse of how the present bondonic approach (Putz 2010a, b; Putz and Ori 2015, see Chap. 10; Putz et al. 2015a, b, see Chaps. 11 and 12; Putz 2015) may be employed, the scattering phenomena are considered within its Raman realization (Smekal 1923; Raman and Krishnan 1928, 1929; Landsberg and Mandelstam 1928), viewed as a sort of generalized Compton (1923) scattering process, *i.e.*, extracting the structural information from various systems (atoms,



**Fig. 13.3** The Feynman diagrammatical sum of interactions entering the Raman effect by connecting the single and double photonic particles' events in absorption (*incident wave light*  $\vec{q}_0, \nu_0$ ) and emission (*scattered wave light*  $\vec{q}, \nu$ ) induced by the quantum first  $H^{(1)}$  and second  $H^{(2)}$  order interaction Hamiltonians of Eqs. (13.1) and (13.2) through the initial  $|B_i\rangle$ , final  $|B_f\rangle$ , and virtual  $|B_v\rangle$  bondonic states. The first term accounts for absorption (A)-emission (E) at once, the second term sums over the virtual states connecting the absorption followed by emission, while the third term sums over virtual states connecting the absorption following the emission events. (Putz 2010a, 2012a)

molecules, crystals, *etc.*) by modeling the inelastic interaction between an incident IR photon and a quantum system (here the bondons of chemical bonds in molecules), leaving a scattered wave with different frequency and the resulting system in its final state (Freeman 1974; Thomas 1991; Sutton 2009). Quantitatively, one firstly considers the interaction Hamiltonian as being composed by two parts (Putz 2010a)

$$H^{(1)} = -\frac{e_B}{m_B} \sum_j \left[ \vec{p}_{Bj} \cdot \vec{A}(\vec{r}_j, t) \right] \quad (13.1)$$

$$H^{(2)} = \frac{e_B^2}{2m_B} \sum_j \vec{A}^2(\vec{r}_j, t) \quad (13.2)$$

accounting for the linear and quadratic dependence of the light field potential vector  $\vec{A}(\vec{r}_j, t)$  acting on the bondons "j", carrying the kinetic moment  $p_{Bj} = m_{Bj} v_{Bj}$ , charge  $e_B$  and mass  $m_B$ . Then, noting that, while considering the quantified incident ( $\vec{q}_0, \nu_0$ ) and scattered ( $\vec{q}, \nu$ ) light beams, the interactions driven by  $H^{(1)}$  and  $H^{(2)}$  model the changing in one- and two- occupation numbers of photonic trains, respectively.

In this context, the transition probability between the initial  $|B_i\rangle$  and final  $|B_f\rangle$  bondonic states writes by squaring the sum of all scattering quantum probabilities that include absorption (A, with  $n_A$  number of photons) and emission (E, with  $n_E$  number of photons) of scattered light on bondons, see Fig. 13.3.

Analytically, one has the *initial-to-final* total transition probability (Heitler 1954) dependence here given as

$$\begin{aligned} d^2 \Pi_{fi} &\sim \frac{1}{\hbar} |\pi_{fi}|^2 \delta(E_{|B_i\rangle} + h\nu_0 - E_{|B_f\rangle} - h\nu) \nu^2 d\nu d\Omega \\ &= \frac{1}{\hbar} |\langle f; n_A - 1, n_E + 1 | H^{(2)} | n_A, n_E; i \rangle| \end{aligned}$$

$$\begin{aligned}
& + \sum_{\mathcal{B}_v} \left\{ \frac{\langle \mathcal{B}_f; n_A - 1, n_E + 1 | H^{(1)} | n_A - 1, n_E; \mathcal{B}_v \rangle}{E_{|\mathcal{B}_i\rangle} - E_{|\mathcal{B}_v\rangle} + h\nu_0} \right. \\
& \quad \times \left. \langle \mathcal{B}_v; n_A - 1, n_E | H^{(1)} | n_A, n_E; \mathcal{B}_i \rangle \right\} \\
& + \sum_{\mathcal{B}_v} \left\{ \frac{\langle \mathcal{B}_f; n_A - 1, n_E + 1 | H^{(1)} | n_A, n_E + 1; \mathcal{B}_v \rangle}{E_{|\mathcal{B}_i\rangle} - E_{|\mathcal{B}_v\rangle} - h\nu} \right. \\
& \quad \times \left. \langle \mathcal{B}_v; n_A, n_E + 1 | H^{(1)} | n_A, n_E; \mathcal{B}_i \rangle \right\}^2 \\
& \quad \times \delta \left( E_{|\mathcal{B}_i\rangle} + h\nu_0 - E_{|\mathcal{B}_f\rangle} - h\nu \right) \nu^2 d\nu d\Omega
\end{aligned} \tag{13.3}$$

At this point, the conceptual challenge appears to explore the existence of the Raman process itself from the bondonic description of the chemical bond that turns the incoming IR photon into the (induced, stimulated, or spontaneous) structural frequencies

$$\nu_{v \leftarrow i} = \frac{E_{|\mathcal{B}_i\rangle} - E_{|\mathcal{B}_v\rangle}}{h} \tag{13.4}$$

As such, the problem may be reshaped in expressing the virtual state energy  $E_{|\mathcal{B}_v\rangle}$  in terms of bonding energy associated with the initial state

$$E_{|\mathcal{B}_i\rangle} = E_{bond} \tag{13.5}$$

that can be eventually measured or computationally predicted by other means. However, this further implies the necessity of expressing the incident IR photon with the aid of bondonic quantification; to this end the Einstein photo-electric relationship is appropriately reloaded in the form

$$h\nu_{v \leftarrow i} = \frac{m_{\mathcal{B}} v_{\mathcal{B}}^2}{2} = \frac{1}{4} \frac{v_{\mathcal{B}}^2 \hbar^2}{E_{bond} X_{bond}^2} (2\pi n_v + 1)^2 \tag{13.6}$$

where the bondonic mass (Putz 2010a, b, 2012a, b, 2015a, b; Putz and Ori 2015, see Chap. 10 of this monograph; Putz et al. 2015a, b, see Chaps. 11 and 12 of this monograph)

$$m_{\mathcal{B}} = \frac{\hbar^2 (2\pi n + 1)^2}{2 E_{bond} X_{bond}^2}, n = 0, 1, 2, \dots \tag{13.7}$$

was firstly implemented. Next, in terms of representing the turn of the incoming IR photon into the structural *wave*-frequency related with the bonding energy of initial state, see Eq. (13.5); the time of wave-bond  $t_{bond} = \hbar/E_{bond}$  is here considered to further transform Eq. (13.6) to the yield

$$h\nu_{v \leftarrow i} = \frac{1}{4} \frac{v_{\mathcal{B}}^2 E_{bond}^2 t_{bond}^2}{E_{bond} X_{bond}^2} (2\pi n_v + 1)^2 = \frac{1}{4} E_{bond} \frac{v_{\mathcal{B}}^2}{v_{bond}^2} (2\pi n_v + 1)^2 \tag{13.8}$$

where also the corresponding wave-bond velocity was introduced

$$v_{bond} = \frac{X_{bond}}{t_{bond}} = \frac{1}{\hbar} E_{bond} X_{bond} \quad (13.9)$$

It is worth noting that, as previously was the case with the dichotomy between bonding and bondonic times respectively, (Putz et al., see Chap. 12), the bonding velocity of Eq. (13.9) clearly differs by the previous bondonic velocity, see Eq. (12.6) from Putz et al. 2015b, Chap. 12 of this book, since the actual working expression

$$\frac{v_{bond}}{c} = (E_{bond}[kcal/mol])(X_{bond}[A])^0 2.19758 \times 10^{-3}[\%] \quad (13.10)$$

provides considerably lower values than those listed in Table 13.1—again, due to missing the inclusion of the particle mass' information, unlike is the case for the bondonic velocity.

Returning to the bondonic description of the Raman scattering, one replaces the virtual photonic frequency of Eq. (13.8) together with Eq. (13.5) back in the Bohr-type Eq. (13.4) to yield the searched quantified form of virtual bondonic energies in Eq. (13.3) and Fig. 13.1, analytically (Putz 2010a)

$$\begin{aligned} E_{|\mathcal{B}_v\rangle} &= E_{bond} \left[ 1 - \frac{1}{4} \frac{v_{\mathcal{B}}^2}{v_{bond}^2} (2\pi n_v + 1)^2 \right] \\ &= E_{bond} \left[ 1 - 16\pi^2 \frac{(2\pi n_v + 1)^2}{64\pi^2 \frac{E_{bond}^2 X_{bond}^2}{\hbar^2 c^2} + (2\pi n_v + 1)^4} \right] \end{aligned} \quad (13.11)$$

or numerically as (Putz 2010a):

$$E_{|\mathcal{B}_v\rangle} = E_{bond} \left[ 1 - \frac{16\pi^2 (2\pi n_v + 1)^2}{\left\{ 0.305048 \times 10^{-6} \times \left( E_{bond}[kcal/mol] \times X_{bond}[A] \right)^2 \right\} + (2\pi n_v + 1)^4} \right], n_v = 0, 1, 2 \dots \quad (13.12)$$

Remarkably, the bondonic quantification (13.12) of the virtual states of Raman scattering varies from negative to positive energies as one moves from the ground state to more and more excited states of initial bonding state approached by the incident IR towards virtual ones, as may be easily verified by considering particular bonding data, see (Putz 2010a, b, 2012a, b). In this way, more space is given for future considerations upon the inverse or stimulated Raman processes, proving therefore the direct involvement of the bondonic reality in combined scattering of light on chemical structures.

**Table 13.1** The list of ionic liquids (ILs), being of ecotoxicological interest, worked for the present bondonic analysis; for each IL compound there are listed: their identification code by Chemical Abstract Service ID/CAS (Bremen University Data Base 2014; Chemical Book 2014); the evaluated LogEC<sub>50</sub> for their action on acetylcholinesterase (AChE) enzyme (Torrecilla et al. 2009), the computed, within AM1 (HyperChem 2002), for the anion-cation distance employed for bondonic radius of action (X<sub>bond</sub>), the IL polarizability to be considered jointly with heat of formation (E<sub>heat</sub>) into Eq. (13.28), and along to binding energy (E<sub>bond</sub>) into Eq. (13.12) to produce the bondon quantum level indices solution {n<sub>v/bondon</sub>} along the predicted bondonic information as the bondon-to-electron mass S<sub>m</sub>, bondon-to-light velocity S<sub>v</sub>, bondon-to-electron charge S<sub>e</sub>, and the bondonic life time vs. bonding spectral fluctuation time t<sub>B</sub>, through employing the basic formulas (13.29)-(13.33), respectively; the spectral IL-bondon's identification {n<sub>v</sub>, E<sub>v</sub>, D<sub>v</sub>, D<sub>v</sub>} is given and depicted following the actual Raman-IR algorithm (see text for details), while the molecular 3D-orbital distribution is also given for the immediately below level of the identified bondon (B) in the Raman-IR algorithm

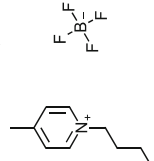
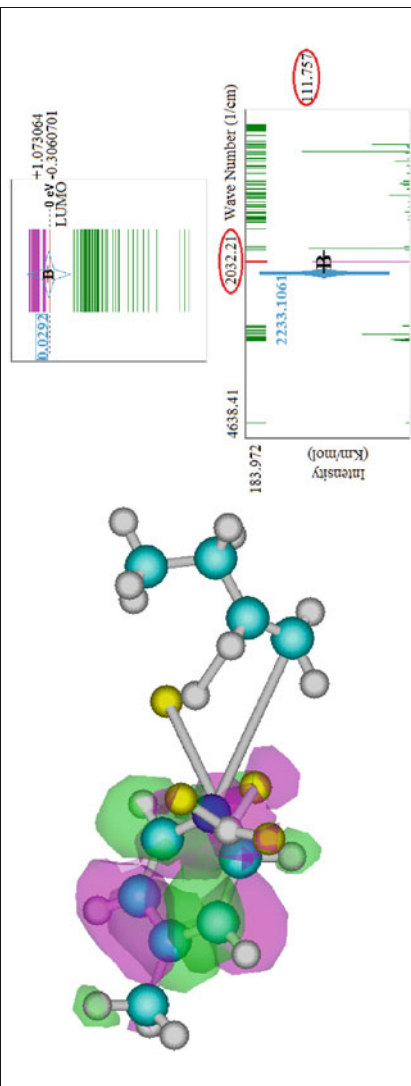
No.	Name Chemical formula (structure weight, D) (ID Code / CAS no.) Ecotoxicity: log <sub>10</sub> EC <sub>50</sub> on AChE systems	Anion-Cation Distance (Å)	Polarizability (Å <sup>3</sup> )	-E <sub>heat</sub> (kcal/mol)	-E <sub>bond</sub> (kcal/mol)	$S_m = \frac{m_B}{m_0}$	$S_v = \frac{v_B}{c}$ [%]	$S_e = \frac{e_B}{e}$	t <sub>B</sub> [×10 <sup>18</sup> ] (seconds) [attoseconds]	t <sub>Bond</sub> [×10 <sup>18</sup> ] (seconds) [attoseconds]	{n <sub>v/bondon</sub> }; E <sub>v</sub> (eV); Next level (eV); D <sub>v</sub> (cm <sup>-1</sup> )
1	1-butyl-4-methylpyridinium tetrafluoroborate (Py4-4Me BF4, 237.05) C <sub>10</sub> H <sub>10</sub> BF <sub>4</sub> N/ 343952-33-0  log <sub>10</sub> EC <sub>50</sub> =1.54	2.468	21.81	225.3467945	3092.139	0.004665	97.2991	0.041927	0.5830 (seconds) [attoseconds]	4.9	{-2.15866, -0.212551, -0.105759, 1.84035}; E <sub>v</sub> = 0.0292; LUMO1 = -0.30607; D <sub>v</sub> = 0.27687; D <sub>0</sub> = 2233.1061
											

Table 13.1 (continued)

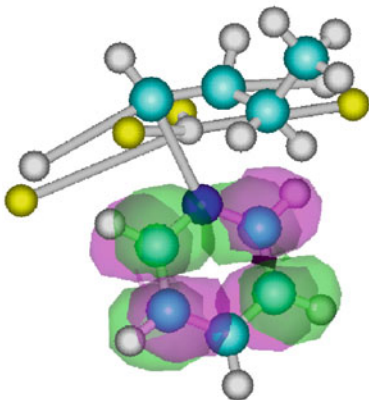
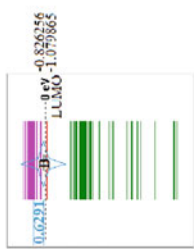
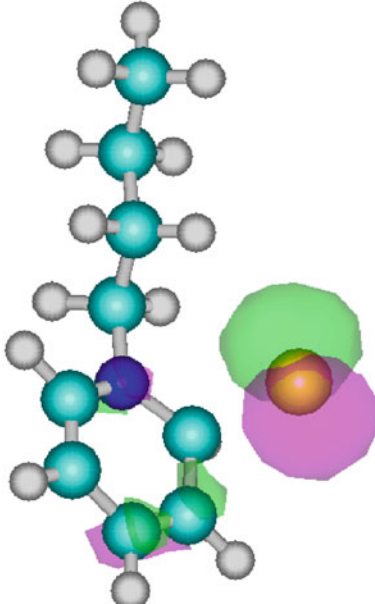
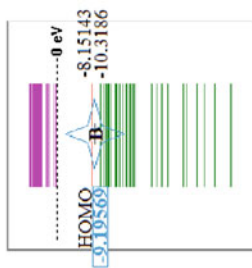
2	<p>1-butylpyridinium tetrafluoroborate (Py4 BF<sub>4</sub>, 223.02) (C<sub>8</sub>H<sub>10</sub>BF<sub>4</sub>N) 203389-28-0</p>  <p><math>\log_{10}EC_{50}=1.8</math></p>	<p>{-2.16403, -0.191054, -0.127256, 1.84572}; E<sub>v</sub> = 0.62909; LUMO2= -0.856256</p>	<p>1.611</p> <p>19.98</p> <p>245.8183119</p> <p>2837.516</p> <p>0.011931</p> <p>92.9728</p> <p>0.025114</p> <p>0.25</p> <p>5.35</p>	
3	<p>1-butylpyridinium bromide (Py4 Br, 216.2) (C<sub>8</sub>H<sub>10</sub>BrN/ 874-80-6)</p>  <p><math>\log_{10}EC_{50}=1.77</math></p>	<p>{-2.07531, -0.209704, -0.108606, 1.757}; E<sub>v</sub> = -9.19573; HOMO2= -10.3186</p>	<p>2.897</p> <p>20.53</p> <p>17.3296020</p> <p>2389.848</p> <p>0.004381</p> <p>96.7465</p> <p>0.03804</p> <p>0.629</p> <p>6.35</p>	

Table 13.1 (continued)

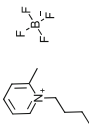
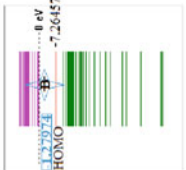
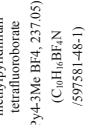
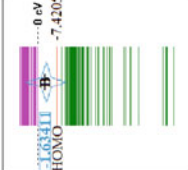
4	<p>1-butyl-2-methylpyridinium tetrafluoroborate (Py4-2Me BF<sub>4</sub>, 237.045328) (C<sub>10</sub>H<sub>10</sub>F<sub>4</sub>N) (286453-46-1)</p>  <p><math>\log_{10}EC_{50}=0.82</math></p>	<p>4.471</p> <p>21.81</p> <p>195.1675993</p> <p>3061.960</p> <p>0.0014354</p> <p>99.1367</p> <p>0.0752123</p> <p>1.826</p> <p>4.957</p>  <p> <math>\epsilon</math>-2.14726,  <math>\epsilon</math>-0.255491,  <math>\epsilon</math>-0.0628187,  1.828951;  <math>E_v</math> =  -1.27974;  HOMO1 =  -7.26457 </p>	<p>5</p> <p>1-butyl-3-methylpyridinium tetrafluoroborate (Py4-3Me BF<sub>4</sub>, 237.05) (C<sub>10</sub>H<sub>10</sub>BF<sub>4</sub>N) (597581-48-1)</p>  <p><math>\log_{10}EC_{50}=1.27</math></p>	<p>1.427</p> <p>21.81</p> <p>187.0139076</p> <p>3053.806</p> <p>0.0141287</p> <p>92.3465</p> <p>0.0239414</p> <p>0.213812</p> <p>4.9704</p>  <p> <math>\epsilon</math>-2.1467,  <math>\epsilon</math>-0.189829,  <math>\epsilon</math>-0.128481,  1.828391;  <math>E_v</math> =  -1.63411;  HOMO1 =  -7.420555 </p>
---	---	---	---	--



Table 13.1 (continued)

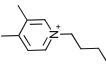
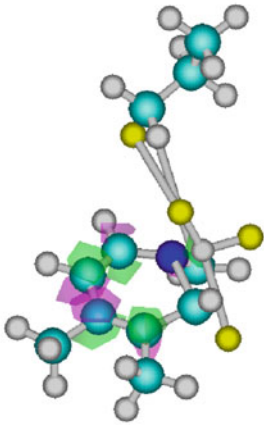
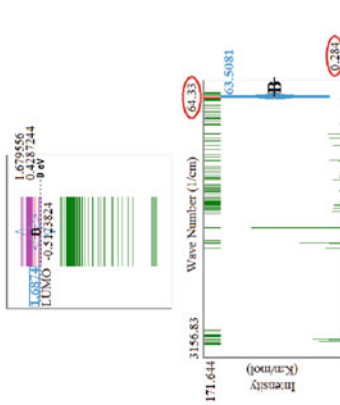
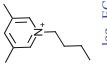
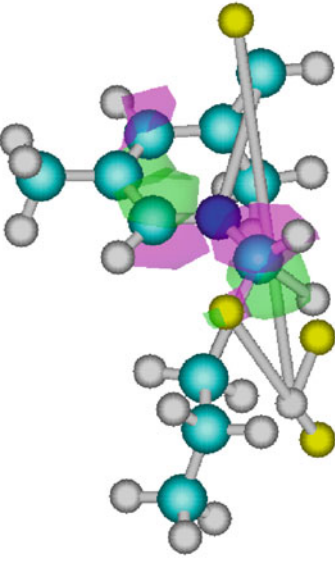
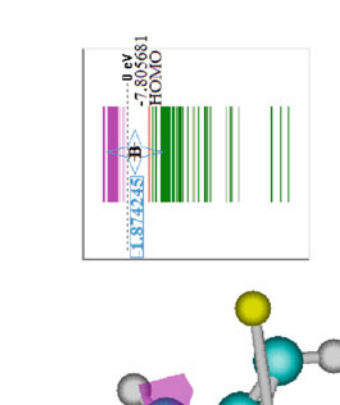
6	<p>1-butyl-3-(4-dimethylpyridinium tetrafluoroborate) (Py4-3Me-4Me BF<sub>4</sub>, 251.0716) (C<sub>11</sub>H<sub>18</sub>BF<sub>4</sub>N) /952429-71-9</p>  <p><math>\log_{10}(\text{EC}_{50})=1.1</math></p>	1.785	23.65	257.5566126	3399.443	0.00811164	95.8252	0.0333373	0.34587	4.4651	<p>{-2.17025, -0.201367, -0.116943, 1.85194}; E<sub>v</sub> = +1.68743; LUMO02 = 1.679556; D<sub>v</sub> = 0.007874; D<sub>o</sub> = 63.5081</p>
 											
7	<p>1-butyl-3-(5-dimethylpyridinium tetrafluoroborate) (Py4-3Me-5Me BF<sub>4</sub>, 251.0716) (C<sub>11</sub>H<sub>18</sub>BF<sub>4</sub>N) /952429-72-0</p>  <p><math>\log_{10}(\text{EC}_{50})=1.17</math></p>	3.990	23.65	175.0944484	3317.380	0.00166361	99.0774	0.0727198	1.57752	4.5755	<p>{-2.14407, -0.252448, -0.0658616, 1.82576}; E<sub>v</sub> = -1.8742452; HOMO1 = -7.805681</p>
 											

Table 13.1 (continued)

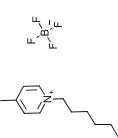

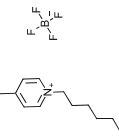
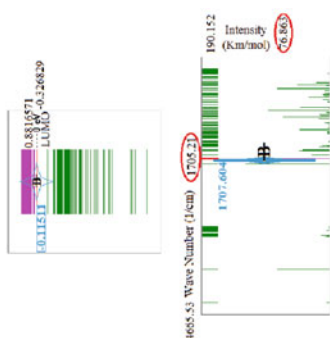
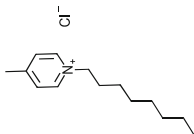
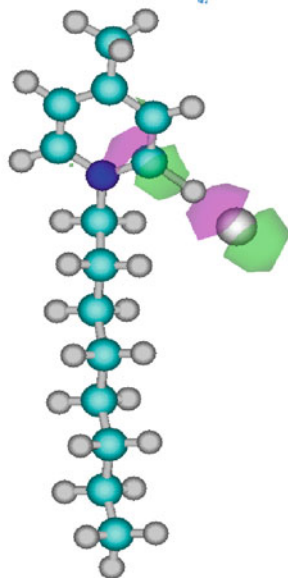
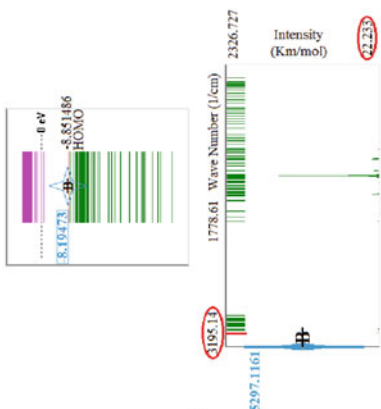
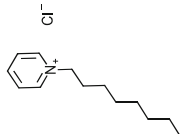
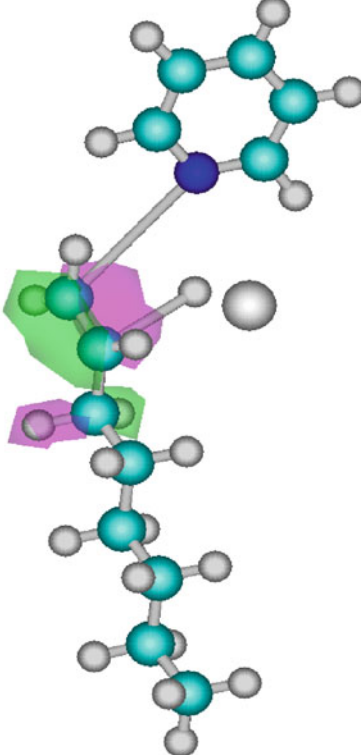
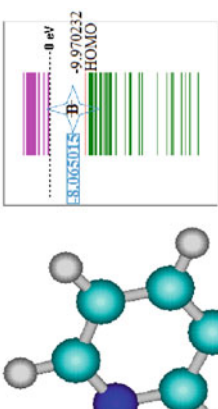
8	<p>1-hexyl-4-methylpyridinium tetrafluoroborate (Py6-Me-BF<sub>4</sub>, 265 (0986) (C<sub>11</sub>H<sub>20</sub>BF<sub>4</sub>N /952429-73-1)</p>  <p><math>\log_{10}EC_{50}=1.48</math></p>	1.711	25.48	282.6013475	3699381	0.00811223	96.1443	0.0347766	0.343549	4.10282	<p>{-2.17767, -0.203028, -0.115282, 1.85936};  <math>E_v =</math>            3.006603;            LUMO4 = 1.840296            LUMO = -0.770937</p> 
9	<p>1-octyl-4-methylpyridinium tetrafluoroborate (Py8-Me-BF<sub>4</sub>, 293.1516) (C<sub>13</sub>H<sub>22</sub>BF<sub>4</sub>N /936239-96-2)</p>  <p><math>\log_{10}EC_{50}=1.22</math></p>	2.562	29.15	201.2906346	4168459	0.00321114	98.5931	0.05866731	0.8253323	3.64132	<p>{-2.15712, -0.233936, -0.0843738, 1.83881};  <math>E_v =</math>            -0.115113;            LUMO1 = -0.326829;            Dv = 0.211716;            Du = 1.707.60389</p> 

Table 13.1 (continued)

<p>10</p> <p>1-octyl-4-methylpyridinium chloride (Py<sub>8</sub>-4Me Cl, 241.8) (C<sub>14</sub>H<sub>23</sub>ClN /141645-91-2)</p>  <p><math>\log_{10}EC_{50}=1.11</math></p>	  <p>3.709</p> <p>15.4563379</p> <p>3800.354</p> <p>0.00168056</p> <p>99.1851</p> <p>0.07744</p> <p>1.55822</p> <p>3.99402</p> <p>{-2.10862, -0.260311, -0.0579992, 1.79031}; E<sub>v</sub> = -8.1947271; HOMO1 = -8.851486; D<sub>v</sub> = 0.656759; D<sub>0</sub> = 5297.11606</p>
<p>11</p> <p>1-octyl-pyridinium chloride (Py<sub>8</sub> Cl, 227.773) (C<sub>13</sub>H<sub>22</sub>ClN /4086-73-1)</p>  <p><math>\log_{10}EC_{50}=1.6</math></p>	  <p>3.543</p> <p>27.17</p> <p>22.9532198</p> <p>3532.757</p> <p>0.00198124</p> <p>98.9699</p> <p>0.0687653</p> <p>1.3275</p> <p>4.29656</p> <p>{-2.10646, -0.249079, -0.0692311, 1.78815}; E<sub>v</sub> = -8.0650148; HOMO1 = -9.970232</p>

Overall, the bondonic characterization of the chemical bond is fully justified by quantum and relativistic considerations, to be advanced as a useful tool in characterizing chemical reactivity, times of reactions, *i.e.*, when tunneling or entangled effects may be rationalized in an analytical manner.

Note that further correction of this bondonic model may be realized when the present point-like approximation of nuclear systems is abolished and replaced by the bare-nuclear assumption in which additional dependence on the bonding distance is involved. While this is left for further communication, in what next we will explore the numerical prediction of the Raman scattering spectra for a series of ionic liquids as based on bondonic information combined with the polarized nature of the chemical structure investigated.

### 13.3 Polarizability Driving Bondonic IL-Spectra

Next, for evaluating the composed polarizability and total energy in the electrostatic anionic-cationic (AC) complex one should rely on the basic principles of electrostatics, starting from the Gauss electric flux law linking the total (source) charge with the electrostatic field created through a closed surface (Putz et al. 2007, 2010; Putz 2012c, 2015c; Putz and Putz 2013)

$$\oint_{\Sigma} \vec{E} d\vec{S} = \frac{1}{\epsilon_0} q_{total} \quad (13.13)$$

With the help of which the Columbus law springs out for a constant electrostatic field on a spherical surface distribution at the given radius ( $r$ ) from the charge point ( $q_{total}$ )

$$\begin{cases} S = 4\pi r^2 \\ E = ct \end{cases}$$

$$\Rightarrow E \oint_{\Sigma} dS = \frac{Q}{\epsilon_0} \Leftrightarrow E \cdot 4\pi r^2 = \frac{Q}{\epsilon_0} \Rightarrow E = \frac{Q}{4\pi \epsilon_0 r^2} \quad (13.14)$$

The electrostatic field immediately relates with the electrostatic force

$$\vec{F} = q \cdot \vec{E} = \frac{1}{4\pi \epsilon_0} \frac{q \cdot Q}{r^3} \vec{r} \quad (13.15)$$

and with the electrostatic potential :

$$U = \int_1^2 \vec{E} \cdot d\vec{l} = \Delta\phi \quad (13.16)$$

which may be further written successively as

$$\begin{aligned}\Delta\phi &= \phi_1 - \phi_2 = \frac{1}{4\pi\epsilon_0} \frac{q}{r_1} - \frac{1}{4\pi\epsilon_0} \frac{q}{r_2} = \frac{q}{4\pi\epsilon_0} \left( \frac{1}{r_1} - \frac{1}{r_2} \right) = \frac{q}{4\pi\epsilon_0} \cdot \frac{r_2 - r_1}{r_1 r_2} \\ &\cong \frac{1}{4\pi\epsilon_0} \frac{ql \cos\theta}{r^2} = \frac{1}{4\pi\epsilon_0} \frac{d \cos\theta}{r^2}\end{aligned}\quad (13.17)$$

when one employed the general expressions for the electrostatic potential

$$\phi = \frac{1}{4\pi\epsilon_0} \frac{\vec{d} \cdot \vec{r}}{r^3}\quad (13.18)$$

and for the dipole moment

$$\vec{d} \cdot \vec{r} = d \cdot r \cdot \cos\theta\quad (13.19)$$

However, from (13.16) to (13.18) there follows that in general one has the electrostatic field-potential relationship

$$\begin{aligned}\vec{E} \cdot \vec{r} &= \phi \\ \Rightarrow \vec{E} \cdot \vec{r} &= \frac{1}{4\pi\epsilon_0} \frac{\vec{d} \cdot \vec{r}}{r^3}\end{aligned}\quad (13.20)$$

leaving with the general electrostatic field-dipole connection too

$$\vec{d} = 4\pi\epsilon_0 r^3 \cdot \vec{E} = \alpha \cdot \vec{E}\quad (13.21)$$

From Eq. (13.21) one recognizes the polarizability basic formulation

$$\alpha = 4\pi\epsilon_0 r^3 \Leftrightarrow POL = ct \cdot R^3, ct = 4\pi\epsilon_0\quad (13.22)$$

allowing further AC-complex polarizability formation as based on the anionic-cationic summation of the associate radii of action

$$R_{AC} = R_A + R_C \cong ct^{-1/3} (POL_A^{1/3} + POL_C^{1/3})\quad (13.23)$$

which corresponds to the actual projective polarizability formulation for the AC (IL) complex

$$POL_{AC} = (POL_A^{1/3} + POL_C^{1/3})^3 [\text{\AA}^3]\quad (13.24)$$

On the same analysis line, when one goes to evaluate the total energy of the AC complex, one has to consider also the electrostatic interaction energy which superimposes to the individual radicalic (atomic or molecular fragments) of A and C subsystems, to get

$$E_{AC} = E_A + E_C - \frac{q_A q_C}{(4\pi\epsilon_0) R_{AC}} \cong E_A + E_C - \frac{q_A q_C}{(4\pi\epsilon_0) ct^{1/3} POL_{AC}^{1/3}}\quad (13.25)$$

Thus producing the working projective form for the total energy produced by the the AC (IL) complex

$$E_{AC} = E_A + E_C - 627.71 \frac{q_A q_C}{P O L_{AC}^{1/3}} [\text{kcal/mol}] \quad (13.26)$$

where one implemented the unitary electrostatic AC conditions  $q_A q_C = (-1)(+1) = -1$  along the atomic units transformation

$$\frac{1}{4\pi\epsilon_0 c t^{1/3}} = 1at = 627.71 \frac{\text{kcal}}{\text{Mol}} \quad (13.27)$$

At this point one could claim that the atomic unit is for energy units/hartrees equal with Hydrogen ground state energy in (13.27) so a factor of  $\frac{1}{2}$  should be added; this was nevertheless absorbed by the fact the bondonic information “travels” back and forth among the pairing electrons in chemical bonding so justifying the working Eq. (13.26).

Worth commenting also about the polarizability influence in chemical bonding structure determined by spectral investigation, the polarizability measures the electronic cloud deformation, so associating with a dipole moment in molecule (electrons-nuclei) which is so involved in scattering reactions: e.g. for a symmetric stretching vibration the polarizability gets smaller and the vibration is Raman-active, yet IR-inactive; contrarily, during the asymmetric stretching vibration the polarizability does not change, and the vibration is IR-active and Raman-inactive (Kendall 1966; Farmer 1974; Nakamoto 1986). However, unlike to IR spectroscopy, a of the deformation of the electron cloud, i.e. of the polarization potential is necessary for a molecule to exhibit a Raman effect; it nevertheless, provides a non-destructive technique by which the chemical structure can be determined with small sample amount without sample preparation requirement; so, Raman spectroscopy is nowadays largely employed for mineral identification and inclusion (including analyses of gemstones and archaeometric objects), characterization of thermal maturity, metamictization, OH content, impurities, speciation & concentration (Cheetham and Day 1987; McMillian and Hofmeister 1988).

The main difference respecting IR spectroscopy resides in the Raman spectroscopy the frequency principle (carrying the energy equal to the energy difference between the two vibrational states, as in Rayleigh scattering) is abolished since higher than the absorption frequency is scattered by molecule so the inelastic photon-structure (bondon in our assessment) occurs and the system (usually in ground states) gains energy from the scattered light so the molecular system reaches a higher energy state—by this process called as—*Stokes scattering*. The other case when the system is already on an excited state from where it loses energy by light (Anti-Stokes) scattering so reaching lower energy level—is much rare at room temperature (Putz 2013).

In the actual photon-bondonic scattering process, there is clear that the Eq. (13.12) is the main analytical structure-spectral tool for determining the bondonic quantum level ( $n_v$ ) as well as their quantum energies levels ( $E_{|B_v\rangle} = E_v$ ); it may be therefore regarded as a kind of eigen-equation for bonding, since it unfolds in terms of bonding

energy  $E_{bond}$  and bondonic radii of action  $X_{bond}$ . However, in order to can solve this equation for the two variables  $\{n_v, E_v\}$  one employs the above polarizability related AC-energy (13.26), yet under the working form:

$$E_v(\text{kcal/mol}) = |E_{Heat}|(\text{kcal/mol}) - 627.71 \frac{1}{(POL[\text{\AA}])^{1/3}} \quad (13.28)$$

in terms of absolute heat of formation which equivalents anion and cation energy summation in Eq. (13.26) since calculated at its turn by subtracting atomic heats of formation from the binding energy, so in formal agreement with Eq. (13.12) too. Accordingly, the present algorithm actually provides the bondonic energy as directly related with the AC-polarizability, which further drives also the bondonic quantum numbers, as well as the energetic spectral placements, see below application. The working AC information of ionic liquids is therefore contained in anion-cation (inter-charged poles) distance ( $\text{\AA}$ ) for working  $X_{bond}$ , the IL polarizability ( $\text{\AA}^3$ ) for the global  $POL_{AC}$ , the IL-binding  $E_{binding}$  (kcal/mol), and IL heat of formation  $E_{heat}$  (kcal/mol), for being combined in the Eqs. (13.12) and (13.28) for the  $\{n_v, E_v\}$  solution for a given IL-system. At this point, the identification of the IL-bondon is made upon the following *Raman-IR algorithm*:

- Once the  $E_v$  is computed and converted in electron-volts (Energy Units Converter 2014) it is identified among the energetic spectra of the concerned ionic liquid;
- One considers the immediate below energetic level, say  $E_i$ , either on bonding (HOMO side) on anti-bonding (LUMO side) parts of molecular spectra;
- The difference  $Dv(eV) = E_v - E_i$  is performed and further considered on the frequency ( $cm^{-1}$ ) scale (Metric Converter 2014)
- For the  $0.05 < Dv < 0.5$  (eV) the  $400 < Dv < 4000$  ( $cm^{-1}$ ) *mid-IR* range is identified for the IL-bondon (e.g. as it is specific for  $H_2O$  bending and stretching vibrations)
- For  $0 < Dv < 0.05$  (eV) that is  $0 < Dv < 400$  ( $cm^{-1}$ ) *far-IR* regime is identified for IL-bondon, as it is specific for  $MO_4, MO_6$  lattice vibrations;
- For  $Dv > 0.5$  (eV) that is  $Dv > 4000$  ( $cm^{-1}$ ) the *near-IR* regime is identified for IL-bondon, which this way is actually associated with Raman-bondon, since being near-IR among the light sources for Raman—Stokes scattering.

Additionally, the IL-bondon is further characterized for the already custom information as the bondon-to-electron mass, bondon-to-light velocity, bondon-to-electron charge, and the bondonic life time vs. bonding spectral fluctuation time, given respectively as (Putz 2010a, 2012a, b, 2015a; Putz et al. 2015b, Chap. 12 of this book):

$$s_m = \frac{m_B}{m_0} = \frac{87.8603}{(E_{bond}[\text{kcal/mol}]) \left( X_{bond}[\text{\AA}] \right)^2} \quad (13.29)$$

$$s_v = \frac{v_B}{c} = \frac{100}{\sqrt{1 + \frac{3.27817 \times 10^6}{(E_{bond}[\text{kcal/mol}])^2 \left( X_{bond}[\text{\AA}] \right)^2}}} [\%] \quad (13.30)$$

$$\zeta_e = \frac{e_B}{e} \sim \frac{1}{32\pi} \frac{(E_{bond}[\text{kcal/mol}]) \left( X_{bond}[\text{\AA}]^0 \right)}{\sqrt{3.27817} \times 10^3} \quad (13.31)$$

$$t_B = \frac{0.0257618}{\zeta_m \zeta_v^2} \times 10^{-15} [\text{s}]_{SI} \quad (13.32)$$

$$t_{bond} = \frac{\hbar}{E_{bond}} = \frac{1.51787}{E_{bond}[\text{kcal/mol}]} \times 10^{-14} [\text{s}]_{SI} \quad (13.33)$$

These bondonic analysis is performed on a representative set of ionic liquids with results displayed in Table 13.1.

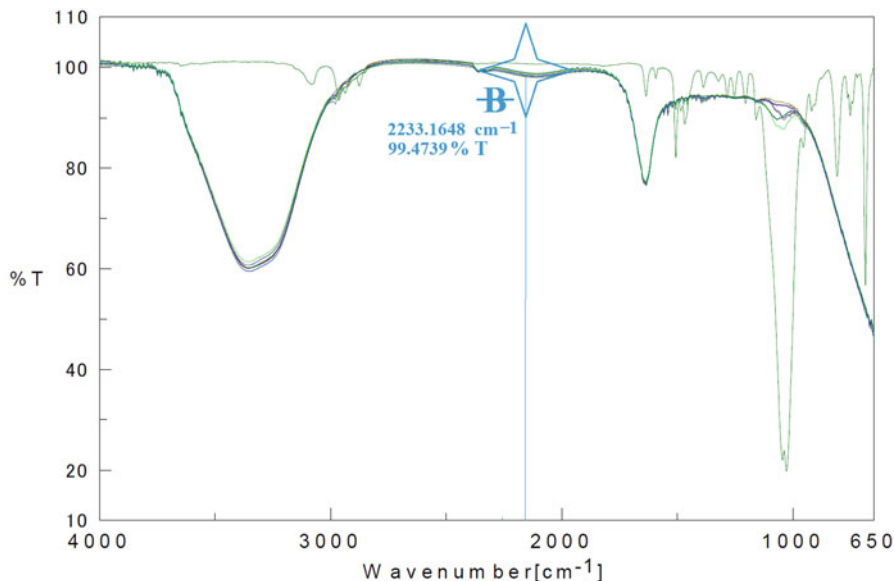
The bondonic IR-Raman identifications of Table 13.1 are discussed and interpreted as following:

- The quantum level indices for all IL-bondons are given invariable in number of four, as a natural consequence of Eq. (13.12), by which always only one is of positive nature, for which also the observed quantum level was identifies, in each case, according with the above bondonic Raman-IR algorithm; however, one can naturally ask “what meaning have the other three bondonic levels?”. Fortunately the answer can be given in the light of entangled chemistry opened by bondonic chemistry, see Chapter 10 of the present monograph (Putz and Ori 2015, see Chap. 10 of this monograph), by which each chemical bonding is predicted in “quaternion states”, so leaving with the answer that the remaining quantum levels with negative quantum indices are in the hidden or entangled spectra of IL-bondons; they nevertheless should be identified by special spectroscopically procedures, eventually involving teleporting information and protocols, not yet available, despite being just started to be imagined (Putz and Ori 2015, see Chap. 10 of this monograph);
- The bondonic prediction/identification in IL-spectra falls as being of IR type (IL nos. 1, 6, 9, and 10 in Table 13.1—being the last case pushed to overtones, almost Raman) and of Raman type (for the rest of ILs of Table 13.1), according with the presented bondonic Raman-IR algorithm; one also may remark that the Raman-bondon generally associates with the no-ring or partially cation ring electronic HOMO occupancy/delocalization, as complementary to IR-bondon which is merely distributed on LUMO ring levels, and vice-versa, respectively. In particular the bondon of Il no.1 (the so called BMPyBF4) was checked with the experimental counterpart identification in the Fig. 13.4, with a reliable rationale as corresponding with 0.5 [%] of IR absorption since belonging to LUMO state.

On the other side, the bondonic specific features for the concerned IL of Table 13.1 are listed as:

- The bondonic mass, although less than that of electron in al case, is not so small as compared with other “classical” carbon systems (Putz et al. 2015a, see Chap. 11 of this monograph) or polymeric ribbons, e.g. silanes as precursors of silicenes (Putz et al. 2015b, see Chap. 12 of this monograph); since mass information is a main information for the bondons, it already qualifies the modeling chemical





**Fig. 13.4** The IR overlapping of the gas-phase (green line) BMPyBF<sub>4</sub> (1-butyl-4-methylpyridinium tetrafluoroborate, the IL no. 1 in the Table 13.1), with the same IL solvated in water, as well as in an acidic buffer with pH = 2.8, and in the TRIS/THAM (tris(hydroxymethyl)aminomethane) base buffer at higher 0.07 and lower 0.007 concentration, respectively; the predicted IL-bondon at 2233.1648 cm<sup>-1</sup> in Table 13.1 corresponds here with a special region of middle IR spectra, actually not assigned to an existing electronic (bending or stretching) vibration, yet being sensitive as for 0.5361 [%] absorption from the total incoming light as characteristic for the AC binding itself

bonding type as being of ionic nature, in accordance with the general bondonic prescriptions (Putz 2010a, 2012a, b, 2015a, Putz et al. 2015b, see Chap. 12 of this monograph);

- The bosonic velocity of bondons is moderate high, so below the predicted extreme value as of 99.9951 [% c], while carrying a less charge than the electron, yet in a range between one—to—two order degrees respecting electronic unity; these feature, further confirms the ionic character of chemical bonding carried by the bondon, so natural for ionic liquids;
- Yet, the bondonic analysis provide also a reminiscence of the multiple bonding character in IL, apart of the dominant ionic bonding, due to the bondonic life time that lays in the range of attoseconds; although with an observable perspective (Koke et al. 2010), this finding truly impedes the nowadays direct observation for IL-bondons, since the associated quantum level lifetime fluctuation period ( $t_{Bond}$  in Table 13.1) actually included from few-to-tenths of bondonic oscillations; nevertheless, for when available the experimental ultra-fast (atto) spectroscopy below the 6 attoseconds (i.e. to a quarter or below of the atomic unit of time that is 24 attoseconds) the present study stil predicts the IL-bondonic observation for the compound no. 10 in Table 13.1, in a Raman spectra.

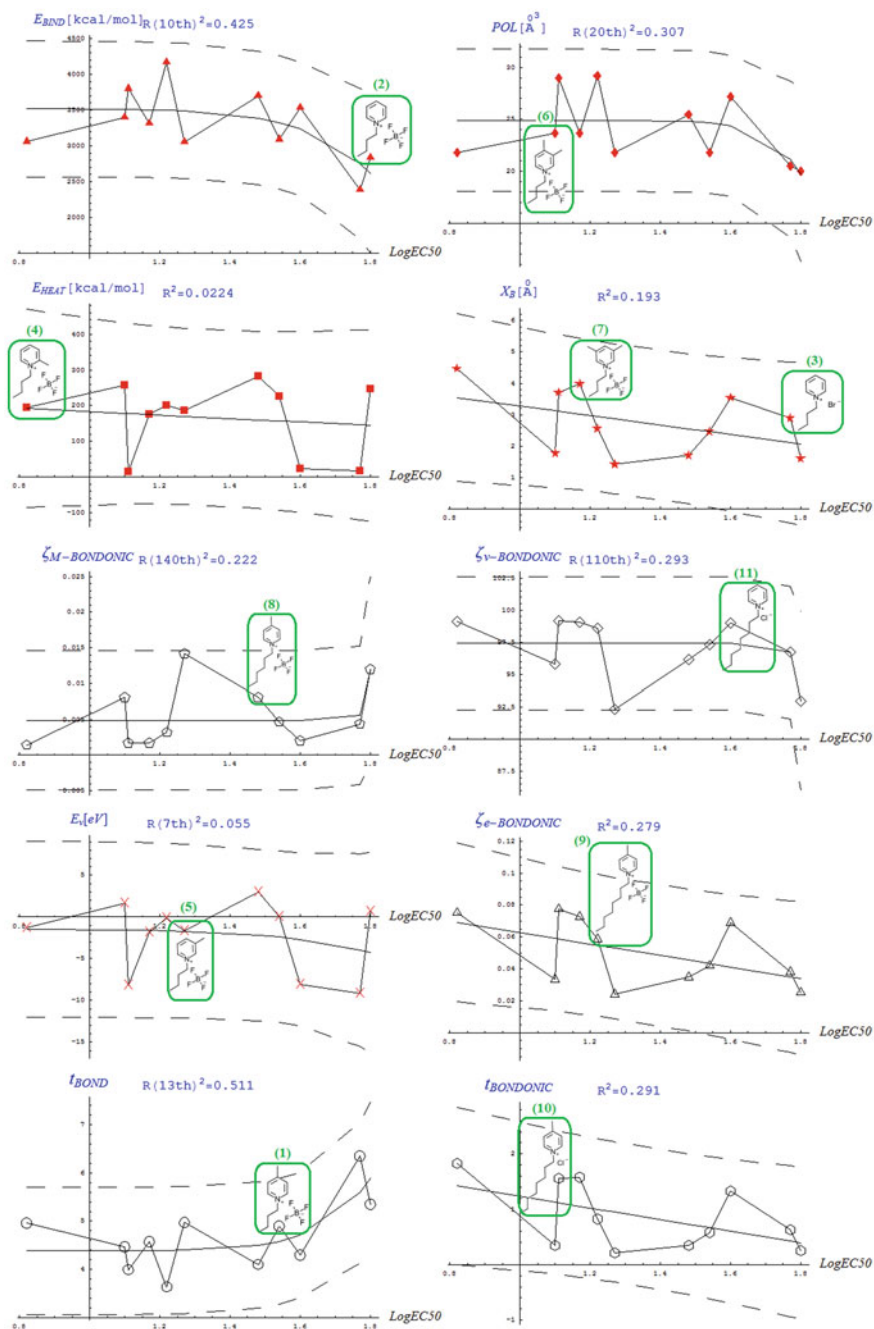
Finally, the structural and bondonic data of IL of Table 13.1 are correlated with the recorded biological activity of the worked IL on the acetylcholinesterase, just to see

how and in which degree these correlation works from a sub-atomic level of bondons to the macroscopic effects of biological activity. These correlations are represented in Fig. 13.5

The results of Fig. 13.5 display intriguing insight in the bondonic chemical influence on biological activity, at least for the present IL cases:

- The shape of bondonic correlations goes in groups like: bondonic mass ratio ( $\zeta_{m(\text{or } M)}$ ) with bondonic level ( $E_v$ ) which goes like heat of formation ( $E_{\text{heat}}$ ); while A-C bondonic radii ( $X_{\text{bond}}$ ) parallels the bondonic time correlation ( $t_{\text{BONDONIC}}$ ) which are followed by bondonic-charge ( $\zeta_e$ ) and the bondonic bosonic velocity ( $\zeta_v$ ); interestingly the AC polarization (POL) barely mirrors the bonding energy ( $E_{\text{BOND}}$ ) and fluctuation life time ( $t_{\text{BOND}}$ );
- All IL considered structural information correlated extremely poor with actual EC50 activity, so confirming the structural-activity relationship should be performed by involving more globally averaged chemical information, so averaging the quantum fluctuations that seems not directly affecting the chemical-biological interaction;
- Moreover, some correlation actually does not exist at all, unless one “magnifies” with higher order of correlations; for instance one needs the 7th order of correlation to produce a square-root of correlation about 0.055 which actually correspond with a “born from vacuum” correlation; till the correlation of the bondonic velocity that has to be considered until the 110th order so that the maximum achievement of  $R^2 = 0.293$  correlation factor to be reached, in the same range for bondonic mass correlation ( $R^2 = 0.222$ ) which nevertheless is obtained in the 140th degree of correlation; this leads with the idea the bondon, although present in chemical bonding, is actually missing in chemical-biological interaction, an issue that should certainly further explored also for other chemical-biological systems;
- Interestingly, “the best” correlation is recorded when the spectral lifetime is considered against EC50 ( $R^2 \sim 0.511$ ), while also bondonic lifetime just follows ( $R^2 \sim 0.291$ ) without the need of higher degrees of correlations to be performed, a matter found also for bondonic charge and action radii; so leaving with the hope of IL-bondonic observation for then when the sub-atto-spectroscopy techniques will be available.

Overall, one remains with the fruitful idea that the bondons for ionic liquids, although predicted in their Raman and IR spectra, depend for their observation by the evolving spectroscopically technique under-atto-seconds, while having actually no direct influence in bio/eco-toxicological activities; however, there is still room for exploring the role of the bondonic information in chemical reactivity indices, as well as in topo-reactivity indices that are susceptibly being directly influenced by them; then with such enriched topo-reactivity indices one can further test for chemical-biological correlation; if the correlation is higher than with no-bondonic information incorporated, then the bondonic influence through the driving chemical reactivity indices appears to be essential; that will be another form of “entangled” bondonic influence. All is to be explored in the near future towards a complete chemical field theory of chemical bonding in special and of chemical interaction (biological included) in general.



**Fig. 13.5** The bonding and bondonic correlations against  $\text{LogEC}_{50}$  activity for the ionic liquids information of Table 13.1 action on acetylcholinesterase enzyme (see text for details)

## 13.4 Conclusions

Ionic liquids with their special physicochemical properties give us a new perspective on the future of chemistry. They find their place in many and diverse applications. Because of their modular nature, their physicochemical properties can be fine-tuned depending on their future purpose, by modifying the structural factors of cations and anions can be obtained a wide diversity of ILs. Even if ILs are considered as the future for a greener chemistry, their impact on the environment should be properly tested. Toxicity, biodegradation, mineralization and bioaccumulation studies for ILs should be made on all Kingdoms in the classification of living organisms. Ionic liquids containing pyridinium cation has been found to be more environmental friendly than those with imidazolium cation. This encourage that by small structural manipulation of the pyridinium skeleton can be obtained IL with proper properties for the desired application and a low environmental risk. It is a challenging for researchers to find the balance between design of ILs which involve certain physicochemical properties required by the scope of the ILs, and their biodegradability and toxicity, minimizing the toxicity and maximizing the biodegradability, even if they do not always vary in this direction. From quantum structure perspective, IL are interesting systems to study their associated bondons—as the quantum quasi particles of chemical bonding; this because, as a coupled anion-cation system, the bondon is mainly localized between the charged poles which offers an implicit dipole momentum which offers the immediate conditions the celebrated complementary Raman-IR spectroscopy may apply so giving the associate spectra for bondon prediction and identification. Accordingly, a dedicated study was unfold with valuable findings among which we are listing: the “quaternion” nature for the quantum indices for bondons, in accordance with earlier entangled nature of bondonic chemistry (Putz and Ori 2015, see Chap. 10 of this monograph) and reinforcing the gravitational space-time bondonic influence at the bondonic level (Putz et al. 2015a, see Chap. 11 of this monograph) to be further investigating; however, from such “quaternionic” folding for IL-bondon, just one level is actually selected to be observable in Raman or IR spectra, upon a specific algorithm respecting the energy (and frequency) difference respecting the next below neighboring level in spectra, thus deciding between vibrational or an excited IR and Raman levels paralleling the increase of the such difference, respectively. However the bondonic observables provides a relatively high mass, bosonic velocity and fermionic charge so placing the IL-Bondon in the ionic chemical bonding category, naturally fro Ionic liquids, yet having also a multi-bonding characteristics by the associated lifetime in the range of attoseconds that also fixes the spectroscopically ultra-fast regime in which these particles may be truly observable; alternatively special spectroscopically quantum information may be designed (Putz and Putz 2012) in order to achieve the bondonic observation by entangled experiments. Finally, the chemical-biological interaction was analyzed through correlating the bondonic information with eco-toxicology data as EC50, yet revealing marginal direct or even high to very high order correlational influence; this actually confirms the sub-atomic nature of the bondon that is actually averaged in the chemical-biological interaction,

yet leaving the open possibility for indirectly influencing it by direct influencing the chemical topo-reactive descriptors and indices (e.g. electronegativity or chemical hardness) that are currently used for such structure-activity relationships (Putz 2015c); these issues remain open for further explorations and communications.

**Acknowledgement** Authors thank West University of Timișoara; Faculty of Chemistry, Biology, Geography; and Biology-Chemistry Department, for working and research facilities provided for the present joint chapter though the recent accredited "Laboratory of Computational and Structural Physical-Chemistry for Nanosciences and QSAR". AMP kindly thanks Romanian Academy too.

## References

- Abrusci C, Palomar J, Pablos JL, Rodriguez F, Catalina F (2011) Efficient biodegradation of common ionic liquids by *Sphingomonas paucimobilis* bacterium. *Green Chem* 13:709–717
- Allen CR, Richard PL, Ward AJ, van de Water LGA, Masters AF, Maschmeyer T (2006) Facile synthesis of ionic liquids possessing chiral carboxylates. *Tetrahedron Lett* 47(41):7367–7370
- Anthony L, Maginn EJ, Brennecke JF (2001) Solution thermodynamics of Imidazolium-Based Ionic liquids and water. *J Phys Chem B* 105(44):10942–10949
- Anthony JL, Maginn EJ, Brennecke JF (2002) Solubilities and thermodynamic properties of gases in the ionic liquid 1-n-Butyl-3-methylimidazolium hexafluorophosphate. *J Phys Chem B* 106(29):7315–7320
- Appetecchi GB, Montanino M, Zane D, Carewska M, Alessandrini F, Passerini S (2009) Effect of the alkyl group on the synthesis and the electrochemical properties of N-alkyl-N-methylpyrrolidinium bis(trifluoromethanesulfonyl)imide ionic liquids. *Electrochim Acta* 54:1325–1332
- Boethling RS (1994) Cationic surfactants. In: Cross J, Singer EJ (Eds) *Surfactant science series*, vol 53. Marcus Dekker, New York; pp 95–135
- Bremen University Data Base (2014) <http://www.il-eco.uft.uni-bremen.de/>. Accessed July 2014
- Calvano CD, Ceglie CD, D'Accolti L, Zambonin CG (2012) MALDI-TOF mass spectrometry detection of extra-virgin olive oil adulteration with hazelnut oil by analysis of phospholipids using an ionic liquid as matrix and extraction solvent. *Food Chem* 134(2):1192–1198
- Carrera GVSM, Frade RFM, Aires-De-Sousa J, Afonso CAM, Branco LC (2010) Synthesis and properties of new functionalized guanidinium based ionic liquids as non-toxic versatile organic materials. *Tetrahedron* 66(45):8785–8794
- Cheatham AK, Day P (1987) *Solid state chemistry—techniques* (Chap. 9). Clarendon Press, Oxford
- Chemical Book (2014) <http://www.chemicalbook.com/>. Accessed July 2014
- Cho CW, Jeon YC, Pham TP, Vijayaraghavan K, Yun YS (2008) The ecotoxicity of ionic liquids and traditional organic solvents on microalga *Selenastrum capricornutum*. *Ecotoxicol Environ Saf* 71(1):166–171
- Coleman D, Gathergood N (2010) Biodegradation studies of ionic liquids *Chem Soc Rev* 39: 600–637
- Compton A (1923) A quantum theory of the scattering of X-rays by light elements. *Phys Rev* 21:483
- Costa Gomes MF (2007) Low-pressure solubility and thermodynamics of solvation of carbon dioxide, ethane, and hydrogen in 1-Hexyl-3-methylimidazolium Bis(trifluoromethylsulfonyl)-amide between temperatures of 283 and 343 K. *J Chem Eng Data* 52:472–475
- Couling DJ, Bernot RJ, Docherty KM, Dixon JK, Maginn EJ (2006) Assessing the factors responsible for ionic liquid toxicity to aquatic organisms via quantitative structure-property relationship modeling. *Green Chem* 8:82–90

- Deng Y, Morrissey S, Gathergood N, Delort A-M, Husson P, Costa Gomes MF (2010) The presence of functional groups key for biodegradation in ionic liquids: effect on gas solubility. *ChemSusChem* 3:377–385
- Deng Y, Husson P, Delort A-M, Besse-Hoggan P, Sancelme M, Costa Gomes MF (2011) Influence of an oxygen functionalization on the physicochemical properties of ionic liquids: density, viscosity, and carbon dioxide solubility as a function of temperature. *J Chem Eng Data* 56(11):4194–4202
- Deng Y, Besse-Hoggan P, Husson P, Sancelme M, Delort AM, Stepnowskic P, Paszkiewicz M, Goelbiowskic M, Costa Gomes MF (2012) Relevant parameters for assessing the environmental impact of some pyridinium, ammonium and pyrrolidinium based ionic liquids. *Chemosphere* 89(3):327–333
- Docherty K, Kulpa C (2005) Toxicity and antimicrobial activity of imidazolium and pyridinium ionic liquids. *Green Chem* 7:185–189
- Docherty KM, Dixon JK, Kulpa CF (2007) Biodegradability of imidazolium and pyridinium ionic liquids by an activated sludge microbial community. *Biodegradation* 18:481–493
- Docherty KM, Joyce MV, Kulacki KJ, Kulpa CF (2010) Novel microbial biodegradation and metabolite toxicity of three Pyridinium-Cation ionic liquids. *Green Chem* 12:701–712
- Energy Units Converter (2014) <http://www.colby.edu/chemistry/PCChem/Hartree.html>. Accessed July 2014
- Farmer VC (1974) The infrared spectra of minerals. Monograph, no. 4. Mineralogical Society of London, London
- Ferraz R, Branco LC, Prudêncio C, Noronha JP, Petrovski Ž (2011) Ionic liquids as active pharmaceutical ingredients. *ChemMedChem* 6(6):975–985
- Florindo C, Araújo JMM, Alves F, Matos C, Ferraz R, Prudêncio C, Noronha JP, Petrovski Ž, Branco L, Rebelo LPN, Marrucho IM (2013) Evaluation of solubility and partition properties of ampicillin-based ionic liquids. *J Pharm* 456(2):553–559
- Ford L, Harjani JR, Atefi F, Garcia MT, Singer RD, Scammells PJ (2010) Further studies on the biodegradation of ionic liquids. *Green Chem* 12: 1783–1789
- Frade RFM, Afonso CAM (2010) Impact of ionic liquids in environment and humans: an overview. *Hum Exp Toxicol* 29(12):1038–1054
- Freeman S (1974) Applications of laser Raman spectroscopy. Wiley, New York
- Fukumoto K, Yoshizawa M, Ohno H (2005) Room temperature ionic liquids from 20 natural aminoacids. *J Am Chem Soc* 127:2398–2399
- Gao H, Zhang Y, Wang HJ, Liu J, Chen J (2010) Theoretical study on the structure and cation-anion interaction of amino acid cation based amino acid ionic liquid  $[Pro]^+ [NO_3]^-$ . *J Phys Chem A* 114(37):10243–10252
- Garcia MT, Gathergood N, Scammells PJ (2005) *Green Chem* 7:9–14
- Gathergood N, Scammells PJ (2002) Design and preparation of room-temperature ionic liquids containing biodegradable side chains. *Aust J Chem* 55:557–560
- Gathergood N, Garcia MT, Scammells PJ (2004) *Green Chem* 6:166–175
- Gathergood N, Scammells PJ, Garcia MT (2006) Biodegradable ionic liquids. Part III: the first readily biodegradable ionic liquids. *Green Chem* 8:156–160
- Harjani JR, Singer RD, Garcia MT, Scammells PJ (2008) *Green Chem* 4:436–438
- Harjani JR, Singer RD, Garcia MT, Peter J (2009) Scammells biodegradable pyridinium ionic liquids: design, synthesis and evaluation. *Green Chem* 11:83–90.
- Heitler W (1954) The quantum theory of radiation, 3rd ed. Cambridge University Press: New York
- Hussey CL (1983) Room temperatures molten salt systems. *Adv Molten Salt Chem* 5:185–229
- Hough WL, Smiglak M, Rodríguez H, Swatloski RP, Spear SK, Daly DT, Pernak J, Grisel JE, Carliss RD, Soutullo MD, Davis JH, Rogers Jr RD (2007) The third evolution of ionic liquids: active pharmaceutical ingredients. *New J Chem* 31:1429–1436
- Howard PH, Boethling RS, Stiteler W, Meylan W, Beauman J (1991) *Sci Total Environ* 635:109–110
- HyperChem (2002) Hypercube Inc. 7.01 [Program package]

- Imperato G, König B, Chiappe C (2007) Ionic green solvents from renewable resources. *Eur J Org Chem* 7:1049–1058
- Jastorff B, Molter K, Behrend P, Weber UB, Filser J, Heimers A, Ondruschka B, Ranke J, Schaefer M, Schroder H, Stark A, Stepnowski P, Stock F, Störmann R, Stolte S, Biermann UW, Ziegert S, Thoming J (2005) *Green Chem* 7:362–372
- Kendall DN (1966) *Applied infrared spectroscopy*. Reinhold Publishing Corporation, NY
- Koke S, Grebing C, Frei H, Anderson A, Assion A, Steinmeyer G (2010) Direct frequency comb synthesis with arbitrary offset and shot-noise-limited phase noise. *Nat Photonics* 4:462–465
- Kumar RA, Papaiconomou N, Lee JM, Salminen J, Clark DS, Prausnitz JM (2009) In vitro cytotoxicities of ionic liquids: effect of cation rings, functional groups, and anions. *Environ Toxicol* 24(4):388–95
- Landsberg G., Mandelstam L. (1928) A novel effect of light scattering in crystals. *Naturwissenschaften* 16:557
- Latala A, Nedzi M, Stepnowski P (2010) Toxicity of imidazolium ionic liquids towards algae. Influence of salinity variations. *Green Chem* 12: 60–64
- Li Y, Li G, Wang X, Zhu Z, Ma H, Zhang T, Jin J (2012) Poly(ionic liquid)-wrapped single-walled carbon nanotubes for sub-ppb detection of CO<sub>2</sub>. *Chem Commun* 48:8222–8224
- Mallakpour S, Rafiee Z (2011a) Ionic liquids as environmentally friendly solvents in macromolecules chemistry and technology, Part I. *J Polym Environ* 19:447–484
- Mallakpour S, Rafiee Z (2011b) Ionic liquids as environmentally friendly solvents in macromolecules chemistry and technology, Part II. *J Polym Environ* 19:485–517
- Marciniak A (2010) The solubility parameters of ionic liquids. *Int J Mol Sci* 11(5):1973–1990
- Marrucho IM, Branco LC, Rebelo LP (2014) Ionic liquids in pharmaceutical applications. *Annu Rev Chem Biomol Eng* 5:527–546
- McMillian PF, Hofmeister A (1988) Infrared and Raman spectroscopy. In: Hawthorne FC (ed) *Spectroscopic methods in mineralogy and geology*. Reviews in mineralogy, vol 18. Mineralogical Society of America, USA, pp 99–159
- Metric Converter (2014) [http://www.ecoterr.com/length\\_units\\_metric\\_standard\\_calculator.htm](http://www.ecoterr.com/length_units_metric_standard_calculator.htm). Accessed July 2014
- Mohajeri A, Ashrafi A (2011) Structure and electronic properties of amino acid ionic liquids. *J Phys Chem A* 115(24):6589–6593
- Mu X, Qi L, Zhang H, Shen Y, Qiao J, Ma H (2012) Ionic liquids with amino acids as cations: novel chiral ligands in chiral ligand-exchange capillary electrophoresis. *Talanta* 97:349–354
- Muldoon MJ, Aki SNVK, Anderson JL, Dixon JK, Brennecke JF (2007) Improving carbon dioxide solubility in ionic liquids. *J Phys Chem B* 111:9001–9009
- Nakamoto K (1986) *Infrared and Raman spectra of inorganic and coordination compounds*. Wiley, New York
- Ohno H, Fukumoto K. (2007) Amino acid ionic liquids. *Acc Chem Res* 40:1122–1129
- Ohno H, Yoshizawa M, Mizumo T (2005) In: Ohno H (Ed) *Electrochemical aspects of ionic liquids*. Wiley, Hoboken, pp 75–81
- Palomar J, Torrecilla JS, Lemus J, Ferro VR, Rodriguez F (2010) *Phys Chem Chem Phys* 12:1991–2000
- Papaiconomou N, Salminen J, Lee J-M, Prausnitz JM (2007) Physicochemical properties of hydrophobic ionic liquids containing 1-Octylpyridinium, 1-Octyl-2-methylpyridinium, or 1-Octyl-4-methylpyridinium Cations. *J Chem Eng Data* 52:833–840
- Papaiconomou N, Estager J, Traore Y, Bauduin P, Bas C, Legeai S, Viboud S, Draye M (2010) Synthesis, physicochemical properties, and toxicity data of new hydrophobic ionic liquids containing dimethylpyridinium and trimethylpyridinium cations. *J Chem Eng Data* 55:1971–1979
- Patrascu C, Sugisaki C, Mingotaud C, Marty J-D, Genisson Y, Lauth-de Viguierie N (2004) New pyridinium chiral ionic liquids. *Heterocycles* 63(9):2033–2041
- Pernak J, Syguda A, Janiszewska D, Materna K, Praczyk T (2011) Ionic liquids with herbicidal anions. *Tetrahedron* 67:4838–4844
- Petkovic M, Seddon KR, Rebelo LPN, Pereira CS (2011) Ionic liquids: a pathway to environmental acceptability *Chem Soc Rev* 40:1383–1403

- Pham TPT, Cho C-W, Jeon C-O, Chung Y-J, Lee M-W, Yun Y-S (2009) Identification of metabolites involved in the biodegradation of the ionic liquid 1-butyl-3-methylpyridinium bromide by activated sludge microorganisms. *Environ Sci Technol* 43:516–521
- Pham TPT, Cho C-W, Yun Y-S (2010) Environmental fate and toxicity of ionic liquids: a review. *Water Res* 44:352–372
- Praczyk T, Kardasz P, Jakubiak E, Syguda A, Materna K, Pernak J (2012) Herbicidal ionic liquids with 2, 4-D. *Weed Sci* 60(2):189–192
- Pretti C, Chiappe C, Baldetti I, Brunini S, Monni G, Intorre L. (2009) Acute toxicity of ionic liquids for three freshwater organisms: pseudokirchneriella subcapitata, Daphnia magna and Danio rerio. *Ecotoxicol. Environ Saf* 72(4):1170–1176
- Putz MV (2010a) The bondons: the quantum particles of the chemical bond. *Int J Mol Sci* 11(11):4227–4256
- Putz MV (2010b) Beyond quantum nonlocality: chemical bonding field. *Int J Environ Sci* 1: 25–31
- Putz MV (2012a) Quantum theory: density, condensation, and bonding. Apple Academic, Toronto
- Putz MV (2012b) Chemical orthogonal spaces, in mathematical chemistry monographs, vol 14. University of Kragujevac, Kragujevac
- Putz MV (ed) (2012c) QSAR & SPECTRAL-SAR in computational Ecotoxicology. Apple Academic, Toronto; CRC Press—Taylor & Francis Group, New Jersey
- Putz MV (2013) Quantum and optical dynamics of matter for nanotechnology. IGI Global, Hershey
- Putz MV (2015a) Quantum nanochemistry, vol 3 (Quantum molecules and reactivity). Apple Academic Press, Toronto
- Putz MV (2015b) Quantum nanochemistry, vol 4 (Quantum solids and orderability). Apple Academic Press, Toronto
- Putz MV (2015c) Quantum nanochemistry, vol. 5 (Quantum structure-activity relationships). Apple Academic Press, Toronto
- Putz AM, Putz MV (2012) Spectral inverse quantum (Spectral-IQ) method for modeling mesoporous systems. Application on silica films by FTIR. *Int J Mol Sci* 13(12):15925–15941
- Putz AM, Putz MV (2013) Spectral-Structure activity relationship (Spectral-SAR) assessment of ionic liquids' in silico ecotoxicity. In: Kadokawa J (Ed) Ionic liquids—new aspects for the future. InTech, Rijeka, pp 85–126. doi:10.5772/51657; Chapter 4.
- Putz MV, Lacrămă A-M, Ostafe V (2007) Spectral-SAR, ecotoxicology of ionic liquids the daphnia magna case. *Int J Ecol (former Research Letters in Ecology)* 12813:5. doi:10.1155/2007/12813
- Putz MV, Putz A-M, Ostafe V, Chiriac A (2010) Spectral-SAR ecotoxicology of ionic liquids-Acetylcholine interaction on E. Electricus Species. *Int J Chem Model* 2:85–96
- Putz MV, Ori O (2015) Bondonic chemistry: physical origins and entanglement prospects. In: Putz MV, Ori O (eds) Exotic properties of carbon nanomatter. Advances in physics and chemistry. Springer, Dordrecht, Chapter 10
- Putz MV, Pitulice L, Dascălu D, Isac D (2015a) Bondonic chemistry: non-classical implications on classical carbon systems. In: Putz MV, Ori O (eds) Exotic properties of carbon nanomatter. Advances in physics and chemistry. Springer, Dordrecht, Chapter 11
- Putz MV, Duda-Seiman C, Duda-Seiman M, Bolcu C (2015b) Bondonic chemistry: consecrating silanes as metallic precursors for silicenes materials. In: Putz MV, Ori O (eds) Exotic properties of carbon nanomatter. Advances in physics and chemistry. Springer, Dordrecht, Chapter 12
- Rahman MBA, Jumbri K, Basri M, Abdulmalek E, Sirat K, Salleh AB (2010) Synthesis and physico-chemical properties of new tetraethylammonium-based amino acid chiral ionic liquids. *Molecules* 15: 2388–2397
- Raman CV, Krishnan KS (1928) The optical analog of the Compton effect. *Nature* 121:711
- Raman CV, Krishnan KS (1929) The production of new radiations by light scattering. *Proc Roy Soc* 122:23
- Ranke J, Molter K, Stock F, BottinWeber U, Poczobutt J, Hoffmann J, Ondruschka B, Filser J, Jastorff B (2004) *Ecotoxicol Environ Saf* 58:396–404
- Ranke J, Muller A, Bottin-Weber U, Stock F, Stolte S, Arning J, Stormann R, Jastorff B (2007a) Lipophilicity parameters for ionic liquid cations and their correlation to in vitro cytotoxicity. *Ecotoxicol Environ Saf* 67:430–438



- Ranke J, Stolte S, Stormann R, Arning J, Jastorff B (2007b) *Chem Rev* 107:2183–2206
- Ranke J, Othman A, Fan P, Müller A (2009) Explaining ionic liquid water solubility in terms of cation and anion hydrophobicity. *Int J Mol Sci* 10(3):1271–1289
- Romero A, Santos A, Tojo J, Rodriguez A (2008) *J Hazard Mater* 151:268–273
- Scammells PJ, Scott JL, Singer RD (2005) Ionic liquids: the neglected issues. *Aust J Chem* 58(3):155–169
- Seddon KR, Stark A, Torres M-J (2000) Influence of chloride, water, and organic solvents on the physical properties of ionic liquids. *Pure Appl Chem* 72(12):2275–2287
- Smekal A (1923) The quantum theory of dispersion. *Naturwissenschaften* 11:873
- Stark A, Seddon KR (2007) In: Seidel A (Ed) *Kirk-Othmer Encyclopaedia of chemical technology*, vol 26. Wiley, New York; pp 836–920
- Stasiewicz M, Mulkiewicz E, Tomczak-Wandzel R, Kumirska J, Siedlecka EM, Goebiowski M, Gajdus J, Czerwicka M, Stepnowski P (2008) Assessing toxicity and biodegradation of novel, environmentally benign ionic liquids (1-alkoxymethyl-3-hydroxypyridinium chloride, saccharinate and acesulfamates) on cellular and molecular level. *Ecotoxicol Environ Saf* 71:157–165
- Stepnowski P, Skladanowski AC, Ludwiczak A, Laczynska E (2004) *Hum Exp Toxicol* 23:513–517
- Stolte S, Arning J, Bottin-Weber U, Mueller A, Pitner W.R, Welz-Biermann U, Jastorff B, Ranke J (2007a) *Green Chem* 9:760–767
- Stolte S, Matzke M, Arning J, Boschen A, Pitner W.R, Welz-Biermann U, Jastorff B, Ranke J (2007b) *Green Chem* 9:1170–1179
- Stolte S, Abdulkarim S, Arning J, Blomeyer-Nienstedt A-K, Bottin-Weber U, Matzke M, Ranke J, Jastorff B, Thoming J (2008) Primary biodegradation of ionic liquid cations, identification of degradation products of 1-methyl-3-octylimidazoliumchloride and electrochemical wastewater treatment of poorly biodegradable compounds. *Green Chem* 10:214–224
- Suarez PAZ, Selbach VM, Dullius JEL, Einloft S, Piatnicki CMS, Azambuja DS, de Souza RF, Dupont J (1997) Enlarged electrochemical window in dialkyl-imidazolium cation based room-temperature air and water-stable molten salts. *Electrochim Acta* 42(16):2533–2535
- Sutton M (2009) Twinkle, twinkle little star—History of spectroscopy. *Chem World* 6(12):50–53
- Thomas NC (1991) The early history of spectroscopy. *J Chem Educ* 68(8):631–634
- Torrecilla JS, Garcia J, Rojo E, Rodriguez F (2009) Estimation of toxicity of Ionic liquids in Leukemia Rat Cell Line and Acetylcholinesterase enzyme by principal component analysis, neural networks and multiple lineal regressions. *J Hazard Mater* 164(1):182–194
- Torrecilla JS, Palomar J, Lemus J, Rodriguez F (2010) *Green Chem* 12:123–134
- Walden P (1914) Molecular weights and electrical conductivity of several fused salts *Bull. Acad Imper Sci (St. Petersburg)* 8:405–422
- Wei D, Ivaska A (2008) Applications of ionic liquids in electrochemical sensors *Analytica Chimica Acta* 607(2):126–135
- Wilkes JS, Zaworotko MJ (1992) Air and water stable 1-Ethyl-3-Methylimidazolium based ionic liquids. *J Chem Soc Chem Comm* 1992:965–967
- Yang X, Chen QY, Li X, Gao J (2012) Functional ionic liquids induced the formation of mitochondria targeted fluorescent core-shell ellipsoidal nanoparticles with anticancer properties. *Coll Surf B Biointerfaces* 98:91–96
- Yoshida Y, Baba O, Saito G (2007) Ionic liquids based on dicyanamide anion: influence of structural variations in cationic structures on ionic conductivity. *J Phys Chem B* 111(18):4742–4749
- Yu YH, Lu XM, Zhou Q, Dong K, Yao HW, Zhang SJ (2008) *Chem Eur J* 14:11174–11182
- Zhang Q, Li Z, Zhang J, Zhang S, Zhu L, Yang J, Zhang X, Deng Y (2007) Physicochemical properties of nitrile-functionalized ionic liquids. *J Phys Chem B* 111:2864–2872
- Zhang S, Lu X, Zhang Y, Zhou Q, Sun J, Han L, Yue G, Liu X, Cheng W, Li S (2009) Ionic liquids and relative process design molecular thermodynamics of complex systems. *Struct Bond* 131:143–191
- Zhao D, Fei Z, Ang WH, Dyson PJ (2007) Sulfonium-based Ionic liquids incorporating the allyl functionality. *Int J Mol Sci* 8:304–315

# Chapter 14

## Electric Field Effects on Graphene Materials

Elton J. G. Santos

**Abstract** Understanding the effect of electric fields on the physical and chemical properties of two-dimensional (2D) nanostructures is instrumental in the design of novel electronic and optoelectronic devices. Several of those properties are characterized in terms of the dielectric constant which play an important role on capacitance, conductivity, screening, dielectric losses and refractive index. Here we review our recent theoretical studies using density functional calculations including van der Waals interactions on two types of layered materials of similar two-dimensional molecular geometry but remarkably different electronic structures, that is, graphene and molybdenum disulphide ( $\text{MoS}_2$ ). We focus on such two-dimensional crystals because of their complementary physical and chemical properties, and the appealing interest to incorporate them in the next generation of electronic and optoelectronic devices. We predict that the effective dielectric constant ( $\epsilon$ ) of few-layer graphene and  $\text{MoS}_2$  is tunable by external electric fields ( $E_{\text{ext}}$ ). We show that at low fields ( $E_{\text{ext}} < 0.01 \text{ V/\AA}$ )  $\epsilon$  assumes a nearly constant value  $\sim 4$  for both materials, but increases at higher fields to values that depend on the layer thickness. The thicker the structure the stronger is the modulation of  $\epsilon$  with the electric field. Increasing of the external field perpendicular to the layer surface above a critical value can drive the systems to an unstable state where the layers are weakly coupled and can be easily separated. The observed dependence of  $\epsilon$  on the external field is due to charge polarization driven by the bias, which show several similar characteristics despite of the layer considered. All these results provide key information about control and understanding of the screening properties in two-dimensional crystals beyond graphene and  $\text{MoS}_2$ .

### 14.1 Introduction

Electron-electron interactions play a central role on a wide range of electronic phenomena in two-dimensional (2D) materials. One of the main ingredients that determines the Coulomb interaction strength in those systems is screening, which

---

E. J. G. Santos (✉)

School of Engineering and Applied Sciences, Harvard University, Cambridge, MA 02138, USA  
e-mail: eltonjos@stanford.edu

Department of Chemical Engineering, Stanford University, Stanford, CA 94305, USA

© Springer Science+Business Media Dordrecht 2015

M. V. Putz, O. Ori (eds.), *Exotic Properties of Carbon Nanomatter*,

Carbon Materials: Chemistry and Physics, DOI 10.1007/978-94-017-9567-8\_14

can be characterized by dielectric constant,  $\epsilon$ . Indeed, screening effects based on  $\epsilon$  play a fundamental role in determining the electron dynamics, the optical exciton binding energy, the electron and hole mobilities as well as charge storage features. In this context the Coulomb interactions are confined in a two-dimensional geometry which can give place to a new set of dielectric properties depending on the electronic nature of the 2D crystal.

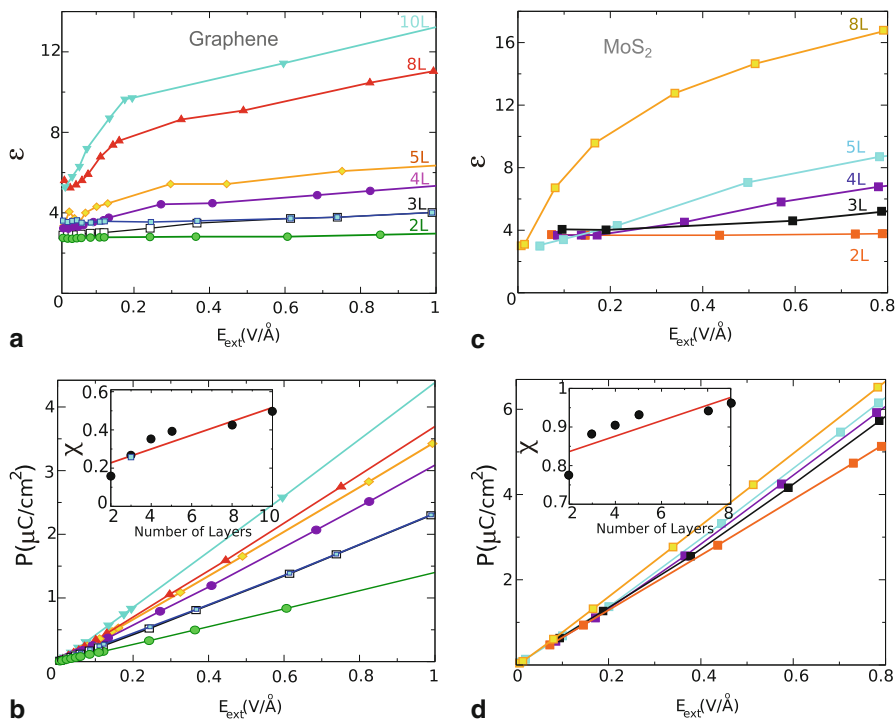
Graphene, a semimetal with zero bandgap, and MoS<sub>2</sub>, a low-dimension direct band gap semiconductor, are two representative members of the 2D family that have been receiving much attention in many fields due to their remarkable chemical and physical properties (Castro Neto et al. 2009; Wang et al. 2012a). One of the main features that influences all these properties is the layer thickness, which determines the charge distribution in the device as well as the electronic structure through the band gap. In particular, graphene can become a semiconductor with a band gap of several tenths of millielectronvolts at a bilayer structure subjected to high electric gate bias (Castro et al. 2007). MoS<sub>2</sub>, in its turn, has a sizable band gap that varies as a function of the number of layers which reaches values of about 1.8 eV at the monolayer limit (Mak et al. 2010). In both situations the electric-field screening is observed to change as the dielectric response depends on the intrinsic electronic properties as well as on  $\epsilon$ .

In fact, the large range of values for  $\epsilon$  found by different experiments on graphene (Elias et al. 2011; Siegel et al. 2011; Bostwick et al. 2010; Reed et al. 2010; Wang et al. 2012b; Sanchez-Yamagishi et al. 2012; Fallahazad et al. 2012; Jellison et al. 2007) and MoS<sub>2</sub> (Zhang et al. 2002; Kim et al. 2012; Bell et al. 1976; Frindt et al. 1963; Beal et al. 1979) has become a subject of considerable discussions. More factors, apart from the external electric fields and layer thickness, indicate that  $\epsilon$  might depend on the underneath substrate as recently measured for graphene (Hwang et al. 2012) and MoS<sub>2</sub> layers (Bao et al. 2013). In practical terms, the dielectric constant is defined by  $\epsilon = (\epsilon_{sub} + \epsilon_{vac})/2$ , with  $\epsilon_{sub}$  and  $\epsilon_{vac}$  the dielectric constant values for the substrate and vacuum, respectively. However, this approach suggests that the environment could play a role in the determination of the intrinsic dielectric constant of these 2D materials. Therefore, it is paramount to determine the intrinsic value of  $\epsilon$  despite of external screening environments.

In the present Chapter, we provide a review of some of our recent computational studies on the effect of electric fields on multilayer graphene and MoS<sub>2</sub>. We will consider both layered systems at different field magnitudes (0–1.0 V/Å) and number of layers (2–10 L). Some differences on the dielectric response between graphene and MoS<sub>2</sub> will be discussed based on simple electrostatic concepts, which will give generality to the calculations for other 2D-layers still to be explored.

## 14.2 Electrical Field Tuning of the Dielectric Constant

Figure 14.1a, c display how  $\epsilon$  evolves with external fields for different number of graphene and MoS<sub>2</sub> layers, respectively. At low fields,  $E_{ext} \leq 0.001$  V/Å,  $\epsilon$  is almost independent of the number of layers having a value close to  $\sim 4$  for both two-dimensional crystals. As the external field  $E_{ext}$  is increased,  $\epsilon$  reaches larger values,



**Fig. 14.1** Calculated  $\varepsilon$  and electric polarization  $P(\mu\text{C}/\text{cm}^2)$  as a function of  $E_{\text{ext}}$  for graphene and  $\text{MoS}_2$  structures. Results for graphene, **a** and **b**, and for  $\text{MoS}_2$ , **c** and **d**, are shown in the range of 2–10L. The insets in **b**, and **d**, show the electric susceptibility  $\chi$  versus the number of layers. A linear fitting is shown by the red line. Calculations for graphene were performed using the Bernal stacking order, which has not shown appreciable changes as compared to the Rhombohedral stacking. 3 L is also shown in Rhombohedral stacking using filled blue squares in **a**. The Bernal stacking was used for all calculations on  $\text{MoS}_2$ . (Adapted from Santos et al. 2013a, b)

up to  $\varepsilon = 12.0$  at  $E_{\text{ext}} = 1.0 \text{ V}/\text{\AA}$  for  $N = 10$  graphene layers. Similar electric response is observed for  $\text{MoS}_2$  with  $\varepsilon = 16.8$  at  $E_{\text{ext}} = 0.8 \text{ V}/\text{\AA}$  for  $N = 8$  layers with an approximately linear dependence of  $\varepsilon$  on the number of layers at a fixed magnitude of the field. These values for  $\varepsilon$  are in good agreement with those found by experimental groups working on graphene (Elias et al. 2011; Siegel et al. 2011; Bostwick et al. 2010; Reed et al. 2010; Wang et al. 2012b; Sanchez-Yamagishi et al. 2012; Fallahzad et al. 2012; Jellison et al. 2007) and on  $\text{MoS}_2$  (Zhang et al. 2002; Kim et al. 2012; Bell et al. 1976; Frindt et al. 1963; Beal et al. 1979) samples. The electric susceptibility  $\chi$  extracted from the polarization  $P$  clearly shows the roughly linear dependence on the number of layers  $N$  as plotted in Fig. 14.1b, d. Moreover, the comparison between graphene and  $\text{MoS}_2$  also gives that the tuning of  $\varepsilon$  with the external field is larger to the latter. At  $N = 8$ ,  $\chi$  is  $\chi = 0.95$  for multilayer  $\text{MoS}_2$  and  $\chi = 0.42$  for multilayer graphene, which is less than half of that value calculated for  $\text{MoS}_2$ . This suggests that the dichalcogenide layer is more electrically polarizable than graphene.

We note that electric fields of the magnitude considered here can in principle be experimentally created, as recently obtained in the case of 3 L graphene (Zou et al. 2013) which fields close to  $\sim 0.6 \text{ V/\AA}$  were achieved taking into account  $\text{HfO}_2$  gates. In the case of  $\text{MoS}_2$ , the high dielectric breakdown, due to the chemical character of the Mo–S covalent bonds, allows the application of large electric bias as recently reported in voltage-current measurements (Lembke et al. 2012).

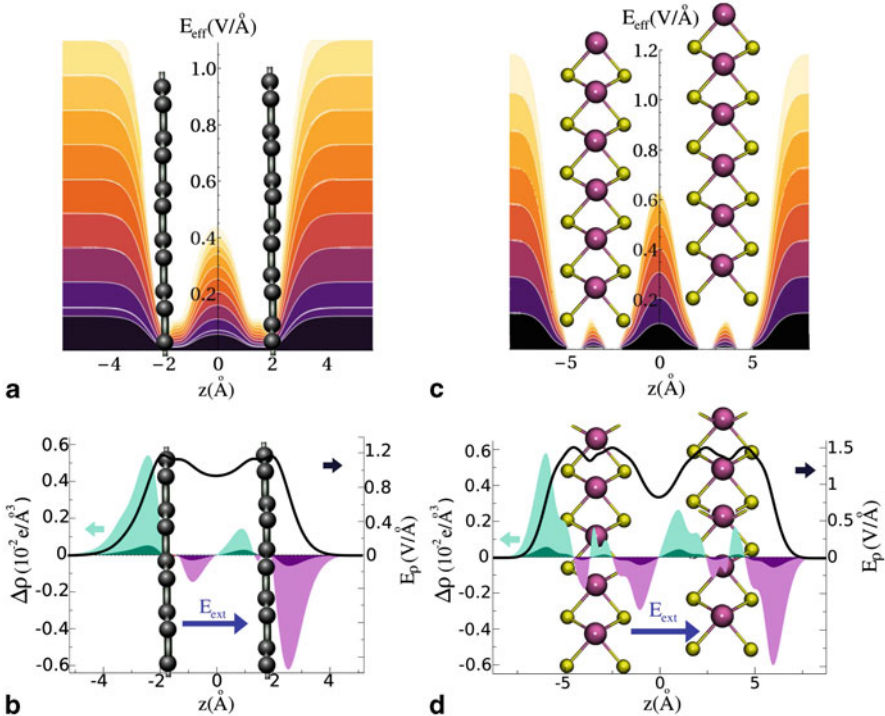
### 14.3 Interlayer Electric Field: Spatial Dependence

Next we discuss the origin of the electric-field mediated tunable dielectric constant in graphene and  $\text{MoS}_2$  layered systems. Figure 14.2 shows the electric response in terms of the effective electric field  $E_{\text{eff}}$  calculated from the Hartree potential  $V_H$  along the supercell for bilayer structures. The application of the external field  $E_{\text{ext}}$  generates an interlayer charge-transfer which partially cancels  $E_{\text{ext}}$  inducing the appearance of  $E_{\text{eff}}$  in the region between the layers. At low  $E_{\text{ext}}$ , all the induced values of  $E_{\text{eff}}$  are approximately constant, within the numerical accuracy of our model, assuming similar shapes as displayed in the dark regions of Fig. 14.2a, c. At fields close to those used to modify the band gap of 2 L graphene (Mak et al. 2009; Zhang et al. 2009; Castro et al. 2007), or used in  $\text{MoS}_2$  transistors (Radisavljevic et al. 2011), that is  $E_{\text{ext}} = 0.08 \text{ V/\AA}$ , the effective field  $E_{\text{eff}}$  is already dependent on position  $z$ , with a maximum at the mid-point between the layers.  $\text{MoS}_2$  has the difference to be formed by S–Mo–S bonds perpendicular to the external field, which induce a smaller but finite contribution between the S atoms. Moreover, the effective field on 2 L  $\text{MoS}_2$  assumes a narrower shape relative to graphene with negligible values close to S. The electric response can also be analyzed based on the induced charge densities,  $\Delta\rho$ , at different fields as plotted in Fig. 14.2b, d. Both layered systems show a charge accumulation at the layer that is under positive potential  $+V$  and a corresponding depletion at the other one  $-V$ . The integration of  $\Delta\rho$  along  $z$ , utilizing the Poisson equation  $\nabla^2 V(z) = -\Delta\rho/\epsilon_0$ , where  $\epsilon_0$  is the vacuum permittivity, results in a response electric field  $E_\rho$  (solid black line in Fig. 14.2b, d) that screens the external electric field, that is,  $E_{\text{eff}} \approx E_{\text{ext}} - E_\rho$ .

### 14.4 Electric Field Damping in Multilayer Systems

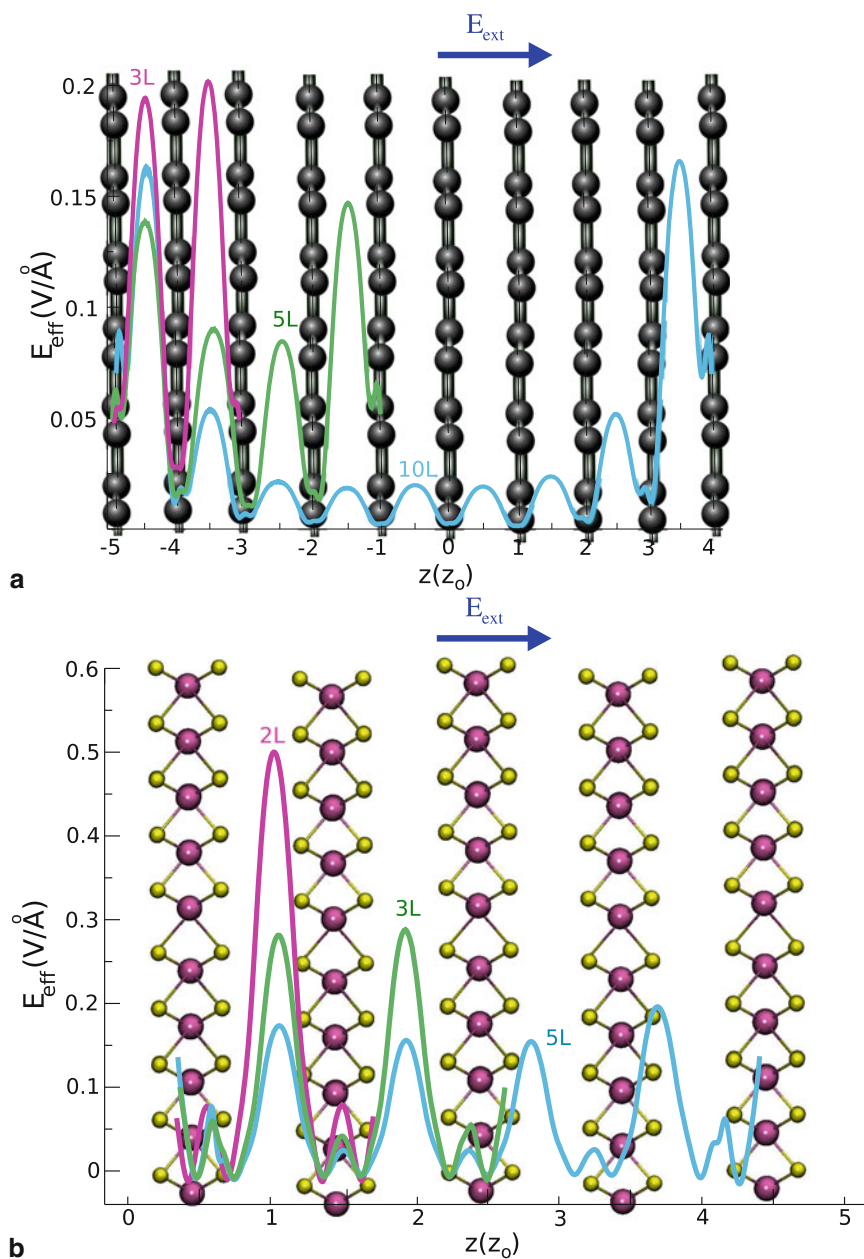
In the previous section, we have considered in detail the electric response due to external fields on graphene and  $\text{MoS}_2$  2 L structures. Although this is an important system, other aspects are also crucial to understand and control the screening associated to two-dimensional crystals. For example, one needs to explore the characteristics of multilayer systems subjected to external bias, as well as the possibility to compare structures with different electronic character. This kind of knowledge is instrumental in possible applications in electronics and optoelectronics.

We address next the dependence of  $\epsilon$  as a function of the number of graphene and  $\text{MoS}_2$  layers  $N$  as shown in Fig. 14.3. Despite the electronic character of each



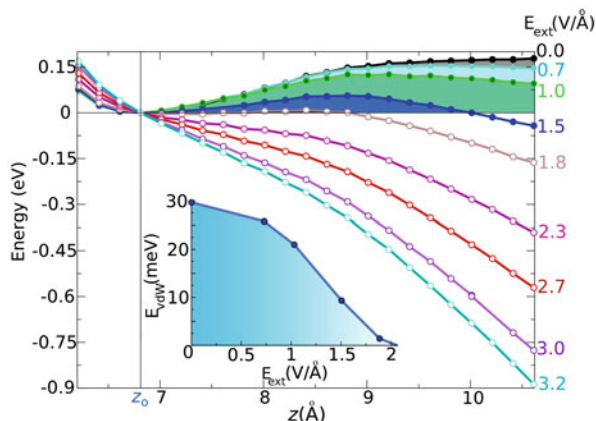
**Fig. 14.2** Effective electric field  $E_{\text{eff}}$  calculated as a function of the interlayer distance at different external fields  $E_{\text{ext}}$  for **a**, bilayer graphene, and **c**, bilayer MoS<sub>2</sub>. The *color gradient* shows the evolution from low (*dark color*) to high (*bright color*) values of the applied electric fields. Induced charge densities,  $\Delta\rho = \rho(E_{\text{ext}}) - \rho(0)$ , in  $e/\text{\AA}^3$ , between the **b**, carbon surfaces and the **d**, MoS<sub>2</sub>-planes. For graphene, the *bolder and lighter shaded curves* correspond to  $E_{\text{ext}} = 0.12 \text{ V/\AA}$  and  $E_{\text{ext}} = 1.22 \text{ V/\AA}$ , respectively. The *solid black curve* corresponds to the electric field generated by the induced charge,  $E_p$ , at  $E_{\text{ext}} = 1.22 \text{ V/\AA}$ . For MoS<sub>2</sub>, the *bolder and lighter shaded curves* correspond to  $E_{\text{ext}} = 0.14 \text{ V/\AA}$  and  $E_{\text{ext}} = 1.5 \text{ V/\AA}$ , respectively. The *solid black curve* corresponds to  $E_p$  at  $E_{\text{ext}} = 1.5 \text{ V/\AA}$ . The *large blue arrow* shows the direction of  $E_{\text{ext}}$  relative to the bilayer structures. (Adapted from Santos et al. 2013a, b)

system, the application of  $E_{\text{ext}}$  on thicker structures creates higher  $E_{\text{eff}}$  in the first few layers with a reduction of field in the innermost regions of the structure. For example in graphene, in the  $N = 10$  case, the maximum value of  $E_{\text{eff}}$  between the two carbon layers at  $z = 3z_o$  and  $4z_o$  is 3.2 times larger than that between the layers at  $z = 2z_o$  and  $3z_o$ . In deeper layers, the field decays further reaching even smaller values. For MoS<sub>2</sub>, the outermost layers show a slightly higher  $E_{\text{eff}}$  and the field decay follows that observed for graphene. However, the damping between internal and external layers, that is, those closer to the gate bias, is slightly different as that observed at the carbon planes. This suggests that the charge polarization of the layers due to the different electronic character (Fig. 14.1c, d) plays an important role on the screening behavior and also on the electrical tuning of the dielectric constant with the number



**Fig. 14.3** Effective electric field  $E_{\text{eff}}$  as a function of the interlayer position  $z_0$  for **a**, 3–10 L graphene and **b**, 2–5 L MoS<sub>2</sub>. Note that  $z_0$  assumes different values for graphene ( $z_0 = 3.41 \text{ \AA}$ ) and MoS<sub>2</sub> ( $z_0 = 6.70 \text{ \AA}$ ). Geometries are shown on the background on each panel. The applied fields are  $0.50 \text{ V}/\text{\AA}$  and  $0.73 \text{ V}/\text{\AA}$  for graphene and MoS<sub>2</sub>, respectively. The *blue arrow* indicates the relative orientation of  $E_{\text{ext}}$ . (Adapted from Santos et al. 2013a, b)

**Fig. 14.4** Energy per MoS<sub>2</sub> unit cell as a function of interlayer distance for different values of  $E_{\text{ext}}$  (V/Å). The *vertical solid line* indicates the equilibrium interlayer distance  $z_0 = 6.70$  Å. The *inset* shows the van der Waals barrier ( $E_{\text{vdW}}$ ) per atom as a function of  $E_{\text{ext}}$ . (Adapted from Santos et al. 2013b)



of layers. As  $\epsilon$  is calculated by the ratio of the external and internal fields to the slabs, the enhancement in the value of the dielectric constant with the number of layers  $N$  is directly related to the reduction of the field in the innermost regions of the structure which leads to lower  $\epsilon$  values for lower values of  $N$ . This decay of field with the layer thickness is in good agreement with recent electrostatic force microscopy and Kelvin probe microscope measurements performed for MoS<sub>2</sub> (Castellanos-Gomez et al. 2013; Li et al. 2013) and graphene (Datta et al. 2009).

## 14.5 Electrostatic Exfoliation on Graphene and MoS<sub>2</sub> Layers

In this section we analyze the possibility to use an electrostatic gate that can be used to exfoliate graphene and MoS<sub>2</sub> layers at different bias. We note that there is an upper limit on the magnitude of  $E_{\text{ext}}$  that can be applied to the systems as the bias induces a shift of the equilibrium position of the layers to higher interlayer separations. Figure 14.4 displays the total energy for MoS<sub>2</sub> 2 L as a function of the interlayer distance  $z$ . We focus on MoS<sub>2</sub> since similar effects are observed for graphene. At  $E_{\text{ext}} = 0.0$  V/Å, a van der Waals barrier  $E_{\text{vdW}}$  of 30 meV/atom prevents the separation of the two layers from  $z_0$  to infinity. At finite  $E_{\text{ext}}$ , the value of  $E_{\text{vdW}}$  decreases, indicating that the MoS<sub>2</sub>-layers become less bound. At  $E_{\text{ext}} = 2.0$  V/Å, the two dichalcogenide layers can be easily separated with a barrier of only 0.45 meV/atom. This indicates that an electrostatic gate can be utilized for exfoliating and printing few-layers MoS<sub>2</sub> in pre-pattern form similarly to that observed for graphene (Liang et al. 2009). Since several challenges of making industrially available large-scale areas of 2D-crystals and fabricating atomic features with precise electronic structure are still to be overcome, the electrostatic exfoliation shown in our calculations could open new avenues for the achievement of such desired properties.



## 14.6 Conclusions

In this Chapter we have reviewed the electrical response of two representative layered materials for future devices-based on graphene and MoS<sub>2</sub>. We have focused on the interplay between electric fields and screening properties of few-layer structures. Density functional theory was the main tool used to compute the properties of the analyzed systems. We have used simple models to understand the observed trends. In particular, we find that the effective dielectric constant of graphene and MoS<sub>2</sub> is electrically tunable, with the layer thickness playing an important role in the enhancement of the effect. The thicker the structure is, the stronger the modulation with electric fields. The driving force for such behavior is due to the linear dependence of the electrical polarization of the layers on the external field. The response field computed from the polarization charge does not screen completely the external bias, which generate higher interlayer fields at thinner structures. Differences due to semi-metallic and semiconducting electronic character of the layers are observed in terms of the field damping inside of the compounds: graphene tends to screen the external field at the outermost layers of system, while MoS<sub>2</sub> the field penetrates deeper in the layers. These results are in sound agreement with recent experiments performed for both materials.

We have also explored the possibility to control the layer exfoliation using electric fields. We have found that the induced interlayer charge imbalance generated by the bias can drive the system to an unstable state where the layers can be separated from each other. The interlayer equilibrium position is modified as a function of the field magnitude, which induces a reduction of the van der Waals barrier that keeps the layers together. As a result, there are variations of the interlayer separations even at low-fields. This investigation is highly relevant in the interpretation of experimental results underway since the field of 2D-materials is just in its beginning where several techniques and effects are still to be developed and explored.

## References

- Bao W, Cai X, Kim D, Sridhara K, Fuhrer MS (2013) High mobility ambipolar MoS<sub>2</sub> field-effect transistors: substrate and dielectric effects. *Appl Phys Lett* 102:042104–042108
- Beal AR, Hughes HP (1979) Kramers-Kronig analysis of the reflectivity spectra of 2H-MoS<sub>2</sub>, 2H-MoSe<sub>2</sub> and 2H-MoTe<sub>2</sub>. *J Phys C Solid State Phys* 12:881–890
- Bell MG, Liang WY (1976) Electron energy loss studies in solids: the transition metal dichalcogenides. *Adv Phys* 1976:53–86
- Bostwick A, Speck F, Seyller T, Horn K, Polini M, Asgari R, MacDonald AH, Rotenberg E (2010) Observation of plasmarons in quasi-freestanding doped graphene. *Science* 328:999–1002
- Castellanos-Gomez A, Cappelluti E, Roldán R, Agrait N, Guinea F, Rubio-Bollinger G (2013) Electric-field screening in atomically thin layers of MoS<sub>2</sub>: the role of interlayer coupling. *Adv Mater* 25:899–903
- Castro EV, Novoselov KS, Morozov SV, Peres NMR, Lopes dos Santos JMB, Nilsson J, Guinea F, Geim AK, Castro-Neto AH (2007) Biased bilayer graphene: semiconductor with a gap tunable by the electric field effect. *Phys Rev Lett* 99:216802–216806

- Castro Neto AH, Guinea F, Peres NMR, Novoselov KS, Geim AK (2009) The electronic properties of graphene. *Rev Mod Phys* 81:109–162
- Datta SS, Strachan DR, Mele EJ, Johnson ATC (2009) Surface potentials and layer charge distributions in few-layer graphene films. *Nano Lett* 9:7–11
- Elias DC, Gorbachev RV, Mayorov AS, Morozov SV, Zhukov AA, Blake P, Ponomarenko LA, Grigorieva IV, Novoselov KS, Guinea F, Geim AK (2011) Dirac cones reshaped by interaction effects in suspended graphene. *Nat Phys* 7:701–704
- Fallahazad B, Hao Y, Lee K, Kim S, Ruoff RS, Tutuc E (2012) Quantum hall effect in Bernal stacked and twisted bilayer graphene grown on Cu by chemical vapor deposition. *Phys Rev B* 85:201408–201413
- Frindt RF, Yoffe AD (1963) Physical properties of layer structures: optical properties and photoconductivity of thin crystals of molybdenum disulphide. *Proc R Soc A* 273:69–83
- Hwang C, Siegel DA, Mo SK, Regan W, Ismach A, Zhang Y, Zettl A, Lanzara A (2012) Fermi velocity engineering in graphene by substrate modification. *Sci Rep* 2:590
- Jellison GE, Hunn JD, Lee HN (2007) Measurement of optical functions of highly oriented pyrolytic graphite in the visible. *Phys Rev B* 76:085125–085133
- Kim S, Konar A, Hwang WS, Lee JH, Lee J, Yang J, Jung C, Kim H, Yoo JB, Choi JY et al (2012) High-mobility and low-power thin-film transistors based on multilayer MoS<sub>2</sub> crystals. *Nat Commun* 3:1011–1018
- Lembke D, Kis A (2012) Breakdown of high-performance monolayer MoS<sub>2</sub> transistors. *Nano Lett* 6:10070–10075
- Li Y, Xu C-Y, Zhen L (2013) Surface potential and interlayer screening effects of few-layer MoS<sub>2</sub> nanoflakes. *Appl Phys Lett* 102:143110–143114
- Liang X, Chang ASP, Zhang Y, Harteneck BD, Choo H, Olynick DL, Cabrini S (2009) Electrostatic force assisted exfoliation of prepatterned few-layer graphenes into device sites. *Nano Lett* 9:467–472
- Mak KF, Lui CH, Shan J, Heinz TF (2009) Observation of an electric-field-induced band gap in bilayer graphene by infrared spectroscopy. *Phys Rev Lett* 102:256405–256409
- Mak KF, Lee C, Hone J, Shan J, Heinz TF (2010) Atomically thin MoS<sub>2</sub>: a new direct-gap semiconductor. *Phys Rev Lett* 105:136805–136809
- Radisavljevic B, Radenovic A, Brivio J, Giacometti V, Kis A (2011) Single-layer MoS<sub>2</sub> transistors. *Nat Nanotechnol* 6:147–150
- Reed JP, Uchoa B, Joe YI, Gan Y, Casa D, Fradkin E, Abbamonte P (2010) The effective fine-structure constant of freestanding graphene measured in graphite. *Science* 330:805–808
- Sanchez-Yamagishi JD, Taychatanapat T, Watanabe K, Taniguchi T, Yacoby A, Jarillo-Herrero P (2012) Quantum hall effect, screening, and layer-polarized insulating states in twisted bilayer graphene. *Phys Rev Lett* 108:076601–076606
- Santos EJG, Kaxiras E (2013a) Electric-field dependence of the effective dielectric constant in graphene. *Nano Lett* 13:898–902
- Santos EJG, Kaxiras E (2013b) Electrically-driven tuning of the dielectric constant in MoS<sub>2</sub> layers. *ACS Nano* 7:10741–10746
- Siegel DA, Park CH, Hwang C, Deslippe J, Fedorov AV, Louie SG, Lanzara A (2011) Many-body interactions in quasi-freestanding graphene. *Proc Natl Acad Sci* 108:11365–11370
- Wang QH, Kalantar-Zadeh K, Kis A, Coleman JN, Strano MS (2012a) Electronics and optoelectronics of two-dimensional transition metal dichalcogenides. *Nat Nanotechnol* 7:699–712
- Wang Y, Brar VW, Shytov AV, Wu Q, Regan W, Tsai HZ, Zettl A, Levitov LS, Crommie MF (2012b) Mapping Dirac quasiparticles near a single Coulomb impurity on graphene. *Nat Phys* 8:653–657
- Zhang X, Hayward, DO, Mingos DMP (2002) Dielectric properties of MoS<sub>2</sub> and Pt catalysts: effects of temperature and microwave frequency. *Catal Lett* 84:225–233
- Zhang Y, Tang TT, Girit C, Hao Z, Martin MC, Zettl A, Crommie MF, Shen YR, Wang F (2009) Direct observation of a widely tunable bandgap in bilayer graphene. *Nature* 459:820–823
- Zou K, Zhang F, Clapp C, MacDonald AH, Zhu J (2013) Transport studies of dual-gated ABC and ABA trilayer graphene: band gap opening and band structure tuning in very large perpendicular electric fields. *Nano Lett* 13:369–373

# Index

## A

Amorphous silica, 119  
Anion-cation polarization in ionic liquids, 371  
Anion-cation structure of ionic liquids, 362  
Aromaticity, 12, 16, 262, 283, 286, 297, 318  
Atomic mass unit, 3, 4

## B

Benzenoid hydrocarbons, 12  
Beta-emitter, 3  
Bonding energy, 271, 272, 274, 280, 319, 360, 371  
Bondon energy, 371  
Bondon velocity, 361

## C

C–C bonds, 16, 70, 75, 77  
C4C8(R/S) nanotorus, 142  
C4C8(R/S) nanotube, 142  
Carbon allotropes, 14  
Carbon atoms, 2–4, 7–9, 11, 12, 14, 46, 276, 297  
Carbon cycle, 4  
Carbon nets, 8, 16  
Carburization, 103  
Catalytic growth mechanisms, 104  
Catamantanes, 9–11  
Cathodoluminescence, 104, 126  
Charge transfer, 51, 60, 67, 84, 86  
Chemical abstracts service, 6  
Chemical bonding, 262, 264, 267–270, 272, 275, 319, 374  
Chemical reactivity, 73, 262, 277, 293, 314, 319, 368, 374  
Clar structures, 13, 14  
Computed spectra, 358  
Conformation, 7, 16

© Springer Science+Business Media Dordrecht 2015

M. V. Putz, O. Ori (eds.), *Exotic Properties of Carbon Nanomatter*,

Carbon Materials: Chemistry and Physics, DOI 10.1007/978-94-017-9567-8

Core-shell nanowires, 104, 109, 119  
Core-shell SiC-SiO<sub>2</sub> nanowires, 108, 119  
Coulomb interaction, 56  
Covalent bonds, 5

## D

“Dewetting” mechanism, 107–110  
Degree, 131, 132, 138, 150, 262  
Delocalization energy, 285, 293, 301, 317  
DFT, 70, 71, 73, 87, 93, 94, 262, 283–292, 299, 306, 318  
Diamantane structures, 9  
Diamond, 7, 8  
Diamondoid hydrocarbons, 9, 16  
Diazonium salts, 262, 299–301, 310, 313  
Dielectric constant, 352  
Diels-Alder reactivity, 92  
Dispersion corrections, 73, 87, 88, 92, 94, 95  
Dispersion interactions, 87, 90, 92, 93

## E

Electrophoretic deposition, 108  
Electrostatic potential, 308, 368, 369  
Exohedral cycloaddition, 70, 71  
Exohedral functionalization, 70, 92

## F

Free valence, 276, 278, 282, 285, 297, 298, 309  
Frozen Cage Model, 67, 83, 93  
Fullerenes, 14, 15, 68, 73, 87  
Fusion, 2

## G

Graphene, 12, 34, 35, 43, 50  
Graphite, 2, 7, 8, 12, 46, 48, 58–61, 103

**H**

*HOMO*, 286, 293–295  
Hückel method, 262, 283, 286  
HOMO, 75, 77, 79, 82, 84–86, 90, 93, 273, 274, 280, 286, 288–290, 293, 299, 301–305, 308, 371, 372  
HOMO-LUMO gaps, 85, 86, 93  
HRTEM, 116, 121  
Hybridization, 5, 7, 8, 43, 59  
Hydrocarbons, 5, 7, 9, 262, 272, 318  
Hyperconjugation, 279

**I**

Ionic liquids biodegradability, 348, 351  
Ionic liquids synthesis, 348  
Isomeric tetramantanes, 10

**L**

*LUMO*, 286, 293–295  
Laser ablation, 103  
LUMO, 75, 77, 79, 82, 84, 86, 89, 93, 273, 274, 280, 286, 289, 293, 301–305, 314–317, 371, 372

**M**

Metal nanoclusters, 105  
Metallic cluster, 67, 68, 71, 73, 75, 79, 86, 92  
Metallofullerenes, 67, 68, 70, 79, 83

**N**

Nanotubes, 14, 16, 133, 140, 141, 145

**O**

Optical emission, 102  
Organic compounds, 5

**P**

Photo-assimilation, 3, 4, 16  
Polyhex nanotorus, 140, 142, 143, 146  
Pyramidalization angles, 67, 77, 79, 93, 95

**R**

Radioactivity, 3  
Radiocarbon, 3  
Rate constant, 310  
Reaction energy, 80, 88  
Regioselectivity, 67, 82, 83, 88, 93

**S**

Screening properties, 38  
SEM, 104, 112–115, 117–121  
Semiconductor nanowires, 104  
SiC nanostructures, 103  
Silanes, 105  
Stacking sequence, 104

**T**

TEM, 104, 116, 118, 119, 121–124  
TEM-EDX analysis, 122  
TEM-HAADF, 116, 121, 122

**V**

van der Waals interaction, 351  
Vapour phase epitaxy, 104, 107, 108, 114

**W**

Wave number, 314, 317

**Z**

Zagreb indices, 139